Insights into the sources of atmospheric aerosols and greenhouse gases in California

Thesis by

Benjamin C. Schulze

In Partial Fulfillment of the Requirements for the

Degree of

Doctor of Philosophy

CALIFORNIA INSTITUTE OF TECHNOLOGY

Pasadena, California

2023

Defended May 18th, 2023

Benjamin Christopher Schulze
ORCID: 0000-0002-6405-8872

ACKNOWLEDGEMENTS

I have had an incredible time at Caltech, thanks in large part to unwavering support from my colleagues, family, and friends.

I would like to especially thank my primary advisors, John Seinfeld, and Paul Wennberg, for their guidance over the last five years. Thank you, John, for being so supportive and allowing me to pursue a wide range of scientific questions during my time at Caltech. I suspect few graduate students are given the opportunity to participate meaningfully in a scientific study within the first few months of their program, as I was. I will always count myself fortunate that I was in your group. And thank you, Paul, for your constant encouragement and insight into the numerous scientific questions I wrestled with over the last few years. I continue to be amazed by your ability to quickly provide detailed guidance on topics as diverse as inorganic aerosol chemistry and greenhouse gas fluxes. Each of our conversations considerably improved my abilities as a scientist.

To the other members of my thesis committee, Rick Flagan and Christian Frankenberg, thank you for your continuous support and availability for helpful discussions. To Rick Flagan, thank you especially for providing me with the opportunity to participate in the CLOUD experiment and further develop my instrumentation skills.

To the members of the Seinfeld and Wennberg groups, thank you for making the last five years so enjoyable. I will miss the afternoon crosswords and informal coffee breaks. I hope we can all stay in touch. To Chris Kenseth, thank you for being a great mentor over the last five years. I am truly fortunate to have had the opportunity to work with you. I appreciated our scientific discussions and the opportunities to work together on the AMS. I will look forward to visiting your lab in a few years. To Yuanlong Huang, thank you for your frequent help with instrumentation and for providing a sounding board for scientific questions. I have never met someone so willing to go out of their way to assist a colleague. To Reina Buenconsejo, thanks for your frequent help with the instruments in the lab. And thank you for doing the innumerable things behind the scenes that kept the group operating smoothly but never got the recognition they deserved. To Ryan Ward, thanks for constantly being available to help with the AMS or jump on a zoom and discuss data. I hope we can continue working together on the ambient datasets you are collecting. To Stavros Amanatidis, thank you for your detailed guidance about the nSEMS and continuous support during my time at CERN.

To Rob Griffin, my first formal scientific advisor, thank you for being an incredible mentor, for stimulating my interest in atmospheric science, and for being a constant source of advice, even after my time at Rice. I have fond memories of my initial introduction to aerosol chemistry at your CEVE 101 seminar. I frequently reflect on how fortunate I was to have attended that talk.

To my parents, thank you so much for your encouragement and support throughout my life. It goes without saying that I could not have asked for better role models. I am constantly appreciative of the relationship we have.

Finally, to my amazing wife, Megan, I will never be able to sufficiently thank you for your support over the last five years. Thank you for being a constant source of encouragement, an amazing role model, and a wonderful mother to our son, Ethan. I love you more than you will ever know.

ABSTRACT

A substantial fraction of atmospheric science research is motivated by uncertainties in the sources of urban particulate matter and greenhouse gases. Such a focus is justified, as particulate matter exposure is responsible for up to nine million annual premature deaths globally, while climate change is rapidly altering ecosystems across the world. Recognizing the urgency of these interrelated problems, regulatory agencies in the U.S. and elsewhere have sought to limit emissions contributing to air quality degradation and global warming.

In this dissertation, we use a combination of ambient measurements, statistical models, and computational models to identify the sources of urban particulate matter and methane in multiple locations in California. In Los Angeles, we investigated the effects of reductions in mobile source pollutant emissions (i.e., on-road and off-road vehicles) on ambient aerosol concentrations. Mobile sources have historically accounted for the dominant fraction of urban particulate matter in Los Angeles, but despite notable reductions in their emissions over the last decade, ambient aerosol concentrations have not declined appreciably. Measurements using an Aerosol Mass Spectrometer demonstrate the complex interplay of direct (i.e., intended) and indirect effects of simultaneous reductions in organic aerosol (OA) precursor and nitrogen oxide emissions from these sources. Mobile sources are found to account for a modest and declining fraction of the total aerosol burden, while the contributions of non-traditional sources such as volatile chemical products (e.g., paints and coatings, cleaning products, adhesives and sealants) have increased. Simulations of organic and inorganic aerosol formation informed by in-situ measurements are developed to identify possible targets of future regulatory efforts.

In the San Joaquin Valley, we used airborne measurements of methane fluxes to evaluate dairy emissions inventories used by state regulatory agencies for policy development. Dairy operations currently account for nearly half of the state's methane emissions, and recent legislation has mandated a 40% reduction in emissions by 2030. Observed methane fluxes align well with emission inventory predictions and demonstrate the utility of

airborne flux measurements to track emission reduction progress in the future. Factor analysis of a combined dataset of greenhouse gas and volatile organic compound concentrations indicates dairy operations account for ~65% of total methane emissions in the southern San Joaquin Valley, with the remainder attributed to fugitive oil and gas emissions.

PUBLISHED CONTENT AND CONTRIBUTIONS

1) Wang, M.; Xiao, M.; Bertozzi, B.; Marie, G.; Rörup, B.; **Schulze, B.;** Bardakov, R.; He, X.-C.; Shen, J.; Scholz, W.; Marten, R.; Dada, L.; Baalbaki, R.; Lopez, B.; Lamkaddam, H.; Manninen, H. E.; Amorim, A.; Ataei, F.; Bogert, P.; Brasseur, Z.; Caudillo, L.; De Menezes, L.-P.; Duplissy, J.; Ekman, A. M. L.; Finkenzeller, H.; Carracedo, L. G.; Granzin, M.; Guida, R.; Heinritzi, M.; Hofbauer, V.; Höhler, K.; Korhonen, K.; Krechmer, J. E.; Kürten, A.; Lehtipalo, K.; Mahfouz, N. G. A.; Makhmutov, V.; Massabò, D.; Mathot, S.; Mauldin, R. L.; Mentler, B.; Müller, T.; Onnela, A.; Petäjä, T.; Philippov, M.; Piedehierro, A. A.; Pozzer, A.; Ranjithkumar, A.; Schervish, M.; Schobesberger, S.; Simon, M.; Stozhkov, Y.; Tomé, A.; Umo, N. S.; Vogel, F.; Wagner, R.; Wang, D. S.; Weber, S. K.; Welti, A.; Wu, Y.; Zauner-Wieczorek, M.; Sipilä, M.; Winkler, P. M.; Hansel, A.; Baltensperger, U.; Kulmala, M.; Flagan, R. C.; Curtius, J.; Riipinen, I.; Gordon, H.; Lelieveld, J.; El-Haddad, I.; Volkamer, R.; Worsnop, D. R.; Christoudias, T.; Kirkby, J.; Möhler, O.; Donahue, N. M. Synergistic HNO3–H2SO4–NH3 Upper Tropospheric Particle Formation. *Nature* **2022**, *605* (7910), 483–489. https://doi.org/10.1038/s41586-022-04605-4.
B.C.S. performed research and edited the manuscript.

2) Van Rooy, P.; Tasnia, A.; Barletta, B.; Buenconsejo, R.; Crounse, J. D.; Kenseth, C. M.; Meinardi, S.; Murphy, S.; Parker, H.; **Schulze, B**.; Seinfeld, J. H.; Wennberg, P. O.; Blake, D. R.; Barsanti, K. C. Observations of Volatile Organic Compounds in the Los Angeles Basin during COVID-19. *ACS Earth Space Chemistry.* **2021**, *5* (11), 3045–3055. https://doi.org/10.1021/acsearthspacechem.1c00248.
B.C.S. performed research and edited the manuscript.

3) Amanatidis, S.; Huang, Y.; Pushpawela, B.; **Schulze, B. C**.; Kenseth, C. M.; Ward, R. X.; Seinfeld, J. H.; Hering, S. V.; Flagan, R. C. Efficacy of a Portable, Moderate-Resolution, Fast-Scanning Differential Mobility Analyzer for Ambient Aerosol Size Distribution Measurements. *Atmos. Meas. Tech*. 2021, 14 (6), 4507–4516. DOI: 10.5194/amt-14-4507-2021.
B.C.S. performed research and edited the manuscript.

4) Kong, W.; Amanatidis, S.; Mai, H.; Kim, C.; **Schulze, B. C**.; Huang, Y.; Lewis, G. S.; Hering, S. V.; Seinfeld, J. H.; Flagan, R. C. The Nano-Scanning Electrical Mobility Spectrometer (NSEMS) and Its Application to Size Distribution Measurements of 1.5–25Nm Particles. *Atmospheric Measurement Techniques* **2021**, *14* (8), 5429–5445. https://doi.org/10.5194/amt-14-5429-2021.
B.C.S. performed research and edited the manuscript.

5) Vasquez, K. T.; Crounse, J. D.; **Schulze, B. C**.; Bates, K. H.; Teng, A. P.; Xu, L.; Allen, H. M.; Wennberg, P. O. Rapid Hydrolysis of Tertiary Isoprene Nitrate

Efficiently Removes NOx from the Atmosphere. *Proc. Nat. Acad. Sci.* **2020**, *117* (52), 33011–33016. https://doi.org/10.1073/pnas.2017442117.
B.C.S performed research and edited the manuscript.

6) **Schulze, B. C**.; Charan, S. M.; Kenseth, C. M.; Kong, W.; Bates, K. H.; Williams, W.; Metcalf, A. R.; Jonsson, H. H.; Woods, R.; Sorooshian, A.; Flagan, R. C.; Seinfeld, J. H. Characterization of Aerosol Hygroscopicity Over the Northeast Pacific Ocean: Impacts on Prediction of CCN and Stratocumulus Cloud Droplet Number Concentrations. *Earth Space Sci.* 2020, 7, e2020EA001098. DOI: 10.1029/2020EA001098.
B. C. S. performed research, analyzed data, and wrote the manuscript.

TABLE OF CONTENTS

LIST OF FIGURES

LIST OF TABLES

Chapter 1

INTRODUCTION

1.1 Overview

The work presented in this thesis investigates questions related to two distinct but important aspects of atmospheric science research – urban air quality and greenhouse gas emissions. Here, we provide a brief overview of the motivating literature related to each topic.

1.2 Background and motivation – urban air quality

Atmospheric aerosols are small, suspended liquid or solid particles that exert considerable effects on global climate (IPCC, 2021a) and negatively impact human health (Burnett et al., 2014; Cohen et al., 2017; Burnett et al., 2018). Aerosols range in size from a few nanometers to multiple micrometers and originate from a variety of natural (e.g., sea spray, dust, biogenic emissions) and anthropogenic (e.g., vehicular combustion, industrial emissions) organic and inorganic sources (Seinfeld and Pandis, 2016). These particles are typically classified as either primary, denoting direct emission in the particulate phase, or secondary, indicating formation in the atmosphere from gas-to-particle conversion.

Aerosols influence climate both directly, by scattering incoming sunlight (direct effect) and indirectly, by acting as seeds for cloud droplet formation (i.e., cloud condensation nuclei (CCN)) (IPCC, 2021a). Changes in CCN concentrations can modulate both cloud reflectivity and cloud lifetime (indirect effect). The negative radiative forcing associated with increased global CCN from anthropogenic activities represents one of the least constrained aspects of global climate change (IPCC, 2021).

Aerosols also influence human health by depositing in alveoli, inducing inflammation, and migrating into the bloodstream, causing increased rates of cerebrovascular disease, ischaemic heart disease, and lung cancer (Burnett et al., 2014). Outdoor aerosol pollution is the fifth largest global mortality risk factor (Cohen et al., 2017) and causes up to nine

million excess mortalities annually (Burnett et al., 2018), with particularly elevated health impacts in urban regions that could increase considerably over the next thirty years (Lelieveld et al., 2015).

The Los Angeles Basin is famous for its historically poor air quality (Warneke et al., 2012; Pollack et al., 2013; SCAQMD, 2023). Aerosol concentrations are particularly pronounced in the region due to the presence of a dense urban population in a valley largely bounded by mountain ranges, leading to considerable aerosol precursor emissions and limited ventilation rates (Blumenthal et al., 1978; Schultz and Warner, 1982). The impacts of the poor air quality, referred to as "smog" given its resemblance to a mixture of smoke and fog, were recognized by the early 1900s (Mitchell et al., 2016; SCAQMD, 2023; CARB, 2023).

In the 1940s, experiments led by Air Haagen-Smit at Caltech recognized the role of hydrocarbon precursors, otherwise known as reactive organic gases (ROG) or volatile organic compounds (VOC), and nitrogen oxides (NO_x) in the formation of particulate matter and ozone, the major components of urban smog (Haagen-Smit, 1952). Industrial emissions were initially blamed for the smog, and concentrated regulatory efforts were implemented to limit emissions of both organic and inorganic gases from these sources (CARB, 2023). Since the implementation of industrial emission controls in the 1950s, exhaust and evaporative emissions from mobile sources (e.g., on-road and off-road vehicles and equipment) have accounted for the majority of local ROG and NO_x contributing to regional smog formation (Pollack et al., 2013; Mitchell et al., 2016; CEPAM, 2019; SCAQMD, 2023).

Mobile sources produce urban aerosol both directly, through emission of lubricating oil particles termed primary organic aerosol (POA), and indirectly through emissions of gaseous organic (e.g., ROG) and inorganic (e.g., NO_x) species that form secondary organic aerosol (SOA) and inorganic aerosol (SIA) following atmospheric oxidation (Gentner et al., 2017). Recognition of the importance of mobile sources to local air pollution in the mid-1900s spawned numerous regulatory efforts aimed at limiting their emissions (SCAQMD, 2023; CARB, 2023). Since the 1960s, California has led the country in

imposing emissions standards on on-road and off-road mobile sources, with increasingly stringent limits for ROG, NO_x, and POA emissions from vehicular exhaust, detailed specifications for fuel composition (e.g., limits on aromatic content), and requirements for installation of technological devices aimed at limiting evaporative emissions (CARB, 2023). Federal legislative efforts, such as the Tier 0-3 programs and non-road source standards, have followed (EPA, 2023a).

The suite of regulatory efforts aimed at reducing mobile source emissions have improved air quality considerably over the last seventy years (Warneke et al., 2012; Pollack et al., 2013). Emission rates of ROG and NO_x (i.e., emissions per mile driven) for new passenger vehicles have declined by 99% (Lu et al., 2018; EPA, 2023b). Off-road emissions have seen similar improvements as a result of the multitude of individual state and federal regulations targeting specific sources (e.g., the Federal Phase 1-3 program aimed at small off-road spark ignition engines) (EPA, 2023c). The effectiveness of these efforts is reflected in ambient concentrations of both primary pollutants, such as NO_x and carbon monoxide (CO), which have declined by more than 80% since 1960, and secondary pollutants such as ozone and OA, which have seen similar declines (Warneke et al., 2012; Pollack et al., 2013; McDonald et al., 2012; 2015).

Despite the clear progress made over the last few decades, however, average aerosol concentrations measured in Los Angeles have remained relatively constant since 2010 (Figure 1.1a). The consistency is particularly notable given that mobile source emissions have continued to decline appreciably during this period, as is clearly seen in concentrations of primary pollutants emitted by mobile sources, such as CO (Figure 1.1a) (CEPAM, 2019). While global climate change is thought to have contributed to increasing wildfire frequency in California, aerosol emissions associated with wildfire events cannot account for the trend (Enhayati Ahanar, 2021).

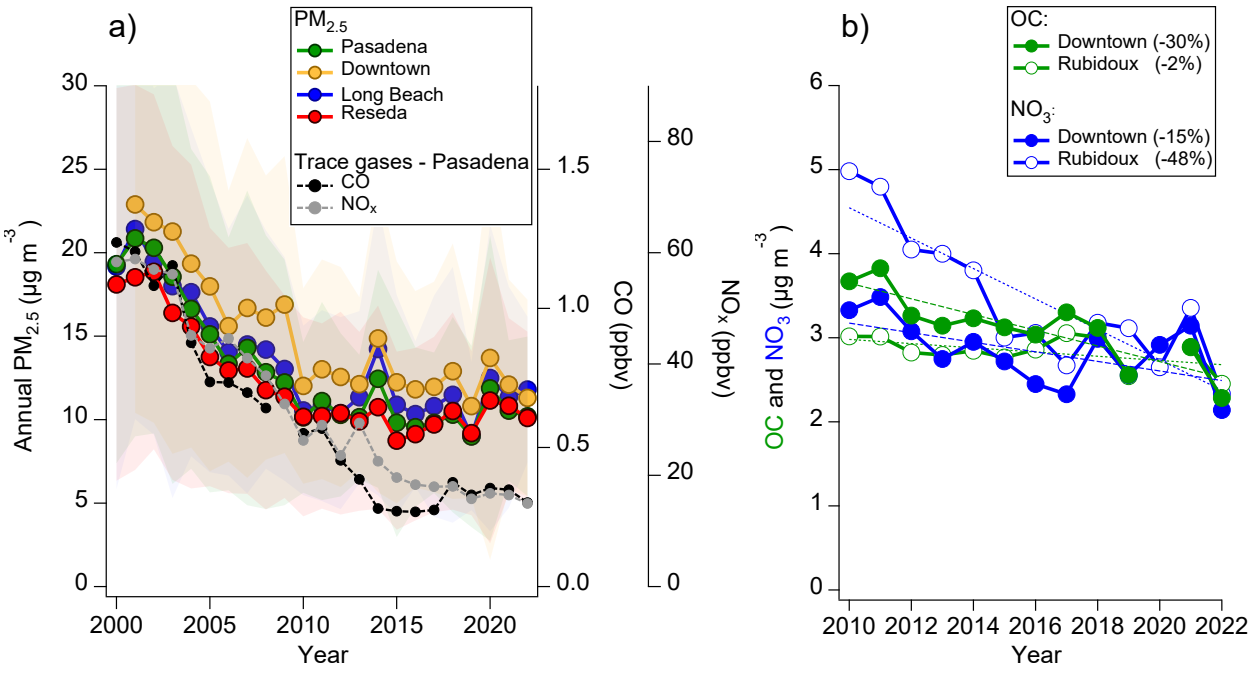

Figure 1.1: Trends in aerosol concentrations in Los Angeles. (a) Annual average $PM_{2.5}$ concentrations measured using Federal Reference Methods at monitoring sites in Los Angeles County from 2000-2020, demonstrating minor changes since 2010. Annual average concentrations of CO and NO_x measured in Pasadena, CA are also shown. (b) Annual average concentrations of organic carbon (OC) and nitrate (NO_3) $PM_{2.5}$ measured in Downtown Los Angeles and Rubidoux, CA demonstrating spatial variability in trends of speciated $PM_{2.5}$.

Multiple factors have been hypothesized to contribute to the lack of recent air quality progress. Due to the effective historical regulation of mobile source emissions, less controlled, non-traditional sources of ROG such as volatile chemical products (e.g., paints, cleaning products, personal care products, industrial solvents) (McDonald et al., 2018; Khare and Gentner, 2018; Seltzer et al., 2021a,b) and asphalt (Khare et al., 2020) have been recognized as potentially important contributors to OA formation. While prior regulatory efforts have focused on limiting emissions from individual classes of VCPs (e.g., paints, industrial solvents), existing policies have primarily focused on ozone-forming emissions rather than aerosol precursors specifically (Seltzer et al., 2021a). Asphalt use is widespread in the Los Angeles Basin because of the sprawling nature of the region's development, and

emissions may now account for as much local OA formation as all mobile sources combined (Khare et al., 2020).

In-basin OA formation rates may have also increased over the last decade as a result of the effective regulation of mobile-source NO_x emissions (Warneke et al., 2013; Pollack et al., 2013). In urban regions with dense NO_x sources (e.g., heavy-duty diesel vehicles), concentrations of the hydroxyl radical (OH), the primary oxidant of anthropogenic SOA precursors, increase as NO_x emissions decline (Seinfeld and Pandis, 2016). This phenomenon has historically been observed in the Los Angeles Basin on weekends, when NO_x emissions decline due to reduced commercial heavy-duty diesel truck traffic, and has also been inferred from long-term ratios of NO_x to the sum of NO_x oxidation products (Pollack et al., 2013). Higher OH concentrations increase the rate of SOA production from emitted precursors, leading to higher SOA concentrations produced before air masses are advected out of the basin (Ortega et al., 2016).

Finally, reductions in NO_x emissions may have altered VOC oxidation chemistry and thereby increased SOA yields (defined as the amount of SOA formed per mass of precursor oxidized). Laboratory studies of both important individual anthropogenic SOA precursors (e.g., toluene and other aromatics) and directly emitted passenger vehicle exhaust have demonstrated that SOA yields increase substantially under low-NO_x experimental conditions (Ng et al., 2007; Chan et al., 2009; Zhao et al., 2017).

While the density of air quality measurements in the Los Angeles Basin is among the highest of any urban location in the U.S. (Pollack et al., 2013), identifying the mechanisms responsible for the aerosol trend using existing datasets remains difficult. Speciated aerosol concentrations have only been measured at two locations in the basin since 2010 (Downtown Los Angeles and Rubidoux), and decadal trends in individual aerosol components differ notably between locations (Figure 1.1b). Gas-phase data provide evidence for decreasing mobile source emissions and shifts in ozone chemistry consistent with increasing OH concentrations, but quantifying the effect of these changes on SOA is complicated by the limited time resolution and chemical specificity of existing aerosol and ROG measurements (Pollack et al., 2013; Baidar et al., 2015).

While three-dimensional simulations of regional air quality could ideally be used to identify the drivers of historical trends, prior simulations of both OA (Lu et al., 2020; Pennington et al., 2021; Seltzer et al., 2021) and IA (Ensberg et al., 2013) in the basin have struggled to accurately reproduce ambient concentrations. Whether historical measurement-model disagreement is the result of inaccuracies in emissions, understanding of aerosol formation efficiencies, or errors in simulated meteorology/atmospheric transport patterns remains unclear (Lu et al., 2020; Seltzer et al., 2021).

The Los Angeles Basin remains in non-attainment of the National Ambient Air Quality Standard (NAAQS) for ambient $PM_{2.5}$, underscoring the need for identification of the underlying reasons for the $PM_{2.5}$ trend and development of additional regulatory policies that can further improve local air quality. This need is particularly urgent given that the Environmental Protection Agency recently proposed further reduction of the $PM_{2.5}$ NAAQS to a value ~20% lower than the current standard (EPA, 2023d), suggesting the basin will remain in non-compliance without dedicated efforts to reduce aerosol-forming emissions.

1.3 Background and motivation – methane emissions

Methane emissions represent the second largest positive anthropogenic forcing on the climate system, leading to accelerated global warming and subsequent impacts on natural ecosystems, sea levels, and the frequency of extreme weather events (IPCC, 2021b). Methane is a much more powerful greenhouse gas than carbon dioxide, with a global warming potential that varies from 84 to 28 when evaluated over 20- or 100-year time horizons (IPCC, 2021b). Globally, methane emissions have doubled over the last two centuries, a trend that is clearly reflected in methane concentrations derived from in-situ measurements and ice core samples (IPCC, 2021b). Given the 20-year GWP, reducing methane emissions in the near-term represents a particularly effective potential method to limit global warming over the next century (Ripple et al., 2014).

Livestock-related sources account for ~30% of global anthropogenic methane emissions and 5% of total anthropogenic greenhouse gas emissions (IPCC, 2021b). Current global

warming targets, such as those developed in the historic Paris Agreement, are therefore unlikely to be met without considerable reductions in emissions from livestock operations (Clark et al., 2020). Recent estimates suggest that on a global scale, livestock methane emissions need to be reduced by 11-30% by 2030 and 24-47% by 2050 to limit warming to 1.5ºC (Arndt et al., 2022).

Ruminant livestock, and dairy/beef cattle in particular, account for the dominant fraction of livestock-related methane emissions (Ripple et al., 2014; IPCC, 2021b). Ruminants produce methane both metabolically, through microbial fermentation of grains and starches in the rumen (enteric fermentation), and indirectly through the anaerobic decomposition of their manure (manure management) (Ripple et al., 2014; Owen and Silver, 2015). Emissions from manure management practices are particularly elevated in developed countries with dense dairy operations, where manure accumulation in large-scale storage systems produces prolonged anoxic conditions (Owen and Silver, 2015; Arndt et al., 2022). Combined, enteric fermentation and manure management practices emit ~109 Tg yr^{-1} of methane globally, an amount equivalent to all fossil-fuel related activities combined (IPCC, 2021b).

Livestock-related methane emissions are particularly substantial in California, which produces approximately 20% of the United States' milk supply from 1.7 million dairy cows. Current inventories produced by the California Air Resources Board (CARB) suggest that enteric fermentation and manure management practices account for ~50% of the state's total methane emissions (CARB, 2022a). Recognizing the urgent need to limit methane emissions, the California Senate recently passed Senate Bill 1383, which requires a 40% reduction in methane emissions from dairy manure management practices relative to 2013 levels by 2030 (SB 1383, 2016).

Most manure management emissions in California originate from waste management ponds, typically referred to as anaerobic lagoons, which store manure until eventual field application (Marklein et al., 2021). Installation of anaerobic digestion systems, which capture and transport emitted methane to processing centers for conversion into pipeline-quality natural gas, currently represents the primary planned mechanism to achieve

emission reduction goals (CARB, 2022b). The development of these anaerobic digester systems, the infrastructure required for effective conversion into natural gas, and the necessary public private partnerships has only recently begun in the state, but development is expected to accelerate with increased direct investment and incentives from federal and state agencies (CDFA, 2023; SoCalGas, 2019).

Effective development and implementation of emission reduction plans requires detailed understanding of the current magnitude of dairy emissions and accurate monitoring as anaerobic digester systems are constructed. Dairy emissions inventories are developed using process-based models that calculate emissions from enteric fermentation and manure management separately based on animal energy intake (i.e., food consumption) and solid waste production, respectively (CARB, 2022a). The emission factors underlying these models are based on a limited number of direct measurements at dairy facilities, and only a modest amount of information about dairy-specific manure management practices exists (e.g., fraction of waste diverted to lagoons vs. stored using solid methods) (Marklein et al., 2021). Considerable effort has therefore been devoted to evaluating the accuracy of emission inventories in California and elsewhere (Jeong et al., 2016; Cui et al., 2019; Marklein et al., 2021).

Two primary top-down methods, inverse modeling of ambient methane concentrations and direct measurements of methane fluxes from individual dairy facilities, have historically been used to evaluate the accuracy of California dairy emission inventories. Inverse modeling studies primarily utilize data from the greenhouse gas monitoring network established by the CARB, which consists of eight locations in California with continuous methane measurements (Jeong et al., 2013; 2016; Cui et al., 2017; 2019). Briefly, in this method, bottom-up prior emissions inventories are combined with detailed atmospheric transport models to evaluate regional methane emissions using Bayesian modeling frameworks (Jeong et al., 2013; 2016; Cui et al., 2017; 2019). Depending on the detail of the prior inventories and the spatial density of measurements utilized, these methods can produce emissions estimates for individual regions and/or source sectors (e.g., dairy/livestock, natural gas, etc.) in the state (Jeong et al., 2016; Cui et al., 2019). Direct

measurements represent an alternative method to evaluate emission inventory accuracy, often using either stationary (Borhan et al., 2011; Arndt et al., 2018) or mobile measurements (Amini et al., 2022; Golston et al., 2020) to quantify emissions from an entire dairy or individual emission sources within an individual dairy operation (e.g., anaerobic lagoons, housing pens, etc.) (Arndt et al., 2018).

In general, top-down estimates using inverse modeling techniques applied to both long-term (Miller et al., 2013; Jeong et al., 2016) and short-term (Zhao et al., 2009; Cui et al., 2017) measurements have suggested that methane emissions from dairy livestock may be twice as large as the California Air Resources Board (CARB) predicts. However, results of recent inventory comparisons are inconsistent, as long-term measurements at individual dairy facilities (Arndt et al., 2018), short-term surveys of multiple dairy facilities (Peischl et al., 2013; Amini et al., 2022; Golston et al., 2022) and short-term inverse modeling studies (Heerah et al., 2021) have supported the accuracy of CARB predictions.

The underlying reasons for these differences remain unclear but could be the result of inaccuracies in the atmospheric transport models used in inverse modeling studies (e.g., simulated mixing heights) (Cui et al., 2019), errors in the spatial allocation of emissions within prior inventories (Marklein et al., 2021), or temporal variability in emissions (Heerah et al., 2021; Amini et al., 2022). Resolution of these inconsistencies is needed to establish confidence in emissions projections and ensure that emission reduction plans will be sufficient.

1.4 Organization of thesis

In Chapter 2, using a combination of atmospheric field measurements and computational modeling techniques, we quantify the complex effects of reductions in mobile source emissions on ambient aerosol concentrations in Los Angeles since 2010. We demonstrate that simultaneous reductions in mobile source emissions of SOA precursors and NO_x has produced relatively consistent SOA concentrations, as increases in oxidant levels have offset the direct effects of reduced emissions of mobile source SOA precursors. However, the relative contribution of mobile sources to the local SOA burden has declined from as

much ~50% in 2010 to only ~25% in 2022. We further show that overnight nitrate aerosol production rates have likely declined by 60% or more over the last decade due to reduced NO_x emissions. Our results demonstrate the declining relevance of mobile source emissions to the ambient aerosol burden in Los Angeles and highlight the need for increased regulatory focus on non-mobile, area, and stationary source emissions.

In Chapter 3, we use airborne measurements of methane fluxes over the San Joaquin Valley (SJV) of California to quantify methane emission rates from dairy operations, which are estimated to account for approximately 50% of California's methane budget. Our measurements suggest average emission rates of ~120 kg hr^{-1} for dairies in this region, corresponding to ~55 g dairy cow^{-1} hr^{-1}. These values align with predictions from emissions inventories currently used by state agencies, supporting their validity and use in policy development. We further provide the first direct demonstration of the improved spatial accuracy of the recently developed VISTA-CA dairy emissions inventory relative to the prior EPA inventory used for methane emissions modeling in the southern SJV. Factor analysis of a combined greenhouse gas and VOC dataset suggests that dairy operations account for ~65% of total methane emissions over the southern San Joaquin Valley, with the remainder likely associated with fugitive oil and gas emissions.

Chapter 4 investigates the relationship between aerosol composition and cloud forming capacity over the N.E. Pacific Ocean, a region where local stratocumulus are thought to be particularly sensitive to variations in cloud condensation nuclei characteristics. Using airborne measurements of aerosol composition and cloud condensation nuclei concentrations, we demonstrate that the sensitivity of simulated cloud droplet number concentrations (CDNC) to aerosol composition is ~40% as large as the sensitivity to the geometric median diameter of size distribution. Model simulations demonstrate that CDNC sensitivity to aerosol hygroscopicity does not decrease monotonically with updraft speed when underlying aerosol size distributions are bimodal, as has been assumed previously.

1.5 References

Amini, S.; Kuwayama, T.; Gong, L.; Falk, M.; Chen, Y.; Mitloehner, Q.; Weller, S.; Mitloehner, F. M.; Patteson, D.; Conley, S. A.; Scheehle, E.; FitzGibbon, M. Evaluating California Dairy Methane Emission Factors Using Short-Term Ground-Level and Airborne Measurements. *Atmospheric Environment: X* **2022**, *14*, 100171. https://doi.org/10.1016/j.aeaoa.2022.100171.

Arndt, C.; Leytem, A. B.; Hristov, A. N.; Zavala-Araiza, D.; Cativiela, J. P.; Conley, S.; Daube, C.; Faloona, I.; Herndon, S. C. Short-Term Methane Emissions from 2 Dairy Farms in California Estimated by Different Measurement Techniques and US Environmental Protection Agency Inventory Methodology: A Case Study. *Journal of Dairy Science* **2018**, *101* (12), 11461–11479. https://doi.org/10.3168/jds.2017-13881.

Arndt, C.; et al. Full Adoption of the Most Effective Strategies to Mitigate Methane Emissions by Ruminants Can Help Meet the 1.5 °C Target by 2030 but Not 2050. *Proc. Natl. Acad. Sci. U.S.A.* **2022**, *119* (20), e2111294119. https://doi.org/10.1073/pnas.2111294119.

Baidar, S.; Hardesty, R. M.; Kim, S.-W.; Langford, A. O.; Oetjen, H.; Senff, C. J.; Trainer, M.; Volkamer, R. Weakening of the Weekend Ozone Effect over California's South Coast Air Basin. *Geophysical Research Letters* **2015**, *42* (21), 9457–9464. https://doi.org/10.1002/2015GL066419.

Blumenthal, D. L.; White, W. H.; Smith, T. B. Anatomy of a Los Angeles Smog Episode: Pollutant Transport in the Daytime Sea Breeze Regime. *Atmospheric Environment (1967)* **1978**, *12* (4), 893–907. https://doi.org/10.1016/0004-6981(78)90028-8.

Borhan, M. S.; Capareda, S.; Mukhtar, S.; Faulkner, W. B.; McGee, R.; Parnell, C. B. Determining Seasonal Greenhouse Gas Emissions from Ground-Level Area Sources in a Dairy Operation in Central Texas. *J Air Waste Manag Assoc* **2011**, *61* (7), 786–795. https://doi.org/10.3155/1047-3289.61.7.786.

Burnett, R. T.; et. al. An Integrated Risk Function for Estimating the Global Burden of Disease Attributable to Ambient Fine Particulate Matter Exposure. *Environmental Health Perspectives* **2014**, *122* (4), 397–403. https://doi.org/10.1289/ehp.1307049.

Burnett, R.; et al. Global Estimates of Mortality Associated with Long-Term Exposure to Outdoor Fine Particulate Matter. *PNAS* **2018**, *115* (38), 9592–9597. https://doi.org/10.1073/pnas.1803222115.

California Air Resources Board (CARB) / *History*. https://ww2.arb.ca.gov/about/history (accessed 2023-02-25).

California Air Resources Board (CARB), *Documentation of California's 2000*-2020 GHG Inventory, **2022a,** Accessed at https://ww2.arb.ca.gov/applications/california-ghg-inventory-documentation.

California Air Resources Board (CARB), *Analysis of Progress Toward Achieving the 2030 Dairy and Livestock Sector Methane Emissions Target,* **2022b.**

California Department of Food and Agriculture (CDFA), *Dairy Digester Research and Development Program,* **2023,** Accessed at: https://www.cdfa.ca.gov/oefi/ddrdp/

Chan, A. W. H.; Kautzman, K. E.; Chhabra, P. S.; Surratt, J. D.; Chan, M. N.; Crounse, J. D.; Kürten, A.; Wennberg, P. O.; Flagan, R. C.; Seinfeld, J. H. Secondary Organic Aerosol Formation from Photooxidation of Naphthalene and Alkylnaphthalenes: Implications for Oxidation of Intermediate Volatility Organic Compounds (IVOCs). *Atmospheric Chemistry and Physics* **2009**, *9* (9), 3049–3060. https://doi.org/10.5194/acp-9-3049-2009.

Clark, M. A.; Domingo, N. G. G.; Colgan, K.; Thakrar, S. K.; Tilman, D.; Lynch, J.; Azevedo, I. L.; Hill, J. D. Global Food System Emissions Could Preclude Achieving the 1.5° and 2°C Climate Change Targets. *Science* **2020**, *370* (6517), 705–708. https://doi.org/10.1126/science.aba7357.

Cohen, A. J.; Brauer, M.; Burnett, R.; Anderson, H. R.; Frostad, J.; Estep, K.; Balakrishnan, K.; Brunekreef, B.; Dandona, L.; Dandona, R.; Feigin, V.; Freedman, G.; Hubbell, B.; Jobling, A.; Kan, H.; Knibbs, L.; Liu, Y.; Martin, R.; Morawska, L.; Pope, C. A.; Shin, H.; Straif, K.; Shaddick, G.; Thomas, M.; van Dingenen, R.; van Donkelaar, A.; Vos, T.; Murray, C. J. L.; Forouzanfar, M. H. Estimates and 25-Year Trends of the Global Burden of Disease Attributable to Ambient Air Pollution: An Analysis of Data from the Global Burden of Diseases Study 2015. *Lancet* **2017**, *389* (10082), 1907–1918. https://doi.org/10.1016/S0140-6736(17)30505-6.

Cui, Y. Y.; et al. Top-down Estimate of Methane Emissions in California Using a Mesoscale Inverse Modeling Technique: The San Joaquin Valley. *Journal of Geophysical Research: Atmospheres* **2017**, *122* (6), 3686–3699. https://doi.org/10.1002/2016JD026398.

Cui, Y. Y.; et al. A Multiplatform Inversion Estimation of Statewide and Regional Methane Emissions in California during 2014–2016. *Environ. Sci. Technol.* **2019**, *53* (16), 9636–9645. https://doi.org/10.1021/acs.est.9b01769.

Enayati Ahangar, F.; Pakbin, P.; Hasheminassab, S.; Epstein, S. A.; Li, X.; Polidori, A.; Low, J. Long-Term Trends of PM2.5 and Its Carbon Content in the South Coast Air

Basin: A Focus on the Impact of Wildfires. *Atmospheric Environment* **2021**, *255*, 118431. https://doi.org/10.1016/j.atmosenv.2021.118431.

Ensberg, J. J.; et a.l Inorganic and Black Carbon Aerosols in the Los Angeles Basin during CalNex. *Journal of Geophysical Research: Atmospheres* **2013**, *118* (4), 1777–1803. https://doi.org/10.1029/2012JD018136.

US EPA, **2023a**, *Basic Information about the Emission Standards Reference Guide for On-road and Nonroad Vehicles and Engines*. https://www.epa.gov/emission-standards-reference-guide/basic-information-about-emission-standards-reference-guide-road (accessed 2023-02-25).

US EPA, **2023b,** *History of Reducing Air Pollution from Transportation in the United States*. https://www.epa.gov/transportation-air-pollution-and-climate-change/history-reducing-air-pollution-transportation (accessed 2023-02-25).

US EPA,. **2023c,** *EPA Emission Standards for Nonroad Engines and Vehicles*. https://www.epa.gov/emission-standards-reference-guide/epa-emission-standards-nonroad-engines-and-vehicles (accessed 2023-02-25).

Gentner, D. R.; Jathar, S. H.; Gordon, T. D.; Bahreini, R.; Day, D. A.; El Haddad, I.; Hayes, P. L.; Pieber, S. M.; Platt, S. M.; de Gouw, J.; Goldstein, A. H.; Harley, R. A.; Jimenez, J. L.; Prévôt, A. S. H.; Robinson, A. L. Review of Urban Secondary Organic Aerosol Formation from Gasoline and Diesel Motor Vehicle Emissions. *Environ. Sci. Technol.* **2017**, *51* (3), 1074–1093. https://doi.org/10.1021/acs.est.6b04509.

Golston, L. M.; Pan, D.; Sun, K.; Tao, L.; Zondlo, M. A.; Eilerman, S. J.; Peischl, J.; Neuman, J. A.; Floerchinger, C. Variability of Ammonia and Methane Emissions from Animal Feeding Operations in Northeastern Colorado. *Environ. Sci. Technol.* **2020**, *54* (18), 11015–11024. https://doi.org/10.1021/acs.est.0c00301.

Haagen-Smit, A. J. Chemistry and Physiology of Los Angeles Smog. *Ind. Eng. Chem.* **1952**, *44* (6), 1342–1346. https://doi.org/10.1021/ie50510a045.

Heerah, S.; Frausto-Vicencio, I.; Jeong, S.; Marklein, A. R.; Ding, Y.; Meyer, A. G.; Parker, H. A.; Fischer, M. L.; Franklin, J. E.; Hopkins, F. M.; Dubey, M. Dairy Methane Emissions in California's San Joaquin Valley Inferred With Ground-Based Remote Sensing Observations in the Summer and Winter. *Journal of Geophysical Research: Atmospheres* **2021**, *126* (24), e2021JD034785. https://doi.org/10.1029/2021JD034785.

IPCC, 2021a. Climate Change 2021: Synthesis Report. The Physical Science Basis, Chapter 7: The Earth's Energy Budget, Climate Feedbacks, and Climate Sensitivity.

IPCC, 2021b. Climate Change 2021: Synthesis Report. The Physical Science Basis, Chapter 5: Global Carbon and other Biogeochemical Cycles and Feedbacks.

Jeong, S.; Hsu, Y.-K.; Andrews, A. E.; Bianco, L.; Vaca, P.; Wilczak, J. M.; Fischer, M. L. A Multitower Measurement Network Estimate of California's Methane Emissions. *Journal of Geophysical Research: Atmospheres* **2013**, *118* (19), 11,339-11,351. https://doi.org/10.1002/jgrd.50854.

Jeong, S.; Newman, S.; Zhang, J.; Andrews, A. E.; Bianco, L.; Bagley, J.; Cui, X.; Graven, H.; Kim, J.; Salameh, P.; LaFranchi, B. W.; Priest, C.; Campos-Pineda, M.; Novakovskaia, E.; Sloop, C. D.; Michelsen, H. A.; Bambha, R. P.; Weiss, R. F.; Keeling, R.; Fischer, M. L. Estimating Methane Emissions in California's Urban and Rural Regions Using Multitower Observations. *Journal of Geophysical Research: Atmospheres* **2016**, *121* (21), 13,031-13,049. https://doi.org/10.1002/2016JD025404.

Khare, P.; Gentner, D. R. Considering the Future of Anthropogenic Gas-Phase Organic Compound Emissions and the Increasing Influence of Non-Combustion Sources on Urban Air Quality. *Atmospheric Chemistry and Physics* **2018**, *18* (8), 5391–5413. https://doi.org/10.5194/acp-18-5391-2018.

Khare, P.; Machesky, J.; Soto, R.; He, M.; Presto, A. A.; Gentner, D. R. Asphalt-Related Emissions Are a Major Missing Nontraditional Source of Secondary Organic Aerosol Precursors. *Science Advances* **2020**, *6* (36), eabb9785. https://doi.org/10.1126/sciadv.abb9785.

Lelieveld, J.; Evans, J. S.; Fnais, M.; Giannadaki, D.; Pozzer, A. The Contribution of Outdoor Air Pollution Sources to Premature Mortality on a Global Scale. *Nature* **2015**, *525* (7569), 367–371. https://doi.org/10.1038/nature15371.

Marklein, A. R.; Meyer, D.; Fischer, M. L.; Jeong, S.; Rafiq, T.; Carr, M.; Hopkins, F. M. Facility-Scale Inventory of Dairy Methane Emissions in California: Implications for Mitigation. *Earth System Science Data* **2021**, *13* (3), 1151–1166. https://doi.org/10.5194/essd-13-1151-2021.

McDonald, B. C.; Dallmann, T. R.; Martin, E. W.; Harley, R. A. Long-Term Trends in Nitrogen Oxide Emissions from Motor Vehicles at National, State, and Air Basin Scales. *Journal of Geophysical Research: Atmospheres* **2012**, *117* (D21). https://doi.org/10.1029/2012JD018304.

McDonald, B. C.; Goldstein, A. H.; Harley, R. A. Long-Term Trends in California Mobile Source Emissions and Ambient Concentrations of Black Carbon and Organic Aerosol. *Environ. Sci. Technol.* **2015**, *49* (8), 5178–5188. https://doi.org/10.1021/es505912b.

McDonald, B. C.; Gouw, J. A. de; Gilman, J. B.; Jathar, S. H.; Akherati, A.; Cappa, C. D.; Jimenez, J. L.; Lee-Taylor, J.; Hayes, P. L.; McKeen, S. A.; Cui, Y. Y.; Kim, S.-W.; Gentner, D. R.; Isaacman-VanWertz, G.; Goldstein, A. H.; Harley, R. A.; Frost, G. J.; Roberts, J. M.; Ryerson, T. B.; Trainer, M. Volatile Chemical Products Emerging as Largest Petrochemical Source of Urban Organic Emissions. *Science* **2018**, *359* (6377), 760–764. https://doi.org/10.1126/science.aaq0524.

Miller, S. M.; Wofsy, S. C.; Michalak, A. M.; Kort, E. A.; Andrews, A. E.; Biraud, S. C.; Dlugokencky, E. J.; Eluszkiewicz, J.; Fischer, M. L.; Janssens-Maenhout, G.; Miller, B. R.; Miller, J. B.; Montzka, S. A.; Nehrkorn, T.; Sweeney, C. Anthropogenic Emissions of Methane in the United States. *PNAS* **2013**, *110* (50), 20018–20022. https://doi.org/10.1073/pnas.1314392110.

Mitchell, D., Clearing the Air: What the Times Called For in 1947. *California Policy Options*. **2016**

Ng, N. L.; Kroll, J. H.; Chan, A. W. H.; Chhabra, P. S.; Flagan, R. C.; Seinfeld, J. H. Secondary Organic Aerosol Formation from *m*-Xylene, Toluene, and Benzene. *Atmospheric Chemistry and Physics* **2007**, *7* (14), 3909–3922. https://doi.org/10.5194/acp-7-3909-2007.

Ortega, A. M.; Hayes, P. L.; Peng, Z.; Palm, B. B.; Hu, W.; Day, D. A.; Li, R.; Cubison, M. J.; Brune, W. H.; Graus, M.; Warneke, C.; Gilman, J. B.; Kuster, W. C.; Gouw, J. de; Gutiérrez-Montes, C.; Jimenez, J. L. Real-Time Measurements of Secondary Organic Aerosol Formation and Aging from Ambient Air in an Oxidation Flow Reactor in the Los Angeles Area. *Atmospheric Chemistry and Physics* **2016**, *16* (11), 7411–7433. https://doi.org/10.5194/acp-16-7411-2016.

Owen, J. J.; Silver, W. L. Greenhouse Gas Emissions from Dairy Manure Management: A Review of Field-Based Studies. *Global Change Biology* **2015**, *21* (2), 550–565. https://doi.org/10.1111/gcb.12687.

Peischl, J.; et al. Quantifying Sources of Methane Using Light Alkanes in the Los Angeles Basin, California. *Journal of Geophysical Research: Atmospheres* **2013**, *118* (10), 4974–4990. https://doi.org/10.1002/jgrd.50413.

Pennington, E. A.; Seltzer, K. M.; Murphy, B. N.; Qin, M.; Seinfeld, J. H.; Pye, H. O. T. Modeling Secondary Organic Aerosol Formation from Volatile Chemical Products. *Atmospheric Chemistry and Physics Discussions* **2021**, 1–26. https://doi.org/10.5194/acp-2021-547.

Pollack, I. B.; Ryerson, T. B.; Trainer, M.; Neuman, J. A.; Roberts, J. M.; Parrish, D. D. Trends in Ozone, Its Precursors, and Related Secondary Oxidation Products in Los Angeles, California: A Synthesis of Measurements from 1960 to 2010. *Journal of*

Geophysical Research: Atmospheres **2013**, *118* (11), 5893–5911. https://doi.org/10.1002/jgrd.50472.

Ripple, W. J.; Smith, P.; Haberl, H.; Montzka, S. A.; McAlpine, C.; Boucher, D. H. Ruminants, Climate Change and Climate Policy. *Nature Clim Change* **2014**, *4* (1), 2–5. https://doi.org/10.1038/nclimate2081.

SB-1383 Short-lived climate pollutants: methane emissions: dairy and livestock: organic waste: landfills., California Legislative Information**, 2016,** Accessed at https://leginfo.legislature.ca.gov/faces/billNavClient.xhtml?bill_id=201520160SB1383

Schultz, P.; Warner, T. T. Characteristics of Summertime Circulations and Pollutant Ventilation in the Los Angeles Basin. *Journal of Applied Meteorology and Climatology* **1982**, *21* (5), 672–682. https://doi.org/10.1175/1520-0450(1982)021<0672:COSCAP>2.0.CO;2.

Seinfeld, J. H., Pandis, S. P. Atmospheric Chemistry and Physics: From Air Pollution to Climate Change, **2016**, *Wiley and Sons*, Hoboken, NJ

Seltzer, K. M.; Pennington, E.; Rao, V.; Murphy, B. N.; Strum, M.; Isaacs, K. K.; Pye, H. O. T. Reactive Organic Carbon Emissions from Volatile Chemical Products. *Atmospheric Chemistry and Physics* **2021**, *21* (6), 5079–5100. https://doi.org/10.5194/acp-21-5079-2021.

Seltzer, K. M.; Murphy, B. N.; Pennington, E. A.; Allen, C.; Talgo, K.; Pye, H. O. T. Volatile Chemical Product Enhancements to Criteria Pollutants in the United States. *Environ. Sci. Technol.* **2021**. https://doi.org/10.1021/acs.est.1c04298.

South Coast Air Quality Management District (SCAQMD): 50 Years of Progress. https://www.aqmd.gov/home/research/publications/50-years-of-progress (accessed 2023-02-25).

Southern California Gas Company (SoCalGas), *Calgren Dairy Fuels,* **2019,** Accessed at: https://www.socalgas.com/sustainability/renewable-gas/rng-success-stories/calgren-dairy-fuels

Warneke, C.; Gouw, J. A. de; Holloway, J. S.; Peischl, J.; Ryerson, T. B.; Atlas, E.; Blake, D.; Trainer, M.; Parrish, D. D. Multiyear Trends in Volatile Organic Compounds in Los Angeles, California: Five Decades of Decreasing Emissions. *Journal of Geophysical Research: Atmospheres* **2012**, *117* (D21). https://doi.org/10.1029/2012JD017899.

Warneke, C.; Gouw, J. A. de; Edwards, P. M.; Holloway, J. S.; Gilman, J. B.; Kuster, W. C.; Graus, M.; Atlas, E.; Blake, D.; Gentner, D. R.; Goldstein, A. H.; Harley, R. A.; Alvarez, S.; Rappenglueck, B.; Trainer, M.; Parrish, D. D. Photochemical Aging of Volatile Organic Compounds in the Los Angeles Basin: Weekday-Weekend Effect.

Journal of Geophysical Research: Atmospheres **2013**, *118* (10), 5018–5028. https://doi.org/10.1002/jgrd.50423.

Zhao, C.; Andrews, A. E.; Bianco, L.; Eluszkiewicz, J.; Hirsch, A.; MacDonald, C.; Nehrkorn, T.; Fischer, M. L. Atmospheric Inverse Estimates of Methane Emissions from Central California. *Journal of Geophysical Research: Atmospheres* **2009**, *114* (D16). https://doi.org/10.1029/2008JD011671.

Zhao, Y.; Saleh, R.; Saliba, G.; Presto, A. A.; Gordon, T. D.; Drozd, G. T.; Goldstein, A. H.; Donahue, N. M.; Robinson, A. L. Reducing Secondary Organic Aerosol Formation from Gasoline Vehicle Exhaust. *PNAS* **2017**, *114* (27), 6984–6989. https://doi.org/10.1073/pnas.1620911114.

C h a p t e r 2

Insights into the complex effects of reduced mobile source emissions on submicron particulate matter concentrations in Los Angeles

Schulze, B.C.; Kenseth, C.M.; Pennington, E.A.; Ward, R.X.; Seltzer, K.M.; Van Rooy, P.; Tasnia, A.; Morris, M.; Jensen, A.; Barletta, B.; Meinardi, S.; Huang, Y.; Parker, H.A.; Hasheminassab, S.; Crounse, J.D.; Day, D.; Campuzano-Jost, P.; de Gouw, J.; Jimenez, J.; Blake, D.R.; Barsanti, K.C.; Pye, H.O.T.; Wennberg, P.O.; Seinfeld, J.H. *Environmental Science & Technology.* In preparation.

Abstract

Despite considerable reductions in mobile source emissions, aerosol concentrations measured in Los Angeles using Federal Reference Methods have not appreciably declined over the last decade. Here, we use measurements and zero-dimensional modeling of aerosol formation in Pasadena, CA in 2010 and 2022 to quantify the impacts of these emissions reductions. Changes in secondary organic aerosol (SOA) concentrations expected from reduced mobile source emissions appear to have been offset by increases in hydroxyl radical concentrations, an indirect effect of reduced emissions of nitrogen oxides. As a result, while the contribution of mobile sources to the SOA burden has declined from ~50% in 2010 to only ~25% in 2022, concentrations of locally-formed SOA have remained effectively constant. In contrast to SOA, reductions in mobile source NO_x emissions have considerably reduced overnight production of nitric acid and ammonium nitrate (AN) aerosol (~60%). We provide evidence that FRM measurements may have underrepresented the reduction in AN concentrations since 2010 due to evaporation of semi-volatile species prior to quantification. Given the effectiveness of regulatory efforts aimed at mobile sources, and on-road sources in particular, further reductions in aerosol concentrations in Los Angeles will likely require increased focus on abating emissions from non-road and area sources.

2.1 Introduction

Exposure to ambient aerosol is associated with increased risk of cardiovascular and respiratory disease and is estimated to cause up to nine million premature deaths per year globally (Cohen et al., 2017; Burnett et al., 2019; Pye et al., 2021). In the U.S., mobile emission sources (i.e., on-road and non-road vehicles and equipment) have historically been responsible for a considerable fraction of organic aerosol (OA) and inorganic aerosol (IA) concentrations in urban areas (Watson et al., 1994; Schauer et al., 1996; Stone et al., 2009; Hasheminassab et al., 2014; McDonald et al. 2015; Ortega et al., 2016; Gentner et al., 2017). Vehicle operation produces OA through both direct particulate emissions, termed primary OA (POA), and via exhaust and/or evaporative emissions of gas-phase fuel components, which undergo atmospheric oxidation to form secondary OA (SOA) (Gentner et al., 2017). Fuel combustion also leads to considerable nitrogen oxide (NO_x) emissions. Atmospheric oxidation of NO_x forms nitric acid (HNO_3), which subsequently reacts with gas-phase ammonia to form ammonium nitrate (AN) aerosol (Ensberg et al., 2013; Schiferl et al., 2014).

The Los Angeles Basin has historically experienced some of the highest aerosol concentrations in the country (Ensberg et al., 2013; Lawson et al., 1990; Docherty et al., 2011; Hayes et al., 2013) and has failed to attain compliance with the 2012 National Ambient Air Quality Standard for fine particulate matter ($PM_{2.5}$) concentrations (EPA, 2012). While implementation of regulatory policies such as the California Low-Emission Vehicle (LEV) program have successfully reduced gaseous and aerosol pollutant concentrations over the last seventy years (McDonald et al., 2015; Warneke et al., 2012; Pollack et al., 2013), regulatory monitoring stations indicate that aerosol concentrations in Los Angeles have remained relatively constant during the last decade, despite considerable declines in mobile source emissions of organic and inorganic aerosol precursors (CEPAM, 2019).

Multiple factors may contribute to the recently observed trend in aerosol concentrations. The reduction of on-road aerosol precursor emissions (Hasheminassab et al., 2014; Altuwayjiri et al., 2021) has likely increased the relative importance of less-controlled, non-vehicular aerosol precursor sources such as volatile chemical products (VCPs) (Khare

and Gentner, 2018; McDonald et al., 2018; Khare et al., 2020; Seltzer et al., 2021a,b). Reductions in urban NO_x emissions may have also increased local hydroxyl radical (OH) concentrations, increasing the rate of volatile organic compound (VOC) oxidation, and thereby increasing the fraction of SOA precursors oxidized in the basin (Warneke et al., 2013; Kim et al., 2016; Van Rooy et al., 2021). Lower NO_x emissions could have also altered photochemical oxidation pathways and in turn increased SOA yields (defined as the amount of OA formed per mass of precursor oxidized) (Ng et al., 2007; Chan et al., 2009; Praske et al., 2018).

Accurate determination of the relative contributions of changing aerosol sources, oxidant concentrations, and oxidative pathways to the recently observed invariance in aerosol mass loadings requires detailed modeling of local aerosol formation informed by speciated measurements of aerosol composition. While model representation of urban aerosol formation is improving, recent simulations of Los Angeles regional air quality using three-dimensional models have poorly captured concentrations of both organic (Jathar et al., 2017; Lu et al., 2020; Pennington et al., 2021; Seltzer et al., 2021a) and inorganic (Ensberg et al., 2013; Schiferl et al., 2014; Heald et al., 2012) aerosol. In the absence of accurate regional models, constrained zero-dimensional box models have been successfully used to provide insight into aerosol sources in Los Angeles (Hayes et al., 2015; Ma et al., 2017) and other urban environments (Dzepina et al., 2009).

In this work, we compare measurements of ambient aerosol concentrations and composition obtained with a High-Resolution Time-of-Flight Aerosol-Mass-Spectrometer (HR-ToF-AMS) at the same location in Pasadena, CA in 2010 and 2022 to the results of detailed model simulations of organic and inorganic aerosol formation. We suggest that recent reductions in on-road vehicle emissions have had complex direct and indirect effects on both OA and IA production. Results further suggest that mobile source emissions now account for a modest and declining fraction of the total aerosol burden in Los Angeles.

2.2 Methods

2.2.1 Field site description

All measurement campaigns discussed here occurred on the campus of the California Institute of Technology (Caltech) in Pasadena, CA. Detailed descriptions of the CalNex-2010 campaign (May 15th – June 15th, 2010) are provided in Hayes et al. (2013). In 2022, aerosol and trace gas measurements were made from the top of Caltech Hall (~40m altitude) from May 13th to June 23rd during the Los Angeles Air Quality Campaign (LAAQC-2022) and from July 4th to August 15th during the California Research at the Nexus of Air Quality and Climate Change-Two field study (CalNexT-2022). The Caltech campus is approximately 18 km northeast of downtown Los Angeles. Prevailing winds in Pasadena were typically from the southwest near midday, transporting air from the urban core of Los Angeles. Diurnal trends in major meteorological parameters during all three campaigns are shown in Figure 2.S1. Temperatures during LAAQC-2022 and CalNexT-2022 were approximately 2^{o}C and 6^{o}C warmer than during CalNex-2010, respectively, and relative humidities were correspondingly lower. Given the considerable meteorological differences between CalNexT-2022 and the other campaigns, we focus our discussion below on comparisons between CalNex-2010 and LAAQC-2022.

2.2.2 Instrumentation

2.2.2.1 AMS sampling and analysis

Ambient submicron, non-refractory PM (NR-PM_1) was measured during all three campaigns using an Aerodyne High Resolution Time-of-Flight Aerosol Mass Spectrometer (HR-ToF-AMS; hereafter "AMS"). A detailed description of AMS operation during CalNex-2010 is provided in Hayes et al. (2013). During LAAQC-2022, the AMS sampled ambient air through approximately 7m of 3/8" stainless steel line connected to a 2.5 μm Teflon-coated cyclone mounted on the roof of Caltech Hall. The sampling setup was similar during CalNexT-2022, but incoming air was first delivered to a valve system capable of alternatively sampling between ambient air and the output of an oxidation flow reactor (OFR). Ambient air was dried using a 24" Nafion dryer during both campaigns.

During CalNexT-2022, ambient data were collected for a five-minute period every ten minutes, with the remaining time spent sampling output from the OFR. Data collected during each campaign were measured using the "V-mode" ion flight path through the time-of-flight chamber. Data were analyzed using the SQUIRREL v1.65C and PIKA v1.25C software packages. Standard methods were used to correct the data for gas-phase interferences and composition-dependent collection efficiencies (Middlebrook et al., 2012). Elemental analysis of organic aerosol composition was performed using the "Improved-Ambient" method (Canagaratna et al., 2015). The ionization efficiency of nitrate and relative ionization efficiencies of ammonium and sulfate were calibrated using dry, 350-400 nm ammonium nitrate and ammonium sulfate particles approximately every week during each campaign. Time series of the calibrated IE values are shown in Figure 2.S2.

Mass loadings of organic and inorganic nitrates measured by the AMS were estimated using two methods. The NO_x ratio method was used to analyze data collected during LAAQC-2022 and CalNexT-2022 (Farmer et al., 2010; Xu et al., 2015). Briefly, laboratory measurements have demonstrated that nitrate functionalities associated with organic and inorganic nitrates fragment to produce considerably different NO^+/NO_2^+ ion ratios in the AMS, termed R_{ON} and R_{AN}, respectively (Farmer et al., 2010). While the specific R_{ON} and R_{AN} values vary between instruments, we used the procedure of Fry et al. (2013) and assumed that the R_{ON}/R_{AN} value is instrument independent. Values of R_{AN} were calculated from calibration data using pure AN particles. We used an R_{ON}/R_{AN} value of 3.99 ± 0.25 following Xu et al. (2015), which represents values observed for β-pinene organic nitrates in laboratory studies. Using an alternative R_{ON}/R_{AN} value of 2.75, as suggested by Day et al. (2022), decreases the inferred inorganic nitrate concentrations in LAAQC-2022 and CalNexT-2022 by 12% and 25%, respectively, which has a negligible effect on our conclusions.

Lacking IE calibration data from 2010, we also used the ionic balance method to estimate organic and inorganic nitrate concentrations during each campaign (Farmer et al., 2010; Zaveri et al., 2020). This method assumes that any ammonium aerosol in excess of the amount required to fully neutralize measured sulfate and chloride (i.e., needed to form

$(NH_4)_2SO_4$ and NH_4Cl) is associated with inorganic nitrate (i.e., NH_4NO_3). Organic nitrates are then assumed to represent the difference between total measured nitrate aerosol concentrations and the inferred concentration of inorganic nitrates. Good agreement was observed between the two nitrate quantification methods during both LAAQC-2022 and CalNexT-2022 (Figure 2.S3).

Positive Matrix Factorization (PMF) was applied to the OA mass spectral datasets collected during each campaign to gain insight into OA sources. PMF is a bilinear unmixing factor analysis model that deconvolves a time series of measured species into a set of compositionally static factors whose contributions to the input dataset vary in time (Paatero and Tapper, 1994; Paatero, 1997). PMF analysis of the 2010 dataset is discussed extensively in Hayes et al. (2013). During LAAQC-2022 and CalNexT-2022, datasets were prepared for PMF analysis following recommendations of Ulbrich et al. (2009). Specifically, "weak" ions were defined as those with a signal-to-noise ratios (SNR) of <2 and down-weighted by a factor of 2. Ions with a SNR of <0.2 were removed from the dataset. Descriptions of PMF solution selection are provided in SI Section 2.S2.

2.2.2.2 Volatile organic compound measurements

Detailed descriptions of VOC measurements performed in 2010 are provided in Borbon et al. (2013) and de Gouw et al. (2017). Briefly, VOC were measured using a custom-built two-channel online gas chromatography-mass spectrometry system (GC-MS) with a time resolution of 30 minutes.

During LAAQC-2022 and CalNexT-2022, ambient whole air samples (WAS) were collected using evacuated 2-liter electropolished stainless steel canisters three times per day. An automated canister sampler located on the roof of Caltech Hall was used to pressurize 32 individual canisters with ambient air to an internal pressure of 20 psi. Samples were collected in the early morning (5:30-6:30 PDT), mid-morning (9:00-10:00 PDT), and in the afternoon during the typical urban plume arrival period (14:00-15:00 PDT). WAS measurements were analyzed at the University of California, Irvine using a multi-detector gas chromatography (GC) system. A detailed description of the analytical

procedure used to quantify VOC concentrations is provided in Simpson et al. (2010) and Van Rooy et al. (2021).

2.2.2.3 Additional aerosol and trace gas measurements

Multiple additional aerosol and trace gas measurements were performed during CalNex-2010, as described by Hayes et al. (2013) and SI Section 2.S1.

Ambient $PM_{2.5}$ measurements were made from the roof of Caltech Hall during both LAAQC-2022 and CalNexT-2022 using a Teledyne T640 PM2.5 analyzer housed in a weatherproof enclosure. The T640 is an optical aerosol spectrometer that uses scattered light to quantify particle size following Lorenz-Mie theory. Aerosols are dried to a maximum of 35% relative humidity prior to sampling by dynamically adjusting the temperature of the incoming sample stream. Data were reported at a time resolution of 1 minute. The effective size range of the T640 is ~180nm to 2.5 μm. Comparisons of AMS mass concentrations with the T640 $PM_{2.5}$ during LAAQC-2022 and CalNexT-2022 are shown in Figure 2.S6.

During CalNexT-2022, a TSI Inc. scanning mobility particle sizer (SMPS) measured ambient particle number distributions from ~20-700 nm diameter. The SMPS used the same inlet line as the AMS, but the aerosol flow passed through an additional 2m of ¼" stainless steel line. The SMPS operated with an aerosol flow rate of 0.3 lpm and a sheath flow rate of 3 lpm, similarly to SMPS operation during CalNex-2010. Individual size distributions were measured every 2.5 minutes. Comparisons of inferred AMS volume concentrations during CalNexT-2022 with volume concentrations inferred from the SMPS are shown in Figure 2.S7.

Ozone concentrations during the 2022 campaigns were measured using a Teledyne T400 UV absorption analyzer, NO and NO_y concentrations were measured using chemiluminescence analyzer with a molybdenum NO_y-NO converter located outside near the sampling inlet (Teledyne T200U), and NO_2 concentrations were measured using Cavity Attenuated Phase Shift (CAPS) with a Teledyne T500U instrument. Concentrations of carbon monoxide were measured using IR spectroscopy with a Teledyne M300EU2

Meteorological data were obtained from measurements associated with the Total Carbon Column Observing Network (TCCON) on the roof of Linde Laboratory, approximately 100m from Caltech Hall.

2.2.3 Zero-dimensional modeling

2.2.3.1 Urban OA box model

We developed a zero-dimensional model of urban OA formation to quantify changes in local OA sources over the last decade in Los Angeles. The model framework is largely based on previously developed zero-dimensional models of OA formation in urban environments (Dzepina et al., 2009; Hayes et al., 2015; Ma et al., 2017). Individual simulations are performed for each hour of an average diurnal cycle during each campaign. Emissions of OA precursors are initialized in the model using measured background-corrected concentrations of carbon monoxide (ΔCO) and inventory-based estimates of speciated OA precursor emissions from on-road, non-road, and area/stationary sources in Los Angeles County relative to total estimated CO emissions (Δprecursor / ΔCO). Total precursor emissions from each source are divided into a set of lumped model species based on volatility and composition, as described in SI Section 2.S4. Emitted precursors are oxidized until the photochemical age (i.e., OH exposure) of the simulated airmass reaches the measured photochemical age, estimated using VOC ratios (SI Section 2.S3). Precursor oxidation forms SOA following established parameterizations (Ma et al., 2017; Pennington et al., 2020). More detailed descriptions of model constraints and relevant parameterizations are provided in SI Section 2.S4.

2.2.3.2 Overnight nitrate box model

We developed a second zero-dimensional model to assess changes in overnight NO_x chemistry and associated impacts on production of inorganic nitrate aerosol since 2010. Model simulations begin at 19:00 local time and simulate NO_x and biogenic VOC (BVOC) emissions, gas-phase chemistry, formation and hydrolysis of N_2O_5, and gas-aerosol partitioning of HNO_3 until 06:00 the following day. Initial simulations were used to tune

NO_x emissions, aerosol uptake parameters, and BVOC emissions to achieve agreement with observations made during CalNex-2010. Following this process, NO_x emissions were reduced to assess effects on overnight inorganic nitrate aerosol formation. A more detailed description of the model simulation procedure is included in SI Section 2.S8.

2.3 Results and discussion

2.3.1 Observed changes in concentrations of major NR-PM_1 species, trace gases, and VOCs

Figure 2.1 compares diurnal trends and average mass fractions of major classes of NR-PM_1 measured by the AMS during CalNex-2010 and LAAQC-2022. Results for CalNexT-2022 are shown in Figure 2.S8. Observed concentrations of all species were reduced in the more recent campaigns relative to CalNex-2010, with much larger differences observed for inorganic species (~35% or more) than organics (~10-35% depending on campaign). In each campaign, OA accounted for the largest fraction of total NR-PM_1 and displayed a clear afternoon maximum, as expected based on the timing of the arrival of processed emissions from the urban core of Los Angles (Blumenthal et al., 1978; Hayes et al., 2013).

As explained in detail in SI Section 2.S2, PMF analysis was performed independently on each dataset. In general, four to five factors were resolved in each campaign, corresponding to less-oxidized oxygenated OA (LO-OOA) (locally-formed SOA), more-oxidized OOA (MO-OOA) (regional/background SOA), hydrocarbon-like OA (HOA) (likely associated with primary OA sources), cooking-influenced OA (CIOA), and local OA (LOA, only observed during CalNex-2010). Detailed descriptions of these factors are provided in Hayes et al. (2013) and SI Section 2.S2 (Table 2.S2, 2.S3).

The PMF results suggest that while the SOA fraction of the OA was relatively consistent between campaigns (~65%), the ratio of total LO-OOA to MO-OOA was larger in the 2022 datasets due to lower average concentrations of MO-OOA. Reductions in MO-OOA concentrations accounted for most of the difference in measured OA between CalNex-2010 and LAAQC-2022, which both occurred during May and June. In contrast, average LO-

OOA concentrations measured during LAAQC-2022 (2.5 μg m^{-3}) were comparable to CalNex-2010 (2.4 μg m^{-3}).

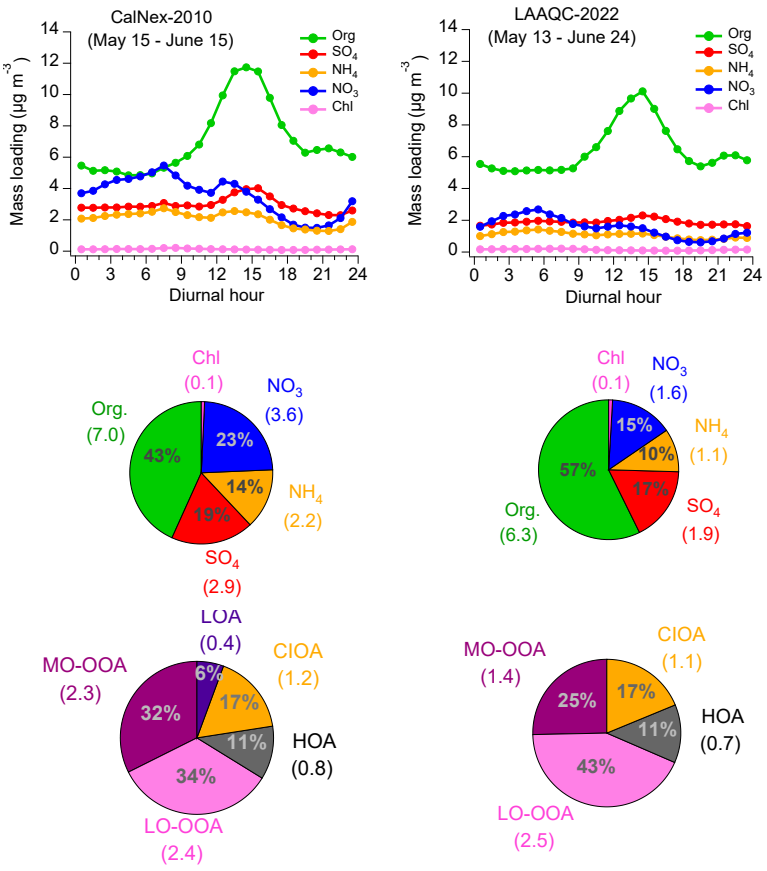

Figure 2.1: Overview of AMS measurements during CalNex-2010 and LAAQC-2022. (Top) Diurnal concentrations of major NR-PM_1 species measured by the AMS (Middle) Average concentrations of $NRPM_1$ species. (Bottom) Average mass fractions of individual PMF factors. Corresponding results for CalNexT-2022 are shown in Figure 2.S8.

Observed HOA concentrations were only slightly lower during LAAQC-2022 than CalNex-2010 (difference of ~13%), in contrast to the observed change in average background-corrected CO concentrations (ΔCO) (29%) and the predicted changes in on-road POA emissions in LA County from the California Emissions Projections Analysis Model (CEPAM) (28%) (CEPAM, 2019). The observed change in ΔCO concentrations (29%) agreed well with predicted changes in CO emissions in LA County (32%) (CEPAM, 2019). We estimated a background CO concentration of 80 ppbv in 2022 based on the relationship of CO to NO_y (Figure 2.S11). A background of 105 ppbv was used for the

2010 dataset based on measurements off the coast of Los Angeles (Hayes et al., 2013). Changes in HOA and CIOA concentrations on weekends relative to weekdays in 2022 aligned well with observations in 2010 (Hayes et al., 2013) (Figure 2.S12).

Estimates of integrated airmass OH exposure (OH_{exp}) (i.e., photochemical age) calculated midday (14:00-15:00) using VOC ratios (SI Section 2.S3) were 53% and 59% higher on average during LAAQC-2022 and CalNexT-2022, respectively, than during CalNex-2010, likely resulting from reduced NO_x emissions (Figure 2.S13) and contributing to the consistency in LO-OOA concentrations, as explained further below. The estimated decline in NO_x emissions since 2010 (~40-50%) (CEPAM, 2019) is comparable to the previously reported drop in NO_x emissions on weekends in 2010 (34-46%) (Warneke et al., 2013), and the change in average airmass (OH_{exp}) is consistent with increases in OH concentrations observed on weekends during CalNex-2010 (Warneke et al., 2013; Griffith et al., 2016).

While average ozone concentrations were relatively similar between campaigns (differences of ~1-6 ppbv), concentrations of NO, NO_2, NO_y, and NO_z were all notably lower in 2022 than in 2010 (~40-60%), in reasonable agreement with long-term trends in NO_x species in the Los Angeles Basin (Figure 2.S16, Table 2.S1) (Pollack et al., 2013). Ambient concentrations of anthropogenic SOA precursors such as benzene, toluene, xylenes, and C_8-C_{10} alkanes were also ~50-60% lower during LAAQC-2022 and CalNexT-2022 than during CalNex-2010 (Figure 2.S15, Table 2.S1). Average isoprene concentrations were relatively similar between CalNex-2010 and LAAQC-2022 (difference of ~10%) but were considerably higher during CalNexT-2022 (+50%), when meteorological conditions were warmer.

As shown in Figure 2.S1, average temperatures during LAAQC-2022 and CalNexT-2022 were ~2ºC and ~6ºC higher, respectively, than during CalNex-2010. Previous measurements in Los Angeles have demonstrated that concentrations of both organic (Nussbaumer and Cohen, 2021) and inorganic (Hersey et al., 2011; Schiferl et al., 2014) aerosol species are heavily dependent on local meteorological conditions.

Figure 2.S17 compares midday concentrations (11:00-17:00) of OA and IA species as a function of midday temperature. Trends in inorganic aerosol species measured during the

more recent campaigns were generally consistent when viewed in this meteorological context, with peak concentrations occurring around 25ºC that were notably lower than those observed during CalNex-2010. Average OA concentrations, in contrast, displayed clearly different trends between 2022 campaigns. During LAAQC-2022 (May-June), concentrations increased consistently from 20-30ºC and mirrored concentrations measured during CalNex-2010, while during CalNexT-2022 (July-August) concentrations were lower on average and consistent from ~25-35ºC. These differences were primarily attributable to variability in the relationship between LO-OOA concentrations and temperature (Figure 2.S18).

Hersey et al. (2011) observed similar variability in OA concentrations with season during the Pasadena Aerosol Characterization Observatory experiment (i.e., between Regime II and III in their study) and hypothesized that the differences were the result of increased amounts of aqueous processing during the late spring/early summer. Figure 2.S19 demonstrates that on days with warm midday temperatures in 2022 (27-32ºC), both OA and LO-OOA concentrations correlated more strongly with ambient ALW and NO_3 ($R^2 > 0.8$) than ΔCO ($R^2 \approx 0.55$), supporting a role for inorganic species and possibly aqueous chemistry in local SOA formation. While the importance of aqueous chemistry in biogenic SOA formation is well established (e.g., Hennigan et al., 2009; Zhang et al., 2012), an increasing body of evidence supports aqueous production of fossil-derived SOA in other urban areas, particularly in Asia, from small carbonyls (e.g., Gkatzelis, 2021; Xu et al., 2022). We note however, that direct measurements of water-soluble organic carbon partitioning during CalNex-2010 suggested a minor role for aerosol liquid water (Zhang et al., 2012).

Here, we focus primarily on the long-term trend in aerosol concentrations/sources during similar meteorological periods. Future work will further investigate the apparent seasonal variability in OA and potential role of aqueous processing. We confirmed that airmass recirculation patterns were similar during meteorologically similar periods (based on temperature and humidity) in 2010 and 2022 by comparing ΔCO concentrations normalized by estimates of CO emissions in Los Angeles County (Figure 2.S20).

2.3.2 Declining contribution of traditional precursors to local SOA

As shown in Figure 2.1, concentrations of LO-OOA (i.e., locally formed SOA) were consistent between CalNex-2010 and LAAQC-2022, despite the notable declines in ambient concentrations of anthropogenic SOA precursors due to reduced mobile source emissions (Table 2.S1) (CEPAM, 2019). In theory, if ambient SOA was entirely derived from traditional anthropogenic sources (i.e., mobile source emissions) distributed evenly throughout an urban region, and SOA yields were constant over time, changes in average SOA concentrations over extended periods should be reasonably well predicted by:

$$\Delta SOA = \Delta(\Delta CO) * \Delta ER * \Delta OH_{exp} \quad (1)$$

Where Δ(ΔCO) represents the change in the ambient ΔCO concentrations, ΔER represents the change in the average emission ratio of traditional SOA precursors relative to CO, and ΔOH_{exp} represents the change in the airmass OH exposure. During LAAQC-2022, average ΔCO concentrations were 29% lower than during CalNex-2010, while the emission ratios of major traditional SOA precursors such as aromatic and alkane VOC (e.g., benzene, toluene, xylenes, C_8-C_{10} alkanes) relative to CO, calculated using the methods described in Van Rooy et al. (2021), have declined by ~25-45% (Figure 2.S21), possibly reflecting a shifting in the relative distribution of on-road and non-road mobile sources (Van Rooy et al., 2021).

The product of these values implies a 50-60% reduction in traditional mobile source SOA precursor emissions since 2010, likely resulting from a combination of improvements in emission control technologies (i.e., catalytic converters), increasing fuel efficiency of on-road and non-road vehicles, and efforts to limit evaporative emissions (Lu et al., 2018). The reduction calculated using Eq. 1 aligns with changes in afternoon concentrations of the same species once corrected for OH_{exp} (to account for increasing OH since 2010) (Figure 2.S22). The inferred decline in emissions is slightly larger than the predicted reduction in mobile source emissions of reactive organic gases (ROG) in LA County since 2010 (~45%) (CEPAM, 2023), in line with previous comparisons of measured and inventory-predicted declines in VOC emissions (Pollack et al., 2013).

Multiplying the change in ΔCO and traditional precursor ER by the observed change in OH_{exp}, which accounts for increases in the rate of SOA production since 2010, predicts a decline in SOA concentrations of ~20-40%. While multiplying by photochemical age assumes that SOA production increases linearly with OH exposure, measurements from both CalNex-2010 (Hayes et al., 2013; Ortega et al., 2016) and the more recent campaigns support this assumption until airmass OH_{exp} reaches ~7.5 x 10^{10} cm^{-3} s (0.6 photochemical days at an assumed OH concentration of 1.5 x 10^6 cm^{-3}), which represents the upper limit of airmass ages observed in 2022 (Figure 2.S13).

The difference between the observed and calculated changes in SOA concentrations suggests that either "non-traditional" urban SOA sources such as VCPs asphalt emissions or biogenics, which are largely excluded from this calculation, accounted for a substantial fraction of total SOA in 2010 and have increased in relative importance over time, or that SOA yields have increased substantially (~30-60%). Kinetic calculations suggest that RO_2 reaction with NO is still expected to be considerably faster than reaction with HO_2 and notably faster than known alkane autooxidation process, though we note that the role of autoxidation in urban SOA formation remains poorly understood and will likely become increasingly relevant over time (SI Section 2.S4) (Praske et al., 2018).

2.3.3 Evidence for a temperature-dependent SOA source

Recent analyses of historical aerosol datasets have noted a strong relationship between OA concentrations and temperature in Los Angeles, thought to result from evaporative, non-combustion emission sources contributing to the local SOA burden (Nussbaumer and Cohen, 2021). During both CalNex-2010 and LAAQC-2022, midday OA concentrations increased considerably with temperature (Figure 2.S17). As shown in Figure 2.S18, this variability is primarily driven by increases in LO-OOA concentrations. Emissions from non-traditional urban SOA sources thought to be increasingly relevant in Los Angeles, such as VCPs and asphalt, may increase with temperature (Khare et al., 2020; Seltzer et al., 2021b).

Relating changes in LO-OOA concentrations to precursor emissions using meteorological variability requires accounting for simultaneous variability in basin ventilation rates and oxidant concentrations. During CalNex-2010, midday planetary boundary layer (PBL) heights decreased with ambient temperature, from ~1100 m at 20ºC to only ~600 m at 29ºC (Figure 2.S23). As midday wind speeds were effectively constant, the change in PBL heights produced a ~50% decline in effective ventilation rates from 20 to 30ºC (Figure 2.S23). This change is clearly reflected in ΔCO concentrations, which nearly doubled over the same temperature range (Figure 2.S20).

However, Figure 2.2 demonstrates that the observed positive relationship between LO-OOA concentrations and temperature remains after concentrations are normalized by ΔCO to account for varying ventilation rates (i.e., LO-OOA/ΔCO), increasing from ~90% from 20ºC to 30ºC. Oxidant concentrations inferred from OH_{exp} estimates also increased notably with temperature (Figure 2.S24), but further normalizing LO-OOA/ΔCO by afternoon OH_{exp} does not fully remove the temperature trend (Figure 2.S24) (remaining increase of 48% from 20ºC to 30ºC), suggesting a possible contribution of temperature-dependent (i.e., evaporative) emissions to local SOA. Interestingly, the temperature trend in LO-OOA/ΔCO is similar during the May-June campaigns in both 2010 and 2022, suggesting at most modest changes in the relative contribution of temperature-dependent sources to the overall SOA burden over the last decade.

Given the strong temperature trend observed, we assessed correlations between LO-OOA/ΔCO and anthropogenic and biogenic VOC/ΔCO measured during each campaign. Anthropogenic VOC concentrations were corrected for measured airmass OH_{exp} to remove the potentially confounding effects of temperature-dependent oxidant concentrations. As shown in Figure 2.2, correlations were strongest with the smallest and largest alkanes measured (i.e., butane and nonane/decane) and isoprene. Negligible correlations were observed between LO-OOA/ΔCO and aromatic VOC/ΔCO, as expected given that the aromatics likely originate from combustion processes (Borbon et al., 2013; Pollack et al., 2013). The trend in LO-OOA/ΔCO with temperature therefore appears to more likely result from evaporative alkane/aromatic IVOC and/or biogenic emissions. While a lack of IVOC

measurements prevents direct assessment of correlations, naphthalene concentrations correlated strongly with temperature during CalNex-2010 (Hayes et al., 2015) and both VCPs and asphalt are known to be major evaporative sources of alkane/aromatic IVOC in the Los Angeles Basin (McDonald et al., 2018; Khare et al., 2020; Seltzer et al., 2021b). Asphalt emissions double over typical summertime in-use temperatures (from 40 ºC to 60ºC) (Khare et al., 2020). The temperature dependence of VCP emissions remains uncertain given the variety of VCP sources and emission pathways, but temperature-driven increases in emissions from specific sectors (e.g., paints and coatings) may be substantial (Seltzer et al., 2021b).

We note that the strengths of the correlations shown in Figure 2.2 are not necessarily indicative of the relative contribution of different emission sources to the SOA burden. As an example, of the VOCs measured during CalNex-2010, LO-OOA/ΔCO correlated most strongly with isoprene. Previous radiocarbon analyses have indicated that 68-74% of LO-OOA measured during CalNex-2010 was derived from fossil (i.e., non-biogenic) carbon sources (Zotter et al., 2014) and bottom-up analyses suggest that isoprene contributes at most 5-25% of the total SOA burden (Hayes et al., 2015; Nussbaumer and Cohen, 2021). Despite our uncertainty regarding the specific drivers of the observed temperature trend in LO-OOA/ΔCO, our observations highlight a potentially important role for evaporative precursors. Additional highly time-resolved measurements of IVOC likely generated through such evaporative processes (e.g., C_{12}+ alkanes and aromatics) would help further constrain SOA sources in Los Angeles.

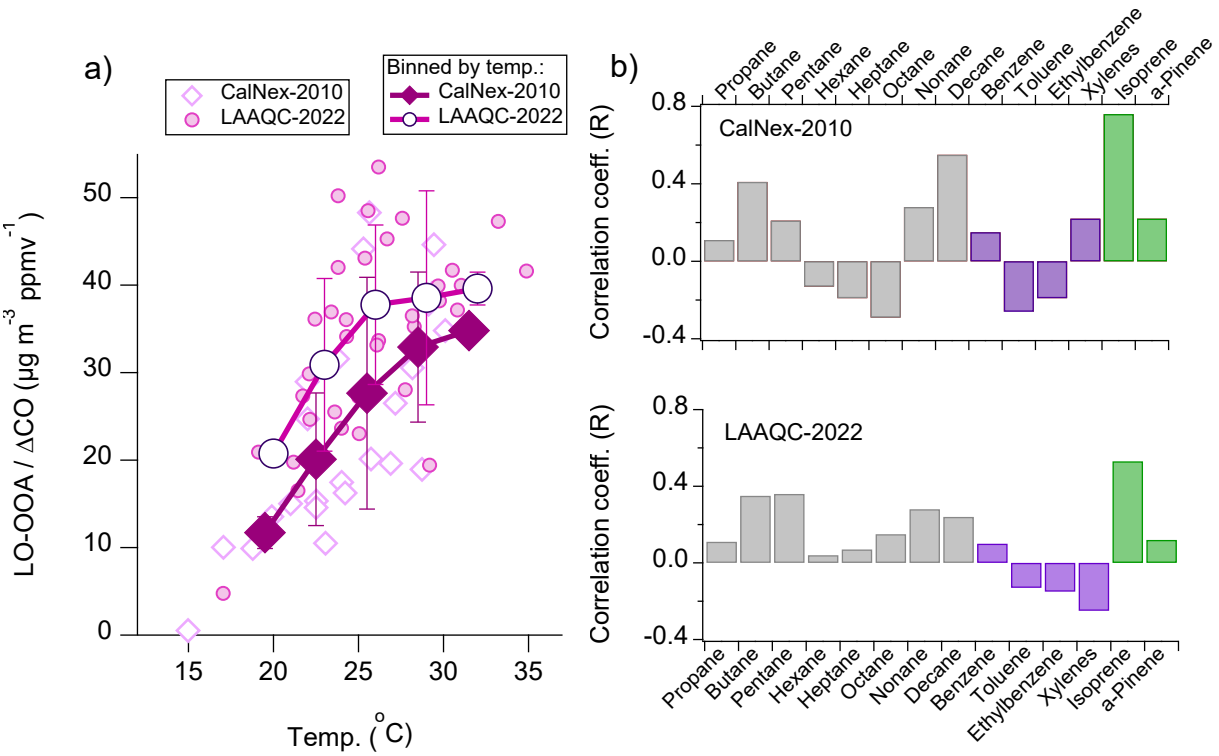

Figure 2.2: (a) Relationship between midday (11:00-16:00) LO-OOA/ΔCO concentrations and temperature during CalNex-2010 and LAAQC-2022. (b) Correlations between midday concentrations of LO-OOA/ΔCO and VOC measured during each campaign. Concentrations of alkanes and aromatics were corrected for measured OH_{exp} to account for temperature-dependent OH concentrations.

2.3.4 Modeled impact of reduced mobile source emissions on SOA formation since 2010

Given the uncertainties involved in the analyses described above, we developed a detailed box model of local SOA formation to quantify changes in the magnitude of individual SOA sources since 2010. The model incorporates emissions from on-road, non-

road mobile, area, and stationary sources, and a description of the model framework, constraints, and SOA formation parameterizations is included in SI Section 2.S5.

Figure 2.3 compares measured and modeled SOA concentrations during CalNex-2010 and LAAQC-2022, which we focus on given their meteorological similarities (Figure 2.S1). The model accurately reproduces average diurnal SOA concentrations measured during CalNex-2010 (bias of 3%) and slightly overpredicts concentrations during LAAQC-2022 (bias of 17%).

Emissions in the base model simulations are constrained using annual average emissions estimates for a variety of mobile and stationary/area sources for Los Angeles County (SI Section 2.S5) (CEPAM, 2019; McDonald et al., 2018; Khare et al., 2020; Seltzer et al., 2021b). We modified gasoline emissions slightly to achieve agreement between modeled and measured alkane and aromatic VOC ER (e.g., benzene/ΔCO), as explained in SI Section 2.S7 (Figure 2.S26). Adjusting emissions to achieve ER agreement only modestly influences the differences between modeled and measured SOA concentrations (Figure 2.3). We adjusted mobile source gasoline emissions as a group, rather than on-road or non-road emissions specifically, given the similarity in emission profiles for on-road and non-road gasoline sources (Lu et al., 2018; Zhao et al., 2022). The remaining bias in simulated SOA concentrations during the 2022 campaigns is likely either the result of uncertainties in the AMS measurements, emissions of lower volatility species, or simulated SOA yields.

While we have limited measurements of less volatile SOA precursors, the model reproduces IVOC concentrations measured during CalNex-2010 with reasonable accuracy (bias of 9%) (Figure 2.S7) (Zhao et al., 2014). Simulated SOA composition also aligns well with ^{14}C measurements made during CalNex-2010 (Zotter et al., 2014), with 80% of modeled SOA and 68-74% of measured SOA derived from fossil sources. SOA formed from biogenic VOC (13%) and cooking-related sources (7%) accounts for the non-fossil fraction in the model.

Overall, the simulated contribution of mobile sources to the SOA burden has declined from ~50% in 2010 to only ~25% in 2022 (Figure 2.3). The relative importance of other, non-traditional SOA sources such as VCPs, cooking emissions, and asphalt are predicted to have increased accordingly, and VCPs are now estimated to contribute the largest

fraction of locally formed SOA (33%), which aligns with recent CMAQ predictions for Los Angeles (Seltzer et al., 2021a). As recently suggested by Khare et al. (2020), asphalt emissions now appear to account for nearly as much local SOA production as mobile sources. In terms of the mobile source distribution, we predict that non-road emissions formed considerably more SOA (16%) than on-road emissions (10%) during the campaigns in 2022.

The relatively small contribution of on-road sources to locally formed SOA in the 2010 simulation explains the inability of previous bottom-up calculations of vehicle SOA production to reproduce ambient SOA concentrations during CalNex-2010 (Ensberg et al., 2014). The modest contribution of all mobile sources is also consistent with recent simulations of the CalNex-2010 field campaign using the Community Multiscale Air Quality (CMAQ) model (Jathar et al., 2017; Lu et al., 2020). Diesel emissions account for a particularly small fraction of local SOA in both years (<10%), in line with prior analyses of hydrocarbon SOA precursor sources during CalNex-2010 (Zhao et al., 2014; 2022). The mass closure (within uncertainty) produced by our model suggests that remaining uncertainties in emissions and/or speciation profiles are unlikely to alter the conclusion that mobile sources now contribute less than one-third of locally formed SOA, as this would require considerable bias in the magnitude of multiple other SOA sources treated in the model.

Despite the ~45% reduction in mobile source emissions since 2010, average measured and simulated concentrations of SOA during LAAQC-2022 were comparable to those in CalNex-2010. Estimated emissions from other anthropogenic sources have either remained effectively constant (VCPs and asphalt) or only increased slightly (e.g., ~10% for cooking emissions) (Khare et al., 2018; Seltzer et al., 2021b; CEPAM, 2019). As modeled SOA yields were identical in each simulation, the consistency in modeled SOA concentrations is attributable to the increase in OH concentrations resulting from reduced mobile source NO_x emissions (Figure 2.S13). As shown in Figure 2.3, if we assume OH concentrations have remained constant since 2010, the model predicts 31% less SOA than in the base 2022 simulation. The direct effect of reduced mobile source SOA precursor emissions appears

to have therefore been offset by the increase in OH concentrations since 2010. We refer to this as the "indirect" effect of mobile source emissions reductions in the discussions below.

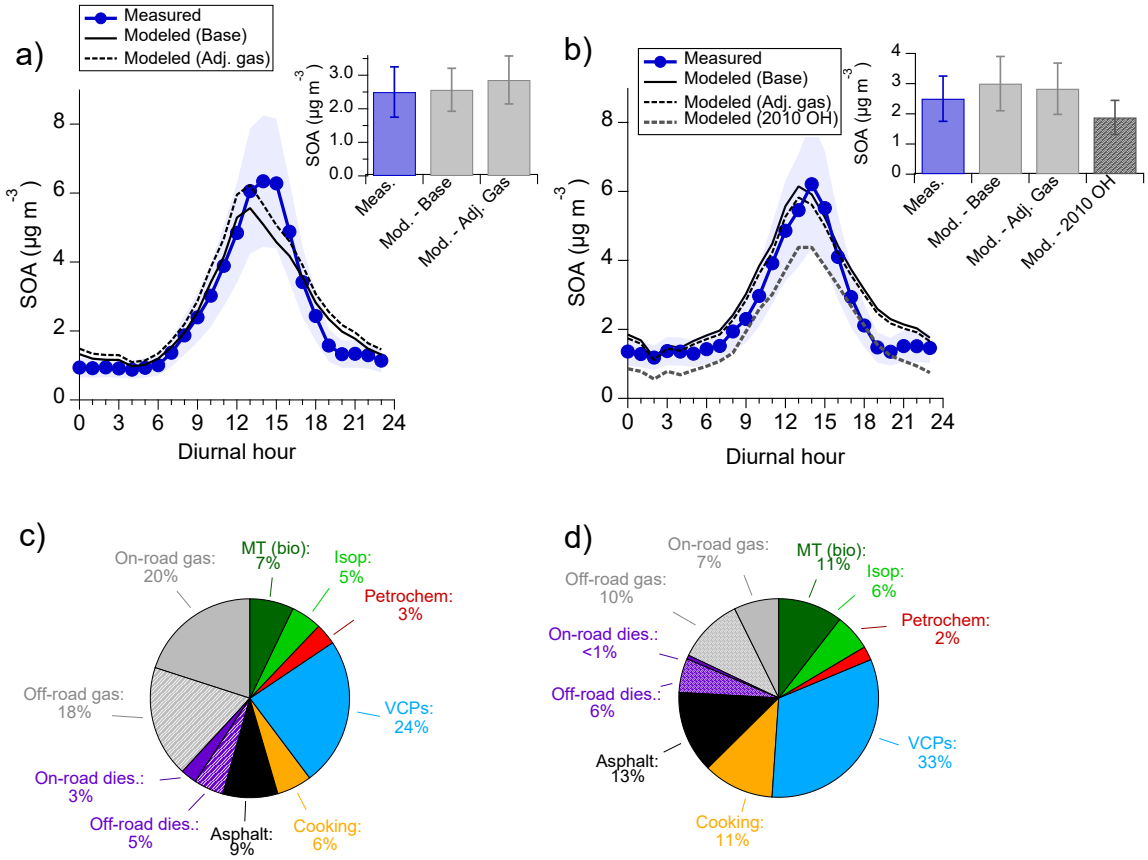

Figure 2.3: Diurnal concentrations of measured and modeled locally-formed SOA during (a) CalNex-2010 and (b) LAAQC-2022. Measured SOA represents the LO-OOA PMF factors resolved during each campaign. Inset bar charts show average measured and simulated concentrations. (c,d) Average contributions of individual precursor sources to modeled SOA during (c) CalNex-2010 and (d) LAAQC-2022.

2.3.6 Notable reductions in overnight nitrate production from reduced NO_x emissions

In contrast to the relatively consistent SOA concentrations, we observed markedly lower nitrate concentrations during LAAQC-2022 (-55%) and CalNexT-2022 (-80%) than were measured during CalNex-2010. Reductions in inorganic nitrate ($NO_{3,inorg.}$) concentrations account for the majority of the difference, suggesting larger changes in $NO_{3,inorg.}$ than organic nitrate ($NO_{3,org.}$) production mechanisms (Figure 2.S3).

The California Air Resources Board (CARB) predicts that NO_x emissions have declined by ~40% in Los Angeles County since 2010, with virtually all of the reduction attributable to mobile sources (80% due to on-road vehicles specifically) (CEPAM, 2019). As noted above, these reductions have produced a 40-60% decline in ambient concentrations in NO, NO_2, NO_y, and NO_z in Pasadena (Table 2.S1, Figure 2.S16). The observed relationship between NO_z and NO_3 concentrations was consistent between campaigns, with day-to-day differences in the NO_3/NO_z ratio likely driven by variations in local temperature/RH (Figure 2.S30).

Linking changes in nitrate concentrations to changes in emissions is complicated by the dependence of inorganic nitrate partitioning on meteorology and other inorganic species (Seinfeld and Pandis, 2016; Guo et al., 2017) (Figure 2.S31). Given the differences in meteorology and sulfate concentrations between campaigns, and the lack of nitric acid measurements in 2022, we first used the ISORROPIA-II thermodynamic model (Fountoukis and Nenes, 2007) to assess whether changes in average $NO_{3,inorg.}$ aerosol concentrations represented reductions in concentrations of total nitrate ($NO_{3,inorg.} + HNO_3$), which would likely indicate changes in total nitrate production, or likely resulted from partitioning differences. These simulations are discussed in detail in SI Section 2.S8. Briefly, as shown in Figure 2.S32, comparison of the thermodynamic model simulations with aerosol observations suggests considerable reductions in total nitrate concentrations (gas + aerosol) at night during the 2022 campaigns relative to CalNex-2010 (>40%) but relatively consistent daytime concentrations.

Analyses of daytime and nighttime nitrate production mechanisms support the changes inferred from the thermodynamic modeling. We calculated a proxy for daytime HNO_3

production in each campaign using the product of ambient NO_2 concentrations and afternoon airmass OH_{exp}. During CalNex-2010, midday OH_{exp} estimates correlated strongly with measured OH concentrations (Figure 2.S33), supporting their use in this calculation in the absence of OH measurements in 2022. As shown in Figure 2.4a, values of the HNO_3 production proxy were largely similar between CalNex-2010 and the more recent campaigns on days with similar temperatures, with average differences of only ~15%. Reductions in afternoon concentrations of NO_2 therefore appear to have been largely "balanced" by increasing OH concentrations from the perspective of daytime nitric acid production.

We then used the box model described in Section 2.3.2 to evaluate changes in overnight nitrate production since 2010 resulting from reduced NO_x emissions. Figure 2.S34 shows that integrated overnight (19:00-06:00) production rates of the nitrate radical ($P(NO_3)$), the precursor to N_2O_5, were ~25% higher during CalNex-2010 than LAAQC-2022. This trend is consistent across Los Angeles County (Figure 2.S35). The decrease since 2010 is attributable to the fact that nighttime NO_2 concentrations have declined considerably, while ozone concentrations have only slightly increased, likely the result of simultaneous reductions in NO_x emissions and anthropogenic VOC (i.e., OH reactivity) (Wang et al., 2023).

After tuning our box model to reproduce overnight concentrations of NO_2, O_3, HNO_3, $ClNO_2$, and $NO_{3,inorg.}$ measured during CalNex-2010 (Figure 2.S36) (Simulation #1), we performed additional simulations with altered trace gas and aerosol surface area concentrations to quantify changes in overnight $NO_{3,inorg.}$ production since 2010. We first reduced the initial NO_2 and increased the initial O_3 concentration to match observations made during LAAQC-2022, while also reducing overnight NO_x emissions by 45% to align with CARB predictions (CEPAM, 2019). As shown in Figure 2.4, changes in trace gas concentrations since 2010 are predicted to have produced a ~60% (58%) reduction in overnight $NO_{3,inorg.}$ production in the absence of any changes in aerosol SA or meteorological differences (Simulation #2).

The third simulation shown in Figure 2.4 incorporates the positive feedback of reduced AN formation on aerosol surface area (SA) available for N_2O_5 hydrolysis, while in the

fourth simulation we also reduced aerosol concentrations associated with non-nitrate related species. The effect of reduced SA available for N_2O_5 hydrolysis in these simulations is largely compensated by slight increases in aerosol pH, which enhances HNO_3 partitioning and leads to a similar overall reduction in overnight $NO_{3,inorg.}$ production (Figure 2.S38). We performed a final simulation identical to the fourth in terms of emissions and trace gas concentrations, with overnight temperature and relative humidity adjusted to match average values observed during LAAQC-2022. An additional ~20% reduction in overnight $NO_{3,inorg.}$ production is predicted in this scenario (82% reduction overall), resulting from notable reductions in ALW, leading to both reduced N_2O_5 hydrolysis rates and higher aerosol pH, which shifts HNO_3 partitioning to the gas phase (Figure 2.S38).

The results of the final model simulation underpredict overnight $NO_{3,inorg.}$ production observed during LAAQC-2022. This could be the result of errors in the ALW concentrations predicted by the thermodynamic model or variability in parameters such as the N_2O_5 uptake coefficient or overnight OH concentrations since 2010, which were assumed constant in our simulations. We discuss these possibilities in SI Section 2.S9. While the remaining model-measurement discrepancy deserves further attention, it is nonetheless evident that reductions in mobile source NO_x emissions have likely notably reduced overnight nitrate aerosol production over the last decade.

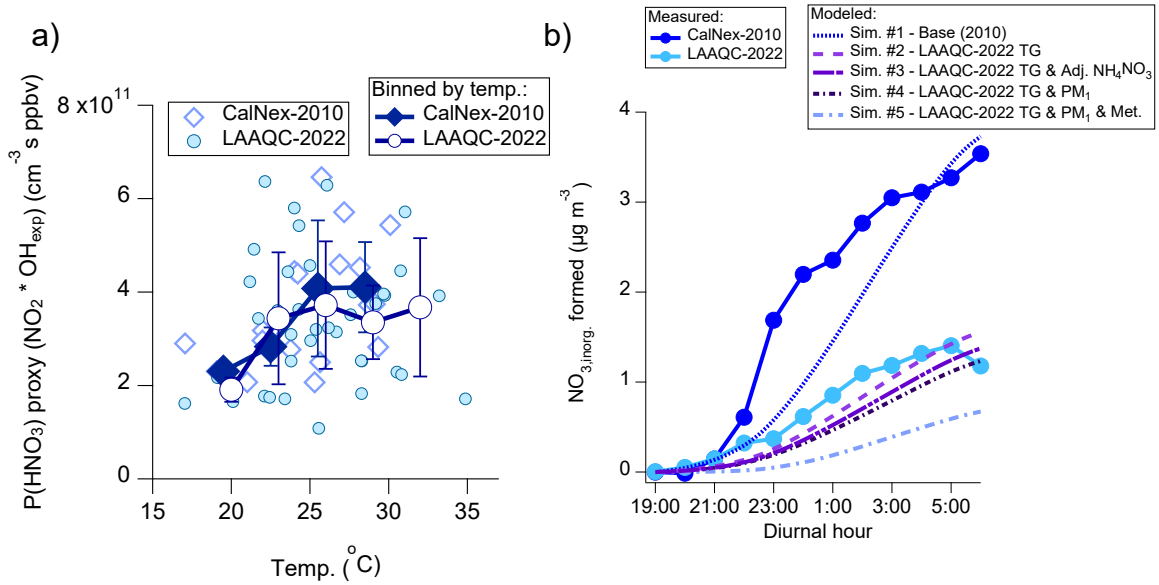

Figure 2.4: Observed and simulated changes in daytime and nighttime nitrate production rates. (a) Comparison of midday (14:00-15:00) estimates of HNO_3 production rates calculated using the product of NO_2 and airmass OH_{exp} during CalNex-2010 and LAAQC-2022. (b) Comparison of measured overnight inorganic nitrate ($NO_{3,inorg.}$) production during CalNex-2010 and LAAQC-2022 with zero-dimensional model simulations described in Section 2.2.3.2 and SI Section 2.S8.

2.4 Implications for urban air quality

We demonstrate that the simultaneous mitigation of mobile source NO_x and SOA precursor emissions has had complex effects on SOA and nitrate aerosol production in Los Angeles. While overnight nitrate aerosol production rates have declined considerably, increases in OH concentrations driven by reduced NO_x emissions, an "indirect" effect of emission controls, appear to have offset expected "direct" changes in both SOA and daytime nitrate aerosol production. As a result, the relative contribution of OA to ambient PM_1 and the fraction of OA attributable to non-mobile sources have both increased.

Interestingly, the differences between average NR-PM_1 concentrations measured during CalNex-2010 and LAAQC-2022 (~30%) were notably larger than long-term changes in $PM_{2.5}$ inferred from gravimetric FRM measurements (Method Reference ID: RFPS-1006-145) in Pasadena (~0-10%) (Figure 2.5). While this could be due to the short-term nature

of the campaigns or measurement uncertainties, the aerosol speciation measurements suggest that reduced AN accounts for a majority of the change in NR-PM_1 since 2010, and previous analyses of FRM measurements have noted substantial evaporation of AN aerosol (75-100%) during spring/summer sampling in Los Angeles and elsewhere (Hering et al., 1999; Zhang and McMurray, 1992; Ashbaugh and Eldred, 2004; Chow et al., 2005; Yu et al., 2005).

As shown in Figure 2.5, comparisons of FRM $PM_{2.5}$ measurements with both the AMS measurements and additional $PM_{2.5}$ measurements made using beta attenuation monitors (BAM), a Federal Equivalent Method (FEM EQPM-1013-209), support this evaporative loss (e.g., FRM $PM_{2.5}$ concentrations in Pasadena during CalNex-2010 were ~35% lower than AMS measurements) (SI Section 2.S10). Hourly AMS data agree particularly well with FEM $PM_{2.5}$ measurements made in Glendora, CA during both campaigns (Figure 2.S40). FRM measurements may have therefore underestimated the true decline in $PM_{2.5}$ concentrations over the last decade due to this evaporative artifact (Figure 2.5b). As discussed in more detail in SI Section 2.S10, these potential biases and their impacts on perceived trends in aerosol concentrations/sources, deserve further attention. In contrast to bulk gravimetric measurements, changes in speciated $PM_{2.5}$ measured from 2010 to 2022 in Los Angeles agreed relatively well with changes inferred from the AMS measurements (Figure 2.S43; 2.S44).

Looking forward, our model results suggest that approximately 25% of local SOA is now attributed to sources that are either difficult to manage from a control perspective (biogenics) (~10-15%) or to on-road sources (~10%), whose emissions are expected to continue to decline quickly due to existing regulations (e.g., California LEV-III and LEV-IV and national Tier 3 standards) and increasing adoption of electric vehicles (CARB, 2023; EPA, 2023). The sources of the remaining ~75% of local SOA represent potential regulatory targets whose mitigation through product reformulation (VCPs, asphalt), increased implementation of emission control technologies such as catalytic converters and/or diesel particulate filters (non-road mobile sources), increased adoption of electric alternatives (e.g., lawn and gardening equipment), and improvement and increased usage

of catalytic oxidation devices (cooking emissions) would likely provide considerable further air quality benefits (McDonald et al., 2018; Seltzer et al., 2021a).

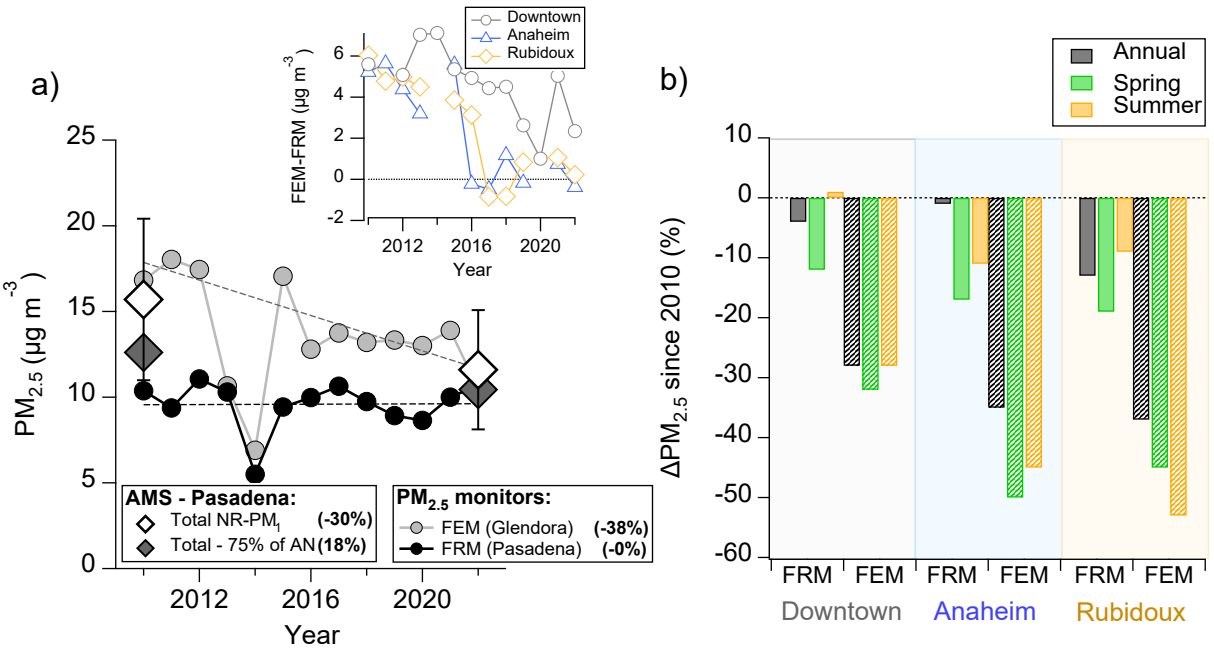

Figure 2.5: Analysis of historical trends in aerosol concentrations in Los Angeles. (a) Comparison of trend in aerosol concentrations inferred from AMS measurements in 2010 and 2022 with trends inferred from FRM (gravimetric) and FEM (beta-attenuation monitor) $PM_{2.5}$ measurements during May and June in Pasadena and Glendora, respectively. White markers represent average NR-PM_1 concentrations measured by the AMS, while grey markers show adjusted concentrations if 75% of AN is removed to represent potential evaporative loss from FRM samples. Inset plot shows the declining difference between May-June FEM and FRM measurements over time at locations in the Los Angeles Basin with co-located FEM and FRM monitors. (b) Inferred trends in $PM_{2.5}$ concentrations measured at three locations in Los Angeles using either FRM or FEM measurements.

While notable increases in OH concentrations are thought to have occurred over the last decade (>50%), comparisons of weekday and weekend OH_{exp} in 2022 suggest that continued reductions in NO_x emissions are unlikely to produce substantial additional increases in local oxidation concentrations (Figure 2.S13). Given that Los Angeles is approaching a NO_x-limited photochemical regime (e.g., Baidar et al., 2015, Parker et al., 2020), continued reductions in mobile source NO_x emissions may be particularly important for local air quality improvement, as controlling NO_x emissions would simultaneously

further reduce nitrate aerosol production, lower peak ozone concentrations, and reduce SOA production rates from non-mobile source emissions through changes in oxidant abundance and potentially NO_3-related ALW concentrations (Figure 2.S19). We note, however, that lower ambient NO_x concentrations may increase SOA yields (e.g., Ng et al., 2007; Crounse et al., 2013; Praske et al., 2018), which could offset the OH- and ALW-related effects on SOA production.

Using a combination of SOA model simulations, analyses of inorganic aerosol precursor emissions inventories, and projected changes in local OH concentrations, we predict that only minor changes in local aerosol concentrations are likely in the near-term unless additional efforts to control emissions from non-road and area emission sources are undertaken (Figure 2.S48) (SI Section 2.S11). Simulated future SOA concentrations are heavily dependent on expected trends in SOA precursor emissions from non-traditional sources (e.g., VCPs) and future modifications to ambient SOA yields due to changing NO_x concentrations, underscoring the importance of additional efforts to refine these predictions. The historical progress made in controlling emissions from mobile sources, and on-road sources in particular, suggests that similarly focused efforts aimed at non-road and area emission sources have the potential to considerably improve local air quality.

2.5 Acknowledgements

We would like to thank Nga Lee Ng, Brian McDonald, Carsten Warneke, and Michael Kleeman for helpful discussions. We would also like to thank the Caltech Facilities Department, and in particular Raul Turcios, for their help during the campaign. This research was funded by the NOAA Climate Program Office's Oceanic and Atmospheric Research Program, grant number NA21OAR4310224.

2.6 Supporting Information

Table of contents

2.S1 Additional measurements during CalNex-2010

2.S1.2 Ammonia (NH_3)

NH_3 was measured during CalNex-2010 using a quantum cascade tunable infrared laser differential absorption spectrometer (QC-TILDAS). Detailed description of instrument design is provided by Ellis et al. (2010). The QC-TILDAS measures NH_3 at the 967 cm^{-1} absorption line using a thermoelectrically cooled pulsed quantum cascade (QC) laser. The inlet of the QC-TILDAS consisted of a 12m heated (40ºC) and insulated 0.95 cm perfluoroalkoxy (PFA) line connected to a 10 cm custom-designed quartz inlet. Data were corrected using periodic zero-air measurements and calibrations performed throughout the campaign. Measured concentrations have an estimated uncertainty of ±10%.

2.S1.2 Nitric acid (HNO_3)

HNO_3 was measured during CalNex-2010 using a negative-ion proton-transfer chemical ionization mass spectrometer (NI-PT-CIMS). Detailed description of instrument design and operation is provided by Veres et al. (2008) and Guo et al. (2017). Acidic species are ionized in the instrument through proton transfer from acetate ions and subsequently detected using a quadrupole mass spectrometer. During CalNex-2010, the NI-PT-CIMS inlet consisted of a 1.3m heated (75ºC) Teflon line. Data were corrected for instrument backgrounds quantified every 190 min. Measured HNO_3 mixing ratios have an estimated uncertainty of ±35%.

2.S1.3 Nitryl chloride ($ClNO_2$)

$ClNO_2$ was measured during CalNex-2010 using an iodide chemical ionization mass spectrometer (CIMS) described extensively in Mielke et al. (2013). $ClNO_2$ was detected as the iodide cluster ions at m/z 208 and m/z 210 using a quadrupole mass spectrometer. During CalNex-2010, sample flow was drawn at a rate of 4 liters per minute through a 10 m long, 1.58 cm outer diameter Kynar tube located approximately 10 m above ground level. A detailed description of the calibration procedure, which involved passing molecular chlorine over concentrated sodium nitrite solution, is provided in Mielke et al. (2013). Measured $ClNO_2$ mixing ratios have an estimated uncertainty of ±30%.

2.S1.4 Hydroxyl radical (OH)

OH mixing ratios were measured during CalNex-2010 using a laser-induced fluorescence assay by gas expansion (LIF-FAGE) technique with the Indiana University FAGE (IU-FAGE) instrument, as described in detail by Griffith et al. (2016). Briefly, the LIF-FAGE technique detects OH using laser-induced fluorescence following expansion of ambient air into a low-pressure chamber. The sampling cell was located approximately 10 m above ground level, and ambient air was drawn into the detection region using a 0.6 mm inlet. Indirect HO_2 measurements were made by intermittently introducing NO into the sampling cell and converting ambient HO_2 into OH for subsequent detection. Calibrations of the IU-FAGE were performed every three days using the UV water photolysis method (Griffith et al., 2016). Measured OH mixing ratios have an estimated uncertainty of ±18%. The detection limit of the IU-FAGE OH measurement was 3.4×10^5 cm^{-3}.

2.S2 Analysis of HR-ToF-AMS organic aerosol data using Positive Matrix Factorization (PMF)

The mass spectra, diurnal profiles, and time series of the four PMF factors resolved from the final LAAQC-2022 and CalNexT-2022 PMF solutions are shown in Figure 2.S4 and S5. Correlations of factor spectra with factors observed during CalNex-2010 are shown in Table S2 and S3, and correlations with measured trace gases and VOCs are shown in Tables S4 and S5. Here we briefly discuss the justification for selecting the four-factor solution in each campaign.

During both campaigns, starting from a three-factor solution, the PMF model resolves factors that appear related to the MO-OOA, LO-OOA, and CIOA/HOA factors resolved in Hayes et al. (2013). The CIOA/HOA factor is difficult to definitively classify as either CIOA or HOA in the three-factor solution. Moving to a four-factor solution clearly separates the CIOA and HOA factors while having little influence on MO-OOA or LO-OOA. In both datasets, the five-factor solution resolves an additional LO-OOA factor with a spectra that correlates somewhat with the limonene + NO_3 spectra reported by Boyd et al. (2017) (R^2 ~ 0.4-0.7) and displays a diurnal profile that increases slightly after sunset, suggesting a possible role for NO_3 chemistry. However, there are no clear indicators for a specific source of this new LO-OOA factor, and correlations with ambient VOC are

inconclusive (e.g., highest R^2 with alkanes, aromatics, and biogenics included in Tables S4 and S5 are 0.32, 0.25, and 0.05, respectively). In both campaigns, the new LO-OOA factor is also relatively well correlated with the other (i.e., original) LO-OOA factor (e.g., $R > 0.7$ during CalNexT-2022), and the most prominent feature in the diurnal profile is an increase midday. The factor may therefore result from splitting and/or mixing of existing factors, which is difficult to conclusively demonstrate (Hayes et al., 2013). Given the difficulty involved in assigning a specific source to the new LO-OOA factor, we conclude that the four-factor solution provides a clearer description of the dataset than the five-factor solution.

Further increasing the number of factors leads to additional factor splitting/mixing, producing new factors that are difficult to classify. As an example, the six-factor solution in the LAAQC-2022 dataset contains two MO-OOA factors that vary in chemical characteristics (O:C of 0.64 and 1.2, respectively) but display little variability in their respective diurnal profiles and lack additional identifying chemical signatures. The presence of two MO-OOA factors also considerably complicates comparison with CalNex-2010. As a result, we conclude that the four-factor solution optimally represents the OA datasets from each campaign and provides the clearest comparison with data collected during CalNex-2010.

2.S3 Calculation of airmass OH exposure (OH_{exp})

We calculated airmass OH_{exp} during each campaign using the average of nine VOC ratios, as shown in Figure 2.S9 (Parrish et al., 2007; Hayes et al., 2013). Emission ratios of VOC relative to CO during LAAQC-2022 and CalNexT-2022 were calculated following the method described in Van Rooy et al. (2021). During LAAQC-2022 and CalNexT-2022, VOC measurements were only made at 5:30, 9:00, and 14:00. As such, we fit a diurnal profile to these OH exposure estimates based on the diurnal trend observed during CalNex-2010. Estimated diurnal trends in OH_{exp} using the average of all nine VOC ratios agree well with ratios calculated using the ratio of 1,2,4-trimethylbenzene to benzene, which has been used in previous work (e.g., Hayes et al., 2015) (Figure 2.S9).

The error in the calculated OH_{exp} estimate in the more recent campaigns based on uncertainties in the measurements (10%) and the calculated emission ratios (~30%) is approximately 35%, which we incorporate into a Monte Carlo analysis of SOA model uncertainty (SI Section 2.S6). We convert OH_{exp} into a photochemical aging timescale for use in the SOA model simulations described below by using an assumed daily-average OH concentration of 1.5 x 10^6 mol. cm^{-3}. Comparisons of average afternoon (14:00-15:00) OH_{exp} estimates from CalNex-2010 and LAAQC-2022 suggest an increase in OH concentrations of ~50-60% since 2010.

We note that, as discussed by Parrish et al. (2007) and Hayes et al. (2013), the OH_{exp} calculation assumes that the VOC measurements were performed at a remote receptor site. If emissions are continuously introduced into an airmass prior to measurement, the OH_{exp} calculation will exhibit a low bias. This results from the fact that aged emissions within an air parcel will have less mathematical "weight" on the OH_{exp} calculation than fresh emissions relative to their volume contribution within the parcel (Hayes et al., 2013). We use a slightly more detailed version of the model developed by Hayes et al. (2013) to estimate this potential error. We assume a hypothetical airmass measured at each diurnal hour is transported for 6 hours over a homogeneous emission source of 1,2,4-trimethylbenzene and benzene prior to measurement. Each hour, emissions are introduced according to the emission ratios calculated during LAAQC-2022 (0.32 pptv $ppbv^{-1}$ for 1,2,4-TMB and 0.68 pptv $ppbv^{-1}$ for benzene). Emissions introduced at each time step are continuously oxidized by ambient OH concentrations until arrival in Pasadena. We increase OH measurements from Griffith et al. (2016) by 55% to account for observed increases in OH_{exp} observed in 2022 for this calculation, although a similar result is expected if the calculation is performed using 2010 emission ratios and OH concentrations. Our simplified model therefore accounts for variable oxidation rates as a function of time, rather than assuming both emissions and oxidation rates are constant during transport. The resulting OH_{exp} error estimate is shown in Figure 2.S10. Ultimately, the effect on simulated diurnally-averaged SOA is minor <20% and the predicted contribution of mobile source emissions is unaffected. Given the minor influence on SOA and the uncertainty in multiple

aspects of the error calculation (e.g., constant six-hour travel time, homogeneous emissions during transport, etc.) we do not attempt to correct photochemical age estimates used in model simulations for this potential bias.

2.S4 Analysis of ambient RO_2 fate

According to the CARB CEPAM inventory, NO_x emissions in Los Angeles County have declined by ~45% since 2010 (CEPAM, 2019). Median ambient afternoon (12:00-16:00) NO mixing ratios were ~1.4 ppbv during LAAQC-2022. Using recommended rate constants for RO_2 reactions with NO (8.6×10^{-12} cm^3 $molec.^{-1}$ s^{-1} at 296 K), HO_2 (1.8×10^{-11} cm^3 $molec.^{-1}$ s^{-1} at 296 K), and HO_2 concentrations measured by Griffith et al. (2016) on weekends during CalNex-2010 (~4.5×10^8 molec. cm^{-3}), we calculate that RO_2 reaction rates with NO still exceed reaction rates with HO_2 by a factor of ~40. However, estimated RO_2 lifetimes at NO concentrations around ~1.4 ppbv are nearly 5s. Praske et al. (2018) have demonstrated that autooxidation rates of functionalized alkane RO_2 (specifically RO_2 formed from 2-hexanol in their experiments) are competitive with NO reactions at RO_2 lifetimes of ~10s. Therefore, while the urban environment in the Los Angeles Basin is likely far from "low-NO_x" conditions from the perspective of NO vs. HO_2 reactivity, RO_2 lifetimes will likely soon be sufficiently long that reaction with NO should not be assumed to be the definitive fate of RO_2 produced from functionalized alkanes, which form from the oxidation of a considerable fraction of anthropogenic SOA precursor emissions (i.e., non-functionalized alkanes). Furthermore, as NO_x emissions continue to decline, it is plausible that RO_2 reaction with HO_2 will eventually become competitive with NO.

2.S5 Model simulation of local SOA formation and the role of mobile source emissions

2.S5.1 Overview of zero-dimensional model

We developed a zero-dimensional model of SOA formation to quantify temporal changes in local SOA sources since 2010. The model design is largely based on previously

developed zero-dimensional models of OA formation in urban environments (Dzepina et al., 2009; Hayes et al., 2015; Ma et al., 2017). Total emissions of OA precursors from on-road, non-road, and area/stationary sources are estimated using the methods described in SI Section 2.S5.2 and are lumped into a smaller set of model species based on volatility and composition. Individual model simulations are performed for each hour of the diurnal cycle. In each simulation, emissions are initialized multiplying background-corrected concentrations of CO (ΔCO) in Pasadena with inventory estimates of lumped precursor emissions from each source relative to CO (Δprecursor / ΔCO) in LA County. Emitted precursors are then oxidized and form SOA according to established parameterizations *(*SI Section 2.S5.2). The total oxidation timescale of each simulation is dictated by the measured OH_{exp} at the same diurnal hour quantified using VOC ratios (SI Section 2.S3).

In the absence of highly time-resolved emissions data, annual emissions were scaled by total annual CO emissions to produce precursor-CO ratios (Δprecursor / ΔCO), which were converted from a mass basis (tons precursor / tons CO) to a molar ratio (pptv precursor / ppbv CO) for implementation into the model. CO is commonly used as a conserved atmospheric dilution tracer in OA source apportionment analyses as it has an atmospheric lifetime of ~1 month while OA formation occurs on timescales of <1 day (Hayes et al., 2015). Scaling inventory-based precursor-CO ratios by measured ΔCO concentrations therefore allows estimation of the initial concentration of OA precursors in the simulated air parcel while accounting for airmass dilution that has occurred during transport (Hayes et al., 2015; Ma et al., 2017). We assumed background CO concentrations of 105 ppbv in 2010 (Hayes et al., 2013) and 80 ppbv in 2022 (Figure 2.S11). Estimates of Los Angeles County emissions from all non-biogenic sources are reported in Table 2.S6.

2.S5.2 Parameterization of emissions and OA formation from individual sources

2.S5*.2.1 Mobile sources*

Mobile source emissions of OA precursors (reactive organic gases (ROG)) and POA implemented in the zero-dimensional SOA model were estimated using scaled inventory data reported by the CARB for Los Angeles County. The EMissions FACtor (EMFAC2021) model is used for initial on-road emissions estimates, while data from the

California Emissions Projection Analysis Model (CEPAM) were used for non-road emissions sources (e.g., off-road equipment, recreational vehicles, commercial harbor craft, farm equipment, etc.) (CEPAM, 2021; EMFAC, 2021).

We note that on-road and non-road mobile gasoline ROG emissions estimates in the South Coast Air Basin (SoCAB) produced by EMFAC (on-road) (54 Gg yr^{-1}) and CEPAM (non-road) (31 Gg yr^{-1}) are 7% and 36% lower than estimates recently reported by McDonald et al. (2018) (58 Gg yr^{-1} from on-road; 52 Gg yr^{-1} from non-road). While we used emissions estimated for Los Angeles County to initialize the model, we assumed that on-road and non-road mobile emissions in Los Angeles County are also underpredicted by 7% and 36%, respectively, and we increased modeled emissions by these magnitudes. Diesel emissions were unadjusted from CARB inventory predictions, as the inventory predictions for on-road and non-road emissions are 40% and 16% larger respectively than those estimated by McDonald et al. (2018) for the SoCAB in 2010. Reducing diesel emissions to obtain agreement with McDonald et al. (2018) in the SoCAB similarly to gasoline emissions would marginally reduce the contribution of on-road sources to SOA; however, as on-road diesel emissions are estimated to account for only 1% of total SOA in 2022, such an adjustment would have virtually no influence on our predicted importance of mobile source emissions.

Volatility distributions of on-road and non-road mobile source OA precursor emissions were parameterized using recently measured, comprehensive volatility-based emission profiles for gasoline and diesel exhaust (Lu et al., 2018). The same volatility profile was used for on- and non-road emission sources burning the same fuel (e.g., gasoline), as measured exhaust volatility distributions are similar (Lu et al., 2018). We used the cold-start gasoline profile reported by Lu et al. (2018) for on- and off-road gasoline sources and the non-diesel particulate filter (DPF) diesel profile for diesel emissions. EMFAC data for Los Angeles County in 2022 suggest that only 14% of total emissions from on-road gasoline vehicles occur after the after-treatment system (catalytic converter) has warmed up (designated “RUNEX” in EMFAC2021 and corresponding to “hot-start” conditions), while the remainder (86%) is emitted while driving without efficient after-treatment (31%), during running losses that bypass after-treatment devices (20%), from diurnal evaporative

emissions (25%), and immediately after a trip while the engine temperature remains elevated (9%). Using the "hot-start" profile, which is enriched in IVOCs relative to the "cold-start" profile, slightly increases SOA formation from gasoline exhaust, but is likely unrealistic given the magnitude of on-road emissions that bypass the catalytic converter, the fact that non-road engines are rarely equipped with exhaust after-treatment technology, and the notable contribution of evaporative emissions, which are expected to be depleted in IVOCs relative to exhaust, to total gasoline emissions. We used the same volatility profile for gasoline exhaust and evaporative emissions. Lu et al. (2018) have demonstrated that gasoline exhaust is considerably enriched in lower volatility species such as IVOCs relative to gasoline fuel, suggesting that the use of the same volatility profile for exhaust and evaporative emissions should produce a conservatively large estimate of the importance of mobile source emissions to the urban SOA budget.

Following Lu et al. (2018), NMOG emissions were apportioned into individual VOC and IVOC volatility bins based on their relative abundance in the emission volatility profile, while POA emissions are apportioned into S/LVOC volatility bins. Initial model precursor concentrations of emissions from each volatility bin (in pptv) were calculated by multiplying precursor-CO ratios by measured background-corrected CO concentrations (ΔCO). Once emitted, VOCs, IVOCs, and S/LVOCs are oxidized and form OA using distinct parameterizations. Volatility bins representative of VOCs were assigned a "volatility analog" from the lumped VOC species simulated by Hayes et al. (2015) and Ma et al. (2017). The oxidation of all gas-phase emissions within a given VOC volatility bin was simulated using the same oxidation rate and product yields as the associated analog. Table 2.S7 lists these volatility bins, their associated lumped volatility analogs, and the mass yields of SVOC oxidation products used to simulate OA formation. The volatility analogs chosen for each volatility bin align well with the composition of each bin reported by Lu et al. (2018) (e.g., the gasoline $\log(C^*) = 10$ bin is predominately alkenes, the $\log(C^*) = 9$ bin is a mixture of alkanes and aromatics, etc.). The volatility analogs chosen produce alkane and aromatic mass fractions within gasoline exhaust of 45% and 26%, respectively, which agrees well with speciated measurements reported by Gentner et al. (2013) (42% alkanes, 26% aromatics). VOC oxidation was simulated using the wall-loss

corrected yields developed by Ma et al. (2017). As described in Ma et al. (2017) incorporation of an aging parameterization in addition to corrections for wall-losses leads to unphysically large SOA yields. Therefore, VOC oxidation products do not age in the base model simulation.

IVOC oxidation and SOA formation was parameterized using the lumped species and SVOC product mass yields described in Lu et al. (2020). As noted by Ma et al. (2017), the rate of gas-wall partitioning of IVOC-derived oxidation products (SVOCs) is expected to be much slower than that for VOC-derived oxidation products given the generally lower volatility of IVOC-derived oxidation products (Ye et al., 2016). As a result of this slower partitioning, the model used by Ma et al. (2017) to correct VOC SOA yields by accounting for vapor wall loss was not able to reproduce SOA yield curves from IVOC oxidation, suggesting a smaller influence of wall losses in IVOC chamber experiments. This aligns with the minor corrections suggested by Zhang et al. (2014) for previously derived high-NO_x SOA yields for long-chain alkanes. We therefore did not implement any estimate of increased IVOC yields to account for vapor wall losses, but we note that this causes model parameterized IVOC yields to potentially represent underestimates. IVOC oxidation products and were aged at a rate of 4×10^{-11} cm^3 mol^{-1} s^{-1}, consistent with previous box- and regional-modeling studies (Murphy et al., 2017; Hayes et al., 2015). Each aging step reduces product volatility by one order of magnitude.

We used vehicular $PM_{2.5}$ composition measurements reported by May et al. (2014) to scale total mobile source $PM_{2.5}$ emissions to POA emissions and to subsequently initialize modeled primary SVOC emissions. POA emissions were estimated to account for 60% and 90% of total on-road and non-road gasoline $PM_{2.5}$ emissions, respectively, while POA emissions are estimated to accounted for 30% of total on-road and non-road diesel-related $PM_{2.5}$ (May et al., 2014). Following the recommendations of Lu et al. (2018), we increased inventory gasoline POA emissions by a factor of 1.4 to account for SVOC breakthrough during measurements of $PM_{2.5}$ emissions from gasoline exhaust. Diesel POA emissions were scaled by a factor of 0.9, as adsorption of IVOCs on sampling filter media more than offsets SVOC breakthrough during recent characterization studies (Lu et al., 2018). SVOC emissions that condense onto the specified background aerosol loading prior to

photochemical aging were assumed to represent POA emissions, while aerosol formed from gas phase SVOC aging is classified as SOA.

Effective SOA yields of gasoline and diesel emissions are shown in Figure 2.S27. The effective yield for gasoline emissions (15%) in the model is larger than the effective yield for Pre-LEV vehicles reported by Zhao et al. (2017) (5%) but lower than the effective yield for LEV vehicles (30%). The SOA yields that the authors report may have also been influenced by vapor wall losses, as the precursor concentrations were low (total OA formation of ~5 μg m^{-3}) and the OH concentrations were moderate (~2 x 10^6 mol. cm^{-3} based on reported photochemical age and experiment timescale) (Zhang et al., 2014). As noted by Zhao et al. (2017), observed yields in their experiments are highly dependent on the NO_x emissions from the vehicles themselves, and therefore it is difficult to determine which effective yield is appropriate for comparison with the ambient atmosphere. Zhao et al. (2017) note that they predict a yield of ~10% for Pre-LEV and LEV gasoline vehicles based on composition and established SOA yields in high-NO_x conditions, which agrees reasonably well with our estimate considering that the yields used by Zhao et al. (2017) are not adjusted for wall losses. We further note that the effective model yield also applies to evaporated gasoline emissions, as we use the same emission profile for exhaust and evaporative emissions. Jathar et al. (2013) report a ~3% SOA yield for evaporated gasoline at an OA mass loading of 10 μg m^{-3}, but the relatively small seed aerosol (7-25 μg m^{-3}) and total OA mass loadings (<15 μg m-3) used in their experiments suggest that vapor wall losses may have been considerable (Zhang et al., 2014; Matsunaga and Ziemann, 2010). As gasoline emissions account for the dominant fraction of on-road SOA produced by the model, any overestimation of the effective SOA yield of gasoline emissions in the model would increase the likelihood that the model overpredicts rather than underpredicts the relevance of on-road emissions to local OA. This would therefore be a conservative error from the perspective of our conclusions.

2.S5.*2.2 Volatile chemical products*

Volatile chemical product emissions used in the base model simulation were calculated using the average of estimates provided by the recently developed VCPy model (Seltzer et al., 2021) and McDonald et al. (2018). VCPy predicts individual compound emissions

using detailed product usage and compositional data, compound-specific physicochemical data to determine evaporation timescales, and estimates of product use timescales. Previous analyses of the VCPy model have confirmed its accuracy in Los Angeles (Seltzer et al., 2021). Detailed description of the datasets used to inform the VCPy model are provided in Seltzer et al. (2021). VCP emissions data for LA County were generated from VCPy directly, while emissions estimates from McDonald et al. (2018) for the SoCAB are scaled to LA County using the relative population in the SoCAB (~17 million) and LA County (~10 million). Speciated VCP emissions were provided directly by VCPy and taken from Table S8 of McDonald et al. (2018). To ensure that the same species emitted by different OA precursor sources have identical oxidation and aerosol formation parameterizations, all alkane and aromatic VOC and IVOC VCP emissions were mapped to the same volatility bin used to simulate oxidation of combustion emissions (Table S7). Emissions of oxygenates and siloxanes are oxidized following the scheme developed by Pennington et al. (2021). We used an effective oxygenate SOA yield of 9.7% calculated from emission-weighted SOA yields of aerosol-forming oxygenates in Los Angeles County produced by VCPy. Terpenes are oxidized and form SOA using the wall-loss corrected yields reported by Ma et al. (2017). The scaled inventory from McDonald et al. (2018) (scaled from the SoCAB to LA County based on population) predicts approximately 33% more VCP emissions than VCPy. As discussed by Seltzer et al. (2021b), differences in predicted emissions arise primarily from differences in predicted evaporation rather than differences in product usage. Mass fractions of individual lumped species in total VCP emissions predicted by McDonald et al. (2018) and by VCPy are shown in Figure 2.S29. We calculated emission ratios (ER) of each lumped species relative to CO from each inventory (e.g., ΔALK5/ΔCO) and used the average ER value for each lumped species as an input to the base model simulation.

2.S5.*2.3 Cooking emissions*

Cooking OA precursor emissions were incorporated into the model using $PM_{2.5}$ emissions published by the CARB CEPAM inventory for cooking activities (commercial charbroiling, deep fat frying, and cooking – unspecified) in Los Angeles County (CEPAM, 2021). All $PM_{2.5}$ emissions were assumed to represent SVOC, and emissions were

apportioned into individual SVOC volatility bins using the average of published volatility profiles for unoxidized canola oil, olive oil, and beef tallow (Takhar et al., 2019), which are commonly used cooking oils in charbroiling and deep fat frying. Gas-phase SVOC were aged at a rate of 4 x 10^{-11} cm^3 mol^{-1} s^{-1}, similarly to SVOCs from mobile sources. Sensitivity simulations suggest that using any of the individual profiles or the Robinson et al. (2007) volatility profile used by previous modeling studies (Hayes et al., 2015; Ma et al., 2017) modifies the diurnal average cooking OA mass loading by -11% to +20% depending on the specific profile used. Cooking-related ROG emissions were negligible (1 ton per day in 2022) in the CEPAM inventory compared to total emissions from other sources (total of 227 in 2020) and cooking $PM_{2.5}$ emissions (7.7 tons per day in 2020) and were therefore excluded from the base model. However, ROG emissions from cooking-activities used by the CARB inventory are based on a study conducted in 1998, and it is unclear whether these emission factors account for the presence of catalytic oxidizers (SCAQMD, 2021). The ROG emission factors listed in the CEPAM documentation are up to two orders of magnitude lower than more recent measurements conducted with a PTR-ToF-MS (Klein et al., 2016), depending on the type of cooking method used. Increasing inventory emissions using the ratio of emission factors for deep fat frying and commercial charbroiling published by Klein et al. (2016) to that used in the CEPAM inventory increases cooking-related daily ROG emissions from 1.3 tons to 33.7 tons. Assuming a relatively large yield of 15%, this factor of 26 increase in cooking ROG emissions increases diurnally averaged cooking OA mass loadings in 2022 by 30% or 0.16 $\mu g\ m^{-3}$. Most of the increase is due to increased mass loadings midday when photochemical ages are longer than a few hours.

2.S5.*2.4 Asphalt Emissions*

Asphalt emissions in the South Coast Air Basin (SoCAB) were recently reported by Khare et al. (2020). Emissions in Los Angeles County were calculated by scaling SoCAB emissions by the relative amount of CO emitted in each location estimated by the CEPAM inventory. Scaling by other reasonable metrics such as total land area or population produce emission estimates 14% larger and 5% smaller, respectively, than scaling by CO

concentrations. These differences are well within the 50% uncertainty reported for asphalt emissions in the SoCAB (Khare et al., 2020).

Emissions were apportioned into individual volatility bins using the speciated emission profile reported for road asphalt at 60ºC (Khare et al., 2020). The EPI-SUITE program is used to determine pure liquid vapor pressures for calculation of compound saturation concentrations (C*). IVOCs, which account for 85% of total emissions, were mapped to the appropriate aromatic or alkane volatility bin developed by Lu et al. (2020). To avoid introducing additional uncertainty by varying the OA formation parameterization depending on the emission source, the aging processes and SVOC product yields associated with asphalt emissions in each volatility bin are identical to the parameterizations used for gasoline, diesel, and VCP emissions in the same bin. The alkane and aromatic fractions of asphalt emissions following this lumping procedure are 57% and 35% respectively, which agrees relatively well with measurements reported by Khare et al. (2020) (68% and 32%, respectively). The remainder of simulated asphalt emissions (8%) are unspeciated SVOCs ($C^* < 100$ μg m^{-3}). The effective SOA yield from asphalt emissions using this framework (~30% without accounting for IVOC oxidation product aging) (Figure 2.S28) is somewhat larger than the amount predicted when assuming a fixed SOA yield of 21% for asphalt emissions, a value estimated for primary road asphalt exposed to sunlight (Khare et al., 2020).

2.S5.*2.5 Petrochemical facility emissions*

Emissions from petrochemical facilities in Los Angeles County were taken from the CARB CEPAM inventory (CEPAM, 2021). We included all emissions from "Petroleum Production and Marketing" except those from oil and gas production, to avoid double counting fugitive oil and gas emissions. The estimate of total emissions in the SoCAB in 2010 (13.45 Gg) agrees relatively well with the value reported by McDonald et al. (2018) (12 Gg). Emissions were speciated using the average of nine EPA SPECIATE profiles for emissions from chemical/industrial plants and oil storage facilities (profiles 2456, 2457, 2461, 2462, 2485, 2487, 2488, 2489, and 2490). Only a small fraction of petrochemical facility emissions (<20%) are predicted to be capable of forming SOA based on these

speciation profiles. SOA forming emissions were apportioned to the appropriate volatility bins used in simulation of SOA formation from other sources.

2.S5.*2.6 Fugitive oil and gas emissions*

Fugitive oil and gas emissions for Los Angeles County in 2010 were scaled from estimates for the SoCAB provided by McDonald et al. (2018). We scaled emissions to LA County using the ratio of fugitive natural gas emissions predicted in LA County relative to the SoCAB by the CEPAM inventory (94%). Emissions estimates reported by the CEPAM for the SoCAB in 2010 are approximately half as large as those estimated by McDonald et al. (2018). Oil and gas emissions were speciated using the average of 20 EPA SPECIATE profiles (95243, 95254, 95255, 95256, 95257, 95260, 95270, 95271, 95274, 95275, 95286, 95287, 95288, 95290, 95291, 95292, 95297, 95298, 95303, 95315). Due to the dominant contribution of methane in fugitive oil and gas emissions (96.3% on average based on SPECIATE profiles), predicted normalized excess mixing ratios of OA precursors analyzed in Figure 2.S26 and simulated SOA mass loadings were unaffected by changes in the assumed emissions from fugitive oil and gas sources. As a result, we assumed 2022 emissions were unchanged from 2010 values.

2.S5.*2.7 Biogenic emissions*

Given the short lifetime of isoprene midday (<1 hour), the fact that the spatial distribution of biogenic emissions and CO emissions may not be similar, and the fact that OH_{exp} estimates quantified using aromatic species are likely not appropriate for modeling biogenic emissions, we used a distinct, simplified Lagrangian method to estimate biogenic SOA formation in LA County. Air mass backward trajectories ending at Pasadena were first calculated using the Hybrid Single-Particle Lagrangian Integrated Trajectory (HYSPLIT4) model (Stein et al., 2015) at 14:00 local time, the approximate time of urban plume arrival, every third day of each campaign. Meteorological data at a resolution of 12 km x 12 km were obtained from the North American Mesoscale Forecast System (NAMS) archive and used to inform the HYSPLIT model. The travel time from the coast to Pasadena is then calculated for each trajectory using the combined dataset (i.e., 2010 and 2022), resulting in average midday transport times of 5.5±2.5 hr.

We used this data to calculate the integrated amount of SOA formed from isoprene and monoterpene oxidation for each hour of the diurnal cycle, assuming a 5 hr (base), 3 hr (low estimate), or 8 hr (high estimate) effective oxidation timescale. For simplicity, we assumed that measured isoprene and monoterpene (α-pinene, β-pinene, and limonene) concentrations are spatially homogeneous across the basin and identical to concentrations measured in Pasadena. During LAAQC-2022 and CalNexT-2022, α-pinene and β-pinene measurements were only performed from 5:30-6:30, 9:00-10:00 and 14:00-15:00. We calculated the average concentrations measured during each sampling period and assume that concentrations are consistent across the diurnal cycle. We assumed the ratio of limonene to β-pinene was the same in 2022 as in 2010. We used OH concentrations measured by Griffith et al. (2016) to simulate BVOC SOA production during CalNex-2010, and 2010 concentrations were increased by 40% in simulations of LAAQC-2020 conditions to account for the increase in afternoon OH_{exp} estimates observed in 2022. Ozone concentrations measured during each campaign were also incorporated to simulate monoterpene SOA formation during transport. We assumed a 5% SOA yield for isoprene photooxidation and a 20% yield for terpene photooxidation and ozonolysis. These photooxidation yields align well with those calculated by Ma et al. (2017) accounting for vapor wall losses (3.5% for isoprene and 22.5% for terpenes at an ambient loading of 10 μg m^{-3}). A 20% yield for terpene ozonolysis at 10 μg m^{-3} is approximately double typical values observed in chambers experiments, but as discussed by Nah et al. (2016), yields from α-pinene ozonolysis in the absence of vapor wall losses are expected to be about twice as large as those historically observed experimentally.

2.S6 Estimation of uncertainties in OA precursor emissions/sources

Monte Carlo analysis was used to estimate uncertainty in the contribution of individual emissions sources to the SOA budget. Emission uncertainty was incorporated by multiplying the inventory-based emissions from each source (e.g., on-road gasoline) by a scalar value randomly sampled from a normal distribution with a mean of one and a

standard deviation representative of the estimated 1σ emissions uncertainty. A total of 1,000 simulations were performed to derive distributions for uncertainty estimation.

2.S6.1 Gasoline and diesel emissions

Uncertainties in gasoline emissions are estimated by comparing emissions estimates published by McDonald et al. (2018) using a fuel-based method with those reported by CARB inventories for the SoCAB in 2010. McDonald et al. (2018) assume evaporative emissions represent 40 ± 20% of total gasoline-related emissions. To obtain individual estimates of on-road and non-road uncertainties, we scale emissions reported for on-road and non-road exhaust in Table S6 of McDonald et al. (2018) to include evaporative emissions (i.e., assume exhaust emissions are 60% of the total). Comparison of the EMFAC total on-road gasoline ROG emissions in the SoCAB (54.3 Gg yr^{-1}) with the McDonald on-road estimate (58.3 Gg yr^{-1}) suggests a difference of ~7%. This value is considerably smaller than the propagated uncertainty obtained from the McDonald et al. (2018) estimate of on-road exhaust uncertainty and evaporative emissions uncertainty (~52%). We therefore assume a 2σ uncertainty of 52% (1σ = 26%) for total gasoline ROG emissions. Non-road gasoline emissions estimates from the CARB CEPAM inventory are 36% lower than those reported by McDonald et al. (2018). We use the McDonald et al. (2018) estimate in the model, as discussed in as discussed in SI Section 2.S5.2, and assume a 1σ uncertainty of 36%. For diesel emissions, we use the on-road and non-road uncertainty estimates published in Table S6 of McDonald et al. (2018) and assume that these represent 2σ uncertainties, leading to 1σ uncertainty estimates of 25% and 28% for on-road and non-road emissions, respectively.

2.S6.2 Volatile chemical product emissions

Volatile chemical product emission uncertainties are derived by comparing estimates reported by the VCPy model (Seltzer et al., 2021b) and McDonald et al. (2018) for LA County. Estimated VCP emissions for the SoCAB from McDonald et al. (2018) are scaled to LA County using the relative population in the SoCAB (~17 million) and LA County (~10 million). For the base model simulation, we use the average (98.7 Gg yr^{-1}) of the VCPy (78.1 Gg yr^{-1}) and McDonald et al. (2018) estimates (119.3 Gg yr^{-1}) estimates and

assume that the 1σ uncertainty can be approximated by the relative difference between the average value and the individual estimates (21%).

2.S6.3 Asphalt emissions

Khare et al. (2020) report asphalt I/SVOC emissions in the SoCAB of 4.3-12.6 Gg yr^{-1}. We scale the midpoint of this range (8.45 Gg yr^{-1}) by the ratio of CO emissions in LA County to those in the SoCAB to produce an estimate of LA County emissions (5.41 Gg yr^{-1}) for use in the base model simulation. We assume that the 2σ uncertainty in asphalt emissions can be approximated by the difference between the midpoint and the bounds of the range reported by Khare et al. (2020) (51%) (1σ uncertainty of 25%).

2.S6.4 Cooking emissions

Given the lack of multiple independent estimates of cooking emissions in LA County or the SoCAB, and the noted variability in cooking emissions with type of food and/or oil, cooking temperature, and cooking style (Klein et al., 2016; Takhar et al., 2019), we conservatively assume that cooking $PM_{2.5}$ emissions have a 2σ uncertainty of 80%. Additional uncertainty is introduced by the lack of SOA formation from cooking-related VOC emissions. As described above, incorporation of cooking-related SOA using recent estimates of cooking-related ROG emissions and reasonable SOA yields increases cooking aerosol mass loadings by ~21%, which is within the range of the emissions uncertainty estimated here. Further observational studies of cooking emissions from realistic sources (i.e., at the exhaust stack) are clearly needed to refine regional emissions estimates.

2.S6.5 Fugitive oil and gas and petrochemical emissions

The uncertainty in fugitive oil and gas emissions is taken directly from McDonald et al. (2018) (23% - 2σ). Given lack of available data, we conservatively assign an 80% uncertainty (2σ) to petrochemical emissions. In the base simulation, oil and gas and petrochemical emissions combined account for less than 2% of anthropogenic urban OA, and as such their uncertainty estimates have virtually no impact on model results.

2.S6.6 Biogenic SOA

In addition to uncertainties in biogenic SOA yields, major uncertainties in our estimate of biogenic SOA formation originate from our assumption of homogeneous terpene and

isoprene concentrations throughout the urban core and the assumption of a constant airmass transport timescale. Without spatially resolved measurements, the uncertainty introduced by the homogenous concentration assumption is difficult to quantify. However, Washenfelder et al. (2011) predicted that isoprene concentrations increased considerably during airmass transport from the coast to Pasadena, suggesting that our assumption of constant concentrations may introduce a positive bias in simulated biogenic SOA. In the absence of more spatially explicit data, we base our uncertainty estimate on the difference in calculated biogenic SOA formed when using the mean calculated afternoon transport time (5 hr) relative to the transport time scale associated with ±1 standard deviation from the calculated mean (3 hr or 8 hr). This results in a 2σ uncertainty estimate of 55%. A scenario in which actual average ambient isoprene and terpene concentrations throughout the urban core were only 50% of concentrations measured in Pasadena would therefore fall into this uncertainty range, provided our estimate of airmass transport time based on backward trajectory data is reasonable.

2.S7 Assessing modeled SOA precursor emissions estimates through comparison of emission ratios (ER) of VOCs to CO

We assessed the accuracy of precursor emissions estimates included in the model by comparing measured and predicted emission ratios (ER) of numerous alkane and aromatic VOCs to CO. To calculate modeled ER, we multiplied Los Angeles County emissions from each OA precursor source (i.e., on-road gasoline emissions) by the fractional abundance of individual species within the emissions and divide by county-wide CO emissions. The mass fraction of individual VOCs within gasoline and diesel exhaust were taken from measurements in the Caldecott Tunnel in Oakland, CA by Gentner et al. (2013) in July 2010. These estimates agree well with estimates for on-road vehicles by May et al. (2014) (~82% of assessed compounds agree within reported standard deviations). The speciation of evaporative gasoline and diesel emissions is based on measurements reported by Gentner et al. (2013) for gasoline and diesel fuel. VCP ER values were calculated by multiplying the average VCP emissions in LA County predicted by VCPy and McDonald et al. (2018) with the average speciation of LA County VCP emissions predicted by VCPy

and McDonald et al. (2018). In cases where the mass fraction of a given species within total VCP emissions is not provided in Table S8 of McDonald et al. (2018), we use the value from VCPy. Petrochemical and oil and gas emissions were speciated using the EPA SPECIATE database, as described above. Asphalt emissions were predicted to contribute negligibly to emissions of the analyzed species, as the largest species analyzed were C_{10} while asphalt emissions are predominately C_{12} to C_{20} (Khare et al., 2020). Results of the ER analysis are shown in Figure 2.S26 and demonstrate that the model reproduces measured values with relatively low bias in 2010 and 2022; however, increasing modeled gasoline SOA precursor emissions by ~30% in 2010 and reducing them by ~20% in 2022 considerably improves the ER comparison.

2.S8 ISOROPPIA-II simulations of nitrate partitioning

Given the differences in meteorology and sulfate concentrations between campaigns, we first used the ISORROPIA-II thermodynamic model to assess whether changes in average $NO_{3,inorg.}$ aerosol concentrations represented reductions in concentrations of total nitrate ($NO_{3,inorg.}$ + HNO_3), which would indicate changes in nitrate production, or could have simply resulted from partitioning differences. For these calculations, ISORROPIA-II was run in "forward" mode using average total aerosol- and gas-phase diurnal concentrations of SO_4, NH_3+NH_4, NO_3+HNO_3, and Chl measured during CalNex-2010. Simulations were performed with meteorological parameters constrained to match those measured during either CalNex-2010, LAAQC-2022, or CalNexT-2022.

We then compared the ratios of $NO_{3,inorg.}$ concentrations observed between the 2022 campaigns and CalNex-2010 (i.e., $NO_{3,inorg\text{-}2022}/NO_{3,inorg\text{-}2010}$) with ratios predicted by ISORROPIA-II if only average meteorological parameters had changed (i.e., $NO_{3,ISOROPPIA\text{-}2010\ w/2022\ met}/NO_{3,ISOROPPIA\text{-}2010\ w/2010\ met}$) or if meteorological conditions and total concentrations (e.g., gas + aerosol) or nitrate and/or sulfate had changed. We compared ratios rather than absolute concentrations given that ISORROPIA-II overpredicts $NO_{3,inorg}$ aerosol measured at night during CalNex-2010 and underpredicts $NO_{3,inorg}$ midday (Guo et al., 2017). The reasons for these discrepancies remain poorly

understood but may be related to HNO_3 uptake on coarse mode sea salt particles (Guo et al., 2017).

As shown in Figure 2.S32, these calculations imply large reductions in nighttime concentrations of total nitrate during the 2022 campaigns relative to CalNex-2010 (i.e., predicted ratios are larger than observed ratios when total nitrate is assumed constant since 2010) but only modest changes in daytime nitrate concentrations, assuming only meteorological parameters were different between the campaigns.

However, given the dependence of AN partitioning on sulfate concentrations, we performed additional simulations that adjusted sulfate concentrations in line with our observations. On average, we measured approximately 35-50% less sulfate during LAAQC-2022 and CalNexT-2022 than was observed during CalNex-2010. This decline aligns with the predicted reduction in sulfur oxide emissions in Los Angeles County since 2010 (~35%) and the likely effect of establishment of the North American Emission Control Area on regional shipping vessel emissions since 2010. Ensberg et al. (2013) estimated that long-range transport accounted for approximately 25-35% of ambient sulfate measured in Pasadena during CalNex-2010, suggesting changes in regional shipping emissions likely influence local concentrations. We assumed total ammonium concentrations were unchanged since 2010 based on CARB predictions of ammonia emissions in Los Angeles County (CEPAM, 2019).

Figure 2.S32 demonstrates that when sulfate concentrations are reduced in line with measured aerosol concentrations, the ISORROPIA-predicted $NO_{3,inorg.}$ ratio aligns with measured ratios midday during LAAQC-2022 and underpredicts ratios measured midday during CalNexT-2022, even without any invoking any reductions in total nitrate concentrations, suggesting similar or larger concentrations of total nitrate during the daytime in 2022 than in 2010. In contrast, the nighttime ratios remain considerably different when sulfate concentrations are reduced, with larger inferred total nitrate concentrations at night during CalNex-2010 than in 2022.

The reduction in daytime sulfate concentrations is therefore predicted to have shifted AN partitioning towards the gas phase, assuming ammonium concentrations have remained relatively constant. We hypothesize this shift results from the fact reducing midday sulfate

concentrations has only a small influence on the abundance of "free" ammonia (increase of ~15%) but considerably increases the AN equilibrium disassociation constant (Seinfeld and Pandis, 2016).

We note that the thermodynamic model results, which suggest similar total nitrate concentrations midday during all three campaigns discussed here, disagree with the trend in NO_z concentrations shown in Figure 2.S16, as a decline in NO_z implies a decline in total nitrate unless the speciation of NO_z has changed drastically. The reasons for this discrepancy remain unclear and warrant further investigation using direct nitric acid measurements/modeling.

2.S9 Zero-dimensional modeling of overnight nitrate aerosol formation

We developed a zero-dimensional model of overnight NO_x chemistry to assess the impacts of reduced NO_x emissions on production of both inorganic ($NO_{3,inorg.}$) and organic ($NO_{3,org.}$) nitrate aerosol. Model simulations begin at 19:00 local time and simulate NO_x and BVOC emissions, gas-phase chemistry, formation and hydrolysis of N_2O_5, and aerosol partitioning of HNO_3 until 06:00 the following day. The gas-phase reactions included in the model are listed in Table S10. As described below, we first constrained trace gas and BVOC concentrations measured in 2010 and performed simulations to estimate critical parameters related to NO_3 aerosol formation (e.g., N_2O_5 uptake coefficient). Following model initialization, trace gas and BVOC concentrations were unconstrained, NO_x and BVOC emissions were tuned to reproduce 2010 measurements, and NO_x emissions were then reduced to assess the impact on NO_3 aerosol formation. Five total simulations were performed. The first (base) simulation (Simulation #1 -Base, below) using unconstrained trace gases is described above and is meant to reproduce conditions observed during CalNex-2010. Comparisons of simulated overnight concentrations of trace gases, $ClNO_2$, HNO_3, $NO_{3,inorg.}$, and BVOC with measurements during CalNex-2010 are shown in Figure 2.S36.

In the second simulation (Simulation #2 – LAAQC-2022 TG), we reduced overnight NO_x emissions by 45% according to CARB emissions estimates for Los Angeles County (CEPAM, 2019), reduced initial NO_2 concentrations (i.e., at 19:00) and increased initial O_3 slightly to match observations made during LAAQC-2022. Total aerosol surface area concentrations were kept constant to assess the implications of changing gas-phase chemistry in the absence of any changes in meteorology or aerosol concentrations. In the third simulation (Simulation #3 – LAAQC-2022 TG & Adj. NH_4NO_3), we adjusted trace gases as in the second simulation while also allowing aerosol surface area to change according to changes in overnight production of $NO_{3,inorg}$ aerosol and associated ALW. The fourth simulation was further used to assess the effects of reductions in non-nitrate aerosol species and associated ALW on $NO_{3,inorg.}$ production through changes in aerosol surface area available for N_2O_5 hydrolysis. Finally, we performed a fifth simulation (Simulation #4 – Adj. TG, SA, Met.) similar to the fourth in terms of trace gases and aerosol surface area concentrations, in which meteorological parameters were also adjusted to match those measured during LAAQC-2022.

For each simulation, prior to simulating overnight chemistry, the ISORROPIA-II thermodynamic model (Fountoukis and Nenes, 2007) was used to calculate mass loadings of inorganic aerosol liquid water (ALW) and aerosol-phase concentrations of H^+ to enable parameterization of N_2O_5 hydrolysis (i.e., HNO_3 formation) and HNO_3 partitioning for various hypothetical total concentrations (i.e., gas + aerosol) of sulfate, ammonium, and nitrate. For Simulations #1-3, we assumed that total overnight concentrations of sulfate and ammonium were equivalent to those measured during CalNex-2010. We then created a lookup table of ALW and aqueous H^+ concentrations by performing overnight ISORROPIA-II calculations while varying the total amount of nitrate from ~3 to 15 μg m^{-3} and maintaining overnight sulfate and ammonium concentrations equivalent to those measured during CalNex-2010. As the zero-dimensional model simulation proceeds, the ALW and H^+ concentrations calculated by ISORROPIA-II for the model-predicted amount of total nitrate and the current model time step (e.g., 23:05 with specific observed meteorological parameters) were used to update aerosol surface area and acidity values for the next model time step. For Simulation #4, the total overnight sulfate and OA

concentration was adjusted to match measurements during LAAQC-2022, while the total ammonia concentration (gas + aerosol) was assumed constant following CARB emission predictions for Los Angeles County (CEPAM, 2019). For Simulations #1-#4, average overnight meteorological conditions measured from Caltech Hall during CalNex-2010 were used as inputs to the ISORROPIA-II model. In the final simulation, these meteorological parameters were adjusted to match values measured during LAAQC-2022. The additional contribution of organic species to aerosol liquid water was estimated using Eq. 5 in Guo et al. (2015). Organic species are assumed to have the median hygroscopicity (κ) observed in CalNex-2010 in all model simulations (Guo et al., 2017).

Aerosol surface area concentrations measured during CalNex-2010 used in calculation of N_2O_5 hydrolysis rates were corrected to account for calculated ALW content uncharacterized by SMPS due to drying upstream of the instrument (Hayes et al., 2013). When adjusting NR-PM_1 concentrations to match those measured during LAAQC-2022 (Simulation #3 and Simulation #4), we modified the initial dry aerosol surface area concentration following the relationship between total AMS NR-PM_1 mass and submicron aerosol surface area measured during CalNex-2010. This allowed us to estimate the average dry submicron aerosol surface area at 19:00 during LAAQC-2022 in the absence of direct SMPS measurements.

Heterogeneous hydrolysis of N_2O_5 to form HNO_3 is parameterized using a reactive uptake probability (γ) of 0.007 and a nitryl chloride yield (Φ) of 0.7 to reproduce total overnight NO_3 formation and nitryl chloride ($ClNO_2$) production measured during CalNex-2010 (Figure 2.S36) when trace gas and BVOC concentrations are constrained. While the $\gamma\Phi$ product (0.0049) used here is slightly smaller than the average value observed during CalNex-2010 reported by Mielke et al. (2013) (0.008), it is well within the range of values observed (0-0.4) and produces reasonable amounts of overnight gas-phase HNO_3, nitrate aerosol, and nitryl chloride production in the constrained 2010 simulation (Figure 2.S36). We assume a constant $\gamma\Phi$ product regardless of simulation, despite the likely dependence on aerosol composition, given the disagreement between established parameterizations and direct measurements of $\gamma\Phi$ observed previously (Mielke et al., 2013). We note that an increasing contribution of OA to total NR-PM_1 mass loadings over time may have caused

reductions in γΦ (Mielke et al., 2013). The lack of NH_3 and HNO_3 measurements in 2022 prevents accurate assessment of aerosol acidity, which inhibits our ability to use overnight AN formation in 2020 to constrain changes in γΦ, as reduced AN formation could be the result of either reduced HNO_3 production through N_2O_5 hydrolysis or reduced HNO_3 partitioning due to increasingly acidic aerosol. Reductions in γΦ since 2010 would increase the predicted reduction of overnight NO_3 formation and therefore would not influence our conclusions.

Partitioning of HNO_3 formed from N_2O_5 hydrolysis between the gas and particle phases is calculated using Eq. 7 in the Supplemental Information of Guo et al. (2017). The HNO_3 partitioning coefficient is calculated during model run using estimates of inorganic (ALW) and aerosol-phase H^+ produced from the ISORROPIA-II model. We use an activity coefficient product for H^+ and NO_3^- ($\gamma_{H+}\gamma_{NO3-}$) of 0.4. The $\gamma_{H+}\gamma_{NO3-}$ product is held constant throughout the simulations given the agreement observed between calculated partitioning of HNO_3 and the partitioning predicted by ISORROPIA-II. The resulting estimates of aerosol acidity and the particle phase fraction of NO_3 in each simulation are shown in Figure 2.S38.

The model directly simulates monoterpene emissions to predict organic NO_3 aerosol formation and ensure accurate nitrate radical reactivity during simulations with reduced NO_x emissions. Monoterpene emissions are estimated by minimizing the difference between measured and modeled monoterpene concentrations.

Monoterpene emissions were assumed to follow the temperature dependence reported by Guenther et al. (1993) in all simulations. The model assumes that overnight isoprene emissions are negligible. Overnight concentrations of all simulated BVOC are shown in Figure 2.S37. We assumed a constant SOA yield for NO_3 oxidation of all simulated monoterpenes of 25% (Fry et al., 2014), while the SOA yield from NO_3 oxidation of isoprene is assumed to be negligible for simplicity. Applying an isoprene SOA yield of 10-20% increases overnight organic NO_3 aerosol formation by 0.07 to 0.15 μg m^{-3} and has no influence on our conclusions.

We assumed an overnight OH concentration of 1 x 10^5 cm^{-3} in our base simulations. Overnight OH concentrations measured by Griffith et al. (2016) during CalNex-2010 were

frequently below the detection limit of the Fluorescence Assay by Gas Expansion instrument (4.4 x 10^5), and true overnight OH concentrations are therefore highly uncertain. However, increasing the estimated overnight OH concentration to 2 x 10^5 cm^{-3} has little influence on predicted overnight $NO_{3,inorg.}$ production assuming 1) OH concentrations and N_2O_5 uptake coefficients were constant between simulations and 2) N_2O_5 uptake coefficients are tuned to achieve model-measurement agreement in $NO_{3,inorg.}$ production in Simulation #1 (Figure 2.S39).

As noted in the main text, the final model simulation (Simulation #5), which is meant to best represent conditions observed during LAAQC-2022 (e.g., trace gases, aerosol concentrations, and meteorology) underpredicts measured $NO_{3,inorg.}$ We evaluated whether this discrepancy could be due to changing overnight OH concentrations or changes in the N_2O_5 uptake coefficient. Briefly, Hansen et al. (2021) demonstrated that NO_2 and CO accounted for at least one-third of overnight OH reactivity during CalNex-2010. If overnight OH production has not appreciably changed, which is reasonable given the similar meteorology (and as a result the inferred strength of local terpene emissions) and overnight ozone concentrations, the decline in OH reactivity may have led to an increase in overnight OH concentrations. Approximately half of OH reactivity was unaccounted for by measured species during CalNex-2010, and a portion of this reactivity may also be attributable to anthropogenic sources whose emissions have declined (Hansen et al., 2021). While Figure 2.S39 shows that we can produce the same overnight $NO_{3,inorg}$ production using constant OH concentrations of either 1x10^5 cm^{-3} or 2x10^5 cm^{-3} by tuning the N_2O_5 uptake coefficient and assuming it is constant between simulations, if we instead assume that OH increased from 1x10^5 cm^{-3} in 2010 to 2x10^5 cm^{-3} in 2022, the predicted amount of $NO_{3,inorg}$ in Simulation #5 increases considerably and only underpredicts measured $NO_{3,inorg}$ by 20% (as opposed to 45% in the scenario with a constant overnight OH concentration of 1x10^5 cm^{-3}).

2.S10 Comparison of AMS and $PM_{2.5}$ measurements at stationary monitors in Los Angeles County

As noted in the main text, the average NR-PM_1 concentration measured during LAAQC-2022 (11.0 μg m^{-3}) was approximately 30% lower than the average concentration measured during CalNex-2010 (15.7 μg m^{-3}). This apparent decline stands in contrast to the consistency in gravimetric FRM $PM_{2.5}$ concentrations measured at the Pasadena South Coast Air Quality Monitoring District (SCAQMD) site during each campaign (10.5 μg m^{-3} during CalNex-2010 and 10.3 μg m^{-3} during LAAQC-2022) and the minor change in annual average $PM_{2.5}$ concentrations from 2010 to 2022 (decline of 10%).

However, while AMS NR-PM_1 concentrations were only slightly higher than FRM $PM_{2.5}$ measurements made in Pasadena during LAAQC-2022, NR-PM_1 concentrations measured during CalNex-2010 exceeded nearby FRM $PM_{2.5}$ concentrations by ~35% on average (Figure 2.S41).

Aerosol composition measurements suggest that reduced ammonium nitrate (AN) concentrations (~55% reduction between CalNex-2010 and LAAQC-2022) account for ~50% (~2.5 μg m^{-3}) of the total reduction in average NR-PM_1 mass loadings observed between CalNex-2010 and LAAQC-2022. Changes in observed OA mass loadings were more modest (<1 μg m^{-3}). Previous analyses of gravimetric aerosol measurements using FRM in Los Angeles and other cities in California have observed substantial evaporation of AN aerosol (80-90%) during spring/summer sampling (Hering et al., 1999; Zhang et al., 1992; Ashbaugh and Eldred, 2004; Chow et al., 2005; Yu et al., 2005). If we assume that 75-100% of AMS-measured AN evaporated from nearby $PM_{2.5}$ filter samples prior to quantification and decrease AMS concentrations accordingly, agreement between the measurements improves considerably (Figure 2.5 in the main text).

We further investigated the potential occurrence of AN evaporation by comparing $PM_{2.5}$ mass loadings measured in the Los Angeles Basin using the gravimetric FRM (Method Reference ID: 390 RFPS-1006-145) (24-hr integrated samples) with measurements performed using a beta attenuation monitor (BAM) (Federal Equivalent Method, FEM EQPM-1013-209) (BAM-1020; Met One Instruments). The BAM instrument measures $PM_{2.5}$ mass loadings continuously by recording attenuation of emitted beta rays by the filter sample using a scintillation detector, resulting in a high time-resolution measurement (1 hr) thought to be less influenced by evaporation artifacts than typical gravimetric FRMs,

as only modest meteorological changes typically occur during a single sampling period (Le et al., 2020).

Figure 2.5 demonstrates that in contrast to the consistency in average FRM $PM_{2.5}$ concentrations measured in May and June in Pasadena since 2010, FEM $PM_{2.5}$ concentrations measured in Glendora, approximately 15 miles to the east, declined by 38% over the same period. As shown in Figure 2.S42, FEM $PM_{2.5}$ measurements made during CalNex-2010 and LAAQC-2022 at four locations across the Los Angeles Basin show approximately the same relative decline from 2010 to 2022 as that inferred from the AMS measurements. Three of these locations have co-located FRM and FEM monitors that have been sampling continuously over the last decade (Downtown Los Angeles, Anaheim, and Rubidoux). As shown in Figure 2.5 in the main text, at each of these locations, the decline in $PM_{2.5}$ concentrations measured by the FEM monitors since 2010 considerably exceeds the decline inferred from the FRM measurements. The absolute differences between FRM and FEM measurements observed during May and June sampling in 2010 (4-6 $\mu g\ m^{-3}$) were also comparable to the differences observed between the AMS and FRM measurements in Pasadena during CalNex-2010 (~6 $\mu g\ m^{-3}$). Furthermore, the differences between the FEM BAM and gravimetric FRM measurements have declined appreciably with time at each location (Figure 2.5), in agreement with the AMS-measured decline in the absolute mass loading and fractional contribution of AN in Pasadena.

While the BAM-FRM comparison supports declining concentrations of evaporative aerosol components, previous comparisons of BAM and FRM measurements have found indirect evidence for positive artifacts in BAM measurements due to acid gas absorption on the glass fiber filters used in BAM instruments (e.g., HNO_3) (Le et al., 2020; Liu et al., 2013). Teflon filters used in FRM measurements, in contrast, are not thought to absorb acidic gases as efficiently (Le et al., 2020; Liu et al., 2013). While difficult to precisely quantify, we use relative differences in measured concentrations of inorganic species on Teflon and glass fiber filters by Liu et al. (2013) (e.g., 36% larger concentrations of NO_3 aerosol on glass fiber than Teflon filters) and AMS-measured NR-PM_1 speciation in Pasadena to calculate an upper limit estimate of the positive artifact in the BAM measurements of ~1.5-2 $\mu g\ m^{-3}$ in 2010. This represents only 20-30% of the difference

between BAM and FRM measurements in downtown Los Angeles in 2010. Furthermore, as HNO_3 exists in equilibrium with AN, the declining difference between the BAM and FRM methods since 2010 supports reduced production of AN aerosol even if the HNO_3 absorption bias in the BAM measurement has historically been substantial. Our analysis therefore suggests that AN mass loadings have declined considerably over the last decade, driven largely by reduced mobile source NO_x emissions, but this decline may not have been fully captured by regulatory FRM monitors due to sampling artifacts (i.e., AN evaporation) (Hering et al., 1999; Chow et al., 2005).

We note that this potential explanation for the AMS-FRM discrepancy does not explain the only modest reductions in NO_3 $PM_{2.5}$ concentrations measured in downtown Los Angeles using nylon filter samples coupled with ion chromatography. Nylon filters retain volatilized nitric acid with much greater efficiency than Teflon filters, and as such are thought to be associated with minimal negative artifacts (Yu et al., 2005). While the average inferred changes in spring/summer $PM_{2.5}$ concentrations of organic carbon, sulfate, and ammonium measured downtown (23-45%, 26-35%, and 50-65%, respectively) (Figure 2.S43) agree well with average differences observed between the CalNex-2010 and LAAQC-2022 AMS measurements (10%, 35%, and 55%, respectively), the measured change in nitrate aerosol downtown (21-38%) is somewhat smaller than the difference in the AMS measurements (55%).

However, the decadal change in nitrate aerosol in Rubidoux (~50% as an annual average and as much as 68% for summertime periods) aligns well with the changes observed from the AMS measurements and exceeds the changes observed downtown, suggesting that temporal trends in individual aerosol components may exhibit considerable spatial variability (Figure 2.S44).

The relatively minor change in nitrate $PM_{2.5}$ concentrations measured downtown is also difficult to reconcile with the considerable simultaneous decline in ammonium aerosol concentrations (Figure 2.S43). We also observed considerably variable levels of agreement between daily average concentrations of inorganic aerosol species measured in Pasadena using the AMS and downtown using nylon filter samples during LAAQC-2022 and CalNexT-2022 (Figure 2.S45). Specifically, while AMS and $PM_{2.5}$ measurements of

ammonium aerosol agree relatively well during both campaigns, $PM_{2.5}$ concentrations of nitrate and sulfate aerosol measured in downtown Los Angeles were notably larger than PM_1 concentrations measured in Pasadena.

To investigate this further, we estimated trends in AN-associated nitrate $PM_{2.5}$ concentrations using an ion balance analysis. Specifically, we assumed that given the considerable measured concentrations of $PM_{2.5}$ nitrate aerosol, all measured sulfate was likely fully neutralized by available ammonium (or other available cations such as sodium and magnesium), as particles would otherwise be highly acidic, shifting nitrate partitioning to the gas phase (Seinfeld and Pandis, 2016). As such, we first calculated ammonium sulfate (AS)-associated ammonium concentrations assuming that either (1) all "free" sodium and magnesium (i.e, not needed to balance measured chloride concentrations) was associated with nitrate anions or (2) 50% of "free" sodium and magnesium was associated with sulfate, with the remainder balanced by nitrate. In scenario 1, all measured sulfate is assumed to be ammonium sulfate, while some sulfate is associated with non-ammonium cations in scenario 2. All ammonium not associated with ammonium sulfate was assumed to be available to form AN. We then calculated the trend in AN-associated NO_3 since 2010 using the AN-associated ammonium concentrations. As shown in Figure 2.S46, this calculation suggests that the concentration of AN-associated NO_3 has declined by ~70-80% or more during spring/summer conditions in downtown Los Angeles and Rubidoux, CA since 2010.

We then calculated the maximum possible nitrate concentration associated with other, non-NH_4 cations measured downtown (i.e., sodium, magnesium, and calcium) to determine whether measured nitrate concentrations could be fully accounted for with available cations. As shown in Figure 2.S47, the sum of NH_4-associated NO_3 (from the ammonium balance) and non-NH_4-associated NO_3 (i.e., NO_3 from $NaNO_3$, $Mg(NO_3)_2$, and $Ca(NO_3)_2$) reproduces both annual and seasonal trends in average measured total NO_3 concentrations with reasonable accuracy in both locations. The closure of the nitrate budget supports the conclusion from Figure 2.S46 that the concentration of NH_4-associated NO_3 may have declined considerably since 2010, in agreement with the AMS measurements and the FRM-BAM comparison discussed above. It may therefore be the case the relative fraction of

nitrate associated with other, non-NH_4 cations has increased. Such a trend would likely be missed when comparing AMS measurements, given that other nitrate species are more likely than AN to be associated with super-micron particles not transmitted through the AMS aerodynamic lens (e.g., $NaNO_3$) and/or not vaporize quickly enough to be detected (Hayes et al., 2013). Additional measurements and direct instrumental comparisons are clearly warranted to further investigate the potential evaporative artifact discussed above, the sources of nitrate $PM_{2.5}$ aerosol, and the resulting implications on our interpretation of trends in aerosol production .

2.S11 Estimated future trends in NR-PM_1 concentrations in Los Angeles

Figure 2.S48 displays predicted trends in average mass loadings of NR-PM1 components and OA subtypes for typical May-June conditions in 2025, 2030, and 2035. Simulations of future SOA concentrations use on-road and non-road gasoline and diesel emissions estimates from the CARB EMFAC and CEPAM inventories scaled similarly to the 2010 and 2022 simulations described in SI Section 2.S5.1. VCP emissions are assumed to increase according to relative changes in population, and population projections are obtained from the California Department of Finance (California Department of Finance, 2021). Cooking emissions are obtained from CEPAM model projections. Asphalt and biogenic emissions are assumed unchanged relative to the base simulation. Diurnal concentrations of ΔCO are reduced according to predicted changes in the sum of on-road and non-road CO emissions in Los Angeles County estimated by the CARB EMFAC and CEPAM inventories, respectively. Based on the analysis of weekend effects in afternoon OH_{exp} estimates in 2020 as shown in Figure 2.S13, we assume that diurnal trends in airmass OH exposures and therefore model aging timescales are unchanged from 2020-2035. The CEPAM model predicts an 18% reduction in NO_x emissions over the next 15 years, which is smaller than the average change in NO concentrations on weekends in 2022 (-48%), when average OH_{exps} were similar to average weekday values (Figure 2.S13).

SOA yields are unadjusted relative to the 2022 simulation given the modest predicted changes in NO_x emissions; however, application of low-NO_x SOA yields produces SOA concentrations approximately twice as large as those predicted using base SOA yields

(Figure 2.S48), underscoring the importance of improving understanding of future trends in RO_2 fate. We assume that alkane and aromatic SOA yields in low-NO_x conditions are increased by 0-100% and 200-300%, respectively, relative to high-NO_x conditions, based on available laboratory data (Ng et al., 2007; Cappa et al., 2013; Zhang et al., 2014). Isoprene SOA yields are increased by a factor of two in low-NO_x simulations following the Odum two-product model parameterizations presented in Carlton et al. (2009). Monoterpene SOA yields are also increased by a factor of two following results reported by Eddingsaas et al. (2012) for α-pinene photooxidation in the presence of ammonium sulfate seed. While experimental investigations of oxygenate SOA yields have been published recently, it remains unclear how SOA yields of various classes of oxygenated emissions, including oxygenated aromatics (Charan et al., 2020), glycol ethers (Li and Cocker et al., 2018), and siloxanes (Charan et al., 2021), vary as a function of NO concentration. As products of oxygenate emissions are predicted to account for <5% of AU-OA, reasonable adjustments of oxygenate yields (-50% to 300%) have a minor influence on the predicted contribution of SOA.

The total concentration of MO-OOA is assumed unchanged from 2020-2035. CIOA and HOA concentrations are adjusted following predicted cooking emissions and mobile source PM2.5 emissions from the CARB CEPAM model, respectively. Concentrations of SO_4, NO_3, and NH_4 aerosol are assumed to change proportionally with projected emissions of SO_2, NO_x, and NH_3 emissions, respectively, in Los Angeles County reported by the CARB CEPAM inventory. While such direct scaling of concentrations based on emissions changes in clearly simplistic, it nevertheless demonstrates that only minor changes in aerosol concentrations are predicted unless 1) currently unaccounted for emissions reductions are implemented or 2) non-linear/synergistic effects on aerosol production are considerable.

Figures 2.S1-2.S48

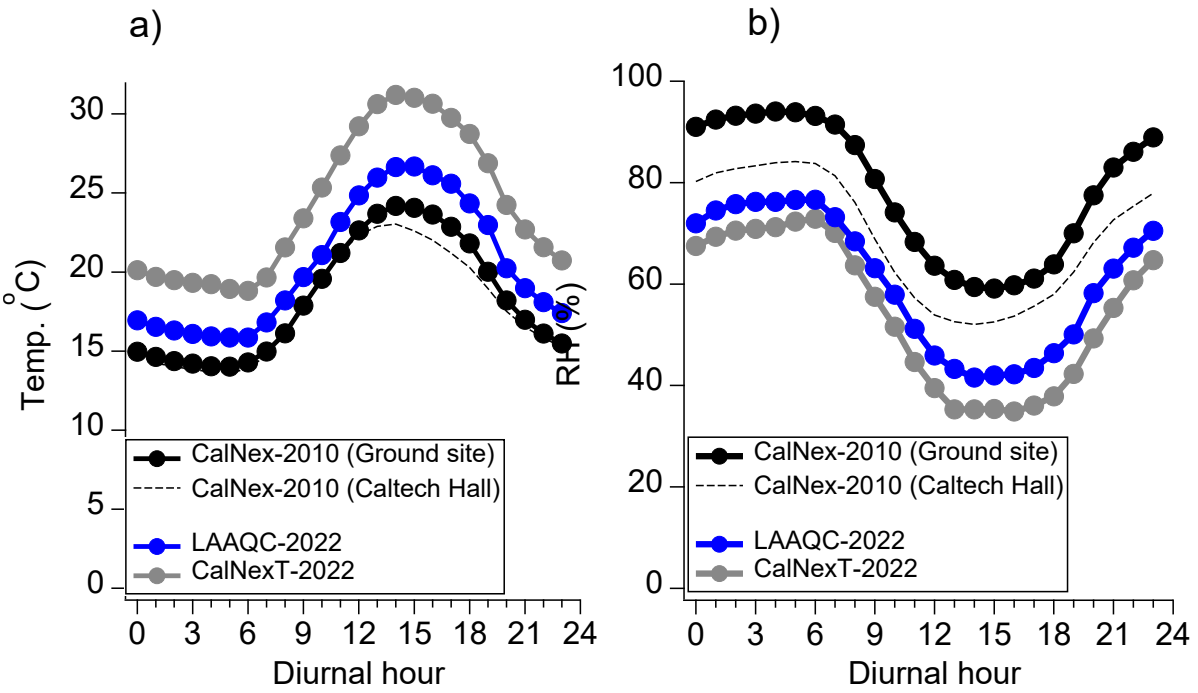

Figure 2.S1: Diurnal profiles of (a) temperature and (b) relative humidity during CalNex-2010, LAAQC-2022, and CalNexT-2022. Data collected from both the ground-site and the top of Caltech Hall during CalNex-2010 are shown. Meteorological data were measured in 2022 from the roof of Linde Robinson Laboratory during the 2022 campaigns (approximately 100m from Caltech Hall).

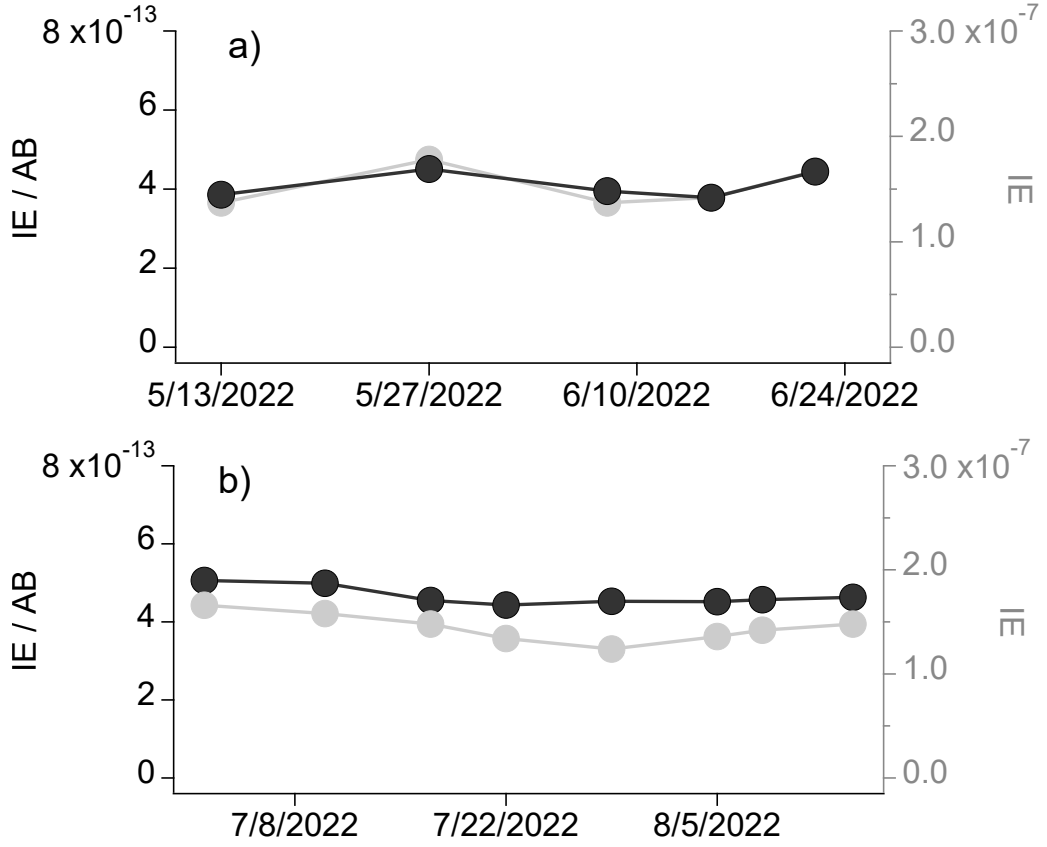

Figure 2.S2: Time series of the HR-ToF-AMS ionization efficiency (IE) and the IE normalized to the instrumental airbeam (IE/AB) during (a) LAAQC-2022 and (b) CalNexT-2022.

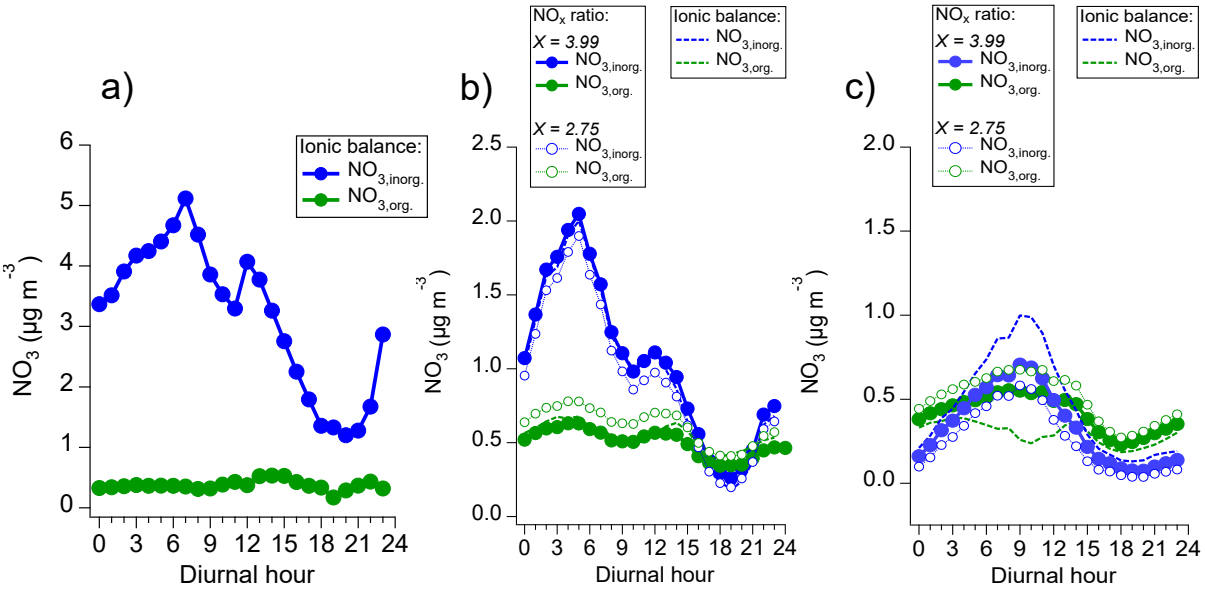

Figure 2.S3: Diurnal profiles of organic ($NO_{3,org.}$) and inorganic ($NO_{3,inorg.}$) nitrate aerosol calculated during (a) CalNex-2010, (b) LAAQC-2022, and (c) CalNexT-2022 using either the NO_x ratio method or the ionic balance method. The NO_x ratio method was not used to analyze CalNex-2010 data as ammonium nitrate calibration data were unavailable.

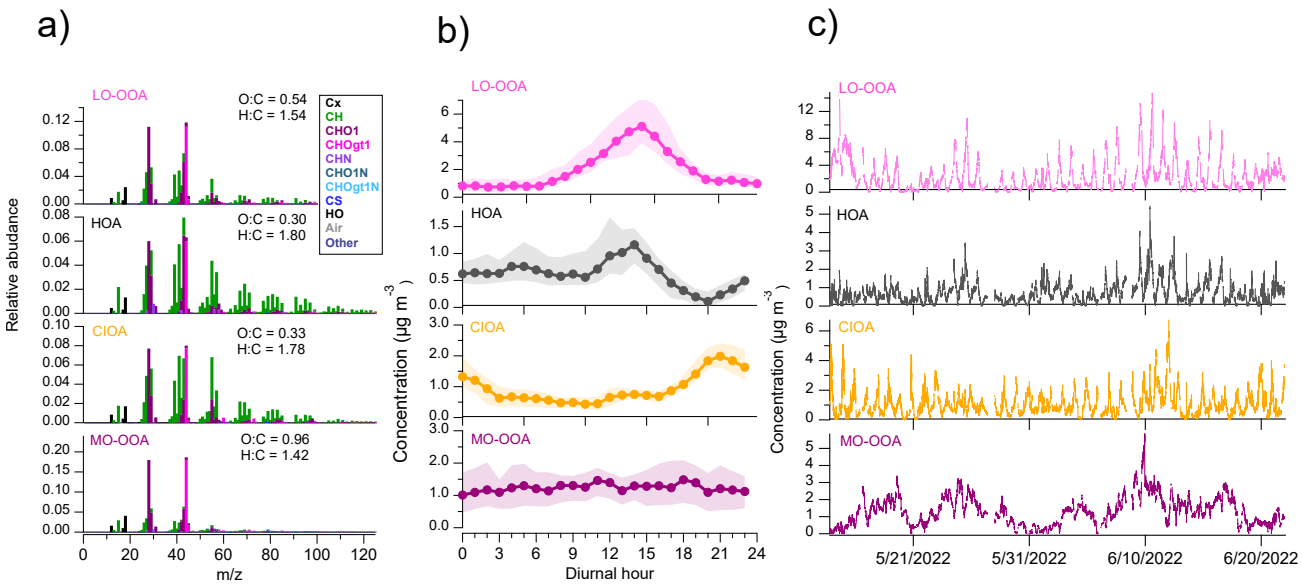

Figure 2.S4: (a) Mass spectra, (b) diurnal profiles, and (c) time series of PMF factors resolved from the LAAQC-2022 OA dataset. Median diurnal values are shown, and shaded regions represent the interquartile range of measurements.

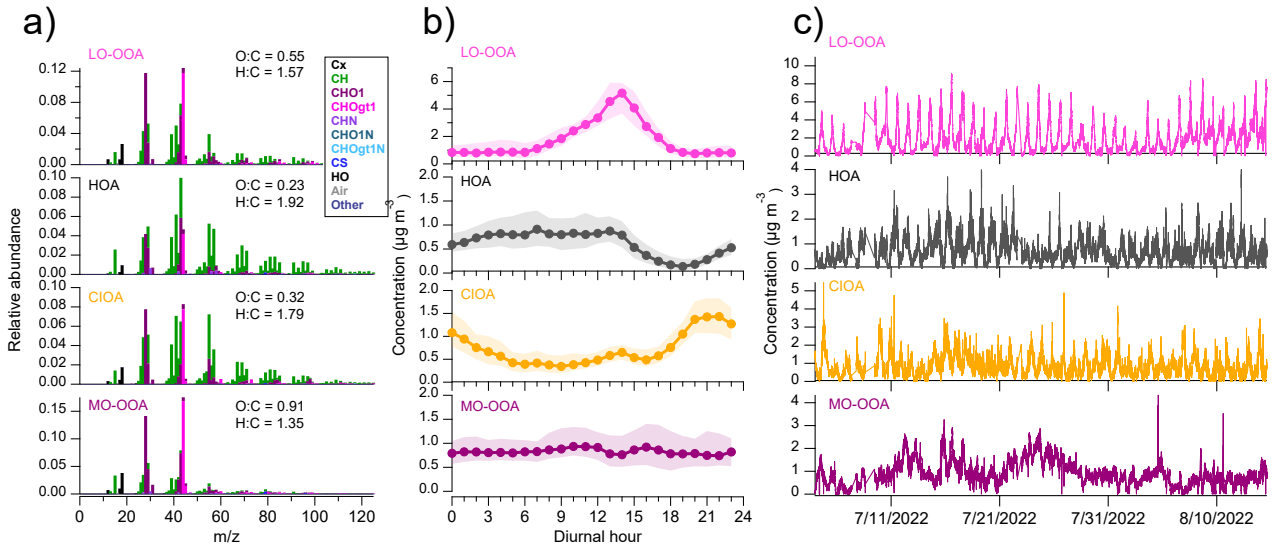

Figure 2.S5: (a) Mass spectra, (b) diurnal profiles, and (c) time series of PMF factors resolved from the CalNexT-2022 OA dataset. Median diurnal values are shown, and shaded regions represent the interquartile range of measurements.

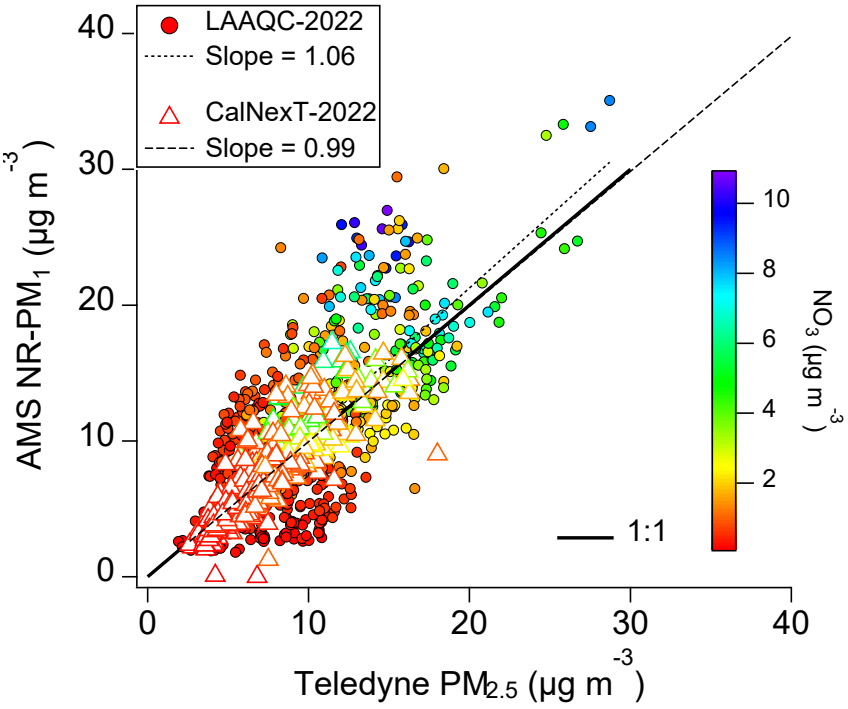

Figure 2.S6: Comparison of AMS NR-PM_1 and Teledyne T640 $PM_{2.5}$ concentrations measured during LAAQC-2022, and CalNexT-2022.

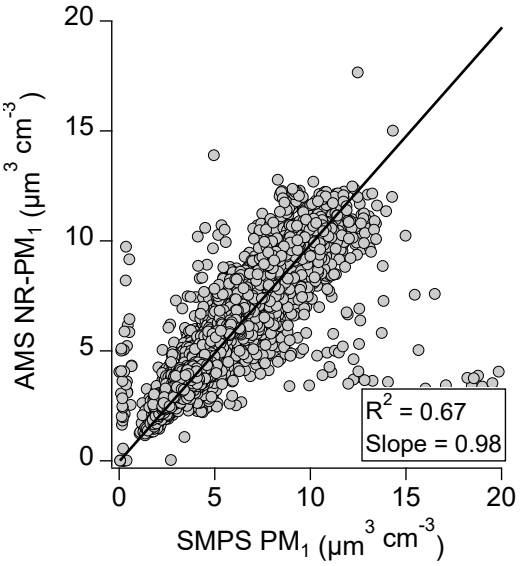

Figure 2.S7: Comparison of AMS and SMPS PM_1 volume measured during CalNexT-2022. Mass loadings measured by the AMS were converted to volume concentrations by assuming organic and inorganic aerosol densities of 1.25 and 1.77 g cm^{-3}, respectively.

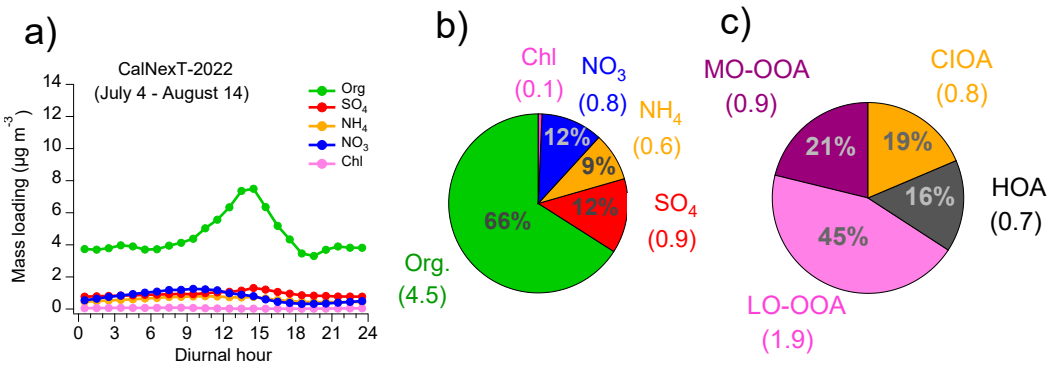

Figure 2.S8: (a) Diurnal concentrations of NR-PM_1 species measured by the AMS during CalNexT-2022. (b) Average concentrations of NR-PM_1 species. (c) Average concentrations of PMF factors.

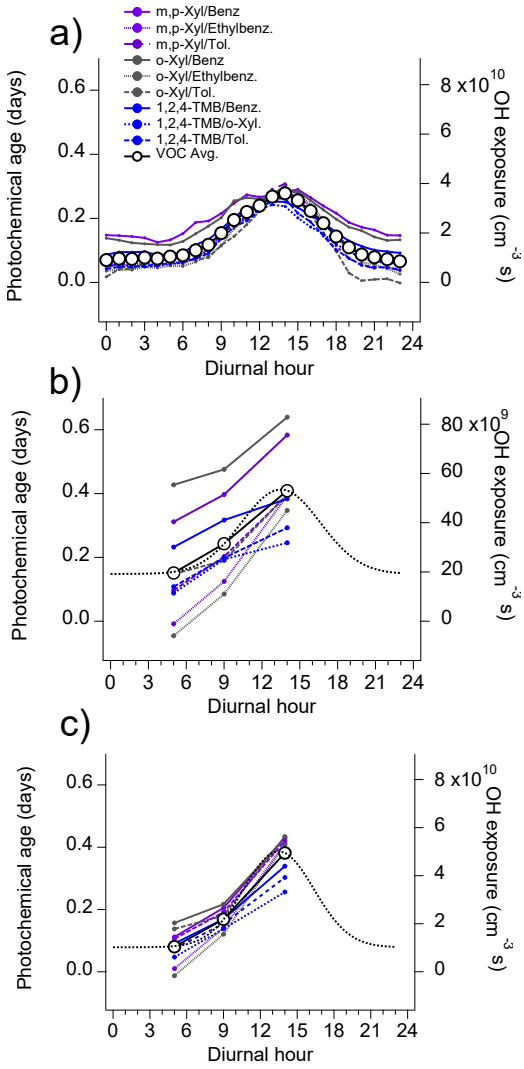

Figure 2.S9: Diurnal estimates of airmass OH exposure and inferred photochemical age during (a) CalNex-2010, (b) LAAQC-2022, and (c) CalNexT-2022. Photochemical age was calculated from OH exposure assuming an OH concentration of 1.5 x 10^6 cm^{-3}. Diurnal fits were applied to measurements made at 5:30, 9:00, and 14:00 during LAAQC-2022 and CalNexT-2022.

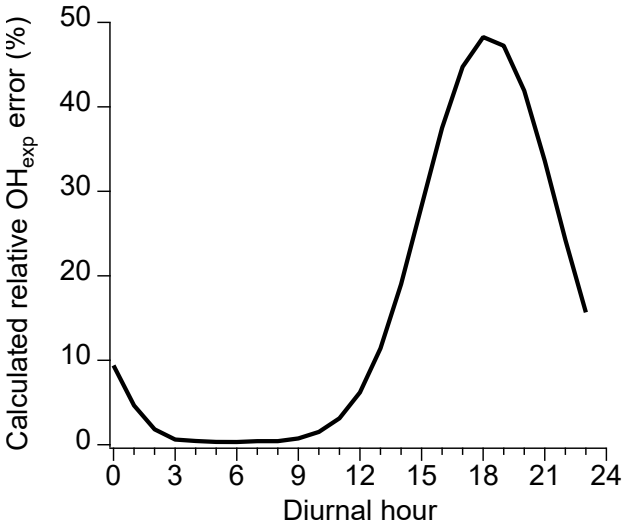

Figure 2.S10: Estimated potential relative error in calculated OH exposure due to the assumption that VOC measurements were performed at a remote receptor site (SI Section 2.S3).

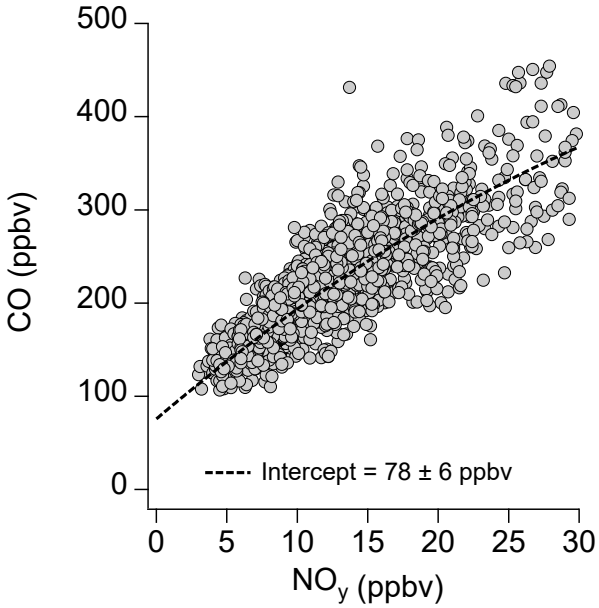

Figure 2.S11: Relationship between CO and NO_y measured during LAAQC-2022 and CalNexT-2022. A three-term polynomial fit was used to determine the background CO concentration, which is taken as the intercept of the fit (i.e., concentration associated with negligible ambient NO_y).

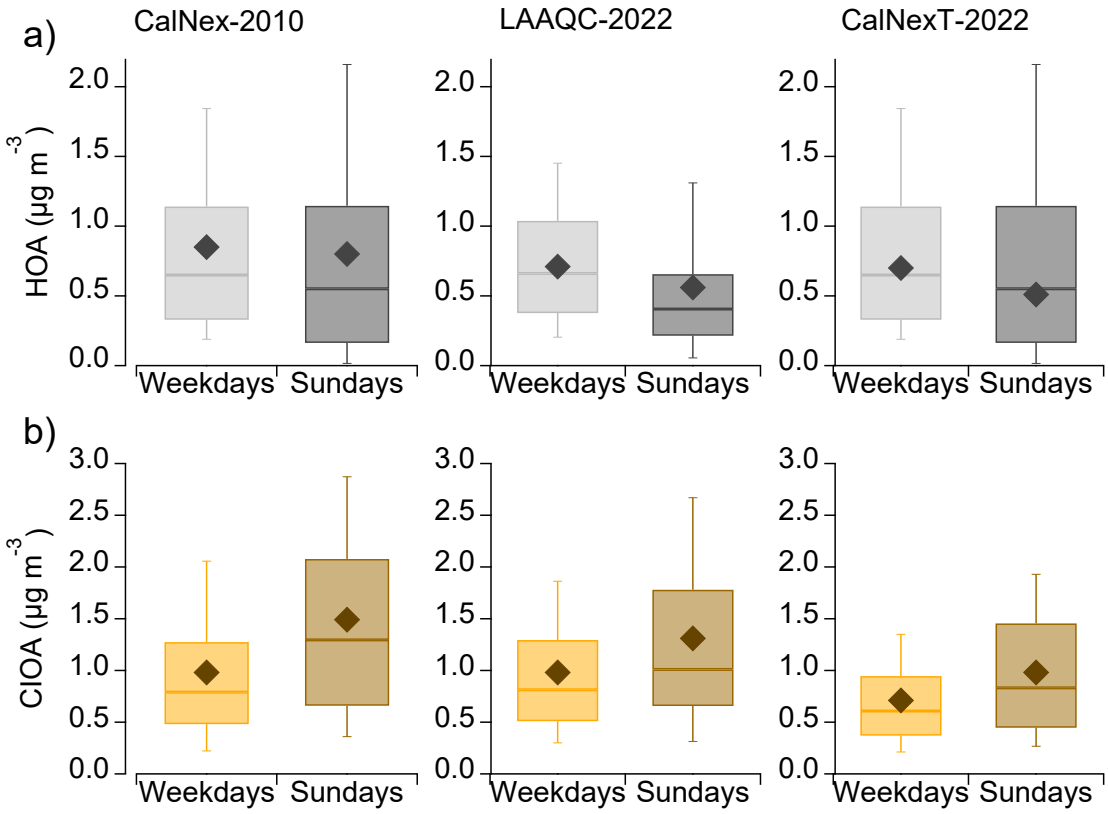

Figure 2.S12: Concentrations of (a) HOA and (b) CIOA on weekdays and Sundays during CalNex-2010, LAAQC-2022, and CalNexT-2022. Diamond markers represent averages. Box plots show the 10th, 25th, 50th, 75th, and 90th percentile values.

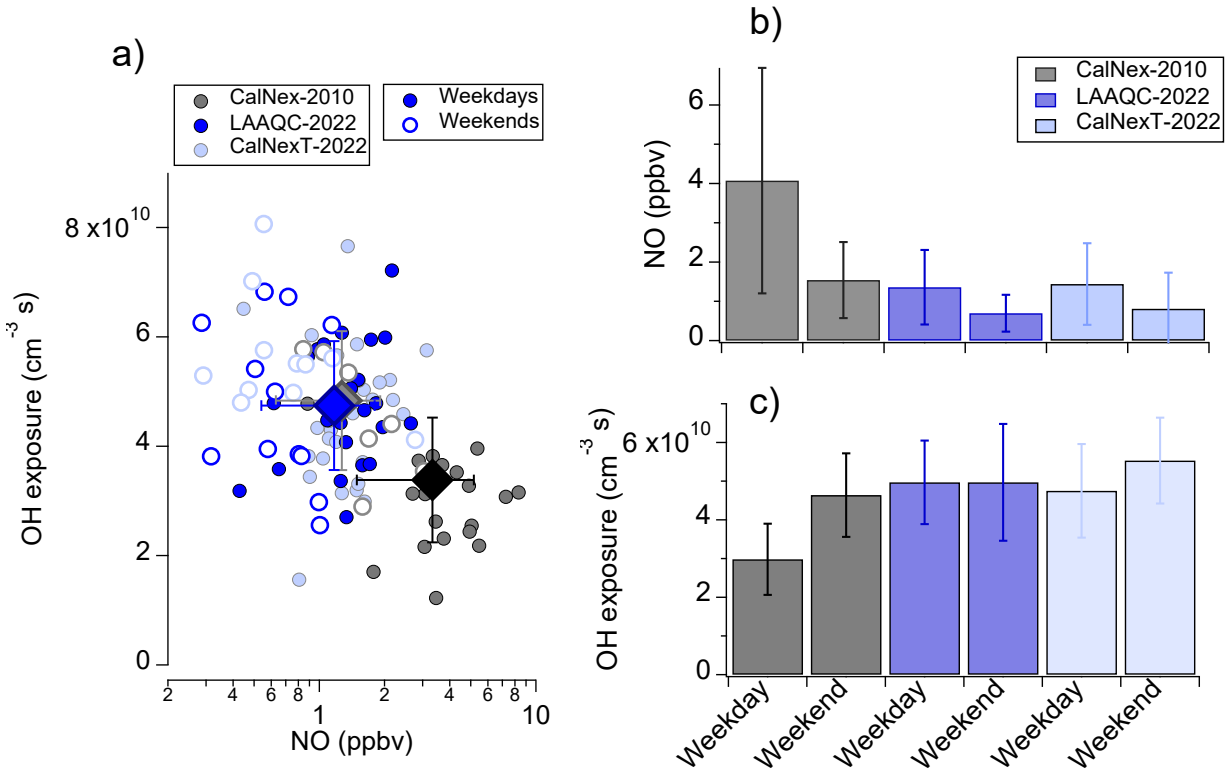

Figure 2.S13: (a) Observed relationship between inferred afternoon airmass OH exposure (OH_{exp}) and ambient NO concentrations during CalNex-2010, LAAQC-2022, and CalNexT-2022. Filled circles denote weekday values, while open circles represent weekends. Diamond markers indicate average values measured during each campaign. (b) Comparison of average afternoon (11:00-17:00) NO concentrations on weekdays and weekends during each campaign. (c) Comparison of afternoon (14:00) OH exposure estimates on weekdays and weekends during each campaign. Error bars represent standard deviations.

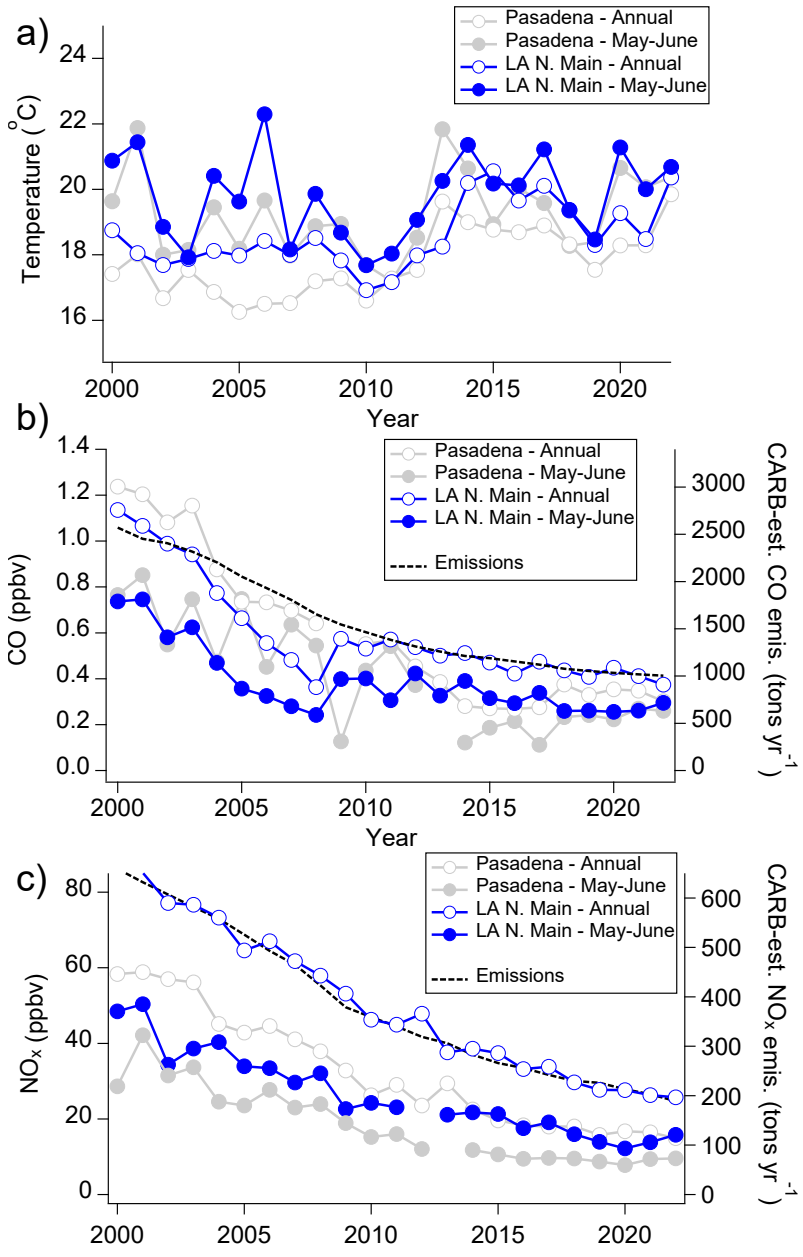

Figure 2.S14: Time series of (a) temperature, (b) CO, and (c) NO_x measured at the Pasadena and downtown (LA North Main) South Coast Air Quality Management District (SCAQMD) monitoring sites. CARB-estimated emissions of CO and NO_x in Los Angeles County are also shown.

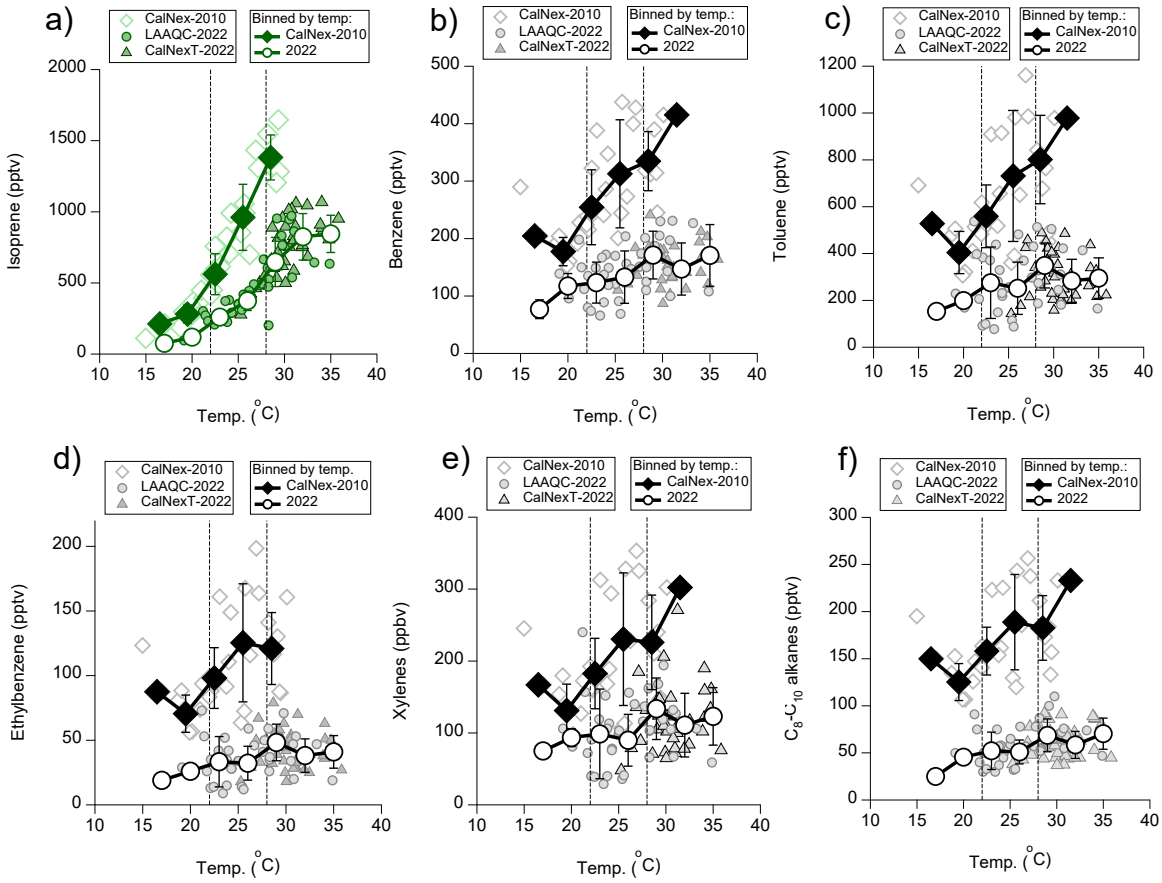

Figure 2.S15: Observed variability in midday (11:00-16:00) concentrations of (a) isoprene, (b) benzene, (c) toluene, (d) ethylbenzene, (e) xylenes, and (f) C_8-C_{10} alkanes with temperature during CalNex-2010, LAAQC-2022, and CalNexT-2022. Larger makers denote average values binned by temperature. Error bars represent standard deviations. Averages calculated from 2022 data have been offset by 0.5ºC to show standard deviations.

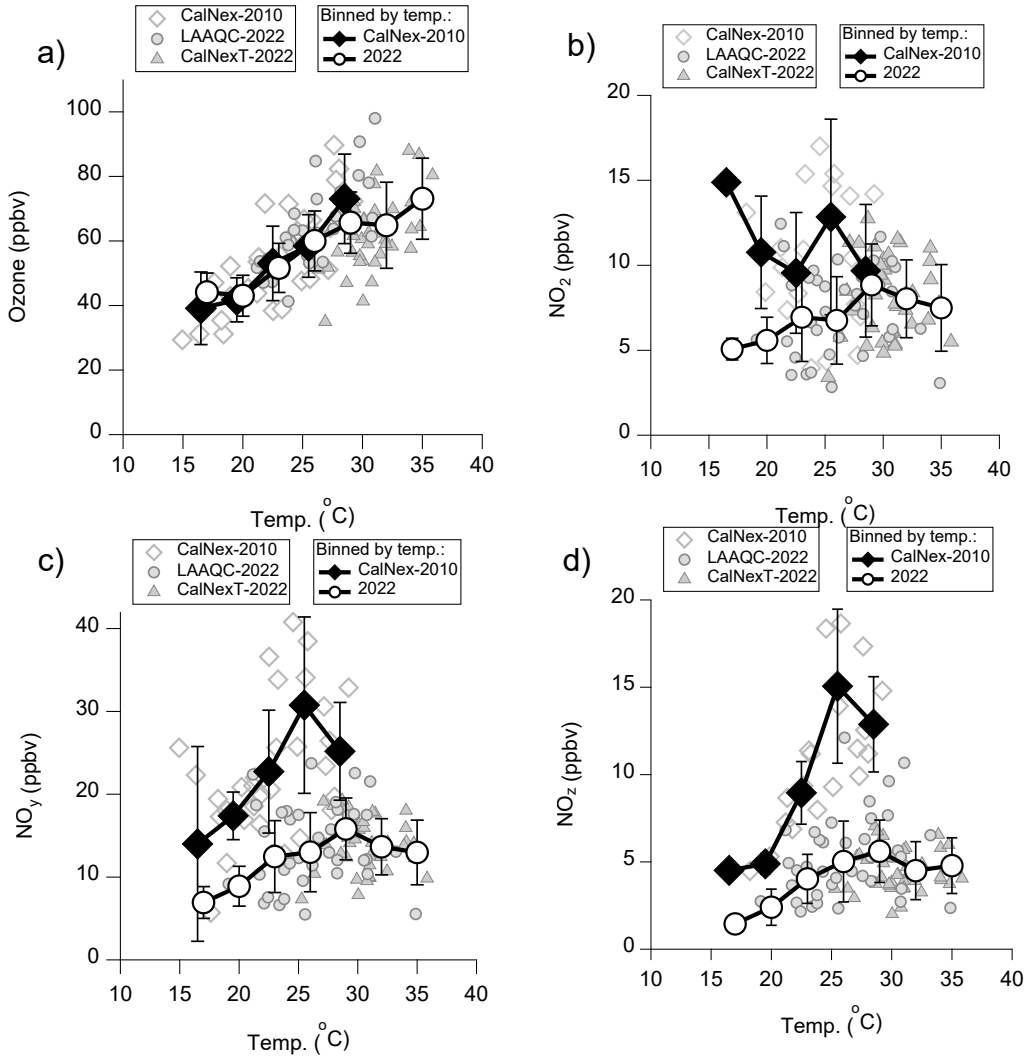

Figure 2.S16: Observed variability in midday (11:00-16:00) concentrations of (a) O_3, (b) NO_2, (c) NO_y, and (d) NO_z with temperature during CalNex-2010, LAAQC-2022, and CalNexT-2022. Larger makers denote average values binned by temperature. Error bars represent standard deviations. Averages calculated from 2022 data have been offset by 0.5ºC to show standard deviations

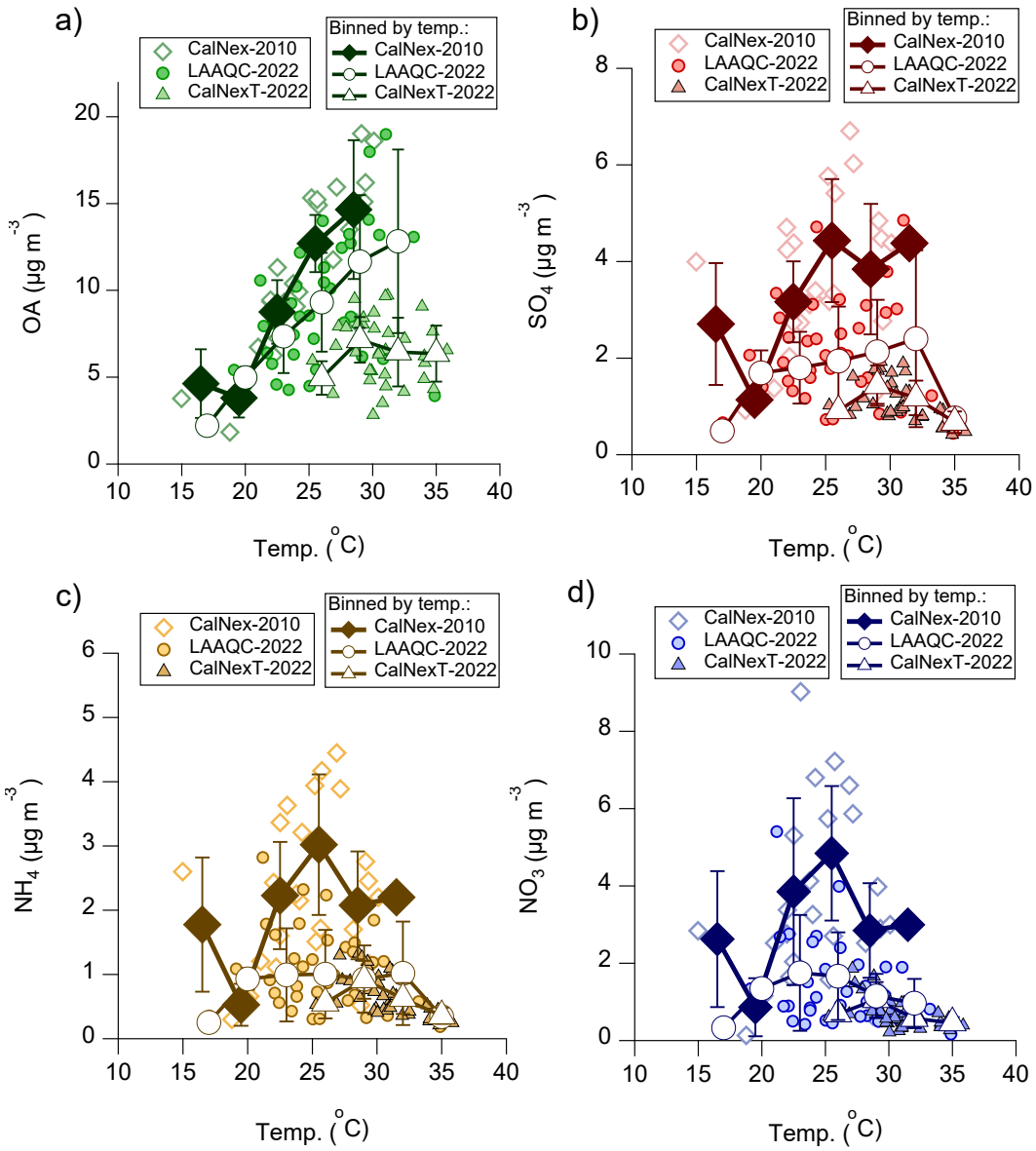

Figure 2.S17: Observed variability in midday (11:00-16:00) concentrations of (a) OA, (b) SO_4, (c) NH_4, and (d) NO_3 with temperature during CalNex-2010, LAAQC-2022, and CalNexT-2022.

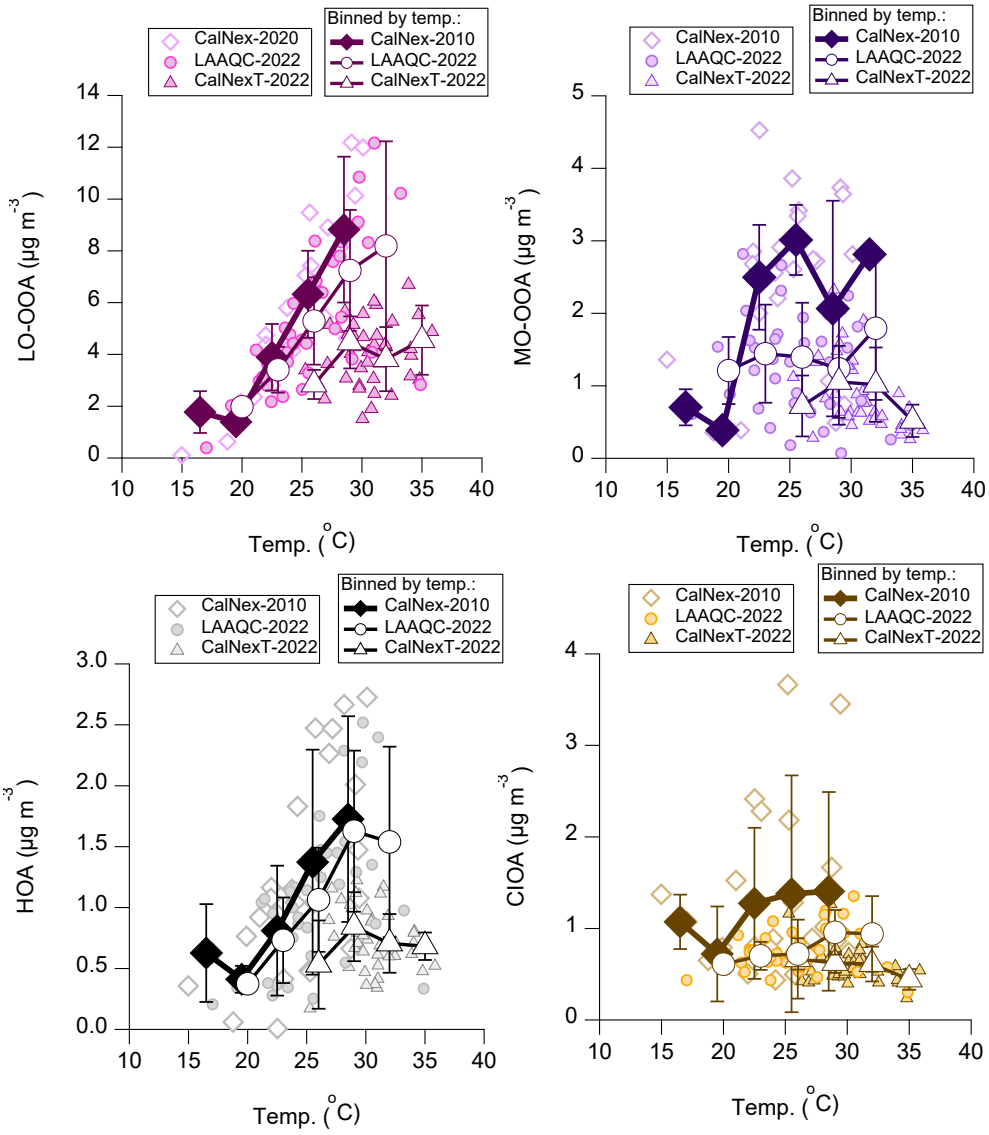

Figure 2.S18: Observed variability in midday (11:00-16:00) concentrations of (a) LO-OOA, (b) MO-OOA, (c) HOA, and (d) CIOA with temperature during CalNex-2010, LAAQC-2022, and CalNexT-2022.

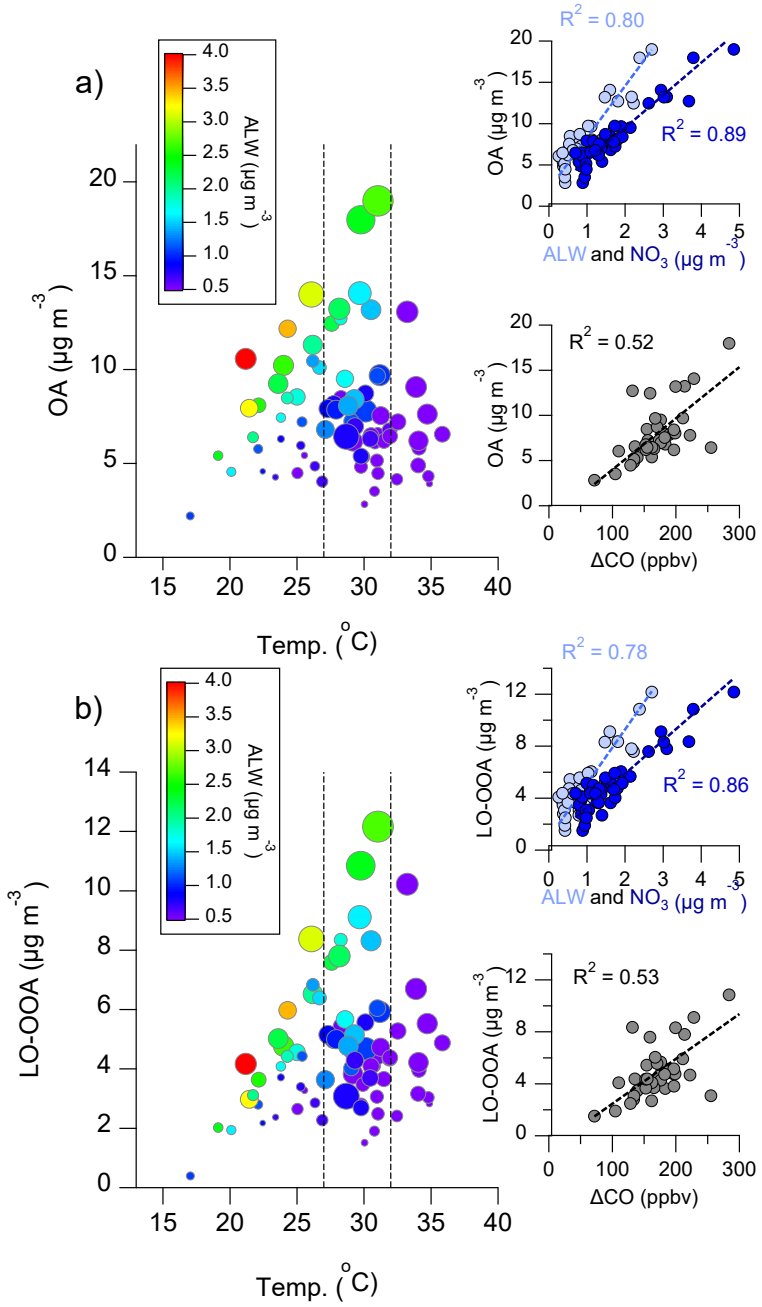

Figure 2.S19: Observed variability in midday (11:00-16:00) concentrations of (a) OA and (b) LO-OOA with temperature during both campaigns in 2022 (LAAQC-2022 and CalNexT-2022). Data points are colored by aerosol liquid water concentrations associated with inorganic NR-PM_1 species calculated using ISORROPIA-II (Fountoukis and Nenes, 2007) and sized by ΔCO concentrations. Inset plots show correlations of OA and LO-OOA concentrations measured between 27 and 32°C with ALW, NO_3, and ΔCO concentrations.

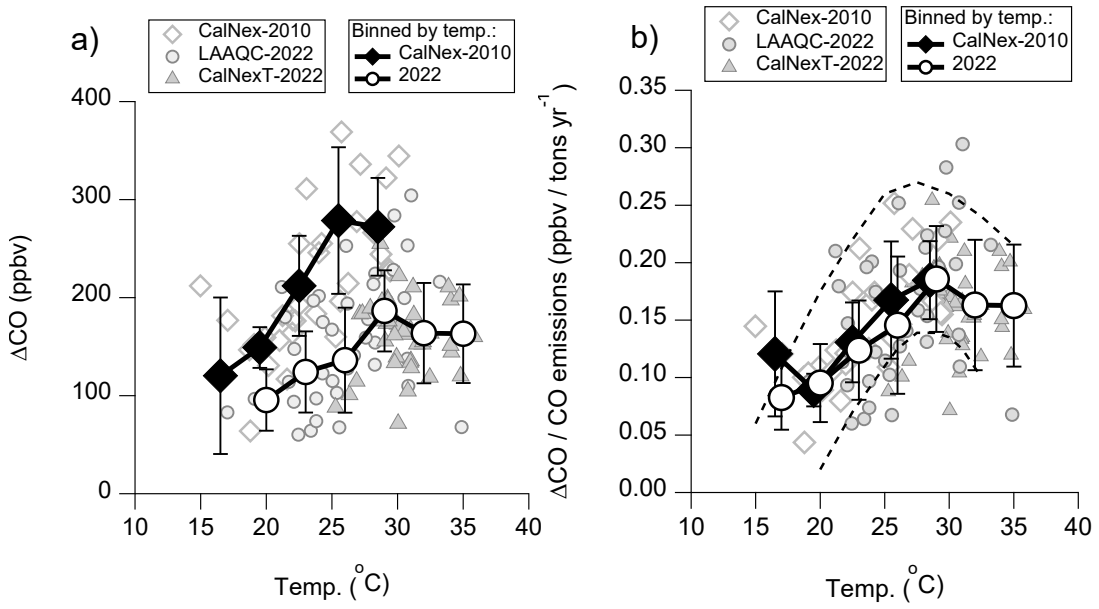

Figure 2.S20: Observed relationship between midday (11:00-16:00) concentrations of (a) ΔCO and (b) ΔCO divided by Los Angeles County CO emissions estimated by the CARB and temperature during CalNex-2010, LAAQC-2022, and CalNexT-2022. Larger makers denote average values binned by temperature. Error bars represent standard deviations. Averages calculated from 2022 data have been offset by 0.5ºC to show standard deviations. Dotted lines shown in (b) are meant to guide the eye.

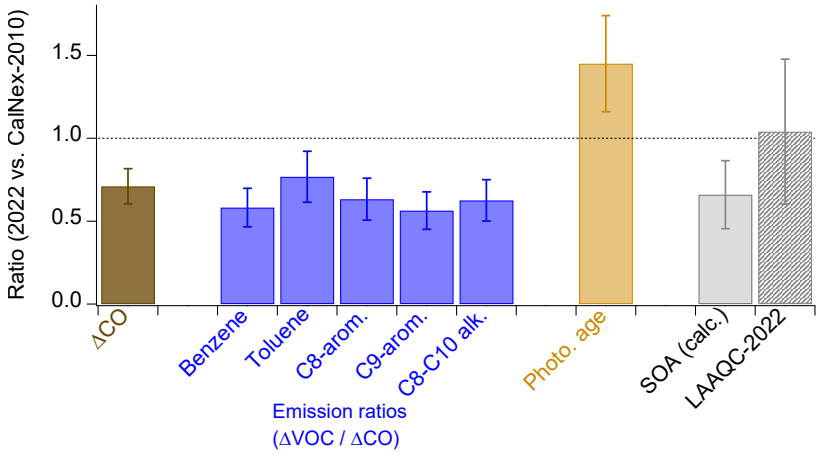

Figure 2.S21: Ratios of ΔCO concentrations, emission ratios of measured traditional SOA precursors, midday (14:00-15:00) photochemical age (i.e., OH exposure), and SOA either calculated using Eq. 1 or measured during LAAQC-2022 relative to CalNex-2010. Measured SOA corresponds to the LO-OOA factor derived from PMF analysis. Estimates of airmass photochemical age were calculated using VOC ratios, as described in SI Section 2.S3.

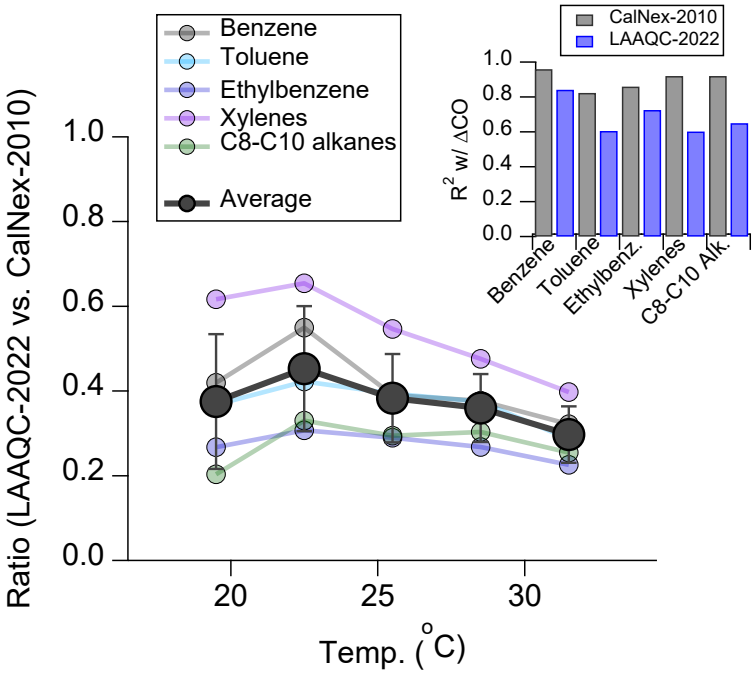

Figure 2.S22: Ratios of OH_{exp}-corrected afternoon (14:00-15:00) concentrations of aromatic and alkane species linked to mobile source emissions measured during LAAQC-2022 and CalNex-2010. The average ratio implies a ~60% reduction in emissions since 2010. Inset plot shows correlations of OH_{exp}-corrected afternoon concentrations with ΔCO during both campaigns.

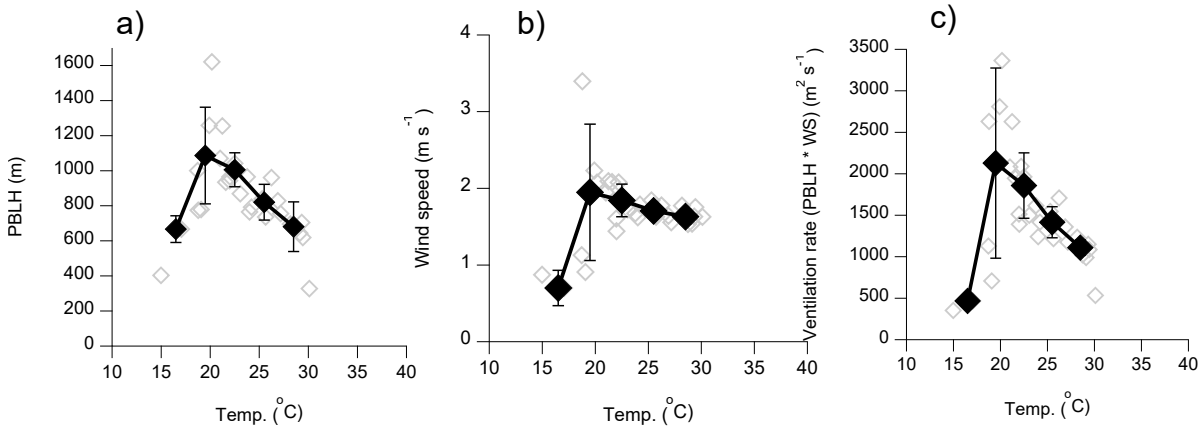

Figure 2.S23: Observed relationship between afternoon (11:00-16:00) (a) planetary boundary layer heights (PBLH), (b) wind speeds, and (c) inferred PBL ventilation rates with temperature during CalNex-2010. Larger makers denote average values binned by temperature. Error bars represent standard deviations.

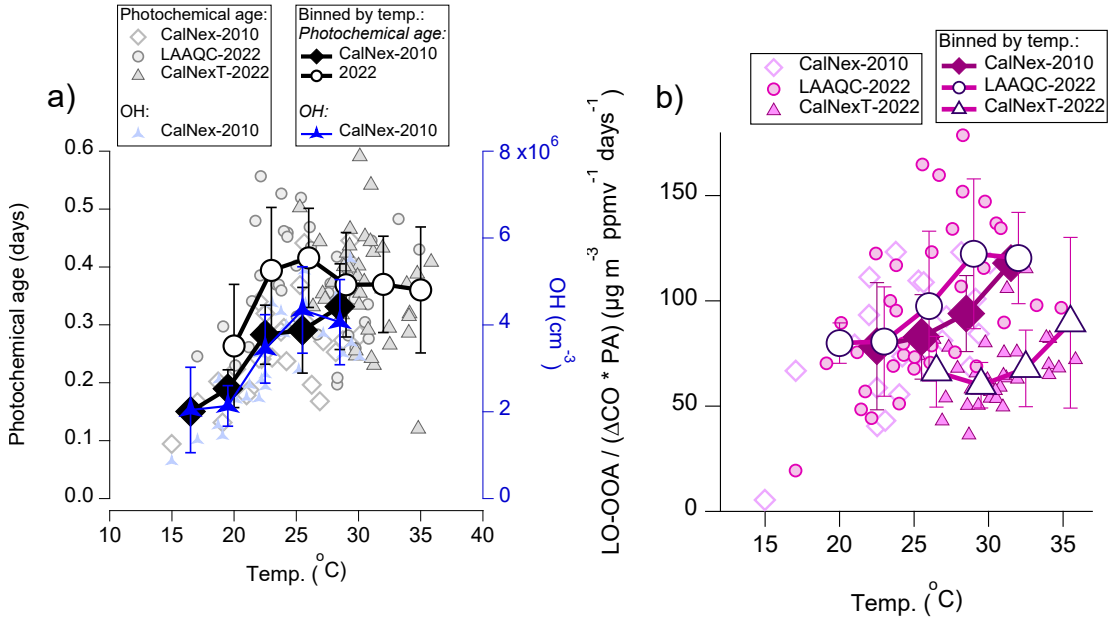

Figure 2.S24: Observed relationship between midday (11:00-16:00) (a) airmass photochemical age (i.e., OH exposure) and OH concentrations and (b) LO-OOA normalized by ΔCO and photochemical age and temperature during CalNex-2010, LAAQC-2022, and CalNexT-2022. Larger makers denote average values binned by temperature. Error bars represent standard deviations. Averages calculated from 2020-2022 data have been offset by 0.5°C to show standard deviations.

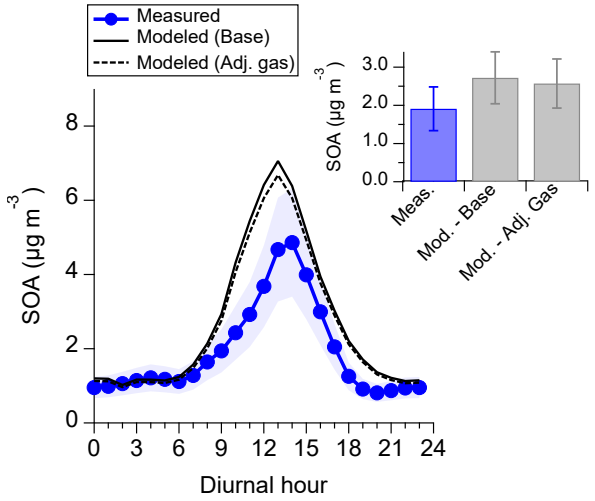

Figure 2.S25: Comparison of measured and modeled SOA during CalNexT-2022. Measured SOA refers to the measured LO-OOA PMF factor.

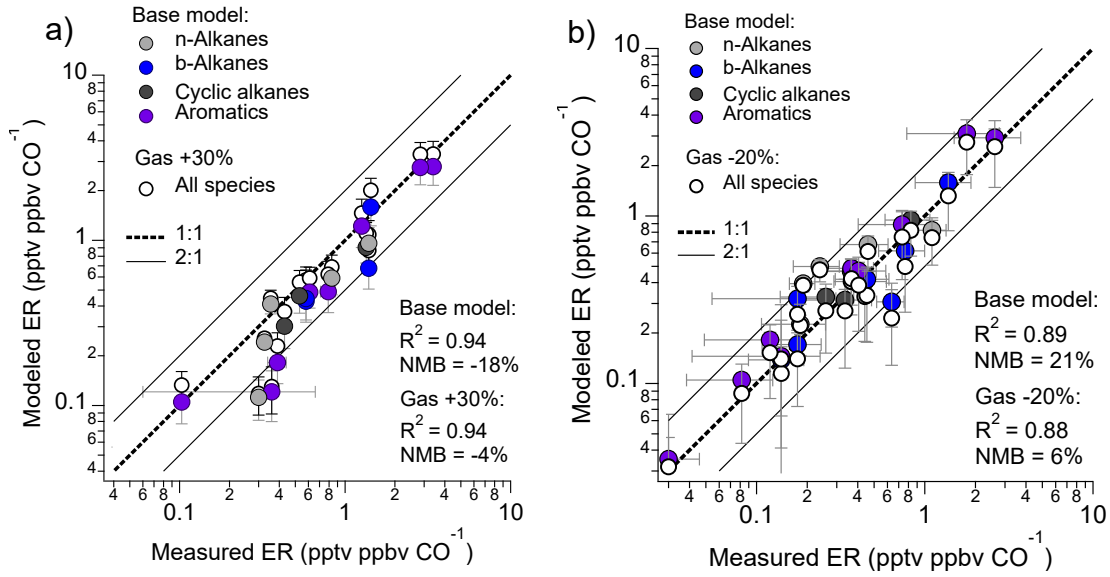

Figure 2.S26: Comparison of modeled and measured emission ratios (ER) of alkane and aromatic VOC for simulations of (a) CalNex-2010 and (b) LAAQC-2022. White markers denote final values once gasoline emissions are adjusted by +30% and -20% in 2010 and 2022, respectively. NMB represents normalized mean bias.

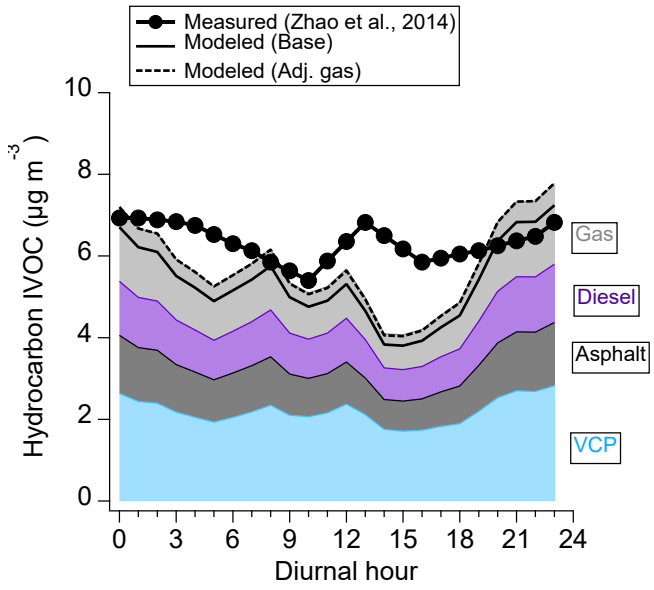

Figure 2.S27: Comparison of measured and modeled concentrations of hydrocarbon IVOC during CalNex-2010. Results from both the base simulation and the simulation with adjusted gasoline emissions are shown.

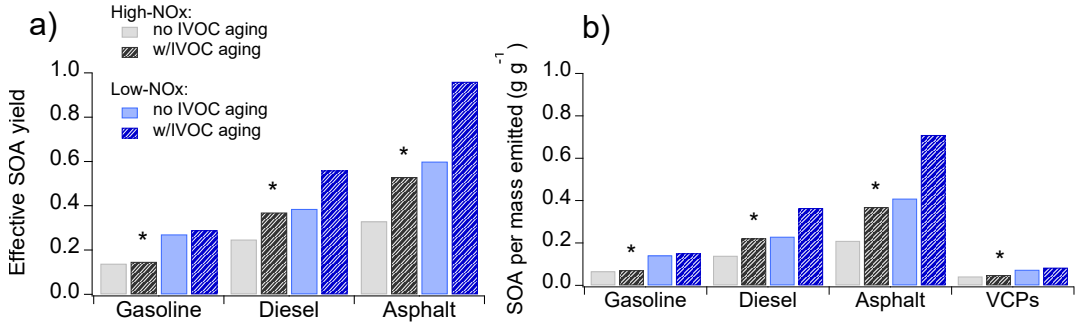

Figure 2.S28: (a) Modeled effective SOA yield (mass of SOA formed per total mass of reactant consumed) of gasoline, diesel, and asphalt emissions in the zero-dimensional model. Results are shown for high-NO_x and low-NO_x conditions, as well as when either including or excluding IVOC oxidation product aging. Yields are calculated after 12 hours of photochemical aging at an OH concentration of 1.5 x 10^6 molec. cm^{-3} and a background OA mass loading of 10 μg m^{-3}. VCPs are not included as the model does not simulate aging of the ~65% of VCP emissions not expected to form any SOA, which prevents an accurate assessment of effective yield. (b) Total amount of SOA mass formed per total mass of precursor emitted. The VCP value presented in (b) accounts for non-SOA forming mass emitted. In both cases, markers indicate the values used in the base model simulations described in the main text.

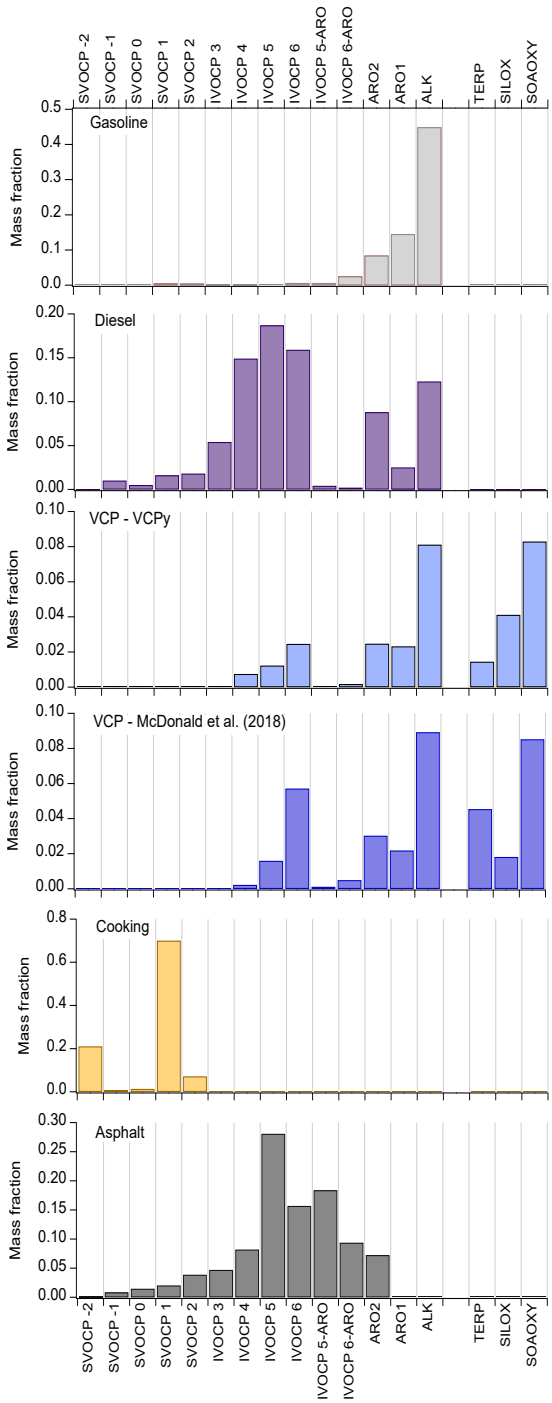

Figure 2.S29: Emission profile of each major anthropogenic OA precursor source included in the zero-dimensional model. Emissions assumed to form no POA or SOA (e.g., small alkenes in gasoline emissions, small oxygenates in VCP emissions, etc.) are not shown. Petrochemical emissions are not shown given that they are expected to account for <2% of SOA.

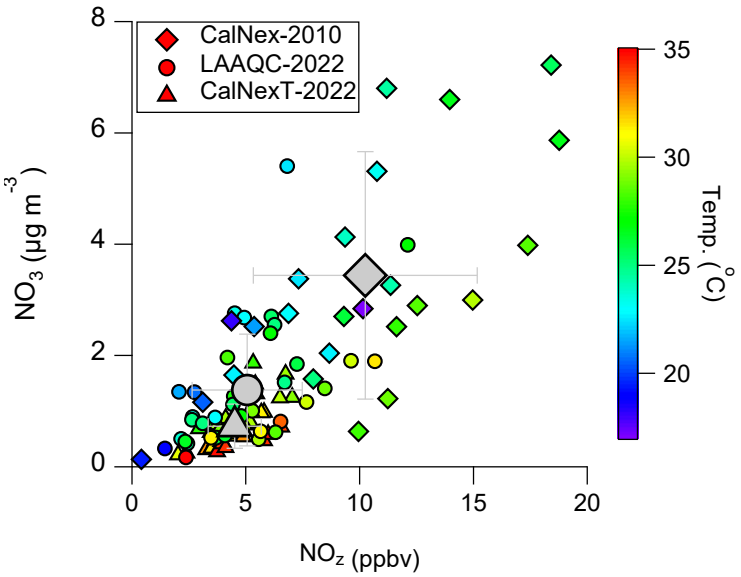

Figure 2.S30: Relationship between afternoon (11:00-16:00) concentrations of NO_3 and NO_z during CalNex-2010, LAAQC-2022, and CalNexT-2022.

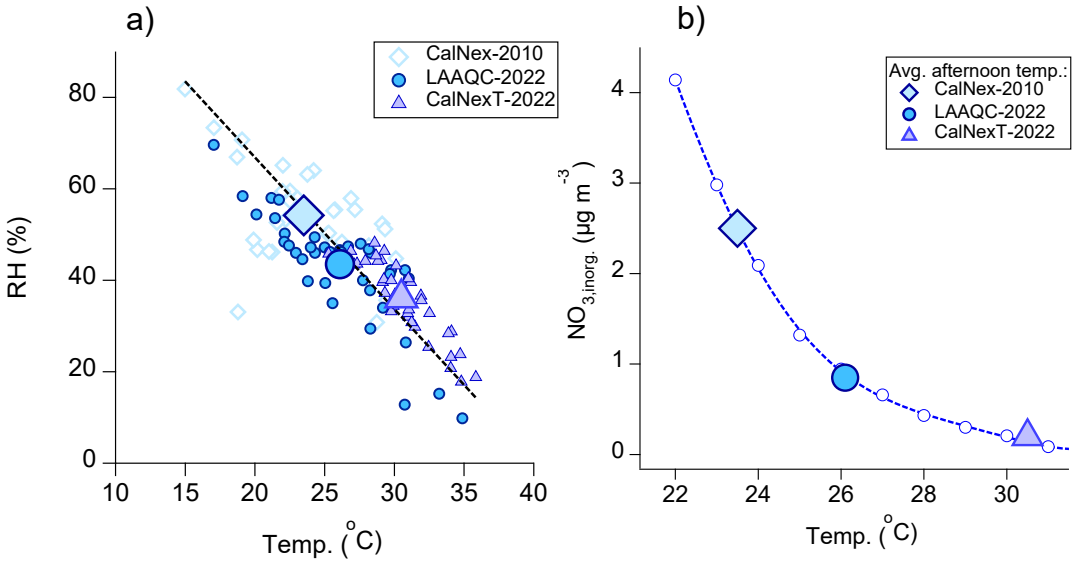

Figure 2.S31: (a) Observed relationship between midday (11:00-17:00) RH and temperature during CalNex-2010, LAAQC-2022, and CalNexT-2022. Large markers denote campaign averages. Dotted line is a linear fit to the data from all three campaigns. (b) Concentration of inorganic nitrate aerosol ($NO_{3,inorg.}$) predicted by ISORROPIA-II as a function of midday temperature when run in "forward" mode using total concentrations of SO_4, NH_3 (NH_4 (p) + NH_3 (g), and NO_3 (HNO_3 (g) + NO_3 (p)) measured at noon during CalNex-2010. Ambient RH values were scaled with temperature in the ISORROPIA-II simulations following the relationship shown in (a). The ISORROPIA-II results demonstrate that an average temperature difference of ~2-3°C is predicted to reduce ambient $NO_{3,inorg.}$ concentrations by over 50%.

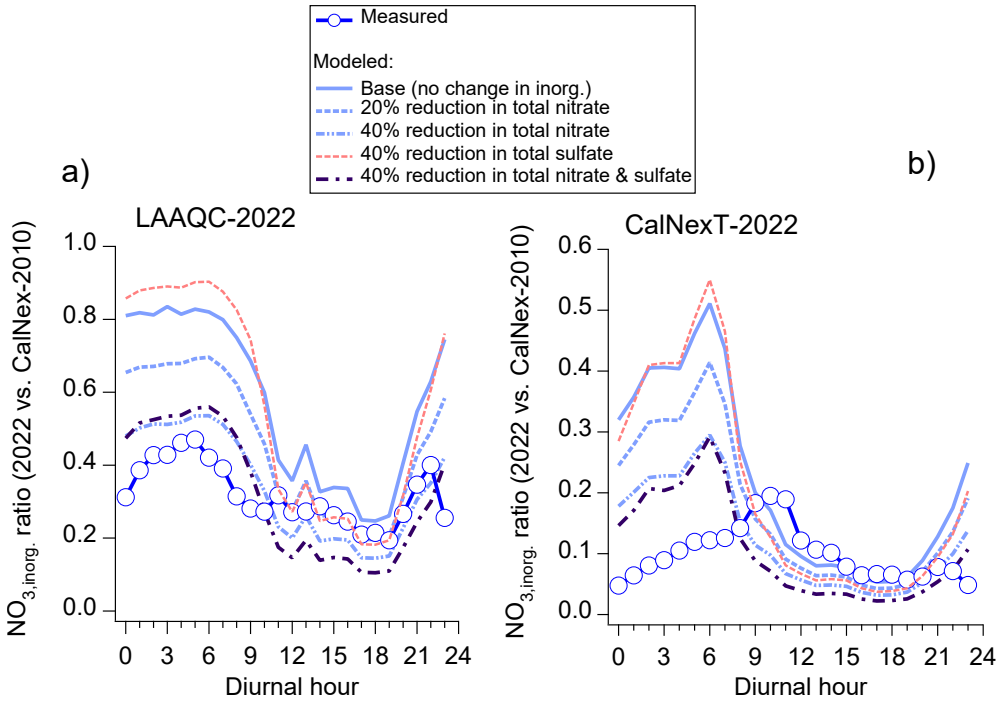

Figure 2.S32: Comparison of measured ratios of inorganic nitrate ($NO_{3,inorg.}$) between (a) LAAQC-2022 and CalNex-2010 and (c) CalNexT-2022 and CalNex-2010 with ratios calculated using ISORROPIA-II simulations assuming that either only meteorological parameters had changed between campaigns (base simulation) or that meteorological parameters and total concentrations (gas + aerosol) of nitrate and sulfate had shifted between campaigns by the noted relative amounts. Results demonstrate that measured nighttime $NO_{3,inorg.}$ ratios are only reproduced by ISORROPIA-II if total nitrate concentrations in 2022 are reduced considerably (>40%) relative to CalNex-2010. In contrast, daytime ratios are reproduced (LAAQC-2022) or even underpredicted (CalNexT-2022) if sulfate concentrations are changed but total nitrate concentrations are assumed constant.

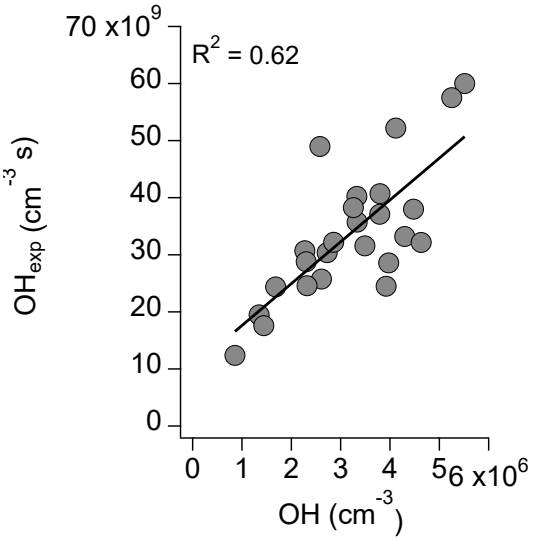

Figure 2.S33: Correlation between midday (11:00-17:00) estimates of airmass OH exposure calculated using VOC ratios (OH_{exp}) (SI Section 2.S3) and measured OH concentrations during CalNex-2010.

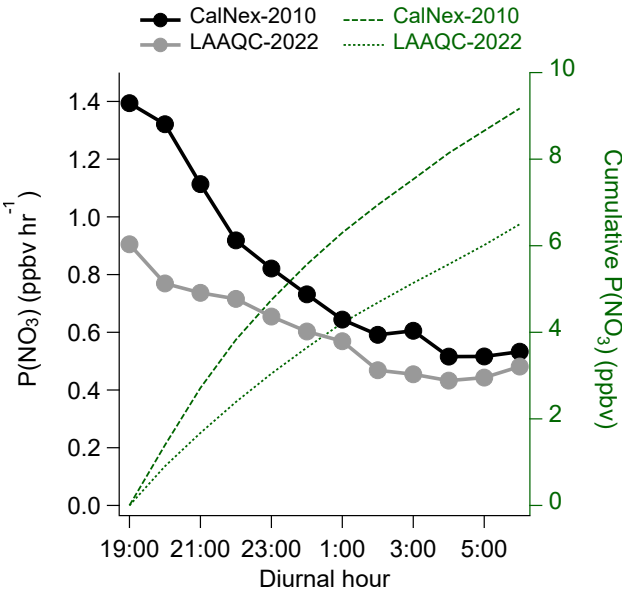

Figure 2.S34: Calculated overnight nitrate radical production rate and cumulative nitrate radical production during CalNex-2010 and LAAQC-2022.

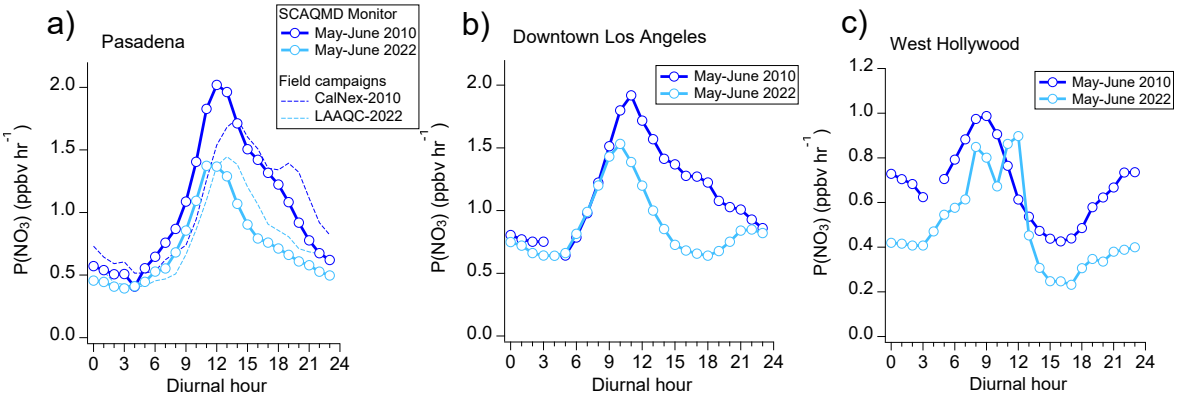

Figure 2.S35: Diurnal nitrate radical production rates inferred from measurements at SCAQMD monitoring sites in (a) Pasadena, (b) downtown Los Angeles, and (c) West Hollywood during May-June 2010 and 2022.

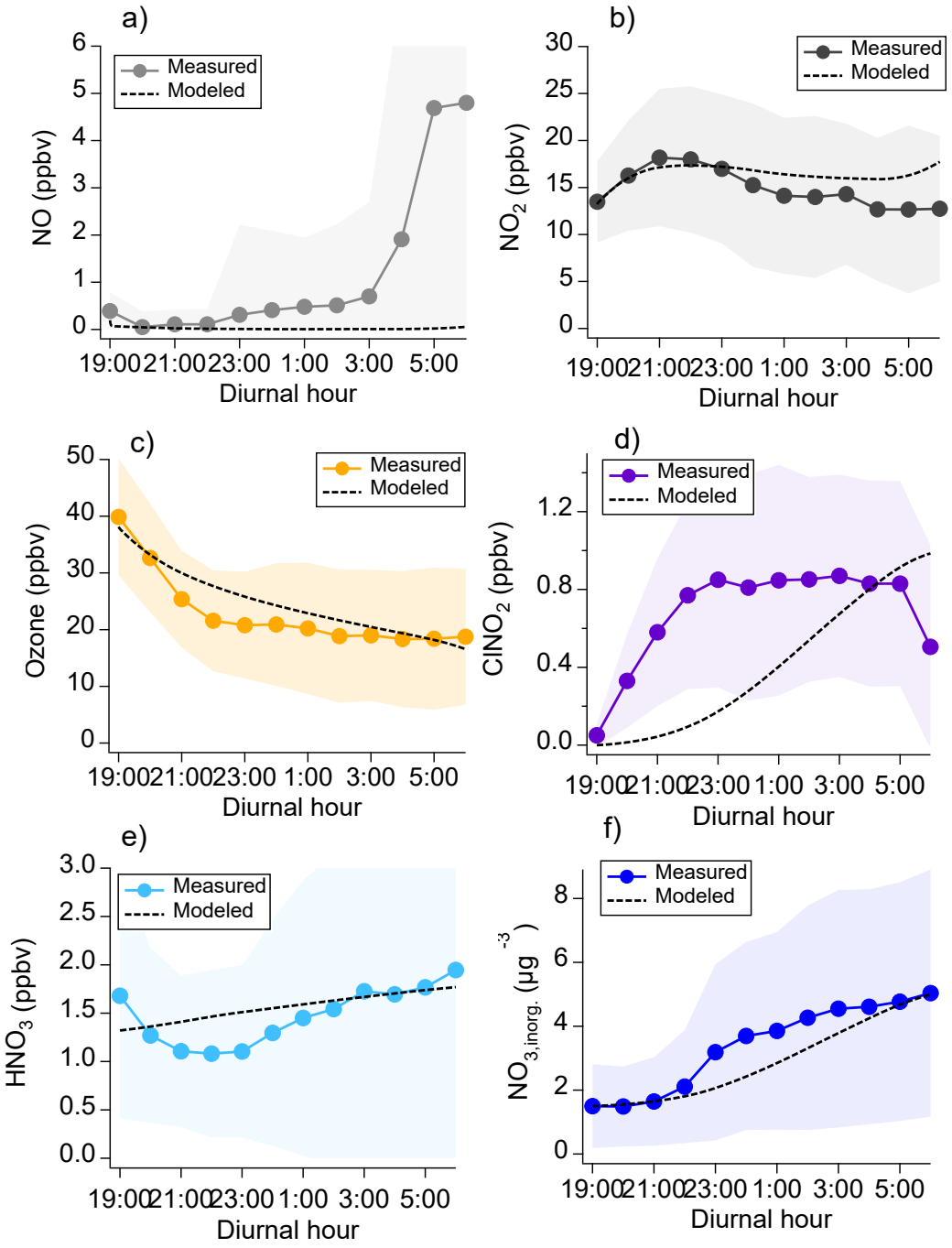

Figure 2.S36: Comparison of overnight measured concentrations of (a) NO, (b) NO_2, (c) ozone, (d) $ClNO_2$, (e) HNO_3, and (d) $NO_{3,inorg.}$ during CalNex-2010 with concentrations simulated in the base overnight model run (Simulation #1) described in SI Section 2.S9. Markers represent average values measured during CalNex-2010, while shaded areas denote standard deviations.

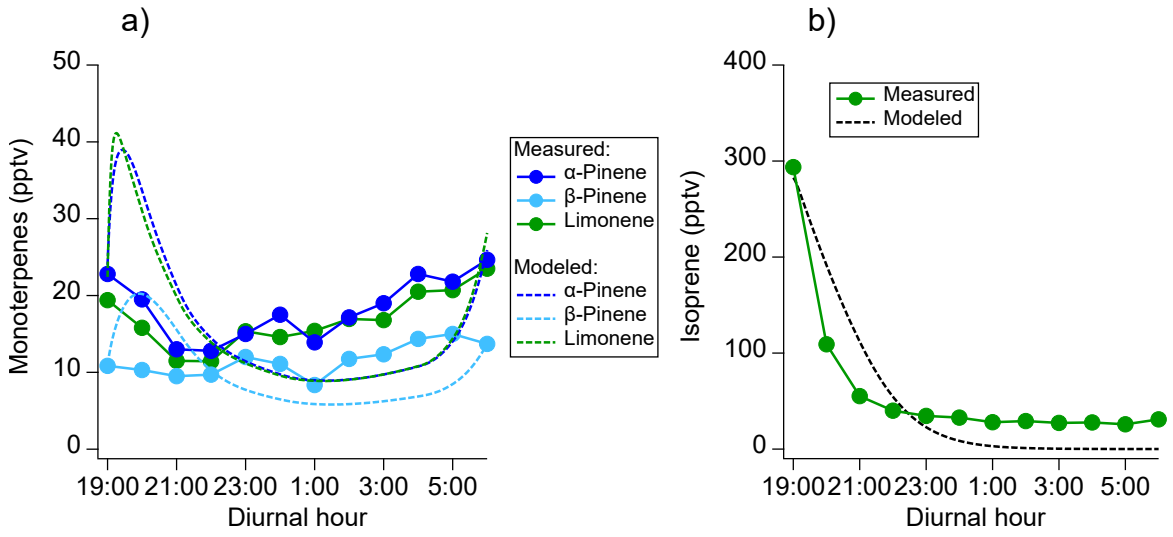

Figure 2.S37: Comparison of overnight measured concentrations of (a) monoterpenes and (b) isoprene during CalNex-2010 with concentrations simulated in the base overnight model run (Simulation #1) described in SI Section 2.S9. Markers represent average values measured during CalNex-2010.

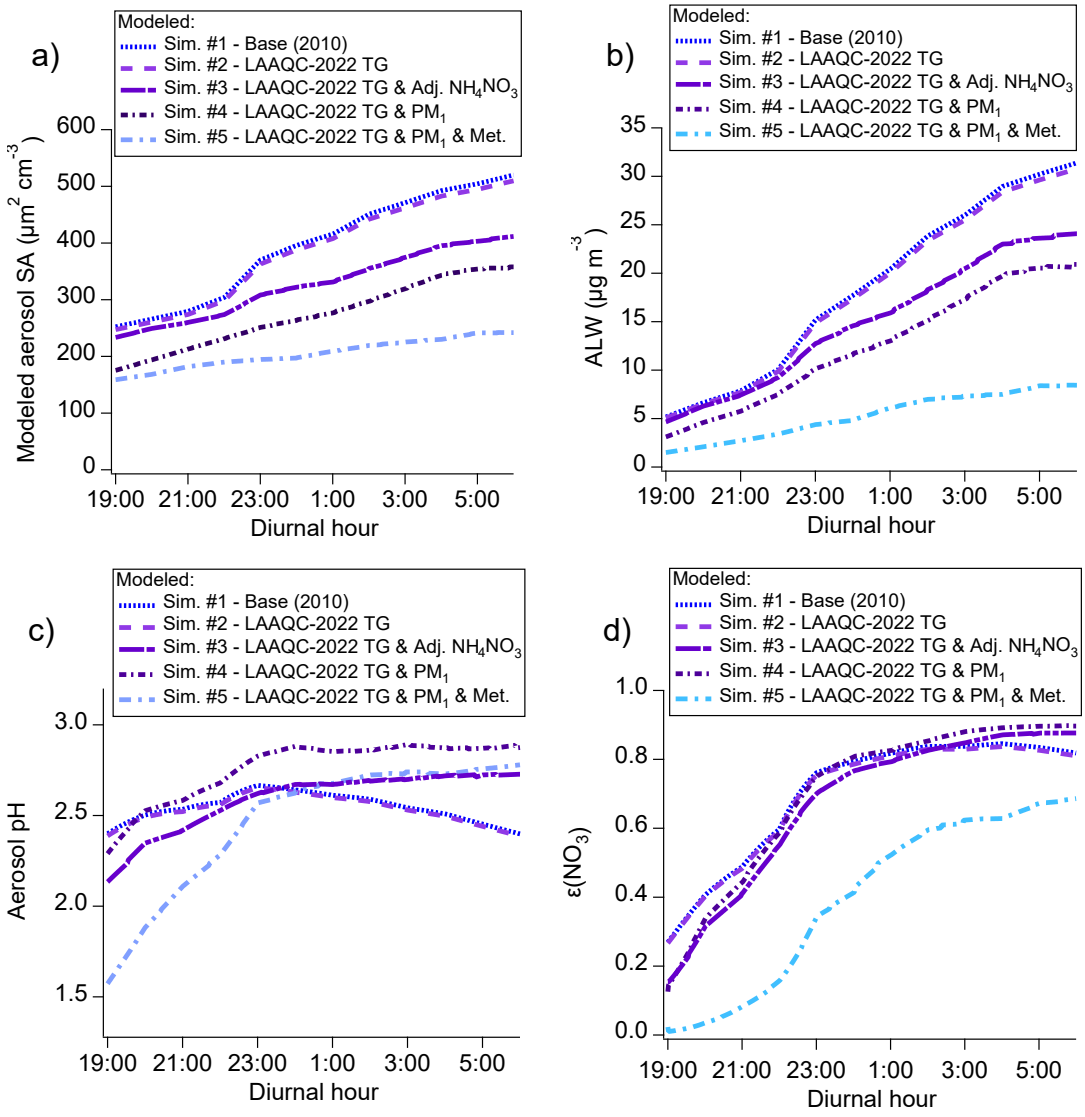

Figure 2.S38: Modeled overnight (a) aerosol surface area concentrations, (b) aerosol liquid water concentrations, (c) aerosol pH, and (d) NO_3 partitioning ratio (aerosol/gas + aerosol) for each of the simulations discussed in SI Section 2.S9.

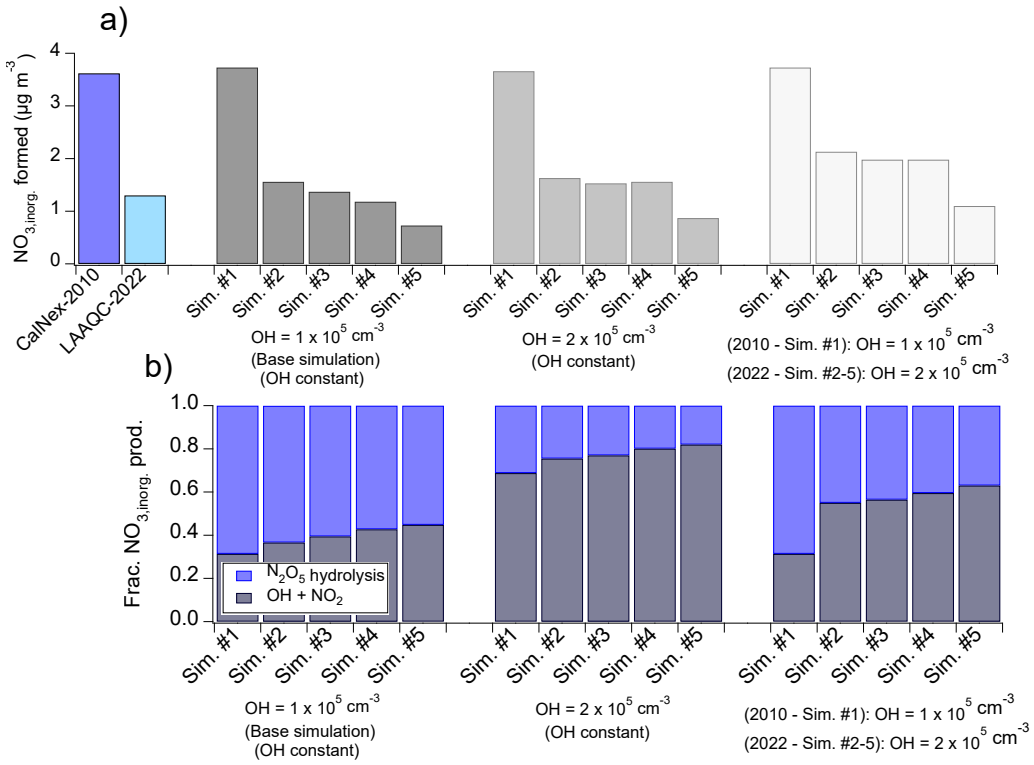

Figure 2.S39: (a) Comparison of measured overnight $NO_{3,inorg.}$ formation with simulation results assuming either constant overnight OH concentrations of 1 x 10^5 cm^{-3} or 2 x 10^5 cm^{-3} or variable OH concentrations, with OH increasing from 1 x 10^5 cm^{-3} in 2010 to 2 x 10^5 cm^{-3} in 2022. In all cases, N_2O_5 uptake coefficients were tuned to achieve model-measurement agreement in Simulation #1 and held constant throughout the simulations. Simulation #5 is meant to best represent both trace gas and aerosol conditions observed during LAAQC-2022. (b) Fraction of overnight $NO_{3,inorg.}$ production attributed to N_2O_5 hydrolysis or OH + NO_2 for each simulation.

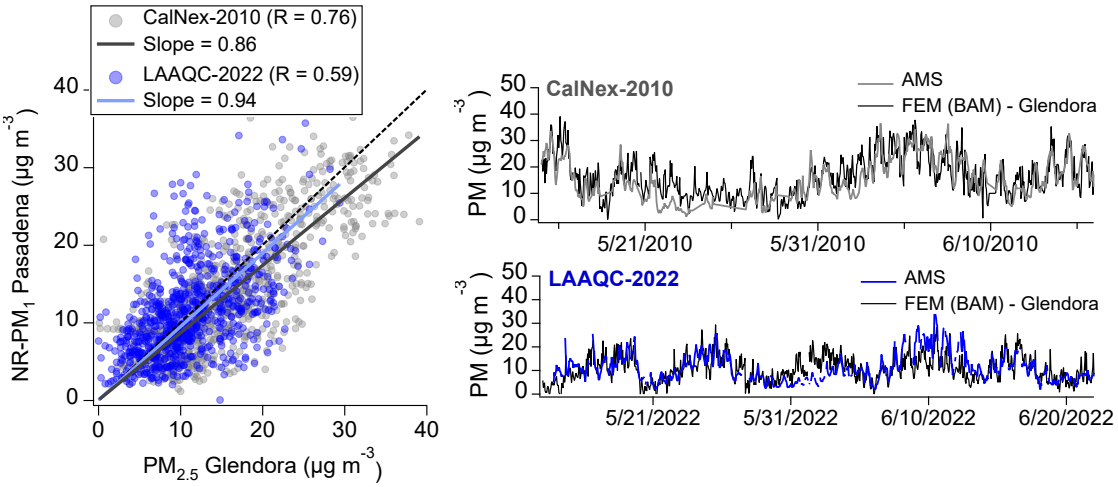

Figure 2.S40: (a) Correlation between hourly NR-PM1 measurements during CalNex-2010 and LAAQC-2022 with FEM PM2.5 measurements in Glendora. (b) Time series of total NR-PM1 and FEM PM2.5 during each campaign.

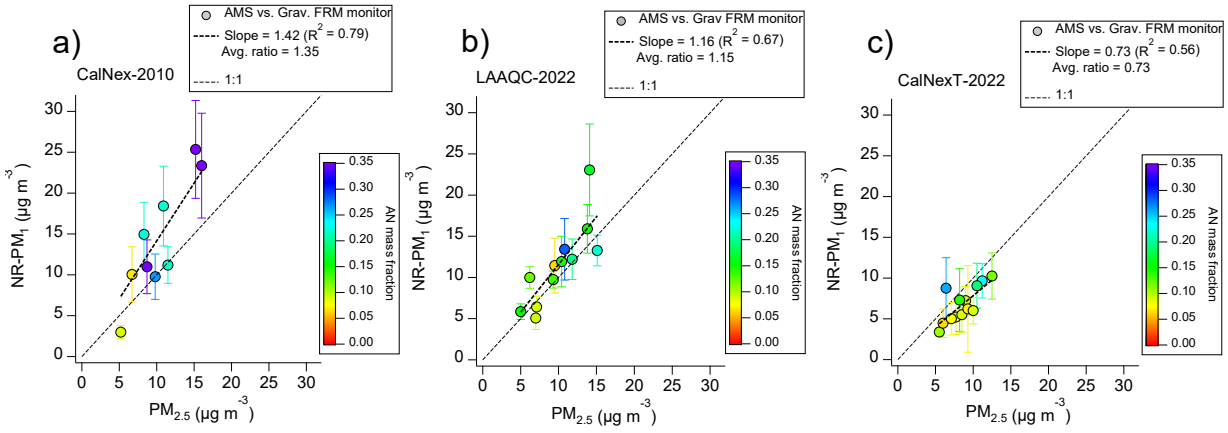

Figure 2.S41: Comparisons between daily average NR-PM_1 concentrations measured by the AMS and $PM_{2.5}$ concentrations measured by the Pasadena SCAQMD gravimetric FRM monitor during (a) CalNex-2010, (b) LAAQC-2022, and (c) CalNexT-2022.

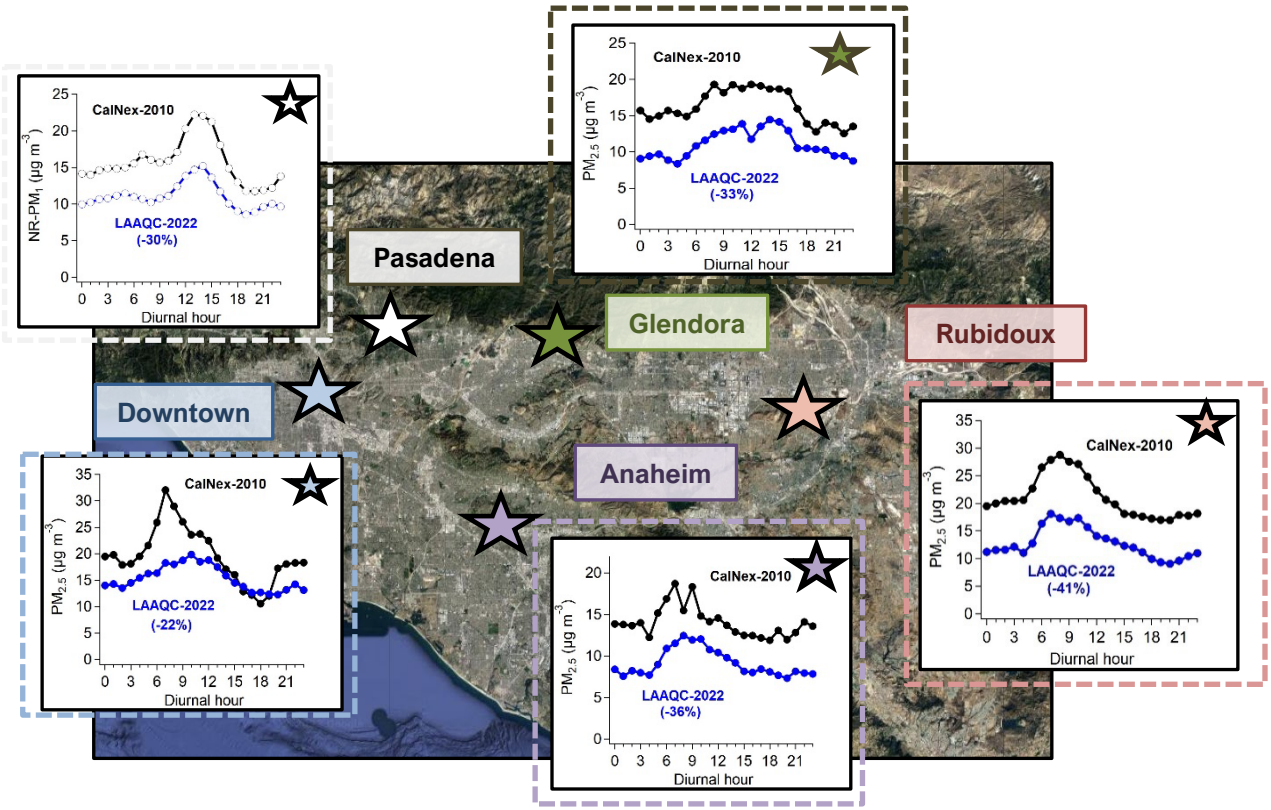

Figure 2.S42: Comparison of AMS diurnal trends in Pasadena measured during CalNex-2010 and LAAQC-2022 with FEM measurements at four additional sites in the Los Angeles Basin, demonstrating consistent reductions from 2010 to 2022.

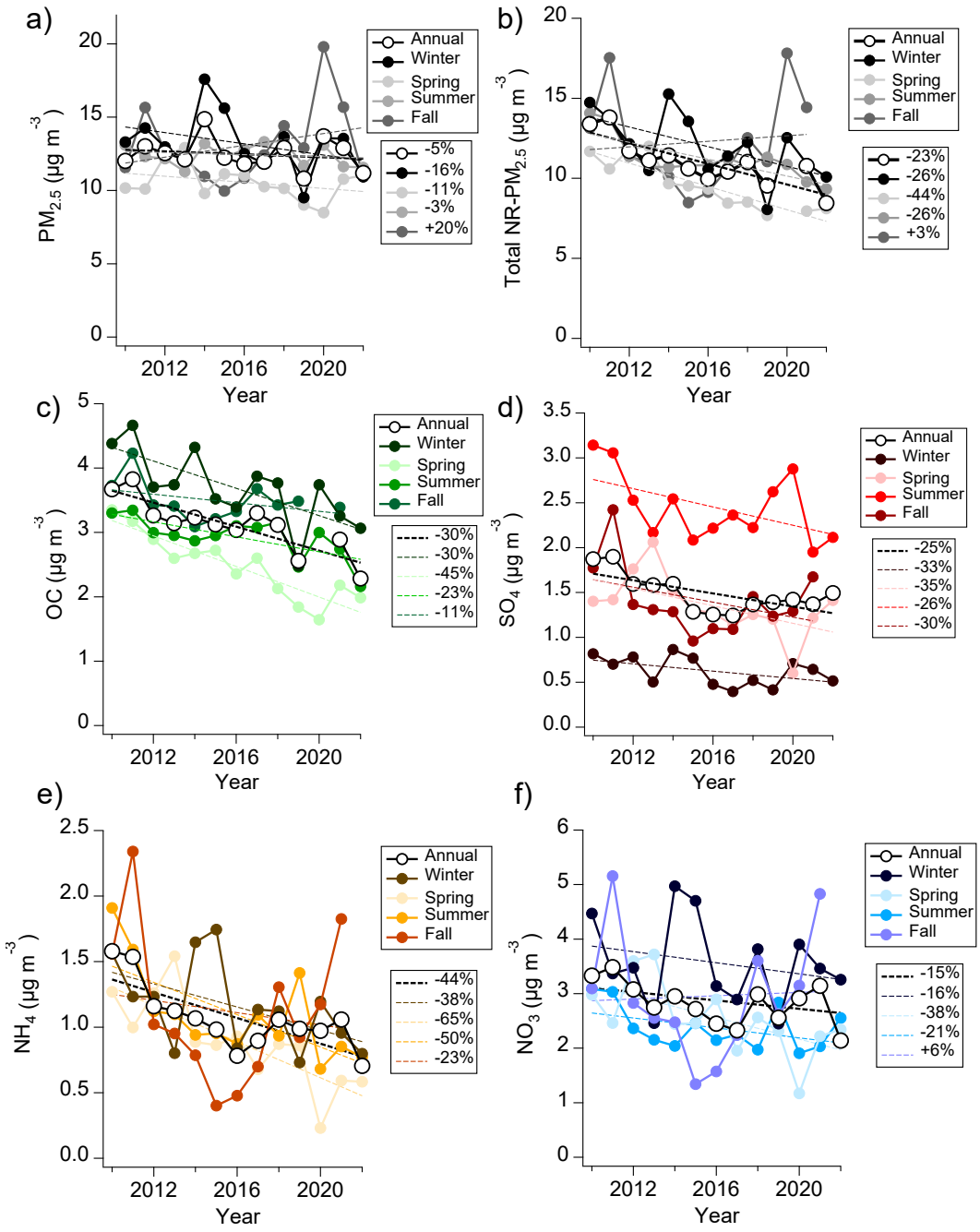

Figure 2.S43: Trends in seasonally-averaged concentrations of (a) total $PM_{2.5}$ measured using the FRM (gravimetric) method, (b) sum of speciated $PM_{2.5}$ components also measured by the AMS (OM+SO4+NH4+NO3), (c) organic carbon (OC), (b) sulfate, (c) ammonium, and (d) nitrate aerosol measured at the downtown Los Angeles SCAQMD monitoring site. Relative changes in average concentrations since 2010 calculated from linear fits are shown. OM concentrations used in the sum in (b) were calculated assuming an OM:OC ratio of 1.8.

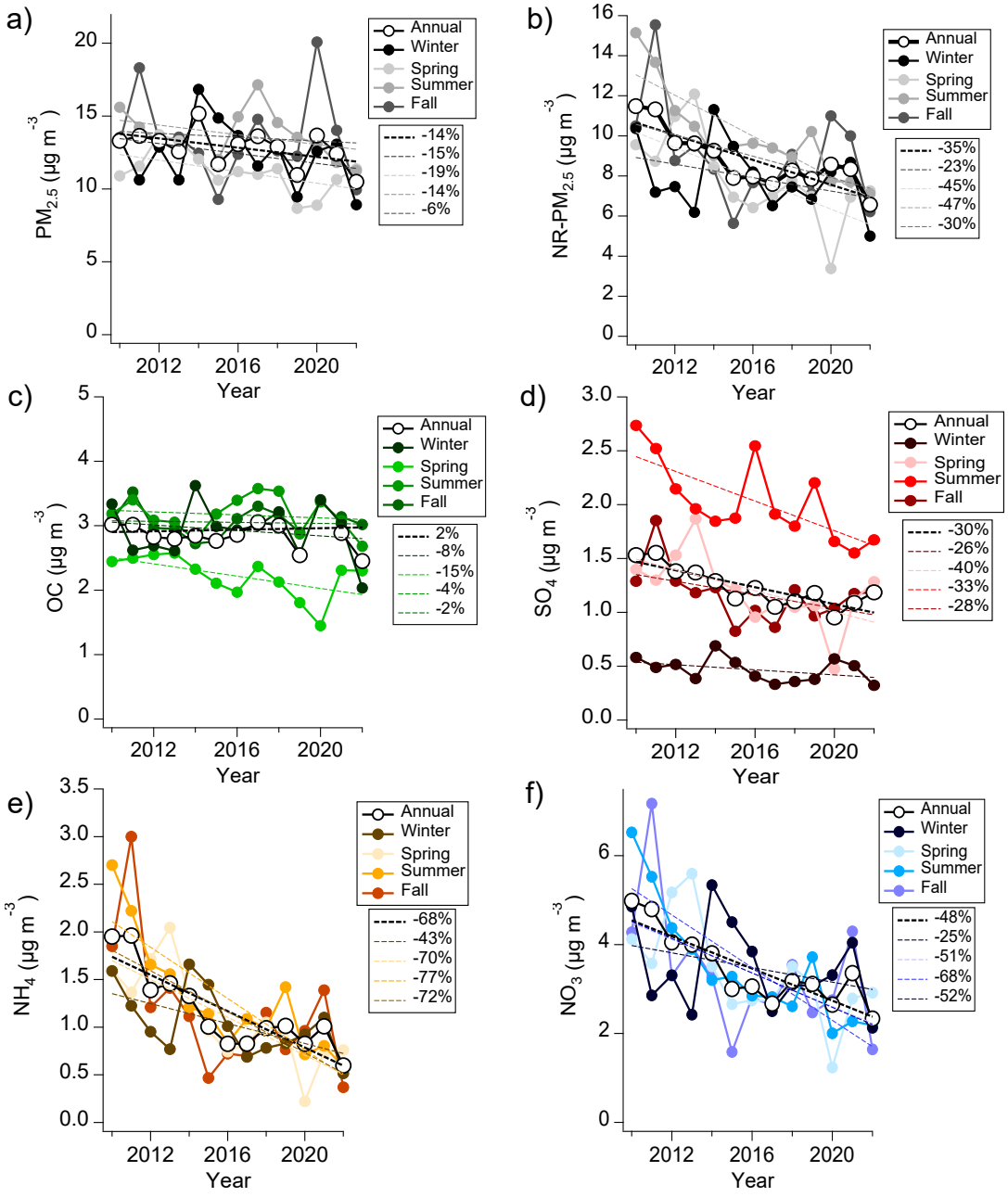

Figure 2.S44: Trends in seasonally-averaged concentrations of (a) total $PM_{2.5}$ measured using the FRM (gravimetric) method, (b) sum of speciated $PM_{2.5}$ components also measured by the AMS (OM+SO4+NH4+NO3), (c) organic carbon (OC), (b) sulfate, (c) ammonium, and (d) nitrate aerosol measured at the Rubidoux SCAQMD monitoring site. Relative changes in average concentrations since 2010 calculated from linear fits are shown. OM concentrations used in the sum in (b) were calculated assuming an OM:OC ratio of 1.8.

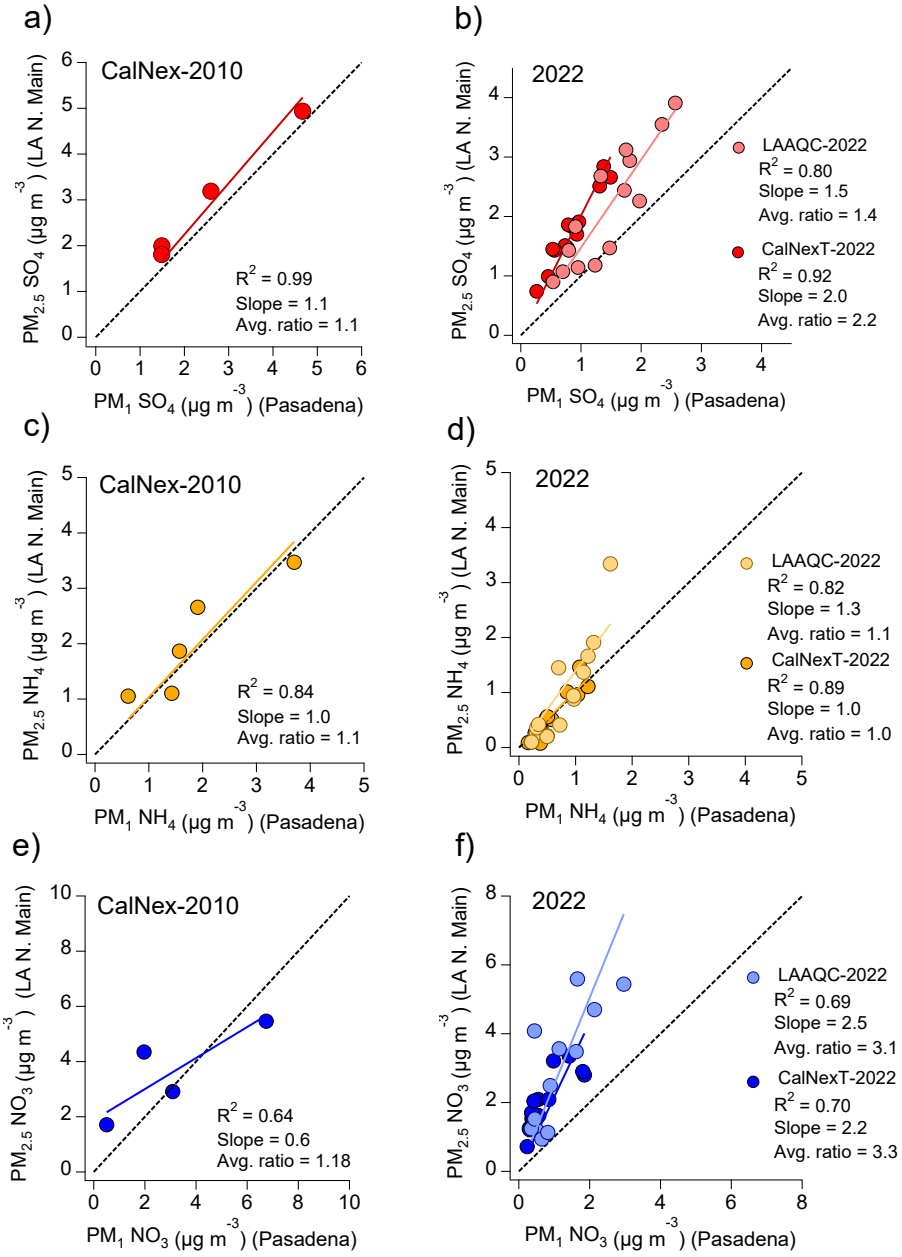

Figure 2.S45: Relationship between $PM_{2.5}$ concentrations of (a-b) sulfate, (c-d) ammonium, and (e-f) nitrate aerosol measured in downtown Los Angeles with AMS NR-PM_1 concentrations measured during CalNex-2010 (a,c,e – left column), and 2022 (LAAQC-2022 and CalNexT-2022) (b,d,f – left column).

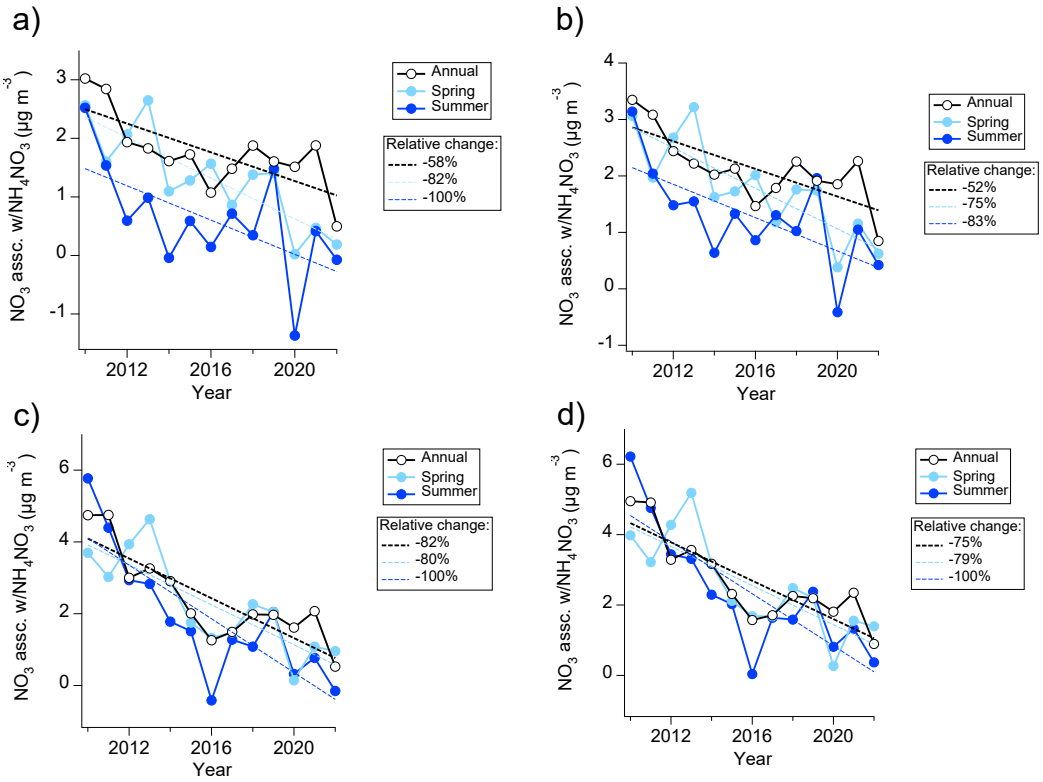

Figure 2.S46: Trends in seasonal and annual concentrations of nitrate aerosol associated with NH_4NO_3 assuming NH_4NO_3 concentrations can be calculated from an ammonium balance (SI Section 2.S10). (a-b) Concentrations in downtown Los Angeles assuming that either (a) all free sodium and magnesium (i.e., not associated with chloride) represents sodium nitrate and magnesium nitrate and (b) assuming that 50% of free sodium and magnesium is sodium sulfate and magnesium sulfate, with the remaining free sodium and magnesium associated with nitrate. (c-d) Same as (a-b) for measurements in Rubidoux, CA.

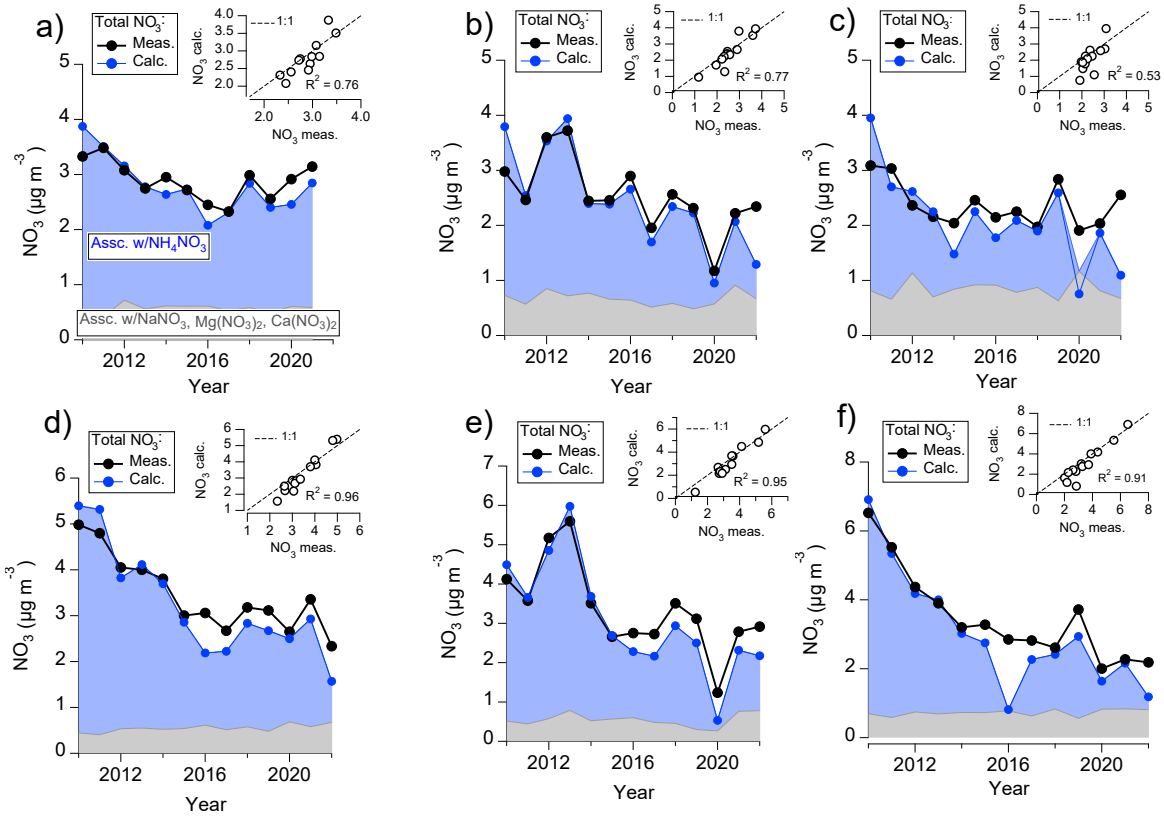

Figure 2.S47: Trends in $PM_{2.5}$ concentrations of total measured NO_3, calculated NO_3 associated with ammonium nitrate (blue), and calculated NO_3 associated with other cations (grey) in downtown Los Angeles (top row) and Rubidoux (bottom row). Calculations follow the method described in SI Section 2.S10 and assume that 50% of free sodium and magnesium is associated with sulfate, with the remainder associated with nitrate anions. Concentrations shown represent (a,d) annual, (b,e) spring, and (c,f) summertime averages. Inset plots show correlations of total calculated $PM_{2.5}$ NO_3 based on other cation and anion concentrations with measured NO_3 concentrations.

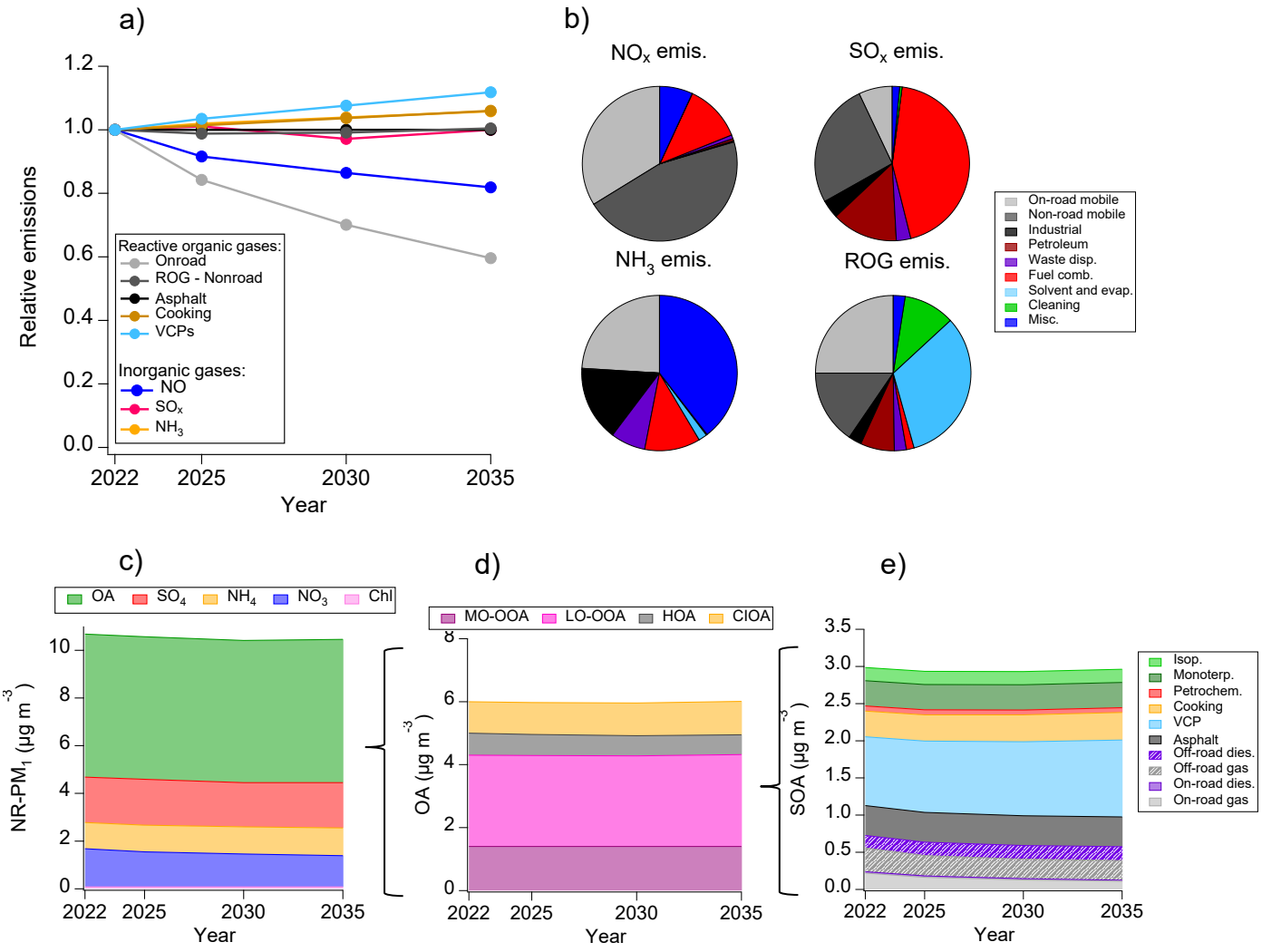

Figure 2.S48: (a) Relative trend in emissions of OA and IA precursors in Los Angeles County from 2022-2035 predicted by the CARB CEPAM inventory (CEPAM, 2029). (b) Relative contributions of individual emission sources to 2022 NO_x, SO_x, NH_3, and ROG emissions in Los Angeles County predicted by the CEPAM inventory. (c) Predicted trend in NR-PM1 components using emissions trends as explained in Section 4.S11. (d) Same as (c) for individual PMF factors. (e) Same as (c) for modeled SOA composition.

Tables 2.S1-2.S10

Table 2.S1: Average (± standard deviation) concentrations of measured trace gases (ppbv) and VOCs (pptv) during CalNex-2010, LAAQC-2022, and CalNexT-2022

Species	CalNex-2010	LAAQC-2022	CalNexT-2022
Trace gases			
O_3	33.3 ± 18.2	39.9 ± 18.4	34.0 ± 21.5
NO	2.4 ± 4.4	0.9 ± 1.7	1.7 ± 2.9
NO_2	12.6 ± 6.7	7.8 ± 4.2	10.3 ± 5.5
NO_y	20.9 ± 10.3	12.1 ± 6.4	15.2 ± 8.1
NO_z	7.1 ± 4.0	3.4 ± 2.1	3.2 ± 1.8
CO	301 ± 88	221 ± 72	236 ± 69
Alkanes			
n-Hexane	266 ± 178	112 ± 81	138 ± 108
n-Heptane	147 ± 61	49 ± 26	57 ± 27
n-Octane	59 ± 29	25 ± 12	28 ± 14
n-Nonane	56 ± 18	17 ± 8	21 ± 9
2-Methylhexane	94 ± 54	43 ± 24	55 ± 28
3-Methylhexane	95 ± 53	45 ± 26	57 ± 29
Cyclohexane	88 ± 48	37 ± 21	42 ± 19
Aromatics			
Benzene	262 ± 108	133 ± 51	152 ± 85
Toluene	579 ± 274	276 ± 147	312 ± 144
Ethylbenzene	103 ± 47	35 ± 19	44 ± 21
m,p-Xylene	286 ± 142	98 ± 62	129 ± 75
o-Xylene	117 ± 53	38 ± 23	48 ± 26
1,2,4-TMB	94 ± 50	20 ± 15	33 ± 2
Biogenics			
Isoprene	325 ± 451	299 ± 344	499 ± 436
α-Pinene	30 ± 28	49 ± 139	29 ± 21

Table 2.S2: Correlation (R^2) of PMF factor spectra resolved from the four-factor PMF solution from the LAAQC-2022 dataset with spectra observed during CalNex-2010 in Pasadena, CA by Hayes et al. (2013)

Factor	LO-OOA[1]	MO-OOA[2]	HOA	CIOA	LOA
LO-OOA	0.97	0.84	0.68	0.82	0.86
MO-OOA	0.79	0.97	0.36	0.48	0.72
HOA	0.82	0.48	0.84	0.91	0.74
CIOA	0.84	0.52	0.92	0.97	0.77

[1]Referred to as "SV-OOA" in Hayes et al. (2013). [2]Referred to as "LV-OOA" in Hayes et al. (2013)

Table 2.S3: Correlation (R^2) of PMF factor spectra resolved from the five-factor PMF solution from the CalNexT-2022 dataset with spectra observed during CalNex-2010 in Pasadena, CA by Hayes et al. (2013)

Factor	LO-OOA[1]	MO-OOA[2]	HOA	CIOA	LOA
LO-OOA	0.97	0.85	0.68	0.81	0.86
MO-OOA	0.88	0.96	0.43	0.58	0.78
HOA	0.67	0.31	0.84	0.85	0.61
CIOA	0.85	0.55	0.92	0.95	0.79

[1]Referred to as "SV-OOA" in Hayes et al. (2013). [2]Referred to as "LV-OOA" in Hayes et al. (2013)

Table 2.S4: Correlation (R^2) of PMF factors measured during LAAQC-2022 with VOCs and trace gases.

Species	LO-OOA	MO-OOA	HOA	CIOA
Trace gases				
O_3	0.55	0.04	0.03	0.02
NO	0.04	0.01	0.25	0.01
NO_2	0.04	0.01	0.38	0.14
NO_y	0.19	0.06	0.60	0.04
CO	0.33	0.10	0.53	0.12
Alkanes				
n-Hexane	0.20	0.03	0.59	0.42
n-Heptane	0.20	0.07	0.76	0.48
n-Octane	0.12	0.07	0.70	0.51
n-Nonane	0.13	0.09	0.75	0.49
2,2-Dimethylbutane	0.48	0.02	0.73	0.38
2-Methylpentane	0.28	0.04	0.78	0.45
3-Methylpentane	0.19	0.03	0.75	0.48
Cyclopentane	0.19	0.02	0.68	0.37
Aromatics				
Benzene	0.34	0.10	0.8	0.43
Toluene	020	0.10	0.77	0.49
Ethylbenzene	0.16	0.11	0.77	0.50
m,p-Xylene	0.00	0.11	0.52	0.44
o-Xylene	0.03	0.12	0.63	0.49
1,2,4-TMB	0.01	0.06	0.39	0.43
Biogenics				
Isoprene	0.46	0.01	0.18	0.08
α-Pinene	0.00	0.01	0.00	0.00

Table 2.S5: Correlation (R^2) of PMF factors measured during CalNexT-2022 with VOCs and trace gases.

Species	LO-OOA	MO-OOA	HOA	CIOA
Trace gases				
O_3	0.47	0.04	0.05	0.02
NO	0.00	0.00	0.30	0.02
NO_2	0.00	0.03	0.52	0.02
NO_y	0.03	0.01	0.60	0.00
CO	0.18	0.00	0.46	0.03
Alkanes				
n-Hexane	0.02	0.00	0.53	0.06
n-Heptane	0.04	0.02	0.87	0.07
n-Octane	0.01	0.02	0.77	0.07
n-Nonane	0.01	0.03	0.67	0.05
2,2-Dimethylbutane	0.29	0.03	0.65	0.10
2-Methylpentane	0.14	0.02	0.77	0.10
3-Methylpentane	0.05	0.02	0.77	0.07
Cyclopentane	0.01	0.04	0.59	0.02
Aromatics				
Benzene	0.19	0.10	0.71	0.06
Toluene	0.07	0.02	0.84	0.06
Ethylbenzene	0.07	0.02	0.78	0.10
m,p-Xylene	0.01	0.00	0.63	0.08
o-Xylene	0.00	0.01	0.71	0.08
1,2,4-TMB	0.07	0.00	0.32	0.06
Biogenics				
Isoprene	0.31	0.00	0.01	0.00
α-Pinene	0.0	0.00	0.30	0.13

Table 2.S6: Summary of annual Los Angeles County reactive organic gas (i.e., SOA precursor) emissions estimates in 2010 and 2022 used to inform the zero-dimensional SOA model.

Emission source	Emissions (Gg yr^{-1})	
	2010	2022
On-road gasoline[a]	39.8	16.0
Non-road gasoline[b]	27.4	19.5
On-road diesel	2.2	0.4
Non-road diesel	3.5	2.5
Volatile chemical products[c]	91.2	83.0
Asphalt	5.2	5.2
Cooking	0.38	0.30
Petrochemical facilities	10.9	4.1
Oil & Gas production	32.9	32.9

[a]On-road gasoline emissions increased by 7% relative to base EMFAC estimates following comparison of EMFAC emissions with those reported in McDonald et al. (2018)
[b]Non-road gasoline emissions increased by 56% relative to base CEPAM estimates following comparison of CEPAM emissions with those reported in McDonald et al. (2018)
[c]Values represent the average of estimates reported by the VCPy model for Los Angeles County and scaled from the SoCAB to Los Angeles County from estimates reported by McDonald et al. (2018), as described in *SI Appendix*, S5

Table 2.S7: Volatile organic compound (VOC) and intermediate VOC (IVOC) volatility bins, associated OH oxidation rates, and oxidation product mass yields used for combustion emissions, asphalt emissions, and alkane and aromatic species within VCP emissions in the zero dimensional model under high-NO_x conditions. Species emitted in the volatility range C* = 10^7-10^{10} μg m^{-3} were assigned a lumped volatility analog from Ma et al. (2017), as shown. Species more volatile than C* = 10^{10} were assumed to produce no secondary organic aerosol following oxidation. IVOC volatility assignments and oxidation product yields follow Lu et al. (2020). Species less volatile than C* = 10^3 directly undergo SVOC aging following emission as described in *SI Appendix, S5*.

C* (μg m^{-3})	MW	k_{OH} x 10^{-11} (cm^{-3} $molec^{-1}$ s^{-1})	Volatility Analog	Oxidation product mass yields				
				C* = 0.1	C* = 1	C* = 10	C* = 100	C* = 1000
10^{10}	61.7	3.64	OLE1	0	0.014	0	0.098	0.088
10^9	110.0	0.74	ALK5	0	0.157	0	0	0
10^8 – ARO[1]	103.4	0.51	ARO1	0	0.276	0.002	0.431	0.202
10^8 – ALK[1]	110.0	0.74	ALK5	0	0.157	0	0	0
10^7	116.2	2.59	ARO2	0	0.31	0	0.42	0.209
10^6 – ARO	162.3	3.05	N/A	0.022	0.109	0.251	0.005	0
10^5 – ARO	197.3	7.56	N/A	0.143	0.021	0.329	0.358	0
10^6 – ALK	184.4	1.55	N/A	0.009	0.045	0.118	0.47	0
10^5 – ALK	219.4	1.89	N/A	0.051	0.061	0.394	0.494	0
10^4 – ALK	254.9	2.25	N/A	0.068	0.083	0.523	0.239	0
10^3 - ALK	296.6	2.65	N/A	0.067	0.086	0.544	0.198	0

[1]Mass associated with the C* = 10^8 volatility bin emitted from gasoline sources is evenly divided into the ARO1 and ALK5 lumped species to ensure that mass fractions of aromatic and alkane species within gasoline and diesel exhaust agree with measurements reported by Gentner et al. (2013).

Table 2.S8: Oxidation product mass yields and OH reaction rates for non-alkane or aromatic OA precursors simulated by the zero-dimensional model under high-NO_x conditions. Mass yields for terpenes and isoprene are taken from Ma et al. (2017) and represent wall loss-corrected estimates in high-NO_x conditions. Siloxanes are oxidized following the parameterization developed by Pennington et al. (2021).

Compound class	MW	k_{OH} x 10^{-11} (cm^{-3} $molec^{-1}$ s^{-1})	Oxidation product mass yields				
			C* = 0.1	C* = 1	C* = 10	C* = 100	C* = 1000
Oxy. IVOC	164.5	2.81	0.097	0	0	0	0
SILOX	344.4	0.17	0.0	0.14[a]	0	0.82[a]	0
TERP	136.2	16.0	0	0.210	0	0.348	0.297
ISOP	68.1	10.0	0	0.034	0	0.005	0

[a]Following Pennington et al. (2021), oxidation products of siloxanes have C* values of 0.95 and 484 rather than 1 and 100. Siloxanes are the only modeled compound class whose oxidation products do not occupy the standard volatility bins.

Table 2.S9: Effective SOA yield of each major lumped SOA precursor species at a background OA mass loading of 10 μg m^{-3}. Yields shown below for IVOCs do not account for oxidation product aging, which is included in the model as described in *SI Appendix*, S5

Compound class	Effective SOA yield at 10 μg m^{-3}	
	High-NO_x	Low-NO_x
OLE1	0.02	0.02
ALK5	0.14	0.14-0.29
ARO1	0.29	0.59-0.88
ARO2	0.32	0.64-0.97
IVOC6-Aro	0.25	0.49-0.74
IVOC5-Aro	0.36	0.72-1.07
IVOC6-Alk	0.15	0.15-0.30
IVOC5-Alk	0.35	0.35-0.70
IVOC4-Alk	0.43	0.43-0.85
IVOC3-Alk	0.43	0.43-0.87
Oxy. IVOC	0.10	0.10
SILOX	0.14	0.14
ISOP	0.03	0.06
TERP	0.23	0.48

Table 2.S10: Gas-phase chemical reactions included in the zero-dimensional model of overnight nitrate aerosol formation.

No.	Reactants		Products	Rate coefficient (cm^3 $molec.^{-1}$ s^{-1} unless stated otherwise)	Source
1	$NO + O_3$	→	$NO_2 + O_2$	$1.4 \times 10^{-12} e^{(-1310/temp)}$	MCM[a]
2	$NO_2 + O_3$	→	$NO_3 + O_2$	$1.4 \times 10^{-13} e^{(-2470/temp)}$	MCM
3	$NO_3 + NO$	→	$2NO_2$	$1.8 \times 10^{-11} e^{(110/temp)}$	MCM
4	$NO_3 + NO_2$	→	$NO + NO_2$	$4.5 \times 10^{-14} e^{(-1260/temp)}$	MCM
5	$NO_3 + NO_2$	→	N_2O_5	$(k_0*k\infty)*F/(k_0 + k\infty)$[c]	Atkinson et al. (2004)[b]
6	N_2O_5	→	$NO_3 + NO_2$	$(k_0*k\infty)*F/(k_0 + k\infty)$[d] ($s^{-1}$)	Atkinson et al. (2004)
7	N_2O_5	→	(2-Φ)HNO3 + $\Phi ClNO_2$	¼(γv)SA (s^{-1})	Mielke et al. (2013)
8	$NO_2 + OH$	→	HNO_3	$k_0*M/(1+(k_0*M/k\infty))*$ $0.6^{(1+\log10(k0*M/k\infty\text{^}2)\text{^}-1}$	Seinfeld and Pandis (2016)
9	$NO_3 + hv$	→	$NO_2 + O$	$j(NO_3)$[e] (s^{-1})	MCM
10	α-pinene + NO_3	→	RO_2	$1.20 \times 10^{-12} e^{(490/temp)}$	MCM
11	α-pinene + O_3	→	RO_2	$8.05 \times 10^{-16} e^{(-640/temp)}$	MCM
12	α-pinene + OH	→	RO_2	$1.20 \times 10^{-11} e^{(440/temp)}$	MCM
13	β-pinene + NO_3	→	RO_2	2.51×10^{-12}	MCM
14	β-pinene + O_3	→	RO_2	$1.35 \times 10^{-15} e^{(-1270/temp)}$	MCM
15	β-pinene + OH	→	RO_2	$2.38 \times 10^{-11} e^{(357/temp)}$	MCM
16	Limonene + NO_3	→	RO_2	1.22×10^{-11}	MCM
17	Limonene + O_3	→	RO_2	$2.80 \times 10^{-15} e^{(-770/temp)}$	MCM
18	Limonene + OH	→	RO_2	$4.28 \times 10^{-11} e^{(401/temp)}$	MCM
19	Ocimene + NO_3	→	RO_2	2.20×10^{-11}	Atkinson et al. (1997)
20	Ocimene + O_3	→	RO_2	$3.15 \times 10^{-15} e^{(-626/temp)}$	Kim et al. (2011)
21	Ocimene + OH	→	RO_2	$4.35 \times 10^{-11} e^{(579/temp)}$	Kim et al. (2011)
22	Isoprene + NO_3	→	RO_2	$3.15 \times 10^{-12} e^{(-450/temp)}$	MCM
23	Isoprene + O_3	→	RO_2	$1.03 \times 10^{-14} e^{(-1995/temp)}$	MCM
24	Isoprene + OH	→	RO_2	$2.70 \times 10^{-11} e^{(390/temp)}$	MCM
25	$NO_3 + RO_2$	→	Products	2×10^{-12}	Vaughan et al. (2006)

26	$NO_3 + OH$	→	$HO_2 + NO_2$	2×10^{-11}	MCM
27	$NO_3 + HO_2$	→	$OH + NO_2$	4×10^{-12}	MCM
28	$RO_2 + RO_2$	→	Products	2×10^{-12}	Jenkin and Boyd (1998)

[a]"MCM" refers to the Master Chemical Mechanism v3.3.1 (http://mcm.york.ac.uk/home.htt). [b]IUPAC data accessed from https://iupac-aeris.ipsl.fr/. [c]$k_0 = 3.6x10^{-30}*M*(temp/300)^{-4.1}$, $k\infty = 1.9x10^{-12}*(temp/300)^{0.2}$, $KR = k_0/k\infty$, NC = 0.75-1.27*log10(0.35), $F = 10^{(log10(0.35)/(1+log10(KR)/NC)^2)}$, $M = 2.42x10^{19}$. [d]$k_0 = 1.3x10^{-3}*M*(temp/300)^{-3.5}$, $k\infty = 9.7x10^{14}*(temp/300)^{0.1}$, $KR = k_0/k\infty$, NC = 0.75-1.27*log10(0.35), $F = 10^{(log10(0.35)/(1+log10(KR)/NC)^2)}$. [e]j(NO3) is represented by J5 and J6 in the MCM.

2.7 References

Ashbaugh, L. L.; Eldred, R. A. Loss of Particle Nitrate from Teflon Sampling Filters: Effects on Measured Gravimetric Mass in California and in the IMPROVE Network. *Journal of the Air & Waste Management Association* **2004**, *54* (1), 93–104. https://doi.org/10.1080/10473289.2004.10470878.

Baidar, S.; Hardesty, R. M.; Kim, S.-W.; Langford, A. O.; Oetjen, H.; Senff, C. J.; Trainer, M.; Volkamer, R. Weakening of the Weekend Ozone Effect over California's South Coast Air Basin. *Geophysical Research Letters* **2015**, *42* (21), 9457–9464. https://doi.org/10.1002/2015GL066419.

Blumenthal, D. L.; White, W. H.; Smith, T. B. Anatomy of a Los Angeles Smog Episode: Pollutant Transport in the Daytime Sea Breeze Regime. *Atmospheric Environment (1967)* **1978**, *12* (4), 893–907. https://doi.org/10.1016/0004-6981(78)90028-8.

Borbon, A.; Gilman, J. B.; Kuster, W. C.; Grand, N.; Chevaillier, S.; Colomb, A.; Dolgorouky, C.; Gros, V.; Lopez, M.; Sarda-Esteve, R.; Holloway, J.; Stutz, J.; Petetin, H.; McKeen, S.; Beekmann, M.; Warneke, C.; Parrish, D. D.; Gouw, J. A. de. Emission Ratios of Anthropogenic Volatile Organic Compounds in Northern Mid-Latitude Megacities: Observations versus Emission Inventories in Los Angeles and Paris. *Journal of Geophysical Research: Atmospheres* **2013**, *118* (4), 2041–2057. https://doi.org/10.1002/jgrd.50059.

Boyd, C. M.; Nah, T.; Xu, L.; Berkemeier, T.; Ng, N. L. Secondary Organic Aerosol (SOA) from Nitrate Radical Oxidation of Monoterpenes: Effects of Temperature, Dilution, and Humidity on Aerosol Formation, Mixing, and Evaporation. *Environ. Sci. Technol.* **2017**, *51* (14), 7831–7841. https://doi.org/10.1021/acs.est.7b01460.

Burnett, R.; Chen, H.; Szyszkowicz, M.; Fann, N.; Hubbell, B.; Pope, C. A.; Apte, J. S.; Brauer, M.; Cohen, A.; Weichenthal, S.; Coggins, J.; Di, Q.; Brunekreef, B.; Frostad, J.; Lim, S. S.; Kan, H.; Walker, K. D.; Thurston, G. D.; Hayes, R. B.; Lim, C. C.; Turner, M. C.; Jerrett, M.; Krewski, D.; Gapstur, S. M.; Diver, W. R.; Ostro, B.; Goldberg, D.; Crouse, D. L.; Martin, R. V.; Peters, P.; Pinault, L.; Tjepkema, M.; Donkelaar, A. van; Villeneuve, P. J.; Miller, A. B.; Yin, P.; Zhou, M.; Wang, L.; Janssen, N. A. H.; Marra, M.; Atkinson, R. W.; Tsang, H.; Thach, T. Q.; Cannon, J. B.; Allen, R. T.; Hart, J. E.; Laden, F.; Cesaroni, G.; Forastiere, F.; Weinmayr, G.; Jaensch, A.; Nagel, G.; Concin, H.; Spadaro, J. V. Global Estimates of Mortality Associated with Long-Term Exposure to Outdoor Fine Particulate Matter. *PNAS* **2018**, *115* (38), 9592–9597. https://doi.org/10.1073/pnas.1803222115.

California Air Resources Board (CARB), Low-Emission Vehicle Program, Accessed at: https://ww2.arb.ca.gov/our-work/programs/low-emission-vehicle-program. Last accessed: Feb. 7, 2022

California Emissions Projections Analysis Model (CEPAM) 2019 v1.03. Accessed at: https://ww2.arb.ca.gov/applications/cepam2019v103-standard-emission-tool. Last accessed: Feb 7, 2022.

Canagaratna, M. R.; Jimenez, J. L.; Kroll, J. H.; Chen, Q.; Kessler, S. H.; Massoli, P.; Hildebrandt Ruiz, L.; Fortner, E.; Williams, L. R.; Wilson, K. R.; Surratt, J. D.; Donahue, N. M.; Jayne, J. T.; Worsnop, D. R. Elemental Ratio Measurements of Organic Compounds Using Aerosol Mass Spectrometry: Characterization, Improved Calibration, and Implications. *Atmospheric Chemistry and Physics* **2015**, *15* (1), 253–272. https://doi.org/10.5194/acp-15-253-2015.

Cappa, C. D.; Zhang, X.; Loza, C. L.; Craven, J. S.; Yee, L. D.; Seinfeld, J. H. Application of the Statistical Oxidation Model (SOM) to Secondary Organic Aerosol Formation from Photooxidation of C_{12} Alkanes. *Atmospheric Chemistry and Physics* **2013**, *13* (3), 1591–1606. https://doi.org/10.5194/acp-13-1591-2013.

Carlton, A. G.; Wiedinmyer, C.; Kroll, J. H. A Review of Secondary Organic Aerosol (SOA) Formation from Isoprene. *Atmospheric Chemistry and Physics* **2009**, *9* (14), 4987–5005. https://doi.org/10.5194/acp-9-4987-2009.

Chan, A. W. H.; Kautzman, K. E.; Chhabra, P. S.; Surratt, J. D.; Chan, M. N.; Crounse, J. D.; Kürten, A.; Wennberg, P. O.; Flagan, R. C.; Seinfeld, J. H. Secondary Organic Aerosol Formation from Photooxidation of Naphthalene and Alkylnaphthalenes: Implications for Oxidation of Intermediate Volatility Organic Compounds (IVOCs). *Atmospheric Chemistry and Physics* **2009**, *9* (9), 3049–3060. https://doi.org/10.5194/acp-9-3049-2009

Chow, J. C.; Watson, J. G.; Lowenthal, D. H.; Magliano, K. L. Loss of PM2.5 Nitrate from Filter Samples in Central California. *Journal of the Air & Waste Management Association* **2005**, *55* (8), 1158–1168. https://doi.org/10.1080/10473289.2005.10464704

Cohen, A. J.; Brauer, M.; Burnett, R.; Anderson, H. R.; Frostad, J.; Estep, K.; Balakrishnan, K.; Brunekreef, B.; Dandona, L.; Dandona, R.; Feigin, V.; Freedman, G.; Hubbell, B.; Jobling, A.; Kan, H.; Knibbs, L.; Liu, Y.; Martin, R.; Morawska, L.; Pope, C. A.; Shin, H.; Straif, K.; Shaddick, G.; Thomas, M.; van Dingenen, R.; van Donkelaar, A.; Vos, T.; Murray, C. J. L.; Forouzanfar, M. H. Estimates and 25-Year Trends of the Global Burden of Disease Attributable to Ambient Air Pollution: An Analysis of Data from the Global Burden of Diseases Study 2015. *Lancet* **2017**, *389* (10082), 1907–1918. https://doi.org/10.1016/S0140-6736(17)30505-6.

Crounse, J. D.; Nielsen, L. B.; Jørgensen, S.; Kjaergaard, H. G.; Wennberg, P. O. Autoxidation of Organic Compounds in the Atmosphere. *J. Phys. Chem. Lett.* **2013**, *4* (20), 3513–3520. https://doi.org/10.1021/jz4019207.

Day, D. A.; Campuzano-Jost, P.; Nault, B. A.; Palm, B. B.; Hu, W.; Guo, H.; Wooldridge, P. J.; Cohen, R. C.; Docherty, K. S.; Huffman, J. A.; de Sá, S. S.; Martin, S. T.; Jimenez, J. L. A Systematic Re-Evaluation of Methods for Quantification of Bulk Particle-Phase Organic Nitrates Using Real-Time Aerosol Mass Spectrometry. *Atmospheric Measurement Techniques* **2022**, *15* (2), 459–483. https://doi.org/10.5194/amt-15-459-2022.

De Gouw, J. A.; Gilman, J. B.; Kim, S.-W.; Lerner, B. M.; Isaacman-VanWertz, G.; McDonald, B. C.; Warneke, C.; Kuster, W. C.; Lefer, B. L.; Griffith, S. M.; Dusanter, S.; Stevens, P. S.; Stutz, J. Chemistry of Volatile Organic Compounds in the Los Angeles Basin: Nighttime Removal of Alkenes and Determination of Emission Ratios. *Journal of Geophysical Research: Atmospheres* **2017**, *122* (21), 11,843-11,861. https://doi.org/10.1002/2017JD027459.

Docherty, K. S.; Aiken, A. C.; Huffman, J. A.; Ulbrich, I. M.; DeCarlo, P. F.; Sueper, D.; Worsnop, D. R.; Snyder, D. C.; Peltier, R. E.; Weber, R. J.; Grover, B. D.; Eatough, D. J.; Williams, B. J.; Goldstein, A. H.; Ziemann, P. J.; Jimenez, J. L. The 2005 Study of Organic Aerosols at Riverside (SOAR-1): Instrumental Intercomparisons and Fine Particle Composition. *Atmospheric Chemistry and Physics* **2011**, *11* (23), 12387–12420. https://doi.org/10.5194/acp-11-12387-2011.

Dzepina, K.; Volkamer, R. M.; Madronich, S.; Tulet, P.; Ulbrich, I. M.; Zhang, Q.; Cappa, C. D.; Ziemann, P. J.; Jimenez, J. L. Evaluation of Recently-Proposed Secondary Organic Aerosol Models for a Case Study in Mexico City. *Atmospheric Chemistry and Physics* **2009**, *9* (15), 5681–5709. https://doi.org/10.5194/acp-9-5681-2009

Eddingsaas, N. C.; Loza, C. L.; Yee, L. D.; Chan, M.; Schilling, K. A.; Chhabra, P. S.; Seinfeld, J. H.; Wennberg, P. O. α-Pinene Photooxidation under Controlled Chemical Conditions – Part 2: SOA Yield and Composition in Low- and High-NO_x Environments. *Atmospheric Chemistry and Physics* **2012**, *12* (16), 7413–7427. https://doi.org/10.5194/acp-12-7413-2012.

Ellis, R. A.; Murphy, J. G.; Pattey, E.; van Haarlem, R.; O'Brien, J. M.; Herndon, S. C. Characterizing a Quantum Cascade Tunable Infrared Laser Differential Absorption Spectrometer (QC-TILDAS) for Measurements of Atmospheric Ammonia. *Atmospheric Measurement Techniques* **2010**, *3* (2), 397–406. https://doi.org/10.5194/amt-3-397-2010

Ensberg, J. J.; Craven, J. S.; Metcalf, A. R.; Allan, J. D.; Angevine, W. M.; Bahreini, R.; Brioude, J.; Cai, C.; Coe, H.; Gouw, J. A. de; Ellis, R. A.; Flynn, J. H.; Haman, C. L.; Hayes, P. L.; Jimenez, J. L.; Lefer, B. L.; Middlebrook, A. M.; Murphy, J. G.; Neuman, J. A.; Nowak, J. B.; Roberts, J. M.; Stutz, J.; Taylor, J. W.; Veres, P. R.; Walker, J. M.; Seinfeld, J. H. Inorganic and Black Carbon Aerosols in the Los Angeles Basin during CalNex. *Journal of Geophysical Research: Atmospheres* **2013**, *118* (4), 1777–1803. https://doi.org/10.1029/2012JD018136.

Ensberg, J. J.; Hayes, P. L.; Jimenez, J. L.; Gilman, J. B.; Kuster, W. C.; de Gouw, J. A.; Holloway, J. S.; Gordon, T. D.; Jathar, S.; Robinson, A. L.; Seinfeld, J. H. Emission Factor Ratios, SOA Mass Yields, and the Impact of Vehicular Emissions on SOA Formation. *Atmospheric Chemistry and Physics* **2014**, *14* (5), 2383–2397. https://doi.org/10.5194/acp-14-2383-2014.

Environmental Protection Agency (EPA), PM-2.5 (2012) Designated Area/State Information, Accessed at: https://www3.epa.gov/airquality/greenbook/kbtc.html. Last accessed: Feb. 23, 2022

Environmental Protection Agency (EPA), Regulations for On-road Vehicles and Engines, Accessed at: https://www.epa.gov/regulations-emissions-vehicles-and-engines/regulations-onroad-vehicles-and-engines. Last accessed: Feb 7, 2022.

Emissions Factor Analysis Model (EMFAC2021), California Air Resources Board, Accessed at: https://arb.ca.gov/emfac/

Farmer, D. K.; Matsunaga, A.; Docherty, K. S.; Surratt, J. D.; Seinfeld, J. H.; Ziemann, P. J.; Jimenez, J. L. Response of an Aerosol Mass Spectrometer to Organonitrates and Organosulfates

and Implications for Atmospheric Chemistry. *PNAS* **2010**, *107* (15), 6670–6675. https://doi.org/10.1073/pnas.0912340107.

Fountoukis, C.; Nenes, A. ISORROPIA II: A Computationally Efficient Thermodynamic Equilibrium Model for K^+;Ca^{2+};Mg^{2+};NH_4^+;Na^+;SO_4^{2-};NO_3^-;Cl^- ;H_2O Aerosols. *Atmospheric Chemistry and Physics* **2007**, *7* (17), 4639–4659. https://doi.org/10.5194/acp-7-4639-2007

Fry, J. L.; Draper, D. C.; Zarzana, K. J.; Campuzano-Jost, P.; Day, D. A.; Jimenez, J. L.; Brown, S. S.; Cohen, R. C.; Kaser, L.; Hansel, A.; Cappellin, L.; Karl, T.; Hodzic Roux, A.; Turnipseed, A.; Cantrell, C.; Lefer, B. L.; Grossberg, N. Observations of Gas- and Aerosol-Phase Organic Nitrates at BEACHON-RoMBAS 2011. *Atmos. Chem. Phys.* **2013**, *13* (17), 8585–8605. https://doi.org/10.5194/acp-13-8585-2013.

Gentner, D. R.; Worton, D. R.; Isaacman, G.; Davis, L. C.; Dallmann, T. R.; Wood, E. C.; Herndon, S. C.; Goldstein, A. H.; Harley, R. A. Chemical Composition of Gas-Phase Organic Carbon Emissions from Motor Vehicles and Implications for Ozone Production. *Environ. Sci. Technol.* **2013**, *47* (20), 11837–11848. https://doi.org/10.1021/es401470e.

Gentner, D. R.; Jathar, S. H.; Gordon, T. D.; Bahreini, R.; Day, D. A.; El Haddad, I.; Hayes, P. L.; Pieber, S. M.; Platt, S. M.; de Gouw, J.; Goldstein, A. H.; Harley, R. A.; Jimenez, J. L.; Prévôt, A. S. H.; Robinson, A. L. Review of Urban Secondary Organic Aerosol Formation from Gasoline and Diesel Motor Vehicle Emissions. *Environ. Sci. Technol.* **2017**, *51* (3), 1074–1093. https://doi.org/10.1021/acs.est.6b04509.

Gordon, T. D.; Presto, A. A.; May, A. A.; Nguyen, N. T.; Lipsky, E. M.; Donahue, N. M.; Gutierrez, A.; Zhang, M.; Maddox, C.; Rieger, P.; Chattopadhyay, S.; Maldonado, H.; Maricq, M. M.; Robinson, A. L. Secondary Organic Aerosol Formation Exceeds Primary Particulate Matter Emissions for Light-Duty Gasoline Vehicles. *Atmospheric Chemistry and Physics* **2014**, *14* (9), 4661–4678. https://doi.org/10.5194/acp-14-4661-2014.

Griffith, S. M.; Hansen, R. F.; Dusanter, S.; Michoud, V.; Gilman, J. B.; Kuster, W. C.; Veres, P. R.; Graus, M.; Gouw, J. A. de; Roberts, J.; Young, C.; Washenfelder, R.; Brown, S. S.; Thalman, R.; Waxman, E.; Volkamer, R.; Tsai, C.; Stutz, J.; Flynn, J. H.; Grossberg, N.; Lefer, B.; Alvarez, S. L.; Rappenglueck, B.; Mielke, L. H.; Osthoff, H. D.; Stevens, P. S. Measurements of Hydroxyl and Hydroperoxy Radicals during CalNex-LA: Model Comparisons and Radical Budgets. *Journal of Geophysical Research: Atmospheres* **2016**, *121* (8), 4211–4232. https://doi.org/10.1002/2015JD024358

Guo, H.; Liu, J.; Froyd, K. D.; Roberts, J. M.; Veres, P. R.; Hayes, P. L.; Jimenez, J. L.; Nenes, A.; Weber, R. J. Fine Particle PH and Gas–Particle Phase Partitioning of Inorganic Species in Pasadena, California, during the 2010 CalNex Campaign. *Atmospheric Chemistry and Physics* **2017**, *17* (9), 5703–5719. https://doi.org/10.5194/acp-17-5703-2017

Gkatzelis, G. I.; Papanastasiou, D. K.; Karydis, V. A.; Hohaus, T.; Liu, Y.; Schmitt, S. H.; Schlag, P.; Fuchs, H.; Novelli, A.; Chen, Q.; Cheng, X.; Broch, S.; Dong, H.; Holland, F.; Li, X.; Liu, Y.; Ma, X.; Reimer, D.; Rohrer, F.; Shao, M.; Tan, Z.; Taraborrelli, D.; Tillmann, R.; Wang, H.; Wang, Y.; Wu, Y.; Wu, Z.; Zeng, L.; Zheng, J.; Hu, M.; Lu, K.; Hofzumahaus, A.; Zhang, Y.; Wahner, A.; Kiendler-Scharr, A. Uptake of Water-Soluble Gas-Phase Oxidation Products Drives

Organic Particulate Pollution in Beijing. *Geophysical Research Letters* **2021**, *48* (8), e2020GL091351. https://doi.org/10.1029/2020GL091351.

Hasheminassab, S.; Daher, N.; Ostro, B. D.; Sioutas, C. Long-Term Source Apportionment of Ambient Fine Particulate Matter (PM2.5) in the Los Angeles Basin: A Focus on Emissions Reduction from Vehicular Sources. *Environmental Pollution* **2014**, *193*, 54–64. https://doi.org/10.1016/j.envpol.2014.06.012

Hayes, P. L.; Ortega, A. M.; Cubison, M. J.; Froyd, K. D.; Zhao, Y.; Cliff, S. S.; Hu, W. W.; Toohey, D. W.; Flynn, J. H.; Lefer, B. L.; Grossberg, N.; Alvarez, S.; Rappenglück, B.; Taylor, J. W.; Allan, J. D.; Holloway, J. S.; Gilman, J. B.; Kuster, W. C.; de Gouw, J. A.; Massoli, P.; Zhang, X.; Liu, J.; Weber, R. J.; Corrigan, A. L.; Russell, L. M.; Isaacman, G.; Worton, D. R.; Kreisberg, N. M.; Goldstein, A. H.; Thalman, R.; Waxman, E. M.; Volkamer, R.; Lin, Y. H.; Surratt, J. D.; Kleindienst, T. E.; Offenberg, J. H.; Dusanter, S.; Griffith, S.; Stevens, P. S.; Brioude, J.; Angevine, W. M.; Jimenez, J. L. Organic Aerosol Composition and Sources in Pasadena, California, during the 2010 CalNex Campaign. *J. Geophys. Res. Atmos.* **2013**, *118* (16), 9233–9257. https://doi.org/10.1002/jgrd.50530

Hayes, P. L.; Carlton, A. G.; Baker, K. R.; Ahmadov, R.; Washenfelder, R. A.; Alvarez, S.; Rappenglück, B.; Gilman, J. B.; Kuster, W. C.; de Gouw, J. A.; Zotter, P.; Prévôt, A. S. H.; Szidat, S.; Kleindienst, T. E.; Offenberg, J. H.; Ma, P. K.; Jimenez, J. L. Modeling the Formation and Aging of Secondary Organic Aerosols in Los Angeles during CalNex 2010. *Atmospheric Chemistry and Physics* **2015**, *15* (10), 5773–5801. https://doi.org/10.5194/acp-15-5773-2015.

Heald, C. L.; Collett, J. L. J.; Lee, T.; Benedict, K. B.; Schwandner, F. M.; Li, Y.; Clarisse, L.; Hurtmans, D. R.; Van Damme, M.; Clerbaux, C.; Coheur, P.-F.; Philip, S.; Martin, R. V.; Pye, H. O. T. Atmospheric Ammonia and Particulate Inorganic Nitrogen over the United States. *Atmospheric Chemistry and Physics* **2012**, *12* (21), 10295–10312. https://doi.org/10.5194/acp-12-10295-2012.

Hennigan, C. J.; Bergin, M. H.; Russell, A. G.; Nenes, A.; Weber, R. J. Gas/Particle Partitioning of Water-Soluble Organic Aerosol in Atlanta. *Atmospheric Chemistry and Physics* **2009**, *9* (11), 3613–3628. https://doi.org/10.5194/acp-9-3613-2009.

Hering, S.; Cass, G. The Magnitude of Bias in the Measurement of PM_{25} Arising from Volatilization of Particulate Nitrate from Teflon Filters. *Journal of the Air & Waste Management Association* **1999**, *49* (6), 725–733. https://doi.org/10.1080/10473289.1999.10463843

Hersey, S. P.; Craven, J. S.; Schilling, K. A.; Metcalf, A. R.; Sorooshian, A.; Chan, M. N.; Flagan, R. C.; Seinfeld, J. H. The Pasadena Aerosol Characterization Observatory (PACO): Chemical and Physical Analysis of the Western Los Angeles Basin Aerosol. *Atmos. Chem. Phys.* **2011**, *11* (15), 7417–7443. https://doi.org/10.5194/acp-11-7417-2011.

Jathar, S. H.; Miracolo, M. A.; Tkacik, D. S.; Donahue, N. M.; Adams, P. J.; Robinson, A. L. Secondary Organic Aerosol Formation from Photo-Oxidation of Unburned Fuel: Experimental Results and Implications for Aerosol Formation from Combustion Emissions. *Environ. Sci. Technol.* **2013**, *47* (22), 12886–12893. https://doi.org/10.1021/es403445q.

Jathar, S. H.; Gordon, T. D.; Hennigan, C. J.; Pye, H. O. T.; Pouliot, G.; Adams, P. J.; Donahue, N. M.; Robinson, A. L. Unspeciated Organic Emissions from Combustion Sources and Their Influence on the Secondary Organic Aerosol Budget in the United States. *PNAS* **2014**, *111* (29), 10473–10478. https://doi.org/10.1073/pnas.1323740111.

Jathar, S. H.; Woody, M.; Pye, H. O. T.; Baker, K. R.; Robinson, A. L. Chemical Transport Model Simulations of Organic Aerosol in Southern California: Model Evaluation and Gasoline and Diesel Source Contributions. *Atmospheric Chemistry and Physics* **2017**, *17* (6), 4305–4318. https://doi.org/10.5194/acp-17-4305-2017.

Khare, P.; Gentner, D. R. Considering the Future of Anthropogenic Gas-Phase Organic Compound Emissions and the Increasing Influence of Non-Combustion Sources on Urban Air Quality. *Atmospheric Chemistry and Physics* **2018**, *18* (8), 5391–5413. https://doi.org/10.5194/acp-18-5391-2018.

Khare, P.; Machesky, J.; Soto, R.; He, M.; Presto, A. A.; Gentner, D. R. Asphalt-Related Emissions Are a Major Missing Nontraditional Source of Secondary Organic Aerosol Precursors. *Science Advances* **2020**, *6* (36), eabb9785. https://doi.org/10.1126/sciadv.abb9785.

Kim, B. M.; Cassmassi, J.; Hogo, H.; Zeldin, M. D. Positive Organic Carbon Artifacts on Filter Medium During PM2.5 Sampling in the South Coast Air Basin. *Aerosol Science and Technology* **2001**, *34*, 35–41. https://doi.org/10.1080/02786820118227.

Kim, S.-W.; McDonald, B. C.; Baidar, S.; Brown, S. S.; Dube, B.; Ferrare, R. A.; Frost, G. J.; Harley, R. A.; Holloway, J. S.; Lee, H.-J.; McKeen, S. A.; Neuman, J. A.; Nowak, J. B.; Oetjen, H.; Ortega, I.; Pollack, I. B.; Roberts, J. M.; Ryerson, T. B.; Scarino, A. J.; Senff, C. J.; Thalman, R.; Trainer, M.; Volkamer, R.; Wagner, N.; Washenfelder, R. A.; Waxman, E.; Young, C. J. Modeling the Weekly Cycle of NOx and CO Emissions and Their Impacts on O3 in the Los Angeles-South Coast Air Basin during the CalNex 2010 Field Campaign. *Journal of Geophysical Research: Atmospheres* **2016**, *121* (3), 1340–1360. https://doi.org/10.1002/2015JD024292.

Klein, F.; Platt, S. M.; Farren, N. J.; Detournay, A.; Bruns, E. A.; Bozzetti, C.; Daellenbach, K. R.; Kilic, D.; Kumar, N. K.; Pieber, S. M.; Slowik, J. G.; Temime-Roussel, B.; Marchand, N.; Hamilton, J. F.; Baltensperger, U.; Prévôt, A. S. H.; El Haddad, I. Characterization of Gas-Phase Organics Using Proton Transfer Reaction Time-of-Flight Mass Spectrometry: Cooking Emissions. *Environ. Sci. Technol.* **2016**, *50* (3), 1243–1250. https://doi.org/10.1021/acs.est.5b04618.

Lawson, D. R. The Southern California Air Quality Study. *Journal of the Air & Waste Management Association* **1990**, *40* (2), 156–165. https://doi.org/10.1080/10473289.1990.10466671

Le, T.-C.; Shukla, K. K.; Chen, Y.-T.; Chang, S.-C.; Lin, T.-Y.; Li, Z.; Pui, D. Y. H.; Tsai, C.-J. On the Concentration Differences between PM2.5 FEM Monitors and FRM Samplers. *Atmospheric Environment* **2020**, *222*, 117138. https://doi.org/10.1016/j.atmosenv.2019.117138.

Liu, C.-N.; Lin, S.-F.; Tsai, C.-J.; Wu, Y.-C.; Chen, C.-F. Theoretical Model for the Evaporation Loss of PM2.5 during Filter Sampling. *Atmospheric Environment* **2015**, *109*, 79–86. https://doi.org/10.1016/j.atmosenv.2015.03.012.

Liu, C.-N.; Awasthi, A.; Hung, Y.-H.; Gugamsetty, B.; Tsai, C.-J.; Wu, Y.-C.; Chen, C.-F. Differences in 24-h Average PM2.5 Concentrations between the Beta Attenuation Monitor (BAM) and the Dichotomous Sampler (Dichot). *Atmospheric Environment* **2013**, *75*, 341–347. https://doi.org/10.1016/j.atmosenv.2013.04.062.

Lu, Q.; Zhao, Y.; Robinson, A. L. Comprehensive Organic Emission Profiles for Gasoline, Diesel, and Gas-Turbine Engines Including Intermediate and Semi-Volatile Organic Compound Emissions. *Atmospheric Chemistry and Physics* **2018**, *18* (23), 17637–17654. https://doi.org/10.5194/acp-18-17637-2018.

Lu, Q.; Murphy, B. N.; Qin, M.; Adams, P. J.; Zhao, Y.; Pye, H. O. T.; Efstathiou, C.; Allen, C.; Robinson, A. L. Simulation of Organic Aerosol Formation during the CalNex Study: Updated Mobile Emissions and Secondary Organic Aerosol Parameterization for Intermediate-Volatility Organic Compounds. *Atmos. Chem. Phys.* **2020**, *20* (7), 4313–4332. https://doi.org/10.5194/acp-20-4313-2020.

Ma, P. K.; Zhao, Y.; Robinson, A. L.; Worton, D. R.; Goldstein, A. H.; Ortega, A. M.; Jimenez, J. L.; Zotter, P.; Prévôt, A. S. H.; Szidat, S.; Hayes, P. L. Evaluating the Impact of New Observational Constraints on P-S/IVOC Emissions, Multi-Generation Oxidation, and Chamber Wall Losses on SOA Modeling for Los Angeles, CA. *Atmospheric Chemistry and Physics* **2017**, *17* (15), 9237–9259. https://doi.org/10.5194/acp-17-9237-2017.

Matsunaga, A.; Ziemann ‡, P. J. Gas-Wall Partitioning of Organic Compounds in a Teflon Film Chamber and Potential Effects on Reaction Product and Aerosol Yield Measurements. *Aerosol Science and Technology* **2010**, *44* (10), 881–892. https://doi.org/10.1080/02786826.2010.501044.

May, A. A.; Nguyen, N. T.; Presto, A. A.; Gordon, T. D.; Lipsky, E. M.; Karve, M.; Gutierrez, A.; Robertson, W. H.; Zhang, M.; Brandow, C.; Chang, O.; Chen, S.; Cicero-Fernandez, P.; Dinkins, L.; Fuentes, M.; Huang, S.-M.; Ling, R.; Long, J.; Maddox, C.; Massetti, J.; McCauley, E.; Miguel, A.; Na, K.; Ong, R.; Pang, Y.; Rieger, P.; Sax, T.; Truong, T.; Vo, T.; Chattopadhyay, S.; Maldonado, H.; Maricq, M. M.; Robinson, A. L. Gas- and Particle-Phase Primary Emissions from in-Use, on-Road Gasoline and Diesel Vehicles. *Atmospheric Environment* **2014**, *88*, 247–260. https://doi.org/10.1016/j.atmosenv.2014.01.046.

McDonald, B. C.; Goldstein, A. H.; Harley, R. A. Long-Term Trends in California Mobile Source Emissions and Ambient Concentrations of Black Carbon and Organic Aerosol. *Environ. Sci. Technol.* **2015**, *49* (8), 5178–5188. https://doi.org/10.1021/es505912b.

McDonald, B. C.; Gouw, J. A. de; Gilman, J. B.; Jathar, S. H.; Akherati, A.; Cappa, C. D.; Jimenez, J. L.; Lee-Taylor, J.; Hayes, P. L.; McKeen, S. A.; Cui, Y. Y.; Kim, S.-W.; Gentner, D. R.; Isaacman-VanWertz, G.; Goldstein, A. H.; Harley, R. A.; Frost, G. J.; Roberts, J. M.; Ryerson, T. B.; Trainer, M. Volatile Chemical Products Emerging as Largest Petrochemical Source of Urban Organic Emissions. *Science* **2018**, *359* (6377), 760–764. https://doi.org/10.1126/science.aaq0524.

Middlebrook, A. M.; Bahreini, R.; Jimenez, J. L.; Canagaratna, M. R. Evaluation of Composition-Dependent Collection Efficiencies for the Aerodyne Aerosol Mass Spectrometer Using Field

Data. *Aerosol Science and Technology* **2012**, *46* (3), 258–271. https://doi.org/10.1080/02786826.2011.620041.

Mielke, L. H.; Stutz, J.; Tsai, C.; Hurlock, S. C.; Roberts, J. M.; Veres, P. R.; Froyd, K. D.; Hayes, P. L.; Cubison, M. J.; Jimenez, J. L.; Washenfelder, R. A.; Young, C. J.; Gilman, J. B.; Gouw, J. A. de; Flynn, J. H.; Grossberg, N.; Lefer, B. L.; Liu, J.; Weber, R. J.; Osthoff, H. D. Heterogeneous Formation of Nitryl Chloride and Its Role as a Nocturnal NOx Reservoir Species during CalNex-LA 2010. *Journal of Geophysical Research: Atmospheres* **2013**, *118* (18), 10,638-10,652. https://doi.org/10.1002/jgrd.50783.

Murphy, B. N.; Woody, M. C.; Jimenez, J. L.; Carlton, A. M. G.; Hayes, P. L.; Liu, S.; Ng, N. L.; Russell, L. M.; Setyan, A.; Xu, L.; Young, J.; Zaveri, R. A.; Zhang, Q.; Pye, H. O. T. Semivolatile POA and Parameterized Total Combustion SOA in CMAQv5.2: Impacts on Source Strength and Partitioning. *Atmospheric Chemistry and Physics* **2017**, *17* (18), 11107–11133. https://doi.org/10.5194/acp-17-11107-2017.

Nah, T.; McVay, R. C.; Zhang, X.; Boyd, C. M.; Seinfeld, J. H.; Ng, N. L. Influence of Seed Aerosol Surface Area and Oxidation Rate on Vapor Walldeposition and SOA Mass Yields: A Case Study with <I>A</I>-Pineneozonolysis. *Atmos. Chem. Phys.* **2016**, *16* (14), 9361–9379. https://doi.org/10.5194/acp-16-9361-2016.

Ng, N. L.; Kroll, J. H.; Chan, A. W. H.; Chhabra, P. S.; Flagan, R. C.; Seinfeld, J. H. Secondary Organic Aerosol Formation from *m*-Xylene, Toluene, and Benzene. *Atmospheric Chemistry and Physics* **2007**, *7* (14), 3909–3922. https://doi.org/10.5194/acp-7-3909-2007.

Nussbaumer, C. M.; Cohen, R. C. Impact of OA on the Temperature Dependence of PM 2.5 in the Los Angeles Basin. *Environ. Sci. Technol.* **2021**, *55* (6), 3549–3558. https://doi.org/10.1021/acs.est.0c07144.

Ortega, A. M.; Hayes, P. L.; Peng, Z.; Palm, B. B.; Hu, W.; Day, D. A.; Li, R.; Cubison, M. J.; Brune, W. H.; Graus, M.; Warneke, C.; Gilman, J. B.; Kuster, W. C.; Gouw, J. de; Gutiérrez-Montes, C.; Jimenez, J. L. Real-Time Measurements of Secondary Organic Aerosol Formation and Aging from Ambient Air in an Oxidation Flow Reactor in the Los Angeles Area. *Atmospheric Chemistry and Physics* **2016**, *16* (11), 7411–7433. https://doi.org/10.5194/acp-16-7411-2016.

Paatero, P.; Tapper, U. Positive Matrix Factorization: A Non-Negative Factor Model with Optimal Utilization of Error Estimates of Data Values. *Environmetrics* **1994**, *5* (2), 111–126. https://doi.org/10.1002/env.3170050203.

Paatero, P. Least Squares Formulation of Robust Non-Negative Factor Analysis. *Chemometrics and Intelligent Laboratory Systems* **1997**, *37* (1), 23–35. https://doi.org/10.1016/S0169-7439(96)00044-5.

Parker, H. A.; Hasheminassab, S.; Crounse, J. D.; Roehl, C. M.; Wennberg, P. O. Impacts of Traffic Reductions Associated With COVID-19 on Southern California Air Quality. *Geophysical Research Letters* **2020**, *47* (23), e2020GL090164. https://doi.org/10.1029/2020GL090164.

Parrish, D. D.; Stohl, A.; Forster, C.; Atlas, E. L.; Blake, D. R.; Goldan, P. D.; Kuster, W. C.; Gouw, J. A. de. Effects of Mixing on Evolution of Hydrocarbon Ratios in the Troposphere.

Journal of Geophysical Research: Atmospheres **2007**, *112* (D10). https://doi.org/10.1029/2006JD007583.

Pennington, E. A.; Seltzer, K. M.; Murphy, B. N.; Qin, M.; Seinfeld, J. H.; Pye, H. O. T. Modeling Secondary Organic Aerosol Formation from Volatile Chemical Products. *Atmospheric Chemistry and Physics Discussions* **2021**, 1–26. https://doi.org/10.5194/acp-2021-547.

Pollack, I. B.; Ryerson, T. B.; Trainer, M.; Parrish, D. D.; Andrews, A. E.; Atlas, E. L.; Blake, D. R.; Brown, S. S.; Commane, R.; Daube, B. C.; Gouw, J. A. de; Dubé, W. P.; Flynn, J.; Frost, G. J.; Gilman, J. B.; Grossberg, N.; Holloway, J. S.; Kofler, J.; Kort, E. A.; Kuster, W. C.; Lang, P. M.; Lefer, B.; Lueb, R. A.; Neuman, J. A.; Nowak, J. B.; Novelli, P. C.; Peischl, J.; Perring, A. E.; Roberts, J. M.; Santoni, G.; Schwarz, J. P.; Spackman, J. R.; Wagner, N. L.; Warneke, C.; Washenfelder, R. A.; Wofsy, S. C.; Xiang, B. Airborne and Ground-Based Observations of a Weekend Effect in Ozone, Precursors, and Oxidation Products in the California South Coast Air Basin. *Journal of Geophysical Research: Atmospheres* **2012**, *117* (D21). https://doi.org/10.1029/2011JD016772.

Pollack, I. B.; Ryerson, T. B.; Trainer, M.; Neuman, J. A.; Roberts, J. M.; Parrish, D. D. Trends in Ozone, Its Precursors, and Related Secondary Oxidation Products in Los Angeles, California: A Synthesis of Measurements from 1960 to 2010. *Journal of Geophysical Research: Atmospheres* **2013**, *118* (11), 5893–5911. https://doi.org/10.1002/jgrd.50472.

Praske, E.; Otkjær, R. V.; Crounse, J. D.; Hethcox, J. C.; Stoltz, B. M.; Kjaergaard, H. G.; Wennberg, P. O. Atmospheric Autoxidation Is Increasingly Important in Urban and Suburban North America. *PNAS* **2018**, *115* (1), 64–69. https://doi.org/10.1073/pnas.1715540115.

Pye, H. O. T.; Ward-Caviness, C. K.; Murphy, B. N.; Appel, K. W.; Seltzer, K. M. Secondary Organic Aerosol Association with Cardiorespiratory Disease Mortality in the United States. *Nat Commun* **2021**, *12* (1), 7215. https://doi.org/10.1038/s41467-021-27484-1.

Robinson, A. L.; Donahue, N. M.; Shrivastava, M. K.; Weitkamp, E. A.; Sage, A. M.; Grieshop, A. P.; Lane, T. E.; Pierce, J. R.; Pandis, S. N. Rethinking Organic Aerosols: Semivolatile Emissions and Photochemical Aging. *Science* **2007**, *315* (5816), 1259–1262. https://doi.org/10.1126/science.1133061.

Schauer, J. J.; Rogge, W. F.; Hildemann, L. M.; Mazurek, M. A.; Cass, G. R.; Simoneit, B. R. T. Source Apportionment of Airborne Particulate Matter Using Organic Compounds as Tracers. *Atmospheric Environment* **1996**, *30* (22), 3837–3855. https://doi.org/10.1016/1352-2310(96)00085-4.

Schiferl, L. D.; Heald, C. L.; Nowak, J. B.; Holloway, J. S.; Neuman, J. A.; Bahreini, R.; Pollack, I. B.; Ryerson, T. B.; Wiedinmyer, C.; Murphy, J. G. An Investigation of Ammonia and Inorganic Particulate Matter in California during the CalNex Campaign. *Journal of Geophysical Research: Atmospheres* **2014**, *119* (4), 1883–1902. https://doi.org/10.1002/2013JD020765.

Seinfeld, J. H. and Pandis, S. Atmospheric Chemistry and Physics: From Air Pollution to Climate Change, Third Edition, **2016**, *Wiley & Sons*, Hoboken, New Jersey

Seltzer, K. M.; Murphy, B. N.; Pennington, E. A.; Allen, C.; Talgo, K.; Pye, H. O. T. Volatile Chemical Product Enhancements to Criteria Pollutants in the United States. *Environ. Sci. Technol.* **2021a**. https://doi.org/10.1021/acs.est.1c04298.

Seltzer, K. M.; Pennington, E.; Rao, V.; Murphy, B. N.; Strum, M.; Isaacs, K. K.; Pye, H. O. T. Reactive Organic Carbon Emissions from Volatile Chemical Products. *Atmospheric Chemistry and Physics* **2021b**, *21* (6), 5079–5100. https://doi.org/10.5194/acp-21-5079-2021.

Simpson, I. J.; Blake, N. J.; Barletta, B.; Diskin, G. S.; Fuelberg, H. E.; Gorham, K.; Huey, L. G.; Meinardi, S.; Rowland, F. S.; Vay, S. A.; Weinheimer, A. J.; Yang, M.; Blake, D. R. Characterization of Trace Gases Measured over Alberta Oil Sands Mining Operations: 76 Speciated C_2–C_{10} Volatile Organic Compounds (VOCs), CO_2, CH_4, CO, NO, NO_2, NO_y, O_3 and SO_2. *Atmospheric Chemistry and Physics* **2010**, *10* (23), 11931–11954. https://doi.org/10.5194/acp-10-11931-2010.

Stein, A. F.; Draxler, R. R.; Rolph, G. D.; Stunder, B. J. B.; Cohen, M. D.; Ngan, F. NOAA's HYSPLIT Atmospheric Transport and Dispersion Modeling System. *Bull. Amer. Meteor. Soc.* **2015**, *96* (12), 2059–2077. https://doi.org/10.1175/BAMS-D-14-00110.1.

Stone, E. A.; Zhou, J.; Snyder, D. C.; Rutter, A. P.; Mieritz, M.; Schauer, J. J. A Comparison of Summertime Secondary Organic Aerosol Source Contributions at Contrasting Urban Locations. *Environ. Sci. Technol.* **2009**, *43* (10), 3448–3454. https://doi.org/10.1021/es8025209.

Takhar, M.; Stroud, C. A.; Chan, A. W. H. Volatility Distribution and Evaporation Rates of Organic Aerosol from Cooking Oils and Their Evolution upon Heterogeneous Oxidation. *ACS Earth Space Chem.* **2019**, *3* (9), 1717–1728. https://doi.org/10.1021/acsearthspacechem.9b00110.

Tkacik, D. S.; Lambe, A. T.; Jathar, S.; Li, X.; Presto, A. A.; Zhao, Y.; Blake, D.; Meinardi, S.; Jayne, J. T.; Croteau, P. L.; Robinson, A. L. Secondary Organic Aerosol Formation from In-Use Motor Vehicle Emissions Using a Potential Aerosol Mass Reactor. *Environ. Sci. Technol.* **2014**, *48* (19), 11235–11242. https://doi.org/10.1021/es502239v.

Ulbrich, I. M.; Canagaratna, M. R.; Zhang, Q.; Worsnop, D. R.; Jimenez, J. L. Interpretation of Organic Components from Positive Matrix Factorization of Aerosol Mass Spectrometric Data. *Atmospheric Chemistry and Physics* **2009**, *9* (9), 2891–2918. https://doi.org/10.5194/acp-9-2891-2009.

Van Rooy, P.; Tasnia, A.; Barletta, B.; Buenconsejo, R.; Crounse, J. D.; Kenseth, C. M.; Meinardi, S.; Murphy, S.; Parker, H.; Schulze, B.; Seinfeld, J. H.; Wennberg, P. O.; Blake, D. R.; Barsanti, K. C. Observations of Volatile Organic Compounds in the Los Angeles Basin during COVID-19. *ACS Earth Space Chem.* **2021**, *5* (11), 3045–3055. https://doi.org/10.1021/acsearthspacechem.1c00248.

Vecchi, R.; Valli, G.; Fermo, P.; D'Alessandro, A.; Piazzalunga, A.; Bernardoni, V. Organic and Inorganic Sampling Artefacts Assessment. *Atmospheric Environment* **2009**, *43* (10), 1713–1720. https://doi.org/10.1016/j.atmosenv.2008.12.016.

Veres, P.; Roberts, J. M.; Warneke, C.; Welsh-Bon, D.; Zahniser, M.; Herndon, S.; Fall, R.; de Gouw, J. Development of Negative-Ion Proton-Transfer Chemical-Ionization Mass Spectrometry

(NI-PT-CIMS) for the Measurement of Gas-Phase Organic Acids in the Atmosphere. *International Journal of Mass Spectrometry* **2008**, *274* (1), 48–55. https://doi.org/10.1016/j.ijms.2008.04.032.

Wang, H.; Wang, H.; Lu, X.; Lu, K.; Zhang, L.; Tham, Y. J.; Shi, Z.; Aikin, K.; Fan, S.; Brown, S. S.; Zhang, Y. Increased Night-Time Oxidation over China despite Widespread Decrease across the Globe. *Nat. Geosci.* **2023**, 1–7. https://doi.org/10.1038/s41561-022-01122-x.

Warneke, C.; Gouw, J. A. de; Holloway, J. S.; Peischl, J.; Ryerson, T. B.; Atlas, E.; Blake, D.; Trainer, M.; Parrish, D. D. Multiyear Trends in Volatile Organic Compounds in Los Angeles, California: Five Decades of Decreasing Emissions. *Journal of Geophysical Research: Atmospheres* **2012**, *117* (D21). https://doi.org/10.1029/2012JD017899.

Warneke, C.; Gouw, J. A. de; Edwards, P. M.; Holloway, J. S.; Gilman, J. B.; Kuster, W. C.; Graus, M.; Atlas, E.; Blake, D.; Gentner, D. R.; Goldstein, A. H.; Harley, R. A.; Alvarez, S.; Rappenglueck, B.; Trainer, M.; Parrish, D. D. Photochemical Aging of Volatile Organic Compounds in the Los Angeles Basin: Weekday-Weekend Effect. *Journal of Geophysical Research: Atmospheres* **2013**, *118* (10), 5018–5028. https://doi.org/10.1002/jgrd.50423.

Washenfelder, R. A.; Young, C. J.; Brown, S. S.; Angevine, W. M.; Atlas, E. L.; Blake, D. R.; Bon, D. M.; Cubison, M. J.; Gouw, J. A. de; Dusanter, S.; Flynn, J.; Gilman, J. B.; Graus, M.; Griffith, S.; Grossberg, N.; Hayes, P. L.; Jimenez, J. L.; Kuster, W. C.; Lefer, B. L.; Pollack, I. B.; Ryerson, T. B.; Stark, H.; Stevens, P. S.; Trainer, M. K. The Glyoxal Budget and Its Contribution to Organic Aerosol for Los Angeles, California, during CalNex 2010. *Journal of Geophysical Research: Atmospheres* **2011**, *116* (D21). https://doi.org/10.1029/2011JD016314.

Watson, J. G.; Chow, J. C.; Lu, Z.; Fujita, E. M.; Lowenthal, D. H.; Lawson, D. R.; Ashbaugh, L. L. Chemical Mass Balance Source Apportionment of PM10 during the Southern California Air Quality Study. *Aerosol Science and Technology* **1994**, *21* (1), 1–36. https://doi.org/10.1080/02786829408959693.

Xu, L.; Suresh, S.; Guo, H.; Weber, R. J.; Ng, N. L. Aerosol Characterization over the Southeastern United States Using High-Resolution Aerosol Mass Spectrometry: Spatial and Seasonal Variation of Aerosol Composition and Sources with a Focus on Organic Nitrates. *Atmos. Chem. Phys.* **2015**, *15* (13), 7307–7336. https://doi.org/10.5194/acp-15-7307-2015.

Xu, B.; Zhang, G.; Gustafsson, Ö.; Kawamura, K.; Li, J.; Andersson, A.; Bikkina, S.; Kunwar, B.; Pokhrel, A.; Zhong, G.; Zhao, S.; Li, J.; Huang, C.; Cheng, Z.; Zhu, S.; Peng, P.; Sheng, G. Large Contribution of Fossil-Derived Components to Aqueous Secondary Organic Aerosols in China. *Nat Commun* **2022**, *13* (1), 5115. https://doi.org/10.1038/s41467-022-32863-3.

Yu, X.-Y.; Lee, T.; Ayres, B.; Kreidenweis, S. M.; Collett, J. L.; Malm, W. Particulate Nitrate Measurement Using Nylon Filters. *Journal of the Air & Waste Management Association* **2005**, *55* (8), 1100–1110. https://doi.org/10.1080/10473289.2005.10464721.

Zhang, X.; McMurry, P. H. Evaporative Losses of Fine Particulate Nitrates during Sampling. *Atmospheric Environment. Part A. General Topics* **1992**, *26* (18), 3305–3312. https://doi.org/10.1016/0960-1686(92)90347-N.

Zhang, Q.; Worsnop, D. R.; Canagaratna, M. R.; Jimenez, J. L. Hydrocarbon-like and Oxygenated Organic Aerosols in Pittsburgh: Insights into Sources and Processes of Organic Aerosols. *Atmospheric Chemistry and Physics* **2005**, *5* (12), 3289–3311. https://doi.org/10.5194/acp-5-3289-2005.

Zhang, X.; Liu, J.; Parker, E. T.; Hayes, P. L.; Jimenez, J. L.; de Gouw, J. A.; Flynn, J. H.; Grossberg, N.; Lefer, B. L.; Weber, R. J. On the Gas-Particle Partitioning of Soluble Organic Aerosol in Two Urban Atmospheres with Contrasting Emissions: 1. Bulk Water-Soluble Organic Carbon. *Journal of Geophysical Research: Atmospheres* **2012**, *117* (D21). https://doi.org/10.1029/2012JD017908.

Zhang, X.; Cappa, C. D.; Jathar, S. H.; McVay, R. C.; Ensberg, J. J.; Kleeman, M. J.; Seinfeld, J. H. Influence of Vapor Wall Loss in Laboratory Chambers on Yields of Secondary Organic Aerosol. *PNAS* **2014**, *111* (16), 5802–5807. https://doi.org/10.1073/pnas.1404727111.

Zhao, Y.; Hennigan, C. J.; May, A. A.; Tkacik, D. S.; de Gouw, J. A.; Gilman, J. B.; Kuster, W. C.; Borbon, A.; Robinson, A. L. Intermediate-Volatility Organic Compounds: A Large Source of Secondary Organic Aerosol. *Environ. Sci. Technol.* **2014**, *48* (23), 13743–13750. https://doi.org/10.1021/es5035188.

Zhao, Y.; Saleh, R.; Saliba, G.; Presto, A. A.; Gordon, T. D.; Drozd, G. T.; Goldstein, A. H.; Donahue, N. M.; Robinson, A. L. Reducing Secondary Organic Aerosol Formation from Gasoline Vehicle Exhaust. *PNAS* **2017**, *114* (27), 6984–6989. https://doi.org/10.1073/pnas.1620911114.

Zhao, Y.; Tkacik, D. S.; May, A. A.; Donahue, N. M.; Robinson, A. L. Mobile Sources Are Still an Important Source of Secondary Organic Aerosol and Fine Particulate Matter in the Los Angeles Region. *Environ. Sci. Technol.* **2022**. https://doi.org/10.1021/acs.est.2c03317.

Zotter, P.; El-Haddad, I.; Zhang, Y.; Hayes, P. L.; Zhang, X.; Lin, Y.-H.; Wacker, L.; Schnelle-Kreis, J.; Abbaszade, G.; Zimmermann, R.; Surratt, J. D.; Weber, R.; Jimenez, J. L.; Szidat, S.; Baltensperger, U.; Prévôt, A. S. H. Diurnal Cycle of Fossil and Nonfossil Carbon Using Radiocarbon Analyses during CalNex. *Journal of Geophysical Research: Atmospheres* **2014**, *119* (11), 6818–6835. https://doi.org/10.1002/2013JD021114.

C h a p t e r 3

Estimates of methane emissions from dairy operations in California's San Joaquin Valley using airborne measurements

Benjamin C. Schulze, Ryan X. Ward, Eva Y. Pfannerstill, Qindan Zhu, Caleb Arata, Bryan Place, Clara Nussbaumer, Paul Wooldridge, Roy Woods, Anthony Bucholz, Ronald C. Cohen, Allen H. Goldstein, Paul O. Wennberg, John H. Seinfeld. *Environmental Science & Technology*. Submitted.

Abstract

State inventories indicate that dairy operations account for nearly half of California's methane budget. Recent analyses suggest, however, that these emissions may be underestimated, complicating efforts to develop emission reduction strategies. Here, we report estimates of dairy methane emissions in the southern San Joaquin Valley (SJV) of California in June of 2021 using airborne flux measurements. We find average methane emission rates of 120 ± 35 kg dairy^{-1} hour^{-1} in this region, corresponding to 60 ± 18 g dairy cow^{-1} hr^{-1}. These values are ~20% larger than annual average estimates from the recently-developed VISTA-CA inventory. We observed notable increases in emissions with temperature. Our estimates align well with inventory predictions when parameterizations for the temperature dependence of emissions are applied. Our measurements further demonstrate that the VISTA-CA emission inventory is considerably more accurate than the EPA GHG-I inventory in this region. Source apportionment analyses confirm that dairy operations produce the majority of methane emissions in the southern SJV (~65%). Fugitive oil and gas (O&G) sources account for the remaining ~35%. Our results support the accuracy of the process-based models used to develop dairy emission inventories and highlight the need for additional investigation of the meteorological dependence of these emissions.

3.1 Introduction

Considerable reductions in emissions of short-lived greenhouse gases are needed to prevent global temperatures from rising more than 1.5oC by the end of the century1. Methane emissions have been prioritized for near-term reduction as methane has a global warming potential (GWP) of 84 over a 20-year period and a lifetime of only 9-10 years[2]. In California, methane emissions represent ~10% of the total greenhouse gas budget, and inventories suggest dairy operations account for nearly 50% of the total[3]. Emissions from dairy operations are approximately equally divided between enteric fermentation and manure management practices[3]. California Senate Bill 1383 aims to reduce methane emissions from manure management at California's dairies by 40% relative to 2013 levels by 2030[4.]

Effective implementation of emission reduction plans requires detailed understanding of the current magnitude of dairy emissions and accurate monitoring as control technologies are adopted. Despite their importance as an emission source, recent analyses have noted discrepancies between top-down estimates of dairy emissions and bottom-up inventory calculations. Estimates using inverse modeling techniques applied to both long-term[5,6] and short-term[7,8] measurements suggest that methane emissions from dairy livestock may be twice as large as the California Air Resources Board (CARB) predicts. However long-term measurements at individual dairy facilities[9], short-term surveys of multiple dairy facilities[10,11], and short-term inverse modeling studies[12] have supported the accuracy of CARB emission predictions.

Efforts to verify bottom-up inventories with top-down measurements are often complicated by the need to assess long-term average estimates (e.g., annual inventory emissions estimates) using the results of short-term measurement campaigns. Emissions from dairies may vary on seasonal and daily timescales[9,12,13] and may be highly intermittent, driven either by temporal variability in routine operations or spontaneous leaks in emission containment devices[14]. Given this complexity and the relative lack of coordinated observational emissions studies in California[9,11,12,15], additional direct measurements of dairy emissions are needed to evaluate the accuracy of the state emission inventory.

In this study, we report estimates of methane emissions from dairy operations in the San Joaquin Valley (SJV) using airborne measurements of methane fluxes during the 2021 Re-Evaluating the Chemistry of Air Pollutants in California (RECAP-CA) campaign. Approximately 90% of the state's dairy cows reside in the SJV, and the region is predicted to have the largest methane emissions per cow in the state due to the specific manure management practices utilized[3].

A total of seven flights were conducted over the SJV in June of 2021, covering approximately 5000 km at an altitude of 400 m. Each of the seven flights intersected the region of dense dairy operations in Tulare and Kings Counties while also including legs upwind of most dairy operations, enabling both eddy-covariance (EC) and mass-balance (MB) based estimates of dairy methane fluxes.

Our results support the validity of the process-based models used to develop dairy methane emission inventories. Our data further suggest that airborne EC measurements may represent a useful component of a future multi-tiered methane emission monitoring network in California.

3.2 Methods

3.2.1 Overview of RECAP-CA flights

Sixteen total flights were conducted during RECAP-CA using a two-engine UV-18A Twin Otter research aircraft operated by the Naval Postgraduate School (NPS). Seven of these flights took place over California's San Joaquin Valley (Figure 3.S1). Flights were based out of the Burbank, CA airport and lasted 4-5 hours during the middle of the day (~11:00 AM-4:00 PM local time).

Ambient air was sampled into the Twin Otter using a 3-inch diameter isokinetic inlet extending above the nose of the aircraft. Vertical wind speeds used in eddy covariance (EC) flux calculations were measured using a five-hole radome probe at the nose of the aircraft. Detailed descriptions of the NPS Twin Otter can be found elsewhere16.

San Joaquin Valley flight tracks were chosen to ensure coverage of a variety of potential emission sources including dairy operations in the Visalia/Tulare region, croplands, the

cities of Bakersfield and Fresno, CA, the I-99 highway, and the Kern River Oil Field. Flight tracks were optimized to minimize turns for EC flux calculations.

3.2.2 Instrumentation

Methane concentrations were measured using a Picarro G2401-m cavity ringdown spectrometer (CRDS) at a frequency of 0.5 Hz. Ambient air was drawn into the instrument from the primary aircraft inlet using a 2 m ¼" Teflon line. The Picarro G2401-m was located towards the rear of the aircraft, and the approximate lag time between the vertical wind sensor on the aircraft nose and the G2401-m measurement was ~8-10s. As discussed in SI Section 3.S1, we estimate a measurement precision of 1 ppbv based on in-flight measurements of standard gases and an accuracy of 2 ppbv based on ground-level calibrations performed following every flight (all uncertainties 1σ), in line with previous studies that utilized Picarro CRDS systems[17,18]. Methane concentrations are reported as dry air mole fractions.

Concentrations of volatile organic compounds (VOC) used in the positive matrix factorization (PMF) analysis described below were measured using a Vocus proton transfer reaction time-of-flight mass spectrometer (PTR-ToF-MS). A detailed description of the operation of the PTR-ToF-MS is provided in Pfannerstill et al. (2023)[19]. Precision in individual VOC concentrations is estimated at <10%.

3.2.3 Estimation of methane emissions using the mass balance method

Methane emissions from dairy operations in the SJV were estimated using the mass balance (MB) technique, which has been used extensively for airborne quantification of emissions from area and point sources[17,18,20,21]. Briefly, following temporally invariant emissions from a point or area source, the flux of a conserved tracer through a sufficiently large two-dimensional plane can be assumed constant if the wind field throughout a survey region is stable. This allows flux quantification downwind using individual passes through the emission plume if a) emissions have mixed vertically and b) the mixing height is known. The inferred emission rate can be calculated using the following18:

$$Emission\ rate = vcos(\alpha) \int_0^z \int_{-y}^{y} (X - X_{bg}) dy\ dz \quad (1)$$

Where vcos(α) represents the component of the measured horizontal wind velocity normal to the flight track, z is the estimated mixing height, here assumed to be the altitude of the planetary boundary layer (PBL), y is the crosswind distance covered during the flight leg, and (X-Xbg) is the methane enhancement above the local estimated background concentration.

We applied the MB method to three flight legs that largely encompassed the region of intensive dairy operations near Visalia, CA (Figure 3.S3, 3.S12). Local wind fields were inconsistent in the region on three of the seven flights, preventing MB calculations (Figure 3.S3). Additional descriptions of associated uncertainties and estimates of emissions from non-dairy sources within the region are included in SI Section 3.S2 and SI Section 3.S3.

3.2.4 Calculation of airborne EC fluxes using the continuous wavelet transform

In addition to the MB method, we estimated methane emissions from dairies using measured EC fluxes. We quantified fluxes using the continuous wavelet transform (CWT), a technique being increasingly adopted for airborne flux measurements[19,22-26.]

The CWT deconvolves contributions to time series variance along both time and frequency domains and does not require airmass stationarity. A more detailed description of the calculation procedure is provided in SI Section 3.S3.

We used a disjunct method to quantify CWT fluxes from the Picarro G2401-m measurements, as described in further detail in SI Section 3.S4. Descriptions of uncertainty calculations are provided in SI Section 3.S4.1. As noted in SI Section 3.S4, we correct the CWT fluxes for high-frequency losses related to the time resolution (0.5 Hz) of the Picarro-G2401-m measurements. Figure 3.S7 demonstrates that following these corrections, average H2O fluxes calculated from the non-continuous G2401-m data agree well with fluxes calculated from 10Hz measurements made with the fast, continuous, LICOR LI-7500DS H2O analyzer.

Flux footprints, defined as the surface region that encompasses emission sources capable of contributing to a given measured flux, were calculated following Metzger et al.

(2012)[27], as explained in SI Section 3.S5[19,24]. Calculated footprints were used to apportion measured fluxes to surface level latitude-longitude grid cells for comparisons with published emission inventories.

3.2.5 Positive Matrix Factorization (PMF) of the combined GHG + VOC dataset

We performed Positive Matrix Factorization (PMF) on a combined dataset consisting of greenhouse gas measurements collected by the Picarro G2401-m and VOC measurements made by the VOCUS PTR-ToF-MS to gain further insight into methane sources in the SJV. Briefly, PMF is a bilinear unmixing factor analysis model that deconvolves a time series of measured species into a set of compositionally static factors whose contributions to the input dataset vary in time[28,29].

For this study, greenhouse gases measured by the Picarro G2401-m (CH4, CO, and CO2) were combined with 38 VOCs measured by the VOCUS PTR-ToF-MS to form the input data matrix. Detailed descriptions of the data preparation, input error estimation, solution selection, and uncertainty quantification processes are provided in SI Section 3.S6. A five-factor solution was identified as optimally describing the input dataset.

3.3 Results and discussion

3.3.1 Overview of observed methane concentrations and eddy covariance fluxes

Figure 3.1 shows average methane concentrations and inferred surface fluxes measured during seven flights over the SJV as part of RECAP-CA. Average concentrations within the region of intensive dairy operations near Visalia, CA were ~50-100 ppbv higher than in the urban regions surveyed, while the average flux (16.1 ± 6.8 mg m^{-2} hr^{-1} (1σ uncertainty)) was nearly three times as large as that observed over the urban areas (5.7 ± 2.1 and 6.1 ± 2.2 mg m^{-2} hr^{-1} in Fresno and Bakersfield, respectively). Oil and gas production is virtually absent in the dairy region, and natural gas emissions from leaking transmission and distribution lines are expected to be much lower than in the urban areas (SI Section 3.S3)[30]. The only considerable point sources of methane emissions in the dairy region are three landfills and two power generating stations near the cities of Visalia,

Hanford, and Tulare[31]. As discussed in SI Section 3.S3, the total estimated emissions from these point sources represent a small fraction of the total dairy-related emissions. Spatial correlations between methane concentrations and dairy-related VOC tracers (e.g., methanol, ethanol, and acetaldehyde) were also considerably larger ($R \approx 0.7$) than correlations with combustion tracers (e.g., CO and aromatics) ($R = 0.1$-0.5 depending on species) when averaged to 0.1° x 0.1° grid cells (Figure 3.S10)[32,33,34].

While all seven flights occurred within a single month, meteorological conditions varied considerably between flights, with median ambient temperatures at flight altitude ranging from ~15°C to 30°C. Observed methane fluxes varied considerably with temperature in each of the three major regions surveyed. In the dairy region specifically, fluxes increased by approximately ~70% from the lowest temperature tercile (inferred ground-level temperature of <23°C) (12 mg m^{-2} hr^{-1}) to the highest tercile (>29°C) (22 mg m^{-2} hr^{-1}) (Figure 3.S11).

3.3.2 Estimates of methane emissions from dairy operations

3.3.2.1 Mass-balance based estimates

Figure 3.S12 shows methane concentrations measured on four flights during the three flight legs that largely encompassed the region of intensive dairy operations in the southern SJV. Observed winds were consistently from the north-northwest at ~3-4 m s^{-1}, and methane concentrations were typically elevated by ~50-200 ppbv on the eastern legs near the southernmost dairy farms relative to the western legs. Wind fields were inconsistent within the region on RF2, RF11, and RF16 (Figure 3.S3), and as a result we used measurements from the four remaining SJV flights (RF5, RF6, RF10, and RF12) to estimate methane emissions using the mass balance method[18,20] (Figure 3.S12). Table 3.S1 provides an example of the parameters used to calculate the methane flux through each leg, the associated uncertainties, and the total calculated emissions within the region during RF5.

Emissions from dairy operations in the MB region were estimated by subtracting emissions from local point sources and natural gas leakage from the total calculated using

Eq. 1, as detailed in SI Section 3.S3. Ultimately, the sum of estimated point source and natural gas leakage emissions accounted for less than 1% of the total emissions inferred from the mass balance calculations, while total cropland emissions may account for up to 3% of total emissions.

To calculate effective emissions per dairy, we divided the dairy-associated emissions by the number of dairies in the MB region (330 ± 50) according to VISTA-CA[35]. We assume a 15% uncertainty in the total number of dairies captured by our measurements given that emission plumes from dairies near the eastern flight leg may have been advected east of the flight track by the time they reached 400 m. Results are shown in Table 3.S2 and suggest an average dairy emission rate of 113 ± 44 kg hr^{-1} during the sampling period. If results from RF12, which represents somewhat of an outlier, are excluded from the calculation, the average emission rate increases to 141 ± 53 kg hr^{-1}.

We analyzed satellite imagery to determine that an average dairy within the surveyed region has a physical area of ~0.25 km^2 (Figure 3.S14), leading to an average effective flux of 450 ± 160 mg m^{-2} hr^{-1}. Dividing the dairy-wide emissions by the average number of dairy cows within each dairy in Tulare and Kings counties (2005 ± 200) according to the 2017 USDA Census of Agriculture produces an effective emission factor (EF) of 56 ± 22 g dairy cow^{-1} hr^{-1} [36].

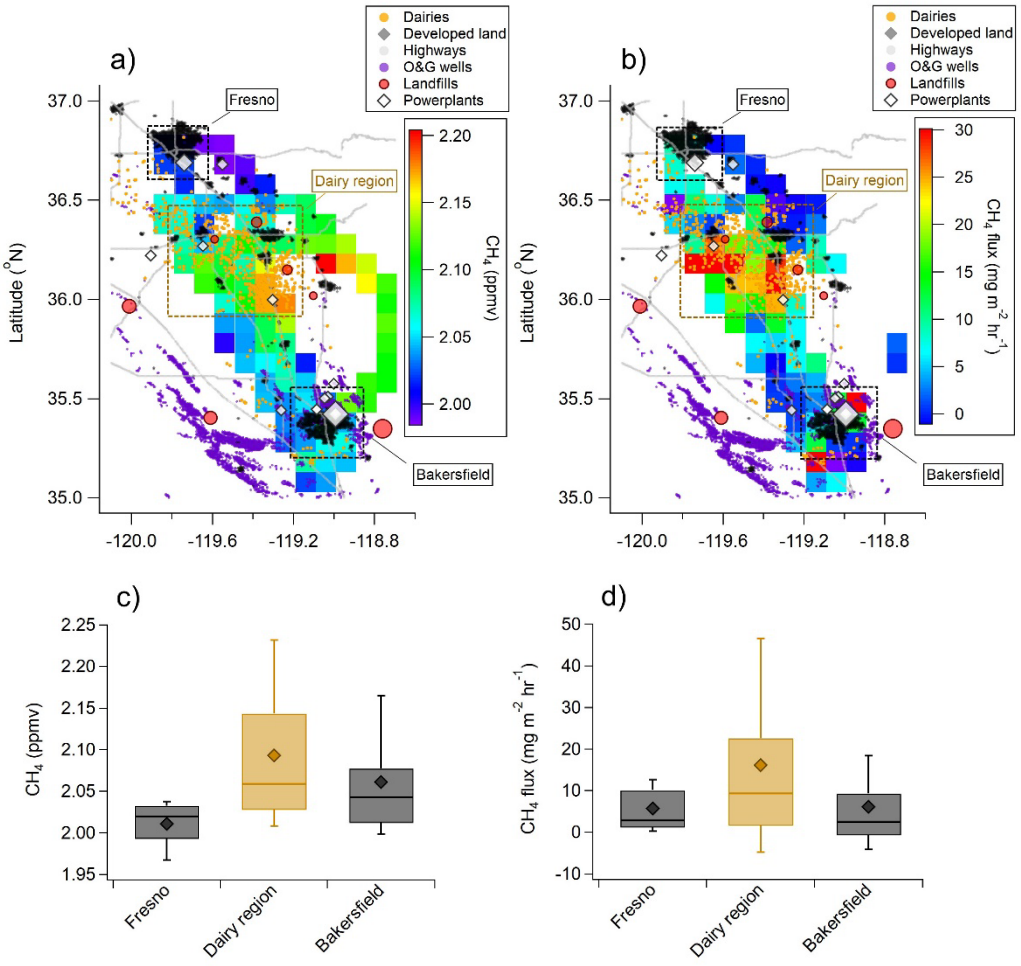

Figure 3.1: Maps of (a) average methane concentrations and (b) inferred surface fluxes measured during seven flights over the SJV during RECAP-CA. Potential methane emission sources, including dairies, oil and gas wells, landfills, developed areas, and highways are shown for reference. (c-d) Boxplots of (c) methane concentrations and (d) inferred surface fluxes in the spatial regions shown in a-b. Boxes denote the interquartile range of measurements, while bars represent the 10th and 90th percentiles. Diamond markers denote averages.

3.3.2.2 Eddy covariance-based estimates

We calculated a second estimate of dairy methane emission rates using EC fluxes. Flux footprints were first used to assign measured fluxes to 0.1° x 0.1° grid cells defined by the VISTA-CA methane emission inventory[3], as shown in Figure 3.2. Given the considerable random errors in individual flux measurements, grid cells that were sampled

infrequently and had relatively small average fluxes had relative uncertainties that exceeded 100% (e.g., segment between Fresno and the Sierra Nevada Mountains) (Figure 2b). However, uncertainties in individual grid cell estimates for regions with notable dairy presence were typically 30-60%.

Figure 3.2c shows the total area of each 0.1° x 0.1° grid cell attributable to dairy operations. Dividing the average grid cell flux by the fractional area encompassed by dairies produces an estimated dairy-level flux for dairies within the grid cell. To develop an aggregate dairy flux estimate, we only averaged grid cells that 1) contain no obvious point sources and 2) contain a notable dairy presence (total area of dairies > 1 km^2). The dairy area threshold is chosen to minimize the probability that flux footprints within a grid cell under-sampled dairies relative to their fractional area with the cell.

The average dairy flux calculated using the EC flux method was 536 ± 160 mg m^{-2} hr^{-1} (Figure 3.2), corresponding to an average emission rate of 134 ± 40 kg hr^{-1} assuming an average dairy size of 0.25 km^2 (67 ± 20 g dairy cow^{-1} hr^{-1}), which agrees with the MB-based estimate within the respective uncertainties. Changing the dairy area threshold to 2 km^2 (i.e., eight average size dairies per grid cell) or reducing it to 0.5 km^2 modifies the inferred emission rate by -14% and +5%, respectively. We note that dairies are larger on average in the southernmost SJV near Bakersfield than near Visalia (Figure 3.S13). However, accounting for this variability in our calculation only increases the inferred average dairy emission rate by 8%.

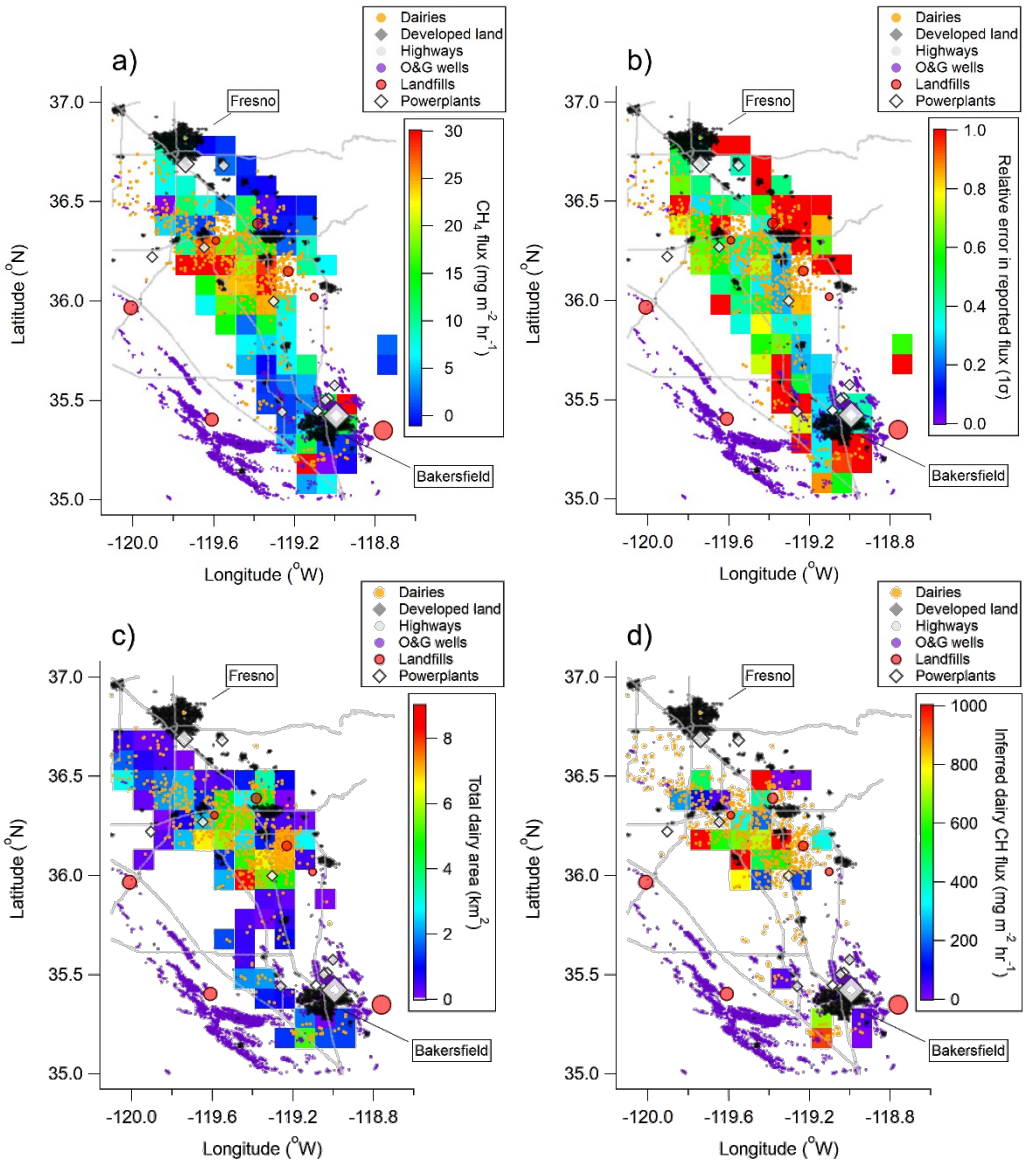

Figure 3.2: Maps of (a) inferred surface-level CH_4 fluxes (mg m^2 hr^{-1}), (b) calculated relative errors in reported fluxes, (c) total calculated area of dairy of farms in each grid cell, and (d) inferred dairy fluxes for grid cells with a notable number of dairies (>1 km^2 total area) and no other major CH_4 sources (e.g., landfills, power plants, etc.) during RECAP-CA.

3.3.3 Comparison of inferred emissions with inventory estimates and observational studies

3.3.3.1 Annual average estimates

The two methods used to calculate dairy methane emissions (MB and EC fluxes) align well with one another and suggest an average emission rate of 123 ± 35 kg hr^{-1} or an EF of 61 ±18 g dairy cow^{-1} hr^{-1} for an average-sized dairy in the southern SJV during the measurement period (Figure 3.3). Given an average area of 0.25 km^2, this corresponds to a flux of 350-630 mg m^{-2} hr^{-1}. We compare this observationally-derived emission rate with annual average dairy emissions estimates in the same region obtained from two inventories. Using CARB inventory methodology, we calculated an annual average emission rate of 94 ± 19 kg hr^{-1} for an average sized dairy in the SJV region surveyed by our flights (Figure 3.3). A detailed description of this calculation is provided in SI Section 3.S7. Dairies in this region primarily use liquid storage systems for manure management[3]. Approximately 60% of total predicted emissions are attributable to manure management, with the remainder produced by enteric fermentation (SI Section 3.S7). The inferred dairy emissions estimate based on our measurements is 31% larger than this annual inventory estimate (1σ uncertainty of -7 to +70%).

We also calculated dairy emissions in the surveyed region using the VISTA-CA inventory[3]. Figure 3.3 shows that the average dairy emission rates calculated from VISTA-CA data in either 1) the mass balance region specifically or 2) the entire region surveyed by our flux measurements agree well with one another and suggest an average dairy emission rate of ~100 kg hr^{-1}. Our inferred emission rates are ~20% larger than these values.

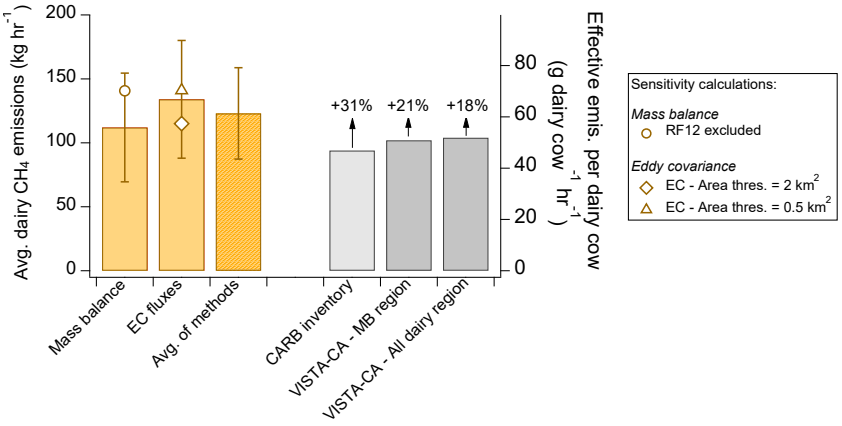

Figure 3.3: Comparison of inferred average dairy methane emission rates and emissions per dairy cow with annual average estimates calculated from CARB emission factors and the VISTA-CA inventory[3]. Emissions per dairy cow were calculated assuming an average of 2005 dairy cows per dairy according to the 2017 USDA Census of Agriculture[40] for counties in the surveyed region (Tulare, Kings, and Kern) (SI Section 3.S7). Results of sensitivity calculations are also shown.

3.3.3.2 Temperature dependence of inferred emissions

While the discussion above compares our measurements with annual average inventory estimates, observations suggest dairy methane emissions may vary considerably on seasonal timescales[9,15,37]. Such variability is likely driven by temperature and dissolved oxygen fluctuations and resulting impacts on microbial activity[9,15].

As shown in Figure 3.S16, average dairy emission rates inferred from our EC measurements increased from ~103 ± 40 kg hr^{-1} at ~18-23ºC (lowest tercile of inferred ground-level temperatures) to ~220 ± 105 kg hr^{-1} at 29-33ºC (highest tercile). We compared the measured temperature trend with predictions using CARB EF adjusted for observed temperature changes based on the parameterization developed by Maasakkers et al. (2016)[37] for manure management emissions (SI Section 3.S8).

As shown in Figure 3.S16, the predicted trend in emissions aligns with our measurements within uncertainty. We then used average monthly temperatures in Visalia, CA to calculate effective monthly average dairy emission rates by scaling CARB EF. Figure 3.S15 shows that when temperature effects are considered using the Maasakkers et al. (2016)[37] parameterization, our measured fluxes are slightly lower than inferred average June emission rates according to the scaled CARB EF (-11%), though the values agree

within the uncertainty of our measurements. These calculations demonstrate that while emission rates inferred from our June measurements are larger than annual average inventory estimates, they agree well once likely temperature effects are considered.

We further note that our measurements were only performed midday, which could also influence comparisons with annual average inventory estimates. Multiple recent studies have shown only minor differences between daytime and nighttime methane emissions from manure storage lagoons[9,38], animal housing pens[9,39,40], and overall dairy facilities[41], even when observed seasonal variability was substantial[9], while other measurements have suggested overnight emissions from housing pens may be 50% lower than those midday[42]. Additional investigation of the temperature dependence and diurnal variability of emissions is clearly warranted given the timing and limited number of flights performed in this study.

3.3.3.3 Comparison with previous observational and inverse modeling studies

Table 3.S3 compares the effective dairy cow methane EF inferred from our measurements with the results of multiple recent observational studies in California and Colorado[9,11,41]. All measurements were performed during summer months (June-August), and average diurnal ground-level temperatures varied from 24-30ºC. Dairies sampled in the studies conducted in California used similar manure management practices (primarily liquid storage systems), and we suspect that the same is true for the Colorado dairies[41] based on satellite imagery. As shown in Table 3.S3, inferred EF agree well and suggest average values of 60 ± 16 g dairy cow hr^{-1} for these regions during the summer. We note that Arndt et al. (2018)[9] report substantial differences in EF from the two Northern California dairies sampled in their study (92 vs. 64 g dairy cow hr^{-1}), potentially due to subtle farm-to-farm differences in manure management practices. Our EF estimates agree particularly well with the results of Amini et al. (2022)[11], which aggregated emissions from dozens of individual dairy facilities in California, similarly to our study.

We then scaled our dairy cow EF to estimate total dairy methane emissions in the SJV (Table 3.S4). Briefly, our estimate of 97 ± 29 Mg hr^{-1} aligns well with that of Cui et al. (2017)[8] for measurements in June 2010 in the southern SJV (105 ± 25 Mg hr^{-1}).

Comparisons with annual average inverse-model estimates are more complicated given the likely temperature dependence of emissions, however, if we convert our June estimate into an annual average using the Maasakkers et al. (2016)[37] parameterization for likely temperature effects (SI Section 3.S8), our inferred value (584 ± 172 Gg yr^{-1}) is between the estimates of Cui et al. (2019)[43] (440 ± 360 Gg yr^{-1}) and Jeong et al. (2013)[44] (1130 ± 420 Gg yr^{-1}).

Despite the general agreement between our results, previously published summertime observational studies[11,41], and inverse model predictions for May-June conditions[8], considerable disagreement remains in the temperature dependence of dairy emissions. While we observe a substantial increase in emissions with temperature (Figure 3.S16), in line with Arndt et al. (2018)[9] and the Maasakkers et al. (2016)[37] parameterization, both observational studies[11] and recent inverse models[6,12] have suggested little to no variability between wintertime and summertime emissions. Higher wind speeds during cooler months have been suggested to account for the lack of seasonality in emissions[11,12]. During RECAP-CA, lower temperatures were not associated with considerably higher wind speeds (average of ~3.3 m s^{-1} in the lowest temperature tercile and 2.8 m s^{-1} in the highest), and therefore the seemingly contradictory results regarding emission temperature dependence may not be inconsistent. Assumptions regarding the seasonality/meteorological dependence of dairy methane emissions critically influence assessments of annual average inventory predictions using short-term measurements. Additional systematic study of this dependence is clearly warranted.

3.3.3.4 Comparison with VISTA-CA and EPA-GHGI inventories

We compared our gridded methane flux measurements to existing inventories that estimate dairy methane emissions at the state (VISTA-CA)[3] and national levels (EPA-GHGI)[37] (Figure 3.4). While these inventories predict similar total emissions from dairy operations in California[3], the spatial distributions of the published inventories vary considerably, especially in the southern SJV (Figure 3.S17), with implications for their use as model priors in inversion-based analyses of methane emission sources[8,12,43].

Correlations between our measurements and the VISTA-CA dairy inventory (R = 0.51) are considerably stronger than with the EPA 2016 livestock GHGI (R = 0.28) over the surveyed region (Figure 3.4). VISTA-CA uses detailed facility-level information (e.g., latitude-longitude) to spatially distribute dairy-related emissions in California[3], and our measurements confirm that those efforts markedly improve the inventory's spatial representativeness relative to the EPA 2016 GHGI, which assigned emissions using general livestock probability maps based on landtype[37]. The clear disagreement between our measurements and the EPA-GHGI (normalized mean bias of -81%) suggests that incorporation of the EPA inventory into hybridized inversion priors, as in Cui et al. (2019)[43], will likely decrease the accuracy of inverse model predictions of methane sources in this region.

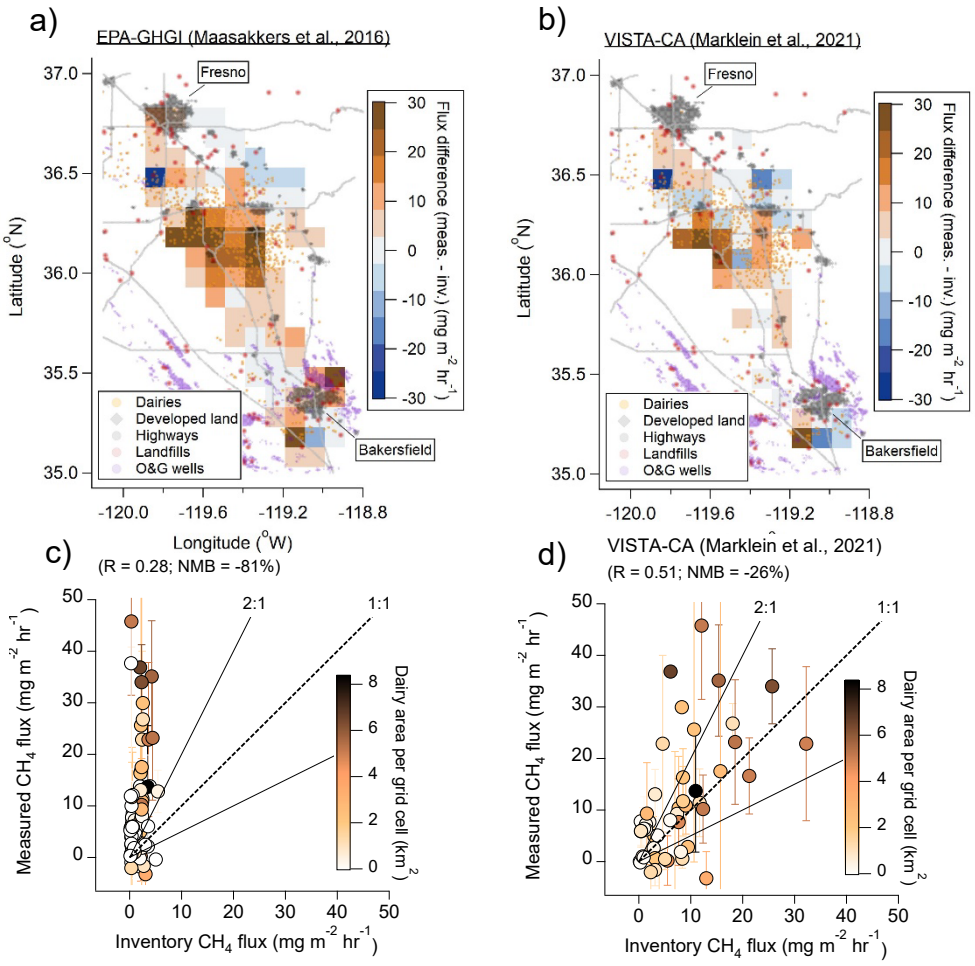

Figure 3.4: (Top) Differences between observed dairy methane fluxes during RECAP-CA and predictions from (a) the 2012 EPA-GHGI methane inventory for livestock operations[17], and (b) the VISTA-CA inventory[3]. (Bottom) Correlations of grid-cell level flux estimates across the surveyed region. The EPA-GHGI values represent predicted emissions in June, while the VISTA-CA inventory values are annual average estimates.

While some of the disagreement between our measurements and the VISTA-CA inventory could be due to non-dairy methane sources in the EC region, these sources, such as fugitive natural gas emissions, are predicted to account for a small fraction of methane emissions in grid cells where dairies are abundant, as discussed in SI Section 3.3. It is therefore more likely that the observed disagreement between the measurements and VISTA-CA inventory represents a combination of 1) temporal variability in emissions, 2) uncertainty in the flux measurements, and/or 3) uncertainty in the attribution of measured

fluxes to grid cells using flux footprints. Additional airborne flux measurements that dedicate increased flight time to surveying this region and quantifying vertical flux divergence could be used to assess the accuracy of VISTA-CA at a more granular (i.e., grid cell) level.

3.3.4 PMF analysis of the combined GHG + VOC dataset

While the flux data allow quantification of dairy methane emissions in the Tulare and Kings counties, our combined GHG + VOC PMF analysis provides further insight into the contribution of dairy emissions to methane enhancements across the broader surveyed SJV region. Five distinct factors (i.e., emission source types) were resolved from the PMF analysis. These factors are classified as emissions from dairies and livestock (Factor 1), hot-running combustion + fugitive O&G sources (Factor 2), non-dairy agricultural sources (Factor 3), cold-start combustion processes (Factor 4), and power generation/refinery facilities (Factor 5). As shown in the factor source profiles (Figure 3.S18), the dairy/livestock and hot-running combustion + fugitive O&G factors accounted for virtually all of the observed methane enhancements over the SJV (>99%). We focus our discussion on these specific factors. Descriptions of factors 3-5 are provided in the SI.

Factor 1 is classified as dairy/livestock emissions given the notable contribution of methane and VOCs previously associated with dairy emissions such as methanol, ethanol, acetaldehyde and acetic acid to the factor source profile (Figure 3.S18)[32,33,34]. Table 3.S5 demonstrates the agreement between the relative contributions of methane, methanol, and ethanol in the dairy/livestock factor and emission ratios (ER) reported from previous VOC measurements at dairy facilities[32,33,34]. The spatial distribution of the factor magnitude provides further evidence for a dairy source (Figure 3.5), with clear enhancements over the region of intensive dairy operations in Tulare and Kings Counties.

The chemical signature and spatial variability of Factor 2 suggest an association with combustion and fugitive O&G emissions. The chemical source profile contains considerable contributions from multiple combustion tracers, including CO, CO_2, alkenes, and toluene. The CO/CO_2 and toluene/CO ratios align well with predictions for on-road

gasoline vehicles from the CARB Emission Factor model (EMFAC) and with direct measurements (Table 3.S5)[45,46].

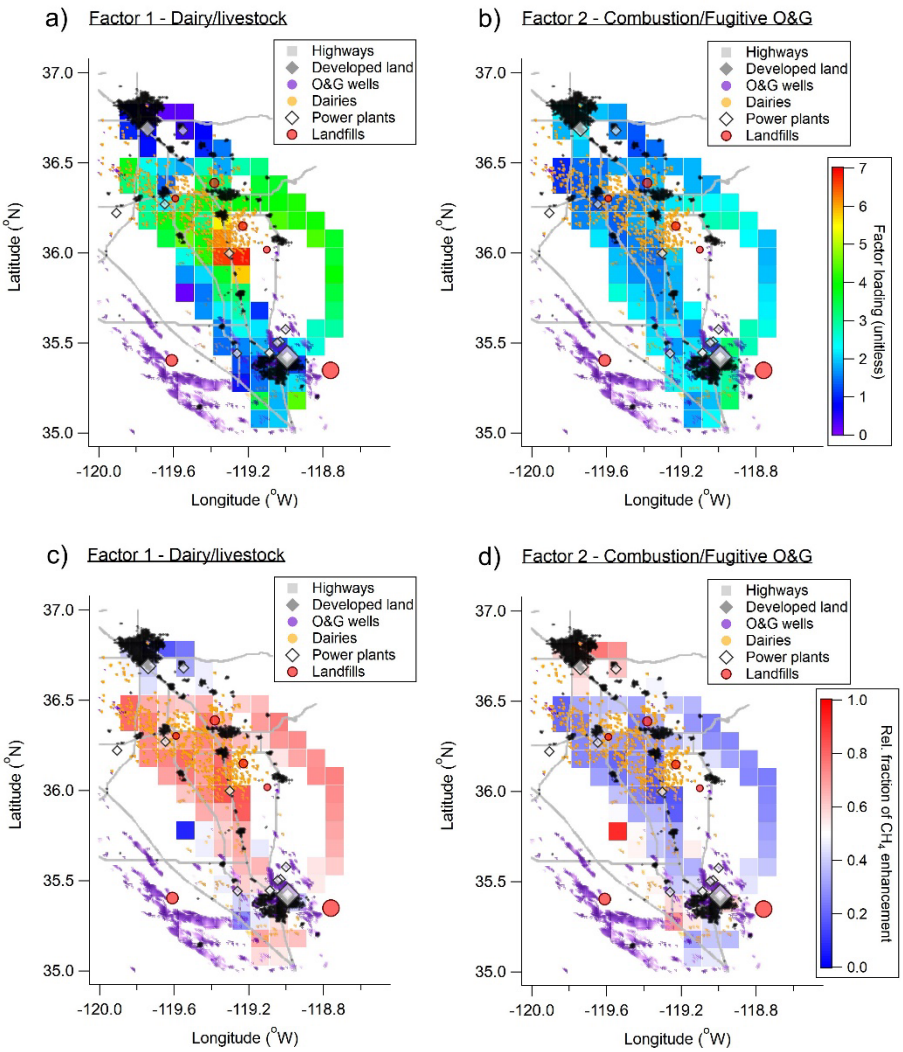

Figure 3.5: (a-b) Maps of the total concentration of the (a) dairy and livestock PMF factor (Factor 1) and (b) the combustion/fugitive oil and gas PMF factor (Factor 2) during RECAP-CA. (c-d) Contributions of factors shown in (a) and (b) to observed methane enhancements over the surveyed region. Enhancements represent the difference between ambient concentrations and the lowest concentration observed during the campaign (SI Section 3.S6). The average contribution of Factors 1 and 2 to the total methane enhancement over the surveyed region is >99%. Locations of possible emission sources are noted. Markers denoting power plants and landfills are sized in proportion to annual emissions estimates.

While many of the chemical tracers included in the source profile support a combustion source, the CH_4/CO and CH_4/CO_2 ratios in Factor 2 are roughly two orders of magnitude

larger than those estimated for on-road vehicles by EMFAC[45]. Within the SJV region surveyed during this study, areas likely associated with considerable fugitive natural gas emissions (i.e., locations of increased production and dense natural gas distribution lines) also have elevated population densities (e.g., Fresno, Bakersfield, and the smaller cities), where vehicular emissions are expected to be elevated relative to the surrounding regions[30]. We hypothesize that this spatial co-location results in the blending of multiple emission sources into a single factor. Such factor mixing was previously reported for PMF results obtained from a GHG + VOC dataset collected in Bakersfield during CalNex-2010[47].

On average, the dairy/livestock PMF factor accounted for 64 ± 10% (1σ) of the observed methane enhancements over the surveyed region, with the remainder (36 ± 9%) contributed by the combustion + fugitive O&G factor (Figure 3.5). As expected, the relative contribution from the dairy/livestock factor peaked near the cities of Visalia and Tulare, with values reacting 80-90% in individual grid cells with the largest dairy abundance. The magnitude (normalized concentration) of Factor 1 increased notably with temperature (Figure 3.S16), in line with the temperature dependence of inferred dairy emission rates.

Recent inversion models have produced a variety of estimates for the fraction of SJV methane emissions attributable to dairy/livestock sources (Figure 3.S26). The considerable differences in the fraction of total emissions from dairies reported by Jeong et al. (2016)[6] (86%) and Cui et al. (2019)[43] (47%) who used similar inverse modeling strategies to simulate emissions over similar time periods, highlights the difficulty involved in methane source apportionment using inverse modeling techniques in this measurement-limited region[43]. Notably, the average inferred fraction of methane emissions from dairies in the SJV from the five studies shown in Figure 3.S26 (70%) aligns well with our estimate (64 ± 10%).

Guha et al. (2015)[47] used a similar PMF method to determine that dairy and livestock emissions accounted for 60-70% of midday (12:00-16:00) average methane enhancements over the Bakersfield region during CalNex-2010, in line with our results. However, our conclusions regarding the source of the non-dairy-related methane emissions differ from Guha et al. (2015)[47]. We discuss these differences in SI Section 3.S6.

If we scale the relative PMF factor contributions to observed methane enhancements by the flux-derived estimate of dairy methane emissions in the SJV, we calculate methane emissions from the combustion/O&G factor of ~40 Mg hr^{-1}. This value is notably larger than the recent inversion-based of estimates of SJV O&G emissions reported by Cui et al. (2017)[8] (~21-27 Mg hr^{-1}). We note, however, that conversion of our PMF results into emissions estimates involves considerable uncertainties that are difficult to precisely quantify.

Dairies therefore accounted for the majority of inferred methane emissions in the surveyed region during our study, as expected. However, the inferred magnitude of a non-dairy source likely linked to O&G emissions underscores the importance of further efforts to characterize the methane source distribution in the SJV. Future airborne campaigns that incorporate greenhouse gas and VOC measurements could provide further insight if more measurements of O&G-associated tracers such as small alkanes are performed[10,48,49].

3.4 Atmospheric implications

We report direct airborne measurements of methane fluxes over the SJV, a region in California associated with particularly large methane emissions from dairy operations. We find midday methane emissions from an average-sized dairy in this region of 120 ± 35 kg hr^{-1}, corresponding to an effective emission rate of ~60 g dairy cow^{-1} hr^{-1}. These values are ~20% larger than annual estimates from the VISTA-CA inventory but agree within our measurement uncertainties. Emissions are observed to increase by ~100% from ~20ºC to ~32ºC, in reasonable agreement with existing parameterizations for the temperature dependence of dairy emissions in the SJV[37]. The results of our PMF analysis confirm that dairy emissions dominate the methane budget across the SJV (~65%), as expected based on previous studies[6,8,43,44,47].

Our results add to the growing body of observational evidence suggesting that the process-based models used to develop dairy methane emission inventories produce reasonably accurate emissions estimates[9,11,41]. While this conflicts with the results of multiple recent inverse modeling studies, inaccuracies in the spatial allocation of dairy

emission priors and a lack of constraining measurement sites often produce uncertainties in inverse model predictions of individual source contributions (e.g., dairy and livestock) that are either substantial (e.g., ±80%)[43] or difficult to quantify[6]. Improved agreement between inventory predictions and inverse models has recently been observed when the number of measurement locations is increased and more spatially detailed dairy emissions inventories, such as the VISTA-CA inventory, are applied[12].

While our results suggest a strong dependence of dairy methane emissions on ambient temperature, the short-term nature of our campaign, the lack of nighttime observations, and the notable uncertainties in inferred emissions estimates underscore the need for further investigation of this relationship. Longer-term datasets collected across seasons may allow development of emission parameterizations that incorporate dependencies on temperature, anaerobic lagoon agitation (e.g., through surface winds and/or rainfall), and subtle differences in manure management practices[9,11,15,38].

Additional precise measurements of methane emissions in the southern SJV will likely be needed to assess statewide progress towards dairy methane emission reduction goals. While improvement and expansion of existing long-term measurements networks will be critical for such monitoring[43], our results suggest that airborne flux measurements could provide a useful complement to the stationary monitoring network. Individual flight campaigns could be used to assess seasonal and inter-annual differences in regional emissions, while flight paths could be tailored to minimize both the systematic and random errors present in our study. Use of a methane analyzer capable of 10Hz measurements and increased characterization of vertical flux divergence could reduce uncertainties reported here by ~50%. Such error reduction would likely be necessary to accurately quantify emissions reductions on the scale expected from implementation of emission control technologies (i.e., anaerobic digesters). Short segments of individual flights could be dedicated to intensive sampling and/or comparison of emissions from individual dairies with/without anaerobic digesters using mass balance methods[11]. The airborne concentration data collected during such campaigns would also provide improved constraints for inverse models[43]. The insights gained from such multi-tiered measurement

networks would assist regulatory agencies in achieving California's methane emission reduction targets.

3.5 Acknowledgements

We would like to thank Greg Cooper, Bryce Kujat, and George Loudakis for their dedicated mission support during RECAP-CA. We would also like to thank Timothy Lueker, Jooil Kim, and Ralph Keeling for assistance with the Picarro G2401-m calibrations at the Scripps Institution of Oceanography. This research was funded by the following sources: California Air Resources Board Contract numbers 20RD003 and 20AQP012, NOAA Climate Program Office's Atmospheric Chemistry, Carbon Cycle, and Climate program, grant number NA22OAR4310540 [UCB]/ NA22OAR4310541 [AD], Office of Naval Research Defense University Research Instrumentation Program grant number N00014-19-1-2108. We thank the Resnick Sustainability Institute at Caltech for funding the purchase of the Picarro G2401-m.

3.6 References

1 IPCC, 2014. Climate Change 2014: Synthesis Report. Contribution of Working Groups I, II and III to the Fifth Assessment Report of the Intergovernmental Panel on Climate Change. In: IPCC, Geneva, Switzerland.

2 Saunois, M.; Bousquet, P.; Poulter, B.; Peregon, A.; Ciais, P.; Canadell, J. G.; Dlugokencky, E. J.; Etiope, G.; Bastviken, D.; Houweling, S.; Janssens-Maenhout, G.; Tubiello, F. N.; Castaldi, S.; Jackson, R. B.; Alexe, M.; Arora, V. K.; Beerling, D. J.; Bergamaschi, P.; Blake, D. R.; Brailsford, G.; Brovkin, V.; Bruhwiler, L.; Crevoisier, C.; Crill, P.; Covey, K.; Curry, C.; Frankenberg, C.; Gedney, N.; Höglund-Isaksson, L.; Ishizawa, M.; Ito, A.; Joos, F.; Kim, H.-S.; Kleinen, T.; Krummel, P.; Lamarque, J.-F.; Langenfelds, R.; Locatelli, R.; Machida, T.; Maksyutov, S.; McDonald, K. C.; Marshall, J.; Melton, J. R.; Morino, I.; Naik, V.; O'Doherty, S.; Parmentier, F.-J. W.; Patra, P. K.; Peng, C.; Peng, S.; Peters, G. P.; Pison, I.; Prigent, C.; Prinn, R.; Ramonet, M.; Riley, W. J.; Saito, M.; Santini, M.; Schroeder, R.; Simpson, I. J.; Spahni, R.; Steele, P.; Takizawa, A.; Thornton, B. F.; Tian, H.; Tohjima, Y.; Viovy, N.; Voulgarakis, A.; van Weele, M.; van der Werf, G. R.; Weiss, R.; Wiedinmyer, C.; Wilton, D. J.; Wiltshire, A.; Worthy, D.; Wunch, D.; Xu, X.; Yoshida, Y.; Zhang, B.; Zhang, Z.; Zhu, Q. The Global Methane Budget 2000–2012. *Earth System Science Data* **2016**, *8* (2), 697–751. https://doi.org/10.5194/essd-8-697-2016.

3 Marklein, A. R.; Meyer, D.; Fischer, M. L.; Jeong, S.; Rafiq, T.; Carr, M.; Hopkins, F. M. Facility-Scale Inventory of Dairy Methane Emissions in California: Implications for Mitigation. *Earth System Science Data* **2021**, *13* (3), 1151–1166. https://doi.org/10.5194/essd-13-1151-2021.

4 SB-1383 Short-lived climate pollutants: methane emissions: dairy and livestock: organic waste: landfills., California Legislative Information, Accessed at https://leginfo.legislature.ca.gov/faces/billNavClient.xhtml?bill_id=201520160SB1383

5 Miller, S. M.; Wofsy, S. C.; Michalak, A. M.; Kort, E. A.; Andrews, A. E.; Biraud, S. C.; Dlugokencky, E. J.; Eluszkiewicz, J.; Fischer, M. L.; Janssens-Maenhout, G.; Miller, B. R.; Miller, J. B.; Montzka, S. A.; Nehrkorn, T.; Sweeney, C. Anthropogenic Emissions of Methane in the United States. *PNAS* **2013**, *110* (50), 20018–20022. https://doi.org/10.1073/pnas.1314392110.

6 Jeong, S.; Newman, S.; Zhang, J.; Andrews, A. E.; Bianco, L.; Bagley, J.; Cui, X.; Graven, H.; Kim, J.; Salameh, P.; LaFranchi, B. W.; Priest, C.; Campos-Pineda, M.; Novakovskaia, E.; Sloop, C. D.; Michelsen, H. A.; Bambha, R. P.; Weiss, R. F.; Keeling, R.; Fischer, M. L. Estimating Methane Emissions in California's Urban and Rural Regions Using Multitower Observations. *Journal of Geophysical Research: Atmospheres* **2016**, *121* (21), 13,031-13,049. https://doi.org/10.1002/2016JD025404.

7 Zhao, C.; Andrews, A. E.; Bianco, L.; Eluszkiewicz, J.; Hirsch, A.; MacDonald, C.; Nehrkorn, T.; Fischer, M. L. Atmospheric Inverse Estimates of Methane Emissions from Central California. *Journal of Geophysical Research: Atmospheres* **2009**, *114* (D16). https://doi.org/10.1029/2008JD011671.

8 Cui, Y. Y.; Brioude, J.; Angevine, W. M.; Peischl, J.; McKeen, S. A.; Kim, S.-W.; Neuman, J. A.; Henze, D. K.; Bousserez, N.; Fischer, M. L.; Jeong, S.; Michelsen, H. A.; Bambha, R. P.; Liu, Z.; Santoni, G. W.; Daube, B. C.; Kort, E. A.; Frost, G. J.; Ryerson, T. B.; Wofsy, S. C.; Trainer, M. Top-down Estimate of Methane Emissions in California Using a Mesoscale Inverse Modeling Technique: The San Joaquin Valley. *Journal of Geophysical Research: Atmospheres* **2017**, *122* (6), 3686–3699. https://doi.org/10.1002/2016JD026398

9 Arndt, C.; Leytem, A. B.; Hristov, A. N.; Zavala-Araiza, D.; Cativiela, J. P.; Conley, S.; Daube, C.; Faloona, I.; Herndon, S. C. Short-Term Methane Emissions from 2 Dairy Farms in California Estimated by Different Measurement Techniques and US Environmental Protection Agency Inventory Methodology: A Case Study. *Journal of Dairy Science* **2018**, *101* (12), 11461–11479. https://doi.org/10.3168/jds.2017-13881.

10 Peischl, J.; Ryerson, T. B.; Brioude, J.; Aikin, K. C.; Andrews, A. E.; Atlas, E.; Blake, D.; Daube, B. C.; Gouw, J. A. de; Dlugokencky, E.; Frost, G. J.; Gentner, D. R.; Gilman, J. B.; Goldstein, A. H.; Harley, R. A.; Holloway, J. S.; Kofler, J.; Kuster, W. C.; Lang, P. M.; Novelli, P. C.; Santoni, G. W.; Trainer, M.; Wofsy, S. C.; Parrish, D. D. Quantifying Sources of Methane Using Light Alkanes in the Los Angeles Basin, California. *Journal of Geophysical Research: Atmospheres* **2013**, *118* (10), 4974–4990. https://doi.org/10.1002/jgrd.50413.

11 Amini, S.; Kuwayama, T.; Gong, L.; Falk, M.; Chen, Y.; Mitloehner, Q.; Weller, S.; Mitloehner, F. M.; Patteson, D.; Conley, S. A.; Scheehle, E.; FitzGibbon, M. Evaluating California Dairy Methane Emission Factors Using Short-Term Ground-Level and Airborne Measurements. *Atmospheric Environment: X* **2022**, *14*, 100171. https://doi.org/10.1016/j.aeaoa.2022.100171.

12 Heerah, S.; Frausto-Vicencio, I.; Jeong, S.; Marklein, A. R.; Ding, Y.; Meyer, A. G.; Parker, H. A.; Fischer, M. L.; Franklin, J. E.; Hopkins, F. M.; Dubey, M. Dairy Methane Emissions in California's San Joaquin Valley Inferred With Ground-Based Remote Sensing Observations in the Summer and Winter. *Journal of Geophysical Research: Atmospheres* **2021**, *126* (24), e2021JD034785. https://doi.org/10.1029/2021JD034785.

13 Saha, C. K.; Ammon, C.; Berg, W.; Fiedler, M.; Loebsin, C.; Sanftleben, P.; Brunsch, R.; Amon, T. Seasonal and Diel Variations of Ammonia and Methane Emissions from a Naturally Ventilated Dairy Building and the Associated Factors Influencing Emissions. *Science of The Total Environment* **2014**, *468–469*, 53–62. https://doi.org/10.1016/j.scitotenv.2013.08.015.

14 Duren, R. M.; Thorpe, A. K.; Foster, K. T.; Rafiq, T.; Hopkins, F. M.; Yadav, V.; Bue, B. D.; Thompson, D. R.; Conley, S.; Colombi, N. K.; Frankenberg, C.; McCubbin, I. B.; Eastwood, M. L.; Falk, M.; Herner, J. D.; Croes, B. E.; Green, R. O.; Miller, C. E. California's Methane Super-Emitters. *Nature* **2019**, *575* (7781), 180–184. https://doi.org/10.1038/s41586-019-1720-3.

15 Owen, J. J.; Silver, W. L. Greenhouse Gas Emissions from Dairy Manure Management: A Review of Field-Based Studies. *Global Change Biology* **2015**, *21* (2), 550–565. https://doi.org/10.1111/gcb.12687.

16 Hegg, D. A.; Covert, D. S.; Jonsson, H.; Covert, P. A. Determination of the Transmission Efficiency of an Aircraft Aerosol Inlet. *Aerosol Science and Technology* **2005**, *39* (10), 966–971. https://doi.org/10.1080/02786820500377814.

17 Pétron, G.; Karion, A.; Sweeney, C.; Miller, B. R.; Montzka, S. A.; Frost, G. J.; Trainer, M.; Tans, P.; Andrews, A.; Kofler, J.; Helmig, D.; Guenther, D.; Dlugokencky, E.; Lang, P.; Newberger, T.; Wolter, S.; Hall, B.; Novelli, P.; Brewer, A.; Conley, S.; Hardesty, M.; Banta, R.; White, A.; Noone, D.; Wolfe, D.; Schnell, R. A New Look at Methane and Nonmethane Hydrocarbon Emissions from Oil and Natural Gas Operations in the Colorado Denver-Julesburg Basin. *Journal of Geophysical Research: Atmospheres* **2014**, *119* (11), 6836–6852. https://doi.org/10.1002/2013JD021272.

18 Peischl, J.; Ryerson, T. B.; Aikin, K. C.; de Gouw, J. A.; Gilman, J. B.; Holloway, J. S.; Lerner, B. M.; Nadkarni, R.; Neuman, J. A.; Nowak, J. B.; Trainer, M.; Warneke, C.; Parrish, D. D. Quantifying Atmospheric Methane Emissions from the Haynesville, Fayetteville, and Northeastern Marcellus Shale Gas Production Regions. *Journal of Geophysical Research: Atmospheres* **2015**, *120* (5), 2119–2139. https://doi.org/10.1002/2014JD022697

19 Pfannerstill, E. Y.; Arata, C.; Zhu, Q.; Schulze, B. C.; Woods, R.; Seinfeld, J. H.; Bucholtz, A.; Cohen, R. C.; Goldstein, A. H. Volatile Organic Compound Fluxes in the San Joaquin Valley; Spatial Distribution, Source Attribution, and Inventory Comparison. *EGUsphere* **2023**, 1–42. https://doi.org/10.5194/egusphere-2023-723.

20 Peischl, J.; Karion, A.; Sweeney, C.; Kort, E. A.; Smith, M. L.; Brandt, A. R.; Yeskoo, T.; Aikin, K. C.; Conley, S. A.; Gvakharia, A.; Trainer, M.; Wolter, S.; Ryerson, T. B. Quantifying Atmospheric Methane Emissions from Oil and Natural Gas Production in the Bakken Shale Region of North Dakota. *Journal of Geophysical Research: Atmospheres* **2016**, *121* (10), 6101–6111. https://doi.org/10.1002/2015JD024631.

21 White, W. H.; Anderson, J. A.; Blumenthal, D. L.; Husar, R. B.; Gillani, N. V.; Husar, J. D.; Wilson, W. E. Formation and Transport of Secondary Air Pollutants: Ozone and Aerosols in the St. Louis Urban Plume. *Science* **1976**, *194* (4261), 187–189. https://doi.org/10.1126/science.959846.

22 Misztal, P. K.; Karl, T.; Weber, R.; Jonsson, H. H.; Guenther, A. B.; Goldstein, A. H. Airborne Flux Measurements of Biogenic Isoprene over California. *Atmospheric Chemistry and Physics* **2014**, *14* (19), 10631–10647. https://doi.org/10.5194/acp-14-10631-2014.

23 Wolfe, G. M.; Kawa, S. R.; Hanisco, T. F.; Hannun, R. A.; Newman, P. A.; Swanson, A.; Bailey, S.; Barrick, J.; Thornhill, K. L.; Diskin, G.; DiGangi, J.; Nowak, J. B.; Sorenson, C.; Bland, G.; Yungel, J. K.; Swenson, C. A. The NASA Carbon Airborne Flux Experiment (CARAFE): Instrumentation and Methodology. *Atmospheric Measurement Techniques* **2018**, *11* (3), 1757–1776. https://doi.org/10.5194/amt-11-1757-2018.

24 Zhu, Q.; Place, B.; Pfannerstill, E. Y.; Tong, S.; Zhang, H.; Wang, J.; Nussbaumer, C. M.; Wooldridge, P.; Schulze, B. C.; Arata, C.; Bucholtz, A.; Seinfeld, J. H.; Goldstein, A. H.; Cohen, R. C. Direct Observations of NO_x Emissions over the San Joaquin Valley Using Airborne Flux Measurements during RECAP-CA 2021 Field Campaign. *Atmospheric Chemistry and Physics Discussions* **2023**, 1–21. https://doi.org/10.5194/acp-2023-3.

25 Nussbaumer, C. M.; Place, B. K.; Zhu, Q.; Pfannerstill, E. Y.; Wooldridge, P.; Schulze, B. C.; Arata, C.; Ward, R.; Bucholtz, A.; Seinfeld, J. H.; Goldstein, A. H.; Cohen, R. C. Measurement Report: Airborne Measurements of NO_x Fluxes over Los Angeles during the RECAP-CA 2021 Campaign. *EGUsphere* **2023**, 1–20. https://doi.org/10.5194/egusphere-2023-601.

26 Yuan, B.; Kaser, L.; Karl, T.; Graus, M.; Peischl, J.; Campos, T. L.; Shertz, S.; Apel, E. C.; Hornbrook, R. S.; Hills, A.; Gilman, J. B.; Lerner, B. M.; Warneke, C.; Flocke, F. M.; Ryerson, T. B.; Guenther, A. B.; Gouw, J. A. de. Airborne Flux Measurements of Methane and Volatile Organic Compounds over the Haynesville and Marcellus Shale Gas Production Regions. *Journal of Geophysical Research: Atmospheres* **2015**, *120* (12), 6271–6289. https://doi.org/10.1002/2015JD023242.

27 Metzger, S.; Junkermann, W.; Mauder, M.; Beyrich, F.; Butterbach-Bahl, K.; Schmid, H. P.; Foken, T. Eddy-Covariance Flux Measurements with a Weight-Shift Microlight Aircraft. *Atmospheric Measurement Techniques* **2012**, *5* (7), 1699–1717. https://doi.org/10.5194/amt-5-1699-2012.

28 Paatero, P.; Tapper, U. Positive Matrix Factorization: A Non-Negative Factor Model with Optimal Utilization of Error Estimates of Data Values. *Environmetrics* **1994**, *5* (2), 111–126. https://doi.org/10.1002/env.3170050203.

29 Paatero, P. Least Squares Formulation of Robust Non-Negative Factor Analysis. *Chemometrics and Intelligent Laboratory Systems* **1997**, *37* (1), 23–35. https://doi.org/10.1016/S0169-7439(96)00044-5.

30 Jeong, S.; Millstein, D.; Fischer, M. L. Spatially Explicit Methane Emissions from Petroleum Production and the Natural Gas System in California. *Environ. Sci. Technol.* **2014**, *48* (10), 5982–5990. https://doi.org/10.1021/es4046692.

31 EPA Facility Level Information on GreenHouse gases Tool (FLIGHT), accessed at: https://ghgdata.epa.gov/ghgp/main.do, last accessed: 12/27/2022

32 Shaw, S. L.; Mitloehner, F. M.; Jackson, W.; DePeters, E. J.; Fadel, J. G.; Robinson, P. H.; Holzinger, R.; Goldstein, A. H. Volatile Organic Compound Emissions from Dairy Cows and Their Waste as Measured by Proton-Transfer-Reaction Mass Spectrometry. *Environ. Sci. Technol.* **2007**, *41* (4), 1310–1316. https://doi.org/10.1021/es061475e.

33 Sun, H.; Trabue, S. L.; Scoggin, K.; Jackson, W. A.; Pan, Y.; Zhao, Y.; Malkina, I. L.; Koziel, J. A.; Mitloehner, F. M. Alcohol, Volatile Fatty Acid, Phenol, and Methane Emissions from Dairy Cows and Fresh Manure. *Journal of Environmental Quality* **2008**, *37* (2), 615–622. https://doi.org/10.2134/jeq2007.0357.

34 Yuan, B.; Coggon, M. M.; Koss, A. R.; Warneke, C.; Eilerman, S.; Peischl, J.; Aikin, K. C.; Ryerson, T. B.; de Gouw, J. A. Emissions of Volatile Organic Compounds (VOCs) from Concentrated Animal Feeding Operations (CAFOs): Chemical Compositions and Separation of Sources. *Atmospheric Chemistry and Physics* **2017**, *17* (8), 4945–4956. https://doi.org/10.5194/acp-17-4945-2017.

35 Hopkins, F.M., T. Rafiq, and R.M. Duren. 2019. Sources of Methane Emissions (Vista-CA), State of California, USA. ORNL DAAC, Oak Ridge, Tennessee, USA. https://doi.org/10.3334/ORNLDAAC/1726

36 USDA 2017 Census of Agriculture, Volume 1, Chapter 2: County Level Data, United States Department of Agriculture, Accessed at: https://www.nass.usda.gov/Publications/AgCensus/2017/Full_Report/Volume_1,_Chapter_2_County_Level/California/

37 Maasakkers, J. D.; Jacob, D. J.; Sulprizio, M. P.; Turner, A. J.; Weitz, M.; Wirth, T.; Hight, C.; DeFigueiredo, M.; Desai, M.; Schmeltz, R.; Hockstad, L.; Bloom, A. A.; Bowman, K. W.; Jeong, S.; Fischer, M. L. Gridded National Inventory of U.S. Methane Emissions. *Environ. Sci. Technol.* **2016**, *50* (23), 13123–13133. https://doi.org/10.1021/acs.est.6b02878.

38 Leytem, A. B.; Bjorneberg, D. L.; Koehn, A. C.; Moraes, L. E.; Kebreab, E.; Dungan, R. S. Methane Emissions from Dairy Lagoons in the Western United States. *Journal of Dairy Science* **2017**, *100* (8), 6785–6803. https://doi.org/10.3168/jds.2017-12777.

39 Joo, H. S.; Ndegwa, P. M.; Heber, A. J.; Ni, J.-Q.; Bogan, B. W.; Ramirez-Dorronsoro, J. C.; Cortus, E. Greenhouse Gas Emissions from Naturally Ventilated Freestall Dairy Barns. *Atmospheric Environment* **2015**, *102*, 384–392. https://doi.org/10.1016/j.atmosenv.2014.11.067

40 Huang, D.; Guo, H. Diurnal and Seasonal Variations of Greenhouse Gas Emissions from a Naturally Ventilated Dairy Barn in a Cold Region. *Atmospheric Environment* **2018**, *172*, 74–82. https://doi.org/10.1016/j.atmosenv.2017.10.051.

41 Golston, L. M.; Pan, D.; Sun, K.; Tao, L.; Zondlo, M. A.; Eilerman, S. J.; Peischl, J.; Neuman, J. A.; Floerchinger, C. Variability of Ammonia and Methane Emissions from Animal Feeding Operations in Northeastern Colorado. *Environ. Sci. Technol.* **2020**, *54* (18), 11015–11024. https://doi.org/10.1021/acs.est.0c00301.

42 Saha, C. K.; Ammon, C.; Berg, W.; Fiedler, M.; Loebsin, C.; Sanftleben, P.; Brunsch, R.; Amon, T. Seasonal and Diel Variations of Ammonia and Methane Emissions from a Naturally Ventilated Dairy Building and the Associated Factors Influencing Emissions. *Science of The Total Environment* **2014**, *468–469*, 53–62. https://doi.org/10.1016/j.scitotenv.2013.08.015.

43 Cui, Y. Y.; Vijayan, A.; Falk, M.; Hsu, Y.-K.; Yin, D.; Chen, X. M.; Zhao, Z.; Avise, J.; Chen, Y.; Verhulst, K.; Duren, R.; Yadav, V.; Miller, C.; Weiss, R.; Keeling, R.; Kim, J.; Iraci, L. T.; Tanaka, T.; Johnson, M. S.; Kort, E. A.; Bianco, L.; Fischer, M. L.; Stroud, K.; Herner, J.; Croes, B. A Multiplatform Inversion Estimation of Statewide and Regional Methane Emissions in California during 2014–2016. *Environ. Sci. Technol.* **2019**, *53* (16), 9636–9645. https://doi.org/10.1021/acs.est.9b01769.

44 Jeong, S.; Hsu, Y.-K.; Andrews, A. E.; Bianco, L.; Vaca, P.; Wilczak, J. M.; Fischer, M. L. A Multitower Measurement Network Estimate of California's Methane Emissions. *Journal of Geophysical Research: Atmospheres* **2013**, *118* (19), 11,339-11,351. https://doi.org/10.1002/jgrd.50854.

45 EMissions FACtor model (EMFAC 2021 v1.02), California Air Resources Board, Accessed at: https://arb.ca.gov/emfac/

46 Gentner, D. R.; Worton, D. R.; Isaacman, G.; Davis, L. C.; Dallmann, T. R.; Wood, E. C.; Herndon, S. C.; Goldstein, A. H.; Harley, R. A. Chemical Composition of Gas-Phase Organic Carbon Emissions from Motor Vehicles and Implications for Ozone Production. *Environ. Sci. Technol.* **2013**, *47* (20), 11837–11848. https://doi.org/10.1021/es401470e.

47 Guha, A.; Gentner, D. R.; Weber, R. J.; Provencal, R.; Goldstein, A. H. Source Apportionment of Methane and Nitrous Oxide in California's San Joaquin Valley at CalNex

2010 via Positive Matrix Factorization. *Atmos. Chem. Phys.* **2015**, *15* (20), 12043–12063. https://doi.org/10.5194/acp-15-12043-2015.

48 Wennberg, P. O.; Mui, W.; Wunch, D.; Kort, E. A.; Blake, D. R.; Atlas, E. L.; Santoni, G. W.; Wofsy, S. C.; Diskin, G. S.; Jeong, S.; Fischer, M. L. On the Sources of Methane to the Los Angeles Atmosphere. *Environ. Sci. Technol.* **2012**, *46* (17), 9282–9289. https://doi.org/10.1021/es301138y.

49 Tribby, A. L.; Bois, J. S.; Montzka, S. A.; Atlas, E. L.; Vimont, I.; Lan, X.; Tans, P. P.; Elkins, J. W.; Blake, D. R.; Wennberg, P. O. Hydrocarbon Tracers Suggest Methane Emissions from Fossil Sources Occur Predominately Before Gas Processing and That Petroleum Plays Are a Significant Source. *Environ. Sci. Technol.* **2022**, *56* (13), 9623–9631. https://doi.org/10.1021/acs.est.2c00927

Supporting information

3.S1 Calibration of the Picarro G2401-m

Prior to the campaign, we performed a two-point calibration of the Picarro G2401-m using an an above-ambient Airgas standard referenced to WMO scales at Scripps Institute of Oceanography (CH_4 concentration 2.981 ± 0.0003 ppmv) and an Airgas Ultrazero Air standard. The initial difference between the measured concentration of the standard tank (based on the factory calibration) and the WMO-referenced concentration was 11 ppbv, and the measured concentration in the Ultrazero air tank was 0.6 ppbv (assumed to be 0 ppbv for calibration purposes). Following application of the two-point calibration, prior to the first flight and following every subsequent flight we performed a one-point calibration using an ambient-level Airgas standard referenced to WMO scales at Scripps Institute of Oceanography (CH_4 concentration 2.0187 ± 0.0005 ppmv). The bias in the measured concentration of the ambient-level standard tank was ~3 ppbv. Subsequent measurements of the standard ambient-level tank varied by less than 1 ppbv (Figure 3.S2). Corrections for post-flight calibrations were applied during data processing (i.e., the internal instrument calibration values were not adjusted during the campaign).

Two additional calibration standards (CH_4 concentrations of 4.117 ppmv and 1.020 ppmv were used to assess in-flight precision and concentration drift. Given time constraints, we were not able to reference these standard concentrations to WMO scales, and as such we only use them to assess relative drift and precision in-flight. Specifically, each standard tank was measured at least once (twice for most flights) for three minutes in-flight, and once again upon landing.

Concentrations measured at altitude were corrected for the one-point calibration performed post-flight using the WMO-referenced standard tank and for differences between the in-flight and post-flight measurements of the in-flight standard tanks. Corrections for the one-point calibrations were typically ~3 ppbv (Figure 3.S2). Corrections based on differences in measurements of the in-flight calibration tanks at altitude and at ground-level were typically less than 1 ppbv. Based on these corrections and

the stability of measured concentrations of in-flight calibration standards (Figure 3.S2), we estimate an uncertainty (1σ) of 2 ppbv and a precision of 1 ppbv.

3.S2 Uncertainties in mass balance emission calculations

Methane emissions from dairy operations in the SJV were estimated using the mass balance (MB) technique, as described briefly in the main text. The flight legs used for MB calculations are shown in Figure 3.S3. Three of the seven flights were deemed unsuitable for MB calculations based on variability in measured wind directions (Figure S3). We used HYSPLIT backward trajectory modeling and ground-level measurements of local wind direction collected at Visalia, CA to confirm that wind fields were consistent for a few hours preceding the four flights deemed suitable for MB calculations based on wind direction measurements (Figure 3.S4).

Planetary boundary layer heights used in calculation of methane emissions were estimated using vertical soundings conducted at the beginning and end of the portion of the flight in the SJV, as well as from soundings conducted prior to each racetrack sampling period, as described in Pfannerstill et al., 2023b. During racetrack sampling, multiple level legs were flown at various altitudes over the same location. Examples of vertical profiles of potential temperature and water vapor concentrations used to estimate PBL heights during two flights with MB calculations are shown in Figure 3.S5. As shown in Figure 3.S5, the soundings were conducted near the legs used for MB calculations. The profiles demonstrate that methane concentrations were mixed uniformly throughout the PBL.

We assume a 25% uncertainty in PBL height (1σ) that incorporates true uncertainty in the PBL height and uncertainty in the extent of vertical mixing of dairy methane plumes. The uncertainties (1σ) in the wind direction and wind speed are estimated to be 5º and 10%, respectively. Following Peischl et al. (2015), background methane concentrations are taken as the lowest concentration measured on upwind flight legs. Given the precision of the Picarro G2401-m and the presence of upwind flight legs, uncertainties related to the background methane concentration are minor.

Figure 3.S9 shows example time series of methane concentrations measured on the upwind (western) and downwind (eastern) legs during RF5 and RF10. During three of the

four flights with consistent wind fields, in-flight calibrations occurred during the western (upwind) leg, adding uncertainty to the calculated flux into the dairy region. We interpolated concentrations during the calibrations using measurements immediately before and after the data gap. An additional 15% error is included in the emission calculations to account for uncertainty related to this interpolation.

As described in SI Section 3.3, we subtracted estimated emissions from non-dairy sources within the encompassed mass balance region from the total calculated emissions to derive dairy-specific emissions estimates.

3.S3 Estimation of point-source, natural gas, and cropland methane emissions within the mass balance region

We estimate point source methane emissions within the mass balance region discussed in Section 3.2 using the EPA GHG database (EPA, 2022), while emissions from natural gas leakage are estimated by scaling pipeline leakage emissions in the South Coast Air Basin reported by Peischl et al. (2013) based on the relative population of the urban areas within the dairy region. Of the eight landfills in the region according to the VISTA-CA inventory (Hopkins, 2019), emissions are only reported for the largest two within the EPA inventory (the Visalia disposal site and the Hanford Sanitary Landfill). The remaining six landfills are inactive (CalRecycle, 2022) and considerably smaller than those with reported emissions. We estimate emissions from these inactive landfills by scaling emissions from the Visalia disposal site based on relative total landfill area. Recent aircraft measurements by Peischl et al. (2013) over the South Coast Air Basin suggest that inventory estimates for landfill methane emissions are reasonably accurate (±20%), while a recent survey of California landfills reported that the median ratio of the directly measured to EPA-estimated methane emissions was 2.1 (Hanson et al., 2020). Overall, the estimated landfill emissions account for 0.3% of the total inferred emissions in the mass balance region. The four non-landfill point sources within the region all have EPA emissions estimates, which we use without adjustment and amount to <0.1% of total inferred emissions.

Emissions from natural gas leakage within the towns of Hanford and Corcoran are estimated by scaling pipeline leakage emissions in the South Coast Air Basin reported by

Peischl et al. (2013) by the relative populations of the SoCAB and the smaller towns. Emissions from Hanford and Corcoran are estimated at ~0.6 and ~0.3 Gg yr^{-1} using this method. When converted to an hourly emission rate, this represents <0.1% of inferred emissions in the mass balance region. We also estimated natural gas emissions using estimates from Jeong et al. (2014) for the mass balance region (1-4 nmol m^{-2} s^{-1}). For an estimated area of 1000 km^2, this corresponds to total emissions of 50-200 kg hr^{-1}, which represents less than 1% of the inferred emissions in the mass balance region.

We assume no net methane emissions from local croplands in the mass balance calculation. While methane emissions from rice cultivation are considerable (e.g., Peischl et al., 2012), limited data exists on emissions from cropland typical of the SJV (e.g., almons, grapes, cherries, tomatoes, etc.). Hannun et al. (2022) recently reported methane emissions from cropland derived from EC measurements in the eastern U.S. Using the average estimate reported by Hannun et al. (2022) (~0.5-2 mg m^{-2} hr^{-1}) and the estimated area of cropland in the mass balance region (~1000 km^2), we predict total cropland emissions of 500-2000 kg hr^{-1}. This represents 1-4% of our estimated total emissions within the mass balance region and is well within our estimated uncertainty.

3.S4 Description of the disjunct eddy covariance flux calculation using the continuous wavelet transform (CWT)

For a given scalar time series x(t), the continuous wavelet transform (CWT) proceeds by calculation of wavelet coefficients as a function of time and scale (i.e., frequency) through convolution of the time series with a wavelet function (ψ)

$$W_s(a,b) = \int_{-\infty}^{\infty} x(t)\, \psi_{a,b}(t)\, dt \tag{3}$$

Where the wavelet function is represented by,

$$\psi_{a,b}(t) = \frac{1}{\sqrt{a}}\, \psi_0\left(\frac{t-b}{a}\right) \tag{4}$$

In the equations above, $\psi_{a,b}$ represent a family of functions related to the "mother wavelet" ψ_0, for which the specific shape (i.e., compression/expansion in frequency space)

and location in time are defined by the scale parameter, *a,* and the translation parameter, *b*. Specific mother wavelets used in CWT vary by application. Here, we use the Morlet wavelet, which is effectively a plane wave modulated by a Gaussian profile and is commonly used in airborne eddy covariance calculations (Torrence and Compo, 1998; Wolfe et al., 2018). Normalization of the mother wavelet by $\frac{1}{\sqrt{a}}$ preserves wavelet energy at different scales. The CWT cospectrum, defined as the cross-wavelet power of W_w and W_s^*, represents the instantaneous covariance (i.e., EC flux) of the vertical wind speed and scalar concentration when integrated across all scales (i.e., frequencies), providing spatially resolved flux information, in contrast to ensemble methods (Torrence and Compo, 1998).

We used a disjunct method to quantify CWT fluxes from the Picarro G2401-m measurements. Specifically, while methane measurements are reported at a frequency of 0.5Hz by the G2401-m, the true elapsed time during methane ringdowns within the Picarro cavity is ≤ 0.4s. The difference between the true measurement time (0.4s) and the reported data interval (2s) is attributable to time spent sampling other species within the cavity (e.g., CO_2, CO, and H_2O). Therefore, rather than using 0.5Hz averaged data, we assume that methane measurements were recorded in 0.4s and occurred at a frequency of 0.5Hz. Given that the sample residence time within the Picarro optical cell is only ~0.8s (500 sccm flow rate at 45ºC and 165 hPa), measurements recorded once every 2s can be assumed distinct. Vertical wind speeds measured at 10Hz were subsequently averaged to a time resolution of 0.4s prior to flux calculations. Following reduction of the vertical wind speed time resolution, the methane time series was shifted to account for lag between the methane and wind speed measurements. Lag times were identified independently for each flight through inspection of lag-covariance plots, and typical lag times were around 8s.

Individual flight segments were selected for flux calculations if a) the segment length was longer than 10 km, b) the aircraft roll and pitch was less than 8º, and c) the flight altitude was stable (±50 m) (Pfannerstill et al., 2023b).

As discussed in Wolfe et al. (2018), wavelet coefficients calculated near the edge of a given flight leg can be considerably influenced by edge effects. The cone of influence (COI) defines the spectral region where these edge effects are prominent. Previous studies

have used a variety of techniques to filter data based on COI influence, and no individual method has been shown to be objectively preferable. Following Wolfe et al. (2018), we used a COI quality flag (q_{COI}), calculated as the fraction of total cospectral power within the COI, to determine whether fluxes are deemed valid or invalid. We used a q_{COI} of ≤ 0.75 in this study to maximize data coverage while removing data points most influenced by edge effects. Fluxes are therefore included unless the fraction of cospectral power within the COI is > 75%. Use of a qCOI of 0.5, as in Wolfe et al. (2018), reduces the number of valid datapoints by 20% and increases the campaign average mean methane flux by ~10%.

3.S4.1 Uncertainties in calculated EC fluxes

Airborne CWT calculations require rigorous attention to methodological uncertainties. In general, we follow the guidance of Wolfe et al. (2018) when calculating both systematic and random errors involved in EC flux calculations. These calculations are described briefly below.

3.S4.2 Systematic uncertainties

Systematic uncertainties in EC fluxes largely arise from 1) under sampling of low-frequency (i.e., large) eddies, 2) under-sampling of high-frequency eddies due to limited instrument time response, and 3) uncertainties in scalar concentrations and vertical wind speed measurements. We used the upper limit estimate derived by Lenschow et al. (1994) to quantify systematic errors related to under sampling of low-frequency eddies.

$$SE_{LF} \leq 2.2\left(\frac{z}{z_i}\right)^{0.5}\frac{z_i}{L} \quad (5)$$

Where z is the aircraft altitude above ground level, z_i is the planetary boundary layer height, and L is the length of the flight leg. Given that the majority of flight legs were long (> 30 km), SE_{LF} was generally a minor contributor to total uncertainty, with an interquartile range of 2-11% of measured fluxes.

We estimated systematic uncertainties related to the limited time response of the Picarro G2401-m by comparing the integrated cospectra of methane fluxes with the integrated cospectra from a 10Hz LI-COR LI-7500DS H_2O analyzer included in the Twin Otter

payload (Figure 3.S6). The decay of methane flux intensity (i.e., cospectral power) with frequency relative to the fast water vapor flux can be accurately described by the transfer function (Horst, 1997):

$$H_s(f) = \frac{Co_{w,CH_4}(f)}{Co_{w,H_2O}(f)} = \frac{1}{1 + (2\pi\tau_R f)^2} \quad (6)$$

The effective response time (τ_R) calculated from a fit to aggregated cospectra from all SJV flight legs is 0.84s (Figure 3.S5), which aligns well with the sample cell residence time (~0.8s). We corrected all measured fluxes using the transfer function. This correction can increase or decrease measured instantaneous fluxes depending on the magnitude of the total fluxes in the frequency range of the corrections. The additional systematic error associated with this time-response correction (SE_{TR}) is ~5%.

We further quantified the uncertainty associated with the fact that a fraction of the total methane flux is contributed by atmospheric eddies with frequencies (i.e., length scales) above the half-power frequency ($f_N = \frac{1}{2\pi\tau_R}$) of the Picarro G2401-m (~0.19 Hz for an instrument time response of 0.84s) (Aubinet et al., 2012). Using the ratio of the total LI-COR fast water vapor cospectra to the fraction of the cospectra present beneath the Picarro G2401-m half-power frequency, we estimate that 14% of the total methane flux may be uncaptured by the G2401-m. We therefore increased all measured fluxes by 14% and assumed an associated systematic uncertainty (SE_{HF}) of 14%. These corrections were also applied to the Picarro G2401-m H_2O flux measurements. Figure 3.S7 demonstrates the agreement between the G2401-m and LICOR LI-7500DS fluxes once these corrections are applied.

Similarly to Wolfe et al. (2018), we assumed that errors in the vertical wind speed and methane measurements added a 5% systematic uncertainty (SE_{acc}) to methane fluxes. All systematic errors were assumed constant for a given flight leg, and the total systematic error (SE_{tot}) was calculated from the root sum square of the individual components. The interquartile range of the combined systematic errors was 13-22%. Values of SE_{tot} were averaged directly when aggregating measurements across a flight leg or within a given spatial location.

3.S4.3 Random errors

Random errors in EC flux measurements generally arise from a combination of the stochastic nature of turbulence and instrument noise. Rather than estimate the magnitude of these effects separately, we calculated the total random flux error using the instantaneous variance of the covariance of methane and vertical wind speed, based on the framework developed by Finkelstein and Sims (2001) and adapted to CWT calculations by Wolfe et al. (2018), where:

$$RE_{EC} = \sqrt{\sum_{p=-m}^{m} \left(\overline{s' s'_p}\ \overline{w' w'_p} + \overline{s' w'_p}\ \overline{w' s'_p} \right)} \quad (7)$$

Where the $\overline{s' s'_p}$ terms represent the auto-covariance or cross-covariance of wind speed and/or scalar concentration for a given lag p. We use a lag time of -10 to 10s following the recommendations of Mauder et al. (2013) and Wolfe et al. (2018), though we note that results are only slightly influenced by increasing the timescale to 20-30s. The instantaneous covariance between vertical wind speed and methane concentration for a given lag p was calculated using Eq. 13 in Wolfe et al. (2018). Instantaneous random errors for methane fluxes at the native 0.5Hz resolution are substantial (interquartile range of 205-670%) but are reduced considerably when averaging across an entire leg or within a specific spatial region (e.g., latitude-longitude grid cell), as random errors reduce as the mean of the root sum square of RE_{EC}. For example, a 300% random error is reduced to only 42% when aggregating 50 independent measurements.

3.S4.4 Correction of EC fluxes for vertical flux divergence

Linking airborne EC fluxes with true ground-level emissions requires accounting for potential flux divergence with altitude, which can be considerable. The underlying mechanisms leading to vertical flux divergence can be understood through the equation describing mass conservation of a scalar in the atmosphere:

$$\frac{dC}{dt} + U\frac{dC}{dx} + \frac{dF_{EC}}{dz} = S \quad (8)$$

The terms on the left-hand side represent scalar storage ($\frac{dC}{dt}$), horizontal advection ($U\frac{dC}{dx}$), and eddy flux divergence ($\frac{dF_{EC}}{dz}$), respectively. *S* is the net atmospheric source or sink of the scalar, which is negligible for methane. Theoretically, vertical flux divergence can be quantified by performing flight legs at multiple altitudes over a given homogeneous source region (Misztal et al., 2014; Wolfe et al., 2018). While such vertical racetrack patterns were flown approximately every other flight during RECAP-CA, with 3-4 altitude levels and 10-20 km of sampling per level, efforts to derive methane flux divergence relationships from the SJV datasets were inconclusive. We hypothesize that this is the result of 1) considerable random errors in flux calculations and 2) the highly variable composition of methane sources within flux footprints as aircraft altitude increased. Generally, the EC flux measured over the SJV in a specific location is highly dependent on whether a single dairy is located within the footprint, as dairies are intense point sources while the surrounding cropland likely emits negligible quantities of methane.

Therefore, rather than use measurements from individual racetrack periods, we calculated a functional relationship between EC flux and aircraft altitude (z) relative to PBL height (z_i) (Wolfe et al., 2018) using the compiled dataset from the entire campaign. Figure 3.S8 shows the vertical flux divergence correction function calculated from this process. For a typical z/z_i of ~0.35-0.45, the correction increases measured EC fluxes by 30-40%. We followed the procedures described by Wolfe et al. (2018) for calculating the VFD-associated random errors, which were ~30-45% based on the correction function and the typical altitude of flux measurements. Given the data aggregation described above, we treat the VFD-associated error as systematic and average individual error VFD-related estimates directly when calculating average flux estimates for a given region/flight leg. While we aggregated the entire dataset for the VFD correction, we also calculated VFD corrections as a function of temperature to ensure that corrections did not vary substantially and thereby bias temperature-based comparisons of inferred surface level fluxes (Figure 3.S9). We note that additional flux measurements as a function of temperature are clearly warranted.

3.S5 Flux footprints

The flux footprint is defined as the surface region that encompasses emission sources capable of contributing to a given measured flux. Following Metzger et al. (2012), we used a combination of the Kljun et al. (2004) crosswind integrated footprint model and a Gaussian crosswind distribution function (Kljun et al., 2015) to calculate flux footprints. The combined model produces a 2D surface probability distribution defining the source region. We opted to use the combined model rather than alternatives such as the 2D parameterization of Kljun et al. (2015) or the half-dome footprint algorithm used by Wolfe et al. (2018) and others after comparison of calculated flux footprints and known ground-level sources with measured VOC fluxes (Pfannerstill et al., 2023).

Calculated footprints were used to apportion measured fluxes to surface level latitude-longitude grid cells for comparisons with published emission inventories. Grid cell-level fluxes were calculated using footprint-based probability weighted averages. We used a minimum probability threshold of 25% when allocating measured fluxes to surface grid cells.

3.S6 Description of positive matrix factorization (PMF) analysis

3.S6.1 Overview

Mathematically, the PMF model is represented by the following (Paatero and Tapper, 1994; Paatero, 1997):

$$X_{i,j} = \sum_{k=1}^{p} g_{i,k} f_{k,j} + e_{i,j}$$

Where $X_{i,j}$ represents the input data matrix with i measurements and j distinct species. The $g_{i,k}$ matrix represents the magnitude or concentration of individual factors (k) at each point in time (i), while the $f_{k,j}$ matrix describes the contributions of each species (j) to each factor (k). The residual matrix $e_{i,j}$ represents the magnitude or concentration of each species that is unrepresented by the model at each point in time. PMF implements a non-negativity constraint on both the factor profiles and magnitudes (e.g., time series and source

profiles must be positive), leading to physically realistic source factors. No *a-priori* information is needed about the specific values of the $g_{i,k}$ or $f_{k,j}$ matrices. A least squares algorithm is used to iteratively calculate the $g_{i,k}$ and $f_{k,j}$ matrices by minimizing a quality of fit parameter Q, which represents the sum of the squared ratios of species residuals to their estimated uncertainties:

$$Q = \sum_{i=1}^{m}\sum_{j=1}^{n}\left(\frac{e_{i,j}}{s_{i,j}}\right)^2$$

3.S6.2 Data preparation

As discussed in the main text, three greenhouse gases (GHG) (CH_4, CO, and CO_2) and 38 VOCs were combined to create the PMF input data matrix. The PMF Evaluation Tool (PET v3.05A) (Ulbrich et al., 2009) and the PMF2 algorithm were used to perform PMF and analyze the results. We followed the procedures described by Guha et al. (2015) for data preparation and error quantification, which simplifies comparison with the results of their PMF study from the Bakersfield area during CalNex-2010. Specifically, rather than using absolute concentrations of greenhouse gases and VOCs as PMF inputs, we removed estimated background concentrations from each species and then normalized by the background-corrected 99th percentile concentration. Scaling the concentrations using this method aids visual analysis of factor profiles, as normalized concentrations of all species are ≤1 for most of the time series. The relative contributions of individual species to factor profiles are therefore relatively similar and not influenced by the substantially different magnitudes of ambient concentrations of GHG and VOC (e.g., when comparing ppm-level CO_2 concentrations with ppb-level benzene concentrations). Background concentrations were defined as the minimum concentration measured during the entire campaign.

VOC concentrations were assumed to have an analytical uncertainty (AU) of 10%. Detection limits varied as a function of specific VOC but were typically 1-2 pptv. The absolute uncertainty of each species was calculated by propagating the analytical uncertainty and detection limits as shown below:

$$s_{i,j} = ((AU * x_{i,j})^2 + LOD^2)^{0.5} \quad for\ x_{i,j} > LOD$$

$$s_{i,j} = 2 * LOD \quad for\ x_{i,j} < LOD$$

Given the much higher precision of the Picarro G2401-m than the VOCUS PTR-ToF, we use the custom uncertainty calculation reported by Guha et al. (2015) for the greenhouse gases, as the resulting Q/Q_{exp} values are reasonable (~2.8 for our final solution) and the GHG and VOC are not split into separate physically implausible factors. The uncertainty of each GHG species is calculated using the following:

$$s_{i,j} = A(x_{i,j})^{0.5}$$

Where $s_{i,j}$ represents the uncertainty for each normalized GHG, A is a scaling factor iteratively chosen to produce reasonable Q/Q_{exp}, and $x_{i,j}$ is the normalized concentration of the GHG at each time step. We used the same scaling factors as Guha et al. (2015) (A = 1 for CH_4, 0.25 for CO_2, and 0.5 for CO).

3.S6.3 Selection of PMF solution

A five-factor PMF solution was found to optimally describe the combined GHG + VOC dataset. Here, we briefly discuss the solution selection process and provide descriptions of Factors 3-5.

While the choice of a final PMF solution requires some subjective input from the analyst, a few quantitative metrics have been typically used to aid selection. The most commonly used of these metrics is the Q/Q_{exp} ratio, where Q is the sum of the squared residuals from the PMF model and Q_{exp} represents the theoretically expected Q value (Ulbrich et al., 2009; Paatero and Tapper, 1994). Values of Q/Q_{exp} near 1 suggest that the billinear model is appropriate and that the input species have been fit to within their estimated error values (i.e., estimated errors are appropriate). Q/Q_{exp} values are ~2, suggesting possible slight underestimation of input errors (Ulbrich et al., 2009). Relatively consistent reductions in Q/Q_{exp} are observed from 3-7 factors (~11-15%), and as a result the Q/Q_{exp} trend provides little insight into the ideal number of factors

The four-factor solution resolves factors resembling the final dairy/livestock and hot-running combustion + fugitive O&G factors, as well as factors linked to non-dairy agriculture emissions and an industrial/power plant emissions factor containing notable contributions from CO_2 and benzene but very little CO or methane. Moving to a five-factor solution resolves an additional factor that appears to be linked to cold-start combustion

given the strong contribution from CO and other combustion tracers such as pentenes, toluene, and C8-aromatics but virtually no CO_2, suggesting emissions before the catalytic converter has reached operating temperature (Kuwayama et al., 2019). None of the regional methane enhancement is associated with this factor, as expected. Solutions with more than five factors become increasingly difficult to interpret, but the six-factor solution warrants specific discussion.

The six-factor solution resolves a new factor with strong contributions from methane and CO_2, as well as other species such as butenes/butanol and CO (Figure 3.S20). The new factor does not appear to result from the direct splitting of either the dairy/livestock or the hot-running combustion/fugitive O&G/landfill factor, as both its source profile and time series are distinct from pre-existing factors. However, based on the analysis discussed below, we hypothesize that this new factor results from mixing of the dairy/livestock and hot-running combustion/fugitive O&G factors.

Prior to the six-factor solution, the dairy/livestock factor accounts for 58-65% of the total regional methane enhancement, depending on the specific solution, while the combined hot-running combustion/fugitive O&G factor accounts for 35-42%; however, in the seven-factor solution, the new uncharacterized factor accounts for 28% of the total, causing the corresponding contributions from the other factors to drop to ~38% and ~34%, respectively. The relatively large CH_4/CO_2 ratio of this new factor (0.0279 mol/mol) suggests that it is not associated with point-source power plant, refinery, or petroleum and natural gas-related emissions (as defined by the EPA GHG inventory) as the EPA GHG point source database indicates that these sources in Tulare, Kings, Kern, and Fresno Counties have average CH_4/CO_2 ratios of ~5.3×10^{-5}, 4.9×10^{-4}, and 8.4×10^{-3} mol/mol, respectively. Methane emissions from these facilities would therefore need to be underestimated by multiple orders of magnitude for the ratios to align. Furthermore, the estimated total methane emissions from non-landfill point sources in these counties represents less than 1% of the estimated dairy-related emissions using our measurement-based estimates of methane emissions per dairy cow and the USDA-estimated number of dairy cows in these counties.

A similar argument suggests that the factor is not predominately linked to landfill emissions. While the EPA-estimated landfill CH_4/CO_2 emission ratio is larger (0.8 mol/mol), emissions from landfills in the surveyed counties represent only 2.5% of the estimated dairy emissions. A recent survey lead by investigators at California Polytechnic State University quantified methane emissions from 16 landfills across California (Hanson et al., 2020). Nine landfills have both an EPA annual methane emissions estimate and a direct measurement from the survey. The median ratio of the measured to EPA-estimated methane emissions was 2.1 (IQR = 0.7 – 4.9). Adjusting estimated landfill methane emissions based on these measurements therefore only increases the total to 5% of the total estimated dairy emissions.

The last possible major source of the new factor, if it is not derived from mixing of pre-existing factors, is fugitive natural gas emissions from transmission/distribution lines. However, the original hot-running combustion/fugitive O&G factor is still present, and it becomes difficult to justify distinct sources for these two factors based on their spectra. If the methane contributions from both factors (the existing combustion/fugitive O&G and new unknown factor) are linked to fugitive O&G emissions, the total contribution of fugitive O&G to the regional methane signal is 62%. To assess the likelihood of this possibility, we use a scaling analysis similarly to the calculations discussed in the mass balance section of the main text. Specifically, we assume that fugitive natural gas emissions will be predominately present in urban regions and will be approximately proportional to population. Scaling the SoCAB fugitive natural gas emissions reported by Peischl et al. (2013) (193 Gg yr^{-1}) by the total population of Kern, Tulare, Kings, and Fresno Counties suggest total emissions of 29 Gg or 29,038 metric tons. This represents 7% of the estimated dairy-related emissions. For fugitive O&G emissions to exceed dairy/livestock emissions, either the fugitive methane emissions would have to be considerably underestimated (by more than a factor of 10) or the dairy-related emissions would have to be considerably overestimated.

In the seven-factor solution, the new unknown factor produced in the six-factor solution is not present, and the methane contributions from the dairy/livestock and hot-running combustion/fugitive O&G factors return to the values produced in the 4-5 factor solutions

(~60% and 40%, respectively). While the seven-factor solution resolves what appears to be a biogenic factor which contains no methane signal, the remaining four factors are more difficult to interpret. As an example, the majority of the benzene signal is associated with the non-dairy agriculture factor in the seven-factor solution, which is difficult to justify.

Given the arguments discussed above and the factor source profiles (Figure 3.S20), we hypothesize that the new methane-containing factor resolved in the six-factor solution results from the mixing of the dairy/livestock, hot-running combustion/fugitive O&G, and non-dairy agriculture factors. As the seven-factor solution produces multiple factors with ambiguous sources, to avoid overinterpretation of the PMF results we conclude that the 5-factor solution provides an optimal description of the GHG + VOC dataset. Brief descriptions of Factors 3-5 are provided below

3.S6.4 Factor descriptions

Non-dairy agriculture

Factor 3 is classified as non-dairy agriculture emissions given the considerable contributions from methanol and acetone (Goldstein and Schade, 2000; Fares et al., 2011), minimal contribution from methane, and prominence over croplands between Bakersfield and Fresno (Figure 3.S19). The molar ratio of acetone to methanol in Factor 3 (0.32 mol mol^{-1}) agrees well with the agriculture and soil-management factor reported by Guha et al. (2015) (0.26 mol mol^{-1}) and with emission ratios reported for a variety of crops typical of the SJV by Gentner et al. (2014) and Fares et al. (2011) (e.g., almonds (0.14), grapes (0.04), pistachios (0.5), oranges (0.5-0.57)). We attribute the CO associated with this factor to agricultural off-road engines, while the minor contribution of CO_2 is likely the result of CO_2 uptake by the same crops responsible for the acetone and methanol emissions. Guha et al. (2015) reported a notable contribution of CO_2 to the agriculture and soil-management PMF factor resolved in Bakersfield, CA; however, the CO_2 contribution was hypothesized to result from overnight plant respiration, which would likely not be detectable in our daytime measurements. The negligible contribution of methane to the factor source profile aligns with the agriculture and soil-management factor reported by Guha et al. (2015) and

with the assumption of minimal methane emissions from croplands in the mass balance calculations discussed in Section S2.

Cold-start combustion

Factor 4 is classified as cold-start combustion emissions given the prominence of combustion-related tracers in the factor source profile (e.g., CO, alkenes, toluene, C8- and C-10 aromatics), lack of contribution from CO_2 (suggesting inefficient combustion), and prominence directly above and downwind of Fresno and Bakersfield (Figure 3.S19). Across the surveyed domain, 12% of the total CO and 32% of the total C8+ aromatic signal is associated with this factor. A similar cold-start combustion-related factor was observed by Kuwayama et al. (2019) in Los Angeles and exhibited many of the same chemical characteristics (e.g., considerable CO associated with very little CO_2, combustion tracers, etc.). While the apparent minor contribution of CO to this factor in Figure 3.S18 suggests that evaporative emissions are a possible source, this perception is skewed by the concentration normalization performed prior to PMF analysis. The true ratios of toluene/CO and C10-aromatics/CO in this factor are only a factor of 2 and 5 larger than the corresponding ratios measured in hot-running combustion engines, respectively (Gentner et al., 2013). The CARB Emission Factor (EMFAC) model predicts that the total emission ratio of reactive organic gases (ROG) to CO from light-duty gasoline passenger vehicles before the catalytic converter has reached operating temperature is 6.6 times larger than that produced during hot-running periods, in reasonable agreement with the comparison above. Furthermore, the prominent contribution of C_5H_{11}, which likely corresponds to C_5 pentenes resulting from incomplete fuel combustion (Gentner et al., 2013) suggests a combustion-related source. This factor accounts for virtually none of the observed methane enhancement (<1%), in agreement with previous cold-start combustion factors (≤6% in Los Angeles) (Kuwayama et al., 2019).

Power-generation/refineries

Factor 5 is interpreted as emissions from power-generation and petroleum refining facilities. Approximately 39% of the domain-wide CO_2 enhancement is contributed by this factor, while the CO/CO_2 ratio (<1e-5 mmol/mol) is clearly lower than expected from gasoline (~7 mmol/mol) and diesel (~0.7 mmol/mol) mobile-source emissions (EMFAC,

2022), suggesting efficient combustion processes likely present at large-scale natural gas-fired power generation facilities. Figure 3.S19 indicates that the factor is prominent nearby and downwind of major power generation facilities near Fresno and Bakersfield, as well as near smaller facilities near the cities of Hanford and Tipton. We hypothesize that the presence of the factor within the Sierra Nevada foothills is the result of upslope winds that transport emissions from generation facilities. While there are relatively few other clearly prominent tracers within the factor profile, the factor accounts for 36% of the domain-wide benzene enhancement and 16% of the C8+-aromatic enhancement, suggesting possible emissions from leaking stock storage tanks at refining facilities. Near Bakersfield, major refining facilities such as Kern Oil Refining, which produces both gasoline and diesel fuel, are in close proximity to major natural gas fueled power-generation facilities (e.g., the Kern River Cogen plant) (EPA, 2022). Such proximity may explain why species expected to be emitted from refining operations are included in a factor with chemical signatures indicating efficient combustion processes (e.g., low CO/CO_2 ratio). Virtually no methane is associated with this factor (<1%), and as a result, uncertainty in the source of this factor has effectively no influence on our conclusions regarding methane sources.

3.S6.5 Quantification of factor uncertainties

Uncertainty in the factor source profiles and time series are estimated using bootstrap analysis (Norris et al., 2008; Ulbrich et al., 2009). Following standard recommendations, 100 bootstrap runs were performed by randomly resampling individual measurements from the original dataset with replacement (Norris et al., 2008). After the random resampling, measurements are sorted chronologically to maintain the general temporal structure of the dataset (i.e., data points collected at the end of the original time series will be forced toward the end of the resampled time series). The PET software automatically determines which factors in each bootstrap run correspond to the base run factors (Ulbrich et al., 2009). The standard deviations of the contributions of individual species to each factor are assumed to represent the 1σ uncertainty in factor source profiles. Similarly, the 1σ uncertainty in the time series of each factor is taken as the standard deviation of the time series from the aggregated bootstrap results.

Figure 3.S22 shows the results of the bootstrapping analysis for the dairy/livestock factor. The uncertainty in the methane contribution to the factor signal is 14% (1σ), while the uncertainty in the average abundance of the factor (i.e., total signal) is 17%. While the propagation of these uncertainties would suggest that the uncertainty in the total contribution of the factor to the methane enhancement is 22%, bootstrap simulations that produce a relative reduction in the methane contribution to the factor signal are associated with larger total factor signals. As such, when the bootstrap results are compiled, the standard deviation of the average contribution of the dairy/livestock factor to the domain-wide methane enhancement is 9.9%, which we take as the 1σ uncertainty in the methane contribution.

In addition to random uncertainties, PMF solutions are associated with inherent rotational ambiguity. Briefly, linear transformations or "rotations" of the factor time series and composition matrices are possible that generate slightly different factors while producing an identical fit to the input dataset (Ulbrich et al., 2009). As a result, resolved solutions are not unique from a mathematical perspective. Within the PET software, such rotations are generated by varying the FPEAK parameter. It is commonly recommended to evaluate solutions with rotations (i.e., varied FPEAKs) that increase Q/Q_{exp} by up to ~10%, though the specific range is subjective (Ulbrich et al., 2009). We evaluated PMF solutions from an FPEAK of -4 to +4, producing Q/Q_{exp} values that increased by up to ~15% (Figure 3.S23). FPEAK values lower than -1 lead to mixing of the dairy/livestock and non-dairy agriculture factors (Figure 3.S24), while values larger than 2.5 produce a factor consisting of almost entirely CO and C_3HO, a likely carbonyl fragment, and fail to resolve the combustion/fugitive O&G factor (Figure 3.S25). Within the range of reasonable PMF solutions ($-1 \leq FPEAK \leq 2.5$), the contribution of the dairy/livestock factor to the domain-wide methane enhancement is ~60-65% (Figure 3.S23) and within the 1σ uncertainty range obtained from bootstrapping analysis of the FPEAK = 0 solution. We use the FPEAK = 0 solution given a lack of justification for alternative solutions within the range of $-1 \leq FPEAK \leq 2.5$.

3.S6.6 Comparison of methane source distribution inferred from PMF with results of Guha et al. (2015)

Guha et al. (2015) used a similar PMF method to determine that dairy and livestock emissions accounted for 60-70% of midday (12:00-16:00) average methane enhancements over the Bakersfield region during CalNex-2010, in line with our results. However, our conclusions regarding the source of the non-dairy-related methane emissions differ from Guha et al. (2015), as we attribute the majority of the remainder to fugitive O&G emissions, while their results suggest that a variety of sources, including motor vehicles, a miscellaneous urban source, and agriculture and soil management account for the remainder. While other sources such as landfill emissions or "miscellaneous urban sources" are likely "mixed" into our combustion + fugitive O&G factor, analysis of regional landfill emissions using the EPA GHG point source inventory[34] suggests that the contribution from landfills is likely small (SI Section 3.S3), and it is unclear what other urban sources could account for such substantial quantities of methane. While we have limited data on direct agricultural methane emissions, calculations using flux measurements from Hannun et al. (2020) suggest that agricultural emissions should represent a small fraction of dairy-related emissions (SI Section 3.S3).

3.S7 Calculation of effective average dairy methane emission rate in the SJV using CARB inventory emission factors

The CARB GHG emission inventory uses a process-based model to estimate dairy emissions from enteric fermentation and manure management practices separately (CARB, 2022). Here we describe calculation of an effective total methane emission rate from dairies in the southern SJV using CARB emission factors and SJV-specific manure management styles.

Enteric fermentation emission rates vary considerably by cattle type (e.g., dairy cows vs. dairy calves vs. dairy replacements) (Marklein et al., 2021). Assuming dairies within the SJV have the same relative proportion of different cattle types as the statewide average,

the effective annual enteric fermentation emission rate is 91 kg cow^{-1} yr^{-1} using CARB emission factors.

The specific manure management practices utilized also have a substantial influence on total methane emissions (Hristov et al., 2017; Marklein et al., 2021), and recent studies have used a variety of assumptions regarding manure management practices in the SJV. For example, Peischl et al. (2013) and Amini et al. (2022) assume that all dairy operations in the SJV use anaerobic lagoons as the primary manure management system, with an effective emission rate of 332 kg dairy cow^{-1} yr^{-1} according to CARB. A recent detailed review of permit information suggests that 30-70% of manure generated in SJV dairies is managed using anaerobic lagoons, depending on the presence/absence of freestalls, with the remainder managed using solid storage practices (Marklein et al., 2021). We assume that all dairies surveyed in our study utilized freestalls and therefore that 70% of manure was managed in anaerobic lagoons (Marklein et al., 2021), which is qualitatively consistent with our survey of 500 dairies in the southern SJV using Google Earth imagery, producing an annual effective dairy cow manure management emission factor of 237.8 kg dairy cow^{-1} yr^{-1}. Here, we note that manure management emissions are calculated based on the number of *dairy cows* and the corresponding emission factor, not the total number of cattle within a dairy. According to the statewide dairy cattle distribution, the total number of cattle on an average dairy is expected to exceed the number of dairy cows by approximately a factor of two (Amini et al., 2022). We further assume no substantial influence from anaerobic digesters, which our review of satellite imagery indicates are only present at ~5% of dairies in the SJV.

Data from the 2017 USDA Census of Agriculture suggests that dairies within Tulare and Kings counties house ~2005 milk cows on average (USDA, 2017). Using the statewide distribution of cattle types, each dairy houses an additional ~1040 dairy calves and ~850 dairy replacements (~250 aged 0-12 months and ~600 aged 12-24 months) on average. Applying the CARB enteric fermentation emission factors to each cattle type, the total enteric fermentation emission rate is 40.2 kg hr^{-1} for an average dairy in the SJV. Multiplying the number of dairy cows by the effective manure management emission factor described above suggests a total manure management emission rate of 54.4 kg hr^{-1} and a

resulting total emission rate of 94.6 kg hr^{-1}. If we assume that all manure is managed using anaerobic lagoons, as in Peischl et al. (2013) and Amini et al. (2022), the total emission rate increases to 116.2 kg hr^{-1}.

3.S8 Calculation of the temperature dependence of dairy methane emission factors

In Section 4.3.3 of the main text, we compared the temperature dependence of dairy methane emissions measured during our study with values calculated using CARB annual emission factors adjusted based on the parameterization for the temperature dependence of manure management emissions reported by Maasakkers et al. (2016). Here we describe those calculations in detail.

Maasakkers et al. (2016) used a specific exponential relationship to parameterize the dependence of manure management emissions on temperature (Eq. 1 in their paper). We first used this parameterization to calculate effective monthly scaling factors for manure management emissions based on average temperatures measured in Visalia and Fresno (Figure 3.S15). We then calculated effective anaerobic lagoon and solid storage emission factors (i.e., emissions per dairy cow per year) based on these scaling factors while ensuring that the annual average dairy-wide emission rate is maintained at 94 kg hr^{-1} (SI Section 3.S8). The scaling factors and the monthly estimated emission rates are shown in Figure 3.S15. Based on the Maasakkers et al. (2016) parameterization, the ratio of manure management emissions to enteric fermentation emissions increases from ~0.4 in January to ~2.1 in July, which agrees well with observations reported by Arndt et al. (2018) for dairies in Northern California. Furthermore, as shown in Figure 3.S15b, the calculated emission rate for an average dairy in this region (2005 dairy cows per dairy) in June, when RECAP-CA was conducted, is 137 kg hr^{-1} using the manure management assumptions described in SI Section 3.S8. This value is only 11% larger than our estimate using the average of the MB and EC methods (123 kg hr^{-1}).

The calculation process described above produces estimated average dairy emission rates by month, while also allowing calculation of the inferred relationship between emission rates and temperature (by fitting the monthly average emission rate vs.

temperature relationship) (Figure 3.S15). We note that this inherently assumes that the average annual temperature in the southern SJV is similar to the annual average temperature across California when weighted by the relative fraction of dairy methane emissions in different regions (from the perspective of the statewide emission inventory). However, as a dominant fraction of dairy methane emissions are produced in the southern SJV (Marklein et al., 2021), this assumption should produce minimal error. Stated differently, given that most dairy methane emissions occur in the SJV, using temperatures in the SJV in the temperature-dependent parameterization of statewide, annual-average manure management emission factors is reasonable.

We then calculated inferred average dairy emission rates from our EC measurements as function of temperature, as shown in Figure 3.S16a. We increased temperatures measured at flight altitude by 4ºC to correct for the difference between temperatures at ground-level and 400 m. Using this method, flight-altitude temperatures of 16ºC, corresponding to the lowest temperature tercile observed in our study, are associated ground-level temperatures of 20ºC, which have a calculated average dairy emission rate of 96 kg hr^{-1}, while flight temperatures of 29ºC (33ºC at ground-level) have an associated emission rate of 198 kg hr^{-1}. As shown in Figure 3.S16a, these values correspond well with emission rates inferred at each temperature from our EC measurements (111 kg hr^{-1} and 224 kg hr^{-1}, respectively).

Given the agreement between the dairy methane emission rate inferred from our June measurements and that calculated for June conditions using CARB EF scaled by the Maasakkers et al. (2016) parameterization, we estimated an effective annual emission rate in the entire SJV based on our measurements. For this calculation, we scaled our average estimate by the ratio of the calculated annual average dairy emission rate (94.6 kg hr^{-1}) to the June emission rate (137 kg hr^{-1}) using CARB EF and the Maasakkers et al. (2016) parameterization (0.69), converted the resulting annual average dairy emission rate to an effective dairy cow emission factor by dividing by 2005 dairy cows per dairy, and multiplied by the total number of dairy cows in counties within the SJV according to the USDA 2017 Census of Agriculture. The resulting value (584 Gg yr^{-1}) is associated with considerable uncertainty given the uncertainty in the temperature dependence of dairy

methane emissions, but it is notable that our calculated value lies between the estimates of Cui et al. (2019) (440 ± 360 Gg yr^{-1}) and Jeong et al. (2013) (1130 ± 420 Gg yr^{-1}).

Figures 3.S1-3.S26

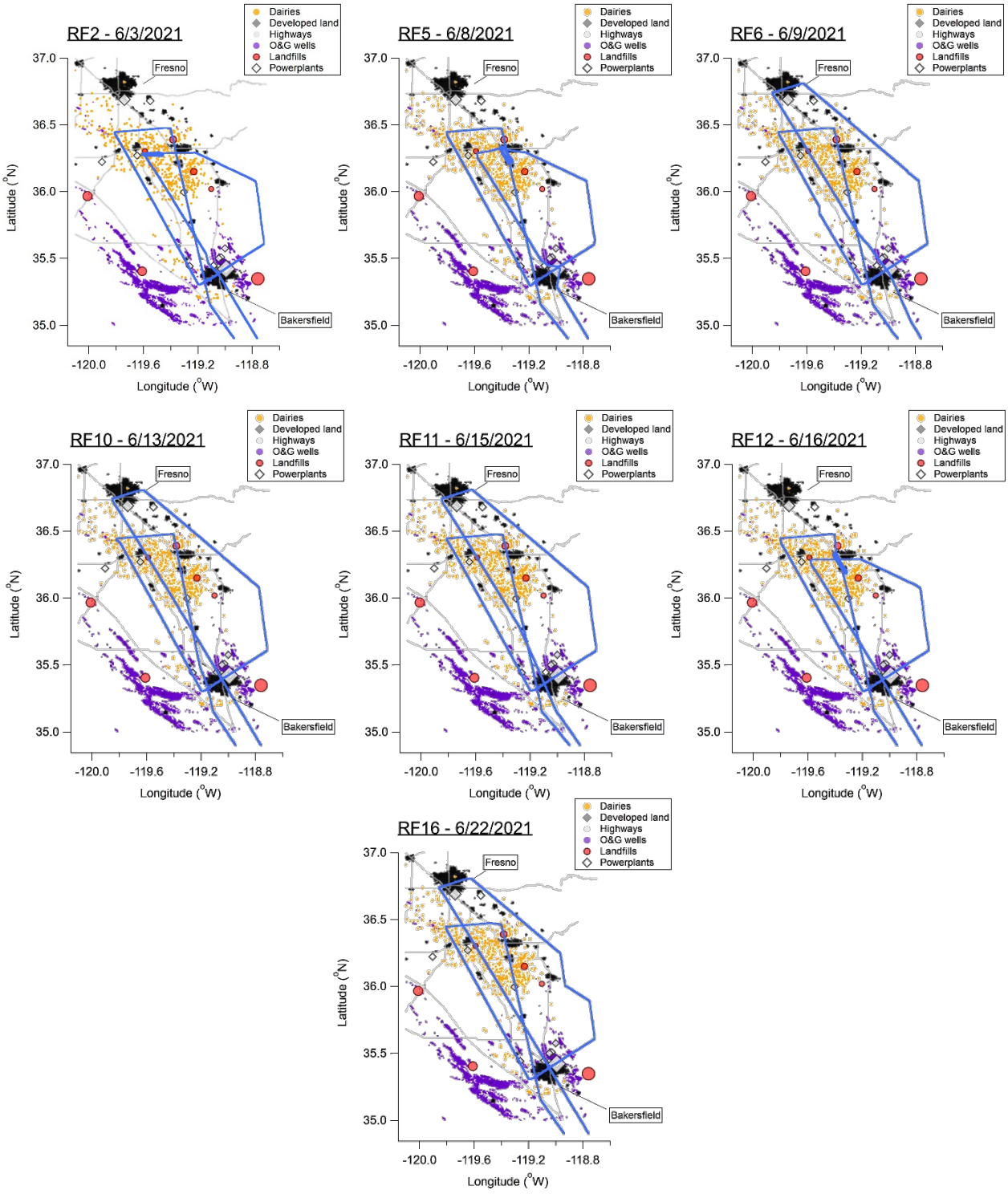

Figure 3.S1: Flight tracks of the seven flights performed over the San Joaquin Valley (SJV) as part of RECAP-CA 2021.

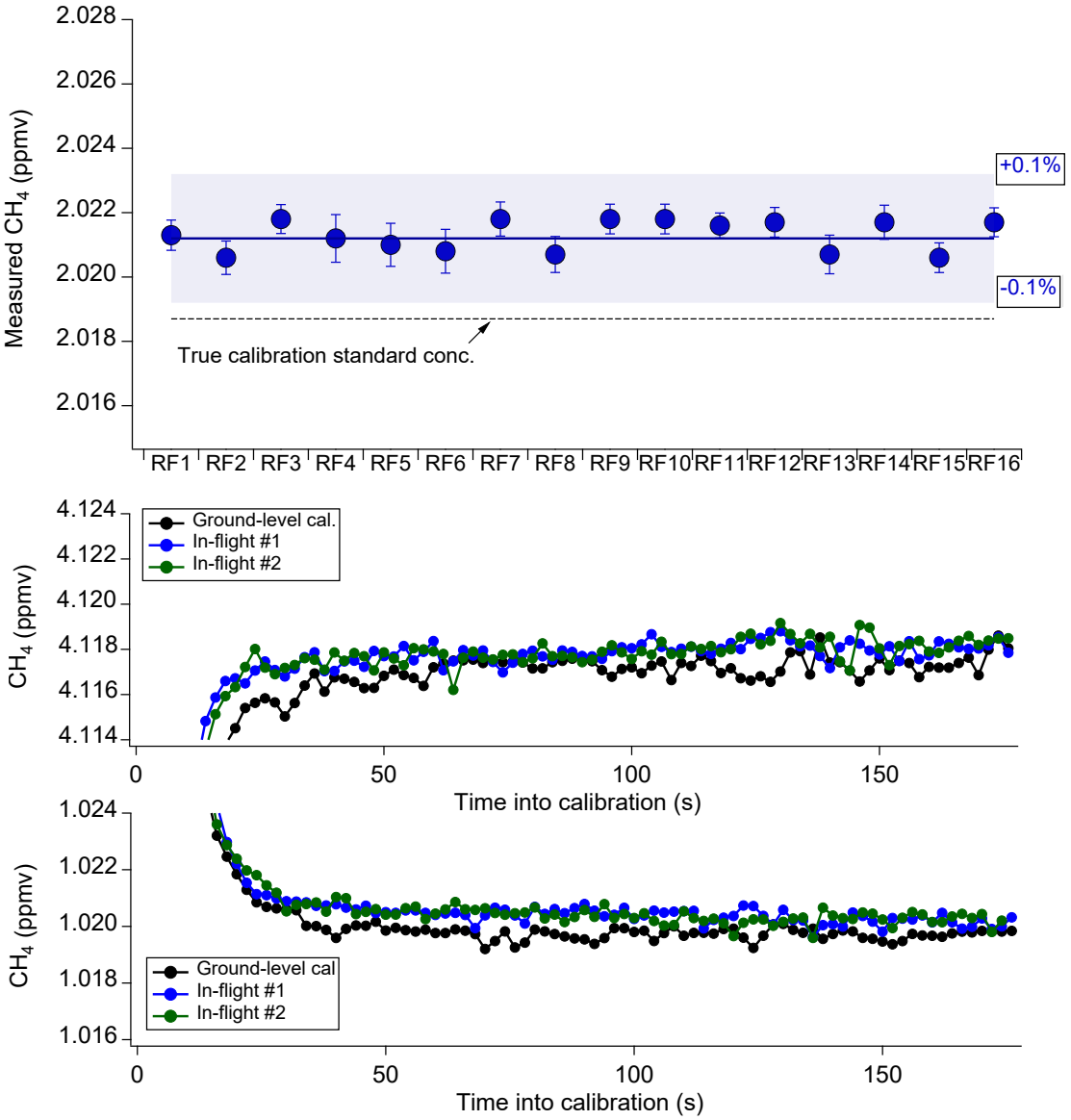

Figure 3.S2: (a) Measured concentration of the WMO-referenced Airgas standard tank after each flight. The true concentration of the standard is shown using the dashed line. Variability between subsequent measurements was ≤1 ppbv. Calibration corrections were applied during data processing. (b) Time series of measured concentrations in the high-span calibration standard from RF5 during three calibrations, two of which occurred in-flight. Calibrations demonstrate precision is ≤ 1 ppbv. (c) Same as (b) for measurements of the low-span calibration standard.

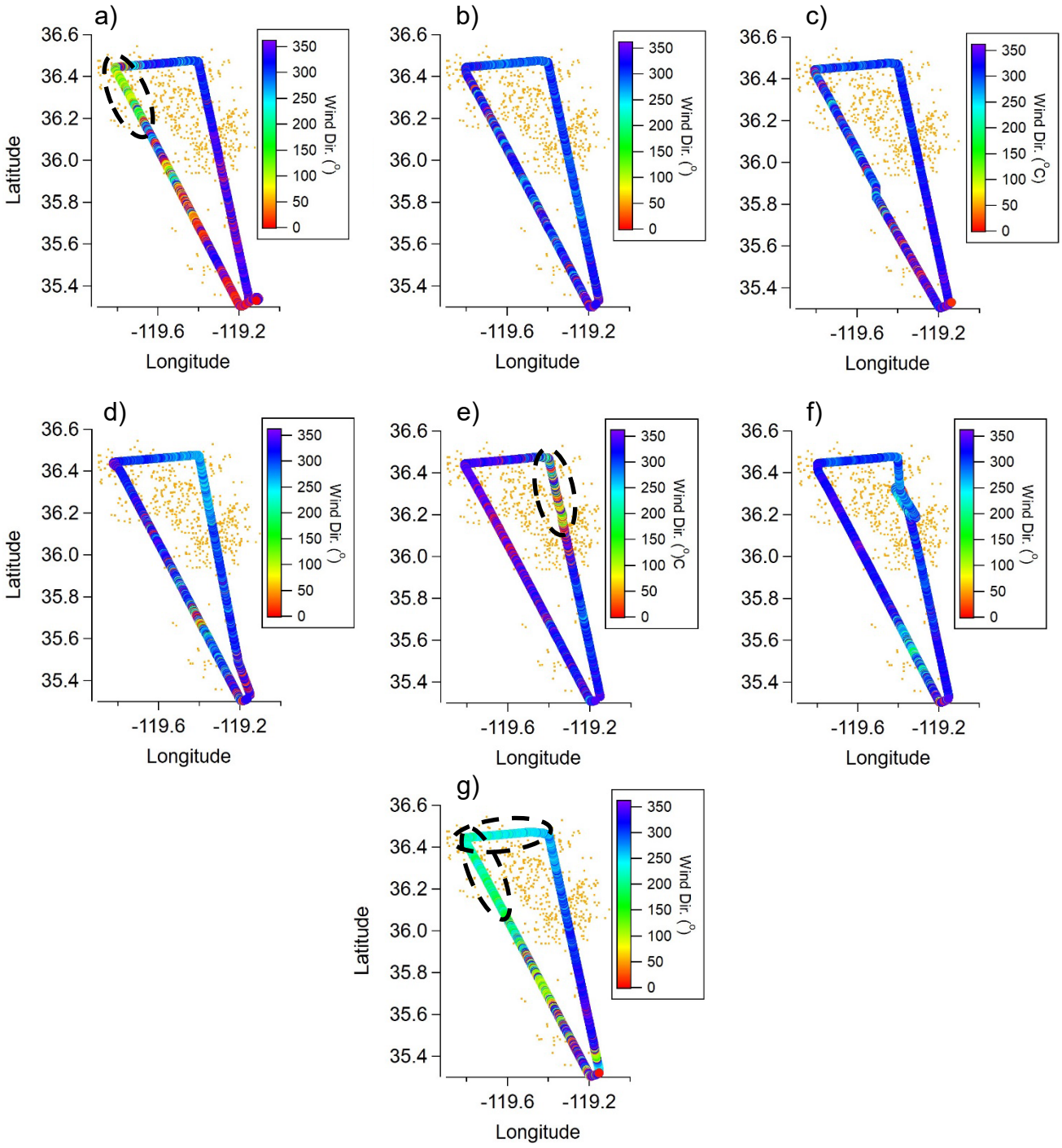

Figure 3.S3: Maps of flight legs used for mass balance calculations from each flight during RECAP-CA. (a) RF2, (b) RF5, (c) RF6, (d) RF10, (e) RF11, (f) RF12, (g) RF16. Points are colored by wind direction. Circles note locations with inconsistent local wind fields (i.e., considerable deviations from the typical northwest origin) during RF2, RF11, and RF16. Orange markers denote local dairy operations.

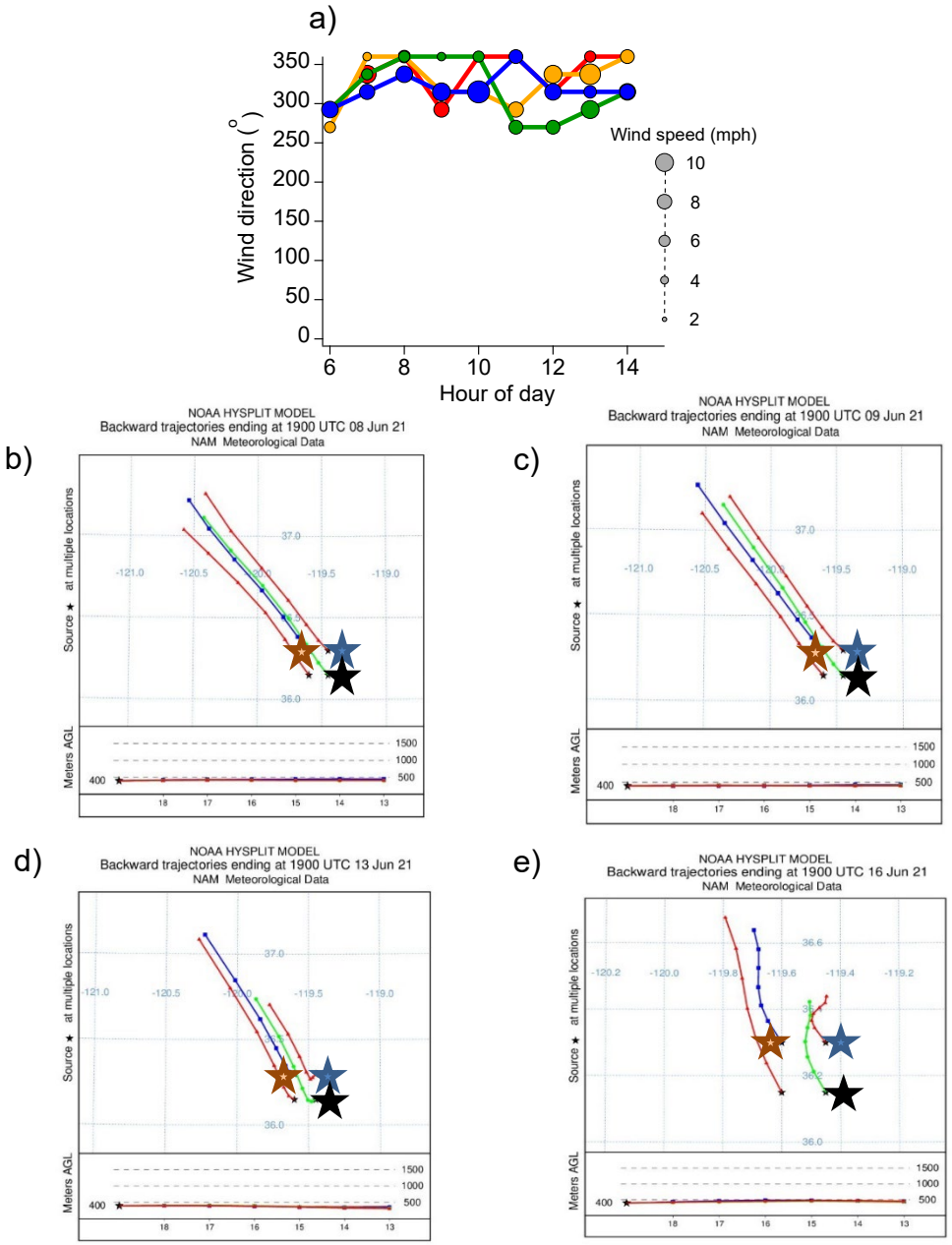

Figure 3.S4: (a) Wind direction and speed measured at the Visalia weather station from 6:00-14:00 on the days corresponding to flights with mass balance CH_4 emissions estimates (RF5, RF6, RF10, and RF12) (Weather Underground, 2022). (b-e) Six-hour airmass backward trajectories ending at noon local time in the region of intensive dairy operations calculated using the HYSPLIT model for RF5, RF6, RF10, and RF12. Blue, green, and black stars denote the locations of the cities of Visalia, Hanford, and Tulare, respectively, which generally bound the mass balance region shown in Figure 3.2 in the main text. Trajectories demonstrate that wind fields were stable and airmasses generally crossed the region of intensive dairy operations within the 3-4 hours prior to measurement.

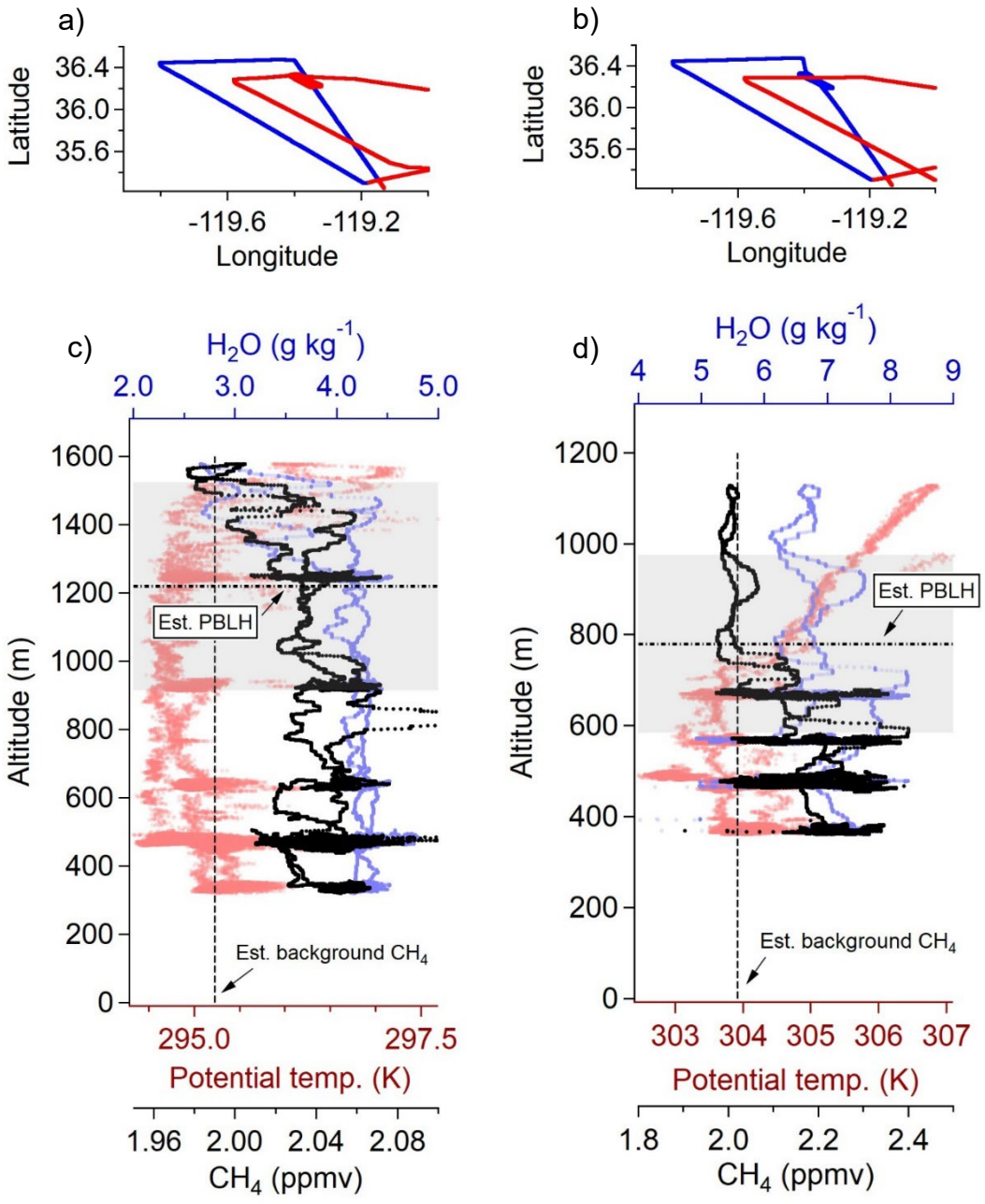

Figure 3.S5: Maps of aircraft latitude and longitude during racetrack sampling in (a) RF5 and (b) RF12 within the mass balance region. Blue points represent flight legs used for MB calculations, while red points denote other portions of the flight. Stars indicate locations of the vertical sounding and racetrack sampling periods. (c-d) Measured potential temperature, water vapor, and methane concentrations as a function of altitude during the sounding and racetrack sampling period. The estimated background methane concentration and PBL height are also shown.

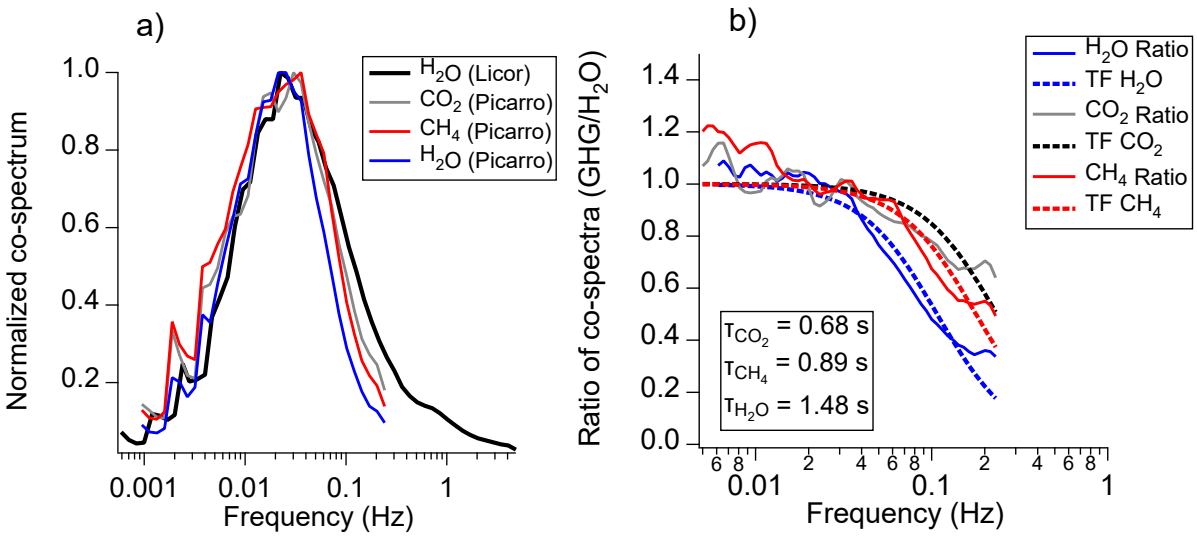

Figure 3.S6: (a) Normalized wavelet cospectrum of water vapor (H_2O) measured by the LI-COR LI-7500DS (10Hz) and H_2O, CH_4, and CO_2 measured by the Picarro G2401-m. (b) Ratio of GHG and H_2O co-spectra showing transfer function fits and effective instrument response times.

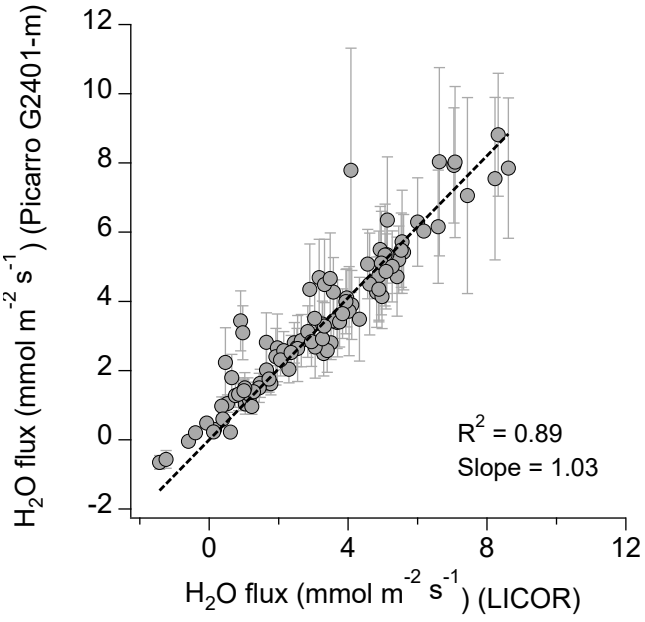

Figure 3.S7: Comparison of average water vapor fluxes measured on each level leg by the Picarro G2401-m and the LICOR LI-7500DS. The G2401-m data have been corrected for the instrument response time and the additional high frequency flux uncaptured by the instrument (SI Section 3.S4).

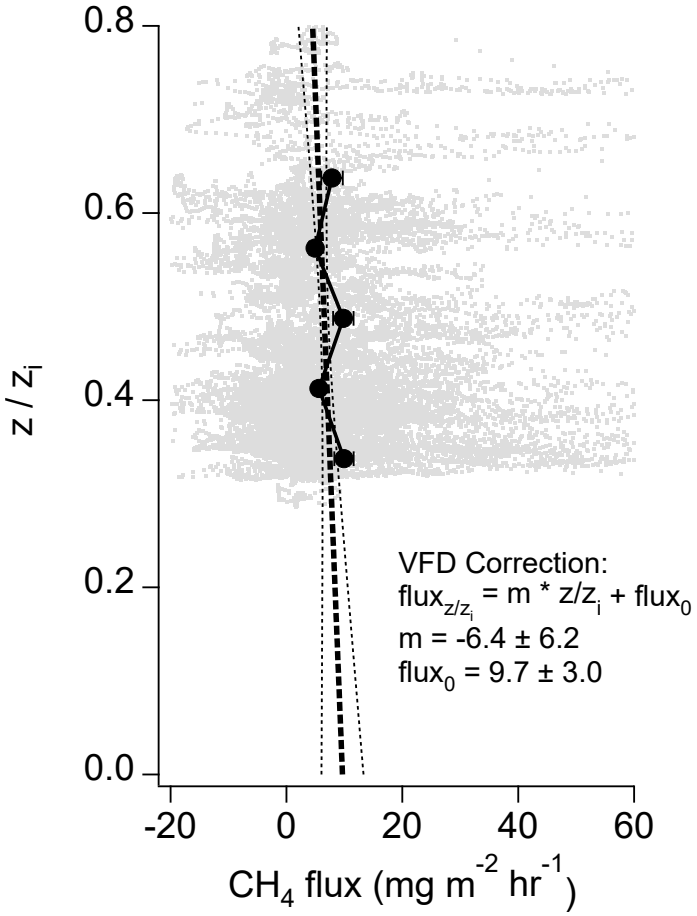

Figure S8: Measured methane flux as a function of aircraft altitude (z) relative to the planetary boundary layer height (z_i). Gray dots represent individual 0.5Hz flux measurements. Black markers denote average fluxes within five z/zi bins containing 95% of the entire dataset. Error bars represent 1σ errors in average fluxes calculated from propagation of random and systematic errors in 0.5Hz fluxes. The thick dashed line represents the extrapolated vertical flux divergence (VFD) correction. Dotted lines denote the 1σ uncertainty in the VFD correction.

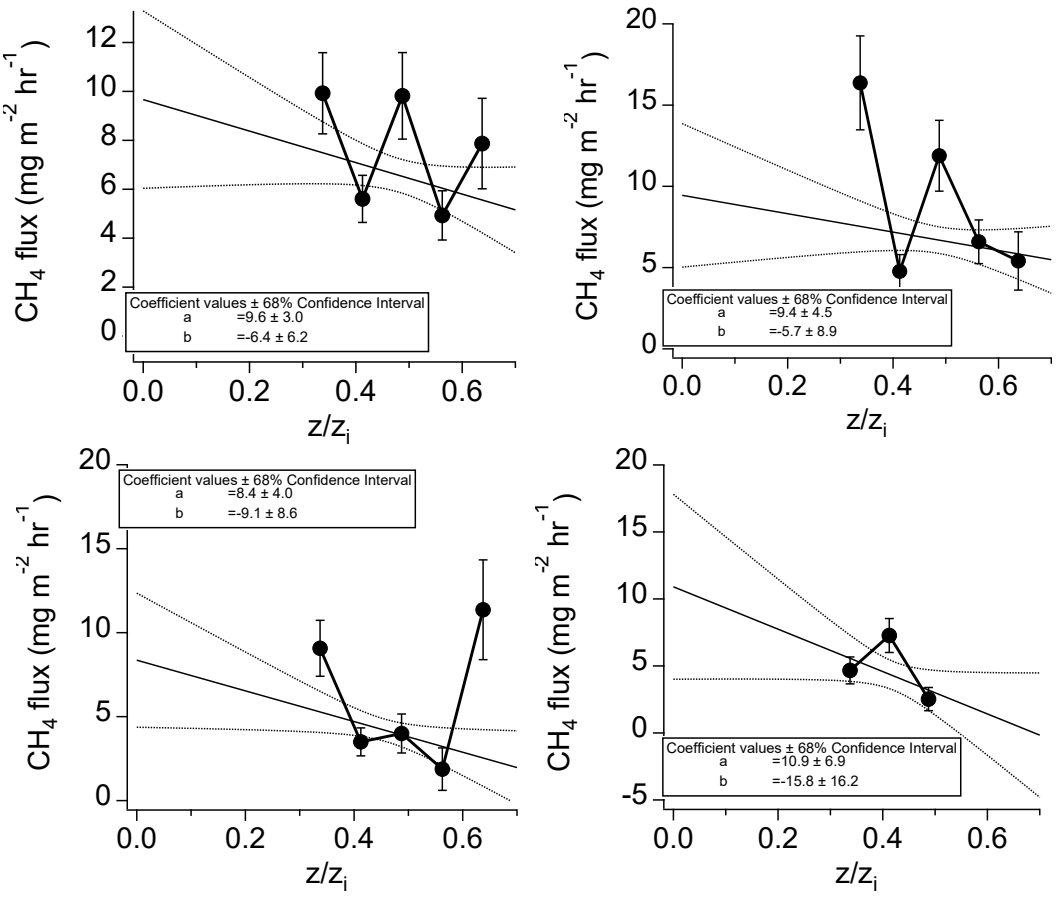

Figure 3.S9: Relationship between the measured methane flux and flight altitude normalized to the planetary boundary layer height (z/z_i) for (a) the entire dataset, and (b-d) periods with temperatures (b) greater than 26°C, (c) between 20°C and 26°C, and (d) less than 20°C. The calculated vertical flux divergence relationship is shown for each dataset, demonstrating that notable flux divergence is predicted in each case. The calculated C_{div} values (Wolfe et al., 2018) are 1.36 ± 0.50, 1.31 ± 0.68, 1.76 ± 1.43, and 2.38 ± 3.95 for a typical z/z_i of 0.4. Considerable uncertainty is associated with the calculated divergence correction for the lowest temperature bin due to a lack of data for $z/z_i > 0.5$. Ground-level fluxes reported in the main text use the flux divergence correction obtained from the entire dataset.

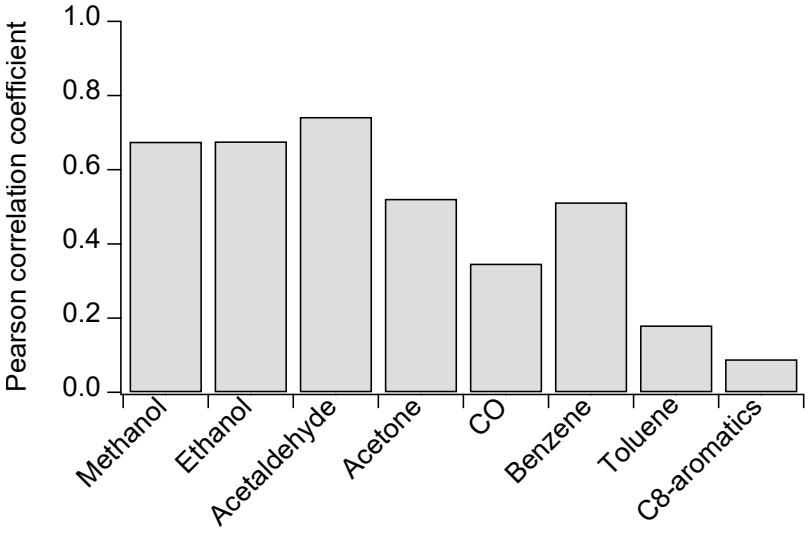

Figure 3.S10: Spatial correlation between average concentrations of methane and various VOC and GHG tracer species in 0.1° x 0.1° grid cells measured during RECAP-CA.

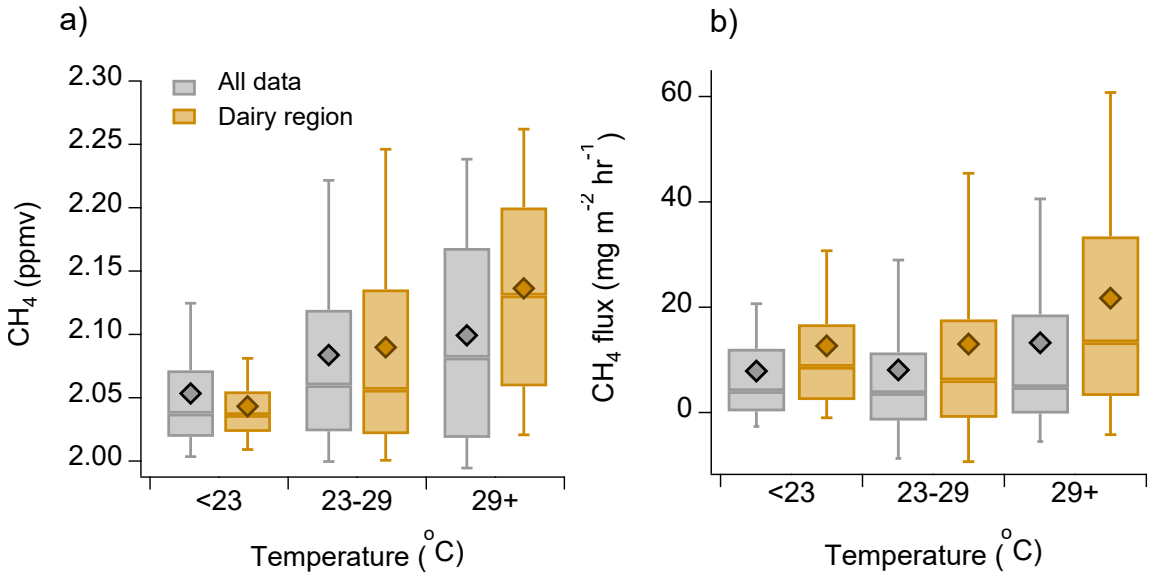

Figure 3.S11: (a) Boxplots of methane concentrations measured as a function of inferred ground-level temperatures across the entire surveyed region and the specific dairy region shown in Figure 1. Boxes represent the interquartile range of measurements, while error bars denote the 10th and 90th percentiles. Diamond markers represent averages. (b) Same as (a) for inferred surface level methane fluxes. Ground-level temperatures were estimated from temperatures at flight-altitude using the observed temperature lapse rate during racetrack sampling.

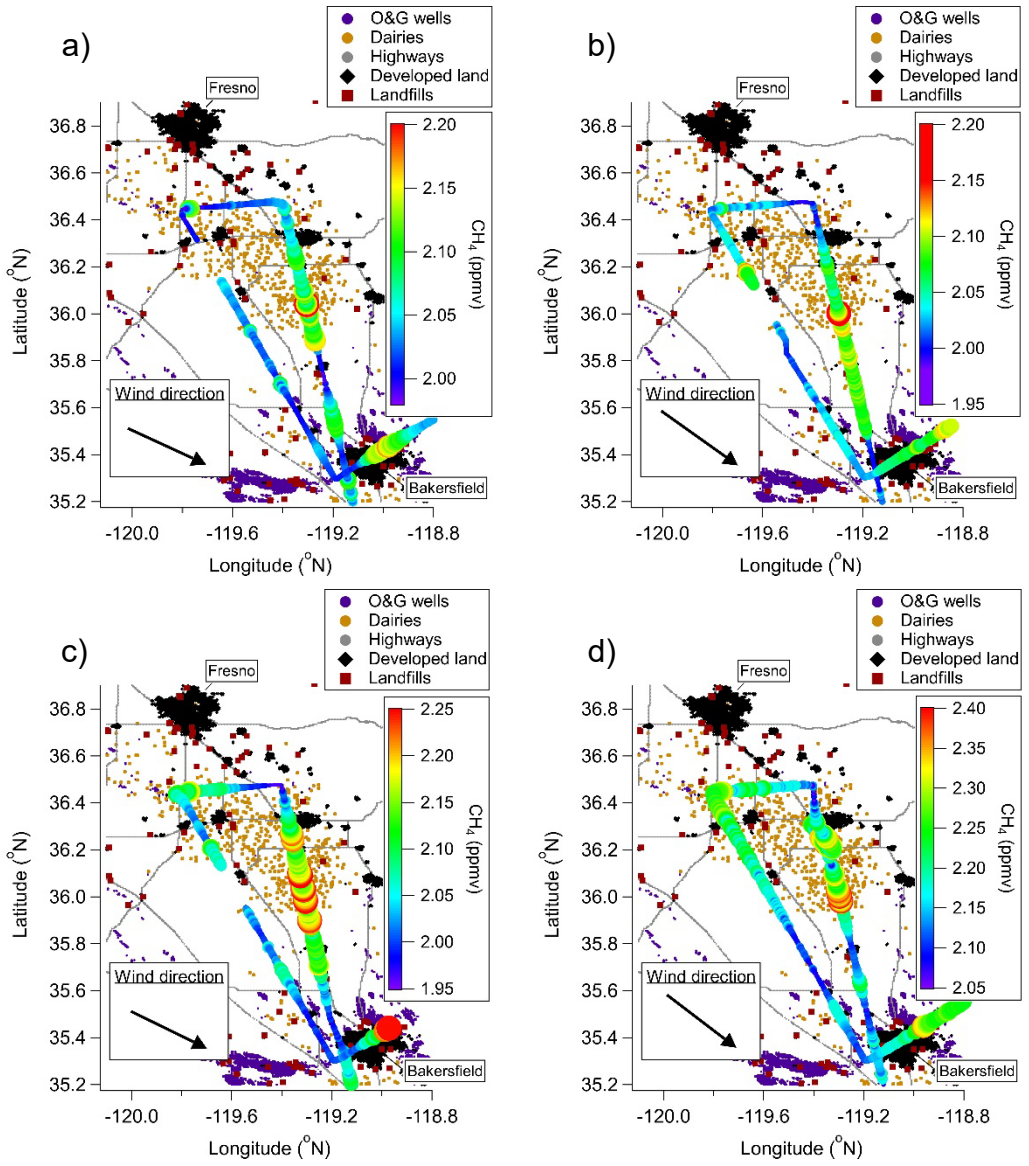

Figure 3.S12: Maps of the San Joaquin Valley region surveyed during flights with mass balance-based methane emissions estimates. (a) RF5, (b) RF6, (c) RF10, and (d) RF12. Markers denoting flight tracks are colored and sized by measured methane mixing ratios.

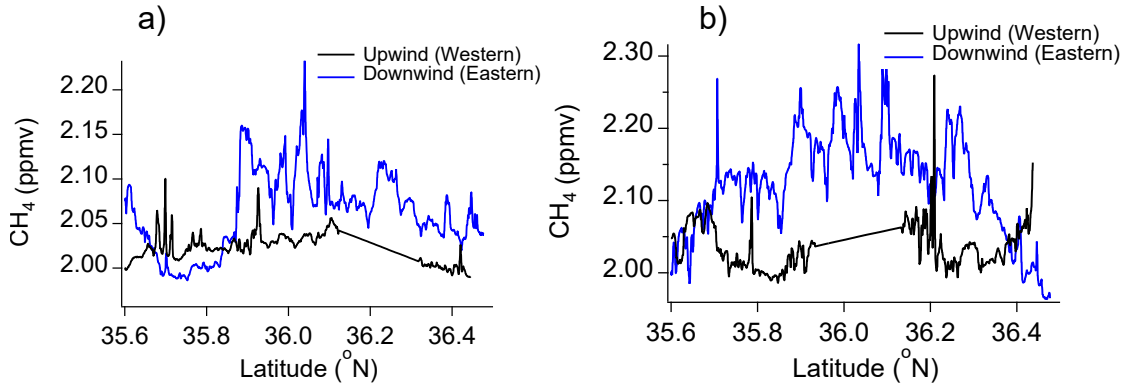

Figure 3.S13: Time series of methane concentrations measured on the western and eastern legs of the mass balance region sampled during (a) RF5 and (b) RF10. Interpolated regions represent in-flight calibrations.

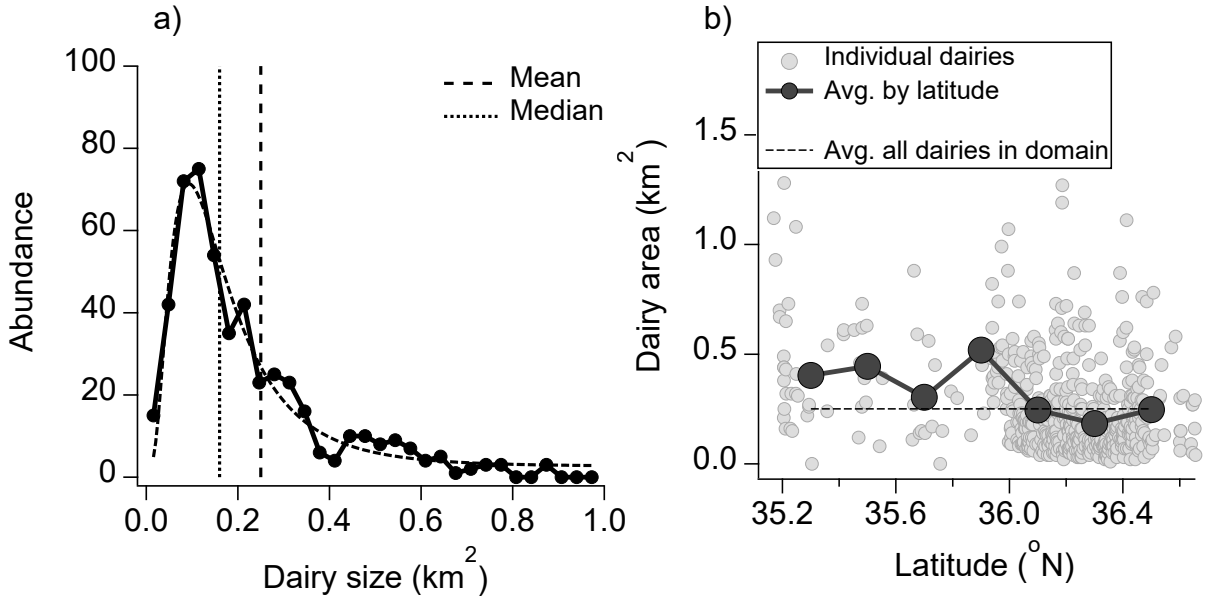

Figure 3.S14: (a) Distribution of dairy sizes in the sampled region of the SJV determined through a survey of Google Earth imagery. A lognormal fit approximately reproduces the distribution. Mean (0.25 km^2) and median (0.16 km^2) values are shown for reference. (b) Average dairy area as a function of latitude, demonstrating larger average dairies in the southernmost SJV near Bakersfield.

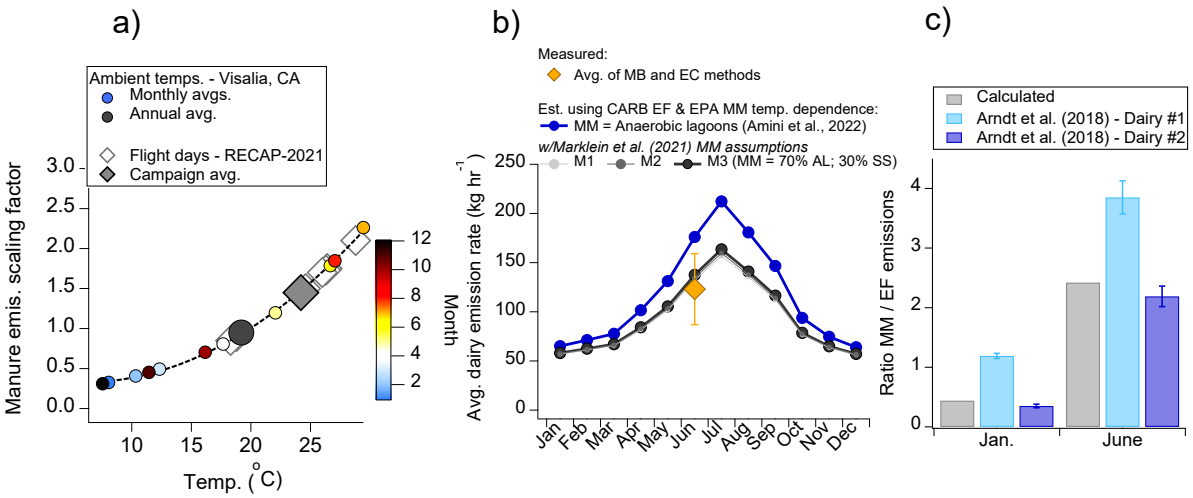

Figure 3.S15: (a) Relative scaling factor describing variation in annual average manure management emission factor with temperature according to the Maasakkers et al. (2016) parameterization. Scaling factors were adjusted equivalently (i.e., all monthly values were increased by a factor of 2.34) to ensure that the annual average calculated dairy emission rate was 94 kg $hr^{-1,}$ as described in SI Section 7. (b) Calculated monthly average dairy emission rate using the scaling factors shown in (a) for a variety of assumptions regarding manure management practices. The blue trace reflects the assumption used in Amini et al. (2022) (all manure managed using anaerobic lagoons). The grey traces represent calculation using assumptions of the different models described in Marklein et al. (2021). Our annual estimate discussed in SI Section 7 uses the M3 model assumptions (70% of manure managed using anaerobic lagoons, with the remainder managed using solid storage). The gold marker represents our average inferred emissions estimate during RECAP-CA, which occurred in June, and demonstrates the agreement between the inventory predictions and our measurements once the temperature dependence of emissions is incorporated. (c) Predicted ratio of manure management (MM) emissions to enteric fermentation (EF) emissions in January and June based on the scaling factors shown in (a) when applied to annual average CARB EF. Blue bars denote values observed by Arndt et al. (2018) at two dairies in Northern California.

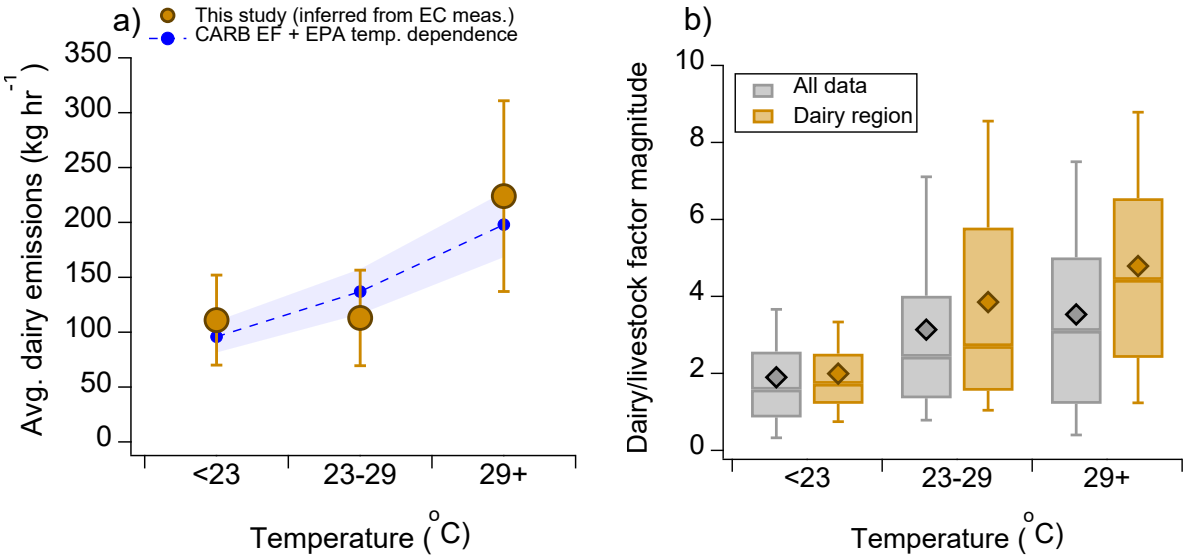

Figure 3.S16: (a) Comparison of observed and predicted average dairy emission rates with temperature during RECAP-CA. Detailed descriptions of the calculations are included in SI Section 8. (b) Variability in the magnitude of the dairy/livestock PMF factor with temperature. The magnitude is unitless due to the normalization procedure performed prior to PMF analysis, as described in SI Section 6. Values are shown for both the entire dataset and for the dairy region shown in Figure 3.1 specifically.

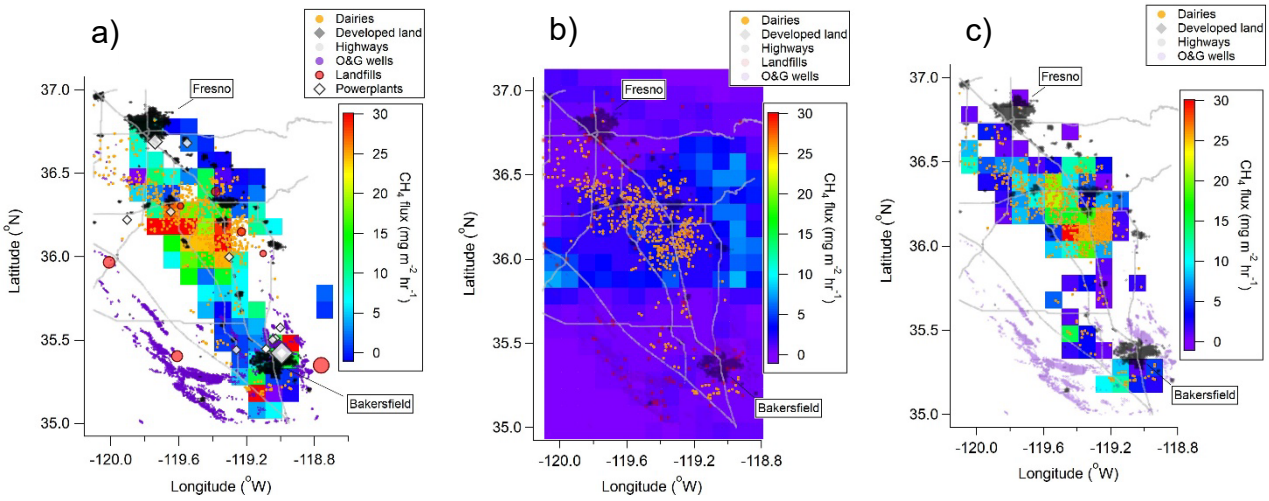

Figure 3.S17: (a) Measured methane fluxes during RECAP-CA. (b) Predicted livestock methane fluxes according to the EPA-GHGI inventory (Maasakkers et al., 2016). (c) Same as (b) for the VISTA-CA inventory (Marklein et al., 2021). Purple regions in (b) represent small but non-zero emissions estimates, while corresponding blank cells in (a) and (c) denote either a lack of measurements (a) or no predicted emissions (c).

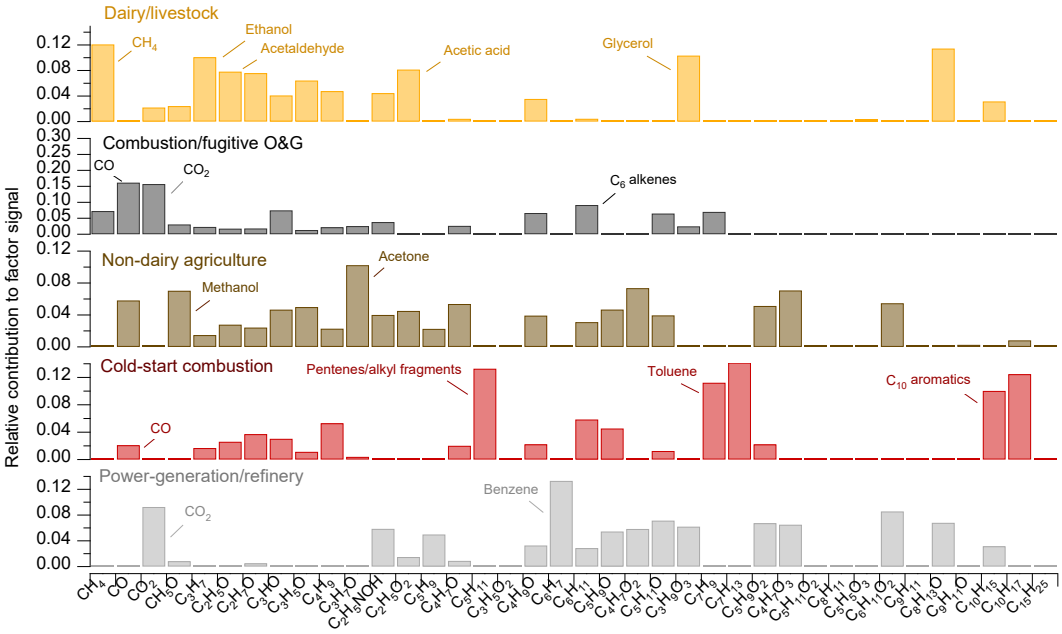

Figure 3.S18: Source profiles of the PMF factors resolved from the combined GHG + VOC dataset collected over the SJV. Factors represent emissions from dairy/livestock, combustion and fugitive oil & gas, non-dairy agriculture, cold-start combustion, and power generation/refining facilities. Species used in factor identification are noted.

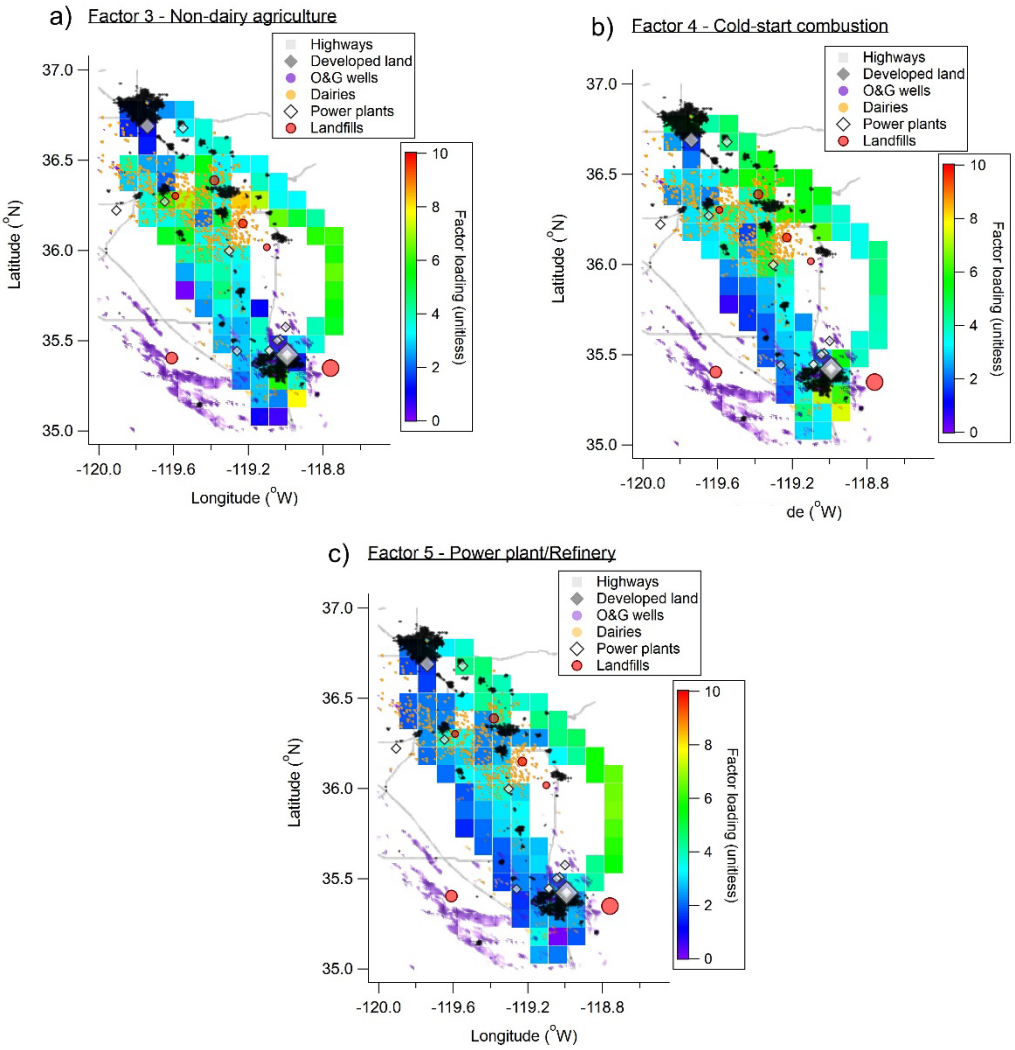

Figure 3.S19: Maps of the total concentration of the (a) non-dairy agriculture, (b) cold-start combustion, and (c) power-plant/refinery PMF factors.

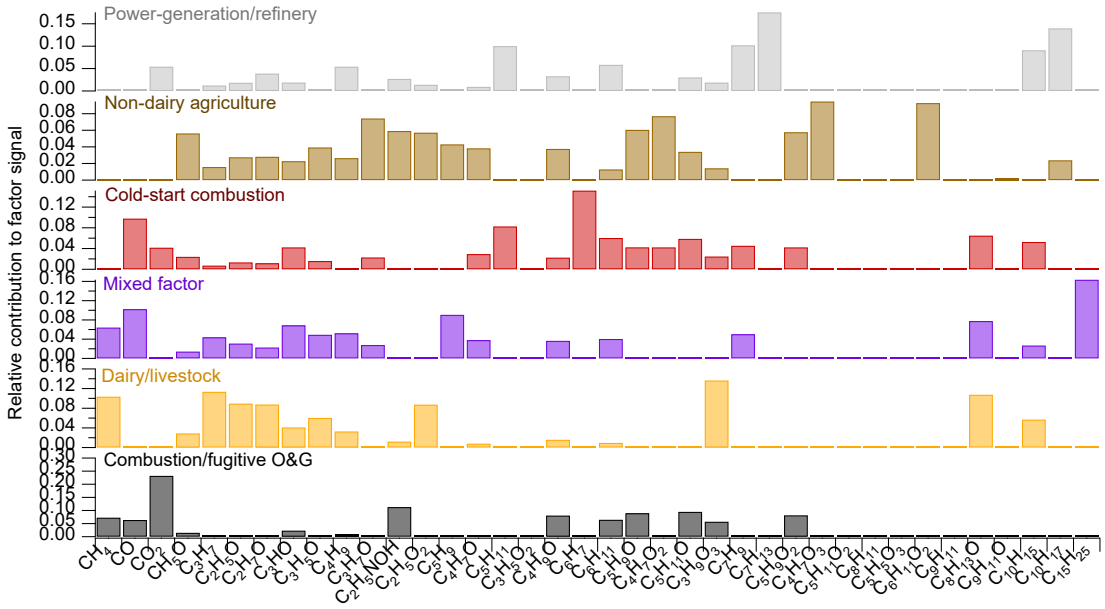

Figure 3.S20: Source profiles of PMF factors resolved in the six-factor solution. Factor assignments are based on similarity to factors resolved in the five-factor solution. An additional factor linked to mixing of pre-existing factors is noted in purple.

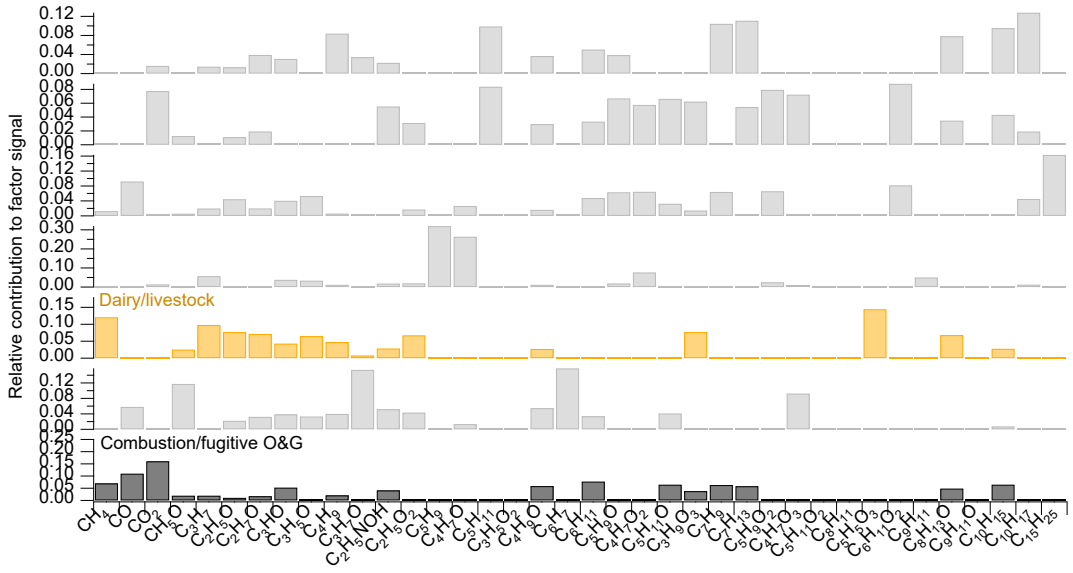

Figure 3.S21: Source profiles of PMF factors resolved in the seven-factor solution. Factors that likely represent dairy/livestock and combustion/fugitive O&G emissions are highlighted orange and black, respectively.

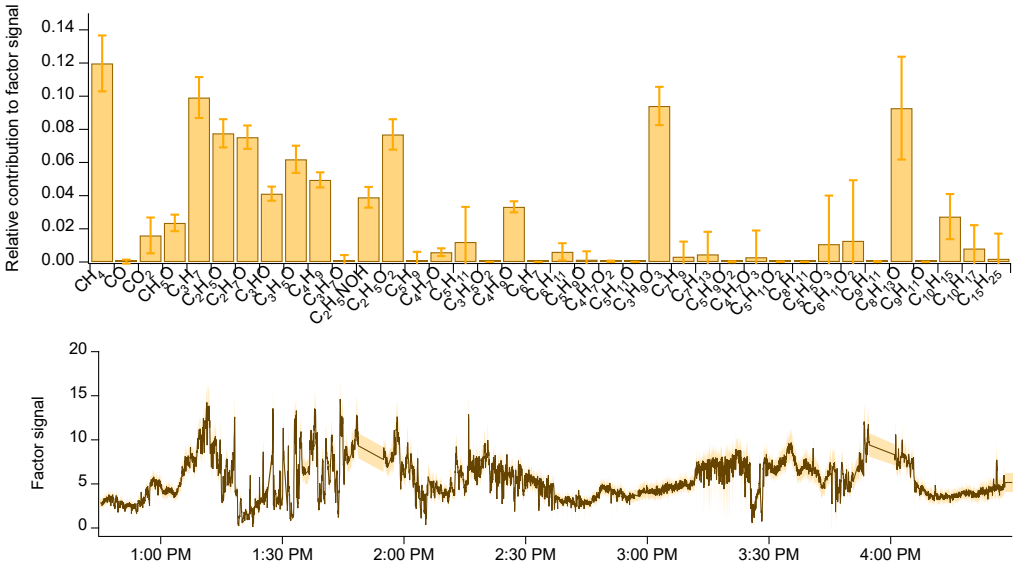

Figure 3.S22: (Top) Source profile of the dairy/livestock PMF factor derived from bootstrap analysis. Error bars represent the standard deviation of the contributions of individual species to the factor signal. (Bottom) Time series of the dairy/livestock factor signal during RF12. Shading indicates the calculated standard deviation of the factor signal.

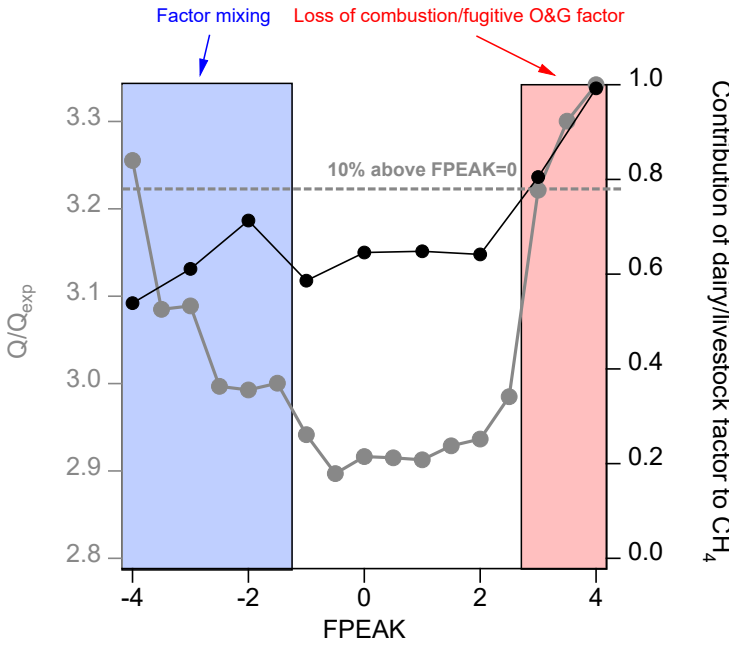

Figure 3.S23: Q/Qexp as a function of the FPEAK parameter. Negative values of FPEAK tend to increase differences between factor time series while decreasing differences in factor spectra. Positive values of FPEAK increase differences in factor spectra. The value of Q/Q_{exp} corresponding to a 10% increase above the value at FPEAK=0 is noted (Ulbrich et al., 2009). FPEAK values lower than -1, highlighted in blue, mix the dairy/livestock and non-dairy agriculture factors into two factors that are not clearly distinguishable.

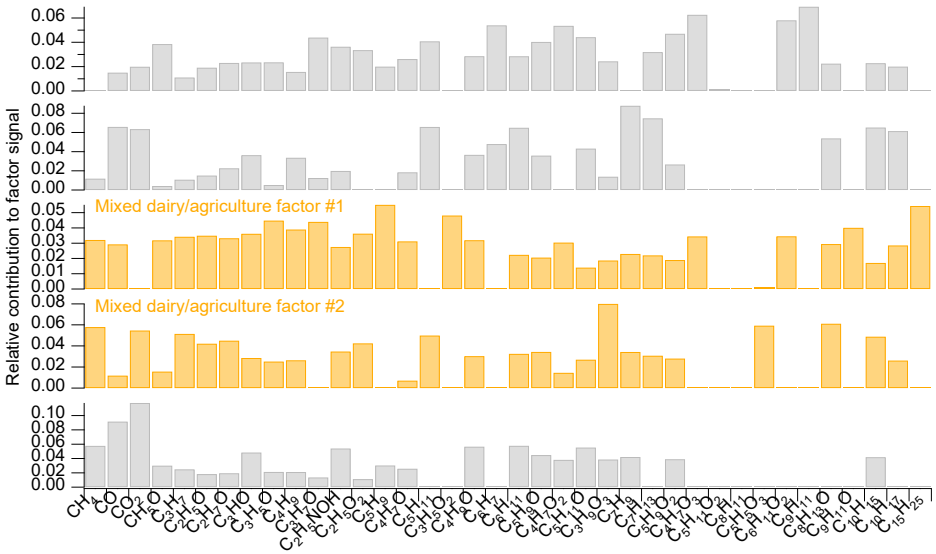

Figure 3.S24: Source profiles of factors resolved from PMF analysis with FPEAK = -3. Factors highlighted in orange are likely formed from mixing of the original dairy/livestock and non-dairy agriculture factors given the considerable contributions from methane, methanol, and methanol.

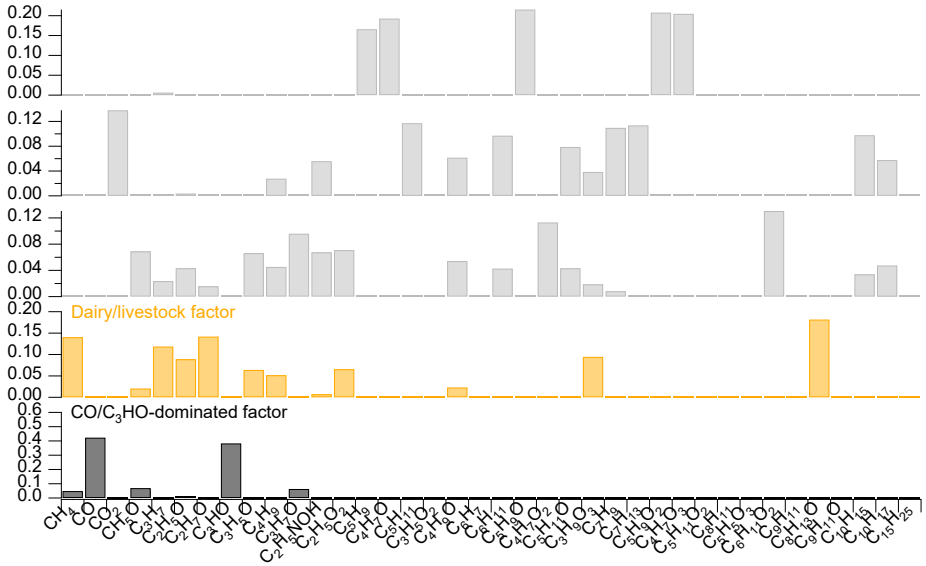

Figure 3.S25: Source profiles resolved from PMF analysis with FPEAK = 3. The factor highlighted in black is almost entirely comprised of CO and C_3HO (~80%) and is difficult to attribute to a specific emission source.

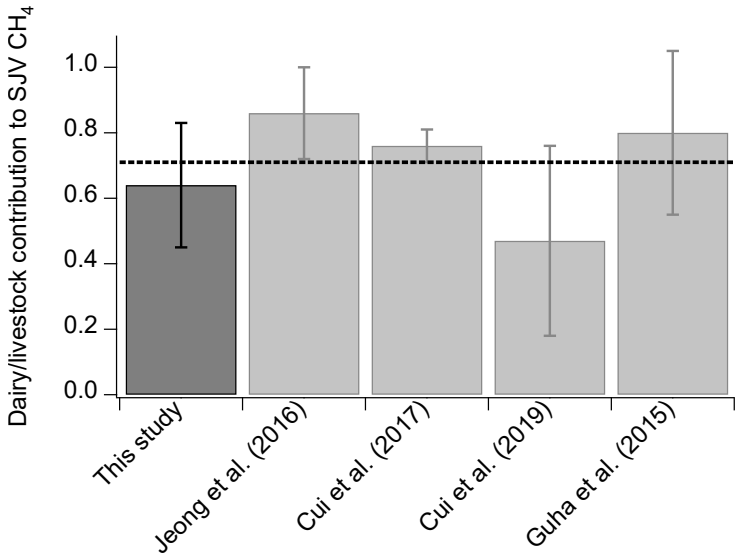

Figure 3.S26: Fraction of methane emissions linked to dairy/livestock sources in the SJV resolved from PMF results reported in this study and other recent atmospheric inversion and PMF studies. Data from Guha et al. (2015) represent results from PMF analysis of combined GHG + VOC dataset in Bakersfield, CA. The remaining studies involve inversion results applicable to the broader SJV region. Error bars represent estimated 2σ uncertainties.

Tables S1-S6

Table S1: Example of data used to calculate emissions from the region of intensive dairy operations during RF5. Negative fluxes represent transport into the mass balance region.

Transect	PBL height (m)	Wind Dir. (deg.)	Wind Speed (m s^{-1})	CH_4 bkgd. (ppmv)	CH_4 flux (kg hr^{-1})
Eastern leg	1212 ± 300	299 ± 12	3.4 ± 0.9	1.982 ± 0.018	57,010 ± 24,040
Northern leg	1218 ± 300	294 ± 14	2.6 ± 1.1	1.982 ± 0.018	-4,950 ± 2,230
Western leg	1222 ± 300	318 ± 25	3.2 ± 1.1	1.982 ± 0.018	-9,110 ± 3,650

Table S2: Inferred methane emissions within the region of intensive dairy operations shown in Figure 2 calculated using the mass balance method from data collected during RF5, RF6, RF10, and RF12.

Research flight	Flux from individual flight legs (10^3 kg hr^{-1})			Net emissions (10^3 kg hr^{-1})	Dairies in region	Emissions per dairy (kg hr^{-1})
	Eastern leg	Northern leg	Western leg			
RF5	57.0	-5.0	-9.2	43.0 ± 18.1	330 ± 50	130 ± 62
RF6	52.6	-6.3	-9.8	36.5 ± 19.8	330 ± 50	110 ± 62
RF10	96.1	-20.3	-15.4	60.4 ± 28.4	330 ± 50	183 ± 90
RF12	52.3	-24.0	-18.9	9.4 ± 32.6	330 ± 50	28 ± 99
Average				33.9 ± 12.1	330 ± 50	113 ± 44

Table 3.S3: Comparison of the effective dairy cow emission factor inferred in this study with results from recently published observational studies in California and Colorado.

Source	Location	Month	Avg. temp (°C)	Effective EF (g CH_4 dairy cow^{-1} hr^{-1})
This study – MB[1]	S. SJV	June	24	56 ± 20
This study – EC	S. SJV	June	24	67 ± 17
This study – Avg.	S. SJV	June	24	61 ± 18
Amini et al. (2022)[2]	S. SJV	June-Aug.	30	62 ± 12
Arndt et al. (2018)[3] (Dairy #1)	N. SJV	June	25	92 ± 5
Arndt et al. (2018) (Dairy #2)	N.E. Colorado	June	27	64 ± 7
Golston et al. (2020)[4]	N.E. Colorado	August	25	70 ± 7

*MB = mass balance. EC = eddy covariance. Avg. = average of methods. Reported avg. temp. represents average value measured in Visalia, CA on flight days according to Weather Underground (wunderground.com). [2]EF calculated by multiplying reported observed-to-estimated ratios for summertime vehicle sampling by calculated EF based on CARB inventory methodology (SI Section 7) assuming all manure management utilized anaerobic lagoons, as was assumed in Amini et al. (2022). [3]EF calculated by dividing the reported facility-level emissions measured by the open path technique by the number of dairy cattle on each dairy farm. [4]EF calculated by dividing total reported CH_4 emissions from dairy operations for August by the total number of dairy cattle in the surveyed region.

Table 3.S4: Comparison of total dairy methane emissions in the SJV estimated from our measurements with previous predictions from inverse modeling studies.

Source	Time period	Extrapolated annual SJV dairy CH_4 emissions (Gg yr^{-1})
This study[1]	June 2021	848 ± 251
This study – adjusted[2]	2021	584 ± 173
Jeong et al. (2013)	Sept-June 2010	1130 ± 420
Cui et al. (2017)[3]	May-June 2010	963 ± 236
Cui et al. (2019)	2014-2016	440 ± 360

[1]Calculated by multiplying effective dairy cow EF (61 g dairy cow^{-1} hr^{-1}) by the total number of dairy cows in eight counties in the SJV according to 2017 USDA Census of Agriculture. [2]Adjusted for annual temperature variability in Visalia, CA using the parameterization for temperature dependence of manure management emissions from Maasakkers et al. (2016) (SI Section 8). [3]Extrapolated from reported Mg hr^{-1} to Gg yr^{-1}.

Table 3.S5: Comparison of the methanol/CH_4, ethanol/CH_4, and methanol/ethanol emission ratios (ER) inferred from the dairy/livestock PMF factor resolved in this study with ER reported from previous measurements at dairy facilities. Uncertainty represents 1σ variability derived from bootstrap analysis.

Source	Methanol/CH_4 (mmol mol^{-1})	Ethanol/CH4 (mmol mol^{-1})	Ethanol/Methanol (mmol $mmol^{-1}$)
Dairy/livestock factor (this study)	9.0 ± 3.0	13.8 ± 1.45	1.54 ± 0.45
Guha et al., 2015[a]	15-47	9-32	0.66
Shaw et al., 2007[b]	3.2	NA	NA
Gentner et al., 2014[c]	7-16	18	2.4
Sun et al., 2008[b]	15-25	18-32	1.3
Yuan et al., 2017[d]	NA	NA	2.3

[a]From PMF factor linked to dairy and livestock emissions derived from measurements in Bakersfield, CA. [b]Direct measurements from environmentally controlled chambers at the University of California, Davis Animal Science Swine Research Facility. [c]Calculated from regression slopes fit to aircraft sampling of dairy plumes. [d]Measurements of dairy plumes near Greeley, CO using a mobile laboratory

Table 3.S6: Comparison of the CO/CO_2, CH_4/CO_2, and toluene/CO emission ratios (ER) inferred from the combustion/fugitive O&G PMF factor resolved in this study with ER reported from the CARB EMFAC model (EMFAC, 2022) and other observational studies. Uncertainty represents 1σ variability derived from bootstrap analysis.

Source	CO / CO_2 (mmol mol^{-1})	CH_4 / CO_2 (mmol mol^{-1})	Toluene / CO (mmol mol^{-1})
Combustion + fugitive O&G factor (this study)	6.0 ± 1.5	21.7 ± 3.5	0.41 ± 0.23
EMFAC – on-road gasoline	7.1	0.12	NA
EMFAC – on-road diesel	0.6	0.01	NA
Guha et al., 2015[a]	NA	NA	0.26
Gentner et al., 2013 – on-road gasoline[b]	NA	NA	1.0
Gentner at al., 2013 – on-road diesel[b]	NA	NA	0.04

[a]From PMF factor linked to motor vehicle emissions derived from measurements in Bakersfield, CA.
[b]Direct measurements of VOCs and CO in the Caldecott Tunnel in Oakland, CA during July 2010.

References

Amini, S.; Kuwayama, T.; Gong, L.; Falk, M.; Chen, Y.; Mitloehner, Q.; Weller, S.; Mitloehner, F. M.; Patteson, D.; Conley, S. A.; Scheehle, E.; FitzGibbon, M. Evaluating California Dairy Methane Emission Factors Using Short-Term Ground-Level and Airborne Measurements. *Atmospheric Environment: X* **2022**, *14*, 100171. https://doi.org/10.1016/j.aeaoa.2022.100171.

Arndt, C.; Leytem, A. B.; Hristov, A. N.; Zavala-Araiza, D.; Cativiela, J. P.; Conley, S.; Daube, C.; Faloona, I.; Herndon, S. C. Short-Term Methane Emissions from 2 Dairy Farms in California Estimated by Different Measurement Techniques and US Environmental Protection Agency Inventory Methodology: A Case Study. *Journal of Dairy Science* **2018**, *101* (12), 11461–11479. https://doi.org/10.3168/jds.2017-13881.

Aubinet, M., Vesala, T., Papale, D., *Eddy Covariance: A Practical Guide to Measurement and Data Analysis*; Eds.; Springer Netherlands: Dordrecht, 2012. https://doi.org/10.1007/978-94-007-2351-1.

CalRecycle SWIS Facility/Site Inspection Details, Accessed at: https://www2.calrecycle.ca.gov/SolidWaste/Site/Search
California Air Resources Board (CARB) Documentation of California's 2000-2020 GHG Inventory. Accessed at: https://ww2.arb.ca.gov/applications/california-ghg-inventory-documentation.
Cui, Y. Y.; Vijayan, A.; Falk, M.; Hsu, Y.-K.; Yin, D.; Chen, X. M.; Zhao, Z.; Avise, J.; Chen, Y.; Verhulst, K.; Duren, R.; Yadav, V.; Miller, C.; Weiss, R.; Keeling, R.; Kim, J.; Iraci, L. T.; Tanaka, T.; Johnson, M. S.; Kort, E. A.; Bianco, L.; Fischer, M. L.; Stroud, K.; Herner, J.; Croes, B. A Multiplatform Inversion Estimation of Statewide and Regional Methane Emissions in California during 2014–2016. *Environ. Sci. Technol.* **2019**, *53* (16), 9636–9645. https://doi.org/10.1021/acs.est.9b01769.

Drozd, G. T.; Zhao, Y.; Saliba, G.; Frodin, B.; Maddox, C.; Weber, R. J.; Chang, M.-C. O.; Maldonado, H.; Sardar, S.; Robinson, A. L.; Goldstein, A. H. Time Resolved Measurements of Speciated Tailpipe Emissions from Motor Vehicles: Trends with Emission Control Technology, Cold Start Effects, and Speciation. *Environ. Sci. Technol.* **2016**, *50* (24), 13592–13599. https://doi.org/10.1021/acs.est.6b04513.
EPA Facility Level Information on GreenHouse gases Tool (FLIGHT), accessed at: https://ghgdata.epa.gov/ghgp/main.do, last accessed: 12/27/2022

Finkelstein, P. L.; Sims, P. F. Sampling Error in Eddy Correlation Flux Measurements. *Journal of Geophysical Research: Atmospheres* **2001**, *106* (D4), 3503–3509. https://doi.org/10.1029/2000JD900731.

Gentner, D. R.; Worton, D. R.; Isaacman, G.; Davis, L. C.; Dallmann, T. R.; Wood, E. C.; Herndon, S. C.; Goldstein, A. H.; Harley, R. A. Chemical Composition of Gas-Phase Organic Carbon Emissions from Motor Vehicles and Implications for Ozone Production. *Environ. Sci. Technol.* **2013**, *47* (20), 11837–11848. https://doi.org/10.1021/es401470e.

Goldstein, A. H.; Schade, G. W. Quantifying Biogenic and Anthropogenic Contributions to Acetone Mixing Ratios in a Rural Environment. *Atmospheric Environment* **2000**, *34* (29), 4997–5006. https://doi.org/10.1016/S1352-2310(00)00321-6.
Guha, A.; Gentner, D. R.; Weber, R. J.; Provencal, R.; Goldstein, A. H. Source Apportionment of Methane and Nitrous Oxide in California's San Joaquin Valley at CalNex 2010 via Positive Matrix Factorization. *Atmos. Chem. Phys.* **2015**, *15* (20), 12043–12063. https://doi.org/10.5194/acp-15-12043-2015.

Hannun, R. A.; Wolfe, G. M.; Kawa, S. R.; Hanisco, T. F.; Newman, P. A.; Alfieri, J. G.; Barrick, J.; Clark, K. L.; DiGangi, J. P.; Diskin, G. S.; King, J.; Kustas, W. P.; Mitra, B.; Noormets, A.; Nowak, J. B.; Thornhill, K. L.; Vargas, R. Spatial Heterogeneity in CO2, CH4, and Energy Fluxes: Insights from Airborne Eddy Covariance Measurements over the Mid-Atlantic Region. *Environ. Res. Lett.* **2020**, *15* (3), 035008. https://doi.org/10.1088/1748-9326/ab7391.

Hanson, J. L., Yesiller, J., and Manheim, D.C. Estimation and Comparison of Methane, Nitrous Oxide, and Trace Volatile Organic Compound Emissions and Gas Collection System Efficiencies in California Landfills, Final Report, Accessed at: https://ww2.arb.ca.gov/sites/default/files/2020-12/CalPoly_LFG_Study_03-30-20.pdf

Hopkins, F.M., T. Rafiq, and R.M. Duren. 2019. Sources of Methane Emissions (Vista-CA), State of California, USA. ORNL DAAC, Oak Ridge, Tennessee, USA. https://doi.org/10.3334/ORNLDAAC/1726

Hristov, A. N.; Harper, M.; Meinen, R.; Day, R.; Lopes, J.; Ott, T.; Venkatesh, A.; Randles, C. A. Discrepancies and Uncertainties in Bottom-up Gridded Inventories of Livestock Methane Emissions for the Contiguous United States. *Environ. Sci. Technol.* **2017**, *51* (23), 13668–13677. https://doi.org/10.1021/acs.est.7b03332

Jeong, S.; Millstein, D.; Fischer, M. L. Spatially Explicit Methane Emissions from Petroleum Production and the Natural Gas System in California. *Environ. Sci. Technol.* **2014**, *48* (10), 5982–5990. https://doi.org/10.1021/es4046692.
Jeong, S.; Hsu, Y.-K.; Andrews, A. E.; Bianco, L.; Vaca, P.; Wilczak, J. M.; Fischer, M. L. A Multitower Measurement Network Estimate of California's Methane Emissions. Journal of Geophysical Research: Atmospheres 2013, 118 (19), 11,339-11,351. https://doi.org/10.1002/jgrd.50854.
Kljun, N.; Calanca, P.; Rotach, M. W.; Schmid, H. P. A Simple Parameterisation for Flux Footprint Predictions. *Boundary-Layer Meteorology* **2004**, *112* (3), 503–523. https://doi.org/10.1023/B:BOUN.0000030653.71031.96.

Kljun, N.; Calanca, P.; Rotach, M. W.; Schmid, H. P. A Simple Two-Dimensional Parameterisation for Flux Footprint Prediction (FFP). *Geosci. Model Dev.* **2015**, *8* (11), 3695–3713. https://doi.org/10.5194/gmd-8-3695-2015.

Kuwayama, T.; Charrier-Klobas, J. G.; Chen, Y.; Vizenor, N. M.; Blake, D. R.; Pongetti, T.; Conley, S. A.; Sander, S. P.; Croes, B.; Herner, J. D. Source Apportionment of Ambient Methane Enhancements in Los Angeles, California, To Evaluate Emission Inventory Estimates. *Environ. Sci. Technol.* **2019**, *53* (6), 2961–2970. https://doi.org/10.1021/acs.est.8b02307.

Lenschow, D. H.; Mann, J.; Kristensen, L. How Long Is Long Enough When Measuring Fluxes and Other Turbulence Statistics? *Journal of Atmospheric and Oceanic Technology* **1994**, *11* (3), 661–673. https://doi.org/10.1175/1520-0426(1994)011<0661:HLILEW>2.0.CO;2.

Maasakkers, J. D.; Jacob, D. J.; Sulprizio, M. P.; Turner, A. J.; Weitz, M.; Wirth, T.; Hight, C.; DeFigueiredo, M.; Desai, M.; Schmeltz, R.; Hockstad, L.; Bloom, A. A.; Bowman, K. W.; Jeong, S.; Fischer, M. L. Gridded National Inventory of U.S. Methane Emissions. *Environ. Sci. Technol.* **2016**, *50* (23), 13123–13133. https://doi.org/10.1021/acs.est.6b02878.

Marklein, A. R.; Meyer, D.; Fischer, M. L.; Jeong, S.; Rafiq, T.; Carr, M.; Hopkins, F. M. Facility-Scale Inventory of Dairy Methane Emissions in California: Implications for Mitigation. *Earth System Science Data* **2021**, *13* (3), 1151–1166. https://doi.org/10.5194/essd-13-1151-2021.

Mauder, M.; Cuntz, M.; Drüe, C.; Graf, A.; Rebmann, C.; Schmid, H. P.; Schmidt, M.; Steinbrecher, R. A Strategy for Quality and Uncertainty Assessment of Long-Term Eddy-Covariance Measurements. *Agricultural and Forest Meteorology* **2013**, *169*, 122–135. https://doi.org/10.1016/j.agrformet.2012.09.006.

Metzger, S.; Junkermann, W.; Mauder, M.; Beyrich, F.; Butterbach-Bahl, K.; Schmid, H. P.; Foken, T. Eddy-Covariance Flux Measurements with a Weight-Shift Microlight Aircraft. *Atmospheric Measurement Techniques* **2012**, *5* (7), 1699–1717. https://doi.org/10.5194/amt-5-1699-2012.

Misztal, P. K.; Karl, T.; Weber, R.; Jonsson, H. H.; Guenther, A. B.; Goldstein, A. H. Airborne Flux Measurements of Biogenic Isoprene over California. *Atmospheric Chemistry and Physics* **2014**, *14* (19), 10631–10647. https://doi.org/10.5194/acp-14-10631-2014.

Norris, G.; Duvall, R.; Brown, S.; Bai, S. Positive Matrix Factorization (PMF) 5.0 Fundamentals and User Guide. 136.

Paatero, P.; Tapper, U. Positive Matrix Factorization: A Non-Negative Factor Model with Optimal Utilization of Error Estimates of Data Values. *Environmetrics* **1994**, *5* (2), 111–126. https://doi.org/10.1002/env.3170050203.

Paatero, P. Least Squares Formulation of Robust Non-Negative Factor Analysis. *Chemometrics and Intelligent Laboratory Systems* **1997**, *37* (1), 23–35. https://doi.org/10.1016/S0169-7439(96)00044-5.

Peischl, J.; Ryerson, T. B.; Holloway, J. S.; Trainer, M.; Andrews, A. E.; Atlas, E. L.; Blake, D. R.; Daube, B. C.; Dlugokencky, E. J.; Fischer, M. L.; Goldstein, A. H.; Guha, A.; Karl, T.; Kofler, J.; Kosciuch, E.; Misztal, P. K.; Perring, A. E.; Pollack, I. B.; Santoni, G. W.; Schwarz, J. P.; Spackman, J. R.; Wofsy, S. C.; Parrish, D. D. Airborne Observations of Methane Emissions from Rice Cultivation in the Sacramento Valley of California. *Journal of Geophysical Research: Atmospheres* **2012**, *117* (D24). https://doi.org/10.1029/2012JD017994.

Peischl, J.; Ryerson, T. B.; Brioude, J.; Aikin, K. C.; Andrews, A. E.; Atlas, E.; Blake, D.; Daube, B. C.; Gouw, J. A. de; Dlugokencky, E.; Frost, G. J.; Gentner, D. R.; Gilman, J. B.; Goldstein, A. H.; Harley, R. A.; Holloway, J. S.; Kofler, J.; Kuster, W. C.; Lang, P. M.; Novelli, P. C.; Santoni, G. W.; Trainer, M.; Wofsy, S. C.; Parrish, D. D. Quantifying Sources of Methane Using Light

Alkanes in the Los Angeles Basin, California. *Journal of Geophysical Research: Atmospheres* **2013**, *118* (10), 4974–4990. https://doi.org/10.1002/jgrd.50413.

Peischl, J.; Ryerson, T. B.; Aikin, K. C.; de Gouw, J. A.; Gilman, J. B.; Holloway, J. S.; Lerner, B. M.; Nadkarni, R.; Neuman, J. A.; Nowak, J. B.; Trainer, M.; Warneke, C.; Parrish, D. D. Quantifying Atmospheric Methane Emissions from the Haynesville, Fayetteville, and Northeastern Marcellus Shale Gas Production Regions. *Journal of Geophysical Research: Atmospheres* **2015**, *120* (5), 2119–2139. https://doi.org/10.1002/2014JD022697

Pfannerstill, E. Y.; Arata, C.; Zhu, Q.; Place, B.; Weber, R. J.; Wooldridge, P. J.; Schulze, B.; Ward, R.; Woods, R.; Seinfeld, J. H.; Bucholtz, A.; Cohen, R. C.; Goldstein, A. H. Temperature-dependent emissions dominate aerosol and ozone formation in Los Angeles. submitted [Online] 2023a.

Pfannerstill, E. Y.; Arata, C.; Zhu, Q.; Schulze, B. C.; Woods, R.; Seinfeld, J. H.; Bucholtz, A.; Cohen, R. C.; Goldstein, A. H. Volatile Organic Compound Fluxes in the San Joaquin Valley; Spatial Distribution, Source Attribution, and Inventory Comparison. *EGUsphere* **2023b**, 1–42. https://doi.org/10.5194/egusphere-2023-723.

Ulbrich, I. M.; Canagaratna, M. R.; Zhang, Q.; Worsnop, D. R.; Jimenez, J. L. Interpretation of Organic Components from Positive Matrix Factorization of Aerosol Mass Spectrometric Data. Atmospheric Chemistry and Physics 2009, 9 (9), 2891–2918. https://doi.org/10.5194/acp-9-2891-2009.

USDA 2017 Census of Agriculture, Volume 1, Chapter 2: County Level Data, United States Department of Agriculture, Accessed at: https://www.nass.usda.gov/Publications/AgCensus/2017/Full_Report/Volume_1,_Chapter_2_County_Level/California/

Torrence, C.; Compo, G. P. A Practical Guide to Wavelet Analysis. *Bulletin of the American Meteorological Society* **1998**, *79* (1), 18.

Wolfe, G. M.; Kawa, S. R.; Hanisco, T. F.; Hannun, R. A.; Newman, P. A.; Swanson, A.; Bailey, S.; Barrick, J.; Thornhill, K. L.; Diskin, G.; DiGangi, J.; Nowak, J. B.; Sorenson, C.; Bland, G.; Yungel, J. K.; Swenson, C. A. The NASA Carbon Airborne Flux Experiment (CARAFE): Instrumentation and Methodology. *Atmospheric Measurement Techniques* **2018**, *11* (3), 1757–1776. https://doi.org/10.5194/amt-11-1757-2018.

Zhu, Q.; Place, B.; Pfannerstill, E. Y.; Tong, S.; Zhang, H.; Wang, J.; Nussbaumer, C. M.; Wooldridge, P.; Schulze, B. C.; Arata, C.; Bucholtz, A.; Seinfeld, J. H.; Goldstein, A. H.; Cohen, R. C. Direct Observations of NO_x Emissions over the San Joaquin Valley Using Airborne Flux Measurements during RECAP-CA 2021 Field Campaign. *Atmospheric Chemistry and Physics Discussions* **2023**, 1–21. https://doi.org/10.5194/acp-2023-3.

Chapter 4

Characterization of aerosol hygroscopicity over the Northeast Pacific Ocean: Impacts on prediction of CCN and stratocumulus cloud droplet number concentrations

Schulze, B. C.; Charan, S. M.; Kenseth, C. M.; Kong, W.; Bates, K. H.; Williams, W.; Metcalf, A. R.; Jonsson, H. H.; Woods, R.; Sorooshian, A.; Flagan, R. C.; Seinfeld, J. H. Characterization of Aerosol Hygroscopicity Over the Northeast Pacific Ocean: Impacts on Prediction of CCN and Stratocumulus Cloud Droplet Number Concentrations. *Earth and Space Science* **2020**, 7 (7), e2020EA001098. https://doi.org/10.1029/2020EA001098.

Abstract:

During the Marine Aerosol Cloud and Wildfire Study (MACAWS) in June and July of 2018, aerosol composition and cloud condensation nuclei (CCN) properties were measured over the N.E. Pacific to characterize the influence of aerosol hygroscopicity on predictions of ambient CCN and stratocumulus cloud droplet number concentrations (CDNC). Three vertical regions were characterized, corresponding to the marine boundary layer (MBL), an above-cloud organic aerosol layer (AC-OAL), and the free troposphere (FT) above the AC-OAL. The aerosol hygroscopicity parameter (κ) was calculated from CCN measurements (κ_{CCN}) and bulk aerosol mass spectrometer (AMS) measurements (κ_{AMS}). Within the MBL, measured hygroscopicities varied between values typical of both continental environments (~0.2) and remote marine locations (~0.7). For most flights, CCN closure was achieved within 20% in the MBL. For five of the seven flights, assuming a constant aerosol size distribution produced similar or better CCN closure than assuming a constant "marine" hygroscopicity (κ = 0.72). An aerosol-cloud parcel model was used to characterize the sensitivity of predicted stratocumulus CDNC to aerosol hygroscopicity, size distribution properties, and updraft velocity. Average CDNC sensitivity to accumulation mode aerosol hygroscopicity is 39% as large as the sensitivity to the geometric median diameter in this environment. Simulations suggest CDNC sensitivity to hygroscopicity is largest in marine stratocumulus with low updraft velocities (<0.2 m s^{-1}), where accumulation mode particles are most relevant to CDNC, and in marine

stratocumulus or cumulus with large updraft velocities (>0.6 m s^{-1}), where hygroscopic properties of the Aitken mode dominate hygroscopicity sensitivity.

4.1 Introduction

Marine stratocumulus (MSc) clouds, commonly observed off the Western coasts of North America, South America, Africa, and Australia, cover nearly one-fifth of the Earth's surface and exert a large impact on its radiative balance (Wood, 2012). These cloud decks are particularly relevant to global climate due to their high albedo contrast with the underlying ocean and relatively low altitude, resulting in stronger shortwave reflectance than longwave absorption (Randall et al., 1984; Brenguier et al., 2000; Wood, 2012). Previous estimates suggest that a ~12% increase in the albedo of these clouds would produce a negative radiative forcing equivalent in magnitude to that of doubling atmospheric CO_2 concentrations (Latham et al., 2008; Stevens and Brenguier, 2009). Remote sensing, parcel modeling, and large eddy simulation (LES) studies have all established that MSc exhibit substantial albedo susceptibility to variations in cloud droplet number concentrations (CDNC) (Platnick and Twomey, 1994; Oreopoulos and Platnick, 2008; Chen et al., 2011; Berner et al., 2015; Sanchez et al., 2016). Understanding the sensitivity of MSc CDNC to aerosols acting as cloud condensation nuclei (CCN) is therefore a critical aspect of reducing uncertainty in climate change predictions (Seinfeld et al., 2016).

The CDNC and albedo of MSc are substantially influenced by the abundance of below-cloud CCN. A recent satellite analysis suggested that variability in below-cloud CCN concentration may be responsible for ~45% of the variability in the radiative effect of marine boundary layer clouds (Rosenfeld et al., 2019). This influence results from the fact that increased CCN abundance enhances cloud reflectivity at constant liquid water path (Twomey, 1977), and has the potential to reduce MSc precipitation rates, increasing cloud lifetime (Albrecht, 1989; Ackerman et al., 1993; Rosenfeld et al., 2006; Goren and Rosenfeld, 2012). As a result, a major component of the uncertainty in the estimated indirect aerosol forcing has been attributed to the prediction of below-cloud CCN

concentrations (Sotiropoulou et al., 2007; Rosenfeld et al., 2014). While the aerosol size distribution is generally thought to be the most important determinant of CCN activity (e.g., Dusek et al., 2006; McFiggans et al., 2006; Ervens et al., 2007; Reutter et al., 2009), particle composition has also been shown to exert a substantial influence (Quinn et al., 2008; Jimenez et al., 2009; Liu and Wang, 2010; Mei et al., 2013; Sanchez et al., 2016).

The propensity of a given aerosol particle to act as a CCN can be described using Köhler theory (Köhler, 1936; Seinfeld and Pandis, 2016), provided sufficient information is known regarding particle size and solute properties (e.g., molecular weight, solubility, density, and activity). A novel framework, κ-Köhler theory, condenses these solute characteristics into a single parameter κ (the aerosol hygroscopicity) that can be easily incorporated into large scale models (Petters and Kreidenweis, 2007). Substantial effort has, therefore, been devoted to quantifying κ values in a multitude of environments (Gunthe et al., 2009; Ervens et al., 2010; Pringle et al., 2010; Rose et al., 2010; Thalman et al., 2017). While κ values characteristic of inorganic aerosol components are relatively well-established, atmospheric organic aerosol is composed of numerous, highly diverse organic compounds, complicating representation of organic hygroscopicity using a single parameter (Kanakidou et al., 2005). Experimental studies have characterized κ values of secondary organic aerosol (SOA) (e.g., Duplissy et al., 2008; 2011; Asa-Awuku et al., 2010; Massoli et al., 2010; Lambe et al., 2011; Frosch et al., 2013; Zhao et al., 2015), and field studies have characterized the typical range of organic κ values (κ_{org}) observed in the atmosphere (Wang et al., 2008; Gunthe et al., 2009; Chang et al., 2010; Mei et al., 2013; Levin et al., 2014; Thalman et al., 2017). Generally, ambient κ_{org} values are found to be 0.1-0.2 for aged aerosol and primary marine organics, and ~0 for freshly emitted combustion aerosol (e.g., soot) (Kreidenweis and Asa-Awuku, 2014). A linear relationship has been noted between observed κ_{org} values and organic aerosol oxygen-to-carbon (O:C) ratios in both the laboratory and the field (Chang et al., 2010; Lambe et al., 2011; Mei et al., 2013; Wang et al., 2019).

Ambient particle hygroscopicity data have been combined with aerosol size distribution measurements in CCN closure studies to assess the extent to which Köhler theory can be used to predict ambient CCN concentrations (e.g., Van Reken et al., 2003;

McFiggans et al., 2006; Medina et al., 2007; Cubison et al., 2008; Asa-Awuku et al., 2011; Moore et al., 2012; Almeida et al., 2014; Ren et al., 2018). Analyzing the accuracy of predicted CCN concentrations can provide insight into the influence of specific aerosol characteristics on CCN activity (Van Reken et al., 2003; Medina et al., 2007; Cubison et al., 2008; Wang et al., 2010; Bougiatioti et al., 2011). For instance, size-resolved compositional (i.e., hygroscopicity) data are often required to accurately reproduce observed CCN concentrations in locations dominated by organic aerosol (Medina et al., 2007; Bhattu and Tripathi, 2015; Ren et al., 2018), while aerosol mixing state has been shown to strongly impact total CCN concentrations in urban environments (Cubison et al., 2008; Quinn et al., 2008; Ervens et al., 2010). By analyzing data from five ambient measurement campaigns, Ervens et al. (2010) found that for aerosol measured farther than a few tens of kilometers from the emission source, CCN activity could be predicted within a factor of two independent of either aerosol mixing state (i.e., internal or external) or organic solubility (i.e., insoluble or slightly soluble). Wang et al. (2010) further demonstrated that CCN concentrations can often be reproduced within 20% assuming internal mixing of aerosol components if the overall κ of the aerosol population is > 0.1. The direct impact of variability in aerosol hygroscopicity on CCN concentrations is often assessed by assuming an invariant chemical composition, represented as a fixed κ, in CCN closure analyses. Field campaigns in continental environments ranging from polluted megacities to the pristine tropical rainforest have shown that CCN concentrations could be reproduced within 20% and 50% respectively assuming a constant $\kappa = 0.3$ (Gunthe et al., 2009; Rose et al., 2010), a value representative of average continental conditions (Andreae and Rosenfeld, 2008; Pringle et al., 2010). However, in coastal regions, MBL aerosol can result from a mixture of distinct marine and continental emissions (e.g., Sorooshian et al., 2009; Coggon et al., 2014; Modini et al., 2015; Mardi et al., 2019), which complicates aerosol representation using regional or global models. CCN closure analysis can provide insight into the uncertainties in CCN concentrations that may result from inaccurate model representation of aerosol composition in these environments.

Due to the importance of the persistent stratocumulus cloud decks over the N.E. Pacific to global climate, aerosol characteristics in this region have received considerable attention.

However, the diverse range of particle sources, including shipping exhaust (Murphy et al., 2009; Coggon et al., 2012; Wonaschutz et al., 2013; Prabhakar et al., 2014), primary and secondary natural marine emissions (Sorooshian et al., 2009; Prabhakar et al., 2014; Modini et al., 2015), anthropogenic and biogenic continental emissions (Hegg et al., 2010; Moore et al., 2012; Coggon et al., 2014), wildfire plumes (Brioude et al., 2009; Mardi et al., 2018), and aged aerosol from the Asian continent (Roberts et al., 2006; 2010), combined with strong temporal and spatial variability due to variable meteorological conditions, has hindered determination of general characteristics of the marine atmosphere in this location. This complexity is reflected in the diversity of hygroscopicity measurements previously reported in the marine boundary layer (MBL) and free troposphere (FT). For instance, average κ values reported from MBL measurements have varied from ~0.2-0.3 (Roberts et al., 2010; Moore et al., 2012) to ~0.5-0.7 (Yakobi-Hancock et al., 2014; Royalty et al., 2017). Measurements in the FT, while sparse, have been even more variable (κ ~0.05-1.0) (Roberts et al., 2006; 2010). While these measurements could largely be reconciled assuming various mixtures of continental (0.27±0.2) and marine (0.72±0.2) aerosol, determining the major emissions sources and meteorological patterns dictating these changes is important for improving model representation of the region (Pringle et al., 2010). CCN-based measurements of aerosol hygroscopicity and the resulting information about small particle composition can be especially useful in this regard, as knowledge of small particle composition can provide substantial insight into particle sources.

While hygroscopicity and mixing state characterization are important components of understanding the CCN activity of ambient aerosol, the dynamic processes controlling supersaturation, droplet nucleation, and droplet growth within clouds lead to nonlinear relationships between aerosol properties and CDNC. As a result, aerosol-cloud parcel modeling is instrumental to fully understand the role of aerosol hygroscopicity and mixing state on CDNC. Reutter et al. (2009) used such a model to distinguish three regimes of aerosol activation, defined as the aerosol-limited, updraft-limited, and transitional regimes, based on the ratio of updraft velocity to aerosol number concentration at the cloud base. The dependence of CDNC on aerosol hygroscopicity, while limited relative to other

parameters such as particle number concentration and updraft velocity, was found to vary substantially between regimes. Additional modeling revealed that CDNC sensitivity to aerosol hygroscopicity is highly dependent on the below-cloud aerosol size distribution, with sensitivity increasing substantially with smaller median radii (Ward et al, 2010). Sanchez et al. (2016) concluded that modeled stratocumulus albedo is insensitive to the assumed hygroscopicity of the organic aerosol fraction; however, the sensitivity of CDNC to bulk hygroscopicity has yet to be fully evaluated in this environment.

The present study uses measurements of aerosol composition and CCN activity collected during the Marine Aerosol Cloud and Wildfire Study (MACAWS), combined with an aerosol-cloud parcel model, to gain insight into near-coastal aerosol hygroscopicity and its influence on prediction of CCN and MSc CDNC. Hygroscopicity measurements are combined with airmass backward trajectories and meteorological parameters to attribute observed particle characteristics to distinct sources when possible. CCN closure analyses are performed to investigate the impact of compositional and mixing state assumptions on CCN predictions. Finally, aerosol-cloud parcel model simulations constrained with MSc microphysical measurements are used to directly investigate the sensitivity of stratocumulus CDNC to aerosol hygroscopicity, mixing state, and size distribution properties.

4.2 Methodology

4.2.1 MACAWS Field Mission

The 2018 Marine Aerosol Cloud and Wildfire Study (MACAWS) consisted of 16 research flights operated out of the Center for Interdisciplinary Remotely-Piloted Aircraft Studies (CIRPAS) in Marina, California during June and July. Measurements were performed on-board the CIRPAS Navy Twin Otter aircraft (Russell et al., 2013; Coggon et al., 2012; 2014; Wang et al., 2016; Sorooshian et al., 2019). The scientific objectives of individual flights included characterization of marine aerosols and clouds, sampling of shipping vessel exhaust plumes, and investigation of nearby wildfire emissions. The present study focuses on 7 research flights primarily aimed at characterization of the

relationship between marine aerosol and the overlying stratocumulus cloud deck. Paths of these 7 flights are depicted in Figure 4.1. Flight strategies typically involved a series of level legs at varying altitudes within the MBL and overlying FT. Slant or spiral soundings were generally performed before and after a series of level legs.

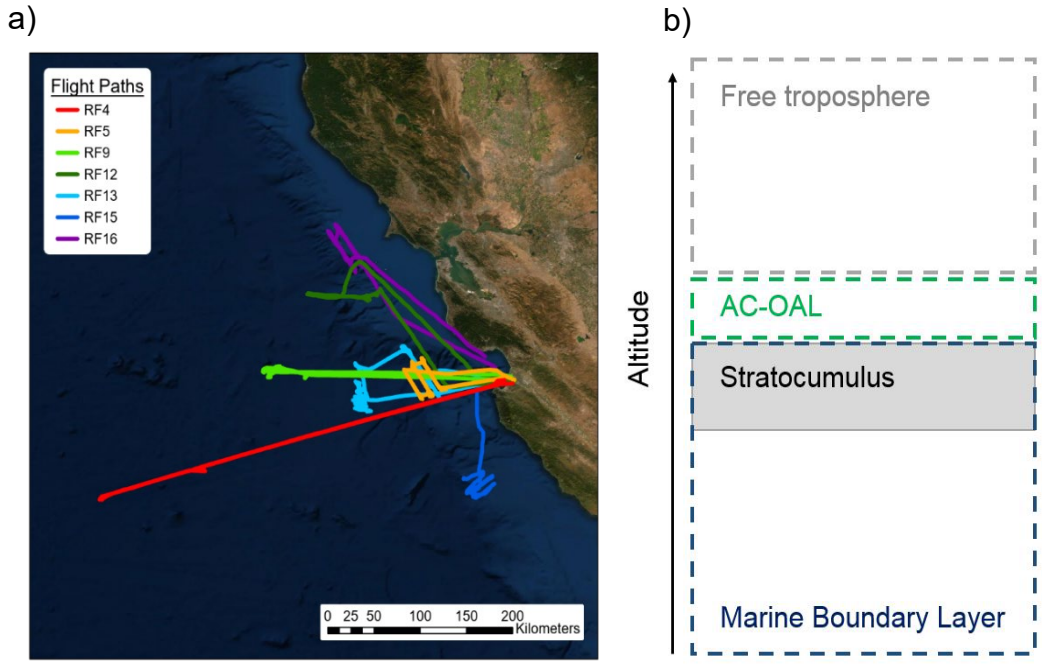

Figure 4.1: a) Trajectories of the 7 MACAWS research flights analyzed in this study. b) Relative vertical locations of the marine boundary layer, the above-cloud organic-aerosol layer, and the free troposphere.

4.2.2 Twin Otter Instrumentation

The navigational and meteorological instrumentation utilized by the Twin Otter aircraft is described in detail by Sorooshian et al. (2018). Ambient aerosol was sampled using a forward-facing sub-isokinetic inlet (Hegg et al., 2005). Aerosol and cloud droplet number concentrations were characterized using a variety of instruments, including multiple condensation particle counters (CPC, TSI 3010, D_p > 10 nm; ultrafine CPC, TSI UFCPC, D_p > 3 nm), a passive cavity aerosol spectrometer probe (PCASP, D_p ~0.11-3.4 µm), and forward scattering spectrometer probe (FSSP, Particle Measuring Systems (PMS), D_p ~1.6-45 µm). Cloud liquid water content was measured using a PVM-100A probe (Gerber et al.,

1994), and a threshold value of 0.02 g m^{-3} was used to distinguish in-cloud sampling (Dadashazar et al., 2018; MacDonald et al., 2018).

Cloud condensation nuclei (CCN) number concentrations were measured at 4 supersaturations (SS) (0.1%, 0.3%, 0.43%, 0.57%) using a Droplet Measurement Technologies (DMT) dual-column streamwise thermal-gradient cloud condensation nuclei counter (CCNC) (Roberts and Nenes, 2005; Lance et al., 2006). The CCNC operates by applying a linear temperature gradient to a cylindrical sampling tube with continuously wetted walls. As the thermal diffusivity of water vapor exceeds the diffusivity of air, supersaturated conditions are produced along the sampling column centerline. For this study, activated droplets grown to sizes larger than 0.75 μm diameter were counted and sized by an optical particle counter. The sheath and sample flows of each column were maintained at 0.45 and 0.05 L min^{-1}, respectively. Instrument pressure was maintained at 750 mb using a flow orifice and active pressure control system at the instrument inlet. Each column of the CCNC was calibrated using ammonium sulfate particles following standard methods as described in Rose et al. (2008). Calibrations were performed before and after the campaign, and observed deviations in applied SS for a given temperature gradient imply uncertainties of ~6%, similar to the 5% value typical of field campaigns, as reported by Rose et al. (2008).

Aerosol size distributions and number concentrations for D_p between ~15 and 800 nm were measured with a custom-built scanning mobility particle sizer (SMPS) consisting of a differential mobility analyzer (DMA, TSI 3081) coupled to a condensation particle counter (TSI 3010). The DMA is operated in a closed-system configuration with a recirculating sheath and excess flow of 2.67 L min^{-1} and an aerosol flow of 0.515 L min^{-1}. The column voltage was scanned from 15 to 9850 V over a ~2-min interval.

Aerosol chemical composition was measured using a high-resolution time-of-flight aerosol mass spectrometer (HR-ToF-AMS, Aerodyne Research Inc., hereafter referred to AMS) (DeCarlo et al., 2006). Incoming air enters the AMS through a 100 μm critical orifice, after which an aerodynamic lens produces a particle beam that is accelerated under high vacuum. The particle beam is flash-vaporized on a resistively heated surface (600°C),

and the resulting gases are ionized by electron impaction (70 eV). Individual ion identity is determined using a high-resolution time-of-flight mass spectrometer. Due to the limited amount of aerosol mass present over the MBL, data were collected in high-sensitivity V-mode. The ionization efficiency (IE) of the AMS was calibrated using dry, 350 nm ammonium nitrate particles before each flight. Data were averaged over 1 min intervals, and all data were analyzed using standard AMS software (SQUIRREL v1.57 and PIKA v1.16l) within Igor Pro 6.37. The collection efficiency (CE) was determined using the composition-dependent calculator within the SQUIRREL and PIKA software packages (Middlebrook et al., 2012). Elemental H:C and O:C ratios were calculated using the "Improved-Ambient" elemental analysis method for AMS mass spectra (Canagaratna et al., 2015). Positive matrix factorization (PMF) analysis (Paatero and Tapper, 1994) was performed on the high-resolution AMS mass spectra in order to distinguish major classes and transformation processes of measured OA. Three factors were extracted, two of which factors correspond to OA subtypes characteristic of the MBL and above-cloud organic aerosol layer (AC-OAL), respectively, and resemble low-volatility oxygenated organic aerosol (LV-OOA). The third factor, which was rarely observed, is likely a result of primary anthropogenic emissions and resembles hydrocarbon-like organic aerosol (HOA). Further discussion of PMF data preparation and factor interpretation is included in the Supplemental Information.

4.2.3 Determination of aerosol hygroscopicity

Aerosol hygroscopicity was calculated using two distinct methods based on measurements with the CCNC and AMS, respectively. Assuming a particle population is internally mixed, the critical activation diameter ($D_{p,c}$) (the diameter at which all larger particles will activate into cloud droplets) produced by a given SS can be determined by integrating the particle size distribution until the total CN concentration is equivalent to the measured CCN concentration:

$$N_{CCN} = \int_{D_{p,c}}^{\infty} n_{CN} dD_p \qquad \text{Eq. 1}$$

Knowledge of the critical diameter can then be used to calculate a single parameter representation of aerosol hygroscopicity from Köhler theory (Petters and Kreidenweis, 2007):

$$s = \frac{D_{wet}^3 - D_{p,c}^3}{D_{wet}^3 - D_{p,c}^3(1-\kappa_{CCN})} \exp\left(\frac{4\sigma M_w}{RT\rho_w D_{wet}}\right) \qquad \text{Eq. 2}$$

where s is the equilibrium supersaturation, $D_{p,c}$ is the critical activation diameter, D_{wet} is the droplet diameter, R is the universal gas constant, T is the absolute temperature, ρ_w is the molar density of water, M_w is the molecular weight of water, and σ is the surface tension of the droplet at the point of activation. Following Rose et al. (2010), κ was determined by applying the observed activation diameter and varying both D_{wet} and κ until s is equivalent to the applied supersaturation of the CCNC and the maximum of a Köhler curve of CCN activation. The droplet surface tension is assumed equal to that of water for comparison with other studies (Petters and Kreidenweis, 2007; Roberts et al., 2010; Yakobi-Hancock et al., 2014; Collins et al., 2013). Hygroscopicity values calculated using this method are referred to as "CCN-derived." Since the likelihood of particle activation at a given SS tends to be a stronger function of size than composition (Dusek et al., 2006), κ_{CCN} values correspond to particles with diameters near the calculated critical diameter.

A Monte Carlo approach was used to estimate the uncertainty in CCN-derived kappa values (Wang et al., 2019). A detailed description is provided in the Supplemental Information. For a given measurement of the aerosol size distribution and CCN number concentration, the distribution of possible κ_{CCN} values calculated by varying these input parameters (i.e., CCN number concentration and size distribution) within their respective uncertainties is lognormally distributed. As a result, uncertainties attributed to κ_{CCN} are not symmetric about the geometric mean values. In general, we estimate 1σ uncertainties of +55%/-40% for κ_{CCN} calculated at SS = 0.3%, ~+75%/-45% at SS = 0.43%, and +100%/-50% to values calculated at SS = 0.57%. Due to the low CCN number concentrations observed at SS = 0.1% (<100 cm^{-3}) and possibility of counting unactivated particles (expected to only be a few per cm^{-3}), κ_{CCN} at SS = 0.1% are not reported, as small absolute deviations in particle number concentration measured by the CCNC and DMA due to differential inlet losses could strongly influence the resulting κ_{CCN} estimates.

Hygroscopicity estimates can also be made using component volume fractions measured by the HR-ToF-AMS using the following equation (Petters and Kreidenweis, 2007):

$$\kappa_{AMS} = \sum_i^N \epsilon_i \kappa_i \qquad \text{Eq. 3}$$

where ϵ_i and κ_i represent the volume fraction and hygroscopicity of the ith NR-PM$_1$ component, respectively. While this calculation cannot capture the contribution of refractory components (sea salt, mineral dust, etc.), further analysis suggests their contribution is minor, as discussed in the Supplemental Information. Organic aerosol density was assumed to be 1.4 g cm^{-3} for volume fraction calculations given the remote nature of the environments sampled and the oxidized character of the measured organic aerosol (e.g., O:C ratios of MBL and AC-OAL PMF factors were 0.91 and 0.76 respectively) (Roberts et al., 2010; Hallquist et al., 2009). The hygroscopicity of individual inorganic components is calculated using:

$$\kappa_i = \left(\frac{M_w}{\rho_w}\right)\left(\frac{\rho_i}{M_i}\right) v_i \qquad \text{Eq. 4}$$

where M_w and ρ_w are the molar mass and density of water, respectively, and M_i, ρ_i, and v_i are the molar mass, density, and van't Hoff factor of the inorganic component. Inorganic aerosol was dominated by sulfate and ammonium. The relative abundances of ammonium sulfate, ammonium bisulfate, and sulfuric acid were calculated using the molar ratio of ammonium to sulfate (Nenes et al., 1998; Asa-Awuku et al., 2011). Ammonium sulfate and bisulfate were assigned van't Hoff factors of 2.5, while sulfuric acid was assigned κ = 0.9 to align with previous measurements (Petters and Kreidenweis et al., 2007). Modifying the van't Hoff factors of ammonium sulfate and ammonium bisulfate and assumed κ of sulfuric acid within reasonable limits had a negligible influence on the presented results. Chloride measured by the AMS was assumed to represent sodium chloride and was assigned a hygroscopicity of 1.28 (Petters and Kreidenweis, 2007). AMS-measured nitrate aerosol was assumed to be ammonium nitrate with a hygroscopicity of 0.67 (Petters and Kreidenweis, 2007). The hygroscopicity of the organic component (κ_{org}) was assumed to be either 0 (non-hygroscopic), 0.1 (slightly-hygroscopic), or a function OA composition using a parameterization based on bulk O:C ratios developed in the literature (Lambe et

al., 2011). Comparisons of κ_{CCN} and κ_{AMS} values, analysis of PMF factor composition, and evaluation of CCN-closure calculations are used to evaluate these different κ_{org} estimates.

An uncertainty analysis similar to that described for κ_{CCN} values was performed for κ_{AMS} values and is described in detail in the Supplemental Information. For median conditions in the MBL and FT, the relative uncertainty in κ_{AMS} is estimated to be ~10-20%, due primarily to uncertainty in the estimated hygroscopicity of the organic component (κ_{org}). In the AC-OAL, the dominant contribution of organic aerosol increases the relative uncertainty to ~50%; however, due to the low absolute κ_{AMS} values observed in the AC-OAL, the absolute uncertainty is only ~0.1 or less.

4.3 Aerosol-cloud parcel model

The aerosol-cloud parcel model used in this study employs a user-specified updraft velocity to induce adiabatic cooling of an air parcel, leading to water vapor supersaturation. The predicted parcel supersaturation at each time step is determined by the relative rates of production through adiabatic cooling and loss through condensation of water vapor onto activated cloud droplets (Pruppacher and Klett, 1997; Seinfeld and Pandis, 2016). In the present study, meteorological parameters such as ambient pressure, temperature, and lapse rate are obtained from MACAWS aircraft measurements and are specified before model execution. The below-cloud dry size distribution is assumed to contain Aitken and accumulation modes, the characteristics of which (i.e., number concentration, geometric mean diameter, hygroscopicity) are set by the user. Particles within each mode can be specified as either internally or externally mixed. Each compositional class, 1 per size mode if internally mixed or 2 per size mode if externally mixed, contains 300 lognormally spaced bins ranging from 1 nm to 3 μm. Droplet activation is assumed to occur when the ambient supersaturation of the parcel exceeds the critical supersaturation of the particles in a given size bin, as determined from κ-Kohler theory (Petters and Kreidenweis, 2007). Following activation, the growth of individual cloud droplet bins due to water vapor diffusion is explicitly represented. Additional physical processes such as droplet coagulation,

coalescence, and deposition are not included, as previous parcel model studies have demonstrated that these processes have little influence on model predictions for typical marine stratocumulus conditions (Sanchez et al., 2016). Model execution proceeds until a user-specified liquid water content (0.4 g m^{-3} in this study) has been reached. Activated particle size bins larger than 1 μm are considered cloud droplets; however, using an alternative size threshold of 2 μm or 0.75 μm has a negligible influence on the results.

4.4 Air mass backward trajectories

Air mass backward trajectories (120 hr) were calculated in the MBL for each flight using the NOAA HYSPLIT v4.2 model with the global data assimilation system (GDAS) 1° x 1° meteorological dataset (Draxler and Hess, 1997; 1998; Stein et al., 2015). The higher spatial resolution EDAS 40 km x 40 km meteorological dataset was not used due to its limited spatial range over the Pacific Ocean. The ending altitude of each trajectory was the approximate midpoint of the MBL during each flight.

4.3. Results and Discussion

4.3.1 Aerosol characteristics over the N. E. Pacific

Results from the seven flights analyzed in this study are summarized in Figure 4.2 and Tables 4.1-4.3. In the subsequent analyses, "all flights" refers to these seven. Typical flight patterns included sampling within the MBL, FT, and when present, the above-cloud organic aerosol layer (AC-OAL). The AC-OAL is operationally defined as the narrow altitude band (generally <200 m) directly above the marine stratocumulus cloud decks where OA mass loadings were relatively large (>1.5 μg m^{-3}) and a distinct AC-OAL PMF factor contributed >80% of total OA mass (Figure 4.S6). This region occupies a similar location as the commonly referenced entrainment interface layer (EIL) above cloud decks (Wood et al., 2012; Dadashazar et al., 2018), but is defined by the aerosol characteristics described above rather than by turbulence and buoyancy characteristics, as is common for the EIL (Carman et al., 2012). Median aerosol properties are reported in Tables 4.1-4.3 for

each of these three regions, while Figure 4.2 displays vertical profiles of aerosol and meteorological properties.

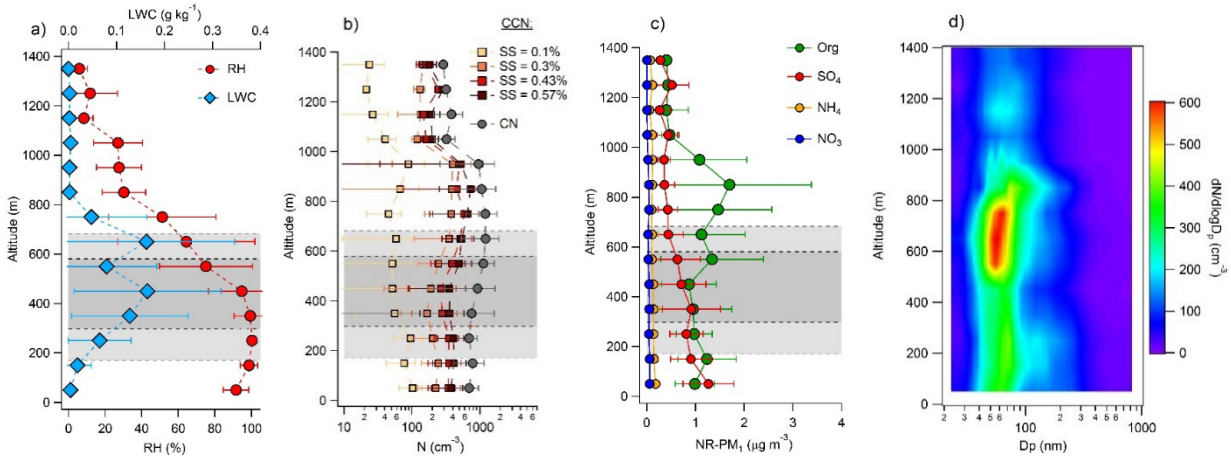

Figure 4.2: Average vertical profiles of (a) RH and LWC, (b) CCN and CN concentrations, and (c) non-refractory (NR) PM_1 component mass loadings for the seven RFs in Figure 4.1. (d) Vertical contour plot of median size distributions measured during the 7 RFs. Horizontal bars represent measurement standard deviations. The dark grey region in panels a-c represents the average stratocumulus cloud depth (avg. cloud top height ≈ 570 m; avg. cloud bottom height ≈ 300 m). The lighter grey region represents the standard deviation of cloud top and bottom heights (e.g., avg. cloud top + cloud top height S.D. ≈ 680 m).

Distinct differences in particle properties were observed within each vertical region. Median aerosol number concentrations observed in the MBL (754 cm^{-3}) exceeded those in the FT (333 cm^{-3}), as expected. Observed particle concentrations were maximized within the AC-OAL (1662 cm^{-3}), where intense actinic fluxes and elevated concentrations of the hydroxyl radical may drive new particle formation (Mauldin et al., 1999; Dadashazar et al., 2018). For all measured SS > 0.1%, observed CCN concentrations were also largest within the AC-OAL, rather than the MBL or FT, underscoring the importance of understanding the hygroscopicity of above-cloud CCN-active particles (Sorooshian et al., 2007a,b; Wang et al., 2008; Coggon et al., 2014).

Table 4.1: Median aerosol number and cloud condensation nuclei (CCN) concentrations measured in the marine boundary layer (MBL), above-cloud organic aerosol layer (AC-OAL), and free troposphere (FT). Values in parenthesis represent the interquartile range. CCN concentrations are provided as a function of the instrument supersaturation (%).

Location	CN (cm^{-3})	CCN: 0.1% (cm^{-3})	CCN: 0.3% (cm^{-3})	CCN: 0.43% (cm^{-3})	CCN: 0.57% (cm^{-3})
MBL	754 (509-978)	75 (33-106)	194 (146-285)	302 (187-410)	410 (229-522)
AC-OAL	1662 (1303-1959)	58 (41-84)	363 (260-537)	574 (403-876)	781 (539-1051)
FT	333 (296-555)	21 (14-35)	115 (89-145)	144 (102-194)	162 (118-240)

Observed aerosol composition in the MBL was relatively evenly divided between organic aerosol (OA) (43%) and sulfate (SO_4) (48%), with a minor contribution from ammonium (NH_4) (~10%) and negligible nitrate (NO_3) (≤1%). Prabhakar et al. (2014) have demonstrated that nitrate is preferentially distributed in super-micron particles in this marine environment, in agreement with the minor contribution observed with the AMS in this study. Using the "clean" versus "perturbed" threshold introduced by Coggon et al. (2012) for this region (where "clean" is defined by aerosol mass concentrations <1 $\mu g\ m^{-3}$), average MBL conditions were "perturbed" by shipping vessel emissions or other anthropogenic sources such as continental outflow. A distinct, highly oxidized MBL PMF factor was extracted from the dataset (Figure 4.S6). The oxidized nature of the MBL factor (O:C = 0.91) precludes the use of marker ions to distinguish individual sources; however, potential sources include shipping and biogenic emissions, as well as oxidized continental outflow aerosol (Sorooshian et al., 2009; Hegg et al., 2010; Coggon et al., 2012). In the AC-OAL, observed aerosol composition was dominated by organics (80%), as has been previously reported (Sorooshian et al., 2007a,b; Wang et al., 2008; Hersey et al., 2009; Coggon et al., 2014). A second, distinct factor displayed large mass loadings (up to 8 $\mu g\ m^{-3}$) within the AC-OAL (Figure 4.S6) (O:C = 0.76), and the mass ratio of the AC-OAL to the MBL PMF factor is used as a tracer of AC-OAL entrainment into the MBL, as discussed in section 3.3.2. Possible aerosol production mechanisms in the AC-OAL include oxidation and transport of biogenic volatile organic compounds emitted by forested regions

in the Northwest U.S., cloud droplet evaporation, and oxidation of sparingly soluble organics vented through the stratocumulus layer (Heald et al., 2005; Sorooshian et al., 2007a; Coggon et al., 2014). While large eddy simulations (LES) have demonstrated that the altitude of the top of the stratocumulus cloud deck can undergo diurnal variations of 10-100 m, providing a potential mechanism for AC-OAL aerosol production through droplet evaporation (Sorooshian et al., 2007a; Chen et al., 2011), the substantially larger mass fraction of organic aerosol in the AC-OAL than the MBL suggests that particle production is primarily a result of continental biogenic sources (Coggon et al., 2014). Observed aerosol mass loadings in the FT were the lowest sampled (1.5 μg m^{-3}) but agree well with previous aircraft measurements by Wang et al. (2008) off the coast of Pt. Reyes, CA at a similar time of year (June-July).

Table 4.2: Median mass loadings of total non-refractory PM1 (NR-PM_1), and organic (Org.), sulfate (SO_4), ammonium (NH_4), and nitrate (NO_3) aerosol components in the marine boundary layer (MBL), above-cloud organic aerosol layer (AC-OAL), and free troposphere (FT). Values in parenthesis represent the interquartile range.

Location	NR-PM_1 (μg m^{-3})	Org. (μg m^{-3})	SO_4 (μg m^{-3})	NH_4 (μg m^{-3})	NO_3 (μg m^{-3})
MBL	2.8 (2.3-2.5)	1.1 (0.8-1.4)	1.5 (0.9-2.0)	0.2 (0.2-0.3)	0.0 (0.0-0.1)
AC-OAL	5.5 (4.5-7.5)	4.4 (3.2-6.1)	0.7 (0.6-1.1)	0.2 (0.2-0.3)	0.1 (0.0-0.1)
FT	1.5 (1.2-2.1)	0.7 (0.5-1.0)	0.6 (0.4-0.7)	0.1 (0.1-0.2)	0.0 (0.0-0.0)

4.3.2 Overview of observed aerosol hygroscopicity

Figure 4.3 displays median aerosol number size distributions, κ_{AMS}, and κ_{CCN} values observed within the MBL, AC-OAL, and FT during each flight. For these comparisons, κ_{AMS} values are calculated assuming $\kappa_{org} = 0.1$, as is typical for non-urban regions (Moore et al., 2011; 2012; Mei et al., 2013). However, we note that using the parameterization developed by Lambe et al. (2011), the calculated κ_{org} values for the MBL and AC-OAL PMF factors are 0.19 and 0.17 respectively, due to their highly oxidized nature (Figure 4.S6), suggesting the true κ_{org} values for large particles may be greater than 0.1.

Table 4.3: Median values of the AMS-derived (κ_{AMS}) and CCN-derived (κ_{CCN}) hygroscopicity factor measured in the marine boundary layer (MBL), above-cloud organic aerosol layer (AC-OAL), and free troposphere (FT). Values in parenthesis represent the interquartile range. κ_{CCN} are provided as a function of the instrument supersaturation (%).

Location	κ_{AMS}	κ_{CCN}: 0.3%	κ_{CCN}: 0.43%	κ_{CCN}: 0.57%
MBL	0.45 (0.35-0.52)	0.39 (0.20-0.61)	0.35 (0.24-0.50)	0.40 (0.27-0.54)
AC-OAL	0.19 (0.17-0.25)	0.13 (0.08-0.20)	0.19 (0.14-0.25)	0.17 (0.12-0.27)
FT	0.37 (0.30-0.43)	0.32 (0.18-0.65)	0.50 (0.29-0.88)	0.37 (0.21-0.72)

Within the MBL, observed hygroscopicity values appear to cluster into three relatively distinct groups that span the range of values previously observed in this environment (Roberts et al., 2010; Yakobi-Hancock et al., 2014; Royalty et al., 2017). The strong temporal variation observed in both particle number size distributions and hygroscopicities underscores the complexity involved in accurately modeling CCN in coastal environments influenced by continental and marine sources. This is further demonstrated in Table 4.3, which depicts estimated organic and inorganic volume fractions of Aitken mode particles derived from MBL κ_{CCN} values. Assuming inorganic aerosol is entirely ammonium sulfate for these calculations, estimated organic fractions vary from effectively zero, as median κ_{CCN} during RF13 are larger than that of ammonium sulfate ($\kappa = 0.61$) to as high as 84%. The low hygroscopicities and subsequently large estimated organic fractions observed during flights RF9 and RF15 are uncharacteristic of remote marine environments and imply a continental influence on particle characteristics. κ_{AMS} values calculated during these flights are ~50-100% larger than κ_{CCN} values, implying addition of particle mass during growth that is more hygroscopic than the Aitken mode particles. While the difference between κ_{AMS} and κ_{CCN} values during these flights are nearly within the uncertainty range of the κ_{CCN} calculation, these observations align with those in many continental locations, where addition of inorganic mass to organic rich Aitken mode particles growth is thought to lead to a positive relationship between particle hygroscopicity and size (Ervens et al., 2010; Rose et al., 2011; Moore et al., 2012; Levin et al., 2014; Kawana et al., 2016). On

the other hand, κ_{AMS} and κ_{CCN} are quite similar during the other five flights, with relative deviations on the order of ~25% or less, which is well within the uncertainty of the κ_{CCN} measurements. A compilation of data reported by Royalty et al. (2017) suggests that minor variation of particle hygroscopicity with size is a common feature of remote marine aerosol, which generally exhibits elevated Aitken mode hygroscopicity. Four individual flights (RF4, RF5, RF13, and RF15) provide specific insight into the combined roles of aerosol sources and meteorological processes in determining aerosol hygroscopicity in the MBL, and these are discussed in further detail in section 3.2.2.

Within the AC-OAL, observed aerosol hygroscopicity is remarkably similar from flight-to-flight, and little difference is observed between κ_{CCN} and κ_{AMS} values. The combination of reduced hygroscopicity (i.e., κ ~0.2) and little variation with particle size suggests that within the AC-OAL, Aitken mode particles are organic-rich and grow through condensation of additional organic vapors, rather than addition of inorganic mass. Even under the assumption that the organic species in Aitken mode AC-OAL particles are entirely insoluble, total particle volume must be at least 66% organic to produce a hygroscopicity of 0.2 (assuming ammonium sulfate as the inorganic component). Chamber studies of monoterpene aerosol often observe κ_{org} of ~0.1-0.15 for Aitken mode particles (Alfarra et al., 2013; Zhao et al., 2015), which increases the estimated organic volume fraction to 80-89%. While the peak in the AC-OAL size distribution varies considerably between flights, the presence of a dominant Aitken mode in three out of four observations suggests particle formation may have occurred recently.

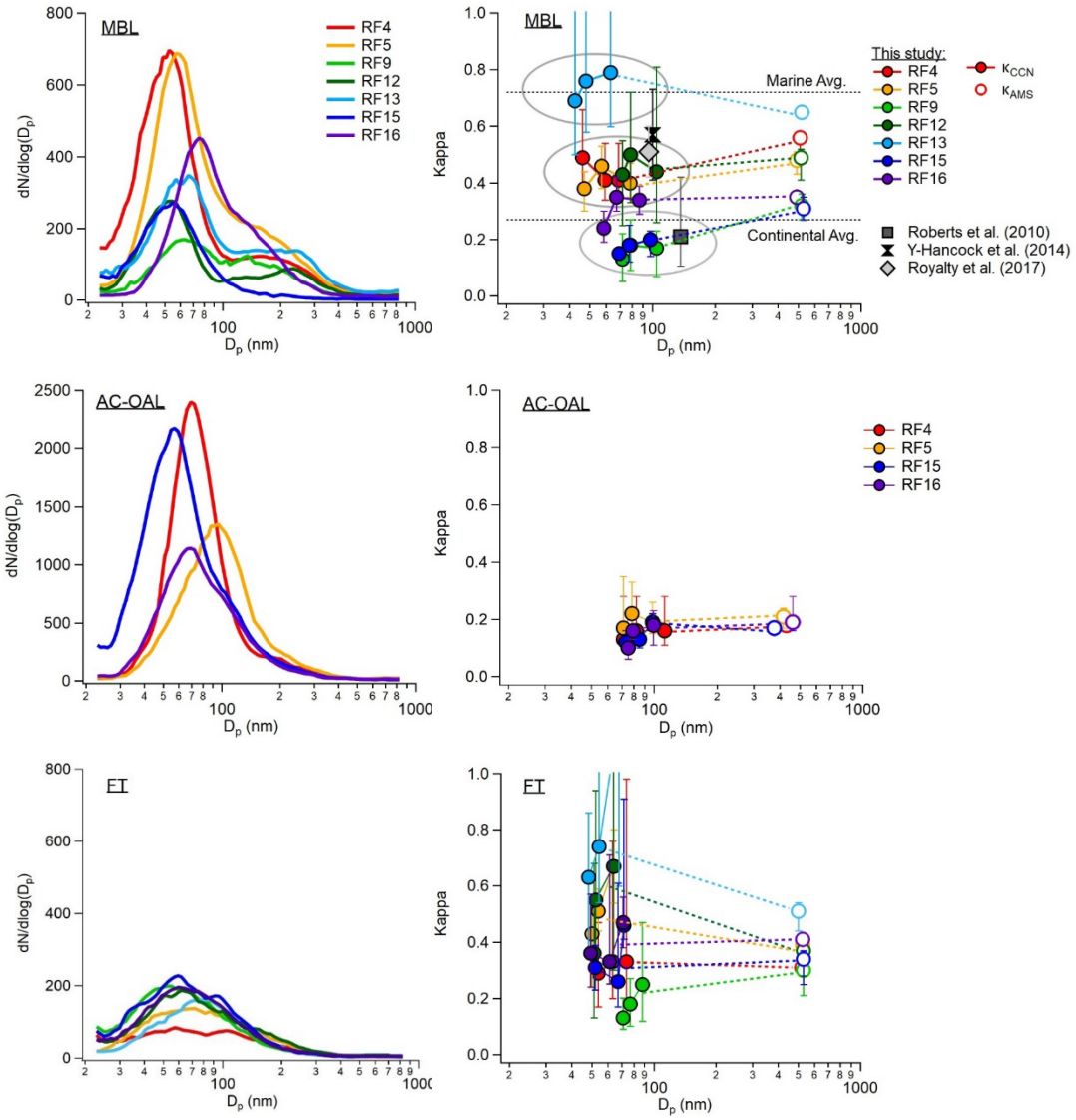

Figure 4.3: Median aerosol size distributions (a-c) and hygroscopicities (κ_{CCN} and κ_{AMS}) (d-f) measured in the marine boundary layer (MBL), above-cloud organic aerosol layer (AC-OAL), and free troposphere (FT), during each flight. Vertical bars represent the interquartile range of hygroscopicity measurements. Previously observed values in the MBL are included for reference in d), as are typical values for continental and marine environments from Andreae and Rosenfeld (2008).

Coggon et al. (2014) first demonstrated that expansive dry air masses originating over the Northwestern U.S. loft biogenic organic aerosol over the MBL and act as the main particle source to the AC-OAL. Our measurements support this conclusion, however an additional contribution from organic gases vented through the stratocumulus layer cannot

be ruled out. Comparing AC-OAL and MBL Aitken mode hygroscopicity suggests cloud droplet evaporation is at most a minor particle source to the AC-OAL, as during three of the four flights in which the AC-OAL was sampled, average MBL Aitken mode particles were substantially more hygroscopic than those in the AC-OAL (κ_{MBL} ~0.4; $\kappa_{AC\text{-}OAL}$ ~0.2). As the most hygroscopic particles in an air mass are likely to activate into cloud droplets, and as addition of inorganic mass is common during cloud processing in marine environments (Faloona et al., 2009; Seinfeld and Pandis, 2016), it is unlikely that residual aerosol formed from evaporated cloud droplets would be less hygroscopic than the MBL aerosol population. Observations during RF15, discussed further in Section 3.2.2., suggest entrainment during precipitation events can lead to a major AC-OAL signature in the MBL, directly demonstrating the importance of understanding the source of these particles.

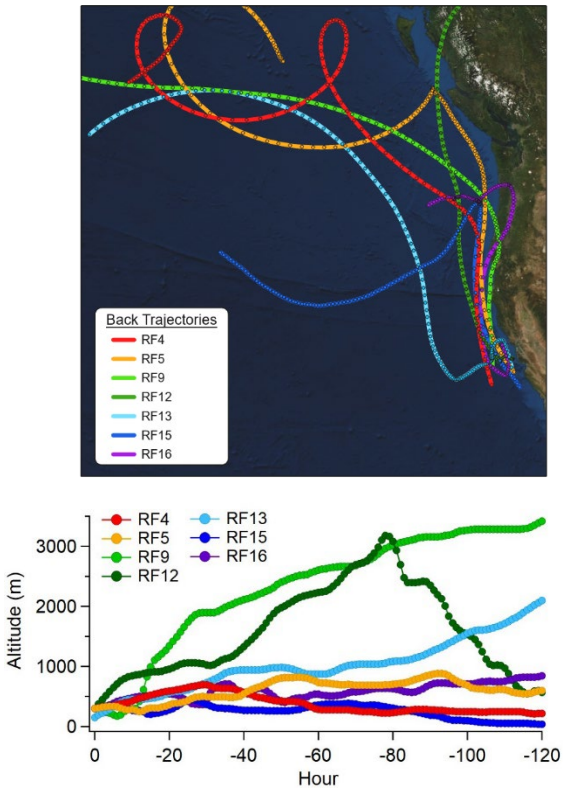

Figure 4.4: (Top) 120-hour backward trajectories calculated from the approximate midpoint of each flight path at an altitude representative of the marine boundary layer. For six of the seven flights, the starting altitude was 300 m, while the starting altitude for the RF13 trajectory was 150 m due to the shallow height of the boundary layer. (Bottom) Airmass altitude during the 120-hour transit to the measurement site.

Due to the low aerosol number concentrations in the FT, observed κ_{CCN} values vary widely between flights and exhibit large variability within individual flights. As a result, we hesitate to draw definitive conclusions based on these data. Other than RF13, average κ_{AMS} values from each flight are near or below 0.4, implying a substantial organic contribution to free tropospheric aerosol. In the absence of continental influence, observation of aerosols of such low hygroscopicity is unexpected, given that particle formation in the upper FT over tropical oceans is driven primarily by sulfuric acid nucleation and growth (Clarke, 1993; Clarke et al., 1998; 1999; 2013). Long range transport of organic aerosol layers from the Asian continent have been noted previously (Roberts et al., 2006; 2010), but estimates of aerosol hygroscopicity in such layers have varied dramatically. For instance, during the CIFEX experiments (Roberts et al., 2006), average κ attributed to aged aerosol layers were only ~0.04, whereas our measurements suggest a more moderate value of ~0.4, while observations by Roberts et al. (2010) indicated a value of 0.93 was more appropriate. While the substantial difference in particle concentrations in the MBL and FT observed during this campaign suggests FT aerosol plays a minor role in dictating MBL CCN activity on average, in remote marine environments entrainment from the FT is the dominant source of MBL particles (Raes et al., 1995; Clarke, 1993; Clarke et al., 1996; 1998; 2013), and as such further research into the variability of FT aerosol composition is warranted.

4.3.3 Observation of distinct influences on MBL particle characteristics

Observations shown in Figure 4.3 indicate highly variable flight-averaged hygroscopicities in the MBL, suggesting that temporal variations in regional meteorology and/or particle source strengths can strongly influence CCN characteristics in this environment. Further analysis suggests that in four of the seven flights discussed in this study, specific meteorological patterns and emissions sources influencing particle characteristics can be identified. We discuss these observations to provide insight into the level of physicochemical detail (both in terms of emissions and atmospheric dynamics) required for atmospheric models to simulate MBL CCN concentrations with high fidelity.

Table 4.4: Calculated Aitken mode organic (f_{org}) and inorganic (f_{inorg}) volume fractions based on median κ_{CCN} values derived from CCN measurements at SS = 0.43% for MBL measurements during each flight. Values of f_{org} and f_{inorg} are calculated assuming the inorganic aerosol component is either ammonium sulfate ($(NH_4)_2SO_4$) or sulfuric acid (H_2SO_4). Note that the hygroscopicity measured during RF13 cannot be reproduced assuming the inorganic component is entirely

Flight	κ_{CCN} – SS = 0.43%	Inorg. = $(NH_4)_2SO_4$		Inorg. = H_2SO_4	
		f_{org}	f_{inorg}	f_{org}	f_{inorg}
RF4	0.41	0.39	0.61	0.61	0.39
RF5	0.46	0.29	0.71	0.55	0.45
RF9	0.18	0.84	0.16	0.90	0.10
RF12	0.50	0.22	0.78	0.50	0.50
RF13	0.76	~	~	0.18	0.82
RF15	0.18	0.84	0.16	0.90	0.10
RF16	0.28	0.65	0.35	0.78	0.22

4.3.3.1 Shipping emissions

Aerosol properties measured during RF4 and RF5 suggest a prominent influence of regional shipping emissions on particle characteristics and hygroscopicity in this environment. During these flights, the dominance of an Aitken mode near ~50-60 nm with much larger concentrations than in the FT suggests relatively recent formation from an MBL-based particle source. While such size distributions could hypothetically result from continental outflow (Moore et al., 2012), air mass backward trajectories remained over the ocean and near or within the MBL (<1000 m) for the previous five days (Figure 4.4). Furthermore, trajectories transited primarily within the major shipping corridor along the coast, as observed for flights "perturbed" by shipping vessel emissions by Coggon et al. (2012), rather than recently arriving from the remote ocean (e.g., RF13). Downward mixing of AC-OAL particles is also ruled out as an Aitken mode particle source during these flights due to the distinctly different hygroscopicities observed in the MBL and AC-OAL (Figure 4.3). Finally, average wind speeds within the MBL were ~12 m s^{-1} and ~9 m s^{-1} during RF4 and RF5 respectively. Modini et al. (2015) previously noted that primary sea spray

emissions produced particle concentrations of only 12 cm^{-3} during periods with similar windspeeds (12 m s^{-1}) in the same marine environment (equivalent to ~2% of particle number concentrations in the MBL during RF4 and RF5).

Shipping emissions have been previously noted as major contributors to aerosol and cloud properties in the N.E. Pacific environment (Murphy et al., 2009; Lack et al., 2011; Coggon et al., 2012; Cappa et al., 2014). Coggon et al. (2012) demonstrated that 70% of cloud residual particles measured in the California shipping lanes were impacted by nearby shipping emissions. Available compositional data further suggests that shipping emissions could be expected to produce Aitken mode hygroscopicities observed during RF4 and RF5. For instance, Lack et al. (2011) observed an effective kappa parameter of 0.68-0.73 from exhaust produced by a large (96,500 ton) container vessel, while the smaller Research Vessel Atlantis sampled during the same study produced a value of ~0.2. Hygroscopic growth factor measurements of shipping exhaust emitted by another large (90,000 ton) container vessel by Murphy et al. (2009) suggest an effective $\kappa = 0.1\text{-}0.5$.

Direct measurements of a large container vessel exhaust plume during RF7 provide further support for the attribution of aerosol characteristics to shipping emissions in RF4 and RF5. As shown in Figure 4.5, the strong Aitken mode peak in the size distribution measured directly within the plume aligns well with those measured in RF4 and RF5, while the total magnitude of the flight-median size distributions agree well with those measured in the diluted plume more than 20 km downwind. As the plume was relatively narrow directly behind the ship, κ_{CCN} values are not available, but κ_{AMS} measurements agree well with those in RF4 and RF5 (Figure 4.5c). However, given the variability in the measured κ values of particulate shipping exhaust just discussed, this agreement cannot be viewed as definitive. Ultimately, while the insights provided by the size distributions, backward trajectories, and κ_{AMS} values would not be definitive on their own, taken together they support a shipping emission signature on aerosol characteristics during these flights. This influence highlights the importance of accurate physicochemical representation of shipping vessel emissions within the California coastal zone. As an example, the implementation of recent regulations on the sulfur content of shipping fuel within coastal waters of the U.S. (up to 200 miles off the coast) should increase the organic:inorganic ratio of particulate

shipping emissions in major shipping lanes over time (Lack et al., 2011; Cappa et al., 2014). Assuming, as a strictly upper limit estimate, that all Aitken mode particles observed during RF4 and RF5 are derived from shipping vessel emissions, changing the assumed hygroscopicity of these emissions from the value observed during ambient measurements in this study (~0.4-0.5) to a value of 0.1 (purely organic, partially hygroscopic), would change the CCN concentration at SS = 0.3% by 15-36%.

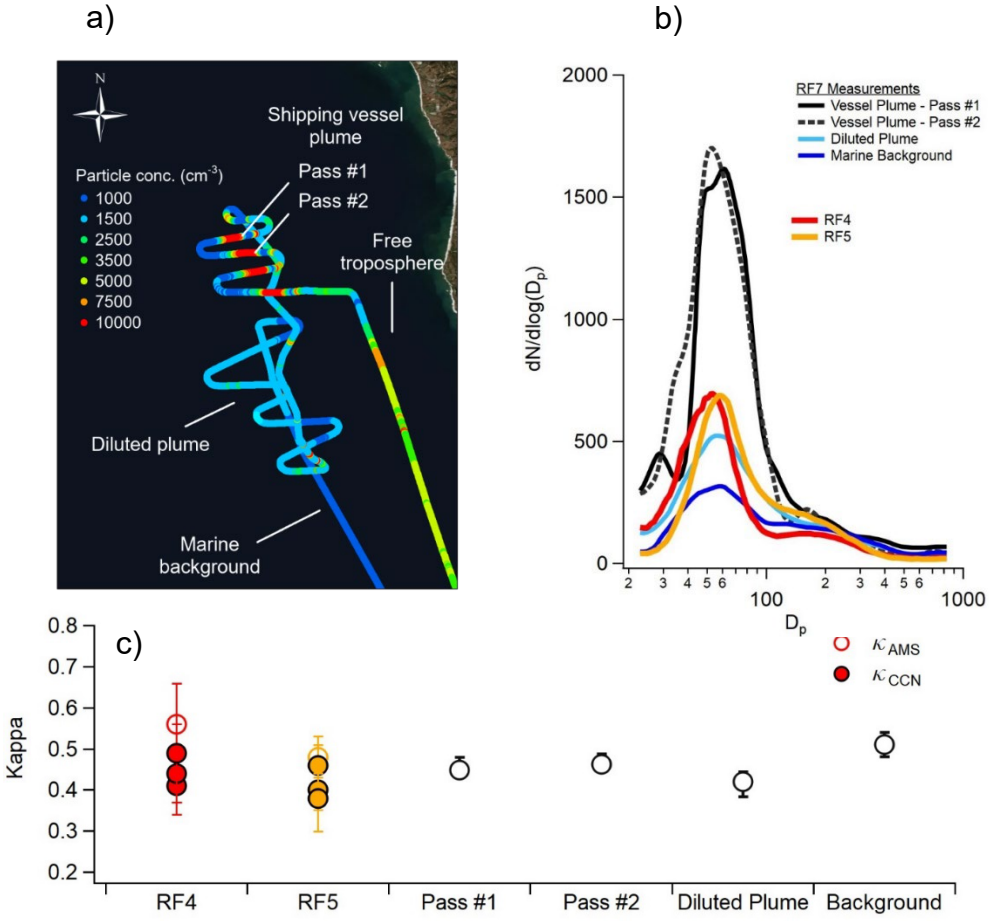

Figure 4.5: (a) Map of the Twin Otter trajectory during repeated sampling of a shipping vessel plume during RF7. Points are colored by the particle concentration measured by the CPC and individual segments of the flight path are labeled. (b) Aerosol size distributions measured during the labeled segments in (a) compared to median distributions measured during RF4 and RF5.

4.3.3.2 Entrainment from the AC-OAL

The observation of a single, dominant Aitken mode with reduced hygroscopicity during RF15 suggests an influence of the AC-OAL on MBL particle properties. According to Figure 4.4, the air mass sampled during RF15 had not recently transited over the continent or within the FT, which has previously shown to occasionally contain distinct layers of reduced hygroscopicity aerosol (Roberts et al., 2006; 2010). Clear evidence of entrainment from the AC-OAL is provided in Figure 4.6, which contrasts size distributions and κ_{AMS} values observed during RF15 and RF4, another flight with a prominent Aitken particle mode and relatively similar backward trajectory. During RF15, the MBL and AC-OAL size distributions are remarkably similar, exhibiting peak diameters at ~55 nm and lacking a larger accumulation mode. Liquid water contents measured within the MBL during RF15 demonstrate a fully developed stratocumulus layer encompassing roughly half of the MBL. κ_{AMS} values vary linearly with altitude from ~0.4 near the ocean surface to ~0.15-0.2 at the top of the cloud layer, aligning with the hypothesis of downward mixing of AC-OAL particles into the MBL. These observations are in stark contrast to those from RF4, where the Aitken mode diameter of the MBL and AC-OAL aerosol differ by ~20-25 nm, and importantly, the Aitken mode diameter in the MBL is smaller than the AC-OAL, suggesting a distinct particle source in each location. Finally, as the AC-OAL and MBL PMF factors are clearly distinguished in each flight where the AC-OAL layer was observed, the AC-OAL:MBL PMF factor mass ratio acts as a tracer for entrainment mixing. During RF15, the median AC-OAL:MBL PMF factor mass ratio was 0.81 in the MBL, in contrast to a value of 0.36 measured during RF4 and a median value of 0.42 in all flights other than RF15 where the AC-OAL was observed. The information obtained from the aerosol size distribution (no accumulation mode) and hygroscopicity (similar to the AC-OAL) in the MBL suggests that the distinct AC-OAL signature may result from entrainment following precipitation scavenging of the preexisting MBL aerosol. As typical AC-OAL particle concentrations are ~5 times as large as those in the overlying FT, failure to simulate this layer will result in underprediction of MBL particle concentrations during such distinct precipitation/entrainment events.

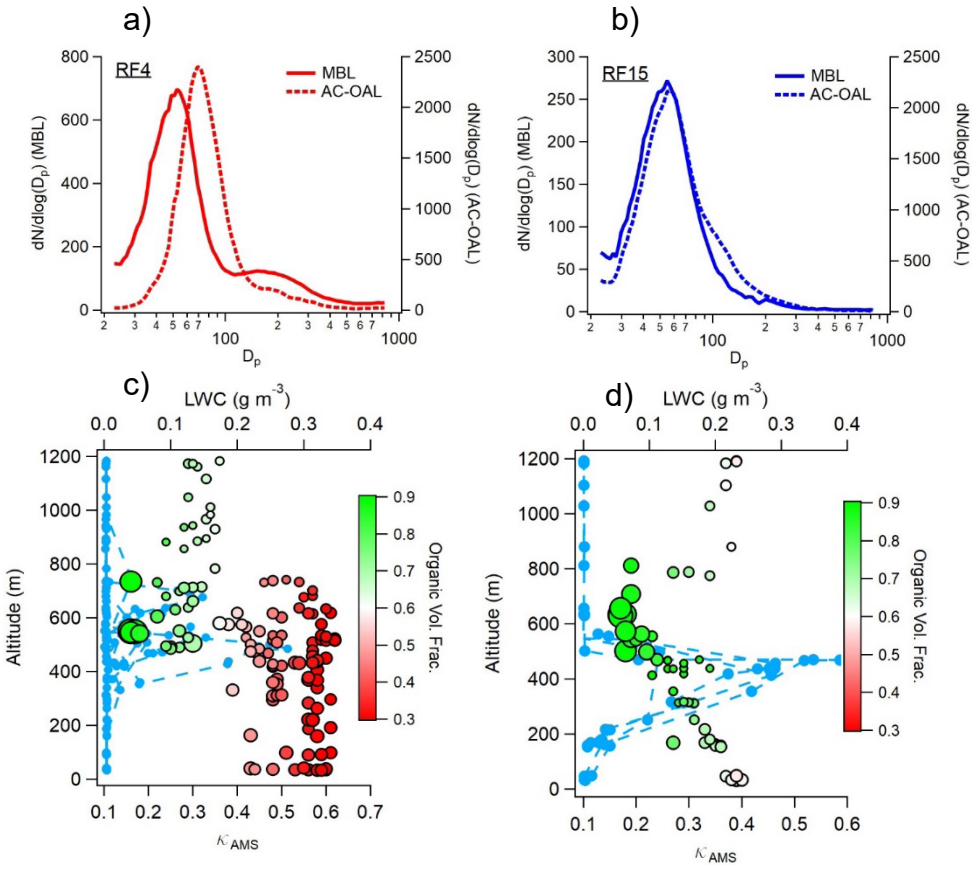

Figure 4.6: (Top) Median aerosol size distributions measured in the marine boundary layer (MBL) and above-cloud organic aerosol layer (AC-OAL) during RF4 (a) and RF15 (c). (Bottom) Vertical profile of AMS-derived hygroscopicity (κ_{AMS}) and liquid water content (LWC) during each flight. Values of κ_{AMS} are colored by the organic volume fraction measured by the AMS to aid interpretation of the figure.

4.3.3.3 Transport from the remote Pacific Ocean

Hygroscopicity measurements made during RF13 are notably larger than those from the other six flights, indicating a lack of organic aerosol across the particle size distribution. As expected, back trajectories calculated within the MBL during this flight indicate recent arrival from the remote Pacific Ocean, rather than extended transport through the major shipping lanes along the coast. The boundary layer was substantially compressed (<300 m) and cloud-free during the flight, suggesting ongoing subsidence of free tropospheric air masses (Fig. 7a). As new particle formation through sulfuric acid nucleation is known to be a notable source of CCN throughout the marine boundary layer (Clarke, 1993; Clarke

et al., 1998; 2013), downwelling and entrainment of such nucleated particles is a possible explanation for the elevated Aitken mode hygroscopicities observed. While low number concentrations in the FT make κ_{CCN} estimates less reliable, the values observed in RF13 are relatively similar to those in the MBL, supporting entrainment. While aerosol size distribution measurements in the FT suggest such entrainment was not responsible for increases in Aitken mode particles locally, as concentrations directly above the MBL are substantially lower than those in the MBL, the elevated aerosol concentrations at ~1000 m suggest entrainment may have produced MBL Aitken mode particles during transport (Figure 4.7b). Furthermore, the vertical profile of the aerosol size distribution in the FT is consistent with past observations of growth of nucleation-produced Aitken mode particles during large scale subsidence (Clarke et al., 1999).

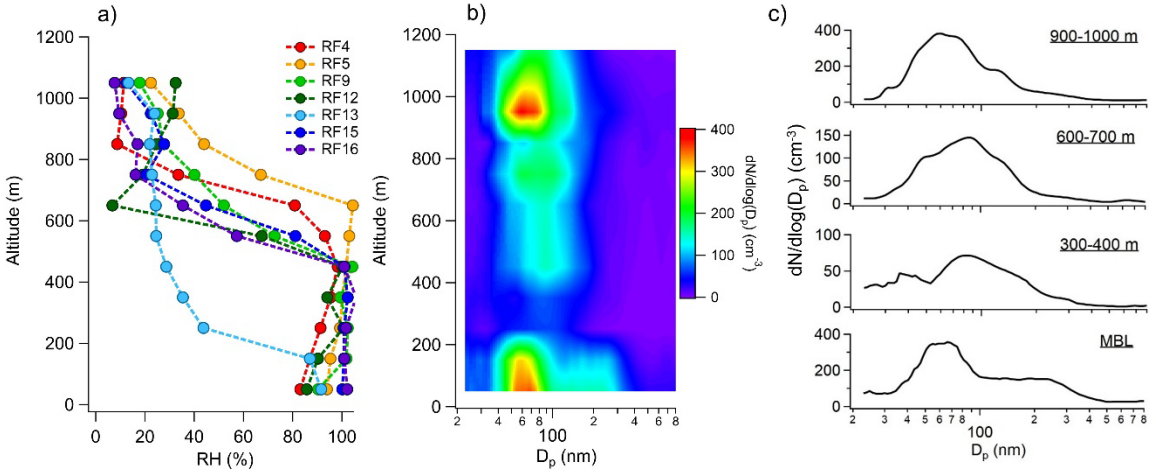

Figure 4.7: (a) Measured relative humidity vertical profile during each flight, demonstrating the reduced marine boundary layer (MBL) height during RF13. (b) Vertical profile of aerosol number size distributions during RF13. (c) Individual aerosol size distributions at different altitudes during

Due to the compressed height of the MBL during RF13, the potential contribution of primary sea spray aerosol to MBL particle characteristics is also enhanced. However, using the size distribution fitting technique established by Modini et al. (2015), the calculated concentration of primary sea spray aerosol is only 18 cm^{-3} or ~4% of the average MBL particle concentration during the flight, suggesting sea spray provides at most a minor contribution.

4.3.4 CCN closure analysis

Figure 4.8 shows CCN closure results for the three sampled environments using six different assumptions regarding aerosol composition and mixing state. Three cases assume internally mixed aerosol components with composition determined by AMS measurements. These cases are differentiated by their assumptions regarding organic aerosol hygroscopicity, with κ_{org} increasing from 0 (first-case), to 0.1 (second-case), and finally to values predicted from time-varying measured OA O:C ratios according to the relationship developed by Lambe et al. (2011) (third-case). The final three cases are similar to the internally mixed cases in their treatment of κ_{org}, however, the organic and inorganic aerosol components are assumed to be externally mixed. Bulk aerosol mass loadings were too low to obtain robust estimates of size-resolved composition, precluding more detailed treatment of composition in CCN closure calculations. Closure was assessed in terms of the normalized mean bias ($NMB = \sum(CCN_{pred,i} - CCN_{meas,i}) / \sum CCN_{meas}$), similarly to Asa-Awuku et al. (2011), which provides a representation of the average CCN prediction error observed for each flight. Data for the MBL and FT are shown for individual flights, while data from the AC-OAL are aggregated from all flights where the layer was observed, as fewer size distributions were obtained from the AC-OAL during each flight (and the AC-OAL was not observed at all during three flights).

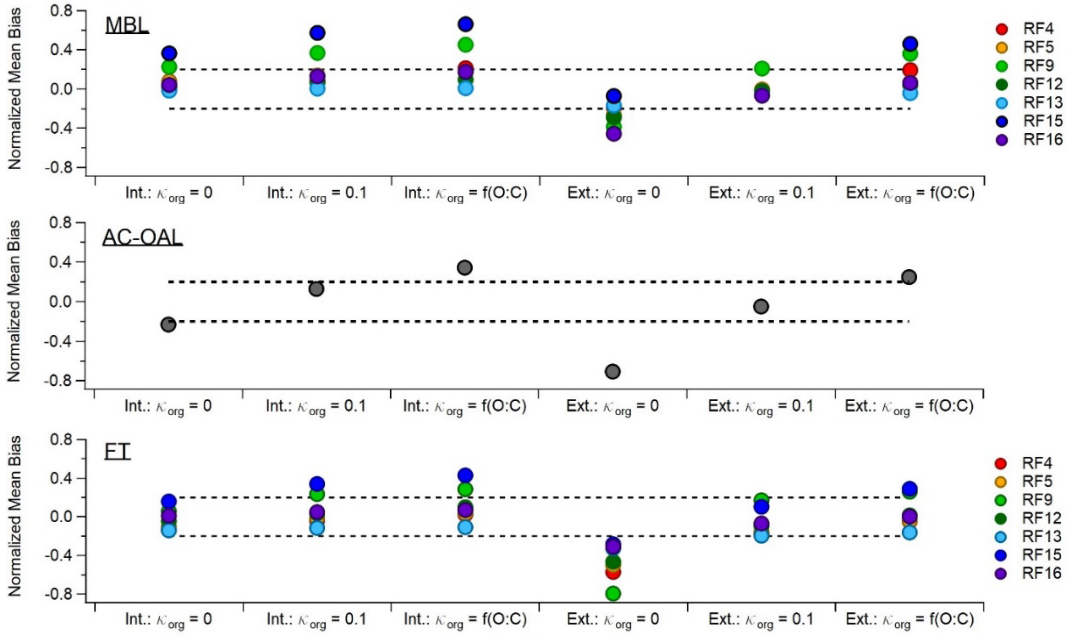

Figure 4.8: Normalized mean bias resulting from CCN closure analysis performed on data from each flight. A value of 0.2 is equivalent to an average overprediction of 20%. Int. indicates aerosol were assumed internally mixed, while Ext. indicates organic and inorganic aerosol were assumed to be externally mixed. κ_{org} represents the assumed hygroscopicity of the organic aerosol component.

For the majority of analyzed flights (5 out of 7), closure is obtained within 20% using AMS-measured bulk composition and an assumption of either insoluble (κ_{org} = 0) or slightly hygroscopic organics (κ_{org} = 0.1). While the assumption of insoluble organics disagrees with observed O:C ratios (e.g., the O:C ratio of the MBL PMF factor is 0.85), CCN closure studies often find this assumption is ideal when assuming internal mixing (Chang et al., 2007; Wang et al., 2008; Lance et al., 2009; Moore et al., 2011). The lack of strong dependence on κ_{org} suggests that in non-urban areas, regional models may be able to assign a single value to organic aerosol rather than attempt to dynamically model changes in organic aerosol hygroscopicity with aging (Wang et al., 2008). This is further highlighted by the fact that closure results assuming a constant κ_{org} value (0.1) are generally more accurate than those produced by parameterizing κ_{org} based on the observed O:C ratio

(Lambe et al., 2011). As larger aerosols are more likely to have undergone cloud-processing, parameterizing organic hygroscopicity based on bulk measurements of the organic O:C ratio, which is biased by the largest particles, may also overpredict the oxidation state of particles near the critical diameter of CCN activation. Without size-resolved compositional data, it is difficult to definitively conclude whether the overprediction observed when κ_{org} is parameterized based on the organic O:C ratio is due to such variability with size or is the result of a different relationship between O:C and κ_{org} for organic aerosols in this environment. However, other published parameterizations between O:C and κ_{org} in the literature either agree well with the Lambe parameterization (Chang et al., 2010; Massoli et al., 2010; Thalman et al., 2017) or predict more hygroscopic particles at the same O:C ratio (and as a result would lead to further overprediction if implemented in the CCN closure analysis) (Mei et al., 2013). The overprediction in CCN observed here when incorporating the Lambe parameterization therefore suggests that small particles near the critical activation diameter are less hygroscopic than larger particles that dominate the mass size distribution and thereby dictate AMS-measured composition.

Overall, generally good closure is expected in a semi-remote environment such as the California coastal zone, as previous studies have noted that closure is likely to be achieved within 20% when the bulk aerosol κ exceeds 0.1 (Wang et al., 2010). Furthermore, it is expected that aerosol in this coastal environment can be modeled as internally mixed, regardless of its true mixing state, due to the substantial contribution of inorganic constituents and distance from emission sources (Ervens et al., 2010; Moore et al., 2013; Fierce et al., 2016). Fierce et al. (2016) have demonstrated that in semi-remote environments (i.e., non-urban locations), initially externally mixed aerosol becomes internally mixed on a time scale of about one day, while the conversion is even faster (on the order of hours) in urban environments, in agreement with the results of Wang et al. (2010). Notable underpredictions (i.e., >20%) of CCN concentrations are produced when assuming externally mixed aerosol with insoluble organics, in agreement with the aged nature of the aerosol in this environment, which should lead to both oxidized organic aerosol and an appreciable amount of internal mixing.

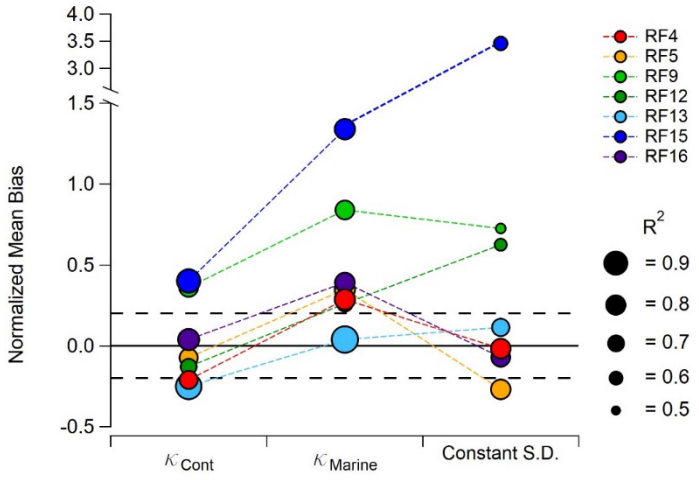

Figure 4.9: Normalized mean bias resulting from additional CCN closure analyses performed on data from each flight. κ_{Cont} and κ_{Marine} refer to analyses assuming a constant κ equivalent to values representative of continental (0.27) and marine (0.72) environments respectively (Pringle et al., 2010). The Constant S.D. case assumes a constant aerosol number size distribution equivalent to the median value observed in the MBL during the campaign. Blacked dashed lines indicate closure error of ±20%. Note the split in the y-axis.

CCN are strongly overpredicted in the MBL during RF9 (37%) and RF15 (57%) when assuming an internal mixture with hygroscopic organics. Aerosol composition during these flights was dominated by organic species in the MBL (59% and 58% of AMS-derived aerosol mass, respectively), indicative of a continental influence on aerosol properties. AMS-derived hygroscopicities are substantially larger than those derived from CCN measurements (Figure 4.3), suggesting that size-dependent composition may lead to the observed overprediction of CCN concentrations when using bulk AMS measurements of aerosol composition. Comparison of CCN closure results when assuming internal versus external mixing suggests that organic and inorganic components are externally mixed, implying either distinct particle sources or a lack of significant aging prior to measurement. In the case of RF15, this external mixing aligns with the hypothesis of downward mixing from the organic-rich AC-OAL. Figure 4.S7 depicts the CCN closure normalized mean bias resulting from an assumption of internally mixed aerosols with hygroscopic organics

as a function of the CCN-derived hygroscopicity. In general, CCN closure error increases rapidly as κ_{CCN} decreases past ~0.25, suggesting that detailed mixing state and/or size resolved compositional information is critical for accurate CCN prediction in this coastal environment during periods of intense organic aerosol intrusion into the MBL. As the aerosol hygroscopicity calculation used in this study relies on an assumption of internal mixing of organic and inorganic aerosol components, it is difficult to determine whether CCN closure error when assuming internal mixing during this flights is a result of externally mixed organic and inorganic aerosol or a result of variable composition with size. Ultimately, as these atypical organic aerosol-dominated marine conditions are the least likely to be accurately reproduced by regional models, further investigation of their frequency, particle characteristics, and resulting impact on cloud properties is warranted.

The analysis presented in Figure 4.8 implies that for typical conditions in the MBL (5 out of 7 flights in this study), mixing state and organic hygroscopicity have relatively little influence on CCN number concentrations. Additional closure analyses were performed assuming a constant κ equivalent to values attributed to average continental (κ = 0.27) and marine (κ = 0.72) environments (Pringle et al., 2010) (Figure 4.9). These results highlight the fact that assuming coastal aerosols have a strictly marine character leads to substantial errors in CCN prediction (>20% for 8 out of 9 flights) even if size distribution parameters are well characterized. Furthermore, for five out of the seven analyzed flights (RF4, RF5, RF9, RF13, RF16), assuming a constant marine κ (0.72) results in CCN prediction error similar to or larger than the error produced by assuming a constant aerosol size distribution derived from the median value measured in the MBL during this study. This underscores the importance of capturing organic contributions to coastal MBL aerosol, whether due to continental outflow, downwelling from the AC-OAL, shipping emissions, or marine biota.

4.3.5 Sensitivity of stratocumulus CDNC to below-cloud aerosol hygroscopicity

In order to investigate directly the sensitivity of N.E. Pacific stratocumulus CDNC to below-cloud aerosol properties, droplet activation was simulated using an aerosol-cloud parcel model constrained with detailed below-cloud aerosol measurements obtained from

three cloud sampling passes performed during the campaign. While a number of previous cloud parcel modeling studies have assumed unimodal size distributions (Reutter et al., 2009; Ward et al., 2010; Chen et al., 2016), observed aerosol size distributions over the N.E. Pacific were frequently bimodal (Figure 4.3). As many current aerosol modules incorporated within global atmospheric chemistry models involve multiple aerosol size modes (Liu and Wang, 2010; Pringle et al., 2010; Rothenberg et al., 2018), we carried out parcel model runs to analyze CDNC sensitivity to properties of the Aitken and accumulation modes separately. Sensitivities were calculated following McFiggans et al. (2006), where $S(X_i) = \delta ln N_{CDNC} / \delta ln X_i$ and X_i is the parameter under investigation. Standard linear regressions of lnN_{CDNC} vs. lnX_i were used to determine $S(X_i)$ values, as is convention (Reutter et al., 2009; Ward et al., 2010; Sánchez-Gácita et al., 2017). Measured aerosol and meteorological properties utilized as model constraints are summarized in Table 4.4. Sensitivity to hygroscopicity was computed across the range of κ = 0.2-0.6. Initial results confirmed that for observed MSc updraft velocities (w = 0.15-0.3 m s^{-1}), below-cloud particle number concentrations (~500-800 cm^{-3}), and typical hygroscopicities ($\kappa \sim$ 0.2-0.4), properties of the Aitken mode have a minor impact on stratocumulus properties ($S(X_i)$<0.05), as minimum simulated activation diameters exceed 100 nm. Therefore, Figure 4.10 depicts the sensitivity of stratocumulus CDNC to properties of the accumulation mode and the simulated updraft velocity.

Table 4.5: Below-cloud aerosol and meteorological data used as aerosol-cloud-parcel model constraints for calculation of CDNC sensitivities depicted in Figure 4.10.

Parameter	RF5-1	RF5-2	RF16
$N_{CN,\ Aitken}$ (cm^{-3})	296	301	128
$D_{pg\ ,\ Aitken}$ (nm)	55	57	70
σ_{Aitken}	1.27	1.27	1.24
κ_{Aitken}	0.36	0.42	0.21
$N_{CN,\ Accum.}$ (cm^{-3})	492	465	406
$D_{pg,\ Accum.}$ (nm)	104	109	124
$\sigma_{Accum.}$	2.21	2.20	1.96
$\kappa_{Accum.}$	0.37	0.34	0.28
w ($m\ s^{-1}$)	0.22	0.26	0.25
w/N_{CN} ($m\ s^{-1}\ cm^{-3}$)	$2.8x10^{-4}$	$3.4x10^{-4}$	$4.7x10^{-4}$
Activation Regime*	Trans.	Trans.	Trans.

*"Activation Regime" refers to the classifications of cloud droplet formation environments developed by Reutter et al. (2009). "Trans." = transitional.

The average sensitivity of CDNC to aerosol hygroscopicity (0.19), while smaller than the sensitivity to size distribution parameters, is 39% as large as the sensitivity to the geometric mean diameter of the accumulation mode. This agrees with the consensus that particle size distribution properties have a larger influence on CCN concentration than particle composition (Dusek et al., 2006; McFiggans et al., 2006; Reutter et al., 2009), but also suggests accurate hygroscopicity reproduction should be included in future model improvement efforts. Observed below-cloud particle number concentrations and updraft velocities suggest that CCN activation occurs in the transitional regime according to the designations defined by Reutter et al. (2009), and simulated sensitivity to hygroscopicity agrees well with those previously reported for the transition regime (0.17-0.2) (Reutter et al., 2009; Ward et al., 2010).

Aging processes during transport likely lead to internally rather than externally mixed aerosol in the MBL. The simulated error in predicted CDNC when assuming fully externally mixed components is only 7.6-8.7% for the three modeled cases. This aligns with the observation of similarly accurate CCN closure results for the MBL when assuming internally or externally mixed components and a κ_{org} of 0.1 or larger. As the volume fraction of inorganic aerosol in the accumulation mode is likely to increase with increasing distance from the coast, this predicted mixing-state-related error may be an upper bound for marine conditions in general.

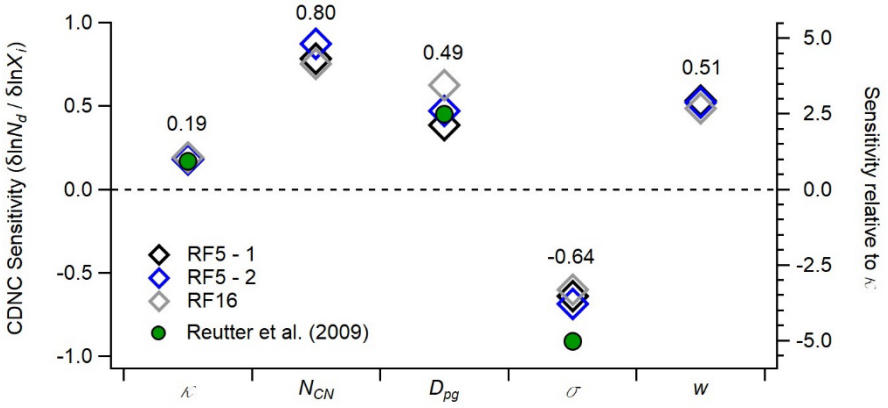

Figure 4.10: Sensitivity of calculated CDNC to accumulation mode aerosol hygroscopicity (κ), below-cloud aerosol particle number concentration (N_{CN}), accumulation mode geometric mean diameter (D_{pg}), accumulation mode standard deviation (σ), and updraft velocity (w). Data obtained during three cloud sampling passes were used as model constraints and are listed in Table 4. Numbers above each group of symbols represent average values from simulations in this study. Green symbols correspond to values reported by Reutter et al. (2009) for the transitional activation regime.

Previous aerosol-cloud parcel modeling studies have demonstrated that the sensitivity of predicted CDNC to aerosol hygroscopicity tends to decrease as bulk hygroscopicity increases, especially for the aerosol-limited and transitional aerosol activation regimes (Reutter et al., 2009; Sánchez-Gácita et al., 2017). If this is the case, accurate hygroscopicity characterization in marine regions subject to organic aerosol inputs, which contain aerosol with lower-than-average κ values, may be more important for global CDNC prediction accuracy than accurate hygroscopicity characterization in remote regions

subject to aerosol sources with different, but elevated, hygroscopicities (e.g., ammonium sulfate (κ = 0.61) vs. sodium chloride (κ = 1.28)). To investigate this possibility, we calculated local CDNC sensitivity to aerosol hygroscopicity for four hypothetical marine aerosol size distributions. Rather than performing a linear regression on data obtained from a broad range of hygroscopicities, as was done for the data shown in Figure 4.10, local sensitivities refer to calculations performed on incremental variations in κ (e.g., κ = 0.1 vs 0.2). Figure 4.11 displays the size distributions used as well as the sensitivity results. In order to span the likely range of size distributions observed in marine environments, the "Coastal" distribution is similar to median distributions observed during RF4 and RF5. A "Remote" distribution was generated using reported size distribution parameters from measurements over the remote subtropical N. Pacific by Ueda et al. (2016). Two additional size distributions were produced by interpolating between the "Coastal" and "Remote" distributions. Total particle concentrations in the simulations varied between 300 cm^{-3} and 800 cm^{-3} depending on the size distribution used. Five different updraft velocities were simulated (w = 0.1-0.5 m s^{-1}), corresponding to the range typically observed within MSc over the Pacific (Zheng et al., 2016).

A few notable trends are evident in the results shown in Figure 4.11. As has been previously reported, CDNC sensitivity to aerosol hygroscopicity tends to decrease as hygroscopicity increases. However, even at low hygroscopicities, calculated sensitivities never exceed 0.3, suggesting that at a maximum, a 50% error in marine aerosol hygroscopicity should lead to an error of only 15% in predicted CDNC. Sensitivity slightly increases as the assumed particle concentration increases, and therefore hygroscopicity is slightly less important in remote marine environments than in more polluted, coastal locations, as expected. In typical remote marine conditions ($\kappa \approx 0.6$) for instance, a 50% error in hygroscopicity is associated with only a ~2.5-7.5% error in predicted CDNC, while in coastal environments ($\kappa \approx 0.35$) the error is estimated to be ~7.5-15%.

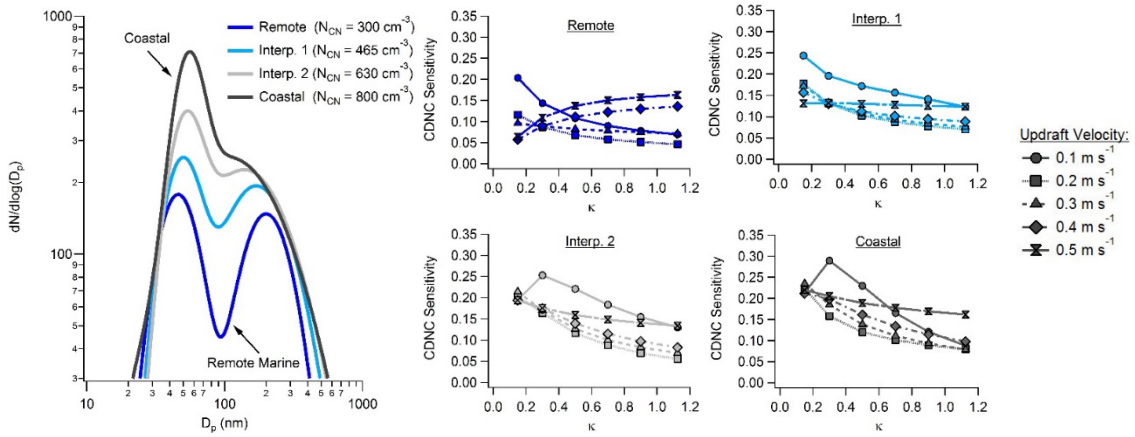

Figure 4.11: (Left) Aerosol number size distributions used as aerosol-cloud-parcel model inputs and (right) local CDNC sensitivities to aerosol hygroscopicity calculated using five updraft velocities. N_{CN} refers to the aerosol number concentration represented by each aerosol size distribution.

When simulating certain combinations of updraft velocity and aerosol size distribution, the sensitivity of predicted CDNC to aerosol hygroscopicity does not decrease monotonically as hygroscopicity increases. Furthermore, at a given hygroscopicity value shown in Figure 4.11, CDNC sensitivity is a non-monotonic function of updraft velocity. Here, we demonstrate that these phenomena are a result of activation of the distinct Aitken aerosol mode. Variation in CDNC sensitivity to hygroscopicity with increasing updraft velocity is shown in Figure 4.12 for κ = 0.6-0.8. Local CDNC sensitivity to hygroscopicity initially decreases with increasing updraft velocity before increasing again at updraft velocities >0.2-0.3 m s^{-1}. This trend is consistent regardless of κ range analyzed; however, the shape of the curve becomes "stretched" horizontally as κ values decrease (Figure 4.12). Using a unimodal size distribution, Reutter et al. (2009) demonstrated that moving from the transitional to the aerosol-limited regime caused CDNC sensitivity to hygroscopicity to decline for all κ > 0.05. For the four marine size distributions simulated in this study, increasing the updraft velocity from 0.1 to 1.0 m s^{-1} shifts activation from the transitional regime to the aerosol-limited regime, implying CDNC sensitivity to hygroscopicity should subsequently decline. Our observation of the opposite phenomenon is due to the fact that

at low (w = 0.1 m s^{-1}) and high (w = 1-1.5 m s^{-1}) updraft velocities, critical diameters produced within the rising air parcel occur near the peak of the accumulation and Aitken aerosol modes, respectively (Figure 4.12b). As the size distribution is peaked at these locations, subtle changes in aerosol hygroscopicity that induce small changes in the critical diameter result in a relatively large change in computed CDNC - hence elevated sensitivity to hygroscopicity. In contrast, for moderate (w ~ 0.2-0.3 m s^{-1}) updraft velocities, minimum critical diameters occur between the peaks of the Aitken and accumulation modes, and for very strong updraft velocities (w > 1.5-2 m s^{-1}) minimum critical diameters occur at sizes smaller than the peak of the Aitken mode, leading to lowered sensitivity (Figure 4.12b). This implies that in aerosol-limited environments with bimodal aerosol size distributions, the sensitivity of CDNC to hygroscopicity cannot necessarily be assumed to be negligible based solely on the ratio of the updraft velocity to particle number concentration. Ultimately, our results suggest that the sensitivity of marine CDNC to hygroscopicity is maximized in weak updraft conditions occurring in MSc (w < 0.2 m s^{-1}), where hygroscopicity of the accumulation, rather than the Aitken, mode is most relevant to accurate CDNC prediction, and in relatively strong updraft conditions (0.5 < w < 2 m s^{-1}) in either MSc or marine cumulus (Clarke et al., 1996), where Aitken mode hygroscopicity has a larger influence on CDNC than that of the accumulation mode.

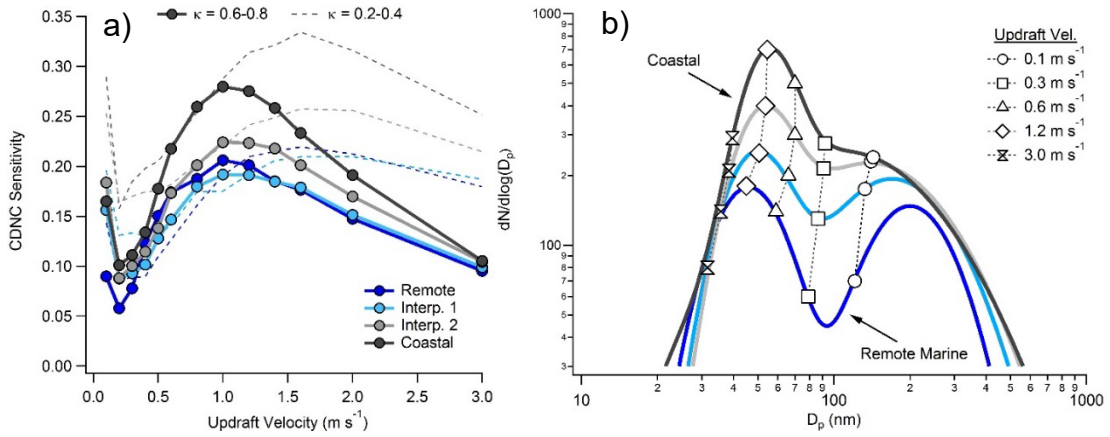

Figure 4.12: (a) Simulated local CDNC sensitivity to hygroscopicity in the range κ = 0.6-0.8 and κ = 0.2-0.4 as a function of updraft velocity. (b) Critical diameter calculated at the maximum supersaturation predicted by the aerosol-cloud-parcel model for four different updraft velocities assuming κ = 0.6.

4.4 Summary and conclusions

Measurements of aerosol properties obtained over the N. E. Pacific Ocean during the MACAWS campaign in June and July 2018 were combined with results from an aerosol-cloud-parcel model to gain insight into aerosol hygroscopicity and its influence on CCN and MSc CDNC prediction in this environment. Three characteristic vertical regions were characterized, corresponding to the MBL, FT, and AC-OAL. Within the MBL, flight-averaged hygroscopicities varied from values typical of continental environments (κ = 0.27), to those representative of remote marine locations (κ = 0.72) (Pringle et al., 2010). In the AC-OAL, observed hygroscopicity suggests a dominant contribution of organic aerosol in both the Aitken and accumulation mode size ranges.

For the majority of flights, measured CCN concentrations could be reproduced within 20% using measurements of the aerosol size distribution, bulk hygroscopicity, and an assumption of either internally or externally mixed organic and inorganic components, in agreement with past results in non-urban locations (e.g., Ervens et al., 2010). Notably, for five of the seven flights, MBL CCN were better predicted when assuming a constant aerosol number size distribution derived from the median value measured in the MBL than when assuming a constant κ typical of remote marine locations (0.72).

Results from an aerosol-cloud-parcel model confirm that the sensitivity of predicted CDNC to accumulation mode aerosol hygroscopicity (0.19) is substantially smaller than sensitivity to size distribution parameters, such as the accumulation mode geometric diameter (0.49) and standard deviation (-0.64). Simulations using a variety of possible MBL aerosol size distributions and hygroscopicities suggest that a 50% error in predicted hygroscopicity should rarely produce a CDNC error greater than 15%. However, model results further suggest that CDNC sensitivity to hygroscopicity does not monotonically decrease with increasing updraft velocity. Rather, sensitivity appears to decrease or remain constant with increasing updraft velocities from low to moderate values (e.g., 0.1-0.3 m s^{-1}) and then increase as updraft velocities increase further (>0.4 m s^{-1}) due to activation of the distinct Aitken mode. This phenomenon is observed despite the fact that at large updraft velocities (>0.4-0.5 m s^{-1}), marine conditions generally occupy the aerosol-limited regime

of cloud droplet activation. Ultimately, CDNC sensitivity to hygroscopicity is predicted to be maximized in weak updraft conditions occurring in MSc (<0.2 m s^{-1}) and in strong updraft conditions (>0.5 m s^{-1}) expected to occur in either MSc or marine cumulus.

4.5 Acknowledgements

This work was supported by Office of Naval Research grants N00014-17-1-2719 and N00014-16-1-2567. AS was partially supported by NASA grant 80NSSC19K0442in support of the ACTIVATE Earth Venture Suborbital-3 (EVS-3) investigation, which is funded by NASA's Earth Science Division and managed through the Earth System Science Pathfinder Program Office. We would like to thank the crew of the CIRPAS Twin Otter for their assistance during the campaign. Airborne field data used in this work can be accessed on the Figshare database (Sorooshian et al., 2017: https://doi.org/10.6084/m9.figshare.5099983.v10.).

4.6 Supporting Information

4.6.1 Determination of uncertainties in reported hygroscopicity parameters

4.6.1.1 CCN-derived hygroscopicity (κ_{CCN})

As calculation of κ_{CCN} requires the use of measured CCN concentrations and aerosol number size distributions, uncertainties in these values were first evaluated. To determine uncertainties in measured CCN concentrations due to uncertainties in instrument supersaturations (SS), hypothetical CCN concentrations were calculated from average size distributions measured in the MBL, AC-OAL, and FT, using the four "true" SS values in the CCNC (0.1%, 0.3%, 0.43%, and 0.57%), as well as SS values offset by the relative deviations observed in the calibrations (±6%) (e.g., 0.094-0.106%, 0.282-0.318%, 0.404-0.456%, and 0.54-0.604%) for a range of possible κ values (0.1-0.8). This calculation suggests a conservative (i.e., upper estimate) relative error in CCN concentrations of 9% due to SS uncertainty. A contour plot demonstrating this error for calculations performed using the median MBL size distribution is shown in Figure 4.S1. Uncertainty in the magnitude of the size distribution from the differential mobility analyzer (DMA) was taken to be 15%, while uncertainty in the DMA bin assignments was ~5% from calibrations performed prior to the campaign. These uncertainties align well with those observed by Wiedensohler et al. (2012) during a comparison of multiple particle size spectrometers. While the authors note that uncertainties in the magnitude of the size distribution increase for particles larger than 200 nm (up to 30%), during this campaign these particles accounted for only ~12% of the total particle concentration in the MBL on average and even less in the AC-OAL (5%), suggesting that the 15% uncertainty used here is reasonable. A depiction of maximum possible uncertainties in critical diameters resulting from errors in CCN concentrations and size distribution parameters is shown in Figure 4.S2 for two SS (0.1% and 0.57%).

Using these uncertainties, 100,000 hypothetical CCN-derived κ values were calculated using the median size distribution and CCN number concentrations in each of the three environments (MBL, AC-OAL, FT). Specifically, prior to calculating CCN-

derived kappa, the average CCN concentration at each SS, aerosol number size distribution magnitude, and aerosol size distribution bin values were each modified by a factor randomly selected from a normal distribution with a mean value of one and standard deviation equivalent to the respective uncertainties (9%, 15%, and 5% respectively). The resulting histogram of CCN-derived kappa values was fit with a lognormal distribution, and the uncertainty is derived from the geometric standard deviation of the fit. An example histogram resulting from this analysis is shown in Figure 4.S3. As the produced distribution is lognormal, uncertainties are not symmetric about the mean values. The numerical data produced by the fitting procedure and resulting uncertainties are displayed in Table S1. Uncertainties increase at larger supersaturations as smaller changes in critical diameter are required to produce equivalent changes in CCN-derived κ. Due to the small CCN concentrations measured at 0.1% SS, the estimated uncertainty at this SS is almost certainly too low, as small variations in absolute number concentration due to differential losses between the CCNC and DMA sampling lines could markedly affect CCN-derived κ. As we could not perform a thorough analysis of differential particle losses within the sampling lines during the campaign, we omit hygroscopicity data measured at a SS of 0.1% from the results.

While the calculated uncertainty of ~+55%/-40% for SS = 0.3% and ~+75%/-45% for SS = 0.43% is substantial, accurate measurement of hygroscopicity on an aircraft platform is an analytically challenging task due to the need for rapid measurements. We note that we cannot quantitatively account for uncertainties introduced by the possibility of externally mixed insoluble particles present in the sampled environments. However, as we primarily focus on data from the MBL and AC-OAL, we expect the concentrations of such particles to be small. For instance, average refractory black carbon concentrations measured by a single particle soot photometer were less than 5 cm^{-3} in these environments.

4.6.1.2 AMS-derived hygroscopicity (κ_{AMS})

Inferred values of the hygroscopicity parameter from AMS measurements (κ_{AMS}) are dependent on the mass fractions of the measured aerosol components (e.g., organics, sulfate, etc.) (converted to volume fractions using known or assumed densities) and the assumed organic aerosol hygroscopicity. Quantification of aerosol component mass loadings requires knowledge of component collection efficiencies, relative ionization efficiencies, and measured ion count rates (Jimenez et al., 2003; Middlebrook et al., 2012). If aerosol components are externally mixed, distinct collection efficiencies for different particle components could introduce uncertainty into measured mass fractions; however, for a semi-remote ambient environment such as the N.E. Pacific MBL, it is likely that observed aerosols are internally mixed. This assumption is supported by CCN closure analyses discussed in the main text as well as internal mixing timescales modeled by Fierce et al. (2016). As a result, uncertainties in the instrument collection efficiency should lead to uncertainties in absolute mass loadings rather than mass fractions. As discussed by Ovadnevaite et al. (2017), for an ambient dataset, the dominant remaining uncertainties in AMS-derived mass fractions result from uncertainty in the relative ionization efficiencies (RIE) of the various species. According to Bahreini et al. (2009), uncertainties in RIEs are 10%, 15%, and 20% for ammonium, sulfate, and organics, respectively. As the propagated uncertainty in κ_{AMS} will be dependent on the assumed "true" κ_{AMS} value (e.g., minor uncertainty would be expected in the case that aerosol was dominated by a single species), we calculated κ_{AMS} uncertainty as a function of the assumed "true" organic mass fraction (Figure 4.S4a). Specifically, for a given assumed organic mass fraction, all inorganic aerosol was assumed to be entirely ammonium sulfate, individual component mass loadings were modified within their respective uncertainties, the identity of the inorganic species was redetermined using the ammonium to sulfate molar ratio (RSO_4), and the κ_{AMS} value was recalculated. Nitrate and chloride were not included due to their minor contributions to observed aerosol mass during the campaign. A histogram of 10,000 calculated κ_{AMS} values was produced for each value across a range of possible organic volume fractions (spanning 0.05 – 1), and a lognormal distribution was subsequently fit to each set of data. Uncertainties were determined from the parameters of the lognormal distribution, similarly to the κ_{CCN} uncertainty analysis.

As shown in Figure 4.S4a, for typical conditions observed during the campaign the estimated uncertainty in κ_{AMS} due to uncertainties in component mass fractions was ~10%.

However, an additional uncertainty is introduced by the need to assume the hygroscopicity of the organic fraction. While this uncertainty is difficult to quantify numerically (i.e., a percentage uncertainty in κ_{org}), we define upper and lower limits as 0.2 and 0 respectively. Figure 4.S4b demonstrates that at large organic volume fractions, the uncertainty in κ_{org} can translate into a relative uncertainty in κ_{AMS} of 75%. However, because the absolute value of κ_{AMS} is low at high organic volume fractions, the maximum absolute uncertainty in κ is ~0.1.

As demonstrated in Figure 4.S4, for organic volume fractions below ~0.4, the relative uncertainty in κ_{AMS} is dictated by the uncertainty in component volume fractions measured by the AMS, while for larger organic volume fractions, uncertainty in κ_{AMS} is dictated by the uncertainty in κ_{org}.

We note that this analysis omits possible uncertainties introduced by the inability of the AMS to accurately quantify refractory aerosol mass (e.g., sea salt, mineral dust, etc.). However, average wind speeds within the MBL (8.1 m s^{-1}) were lower than those measured by Modini et al. (2015) during a period of low sea salt mass loadings (0.14 μg m^{-3}), and measured aerosol number size distributions align with those measured by Modini et al. (2015) during the same period (i.e., no distinct aerosol size mode >500 nm, which would indicate substantial sea spray, was observed). Roberts et al. (2010) analyzed 27 MBL particles in the same N.E. Pacific region with scanning transmission x-ray microscopy and noted that only two particles (7.4%), both of which were super-micron, were likely sea salt. As a result, we are confident that the error related to chloride quantification is minor. Furthermore, there was no indication of distinct aerosol dust layers within the FT, and as shown in Figure 4.S5, the flight-average integrated aerosol mass loadings measured by the differential mobility analyzer agree with those measured by the AMS within the uncertainty of the AMS measurement (40%). Ultimately, we are confident that the possible presence of refractory material did not cause substantially biased κ_{AMS} measurements for this campaign.

4.6.2 Positive matrix factorization of high-resolution organic aerosol mass spectra

Positive matrix factorization (PMF) analysis (Paatero and Tapper, 1994) was performed on the high-resolution AMS mass spectra in order to distinguish major classes and transformation processes of measured OA. The PMF model de-convolves the time series of organic mass spectra measured into a number of temporally unvarying components. Each of these distinct components contributes a variable fraction of total OA mass at each measurement point. Numerous recent studies report use of PMF to describe coastal and marine OA, and often bulk OA can be separated into individual components from marine and anthropogenic sources (Hegg et al., 2008; Hildebrandt et al., 2011; Schmale et al., 2013; Huang et al., 2018). High resolution AMS data preparation, including minimum counting error and variable down-weighting, followed the recommendations of Ulbrich et al. (2009) and Zhang et al. (2011). Model execution was performed using the PMF Evaluation Tool (PET v2.08D) developed by Ulbrich et al. (2009). Examination of PMF results from the present dataset revealed an optimal 3 factor solution with a rotational fPeak parameter of 0 (Ulbrich et al., 2009). Two of these factors correspond to OA subtypes characteristic of the MBL and above-cloud organic aerosol layer (AC-OAL), respectively, and resemble low-volatility oxygenated organic aerosol (LV-OOA). LV-OOA is a commonly observed OA subtype characterized by a relatively large O:C ratio (>0.6), dominance of *m/z* 44 (CO_2^+) within the mass spectrum (an organic acid tracer), and a lack of reduced hydrocarbon fragments (Ng et al., 2010). The third factor is likely a result of primary anthropogenic emissions and resembles hydrocarbon-like organic aerosol (HOA). HOA factors - characterized by a lack of oxygenated ion fragments and low O:C ratios (<0.2) - are typically the result of fossil fuel combustion (either gasoline, diesel, or lubricating oils) (Zhang et al., 2005; Aiken et al., 2008). In marine environments, HOA is often produced by shipping vessel emissions (Murphy et al., 2009; Coggon et al., 2012). Periods sampling biomass burning smoke were excluded from the PMF analysis, as they often contribute OA mass loadings an order of magnitude higher than typical conditions in the region (e.g., >40 μg m^{-3}) and therefore exert a

disproportionately large influence on model output. Direct sampling of biomass burning plumes was identified in the data as DMA scans in the MBL or FT in which average CN concentrations exceeded 1000 cm^{-3} and average organic aerosol mass loadings exceeded 4 $\mu g\ m^{-3}$. Further analysis was performed to ensure these increases were not the result of nearby shipping vessel emissions or sampling of the AC-OAL. Analysis of biomass burning plumes sampled during MACAWS will be the focus of future work.

Figure 4.S6 displays a representative vertical profile of the MBL, AC-OAL, and HOA PMF factors measured during a representative flight (RF5), as well as factor mass spectra extracted from PMF analysis performed on the full dataset. Excluding periods measuring ship plumes, mass loadings of the HOA factor were typically low (<0.1 $\mu g\ m^{-3}$). In general, the MBL factor dominated OA mass below cloud-tops (~0.5-1 $\mu g\ m^{-3}$) and displayed dramatic reductions in mass fraction above-cloud due to increases in AC-OAL factor mass loadings. Similarly to Coggon et al. (2014), we interpret the MBL factor as generally representative of MBL OA in the region. Laboratory and field studies have demonstrated that during oxidative processing, unique organic mass spectra from a variety of aerosol sources (biogenics, anthropogenic emissions, biomass burning, etc.) converge to a consistent, average spectrum typically classified as LV-OOA, as a variety of unique organic species with diverse functionality are converted into organic acids (Ng et al., 2010). The oxidized nature of the MBL factor, therefore, precludes the use of marker ions to distinguish individual sources of this factor, but potential sources include shipping and biogenic emissions, as well as oxidized continental outflow aerosol (Sorooshian et al., 2009; Hegg et al., 2010; Coggon et al., 2012). During the Eastern Pacific Emitted Aerosol Cloud Experiment (E-PEACE), Frossard et al. (2014) reported that ~40% of observed OA in this region could be attributed to a "ship-influenced" source type, while the remaining mass was relatively evenly divided among primary marine aerosol, carboxylic-acid enriched (i.e., aged) aerosol, and a mixture of the three. The MBL factor observed here is likely composed of a mixture of these individual source types. The O:C ratio of the MBL factor extracted from the compiled dataset (0.91) agrees

well with the average value observed by Hersey et al. (2009) (O:C = 0.92±0.33) in the same region.

A second, distinct factor displayed large mass loadings (up to 8 μg m^{-3}) within the AC-OAL. The vertical profile of this AC-OAL factor shown in Figure 4.S6 appears to align with the hypothesis that the presence of the cloud layer is related to production of the AC-OAL factor (e.g., observed increase in mass loading directly above location of LWC decline). During E-PEACE, Coggon et al. (2014) demonstrated that an above-cloud OA layer was linked to continental biogenic emissions from Northern California, suggesting that the AC-OAL factor may be produced by the same mechanism.Tthe substantially larger contribution of organic aerosol in the AC-OAL than the MBL or FT suggests that particle production is likely a result of continental biogenic sources (Coggon et al., 2014) and not upward or downward mixing from the MBL or FT respectively.

Figures 4.S1-4.S7

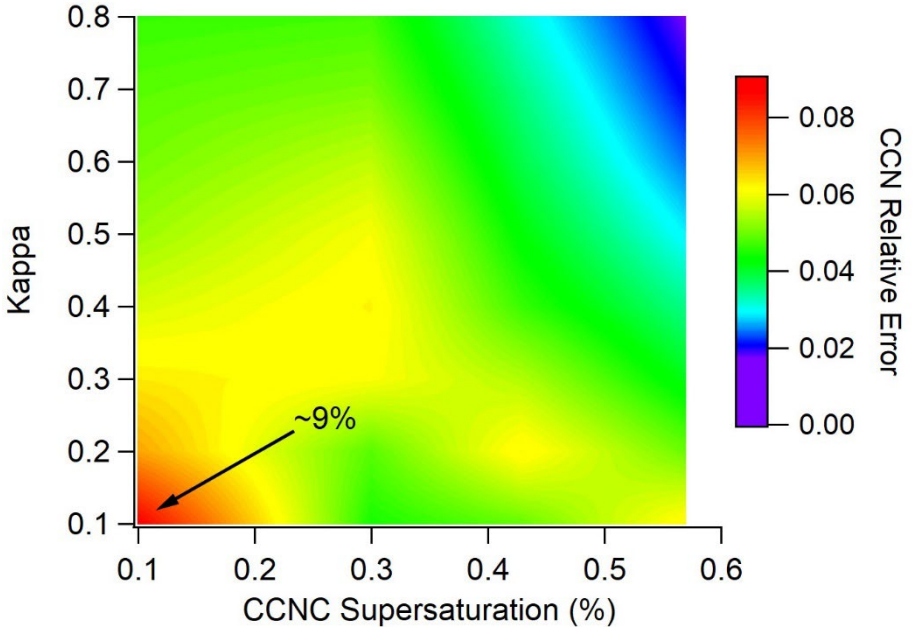

Figure 4.S1: Contour plot of error in predicted cloud condensation nuclei (CCN) concentrations due to uncertainties in instrument supersaturation (±6%) for various possible assumed κ values and instrument supersaturations. The maximum calculated value of ~9% is used in analysis of κ_{ccn} uncertainty.

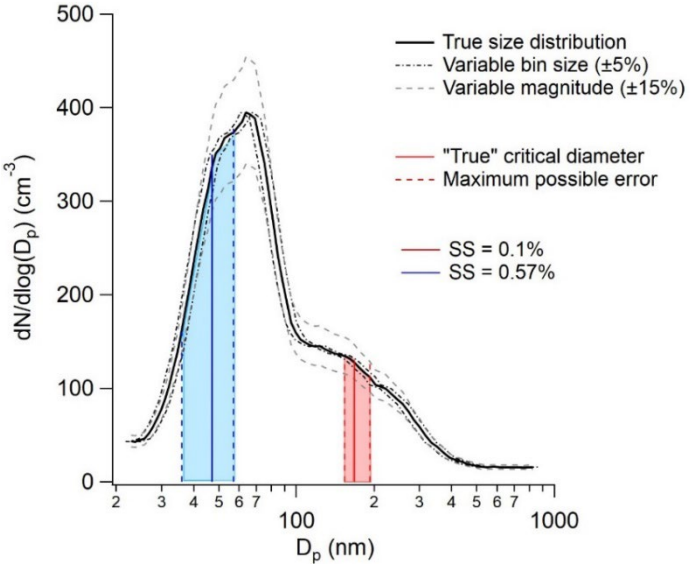

Figure 4.S2: Depiction of possible error in calculated critical diameter at two measurement supersaturations (0.1% - red; 0.57% - blue) due to uncertainties in CCN concentrations (±9%), the magnitude of the size distribution (±15%), and the size distribution bin diameters (±5%). Blue and red highlighted regions represent the range of possible critical diameters calculated due to these uncertainties. Black and grey dashed lines signify possible shifts in the size distribution due to measurement uncertainties.

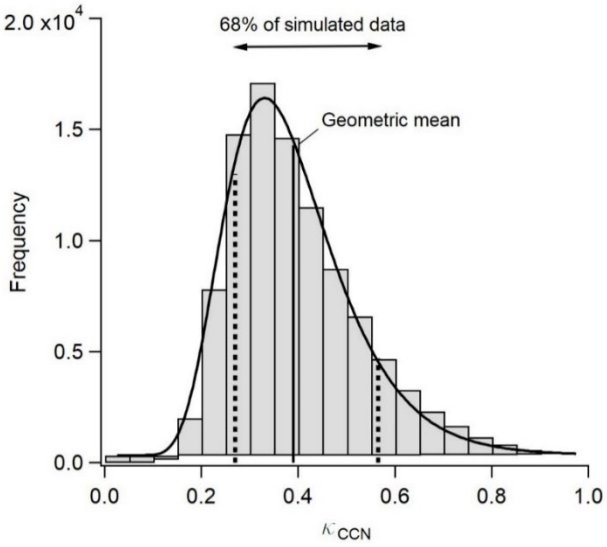

Figure 4.S3: Histogram of 100,000 κ_{CCN} values calculated at SS = 0.3% while varying the observed CCN concentrations and size distribution parameters within their respective uncertainties. The solid vertical line represents the geometric mean (μ_g), while the area between the dashed lines encompasses ~68% of the simulated data and has bounds of $\mu_g * \sigma_g$ and μ_g / σ_g. σ_g is the geometric standard deviation.

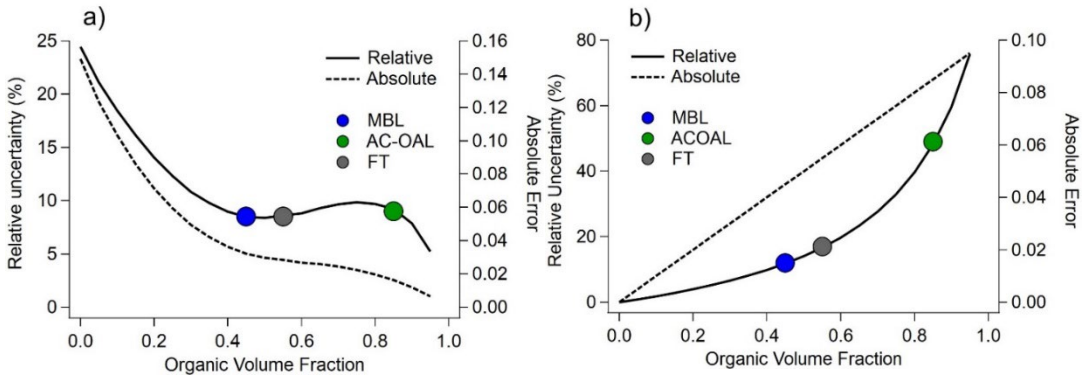

Figure 4.S4: Depiction of relative and absolute uncertainties in derived κ_{AMS} values due to (a) uncertainties in AMS-measured component mass fractions and (b) uncertainties in the assumed organic hygroscopicity parameter (κ_{org}). Uncertainties shown in (b) are determined by comparing κ_{AMS} values calculated assuming $\kappa_{org} = 0.1$ to values calculated for a hypothetical "true" κ_{org} of 0.2. Colored points highlight the relative uncertainty expected for typical conditions in the marine boundary layer (MBL), above-cloud organic aerosol layer (AC-OAL), and free troposphere (FT).

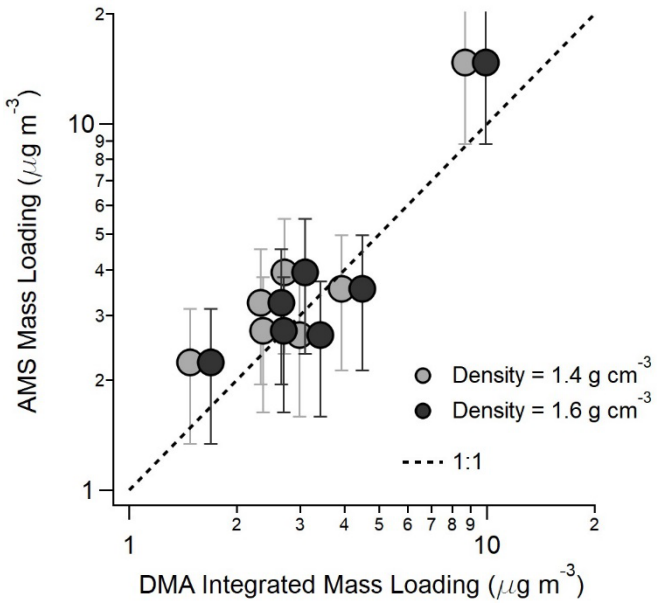

Figure 4.S5: Flight-averaged aerosol mass loadings measured by the aerosol mass spectrometer (AMS) compared to those derived from integrating aerosol number size distribution measurements from the differential mobility analyzer (DMA). Two different densities are shown, both of which could result from varying contributions of organic (1-1.6 g cm^{-3}) and inorganic species (~1.65-1.9 g cm^{-3}). Vertical error bars signify the uncertainty of the AMS mass measurement (35%) (Bahreini et al., 2009).

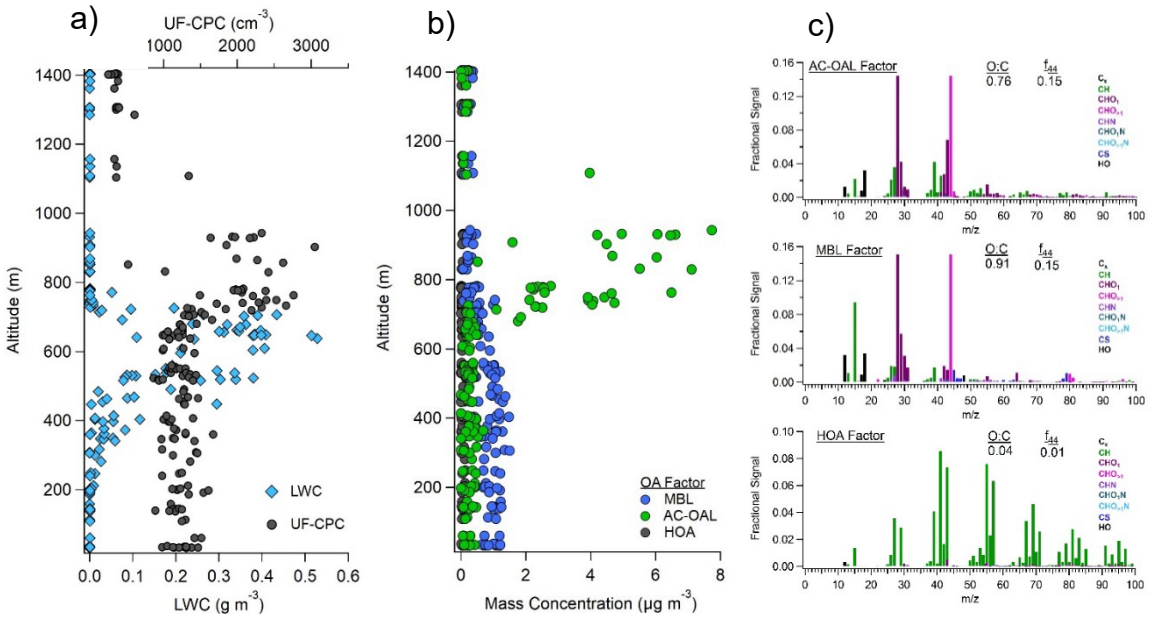

Figure 4.S6: Vertical profiles of (a) LWC and ultra-fine particle concentrations and (b) mass loadings of the extracted MBL, AC-OAL, and HOA factors during RF 5. (c) Individual factor mass spectra extracted from the compiled campaign dataset.

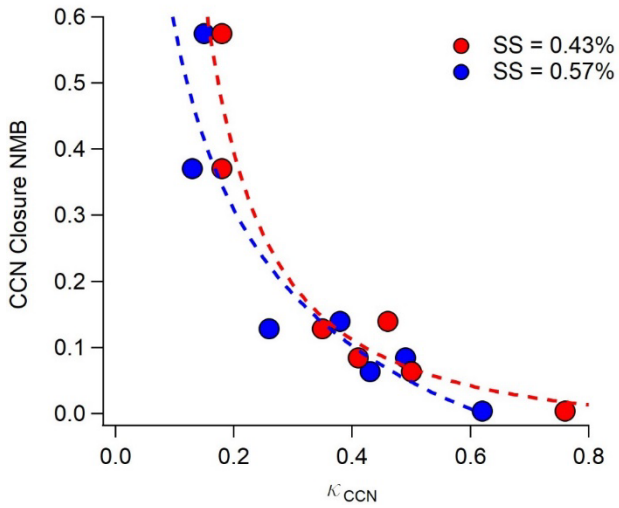

Figure 4.S7: Normalized mean bias (NMB) of flight averaged CCN closure results assuming internal mixing and slightly hygroscopic organics (κ_{org} = 0.1) plotted against κ_{CCN} measured at two supersaturations (0.43% and 0.57%). Power-fits are shown to aid interpretation and are not meant to be predictive.

Table 4.S1: Results of the κ_{CCN} uncertainty analysis for typical marine boundary layer (MBL), above-cloud organic aerosol layer (AC-OAL), and free tropospheric (FT) conditions. Lognormal mean and standard deviation (std. dev.) refer to parameters of a lognormal fit applied to a histogram of 100,000 κ_{CCN} values generated using the iterative procedure discussed in Section S1.1. These values are subsequently transformed to give the geometric mean and standard deviation. The asymmetric uncertainty is then calculated from the geometric standard deviation.

SS (%)	Lognormal mean	Lognormal std. dev.	Geometric mean	Geometric std. dev.	Estimated uncertainty (%)
MBL					
0.1	-1.22	0.36	0.29	1.44	+44; -31
0.3	-1.04	0.42	0.38	1.52	+52; -35
0.43	-0.90	0.49	0.39	1.63	+63; -39
0.57	-0.76	0.66	0.45	1.93	+93; -48
AC-OAL					
0.1	-1.66	0.28	0.19	1.32	+32; -24
0.3	-1.52	0.30	0.21	1.35	+35; -26
0.43	-1.42	0.55	0.23	1.73	+73; -42
0.57	-1.26	0.82	0.26	2.27	+127; -56
FT					
0.1	-1.15	0.29	0.31	1.34	+34; -25
0.3	-0.67	0.44	0.49	1.55	+55; -36
0.43	-0.82	0.57	0.42	1.77	+77; -45
0.57	-1.02	0.65	0.35	1.92	+92; -48

4.7 References

Ackerman, A. S., Toon, O. B. and Hobbs, P. V. (1993). Dissipation of Marine Stratiform Clouds and Collapse of the Marine Boundary Layer Due to the Depletion of Cloud Condensation Nuclei by Clouds, *Science, 262(5131),* 226–229, doi:10.1126/science.262.5131.226

Aiken, A. C., DeCarlo, P. F., Kroll, J. H., Worsnop, D. R., Huffman, J. A., Docherty, K. S., et al. (2008). O/C and OM/OC Ratios of Primary, Secondary, and Ambient Organic Aerosols with High-Resolution Time-of-Flight Aerosol Mass Spectrometry. Environmental Science & Technology, 42(12), 4478–4485. https://doi.org/10.1021/es703009q

Albrecht, B. A. (1989). Aerosols, Cloud Microphysics, and Fractional Cloudiness, *Science, 245(4923),* 1227–1230, doi:10.1126/science.245.4923.1227

Alfarra, M. R., Good, N., Wyche, K. P., Hamilton, J. F., Monks, P. S., Lewis, A. C., & McFiggans, G. (2013). Water uptake is independent of the inferred composition of secondary aerosols derived from multiple biogenic VOCs. Atmospheric Chemistry and Physics, 13(23), 11769–11789. https://doi.org/10.5194/acp-13-11769-2013

Andreae, M. O., & Rosenfeld, D. (2008). Aerosol–cloud–precipitation interactions. Part 1. The nature and sources of cloud-active aerosols. *Earth-Science Reviews*, *89*(1), 13–41. https://doi.org/10.1016/j.earscirev.2008.03.001

Asa-Awuku, A., Nenes, A., Gao, S., Flagan, R. C., & Seinfeld, J. H. (2010). Water-soluble SOA from Alkene ozonolysis: composition and droplet activation kinetics inferences from analysis of CCN activity. *Atmospheric Chemistry and Physics*, *10*(4), 1585–1597. https://doi.org/10.5194/acp-10-1585-2010

Asa-Awuku, A., Moore, R. H., Nenes, A., Bahreini, R., Holloway, J. S., Brock, C. A., et al. (2011). Airborne cloud condensation nuclei measurements during the 2006 Texas Air Quality Study. *Journal of Geophysical Research: Atmospheres*, *116*(D11). https://doi.org/10.1029/2010JD014874

Bahreini, R., Ervens, B., Middlebrook, A. M., Warneke, C., Gouw, J. A. de, DeCarlo, P. F., et al. (2009). Organic aerosol formation in urban and industrial plumes near Houston and Dallas, Texas. Journal of Geophysical Research: Atmospheres, 114(D7). https://doi.org/10.1029/2008JD011493

Berner, A. H., Bretherton, C. S. and Wood, R. (2015). Large eddy simulation of ship tracks in the collapsed marine boundary layer: a case study from the Monterey area ship track experiment, *Atmospheric Chemistry and Physics, 15(10),* 5851–5871, doi:https://doi.org/10.5194/acp-15-5851-2015

Bhattu, D., & Tripathi, S. N. (2015). CCN closure study: Effects of aerosol chemical composition and mixing state. *Journal of Geophysical Research: Atmospheres*, *120*(2), 766–783. https://doi.org/10.1002/2014JD021978

Bougiatioti, A., Nenes, A., Fountoukis, C., Kalivitis, N., Pandis, S. N., & Mihalopoulos, N. (2011). Size-resolved CCN distributions and activation kinetics of aged continental and marine aerosol. *Atmos. Chem. Phys.*, *11*(16), 8791–8808. https://doi.org/10.5194/acp-11-8791-2011

Brenguier, J.-L., Pawlowska, H., Schüller, L., Preusker, R., Fischer, J., & Fouquart, Y. (2000). Radiative Properties of Boundary Layer Clouds: Droplet Effective Radius versus Number Concentration. *Journal of the Atmospheric Sciences*, *57*(6), 803–821. https://doi.org/10.1175/1520-0469(2000)057<0803:RPOBLC>2.0.CO;2

Brioude, J., Cooper, O. R., Feingold, G., Trainer, M., Freitas, S. R., Kowal, D., et al. (2009). Effect of biomass burning on marine stratocumulus clouds off the California coast. Atmospheric Chemistry and Physics, 9(22), 8841–8856. https://doi.org/10.5194/acp-9-8841-2009

Canagaratna, M. R., Jimenez, J. L., Kroll, J. H., Chen, Q., Kessler, S. H., Massoli, P., et al. (2015). Elemental ratio measurements of organic compounds using aerosol mass spectrometry: characterization, improved calibration, and implications. *Atmospheric Chemistry and Physics*, *15*(1), 253–272. https://doi.org/10.5194/acp-15-253-2015

Cappa, C. D., Williams, E. J., Lack, D. A., Buffaloe, G. M., Coffman, D., Hayden, K. L., et al. (2014). A case study into the measurement of ship emissions from plume intercepts of the NOAA ship Miller Freeman. *Atmos. Chem. Phys.*, *14*(3), 1337–1352. https://doi.org/10.5194/acp-14-1337-2014

Carman, J. K., Rossiter, D. L., Khelif, D., Jonsson, H. H., Faloona, I. C., & Chuang, P. Y. (2012). Observational constraints on entrainment and the entrainment interface layer in stratocumulus. *Atmospheric Chemistry and Physics*, *12*(22), 11135–11152. https://doi.org/10.5194/acp-12-11135-2012

Chang, R. Y.-W., Liu, P. S. K., Leaitch, W. R., & Abbatt, J. P. D. (2007). Comparison between measured and predicted CCN concentrations at Egbert, Ontario: Focus on the organic aerosol fraction at a semi-rural site. *Atmospheric Environment*, *41*(37), 8172–8182. https://doi.org/10.1016/j.atmosenv.2007.06.039

Chang, R. Y.-W., Slowik, J. G., Shantz, N. C., Vlasenko, A., Liggio, J., Sjostedt, S. J., et al. (2010). The hygroscopicity parameter (κ) of ambient organic aerosol at a field site subject to biogenic and anthropogenic influences: relationship to degree of aerosol oxidation. *Atmospheric Chemistry and Physics*, *10*(11), 5047–5064. https://doi.org/10.5194/acp-10-5047-2010

Chen, Y.-C., Xue, L., Lebo, Z. J., Wang, H., Rasmussen, R. M. and Seinfeld, J. H. (2011). A comprehensive numerical study of aerosol-cloud-precipitation interactions in marine stratocumulus, *Atmospheric Chemistry and Physics, 11(18),* 9749–9769, doi:https://doi.org/10.5194/acp-11-9749-2011

Chen, J., Liu, Y., Zhang, M., & Peng, Y. (2016). New understanding and quantification of the regime dependence of aerosol-cloud interaction for studying aerosol indirect effects. *Geophysical Research Letters*, *43*(4), 1780–1787. https://doi.org/10.1002/2016GL067683

Clarke, A. D. (1993). Atmospheric nuclei in the Pacific midtroposphere: Their nature, concentration, and evolution. Journal of Geophysical Research: Atmospheres, 98(D11), 20633–20647. https://doi.org/10.1029/93JD00797

Clarke, A. D., Li, Z., & Litchy, M. (1996). Aerosol dynamics in the equatorial Pacific marine boundary layer: Microphysics, diurnal cycles and entrainment. Geophysical Research Letters, 23(7), 733–736. https://doi.org/10.1029/96GL00778

Clarke, A. D., Varner, J. L., Eisele, F., Mauldin, R. L., Tanner, D., & Litchy, M. (1998). Particle production in the remote marine atmosphere: Cloud outflow and subsidence during ACE 1. Journal of Geophysical Research: Atmospheres, 103(D13), 16397–16409. https://doi.org/10.1029/97JD02987

Clarke, A. D., Eisele, F., Kapustin, V. N., Moore, K., Tanner, D., Mauldin, L., et al. (1999). Nucleation in the equatorial free troposphere: Favorable environments during PEM-Tropics. Journal of Geophysical Research: Atmospheres, 104(D5), 5735–5744. https://doi.org/10.1029/98JD02303

Clarke, A. D., Freitag, S., Simpson, R. M. C., Hudson, J. G., Howell, S. G., Brekhovskikh, V. L., et al. (2013). Free troposphere as a major source of CCN for the equatorial pacific boundary layer: long-range transport and teleconnections. Atmospheric Chemistry and Physics, 13(15), 7511–7529. https://doi.org/10.5194/acp-13-7511-2013

Coggon, M. M., Sorooshian, A., Wang, Z., Metcalf, A. R., Frossard, A. A., Lin, J. J., et al. (2012). Ship impacts on the marine atmosphere: insights into the contribution of shipping emissions to the properties of marine aerosol and clouds. *Atmos. Chem. Phys.*, *12*(18), 8439–8458. https://doi.org/10.5194/acp-12-8439-2012

Coggon, M. M., Sorooshian, A., Wang, Z., Craven, J. S., Metcalf, A. R., Lin, J. J., et al. (2014). Observations of continental biogenic impacts on marine aerosol and clouds off the coast of California. *Journal of Geophysical Research: Atmospheres*, *119*(11), 6724–6748. https://doi.org/10.1002/2013JD021228

Collins, D. B., Ault, A. P., Moffet, R. C., Ruppel, M. J., Cuadra-Rodriguez, L. A., Guasco, T. L., et al. (2013). Impact of marine biogeochemistry on the chemical mixing state and cloud forming ability of nascent sea spray aerosol. *Journal of Geophysical Research: Atmospheres*, *118*(15), 8553–8565. https://doi.org/10.1002/jgrd.50598

Cubison, M. J., Ervens, B., Feingold, G., Docherty, K. S., Ulbrich, I. M., Shields, L., et al. (2008). The influence of chemical composition and mixing state of Los Angeles urban aerosol on CCN number and cloud properties. *Atmos. Chem. Phys.*, *8*(18), 5649–5667. https://doi.org/10.5194/acp-8-5649-2008

Dadashazar, H., Braun, R. A., Crosbie, E., Chuang, P. Y., Woods, R. K., Jonsson, H. H., & Sorooshian, A. (2018). Aerosol characteristics in the entrainment interface layer in relation to the marine boundary layer and free troposphere. *Atmospheric Chemistry and Physics*, *18*(3), 1495–1506. https://doi.org/10.5194/acp-18-1495-2018

DeCarlo, P. F., Kimmel, J. R., Trimborn, A., Northway, M. J., Jayne, J. T., Aiken, A. C., et al. (2006). Field-Deployable, High-Resolution, Time-of-Flight Aerosol Mass Spectrometer. *Analytical Chemistry*, *78*(24), 8281–8289. https://doi.org/10.1021/ac061249n

Draxler, R.R. and Hess, G.D. (1997) Description of the HYSPLIT_4 Modeling System. NOAA. Tech. Memo. ERL ARL-224, NOAA Air Resources Laboratory, Silver Spring, 1-24

Draxler, R. R., & Hess, G. D. (1998). An Overview of the HYSPLIT_4 Modelling System for Trajectories, Dispersion, and Deposition, Australian Meteorological Magazine, 47, 295-308.

Duplissy, J., Gysel, M., Alfarra, M. R., Dommen, J., Metzger, A., Prevot, A. S. H., et al. (2008). Cloud forming potential of secondary organic aerosol under near atmospheric conditions. *Geophysical Research Letters*, *35*(3). https://doi.org/10.1029/2007GL031075

Duplissy, J., DeCarlo, P. F., Dommen, J., Alfarra, M. R., Metzger, A., Barmpadimos, I., et al. (2011). Relating hygroscopicity and composition of organic aerosol particulate matter. *Atmospheric Chemistry and Physics*, *11*(3), 1155–1165. https://doi.org/10.5194/acp-11-1155-2011

Dusek, U., Frank, G. P., Hildebrandt, L., Curtius, J., Schneider, J., Walter, S., Chand, D., Drewnick, F., Hings, S., Jung, D., Borrmann, S. and Andreae, M. O. (2006). Size Matters More Than Chemistry for Cloud-Nucleating Ability of Aerosol Particles, *Science, 312(5778),* 1375–1378, doi:10.1126/science.1125261

Ervens, B., Cubison, M., Andrews, E., Feingold, G., Ogren, J. A., Jimenez, J. L., DeCarlo, P. and Nenes, A. (2007). Prediction of cloud condensation nucleus number concentration using measurements of aerosol size distributions and composition and light scattering enhancement due to humidity, *Journal of Geophysical Research: Atmospheres, 112(D10),* doi:10.1029/2006JD007426.

Ervens, B., Cubison, M. J., Andrews, E., Feingold, G., Ogren, J. A., Jimenez, J. L., et al. (2010). CCN predictions using simplified assumptions of organic aerosol composition and mixing state: a synthesis from six different locations. *Atmospheric Chemistry and Physics*, *10*(10), 4795–4807. https://doi.org/10.5194/acp-10-4795-2010

Faloona, I. (2009). Sulfur processing in the marine atmospheric boundary layer: A review and critical assessment of modeling uncertainties. *Atmospheric Environment*, *43*(18), 2841–2854. https://doi.org/10.1016/j.atmosenv.2009.02.043

Fierce, L., Riemer, N., & Bond, T. C. (2016). Toward Reduced Representation of Mixing State for Simulating Aerosol Effects on Climate. Bulletin of the American Meteorological Society, 98(5), 971–980. https://doi.org/10.1175/BAMS-D-16-0028.1

Frosch, M., Bilde, M., Nenes, A., Praplan, A. P., Jurányi, Z., Dommen, J., et al. (2013). CCN activity and volatility of β-caryophyllene secondary organic aerosol. *Atmospheric Chemistry and Physics*, *13*(4), 2283–2297. https://doi.org/10.5194/acp-13-2283-2013

Frossard A. A., Russell L. M., Burrows S. M., Elliott S. M., Bates T. S., & Quinn P. K. (2014). Sources and composition of submicron organic mass in marine aerosol particles. Journal of Geophysical Research: Atmospheres, 119(22), 12,977-13,003. https://doi.org/10.1002/2014JD021913

Gerber, H., Arends, B. G., & Ackerman, A. S. (1994). New microphysics sensor for aircraft use. *Atmospheric Research*, *31*(4), 235–252. https://doi.org/10.1016/0169-8095(94)90001-9

Goren, T. and Rosenfeld, D. (2012). Satellite observations of ship emission induced transitions from broken to closed cell marine stratocumulus over large areas, Journal of Geophysical Research: Atmospheres, 117(D17), doi:10.1029/2012JD017981

Gunthe, S. S., King, S. M., Rose, D., Chen, Q., Roldin, P., Farmer, D. K., et al. (2009). Cloud condensation nuclei in pristine tropical rainforest air of Amazonia: size-resolved measurements and modeling of atmospheric aerosol composition and CCN activity. *Atmospheric Chemistry and Physics*, *9*(19), 7551–7575. https://doi.org/10.5194/acp-9-7551-2009

Hallquist, M., Wenger, J. C., Baltensperger, U., Rudich, Y., Simpson, D., Claeys, M., et al. (2009). The formation, properties and impact of secondary organic aerosol: current and emerging issues. Atmospheric Chemistry and Physics, 9(14), 5155–5236. https://doi.org/10.5194/acp-9-5155-2009

Heald, C. L., Jacob, D. J., Park, R. J., Russell, L. M., Huebert, B. J., Seinfeld, J. H., et al. (2005). A large organic aerosol source in the free troposphere missing from current models. Geophysical Research Letters, 32(18). https://doi.org/10.1029/2005GL023831

Hegg, D. A., Covert, D. S., Jonsson, H., & Covert, P. A. (2005). Determination of the Transmission Efficiency of an Aircraft Aerosol Inlet. *Aerosol Science and Technology*, *39*(10), 966–971. https://doi.org/10.1080/02786820500377814

Hegg, D. A., Covert, D. S., & Jonsson, H. H. (2008). Measurements of size-resolved hygroscopicity in the California coastal zone. *Atmos. Chem. Phys.*, *8*(23), 7193–7203. https://doi.org/10.5194/acp-8-7193-2008

Hegg, D. A., Covert, D. S., Jonsson, H. H., & Woods, R. K. (2010). The contribution of anthropogenic aerosols to aerosol light-scattering and CCN activity in the California coastal zone. *Atmos. Chem. Phys.*, *10*(15), 7341–7351. https://doi.org/10.5194/acp-10-7341-2010

Hersey, S. P., Sorooshian, A., Murphy, S. M., Flagan, R. C., & Seinfeld, J. H. (2009). Aerosol hygroscopicity in the marine atmosphere: a closure study using high-time-resolution, multiple-RH DASH-SP and size-resolved C-ToF-AMS data. *Atmospheric Chemistry and Physics*, *9*(7), 2543–2554. https://doi.org/10.5194/acp-9-2543-2009

Hildebrandt, L., Kostenidou, E., Lanz, V. A., Prevot, A. S. H., Baltensperger, U., Mihalopoulos, N., et al. (2011). Sources and atmospheric processing of organic aerosol in the Mediterranean: insights from aerosol mass spectrometer factor analysis. Atmos. Chem. Phys., 11(23), 12499–12515. https://doi.org/10.5194/acp-11-12499-2011

Huang, S., Wu, Z., Poulain, L., Pinxteren, M. van, Merkel, M., Assmann, D., et al. (2018). Source apportionment of the organic aerosol over the Atlantic Ocean from 53° N to 53°S: significant contributions from marine emissions and long-range transport. Atmospheric Chemistry and Physics, 18(24), 18043–18062. https://doi.org/10.5194/acp-18-18043-2018

Jimenez, J. L., Canagaratna, M. R., Donahue, N. M., Prevot, A. S. H., Zhang, Q., Kroll, J. H., et al. (2009). Evolution of Organic Aerosols in the Atmosphere. *Science*, *326*(5959), 1525–1529. https://doi.org/10.1126/science.1180353

Jimenez, J. L., Jayne, J. T., Shi, Q., Kolb, C. E., Worsnop, D. R., Yourshaw, I., et al. (2003). Ambient aerosol sampling using the Aerodyne Aerosol Mass Spectrometer. Journal of Geophysical Research: Atmospheres, 108(D7). https://doi.org/10.1029/2001JD001213

Kanakidou, M., Seinfeld, J. H., Pandis, S. N., Barnes, I., Dentener, F. J., Facchini, M. C., et al. (2005). Organic aerosol and global climate modelling: a review. *Atmospheric Chemistry and Physics*, *5*(4), 1053–1123. https://doi.org/10.5194/acp-5-1053-2005

Kawana, K., Nakayama, T., & Mochida, M. (2016). Hygroscopicity and CCN activity of atmospheric aerosol particles and their relation to organics: Characteristics of urban aerosols in Nagoya, Japan. Journal of Geophysical Research: Atmospheres, 121(8), 4100–4121. https://doi.org/10.1002/2015JD023213

Köhler, H. (1936). The nucleus in and the growth of hygroscopic droplets. Transactions of the Faraday Society, 32(0), 1152–1161. https://doi.org/10.1039/TF9363201152

Kreidenweis, S. M., & Asa-Awuku, A. (2014). 5.13 - Aerosol Hygroscopicity: Particle Water Content and Its Role in Atmospheric Processes. In H. D. Holland & K. K. Turekian (Eds.), *Treatise on Geochemistry (Second Edition)* (pp. 331–361). Oxford: Elsevier. https://doi.org/10.1016/B978-0-08-095975-7.00418-6

Lack, D. A., Cappa, C. D., Langridge, J., Bahreini, R., Buffaloe, G., Brock, C., et al. (2011). Impact of Fuel Quality Regulation and Speed Reductions on Shipping Emissions: Implications for Climate and Air Quality. *Environmental Science & Technology*, *45*(20), 9052–9060. https://doi.org/10.1021/es2013424

Lambe, A. T., Onasch, T. B., Massoli, P., Croasdale, D. R., Wright, J. P., Ahern, A. T., et al. (2011). Laboratory studies of the chemical composition and cloud condensation nuclei (CCN) activity of secondary organic aerosol (SOA) and oxidized primary organic aerosol (OPOA). *Atmospheric Chemistry and Physics*, *11*(17), 8913–8928. https://doi.org/10.5194/acp-11-8913-2011

Lance, S., Nenes, A., Medina, J., & Smith, J. N. (2006). Mapping the Operation of the DMT Continuous Flow CCN Counter. *Aerosol Science and Technology*, *40*(4), 242–254. https://doi.org/10.1080/02786820500543290

Lance, S., Nenes, A., Mazzoleni, C., Dubey, M. K., Gates, H., Varutbangkul, V., et al. (2009). Cloud condensation nuclei activity, closure, and droplet growth kinetics of Houston aerosol during the Gulf of Mexico Atmospheric Composition and Climate Study (GoMACCS). *Journal of Geophysical Research: Atmospheres*, *114*(D7). https://doi.org/10.1029/2008JD011699

Latham J., Rasch P., Chen C.-C., Kettles L., Gadian A., Gettelman A., Morrison H., Bower K. and Choularton T. (2008). Global temperature stabilization via controlled albedo enhancement of low-level maritime clouds, *Philosophical Transactions of the Royal Society A: Mathematical, Physical and Engineering Sciences, 366(1882),* 3969–3987, doi:10.1098/rsta.2008.0137.

Levin, E. J. T., Prenni, A. J., Palm, B. B., Day, D. A., Campuzano-Jost, P., Winkler, P. M., et al. (2014). Size-resolved aerosol composition and its link to hygroscopicity at a forested site in Colorado. *Atmos. Chem. Phys.*, *14*(5), 2657–2667. https://doi.org/10.5194/acp-14-2657-2014

Liu, X., & Wang, J. (2010). How important is organic aerosol hygroscopicity to aerosol indirect forcing? *Environmental Research Letters*, *5*(4), 044010. https://doi.org/10.1088/1748-9326/5/4/044010

MacDonald, A. B., Dadashazar, H., Chuang, P. Y., Crosbie, E., Wang, H., Wang, Z., et al. (2018). Characteristic Vertical Profiles of Cloud Water Composition in Marine Stratocumulus Clouds and Relationships With Precipitation. *Journal of Geophysical Research: Atmospheres*, *123*(7), 3704–3723. https://doi.org/10.1002/2017JD027900

Mardi, A. H., Dadashazar, H., MacDonald, A. B., Braun, R. A., Crosbie, E., Xian, P., et al. (2018). Biomass Burning Plumes in the Vicinity of the California Coast: Airborne Characterization of Physicochemical Properties, Heating Rates, and Spatiotemporal Features. Journal of Geophysical Research: Atmospheres, 123(23), 13,560-13,582. https://doi.org/10.1029/2018JD029134

Massoli, P., Lambe, A. T., Ahern, A. T., Williams, L. R., Ehn, M., Mikkilä, J., et al. (2010). Relationship between aerosol oxidation level and hygroscopic properties of laboratory generated secondary organic aerosol (SOA) particles. *Geophysical Research Letters*, *37*(24). https://doi.org/10.1029/2010GL045258

Mauldin, R. L., Tanner, D. J., Heath, J. A., Huebert, B. J., & Eisele, F. L. (1999). Observations of H2SO4 and MSA during PEM-Tropics-A. *Journal of Geophysical Research: Atmospheres*, *104*(D5), 5801–5816. https://doi.org/10.1029/98JD02612

McFiggans, G., Artaxo, P., Baltensperger, U., Coe, H., Facchini, M. C., Feingold, G., et al. (2006). The effect of physical and chemical aerosol properties on warm cloud droplet activation. *Atmos. Chem. Phys.*, *6*(9), 2593–2649. https://doi.org/10.5194/acp-6-2593-2006

Medina J., Nenes A., Sotiropoulou R.-E. P., Cottrell L. D., Ziemba L. D., Beckman P. J., & Griffin R. J. (2007). Cloud condensation nuclei closure during the International Consortium for Atmospheric Research on Transport and Transformation 2004

campaign: Effects of size-resolved composition. *Journal of Geophysical Research: Atmospheres*, *112*(D10). https://doi.org/10.1029/2006JD007588

Mei, F., Setyan, A., Zhang, Q. and Wang, J. (2013): CCN activity of organic aerosols observed downwind of urban emissions during CARES, Atmospheric Chemistry and Physics, 13(24), 12155–12169, doi:https://doi.org/10.5194/acp-13-12155-2013.

Middlebrook, A. M., Bahreini, R., Jimenez, J. L., & Canagaratna, M. R. (2012). Evaluation of Composition-Dependent Collection Efficiencies for the Aerodyne Aerosol Mass Spectrometer using Field Data. *Aerosol Science and Technology*, *46*(3), 258–271. https://doi.org/10.1080/02786826.2011.620041

Modini, R. L., Frossard, A. A., Ahlm, L., Russell, L. M., Corrigan, C. E., Roberts, G. C., et al. (2015). Primary marine aerosol-cloud interactions off the coast of California. Journal of Geophysical Research: Atmospheres, 120(9), 4282–4303. https://doi.org/10.1002/2014JD022963

Moore, R. H., Bahreini, R., Brock, C. A., Froyd, K. D., Cozic, J., Holloway, J. S., et al. (2011). Hygroscopicity and composition of Alaskan Arctic CCN during April 2008. *Atmos. Chem. Phys.*, *11*(22), 11807–11825. https://doi.org/10.5194/acp-11-11807-2011

Moore, R. H., Cerully, K., Bahreini, R., Brock, C. A., Middlebrook, A. M., & Nenes, A. (2012). Hygroscopicity and composition of California CCN during summer 2010. *Journal of Geophysical Research: Atmospheres*, *117*(D21). https://doi.org/10.1029/2011JD017352

Murphy, S. M., Agrawal, H., Sorooshian, A., Padró, L. T., Gates, H., Hersey, S., et al. (2009). Comprehensive Simultaneous Shipboard and Airborne Characterization of Exhaust from a Modern Container Ship at Sea. *Environmental Science & Technology*, *43*(13), 4626–4640. https://doi.org/10.1021/es802413j

Nenes, A., S. N. Pandis, & C. Pilinis (1998), ISORROPIA: A new thermodynamic equilibrium model for multiphase multicomponent inorganic aerosols, Aqua. Geochem., 4, 123–152.

Ng, N. L., Canagaratna, M. R., Zhang, Q., Jimenez, J. L., Tian, J., Ulbrich, I. M., et al. (2010). Organic aerosol components observed in Northern Hemispheric datasets from Aerosol Mass Spectrometry. Atmospheric Chemistry and Physics, 10(10), 4625–4641. https://doi.org/10.5194/acp-10-4625-2010

Oreopoulos, L. and Platnick, S.: Radiative susceptibility of cloudy atmospheres to droplet number perturbations: 2. Global analysis from MODIS, Journal of Geophysical Research: Atmospheres, 113(D14), doi:10.1029/2007JD009655, 2008.

Ovadnevaite, J., Zuend, A., Laaksonen, A., Sanchez, K. J., Roberts, G., Ceburnis, D., et al. (2017). Surface tension prevails over solute effect in organic-influenced cloud droplet activation. Nature, 546(7660), 637–641. https://doi.org/10.1038/nature22806

Paatero, P., & Tapper, U. (1994). Positive matrix factorization: A non-negative factor model with optimal utilization of error estimates of data values. *Environmetrics*, *5*(2), 111–126. https://doi.org/10.1002/env.3170050203

Petters, M. D., & Kreidenweis, S. M. (2007). A single parameter representation of hygroscopic growth and cloud condensation nucleus activity. *Atmos. Chem. Phys.*, *7*(8), 1961–1971. https://doi.org/10.5194/acp-7-1961-2007

Platnick, S. & Twomey, S. (1994): Determining the Susceptibility of Cloud Albedo to Changes in Droplet Concentration with the Advanced Very High Resolution Radiometer, J. Appl. Meteor., 33(3), 334–347, doi:10.1175/1520-0450(1994)033<0334:DTSOCA>2.0.CO;2.

Prabhakar, G., Ervens, B., Wang, Z., Maudlin, L. C., Coggon, M. M., Jonsson, H. H., et al. (2014). Sources of nitrate in stratocumulus cloud water: Airborne measurements during the 2011 E-PEACE and 2013 NiCE studies. Atmospheric Environment, 97, 166–173. https://doi.org/10.1016/j.atmosenv.2014.08.019

Pringle, K. J., Tost, H., Pozzer, A., Pöschl, U., & Lelieveld, J. (2010). Global distribution of the effective aerosol hygroscopicity parameter for CCN activation. *Atmospheric Chemistry and Physics*, *10*(12), 5241–5255. https://doi.org/10.5194/acp-10-5241-2010

Pruppacher, H. R., & Klett, J. D. (1997) Microphysics of Clouds and Precipitation, Kluwer, Dordrecht, The Netherlands

Quinn, P. K., Bates, T. S., Coffman, D. J. and Covert, D. S.: Influence of particle size and chemistry on the cloud nucleating properties of aerosols, Atmospheric Chemistry and Physics, 8(4), 1029–1042, doi:https://doi.org/10.5194/acp-8-1029-2008, 2008.

Raes, F. (1995). Entrainment of free tropospheric aerosols as a regulating mechanism for cloud condensation nuclei in the remote marine boundary layer. *Journal of Geophysical Research: Atmospheres*, *100*(D2), 2893–2903. https://doi.org/10.1029/94JD02832

Randall, D. A., Coakley, J. A., Fairall, C. W., Kropfli, R. A., & Lenschow, D. H. (1984). Outlook for Research on Subtropical Marine Stratiform Clouds. Bulletin of the American Meteorological Society, 65(12), 1290–1301. https://doi.org/10.1175/1520-0477(1984)065<1290:OFROSM>2.0.CO;2

Reutter, P., Su, H., Trentmann, J., Simmel, M., Rose, D., Gunthe, S. S., Wernli, H., Andreae, M. O. and Pöschl, U.: Aerosol- and updraft-limited regimes of cloud droplet formation: influence of particle number, size and hygroscopicity on the activation of cloud condensation nuclei (CCN), Atmospheric Chemistry and Physics, 9(18), 7067–7080, doi:https://doi.org/10.5194/acp-9-7067-2009, 2009.

Roberts, G. C., & Nenes, A. (2005). A Continuous-Flow Streamwise Thermal-Gradient CCN Chamber for Atmospheric Measurements. *Aerosol Science and Technology*, *39*(3), 206–221. https://doi.org/10.1080/027868290913988

Roberts G., Mauger G., Hadley O., & Ramanathan V. (2006). North American and Asian aerosols over the eastern Pacific Ocean and their role in regulating cloud condensation nuclei. *Journal of Geophysical Research: Atmospheres*, *111*(D13). https://doi.org/10.1029/2005JD006661

Roberts, G. C., Day, D. A., Russell, L. M., Dunlea, E. J., Jimenez, J. L., Tomlinson, J. M., et al. (2010). Characterization of particle cloud droplet activity and composition in the free troposphere and the boundary layer during INTEX-B. Atmospheric Chemistry and Physics, 10(14), 6627–6644. https://doi.org/10.5194/acp-10-6627-2010

Rose, D., Gunthe, S. S., Mikhailov, E., Frank, G. P., Dusek, U., Andreae, M. O., & Pöschl, U. (2008). Calibration and measurement uncertainties of a continuous-flow cloud condensation nuclei counter (DMT-CCNC): CCN activation of ammonium sulfate and sodium chloride aerosol particles in theory and experiment. *Atmos. Chem. Phys.*, *8*(5), 1153–1179. https://doi.org/10.5194/acp-8-1153-2008

Rose, D., Nowak, A., Achtert, P., Wiedensohler, A., Hu, M., Shao, M., et al. (2010). Cloud condensation nuclei in polluted air and biomass burning smoke near the mega-city Guangzhou, China – Part 1: Size-resolved measurements and implications for the modeling of aerosol particle hygroscopicity and CCN activity. *Atmospheric Chemistry and Physics*, *10*(7), 3365–3383. https://doi.org/10.5194/acp-10-3365-2010

Rose, D., Gunthe, S. S., Su, H., Garland, R. M., Yang, H., Berghof, M., et al. (2011). Cloud condensation nuclei in polluted air and biomass burning smoke near the mega-city Guangzhou, China – Part 2: Size-resolved aerosol chemical composition, diurnal cycles, and externally mixed weakly CCN-active soot particles. *Atmospheric Chemistry and Physics*, *11*(6), 2817–2836. https://doi.org/10.5194/acp-11-2817-2011

Rosenfeld, D.: Aerosol-Cloud Interactions Control of Earth Radiation and Latent Heat Release Budgets, Space Sci Rev, 125(1), 149–157, doi:10.1007/s11214-006-9053-6, 2006.

Rosenfeld, D., Andreae, M. O., Asmi, A., Chin, M., Leeuw, G. de, Donovan, D. P., et al. (2014). Global observations of aerosol-cloud-precipitation-climate interactions. *Reviews of Geophysics*, *52*(4), 750–808. https://doi.org/10.1002/2013RG000441

Rosenfeld, D., Zhu, Y., Wang, M., Zheng, Y., Goren, T. and Yu, S.: Aerosol-driven droplet concentrations dominate coverage and water of oceanic low-level clouds, Science, 363(6427), eaav0566, doi:10.1126/science.aav0566, 2019.

Rothenberg, D., Avramov, A., & Wang, C. (2018). On the representation of aerosol activation and its influence on model-derived estimates of the aerosol indirect effect. *Atmospheric Chemistry and Physics*, *18*(11), 7961–7983. https://doi.org/10.5194/acp-18-7961-2018

Royalty, T. M., Phillips, B. N., Dawson, K. W., Reed, R., Meskhidze, N., & Petters, M. D. (2017). Aerosol Properties Observed in the Subtropical North Pacific Boundary Layer. Journal of Geophysical Research: Atmospheres, 122(18), 9990–10,012. https://doi.org/10.1002/2017JD026897

Russell, L. M., Sorooshian, A., Seinfeld, J. H., Albrecht, B. A., Nenes, A., Ahlm, L., et al. (2013). Eastern Pacific Emitted Aerosol Cloud Experiment. *Bulletin of the American Meteorological Society*, *94*(5), 709–729. https://doi.org/10.1175/BAMS-D-12-00015.1

Sanchez, K. J., Russell, L. M., Modini, R. L., Frossard, A. A., Ahlm, L., Corrigan, C. E., Roberts, G. C., Hawkins, L. N., Schroder, J. C., Bertram, A. K., Zhao, R., Lee, A. K. Y., Lin, J. J., Nenes, A., Wang, Z., Wonaschütz, A., Sorooshian, A., Noone, K. J., Jonsson, H., Toom, D., Macdonald, A. M., Leaitch, W. R. and Seinfeld, J. H.: Meteorological and aerosol effects on marine cloud microphysical properties, Journal of Geophysical Research: Atmospheres, 121(8), 4142–4161, doi:10.1002/2015JD024595, 2016.

Sánchez-Gácita, M., Longo, K. M., Freire, J. L. M., Freitas, S. R., & Martin, S. T. (2017). Impact of mixing state and hygroscopicity on CCN activity of biomass burning aerosol in Amazonia. *Atmospheric Chemistry and Physics*, *17*(3), 2373–2392. https://doi.org/10.5194/acp-17-2373-2017

Schmale, J., Schneider, J., Nemitz, E., Tang, Y. S., Dragosits, U., Blackall, T. D., et al. (2013). Sub-Antarctic marine aerosol: dominant contributions from biogenic sources. Atmos. Chem. Phys., 13(17), 8669–8694. https://doi.org/10.5194/acp-13-8669-2013

Seinfeld, J. H., Bretherton, C., Carslaw, K. S., Coe, H., DeMott, P. J., Dunlea, E. J., Feingold, G., Ghan, S., Guenther, A. B., Kahn, R., Kraucunas, I., Kreidenweis, S. M., Molina, M. J., Nenes, A., Penner, J. E., Prather, K. A., Ramanathan, V., Ramaswamy, V., Rasch, P. J., Ravishankara, A. R., Rosenfeld, D., Stephens, G. and Wood, R.: Improving our fundamental understanding of the role of aerosol−cloud interactions in

the climate system, PNAS, 113(21), 5781–5790, doi:10.1073/pnas.1514043113, 2016.

Sorooshian, A., Lu, M.-L., Brechtel, F. J., Jonsson, H., Feingold, G., Flagan, R. C., & Seinfeld, J. H. (2007a). On the Source of Organic Acid Aerosol Layers above Clouds. *Environmental Science & Technology*, *41*(13), 4647–4654. https://doi.org/10.1021/es0630442

Sorooshian, A., Ng, N. L., Chan, A. W. H., Feingold, G., Flagan, R. C., & Seinfeld, J. H. (2007b). Particulate organic acids and overall water-soluble aerosol composition measurements from the 2006 Gulf of Mexico Atmospheric Composition and Climate Study (GoMACCS). *Journal of Geophysical Research: Atmospheres*, *112*(D13). https://doi.org/10.1029/2007JD008537

Sorooshian A., Padró Luz T., Nenes A., Feingold G., McComiskey A., Hersey S. P., et al. (2009). On the link between ocean biota emissions, aerosol, and maritime clouds: Airborne, ground, and satellite measurements off the coast of California. *Global Biogeochemical Cycles*, *23*(4). https://doi.org/10.1029/2009GB003464

Sorooshian, A., MacDonald, A. B., Dadashazar, H., Bates, K. H., Coggon, M. M., Craven, J. S., et al. (2018). A multi-year data set on aerosol-cloud-precipitation-meteorology interactions for marine stratocumulus clouds. *Scientific Data*, *5*. https://doi.org/10.1038/sdata.2018.26

Sorooshian, A., Anderson, B., Bauer, S. E., Braun, R. A., Cairns, B., Crosbie, E., et al. (2019). Aerosol-Cloud-Meteorology Interaction Airborne Field Investigations: Using Lessons Learned from the US West Coast in the Design of ACTIVATE off the US East Coast. *Bulletin of the American Meteorological Society*. https://doi.org/10.1175/BAMS-D-18-0100.1

Sorooshian, A., et al. (2017), A Multi-Year Data Set on Aerosol-Cloud-Precipitation-Meteorology Interactions for Marine Stratocumulus Clouds. figshare. Dataset. https://doi.org/10.6084/m9.figshare.5099983.v10

Sotiropoulou, R.-E. P., Nenes, A., Adams, P. J., & Seinfeld, J. H. (2007). Cloud condensation nuclei prediction error from application of Köhler theory: Importance for the aerosol indirect effect. *Journal of Geophysical Research: Atmospheres*, *112*(D12). https://doi.org/10.1029/2006JD007834

Stein, A. F., Draxler, R. R., Rolph, G. D., Stunder, B. J. B., Cohen, M. D., & Ngan, F. (2015). NOAA's HYSPLIT Atmospheric Transport and Dispersion Modeling System. Bulletin of the American Meteorological Society, 96(12), 2059–2077. https://doi.org/10.1175/BAMS-D-14-00110.1

Stevens, B., & Brenguier, J.-L. (2009). *Cloud-controlling Factors: Low Clouds*. The MIT Press. Retrieved from https://mitpress.universitypressscholarship.com/view/10.7551/mitpress/9780262012874.001.0001/upso-9780262012874-chapter-8

Suda, S. R., Petters, M. D., Yeh, G. K., Strollo, C., Matsunaga, A., Faulhaber, A., et al. (2014). Influence of Functional Groups on Organic Aerosol Cloud Condensation Nucleus Activity. Environmental Science & Technology, 48(17), 10182–10190. https://doi.org/10.1021/es502147y

Thalman, R., Sá, S. S. de, Palm, B. B., Barbosa, H. M. J., Pöhlker, M. L., Alexander, M. L., et al. (2017). CCN activity and organic hygroscopicity of aerosols downwind of an urban region in central Amazonia: seasonal and diel variations and impact of anthropogenic emissions. *Atmospheric Chemistry and Physics*, *17*(19), 11779–11801. https://doi.org/10.5194/acp-17-11779-2017

Twomey, S.: The Influence of Pollution on the Shortwave Albedo of Clouds, J. Atmos. Sci., 34(7), 1149–1152, doi:10.1175/1520-0469(1977)034<1149:TIOPOT>2.0.CO;2, 1977.

Ueda, S., Miura, K., Kawata, R., Furutani, H., Uematsu, M., Omori, Y., & Tanimoto, H. (2016). Number–size distribution of aerosol particles and new particle formation events in tropical and subtropical Pacific Oceans. *Atmospheric Environment*, *142*, 324–339. https://doi.org/10.1016/j.atmosenv.2016.07.055

Ulbrich, I. M., Canagaratna, M. R., Zhang, Q., Worsnop, D. R., & Jimenez, J. L. (2009). Interpretation of organic components from Positive Matrix Factorization of aerosol mass spectrometric data. Atmospheric Chemistry and Physics, 9(9), 2891–2918. https://doi.org/10.5194/acp-9-2891-2009

VanReken T. M., Rissman T. A., Roberts G. C., Varutbangkul V., Jonsson H. H., Flagan R. C., & Seinfeld J. H. (2003). Toward aerosol/cloud condensation nuclei (CCN) closure during CRYSTAL-FACE. *Journal of Geophysical Research: Atmospheres*, *108*(D20). https://doi.org/10.1029/2003JD003582

Wang, J., Lee, Y.-N., Daum, P. H., Jayne, J., & Alexander, M. L. (2008). Effects of aerosol organics on cloud condensation nucleus (CCN) concentration and first indirect aerosol effect. *Atmospheric Chemistry and Physics*, *8*(21), 6325–6339. https://doi.org/10.5194/acp-8-6325-2008

Wang, J., Cubison, M. J., Aiken, A. C., Jimenez, J. L., & Collins, D. R. (2010). The importance of aerosol mixing state and size-resolved composition on CCN concentration and the variation of the importance with atmospheric aging of aerosols.

Atmospheric Chemistry and Physics, *10*(15), 7267–7283. https://doi.org/10.5194/acp-10-7267-2010

Wang, J., Shilling, J. E., Liu, J., Zelenyuk, A., Bell, D. M., Petters, M. D., et al. (2019). Cloud droplet activation of secondary organic aerosol is mainly controlled by molecular weight, not water solubility. *Atmospheric Chemistry and Physics*, *19*(2), 941–954. https://doi.org/10.5194/acp-19-941-2019

Wang, Z., Ramirez, M. M., Dadashazar, H., MacDonald, A. B., Crosbie, E., Bates, K. H., et al. (2016). Contrasting cloud composition between coupled and decoupled marine boundary layer clouds. *Journal of Geophysical Research: Atmospheres*, *121*(19), 11,679-11,691. https://doi.org/10.1002/2016JD025695

Ward, D. S., Eidhammer, T., Cotton, W. R., & Kreidenweis, S. M. (2010). The role of the particle size distribution in assessing aerosol composition effects on simulated droplet activation. *Atmospheric Chemistry and Physics*, *10*(12), 5435–5447. https://doi.org/10.5194/acp-10-5435-2010

Wiedensohler, A., Birmili, W., Nowak, A., Sonntag, A., Weinhold, K., Merkel, M., et al. (2012). Mobility particle size spectrometers: harmonization of technical standards and data structure to facilitate high quality long-term observations of atmospheric particle number size distributions. Atmospheric Measurement Techniques, 5(3), 657–685. https://doi.org/10.5194/amt-5-657-2012

Wonaschütz, A., Coggon, M., Sorooshian, A., Modini, R., Frossard, A. A., Ahlm, L., et al. (2013). Hygroscopic properties of smoke-generated organic aerosol particles emitted in the marine atmosphere. Atmospheric Chemistry and Physics, 13(19), 9819–9835. https://doi.org/10.5194/acp-13-9819-2013

Wood, R.: Stratocumulus Clouds, Mon. Wea. Rev., 140(8), 2373–2423, doi:10.1175/MWR-D-11-00121.1, 2012.

Yakobi-Hancock, J. D., Ladino, L. A., Bertram, A. K., Huffman, J. A., Jones, K., Leaitch, W. R., et al. (2014). CCN activity of size-selected aerosol at a Pacific coastal location. Atmospheric Chemistry and Physics, 14(22), 12307–12317. https://doi.org/10.5194/acp-14-12307-2014

Zhang, Q., Worsnop, D. R., Canagaratna, M. R., & Jimenez, J. L. (2005). Hydrocarbon-like and oxygenated organic aerosols in Pittsburgh: insights into sources and processes of organic aerosols. Atmospheric Chemistry and Physics, 5(12), 3289–3311. https://doi.org/10.5194/acp-5-3289-2005

Zhang, Q., Jimenez, J. L., Canagaratna, M. R., Ulbrich, I. M., Ng, N. L., Worsnop, D. R., & Sun, Y. (2011). Understanding atmospheric organic aerosols via factor analysis

of aerosol mass spectrometry: a review. Analytical and Bioanalytical Chemistry, 401(10), 3045–3067. https://doi.org/10.1007/s00216-011-5355-y

Zhao, D. F., Buchholz, A., Kortner, B., Schlag, P., Rubach, F., Kiendler-Scharr, A., et al. (2015). Size-dependent hygroscopicity parameter (κ) and chemical composition of secondary organic cloud condensation nuclei. *Geophysical Research Letters*, *42*(24), 10,920-10,928. https://doi.org/10.1002/2015GL066497

Zheng, Y., Rosenfeld, D., & Li, Z. (2016). Quantifying cloud base updraft speeds of marine stratocumulus from cloud top radiative cooling. *Geophysical Research Letters*, *43*(21), 11,407-11,413. https://doi.org/10.1002/2016GL071185

A p p e n d i x A

Rapid hydrolysis of tertiary isoprene nitrate efficiently removes NO_x from the atmosphere

Krystal T. Vasquez , John D. Crounse , Benjamin C. Schulze , Kelvin H. Bates, Alexander P. Teng, Lu Xu, Hannah M. Allen, and Paul O. Wennberg, *Proceedings of the National Academy of Sciences*, pp. 33011-33016, doi: 10.1073/pnas.2017442117

Rapid hydrolysis of tertiary isoprene nitrate efficiently removes NO_x from the atmosphere

Krystal T. Vasquez[a], John D. Crounse[b], Benjamin C. Schulze[b], Kelvin H. Bates[a,1], Alexander P. Teng[b,2], Lu Xu[b], Hannah M. Allen[a], and Paul O. Wennberg[b,c,3]

[a]Division of Chemistry and Chemical Engineering, California Institute of Technology, Pasadena, CA 91125; [b]Division of Geological and Planetary Sciences, California Institute of Technology, Pasadena, CA 91125; and [c]Division of Engineering and Applied Sciences, California Institute of Technology, Pasadena, CA 91125

Edited by Mark Thiemens, University of California San Diego, La Jolla, CA, and approved November 3, 2020 (received for review August 17, 2020)

The formation of a suite of isoprene-derived hydroxy nitrate (IHN) isomers during the OH-initiated oxidation of isoprene affects both the concentration and distribution of nitrogen oxide free radicals (NO_x). Experiments performed in an atmospheric simulation chamber suggest that the lifetime of the most abundant isomer, 1,2-IHN, is shortened significantly by a water-mediated process (leading to nitric acid formation), while the lifetime of a similar isomer, 4,3-IHN, is not. Consistent with these chamber studies, NMR kinetic experiments constrain the 1,2-IHN hydrolysis lifetime to less than 10 s in deuterium oxide (D_2O) at 298 K, whereas the 4,3-IHN isomer has been observed to hydrolyze much less efficiently. These laboratory findings are used to interpret observations of the IHN isomer distribution in ambient air. The IHN isomer ratio (1,2-IHN to 4,3-IHN) in a high NO_x environment decreases rapidly in the afternoon, which is not explained using known gas-phase chemistry. When simulated with an observationally constrained model, we find that an additional loss process for the 1,2-IHN isomer with a time constant of about 6 h best explains our atmospheric measurements. Using estimates for 1,2-IHN Henry's law constant and atmospheric liquid water volume, we show that condensed-phase hydrolysis of 1,2-IHN can account for this loss process. Simulations from a global chemistry transport model show that the hydrolysis of 1,2-IHN accounts for a substantial fraction of NO_x lost (and HNO_3 produced), resulting in large impacts on oxidant formation, especially over forested regions.

atmospheric chemistry | isoprene | hydrolysis | organic nitrates | NO_x

The formation of organic nitrates during the oxidation of volatile organic compounds (VOCs) serves to sequester nitrogen oxides (NO_x = NO + NO_2; NO_x, nitrogen oxide free radicals). This chemistry is expected to become increasingly important as NO_x levels decline (1), as has been occurring in the United States (2). Because the formation and subsequent fate of organic nitrates alters the concentrations and distributions of NO_x in the atmosphere, they, by extension, also significantly impact the production of tropospheric ozone and organic aerosols (3–6), which have known impacts on the environment and human health.

Due to the sheer abundance and reactivity of isoprene in the boundary layer, organic nitrates created from its oxidation are believed to greatly affect the atmospheric NO_x lifetime (7–15). Isoprene-derived hydroxy nitrates (IHNs) are formed primarily during the OH oxidation of isoprene in the presence of NO (16) (Scheme 1). Recent laboratory measurements suggest the branching ratio for this pathway (α) is ~13% (17), which is higher than many previous estimates (18). While eight IHN isomers can form (17), two of these isomers (1,2-IHN and 4,3-IHN; Scheme 1) make up the majority of the total IHN yield at atmospherically relevant conditions. Once formed, current understanding suggests that IHNs are primarily lost from the atmosphere through deposition and chemical oxidation (3, 18, 19).

The relative importance of the IHN-loss pathways determines the extent to which NO_x is recycled back into the atmosphere. For instance, deposition results in the permanent removal of NO_x, but the IHN lifetime against deposition under typical atmospheric conditions is relatively long: $\tau_{dep} \approx 24$ h for $v_{dep} = 1.7$ cm s^{-1} (20) and a boundary layer height of 1.5 km. On the other hand, chemical oxidation by OH is more important, providing a lifetime of 9.3 and 6.9 h (assuming [OH] = 1×10^6 molecules cm^{-3}) for 1,2-IHN and 4,3-IHN, respectively (18). Although studies have shown that the nitrate moiety typically remains attached to these molecules following this chemistry (particularly for 4,3-IHN), subsequent photooxidation of second-generation products can still contribute to significant NO_x recycling (21, 22).

Model simulations of field measurements tend to overestimate daytime concentrations of IHN (19, 23–26). While this might be partially due to assumptions made regarding the isomer distribution of isoprene peroxy radicals (RO_2) and α, this discrepancy has also been attributed to a missing IHN sink. Several possible sinks have been hypothesized. It has been suggested that the tertiary nitrate group on 1,2-IHN allows this molecule to hydrolyze rapidly in clouds or in aerosol (24, 27–30). This loss

Significance

Isoprene-derived hydroxy nitrates (IHNs) play a significant role in controlling the lifetime of NO_x. Here, we showcase isomer-specific measurements of IHN in ambient air, which have allowed us to quantify real-time changes in its isomer distribution. These measurements show that 1,2-IHN undergoes a rapid loss not experienced by the 4,3-IHN isomer. Laboratory studies suggest this sink is likely condensed-phase hydrolysis, forming HNO_3. To match observations, one-dimensional box-model simulations require additional loss rates (here, assigned to hydrolysis) similar in magnitude to the accounted loss processes (OH oxidation and dry deposition). Global simulations included in this process show reduced ozone levels and assign a significant fraction of HNO_3 production to this mechanism within the lower atmosphere.

Author contributions: J.D.C. and P.O.W. designed research; K.T.V., J.D.C., B.C.S., K.H.B., A.P.T., L.X., H.M.A., and P.O.W. performed research; J.D.C. and P.O.W. contributed new reagents/analytic tools; K.T.V., J.D.C., and A.P.T. analyzed data; and K.T.V., J.D.C., and P.O.W. wrote the paper.

The authors declare no competing interest.

This article is a PNAS Direct Submission.

[1]Present address: Center for the Environment, Harvard University, Cambridge, MA 02138.

[2]Private address: Daly City, CA 94014.

[3]To whom correspondence may be addressed. Email: wennberg@caltech.edu.

This article contains supporting information online at https://www.pnas.org/lookup/suppl/doi:10.1073/pnas.2017442117/-/DCSupplemental.

First published December 10, 2020.

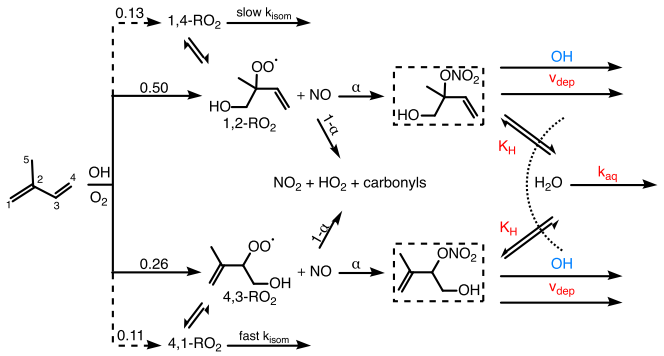

Scheme 1. IHNs are formed through a small, but important, pathway (α) present in the reaction of isoprene and OH (+O_2) in the presence of NO. The dominant pathway ($1-\alpha$) forms NO_2 and promotes ozone production. The formation of the two IHN isomers shown here (1,2-IHN and 4,3-IHN; dashed boxes) represent more than 90% of the IHN produced at atmospherically relevant RO_2 lifetimes (17). We note that the α to 1,2-IHN ($14 \pm 3\%$) is very similar to the α to 4,3-IHN ($13 \pm 3\%$) (18). Once formed, 1,2-IHN and 4,3-IHN can undergo deposition, oxidation, or incorporation into aerosol, where they can hydrolyze. The branching between IHN-loss pathways directly affects isoprene's impact on NO_x and oxidant levels. IHN-loss pathways that result in NO_x recycling are highlighted in blue, while those that result in the permanent loss of NO_x are red.

pathway could contribute significantly to HNO_3 formed over continental regions (28, 31–35). Photolysis has also been proposed (25). Unlike hydrolysis, photolysis of organic nitrates is expected to release NO_2 back into the atmosphere, contributing to tropospheric ozone production downwind of sources (22, 35).

Here, we used newly developed instrumentation (36) to monitor changes in the isomer distribution of IHN during a 2017 summer field study conducted in Pasadena, CA. These ambient observations are interpreted using a combination of laboratory chamber experiments, aqueous hydrolysis experiments, and observationally constrained model simulations. We focus our analysis on the two most abundant isomers, 1,2-IHN and 4,3-IHN. Since 1,2-IHN and 4,3-IHN are thought to undergo similar atmospheric fates (Scheme 1), we use the ratio of their concentrations (1,2-IHN to 4,3-IHN; hereafter, referred to as "IHN isomer ratio," for simplicity) as a proxy for differences in their nonphotochemical loss.

This dataset suggests the 1,2-IHN isomer is rapidly lost via hydrolysis in the atmosphere at a rate competitive with other oxidation and deposition pathways. In addition, global simulations suggest that this loss pathway greatly impacts the global concentration of NO_x, ozone, and nitric acid.

Results and Discussion

Field Observations. Hourly measurements of the ambient concentrations of the IHN isomers were obtained between August 1 and 17, 2017 (37) using a gas chromatography–chemical ionization mass spectrometer (GC-CIMS) deployed atop the main Caltech library (44 m above ground level), which is located on the California Institute of Technology (Caltech) campus in Pasadena, CA: $[OH]_{avg,\ peak} = 5 \times 10^6$ molecules cm^{-3} (38); $[NO]_{avg,\ daytime} =$ 2.5 parts per billion by volume (ppbv). Details of the field site, measurement technique and data processing are provided in *Materials and Methods* and *SI Appendix*.

Daytime observations (1000 to 2000 hours local time) of 1,2-IHN and 4,3-IHN from Caltech (Fig. 1) suggest an additional IHN sink is present in the atmosphere that disproportionately affects the 1,2-IHN isomer. We observed a daily, rapid decline of the IHN isomer ratio starting in the midafternoon (around 1500 hours local time). Chromatograms collected at this site (Fig. 2) (39) illustrate that this was caused by a drop in the concentration of 1,2-IHN relative to 4,3-IHN. However, these observations are not explained using known gas-phase chemistry as the gas-phase lifetime of 1,2-IHN is expected to be longer than 4,3-IHN due to its slower reaction rate with OH (21). This is

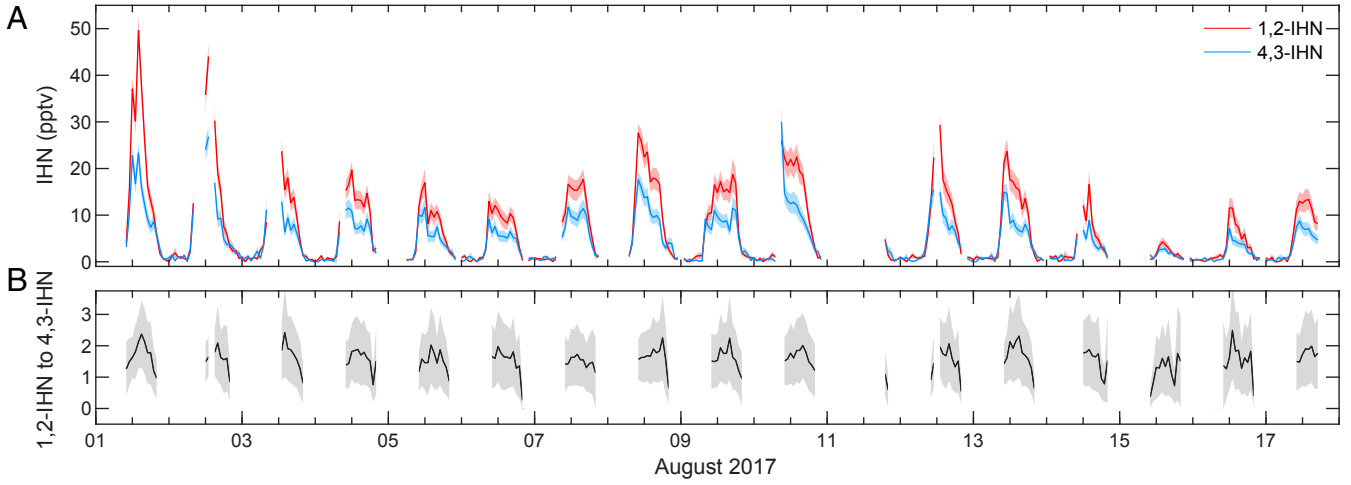

Fig. 1. (*A*) Time series of 1,2-IHN (red) and 4,3-IHN (blue) as measured by the GC-CIMS during the Caltech field study. Solid lines represent the hourly GC measurements, and the shaded regions encompass the error of those measurements. (*B*) The observed daytime (1000 to 2000 hours local time) isomer ratio of 1,2-IHN to 4,3-IHN during the Caltech field study.

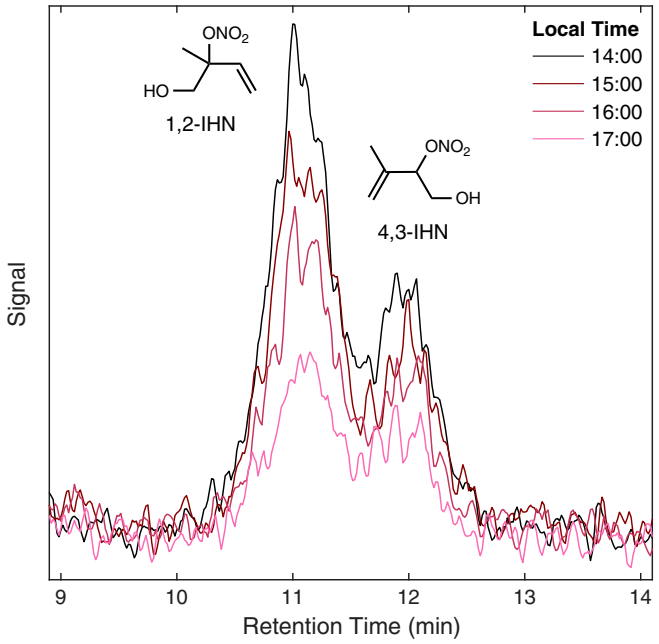

Fig. 2. Four chromatograms of IHN collected during the Caltech field study on August 1, 2017 show that the peak area of 1,2-IHN declines more rapidly than 4,3-IHN in the late afternoon.

verified in Fig. 3, where the IHN isomer ratio simulated with a one-dimensional (1-D) atmospheric model (red) consistently overpredicts the observed ratio (black), with the largest discrepancies occurring in the evening. The model shows that when considering only the gas-phase isoprene chemistry (18) and dry deposition (20), the IHN isomer ratio should steadily increase during this time in contrast with observations.

Laboratory Evidence for IHN Hydrolysis

Chamber Studies. Isoprene-oxidation experiments performed in a 24-m^3 chamber (*SI Appendix*, section 3) suggest that 1,2-IHN is hydrolyzed much faster than 4,3-IHN, lending one possible explanation to the observed trend of the ambient IHN isomer ratio measured at Caltech. In the dark chamber, the lifetime of the 1,2-IHN isomer decreased from 45 min at 50% relative humidity (RH) to 15 min at 85% RH—whereas no change in the 4,3-IHN lifetime was observed. In addition, chromatograms obtained from these experiments (*SI Appendix*, Fig. S2) mirrored those collected in the field (Fig. 2). Accompanying signals of IHN hydrolysis products, such as the isoprene diol and a small yield of 1,4-IHN (17), were observed.

During these experiments, it is likely that IHN hydrolysis was occurring within a condensed-phase reservoir formed by the uptake of water at high RH by salts that had been previously deposited on the chamber walls. Similar experiments with high levels of added ammonium sulphate seed (up to 500 μg m^{-3}) did not measurably alter the decay rate. In contrast, gas-phase experiments performed in a clean 1-m^3 Teflon chamber bag did not show any decay of 1,2-IHN at high RH (>80%) over a 12-h period. Unfortunately, this complicates interpretation of the loss rates observed in the 24-m^3 chamber, as they are likely dependent on the volume of liquid material on the walls, as well as the mixing and transport processes.

^{1}H NMR. As we were unable to provide a quantitative constraint on the hydrolysis loss through the chamber experiments, we use a newly developed synthetic route to 1,2-IHN (*SI Appendix*, section 3) with ^{1}H NMR to probe the kinetics of the 1,2-IHN hydrolysis loss (31). For this experiment, a known volume of synthesized 1,2-IHN was added to a known volume of deuterated chloroform ($CDCl_3$), rapidly mixed, and quickly analyzed using ^{1}H NMR (*SI Appendix*, Fig. S3). In a similar fashion, 1,2-IHN was added to deuterium oxide (D_2O), mixed, and analyzed. No 1,2-IHN ^{1}H NMR signals remained in the D_2O sample (elapsed time from mixing to completion of analysis, <1 min). Based on the signal-to-noise ratio of the 1,2-IHN ^{1}H NMR signals in the CD_3Cl sample, we assign an upper limit of 10 s for the aqueous hydrolysis lifetime of 1,2-IHN in D_2O at 298 K (*SI Appendix*, section 3). For comparison, Jacobs et al. (40) measured the 4,3-IHN hydrolysis lifetime to be approximately 17.5 h in D_2O. The large difference in the hydrolysis lifetimes of these two isomers is consistent with both our chamber and field observations.

Model Simulations of IHN Hydrolysis. Based on laboratory evidence, we incorporated condensed-phase hydrolysis into a 1-D box model to test whether this loss is consistent with the observed diurnal profile of the IHN isomer ratio observed at Caltech. Details of this model are provided in *Materials and Methods* and *SI Appendix*. Briefly, the model uses the recently developed condensed isoprene mechanism (18) and K-theory (41) to simulate the formation, oxidation, and mixing of IHN isomers in an atmospheric column representative of conditions observed at the Calfiornia Nexus Los Angeles Ground Site (CalNex-LA)

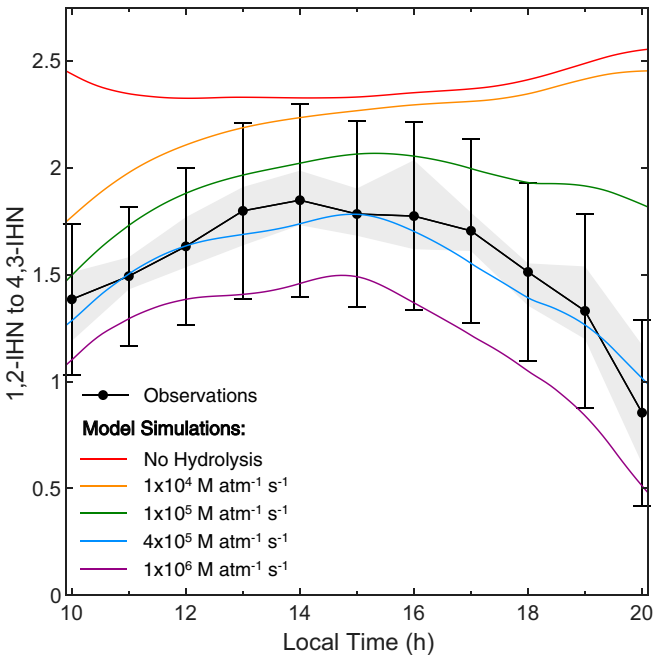

Fig. 3. Comparison of observed (black) and modeled (colored lines) diurnal profiles of the IHN isomer ratio from the Caltech field study. Each black dot represents the median of the hourly IHN isomer ratios, while the gray region encompasses the 25th and 75th percentile values, and the error bars represent the error in the study-averaged results. The model simulation that includes dry deposition and gas-phase chemistry only (red) overpredicted the IHN ratio, particularly in the afternoon, when 4,3-IHN loss should be faster than that of 1,2-IHN due to OH oxidation. Inclusion of a temperature-dependent (*SI Appendix*, Fig. S6) condensed-phase hydrolysis loss coefficient of 1,2-IHN (defined as, k^*_{hydro}, a product of Henry's law constant and aqueous hydrolysis rate [$K_H \times k_{(aq)}$]) enables the model to reproduce the observed IHN isomer ratio using $k^*_{hydro} = 4 \times 10^5$ M atm^{-1} s^{-1} (blue).

(42), which took place on the Caltech campus in 2010. Aerosol liquid water (ALW) concentrations used in the model were calculated with ISORROPIA-II (43), using aerosol measurements obtained from CalNex-LA. Our calculated ALW compares well with results presented in Guo et al. (44). We assume that IHN uptake into the particle is reversible and in instantaneous equilibrium with gas-phase concentrations (45).

The Henry's law coefficient (K_H) of the 1,2-IHN is not known, and, from our NMR study, we have only a lower limit to $k_{(aq)}$. However, provided that $k_{(aq)}$ is less than a few 100 s^{-1}, the hydrolysis loss rate of 1,2-IHN on aerosol (referred to here as the hydrolysis loss coefficient (49), k^*_{hydro}) will occur as the product of these two terms. Therefore, we can vary k^*_{hydro} in our simulations to find the best match to the observed diurnal profile of the IHN isomer ratio.

Fig. 3 shows how modeled IHN isomer ratios compare to observations over a range of hydrolysis loss coefficients (46), with the best agreement occurring when $k^*_{hydro} = 4 \times 10^5$ M atm^{-1} s^{-1} (blue). At this rate, the heterogenous lifetime of 1,2-IHN against hydrolysis ranges between 4 and 7 h in the daytime driven by changes in ALW (3.6 to 6 μg m^{-3}). This loss contributes to ~30% of the mid-day loss of the 1,2-IHN isomer, with that fraction increasing to over 50% in the evening (after 1800 hours local time), as a result of both the increased ALW concentrations and lower OH.

We note that ALW is highly sensitive to both humidity and aerosol composition, and so k^*_{hydro} will be quite variable depending on local conditions. For example, during the Southern Oxidant and Aerosol Study campaign, which took place in the southeastern United States, ALW was typically 1 to 5 μg m^{-3} on most afternoons, and median mass concentrations exceeded 15 μg m^{-3} in the morning (0600 to 0900 hours local time) (47). Furthermore, although not important at the Pasadena field site, hydrolysis by boundary layer cloud processing will also be efficient in many places. To the extent that this is important, our simulations described below will underrepresent the importance of IHN hydrolysis globally.

Our model results are relatively insensitive to additional parameters such as the assumed IHN-deposition velocity, horizontal advective loss, or vertical mixing rates (*SI Appendix*, section 5). However, we find that the modeled ratio is quite sensitive to our assumed ALW. The ALW in our model was estimated from aerosol measurements collected in May to July, which, on average, is a more humid time period than August. In addition, the United States has experienced a steady decline in SO_2 emissions since 2010 (48), which has been repeatedly linked to the reduction of sulphate in aerosols in the summer (49, 50). As sulfate affects the hygroscopicity of the particle, lower humidity and sulfate concentrations would result in lower ALW (51) than would be predicted using CalNex-LA ALW measurements. If we have overestimated ALW, then the inferred k^*_{hydro} is too small.

Atmospheric Implications. We have implemented the inferred k^*_{hydro} of 1,2-IHN into the global chemical transport model, GEOS-Chem, that has been recently updated to reflect the most recent laboratory studies of isoprene photochemistry (52, 53). Shown in Fig. 4 is the change in simulated NO and O_3 when we add 1,2-IHN hydrolysis with a rate similar to that of our 1-D model (in this case, $k^*_{hydro} = 3 \times 10^5$ M atm^{-1} s^{-1}; *SI Appendix*, section 6) to the standard GEOS-Chem model. Consistent with the findings of Paulot et al. (11), we find that over forested regions, the loss of NO_x via the formation of IHN and its subsequent conversion to HNO_3 through condensed-phase hydrolysis (*SI Appendix*, Fig. S8) leads to large reductions in simulated NO levels in the tropics (independent of seasonality; Fig. 4*A*) and during the Northern Hemisphere summer (Fig. 4*B*). This change, in turn, substantially reduces the calculated concentrations of OH (*SI Appendix*, Fig. S9) and O_3 (Fig. 4 *C* and *D*). Of note, surface ozone in the southeastern United States is ~5 parts per billion (ppb) lower in the summer with the addition of 1,2-IHN hydrolysis (Fig. 4*D*)—a change that brings the simulations into agreement with ground-based observations. Previously, to properly simulate surface ozone in GEOS-Chem, an ad hoc reduction between 30 and 60% in NO_x emissions had been suggested (54).

Although our laboratory measurements are unable to quantify the aqueous hydrolysis rate of 1,2-IHN, we find that the global impact of this chemistry is largely insensitive to the assumed hydrolysis loss coefficient, provided that k^*_{hydro} is at least 3×10^5 M atm^{-1} s^{-1} (*SI Appendix*, Fig. S7). The insensitivity of our simulations to k^*_{hydro} above most of the world's forests is a result of the low calculated OH levels ($[OH]_{avg} < 5 \times 10^5$ molecules cm^{-3}; *SI Appendix*, Fig. S10), different from the conditions of the Caltech field site. With such low OH, the gas-phase lifetime of IHN approaches 24 h, and, as a result, hydrolysis outcompetes all other IHN loss processes.

In conclusion, we present a rare observational constraint on the isomer-specific fate of IHN using both laboratory and field measurements obtained using GC-CIMS. Our data suggest that global atmospheric photochemistry is remarkably sensitive to the hydrolysis of a single isoprene hydroxy nitrate isomer, 1,2-IHN. Using GEOS-Chem, we simulate the effect a hydrolysis rate of at least 3×10^5 M atm^{-1} s^{-1} has on NO, O_3, OH, and HNO_3 concentrations in the lower atmosphere. We find that this added loss process represents the majority of the IHN loss over forested regions, resulting in a substantial decrease of simulated NO in the tropics (year-round) and in the Northern Hemisphere during the summer. This drop in NO, in turn, results in lower concentrations of simulated ozone—allowing for better agreement between this model and ground-based observations, especially in the southeastern United States. Lastly, 1,2-IHN hydrolysis acts as a significant source of HNO_3 that is on par with OH + NO_2.

Materials and Methods

Description of Field Site. Measurements described here were collected from a field site located at the Caltech campus in Pasadena, CA, which is located in the Los Angeles metropolitan area approximately 18 km northeast of downtown Los Angeles (DTLA) and 7 km south of the San Gabriel Mountains. The instrument was located on the southwest corner of the roof of the 44-m tall Caltech library (lat 34.137; long −118.126) from August 1 to 17, 2017, sampling into the daytime prevailing winds, which arrived predominantly from the south. Because of its proximity to DTLA, the site experienced high levels of anthropogenic pollution ($[NO]_{avg,\ daytime}$ = 2.5 ppbv). In addition, local vegetation is made up of known isoprene emitters (55), allowing for local biogenic emissions to influence the site.

In addition, a weather station was colocated with our main GC-CIMS instrument to monitor relative humidity (%), air temperature (°C), barometric pressure (mbar), solar radiation (W/m^2), wind speed (m/s), and wind direction. Additional details regarding this field site are provided in *SI Appendix*.

Isomer Measurements. The GC-CIMS instrumentation, and details of its field operation, has been described previously in the literature (36). Briefly, ambient air was pulled at a high flow rate (~2,000 standard liters per minute) through a Teflon-coated glass inlet (3.8-cm inner diameter; 76.2 cm long). A subsampled portion of this gas stream was then directed into the CIMS, either directly or after analytes are separated on a 1-m GC column. Analyte concentrations were quantified using a CF_3O^- reagent ion, which is sensitive toward the detection of oxygenated multifunctional compounds such as organic peroxides and nitrates (16, 56–58). In the field, the instrument collected data in automated 1-h cycles, with GC separation occurring in the latter half hour.

Laboratory experiments were performed on a prototype version of the GC-CIMS field instrument. Analytes were trapped on a portion of a 1-m column that was submerged in an isopropanol bath chilled to approximately

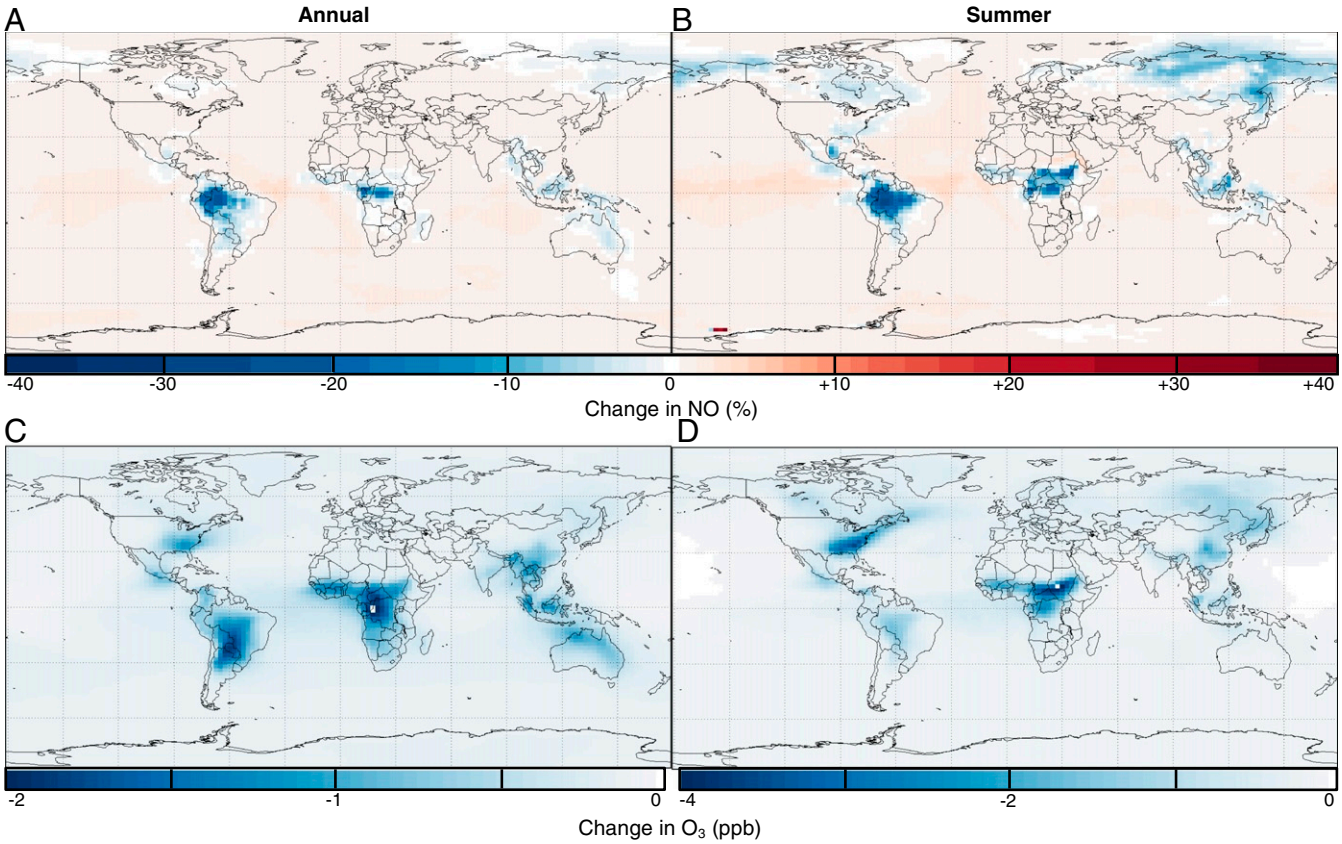

Fig. 4. The standard GEOS-Chem model was updated to include an 1,2-IHN hydrolysis rate of $k^*_{hydro} = 3 \times 10^5$ M atm^{-1} s^{-1}. The impact of this loss on NO and ozone was then assessed through both annual and summer (July 1 to 31) simulations conducted in the lowest 1 km of the atmosphere. The addition of this IHN sink resulted in a ~40% decrease in NO in the tropics throughout the year (*A*) and a lesser, but still substantial, decrease in the Northern Hemisphere during the summer (*B*), with respect to the base model. Likewise, O_3 concentrations also experienced the same spatial and seasonal decrease as NO (*C* and *D*). Of note, surface ozone in the southeastern United States is 5 ppb lower in the summer (*D*), causing this updated model to better agree with ground-based observations.

−20° C. The column was then heated within a Varian CP-3800 GC oven. The column effluent was then directed into a CF_3O^- CIMS.

Measurement uncertainty from field data arose from low analyte signal, caused by a combination of low ambient concentrations and the high instrument dilution needed to prevent simultaneous trapping of water (36). Additional details regarding data processing and measurement uncertainties can be found in *SI Appendix*.

1-D Atmospheric Model. A 1-D atmospheric model was used to interpret ambient measurements collected during the Caltech field study. The model simulates the emission, deposition, vertical transport, and photochemical oxidation of 250 species in an atmospheric column tuned to replicate conditions observed during the 2010 CalNex-LA campaign, which also took place on the Caltech campus. The model combines the latest version of the Regional Atmospheric Chemistry Mechanism (59) with the condensed isoprene-oxidation mechanisms described by Wennberg et al. (18) and IHN deposition rates based on measurements made by Nguyen et al. (20). Vertical transport is simulated in the model using K-theory (41), and its implementation in the model is described in more detail in *SI Appendix*.

Given the uncertainty in local isoprene emissions due to vegetation heterogeneity in and around the Pasadena area, sensitivity tests were performed to determine a reasonable emission rate that produced agreement between measured and modeled isoprene concentrations. ALW concentrations used to model IHN partitioning were calculated using ISORROPIA-II (43) using inputs of temperature, RH, and inorganic aerosol components measured during CalNex-LA. The calculated ALW agreed well with that reported by Guo et al. (44).

Data Availability. Atmospheric trace gas measurements and model output data have been deposited in the California Institute of Technology Research Data Repository CaltechDATA. IHN isomer concentration data used here are available online (http://doi.org/10.22002/D1.971) along with the chromatograms collected at the field site (http://doi.org/10.22002/D1.1671), the output results of the 1-D atmospheric model (http://doi.org/10.22002/D1.1672), and the updated isoprene mechanism used in the global chemical transport model (http://doi.org/10.22002/D1.247). GEOS-Chem is available for public use at http://geos-chem.org/.

ACKNOWLEDGMENTS. Development of the GC-CIMS was supported by the NSF Major Research Instrumentation Program under Grant AGS-1428482 and the field and laboratory studies it participated in were supported by additional NSF funding (Grant AGS-1240604). We thank the Caltech campus and affiliated staff for accommodating our 2017 field study. Work performed by K.T.V. and H.M.A. was also supported by NSF through the Graduate Research Fellowship.

1. E. C. Browne, R. C. Cohen, Effects of biogenic nitrate chemistry on the NOx lifetime in remote continental regions. *Atmos. Chem. Phys.* **12**, 11917–11932 (2012).
2. H. Simon, A. Reff, B. Wells, J. Xing, N. Frank, Ozone trends across the United States over a period of decreasing NO_x and VOC emissions. *Environ. Sci. Technol.* **49**, 186–195 (2015).
3. A. E. Perring, S. E. Pusede, R. C. Cohen, An observational perspective on the atmospheric impacts of alkyl and multifunctional nitrates on ozone and secondary organic aerosol. *Chem. Rev.* **113**, 5848–5870 (2013).
4. J. Mao *et al.*, Southeast atmosphere studies: Learning from model-observation syntheses. *Atmos. Chem. Phys.* **18**, 2615–2651 (2018).
5. L. Xu, S. Suresh, H. Guo, R. J. Weber, N. L. Ng, Aerosol characterization over the southeastern United States using high-resolution aerosol mass spectrometry: Spatial and seasonal variation of aerosol composition and sources with a focus on organic nitrates. *Atmos. Chem. Phys.* **15**, 7307–7336 (2015).
6. A. W. Rollins *et al.*, Evidence for NOx control over nighttime SOA formation. *Science* **337**, 1210–1212 (2012).

7. M. Trainer *et al.*, Observations and modeling of the reactive nitrogen photochemistry at a rural site. *J. Geophys. Res. Atmos.* **96**, 3045–3063 (1991).
8. S. Wu *et al.*, Why are there large differences between models in global budgets of tropospheric ozone? *J. Geophys. Res.* **112**, D05302 (2007).
9. L. W. Horowitz *et al.*, Observational constraints on the chemistry of isoprene nitrates over the eastern United States. *J. Geophys. Res. Atmos.* **112**, D12S08 (2007).
10. M. R. Beaver *et al.*, Importance of biogenic precursors to the budget of organic nitrates: Observations of multifunctional organic nitrates by CIMS and TD-LIF during BEARPEX 2009. *Atmos. Chem. Phys.* **12**, 5773–5785 (2012).
11. F. Paulot, D. K. Henze, P. O. Wennberg, Impact of the isoprene photochemical cascade on tropical ozone. *Atmos. Chem. Phys.* **12**, 1307–1325 (2012).
12. J. Mao *et al.*, Ozone and organic nitrates over the eastern United States: Sensitivity to isoprene chemistry. *J. Geophys. Res. Atmos.* **118**, 11256–11268 (2013).
13. O. J. Squire *et al.*, Influence of isoprene chemical mechanism on modeled changes in tropospheric ozone due to climate and land use over the 21st century. *Atmos. Chem. Phys.* **15**, 5123–5143 (2015).
14. A. G. Carlton *et al.*, Synthesis of the southeast atmosphere studies: Investigating fundamental atmospheric chemistry questions. *Bull. Am. Meteorol. Soc.* **99**, 547–567 (2018).
15. J. Li *et al.*, Decadal changes in summertime reactive oxidized nitrogen and surface ozone over the southeast United States. *Atmos. Chem. Phys.* **18**, 2341–2361 (2018).
16. F. Paulot *et al.*, Isoprene photooxidation: New insights into the production of acids and organic nitrates. *Atmos. Chem. Phys.* **9**, 1479–1501 (2009).
17. A. P. Teng, J. D. Crounse, P. O. Wennberg, Isoprene peroxy radical dynamics. *J. Am. Chem. Soc.* **139**, 5367–5377 (2017).
18. P. O. Wennberg *et al.*, Gas-phase reactions of isoprene and its major oxidation products. *Chem. Rev.* **118**, 3337–3390 (2018).
19. J. A. Fisher *et al.*, Organic nitrate chemistry and its implications for nitrogen budgets in an isoprene- and monoterpene-rich atmosphere: Constraints from aircraft ($SEAC^4RS$) and ground-based (SOAS) observations in the southeast US. *Atmos. Chem. Phys.* **16**, 5969–5991 (2016).
20. T. B. Nguyen *et al.*, Rapid deposition of oxidized biogenic compounds to a temperate forest. *Proc. Natl. Acad. Sci. U.S.A.* **112**, E392–E401 (2015).
21. L. Lee, A. P. Teng, P. O. Wennberg, J. D. Crounse, R. C. Cohen, On rates and mechanisms of OH and O_3 reactions with isoprene-derived hydroxy nitrates. *J. Phys. Chem. A* **118**, 1622–1637 (2014).
22. J. F. Müller, J. Peeters, T. Stavrakou, Fast photolysis of carbonyl nitrates from isoprene. *Atmos. Chem. Phys.* **14**, 2497–2508 (2014).
23. P. Giacopelli, K. Ford, C. Espada, P. B. Shepson, Comparison of the measured and simulated isoprene nitrate distributions above a forest canopy. *J. Geophys. Res. Atmos.* **110**, D01304 (2005).
24. S. Liu *et al.*, Hydrolysis of organonitrate functional groups in aerosol particles. *Aerosol Sci. Technol.* **46**, 1359–1369 (2012).
25. F. Xiong *et al.*, Observation of isoprene hydroxynitrates in the southeastern United States and implications for the fate of NOx. *Atmos. Chem. Phys.* **15**, 11257–11272 (2015).
26. G. M. Wolfe *et al.*, Quantifying sources and sinks of reactive gases in the lower atmosphere using airborne flux observations. *Geophys. Res. Lett.* **42**, 8231–8240 (2015).
27. C. M. Boyd *et al.*, Secondary organic aerosol formation from the β-pinene+NO_3 system: Effect of humidity and peroxy radical fate. *Atmos. Chem. Phys.* **15**, 7497–7522 (2015).
28. J. D. Rindelaub, K. M. McAvey, P. B. Shepson, The photochemical production of organic nitrates from α-pinene and loss via acid-dependent particle phase hydrolysis. *Atmos. Environ.* **100**, 193–201 (2015).
29. J. K. Bean, L. H. Ruiz, Gas-particle partitioning and hydrolysis of organic nitrates formed from the oxidation of α-pinene in environmental chamber experiments. *Atmos. Chem. Phys.* **16**, 2175–2184 (2016).
30. D. A. Day, S. Liu, L. M. Russell, P. J. Ziemann, Organonitrate group concentrations in submicron particles with high nitrate and organic fractions in coastal southern California. *Atmos. Environ.* **44**, 1970–1979 (2010).
31. A. I. Darer, N. C. Cole-Filipiak, A. E. O'Connor, M. J. Elrod, Formation and stability of atmospherically relevant isoprene-derived organosulfates and organonitrates. *Environ. Sci. Technol.* **45**, 1895–1902 (2011).
32. K. S. Hu, A. I. Darer, M. J. Elrod, Thermodynamics and kinetics of the hydrolysis of atmospherically relevant organonitrates and organosulfates. *Atmos. Chem. Phys.* **11**, 8307–8320 (2011).
33. E. C. Browne *et al.*, Observations of total $RONO_2$ over the boreal forest: NOx sinks and HNO_3 sources. *Atmos. Chem. Phys.* **13**, 4543–4562 (2013).
34. P. S. Romer *et al.*, The lifetime of nitrogen oxides in an isoprene-dominated forest. *Atmos. Chem. Phys.* **16**, 7623–7637 (2016).
35. A. Zare *et al.*, A comprehensive organic nitrate chemistry: Insights into the lifetime of atmospheric organic nitrates. *Atmos. Chem. Phys.* **18**, 15419–15436 (2018).
36. K. T. Vasquez *et al.*, Low-pressure gas chromatography with chemical ionization mass spectrometry for quantification of multifunctional organic compounds in the atmosphere. *Atmos. Meas. Tech.* **11**, 6815–6832 (2018).
37. K. T. Vasquez, L. Xu, J. D. Crounse, P. O. Wennberg, IHN GC data from 2017 Caltech Roof Study (Version 1.0). CaltechDATA. http://doi.org/10.22002/D1.971. Deposited 4 July 2018.
38. S. M. Griffith *et al.*, Measurements of hydroxyl and hydroperoxy radicals during CalNex-LA: Model comparisons and radical budgets. *J. Geophys. Res. Atmos.* **121**, 4211–4232 (2016).
39. K. T. Vasquez, L. Xu, J. D. Crounse, P. O. Wennberg, GC chromatograms from 2017 Caltech Roof Study (Version 1.0). CaltechDATA. http://doi.org/10.22002/D1.1671. Deposited 17 November 2020.
40. M. I. Jacobs, W. J. Burke, M. J. Elrod, Kinetics of the reactions of isoprene-derived hydroxynitrates: Gas phase epoxide formation and solution phase hydrolysis. *Atmos. Chem. Phys.* **14**, 8933–8946 (2014).
41. G. M. Wolfe, J. A. Thornton, The Chemistry of Atmosphere-Forest Exchange (CAFE) model - Part 1: Model description and characterization. *Atmos. Chem. Phys.* **11**, 77–101 (2011).
42. T. B. Ryerson *et al.*, The 2010 California research at the nexus of air quality and climate change (CalNex) field study. *J. Geophys. Res. Atmos.* **118**, 5830–5866 (2013).
43. C. Fountoukis, A. Nenes, ISORROPIA II: A computationally efficient thermodynamic equilibrium model for K^+-Ca^{2+}-Mg^{2+}-NH_4^+-Na^+-SO_4^{2-}-NO_3^--Cl^--H_2O aerosols. *Atmos. Chem. Phys.* **7**, 4639–4659 (2007).
44. H. Guo *et al.*, Fine particle pH and gas–particle phase partitioning of inorganic species in Pasadena, California, during the 2010 CalNex campaign. *Atmos. Chem. Phys.* **17**, 5703–5719 (2017).
45. H. O. T. Pye, A. W. H. Chan, M. P. Barkley, J. H. Seinfeld, Global modeling of organic aerosol: The importance of reactive nitrogen (NO_x and NO_3). *Atmos. Chem. Phys.* **10**, 11261–11276 (2010).
46. B. C. Schulze, K. T. Vasquez, J. D. Crounse, P. O. Wennberg, IHN hydrolysis 1D model results. CaltechDATA. http://doi.org/10.22002/D1.1672. Deposited 17 November 2020.
47. T. K. V. Nguyen *et al.*, Trends in particle-phase liquid water during the southern oxidant and aerosol study. *Atmos. Chem. Phys.* **14**, 10911–10930 (2014).
48. US Environmental Protection Agency, Sulfur dioxide trends (2018). https://www.epa.gov/air-trends/sulfur-dioxide-trends. Accessed 13 April 2019.
49. J. L. Hand, B. A. Schichtel, W. C. Malm, M. L. Pitchford, Particulate sulphate ion concentration and so_2 emission trends in the United States from the early 1990s through 2010. *Atmos. Chem. Phys.* **12**, 10353–10365 (2012).
50. F. Paulot, S. Fan, L. W. Horowitz, Contrasting seasonal responses of sulfate aerosols to declining SO_2 emissions in the Eastern U.S.: Implications for the efficacy of SO_2 emission controls. *Geophys. Res. Lett.* **44**, 455–464 (2017).
51. A. G. Carlton, B. J. Turpin, Particle partitioning potential of organic compounds is highest in the Eastern US and driven by anthropogenic water. *Atmos. Chem. Phys.* **13**, 10203–10214 (2013).
52. K. H. Bates, D. J. Jacob, A new model mechanism for atmospheric oxidation of isoprene: Global effects on oxidants, nitrogen oxides, organic products, and secondary organic aerosol. *Atmos. Chem. Phys.* **19**, 9613–9640 (2019).
53. K. H. Bates, P. O. Wennberg, Isoprene oxidation model (Version 5). CaltechDATA. http://doi.org/10.22002/D1.247. Deposited 20 July 2017.
54. K. R. Travis *et al.*, Why do models overestimate surface ozone in the southeast United States? *Atmos. Chem. Phys.* **16**, 13561–13577 (2016).
55. A. Guenther, P. Zimmerman, M. Wildermuth, Natural volatile organic compound emission rate estimates for U.S. woodland landscapes. *Atmos. Environ.* **28**, 1197–1210 (1994).
56. J. D. Crounse, K. A. McKinney, A. J. Kwan, P. O. Wennberg, Measurement of gas-phase hydroperoxides by chemical ionization mass spectrometry. *Anal. Chem.* **78**, 6726–6732 (2006).
57. J. M. St. Clair, D. C. McCabe, J. D. Crounse, U. Steiner, P. O. Wennberg, Chemical ionization tandem mass spectrometer for the in situ measurement of methyl hydrogen peroxide. *Rev. Sci. Instrum.* **81**, 094102 (2010).
58. N. Hyttinen *et al.*, Computational comparison of different reagent ions in the chemical ionization of oxidized multifunctional compounds. *J. Phys. Chem. A* **122**, 269–279 (2018).
59. W. S. Goliff, W. R. Stockwell, C. V. Lawson, The regional atmospheric chemistry mechanism, version 2. *Atmos. Environ.* **68**, 174–185 (2013).

Appendix B

Synergistic HNO_3-H_2SO_4-NH_3 upper tropospheric particle formation

Wang, M.; Xiao, M.; Bertozzi, B.; Marie, G.; Rörup, B.; Schulze, B.; Bardakov, R.; He, X.-C.; Shen, J.; Scholz, W.; Marten, R.; Dada, L.; Baalbaki, R.; Lopez, B.; Lamkaddam, H.; Manninen, H. E.; Amorim, A.; Ataei, F.; Bogert, P.; Brasseur, Z.; Caudillo, L.; De Menezes, L.-P.; Duplissy, J.; Ekman, A. M. L.; Finkenzeller, H.; Carracedo, L. G.; Granzin, M.; Guida, R.; Heinritzi, M.; Hofbauer, V.; Höhler, K.; Korhonen, K.; Krechmer, J. E.; Kürten, A.; Lehtipalo, K.; Mahfouz, N. G. A.; Makhmutov, V.; Massabò, D.; Mathot, S.; Mauldin, R. L.; Mentler, B.; Müller, T.; Onnela, A.; Petäjä, T.; Philippov, M.; Piedehierro, A. A.; Pozzer, A.; Ranjithkumar, A.; Schervish, M.; Schobesberger, S.; Simon, M.; Stozhkov, Y.; Tomé, A.; Umo, N. S.; Vogel, F.; Wagner, R.; Wang, D. S.; Weber, S. K.; Welti, A.; Wu, Y.; Zauner-Wieczorek, M.; Sipilä, M.; Winkler, P. M.; Hansel, A.; Baltensperger, U.; Kulmala, M.; Flagan, R. C.; Curtius, J.; Riipinen, I.; Gordon, H.; Lelieveld, J.; El-Haddad, I.; Volkamer, R.; Worsnop, D. R.; Christoudias, T.; Kirkby, J.; Möhler, O.; Donahue, N. M. Synergistic HNO3–H2SO4–NH3 Upper Tropospheric Particle Formation. *Nature* **2022**, *605* (7910), 483–489. https://doi.org/10.1038/s41586-022-04605-4.

Article

Synergistic HNO_3–H_2SO_4–NH_3 upper tropospheric particle formation

https://doi.org/10.1038/s41586-022-04605-4

Received: 28 July 2021

Accepted: 2 March 2022

Published online: 18 May 2022

Open access

Check for updates

Mingyi Wang[1,2,7], Mao Xiao[3], Barbara Bertozzi[4], Guillaume Marie[5], Birte Rörup[6], Benjamin Schulze[7], Roman Bardakov[8,9], Xu-Cheng He[6], Jiali Shen[6], Wiebke Scholz[10], Ruby Marten[3], Lubna Dada[3,6], Rima Baalbaki[6], Brandon Lopez[1,11], Houssni Lamkaddam[3], Hanna E. Manninen[12], António Amorim[13], Farnoush Ataei[14], Pia Bogert[4], Zoé Brasseur[6], Lucía Caudillo[5], Louis-Philippe De Menezes[12], Jonathan Duplissy[6,15], Annica M. L. Ekman[8,9], Henning Finkenzeller[16], Loïc Gonzalez Carracedo[17], Manuel Granzin[5], Roberto Guida[12], Martin Heinritzi[5], Victoria Hofbauer[1,2], Kristina Höhler[4], Kimmo Korhonen[18], Jordan E. Krechmer[19], Andreas Kürten[5], Katrianne Lehtipalo[6,20], Naser G. A. Mahfouz[1,21], Vladimir Makhmutov[22,23], Dario Massabò[24], Serge Mathot[12], Roy L. Mauldin[1,2,25], Bernhard Mentler[10], Tatjana Müller[5,26], Antti Onnela[12], Tuukka Petäjä[6], Maxim Philippov[22], Ana A. Piedehierro[20], Andrea Pozzer[26], Ananth Ranjithkumar[27], Meredith Schervish[1,2], Siegfried Schobesberger[18], Mario Simon[5], Yuri Stozhkov[22], António Tomé[28], Nsikanabasi Silas Umo[4], Franziska Vogel[4], Robert Wagner[4], Dongyu S. Wang[3], Stefan K. Weber[12], André Welti[20], Yusheng Wu[6], Marcel Zauner-Wieczorek[5], Mikko Sipilä[6], Paul M. Winkler[17], Armin Hansel[10,29], Urs Baltensperger[3], Markku Kulmala[6,15,30,31], Richard C. Flagan[7], Joachim Curtius[5], Ilona Riipinen[9,32], Hamish Gordon[1,11], Jos Lelieveld[26,33], Imad El-Haddad[3], Rainer Volkamer[16], Douglas R. Worsnop[6,19], Theodoros Christoudias[33], Jasper Kirkby[5,12], Ottmar Möhler[4] & Neil M. Donahue[1,2,11,34] ✉

New particle formation in the upper free troposphere is a major global source of cloud condensation nuclei (CCN)[1–4]. However, the precursor vapours that drive the process are not well understood. With experiments performed under upper tropospheric conditions in the CERN CLOUD chamber, we show that nitric acid, sulfuric acid and ammonia form particles synergistically, at rates that are orders of magnitude faster than those from any two of the three components. The importance of this mechanism depends on the availability of ammonia, which was previously thought to be efficiently scavenged by cloud droplets during convection. However, surprisingly high concentrations of ammonia and ammonium nitrate have recently been observed in the upper troposphere over the Asian monsoon region[5,6]. Once particles have formed, co-condensation of ammonia and abundant nitric acid alone is sufficient to drive rapid growth to CCN sizes with only trace sulfate. Moreover, our measurements show that these CCN are also highly efficient ice nucleating particles—comparable to desert dust. Our model simulations confirm that ammonia is efficiently convected aloft during the Asian monsoon, driving rapid, multi-acid HNO_3–H_2SO_4–NH_3 nucleation in the upper troposphere and producing ice nucleating particles that spread across the mid-latitude Northern Hemisphere.

Intense particle formation has been observed by airborne measurements as a persistent, global-scale band in the upper troposphere over tropical convective regions[1,2,4]. Upper tropospheric nucleation is thought to provide at least one-third of global CCN[3]. Increased aerosols since the industrial revolution, and their interactions with clouds, have masked a large fraction of the global radiative forcing by greenhouse gases. Projections of aerosol radiative forcing resulting from future reductions of air pollution are highly uncertain[7]. Present-day nucleation involves sulfuric acid (H_2SO_4) over almost all the troposphere[8]. However, binary nucleation of H_2SO_4–H_2O is slow and, so, ternary or multicomponent nucleation with extra vapours such as ammonia (NH_3)[9] and organics[10,11] is necessary to account for observed new-particle-formation rates[3,8,12].

Ammonia stabilizes acid–base nucleation and strongly enhances particle formation rates[9]. However, ammonia is thought to be extremely scarce in the upper troposphere because its solubility in water and reactivity with acids should lead to efficient removal in convective clouds. However, this assumption is not supported by observation. Ammonia vapour has been repeatedly detected in the Asian monsoon upper troposphere, with mixing ratios of up to 30 pptv (2.5×10^8 cm^{-3}) for a three-month average[5] and up to 1.4 ppbv (1.2×10^{10} cm^{-3}) in hotspots[6].

A list of affiliations appears at the end of the paper.

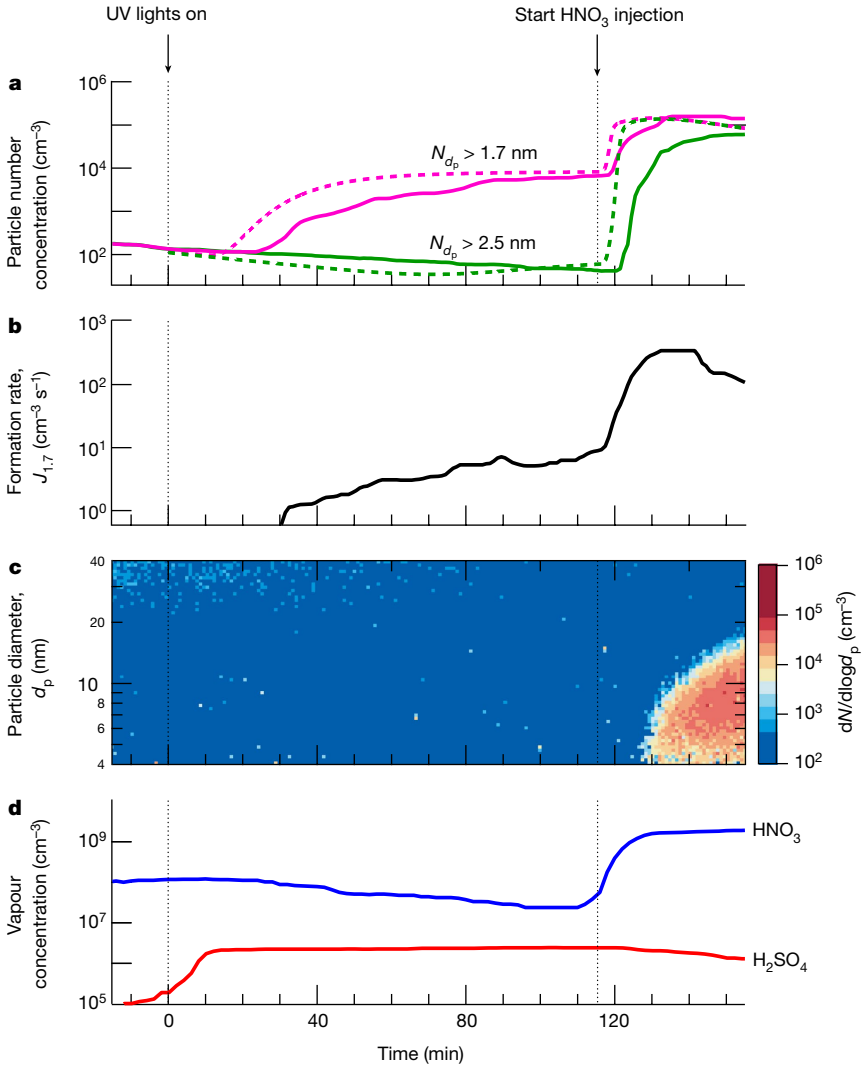

Fig. 1 | Example experiment showing nitric acid enhancement of H_2SO_4–NH_3 particle formation. a, Particle number concentrations versus time at mobility diameters >1.7 nm (magenta) and >2.5 nm (green). The solid magenta trace is measured by a $PSM_{1.7}$ and the solid green trace is measured by a $CPC_{2.5}$. The fixed experimental conditions are about 6.5×10^8 cm^{-3} NH_3, 223 K and 25% relative humidity. A microphysical model reproduces the main features of the observed particle formation (dashed lines; see text for details). **b**, Particle formation rate versus time at 1.7 nm ($J_{1.7}$), measured by a PSM. **c**, Particle size distribution versus time, measured by an SMPS. **d**, Gas-phase nitric acid and sulfuric acid versus time, measured by an I^- CIMS and a NO_3^- CIMS, respectively. Sulfuric acid through SO_2 oxidation started to appear soon after switching on the UV lights at time = 0 min, building up to a steady state of 2.3×10^6 cm^{-3} after a wall-loss-rate timescale of around 10 min. The subsequent H_2SO_4–NH_3 nucleation led to a relatively slow formation rate of 1.7-nm particles. The particles did not grow above 2.5 nm because of their slow growth rate and corresponding low survival probability against wall loss. Following injection of 2.0×10^9 cm^{-3} nitric acid into the chamber after 115 min, while leaving the production rate of sulfuric acid and the injection rate of ammonia unchanged, we observed a sharp increase in particle formation rate (panel **b**), together with rapid particle growth of 40 nm h^{-1} (panel **c**). The overall systematic scale uncertainties of ±30% on particle formation rate, −33%/+50% on sulfuric acid concentration and ±25% on nitric acid concentration are not shown.

The release of dissolved ammonia from cloud droplets may occur during glaciation[13]. Once released in the upper troposphere, ammonia can form particles with nitric acid, which is abundantly produced by lightning[14,15]. These particles will live longer and travel farther than ammonia vapour, with the potential to influence the entire upper troposphere and lower stratosphere of the Northern Hemisphere[6].

Fundamental questions remain about the role and mechanisms of nitric acid and ammonia in upper tropospheric particle formation. Recent CLOUD (Cosmics Leaving Outdoor Droplets) experiments at CERN have shown that nitric acid and ammonia vapours below 278 K can condense onto newly formed particles as small as a few nanometres in diameter, driving rapid growth to CCN sizes[16]. At even lower temperatures (below 258 K), nitric acid and ammonia can directly nucleate to form ammonium nitrate particles, although pure HNO_3–NH_3 nucleation is too slow to compete with H_2SO_4–NH_3 nucleation under comparable conditions. However, the results we present here show that, when all three vapours are present, a synergistic interaction drives nucleation rates orders of magnitude faster than those from any two of the three components. Once nucleated through this multi-acid–ammonia mechanism, the particles can grow rapidly by co-condensation of NH_3 and HNO_3 alone, both of which may be far more abundant than H_2SO_4 in the upper troposphere.

Particle formation measurements in CLOUD

Here we report new-particle-formation experiments performed with mixtures of sulfuric acid, nitric acid and ammonia vapours in the CLOUD chamber[9] at CERN between September and December 2019 (CLOUD 14; see Methods for experimental details). To span ranges typical of the upper troposphere, we established quasi-steady-state

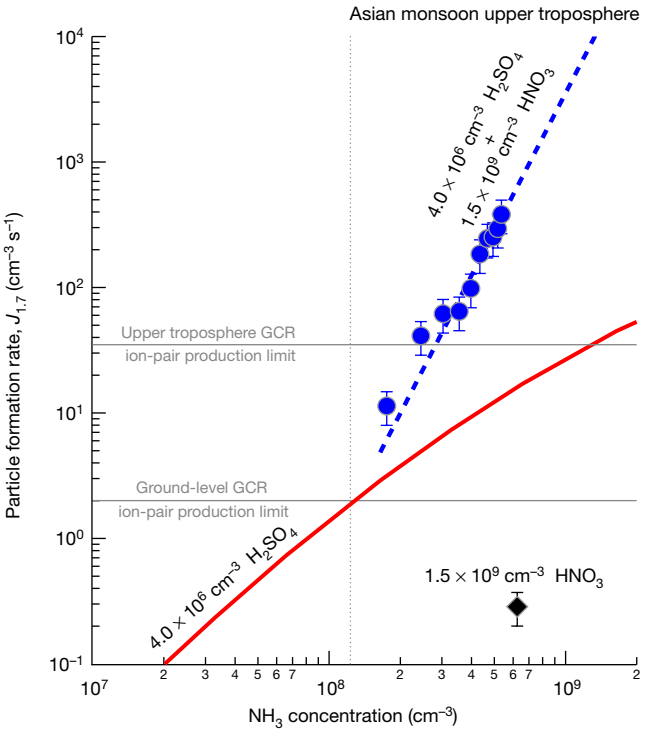

Fig. 2 | Particle formation rates at 1.7 nm ($J_{1.7}$) versus ammonia concentration at 223 K and 25% relative humidity. The chemical systems are HNO_3–NH_3 (black), H_2SO_4–NH_3 (red) and HNO_3–H_2SO_4–NH_3 (blue). The black diamond shows the CLOUD measurement of HNO_3–NH_3 nucleation at 1.5×10^9 cm^{-3} HNO_3, 6.5×10^8 cm^{-3} NH_3 and with H_2SO_4 below the detection limit of 5×10^4 cm^{-3}. The red solid curve is $J_{1.7}$ versus ammonia concentration at 4.0×10^6 cm^{-3} sulfuric acid from a H_2SO_4–NH_3 nucleation parameterization on the basis of previous CLOUD measurements[18,19]. The blue circles show the CLOUD measurements of HNO_3–H_2SO_4–NH_3 nucleation at 4.0×10^6 cm^{-3} H_2SO_4, 1.5×10^9 cm^{-3} HNO_3 and $(1.6–6.5) \times 10^8$ cm^{-3} NH_3. The data are fitted by a power law, $J_{1.7} = k[NH_3]^{3.7}$ (blue dashed curve). The vertical grey dotted line separates ammonia concentrations measured in different regions in the upper troposphere[5]; the region to the right indicates the Asian monsoon conditions. The horizontal grey solid lines show $J_{1.7}$ upper limits for ion-induced nucleation resulting from the GCR ionization rate of around 2 ion pairs cm^{-3} s^{-1} at ground level and 35 ion pairs cm^{-3} s^{-1} in the upper troposphere. Among the three nucleation mechanisms, H_2SO_4–NH_3 nucleation dominates in regions with low ammonia (below around 1.0×10^8 cm^{-3}, or 12 pptv), whereas HNO_3–H_2SO_4–NH_3 nucleation dominates at higher ammonia levels characteristic of the Asian monsoon upper troposphere. The bars indicate 30% estimated total error on the particle formation rates. The overall systematic scale uncertainties are −33%/+50% for sulfuric acid and ±25% for nitric acid concentrations.

vapour concentrations in the chamber of $(0.26–4.6) \times 10^6$ cm^{-3} sulfuric acid (through photochemical oxidation of SO_2), $(0.23–4.0) \times 10^9$ cm^{-3} nitric acid (through either photochemical oxidation of NO_2 or injection from an evaporator) and $(0.95–6.5) \times 10^8$ cm^{-3} ammonia (through injection from a gas bottle). In an extreme experiment to simulate hotspot conditions in the Asian monsoon anticyclone, we raised sulfuric acid, nitric acid and ammonia to maximum concentrations of 6.2×10^7 cm^{-3}, 3.8×10^9 cm^{-3} and 8.8×10^9 cm^{-3}, respectively. The experiments were conducted at 223 K and 25% relative humidity, representative of upper tropospheric conditions.

Figure 1 shows the evolution of a representative new-particle-formation experiment in the presence of around 6.5×10^8 cm^{-3} ammonia. The top three panels show particle number concentrations above 1.7 nm and above 2.5 nm (Fig. 1a), particle formation rate at 1.7 nm ($J_{1.7}$) (Fig. 1b) and particle size distribution (Fig. 1c). The bottom panel shows HNO_3 and H_2SO_4 vapour concentrations (Fig. 1d). We switched on the ultraviolet (UV) lights at $t = 0$ min to oxidize SO_2 with OH radicals and form H_2SO_4. Sulfuric acid started to appear shortly thereafter and built up to a steady state of 2.3×10^6 cm^{-3} over the wall-loss timescale of about 10 min. Under these conditions, the data show a modest formation rate of 1.7-nm particles from H_2SO_4–NH_3 nucleation, consistent with previous CLOUD measurements[8]. These particles grew only slowly (about 0.5 nm h^{-1} at this H_2SO_4 and particle size[17]). No particles reached 2.5 nm within 2 h, owing to their slow growth rate and low survival probability against wall loss.

At $t = 115$ min, we raised the nitric acid concentration to 2.0×10^9 cm^{-3}, through direct injection instead of photochemical production, so that we could independently control the nitric acid and sulfuric acid concentrations. The particle number increased 30-fold and 1,300-fold for particles larger than 1.7 nm and 2.5 nm, respectively. In addition, these newly formed particles grew much more rapidly (40 nm h^{-1}), reaching 20 nm within 30 min. This experiment shows that nitric acid can substantially enhance particle formation and growth rates for fixed levels of sulfuric acid and ammonia.

We also conducted model calculations on the basis of known thermodynamics and microphysics (Methods). Our model results (dashed traces in Fig. 1a) consistently and quantitatively confirm the experimental data: sulfuric acid and ammonia nucleation produces only 1.7-nm particles, whereas addition of nitric acid strongly enhances the formation rates of both 1.7-nm and 2.5-nm particles.

We conducted two further experiments under conditions similar to Fig. 1 but holding the concentrations of a different pair of vapours constant while varying the third. For the experiment shown in Extended Data Fig. 1, we started by oxidizing NO_2 to produce 1.6×10^9 cm^{-3} HNO_3 in the presence of about 6.5×10^8 cm^{-3} NH_3 and then increased H_2SO_4 from 0 to 4.9×10^6 cm^{-3} by oxidizing progressively more injected SO_2. For the experiment shown in Extended Data Fig. 2, we first established 4.6×10^6 cm^{-3} H_2SO_4 and 4.0×10^9 cm^{-3} HNO_3, and then increased NH_3 from 0 to about 6.5×10^8 cm^{-3}. We consistently observed relatively slow nucleation when only two of the three vapours are present, whereas addition of the third vapour increased nucleation rates by several orders of magnitude.

Figure 2 shows particle formation rates measured by CLOUD at 1.7-nm mobility diameter ($J_{1.7}$) versus ammonia concentration, at 223 K. The $J_{1.7}$ data were all measured in the presence of ions from galactic cosmic rays (GCR) and − so − represent the sum of neutral and ion-induced channels. The black diamond shows the measured $J_{1.7}$ of 0.3 cm^{-3} s^{-1} for HNO_3–NH_3 nucleation with 1.5×10^9 cm^{-3} nitric acid, about 6.5×10^8 cm^{-3} ammonia and sulfuric acid below the detection limit of 5×10^4 cm^{-3} (this is the event shown in Extended Data Fig. 1). At this same ammonia concentration, we measured $J_{1.7} = 6.1$ cm^{-3} s^{-1} at 2.3×10^6 cm^{-3} H_2SO_4, demonstrating the much faster rate of H_2SO_4–NH_3 nucleation (not shown). This measurement is consistent with models on the basis of previous CLOUD studies of H_2SO_4–NH_3 nucleation[18,19], as illustrated by the model simulations for 4.0×10^6 cm^{-3} sulfuric acid (red solid curve). The blue circles show our measurements of $J_{1.7}$ for HNO_3–H_2SO_4–NH_3 nucleation at 4.0×10^6 cm^{-3} sulfuric acid and $(1.6–6.5) \times 10^8$ cm^{-3} ammonia, in the presence of 1.5×10^9 cm^{-3} nitric acid (the event shown in Extended Data Fig. 2). The blue dashed curve is a power law fit to the measurements, indicating a strong sensitivity to ammonia concentration ($J_{1.7} = k[NH_3]^{3.7}$).

The vertical grey dotted line in Fig. 2 separates ammonia concentrations measured in different regions in the upper troposphere[5]; Asian monsoon conditions are to the right of this vertical line. Our results indicate that H_2SO_4–NH_3 nucleation is probably responsible for new particle formation in regions with ammonia concentrations below around 10^8 cm^{-3} (12 pptv), but that HNO_3–H_2SO_4–NH_3 nucleation probably dominates at higher ammonia levels in the Asian monsoon upper troposphere. Our nucleation rate measurements confirm that the stronger sulfuric acid is favoured by ammonia in the ammonia-limited regime, so nitric acid will evaporate from the clusters, as it may be displaced by

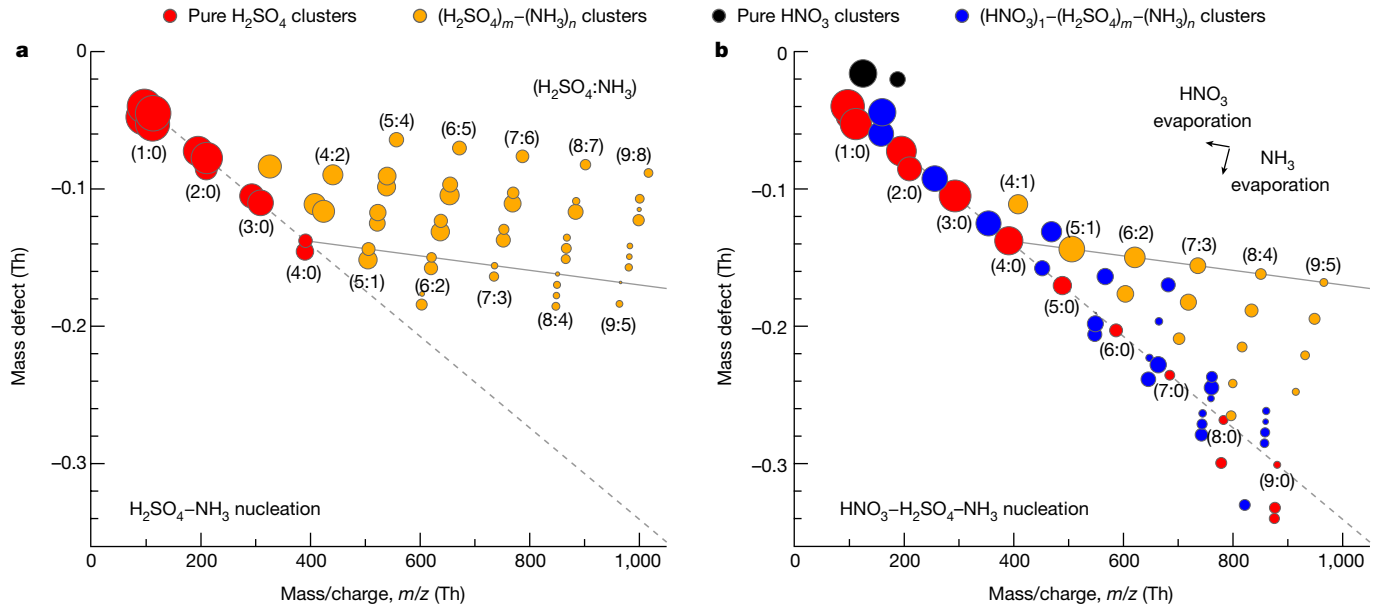

Fig. 3 | Molecular composition of negatively charged clusters during H_2SO_4–NH_3 and HNO_3–H_2SO_4–NH_3 nucleation events at 223 K and 25% relative humidity. Mass defect (difference from integer mass) versus mass/charge (m/z) of negatively charged clusters measured with an APi-TOF mass spectrometer for 1.7×10^6 cm^{-3} sulfuric acid and 6.5×10^8 cm^{-3} ammonia (**a**) and 2.0×10^7 cm^{-3} sulfuric acid, 3.2×10^9 cm^{-3} nitric acid and 7.9×10^9 cm^{-3} ammonia (**b**). The symbol colours indicate the molecular composition as shown. The symbol area is proportional to the logarithm of signal rate (counts per second). The labels (m:n) near the symbols indicate the number of sulfuric acid $(H_2SO_4)_m$ and ammonia $(NH_3)_n$ molecules in the clusters, including both neutral and charged species. The grey dashed lines follow clusters that contain pure H_2SO_4 molecules with an HSO_4^- ion (or SO_4 instead of H_2SO_4 and/or SO_4^- instead of HSO_4^- for pure H_2SO_4 clusters falling below this line in **b**). The grey solid lines follow the 1:1 H_2SO_4–NH_3 addition starting at $(H_2SO_4)_4$–$(NH_3)_0$. Nearly all clusters in panel **a** lie above this line, whereas nearly all clusters in panel **b** fall below it. Most clusters containing HNO_3 lack NH_3 by the time they are measured (they fall near the (m:0) grey dashed line), but the marked difference between **a** and **b** indicates that the nucleating clusters had distinctly different compositions, probably including relatively weakly bound HNO_3–NH_3 pairs in **b**. It is probable that nucleating clusters in the CLOUD chamber at 223 K contain HNO_3–H_2SO_4–NH_3 with a roughly 1:1 acid–base ratio. However, during the transmission from the chamber to the warm APi-TOF mass spectrometer at 293 K, the clusters lose HNO_3 and NH_3, leaving a less volatile core of H_2SO_4 with depleted NH_3. The evaporation of a single NH_3 or HNO_3 molecule from a cluster displaces it on the mass defect plot by a vector distance indicated by the black arrows in **b**.

sulfuric acid. However, as ammonia increases from 1.6 to 6.5×10^8 cm^{-3}, we observe sharp increases in $J_{1.7}$ for HNO_3–H_2SO_4–NH_3 nucleation from 10 to 400 cm^{-3} s^{-1} and in the ratio of particle formation rates (HNO_3–H_2SO_4–NH_3:H_2SO_4–NH_3) from 4 to 30. Our nucleation model (as in Fig. 1) yields slightly higher $J_{1.7}$ than that observed, as shown in Extended Data Fig. 3, but the formation rate variation with ammonia, nonetheless, shows a similar slope.

CLOUD has previously shown that ions enhance nucleation for all but the strongest acid–base clusters; HNO_3–H_2SO_4–NH_3 is probably not an exception. However, the ion enhancement is limited by the GCR ion-pair production rate. We show with the horizontal grey solid lines in Fig. 2 the upper limits on $J_{1.7}$ for ion-induced nucleation of about 2 cm^{-3} s^{-1} at ground level and 35 cm^{-3} s^{-1} in the upper troposphere. Our experimental nucleation rates for HNO_3–H_2SO_4–NH_3 are mostly above upper tropospheric GCR ion production rates. This is confirmed by similar $J_{1.7}$ measured during a neutral nucleation experiment, in which an electric field was used to rapidly sweep ions from the chamber. Thus, for this nucleation scheme, the neutral channel will often prevail over the ion-induced channel in the Asian monsoon upper troposphere. However, when ammonia is diluted away outside the Asian monsoon anticyclone, ions may enhance the nucleation rate up to the GCR limit near 35 cm^{-3} s^{-1}.

In a formal sense, the new-particle-formation mechanism could be one of two types: formation of stable H_2SO_4–NH_3 clusters, followed by nano-Köhler-type activation by nitric acid and ammonia[16]; or else true synergistic nucleation of nitric acid, sulfuric acid and ammonia[9]. In a practical sense, it makes little difference because coagulation loss is a major sink for all small clusters in the atmosphere[20], so appearance of 1.7-nm particles by means of any mechanism constitutes new particle formation. Regardless, we can distinguish between these two possibilities from our measurements of the molecular composition of negatively charged clusters using an atmospheric pressure interface time-of-flight (APi-TOF) mass spectrometer. In Fig. 3, we show cluster mass defect plots during H_2SO_4–NH_3 and HNO_3–H_2SO_4–NH_3 nucleation events at 223 K. The marked difference between Fig. 3a, b indicates that nitric acid changes the composition of the nucleating clusters down to the smallest sizes; thus, the mechanism is almost certainly synergistic HNO_3–H_2SO_4–NH_3 nucleation.

In Fig. 3a, the predominant ions are one of several deprotonated sulfuric acid species, including HSO_4^-, SO_4^-, HSO_5^-, SO_5^- and so on, resulting in a group of points for clusters with similar molecular composition but different mass and mass defect. In the figure, we use the labels (m:n) to indicate the number of sulfuric acid and ammonia molecules in the $(H_2SO_4)_m$–$(NH_3)_n$ clusters, including both neutral and charged species. The mass defect plot closely resembles those previously measured for H_2SO_4–NH_3 nucleation[21]. Negative-ion-induced nucleation proceeds with the known acid–base stabilization mechanism, in which sulfuric acid dimers form as a first step (with HSO_4^- serving as a conjugate base for the first H_2SO_4) and then clusters subsequently grow by 1:1 H_2SO_4–NH_3 addition (that is, as ammonium bisulfate)[9]. We use a grey line to illustrate the 1:1 addition path, beginning at $(H_2SO_4)_4$–$(NH_3)_0$. Clusters larger than the sulfuric acid tetramers mostly contain several ammonia molecules and, so nearly all clusters in Fig. 3a lie above the grey line.

Figure 3b shows a pronounced change in the cluster APi-TOF signal during HNO_3–H_2SO_4–NH_3 nucleation. In addition to pure $(H_2SO_4)_m$–$(NH_3)_n$ clusters, we observe clusters with one extra HNO_3 molecule (or NO_3^- ion), that is, $(HNO_3)_1$–$(H_2SO_4)_m$–$(NH_3)_n$, and the pure nitric acid

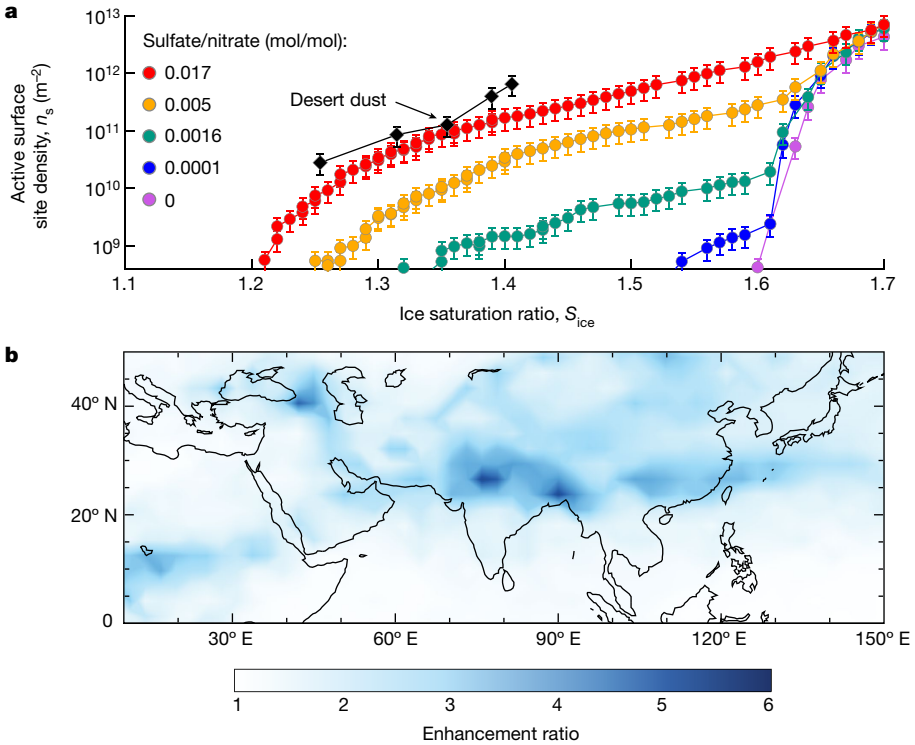

Fig. 4 | Ice nucleation properties and modelled regional contribution of upper tropospheric particles formed from HNO_3–H_2SO_4–NH_3 nucleation. **a**, Active surface site density versus ice saturation ratio, measured by the mINKA instrument at CLOUD, at 233 K and 25% relative humidity. Pure ammonium nitrate particles (purple points) show homogeneous freezing. However, addition of only small amounts of sulfate creates highly ice-nucleation-active particles. At around 1.7% sulfate fraction (red points), the ice nucleating efficiency is comparable with desert dust particles[24]. **b**, Simulation of particle formation in a global model (EMAC) with efficient vertical transport of ammonia into the upper troposphere during the Asian monsoon. Including multi-acid HNO_3–H_2SO_4–NH_3 nucleation (on the basis of the blue dashed curve in Fig. 2) enhances particle number concentrations (nucleation mode) over the Asian monsoon region by a factor of 3–5 compared with the same model with only H_2SO_4–NH_3 nucleation (from Dunne et al.[8], similar to the red solid curve in Fig. 2).

monomer and dimer. In sharp contrast with Fig. 3a, all these clusters are deficient in NH_3, falling below the same grey line as in Fig. 3a. The most deficient contain up to nine bare acids, that is, $(H_2SO_4)_9$ or $(H_2SO_4)_8$–$(HNO_3)_1$. Figure 3b almost certainly does not represent the true cluster composition in the chamber because binary nucleation of H_2SO_4 does not proceed under these exact conditions of H_2SO_4, NH_3, temperature and relative humidity (as demonstrated by Fig. 3a). We can interpret Fig. 3b as follows. It is probable that clusters in the CLOUD chamber (223 K) contain HNO_3–H_2SO_4–NH_3 with a roughly 1:1 acid–base ratio, representing partial neutralization. However, during the transmission from the cold chamber to the warm APi-TOF mass spectrometer (about 293 K), the clusters lose relatively weakly bound HNO_3 and NH_3 molecules but not the lower-volatility H_2SO_4 molecules. Regardless of the interpretation, however, the notable difference between Fig. 3a, b indicates that the sampled clusters had very different compositions and that nitric acid participated in the formation of clusters as small as a few molecules.

Ice nucleation measurements

Nitric acid and ammonia not only enhance the formation rate of new particles but also drive their rapid growth to sizes at which they may act as CCN or ice nucleating particles (INP), above around 50 nm. To assess their effect on cirrus clouds, we measured the ice nucleation ability of particles formed from HNO_3–H_2SO_4–NH_3 nucleation in the CLOUD chamber. Simulating 'hotspot' conditions, we first formed pure ammonium nitrate particles by means of HNO_3–NH_3 nucleation and then increased the H_2SO_4 fraction in the particles by oxidizing progressively more SO_2. We measured their ice nucleation ability using the online continuous flow diffusion instrument, mINKA (Methods and Extended Data Fig. 4). As shown in Fig. 4a, pure ammonium nitrate particles (purple data points) nucleate ice only at high ice saturation ratios (S_{ice}), characteristic of homogeneous nucleation (shown by a steep increase of ice activation above S_{ice} = 1.60 at 215 K). This indicates that pure ammonium nitrate particles, formed by means of HNO_3–NH_3 nucleation, are probably in a liquid state initially, albeit at a relative humidity below the deliquescence point[22]. However, addition of sulfate, with a particulate sulfate-to-nitrate molar ratio as small as 10^{-4}, triggers crystallization of ammonium nitrate. For these particles, we observed a small heterogeneous ice nucleation mode at S_{ice} of 1.54 (blue data points), with other conditions and the particle size distribution held almost constant. Moreover, as the sulfate molar fraction progressively rises to just 0.017 (still almost pure but now solid ammonium nitrate), an active surface site density (n_s) of 10^{10} m^{-2} is reached at S_{ice} as low as 1.26. This is consistent with previous findings, in which particles were generated through nebulization, with a much larger particle diameter and a much higher sulfate-to-nitrate ratio[23]. Our measurements show that HNO_3–H_2SO_4–NH_3 nucleation followed by rapid growth from nitric acid and ammonia condensation — which results in low sulfate-to-nitrate ratio — could provide an important source of INP that are comparable with typical desert dust particles at nucleating ice[24].

Atmospheric implications

Our findings suggest that HNO_3–H_2SO_4–NH_3 nucleation may dominate new particle formation in the Asian monsoon region of the upper troposphere, with a 'flame' of new particles in the outflow of convective

clouds, in which up to 10^{10} cm^{-3} ammonia[6] mixes with low (background) levels of sulfuric acid and nitric acid. Without this mechanism, particle formation through the traditional ternary H_2SO_4–NH_3 nucleation would be much slower and most probably rate-limited by the scarce sulfuric acid. Furthermore, by co-condensing with nitric acid, the convected ammonia also drives the growth of the newly formed particles. Given typical acid-excess conditions in the upper troposphere, condensational growth is governed by the availability of ammonia. Consequently, particles will steadily (and rapidly) grow until ammonia is depleted after several *e*-folding times set by the particle condensation sink. On the basis of condensation sinks generally observed in the tropical upper troposphere[4], this timescale will be several hours. Within this time interval, given the observed ammonia levels, newly formed particles will be able to grow to CCN sizes and even small admixtures of sulfuric acid will render these particles efficient INP.

Our laboratory measurements provide a mechanism that can account for recent observations of abundant ammonium nitrate particles in the Asian monsoon upper troposphere[6]. To evaluate its importance on a global scale, we first parameterized our experimentally measured $J_{1.7}$ for HNO_3–H_2SO_4–NH_3 nucleation as a function of sulfuric acid, nitric acid and ammonia concentrations (Methods). The parameterization is obtained using a power-law dependency for each vapour (Extended Data Fig. 5), given that the critical cluster composition is associated with the exponents according to the first nucleation theorem[25]. Then we implemented this parameterization in a global aerosol model (EMAC, see Methods for modelling details). The EMAC model predicts that HNO_3–H_2SO_4–NH_3 nucleation at 250 hPa (11 km, approximately 223 K) produces an annual average exceeding 1,000 cm^{-3} new particles over an extensive area (Extended Data Fig. 6). This corresponds to an increase in particle number concentration (Fig. 4b) up to a factor of five higher than in a control simulation with only ternary H_2SO_4–NH_3 nucleation[8]. The strongest increase occurs mostly over Asia, in which ammonia is ample because of deep convection from ground sources.

However, another global model (TOMCAT, see Methods) shows much lower ammonia mixing ratios in the upper troposphere than EMAC (<1 pptv compared with <100 pptv, respectively), although with a broadly similar spatial distribution (Extended Data Fig. 7a, b). This large variability of upper tropospheric ammonia is also indicated by recent field measurements on local[6,26] and global[5,27] scales. In view of its importance for both H_2SO_4–NH_3 and HNO_3–H_2SO_4–NH_3 nucleation, there is an urgent need to improve upper tropospheric measurements of ammonia, as well as improve knowledge of its sources, transport and sinks.

We thus turned to a cloud-resolving model to estimate the ammonia vapour fraction remaining after deep convection (see Methods). We show in Extended Data Fig. 8 that around 10% of the boundary layer ammonia can be transported into the upper troposphere and released as vapour by a base-case convective cloud. The sensitivity tests further illustrate that the key factor governing the fraction of ammonia remaining in the cloud outflow is the retention of ammonia molecules by ice particles (Extended Data Fig. 8e), whereas cloud water pH (Extended Data Fig. 8c) and cloud water content (Extended Data Fig. 8d) only play minor roles once glaciation occurs. Given that more than 10 ppbv of ammonia is often observed in the Asian boundary layer[28], it is plausible that the observed 1.4 ppbv (10^{10} cm^{-3}) ammonia in the upper troposphere[6] is indeed efficiently transported by the convective systems.

Although the ammonium–nitrate–sulfate particles are formed locally, they can travel from Asia to North America in just three days by means of the subtropical jet stream, as the typical residence time of Aitken mode particles ranges from one week to one month in the upper troposphere[29]. As a result, these particles can persist as an intercontinental band, covering more than half of the mid-latitude surface area of the Northern Hemisphere (Extended Data Fig. 6). In summary, synergistic nucleation of nitric acid, sulfuric acid and ammonia could provide an important source of new CCN and ice nuclei in the upper troposphere, especially over the Asian monsoon region, and is closely linked with anthropogenic ammonia emissions[27].

Online content

Any methods, additional references, Nature Research reporting summaries, source data, extended data, supplementary information, acknowledgements, peer review information; details of author contributions and competing interests; and statements of data and code availability are available at https://doi.org/10.1038/s41586-022-04605-4.

1. Clarke, A. et al. Nucleation in the equatorial free troposphere: favorable environments during PEM-Tropics. *J. Geophys. Res. Atmos.* **104**, 5735–5744 (1999).
2. Weigel, R. et al. In situ observations of new particle formation in the tropical upper troposphere: the role of clouds and the nucleation mechanism. *Atmos. Chem. Phys.* **11**, 9983–10010 (2011).
3. Gordon, H. et al. Causes and importance of new particle formation in the present-day and pre-industrial atmospheres. *J. Geophys. Res. Atmos.* **122**, 8739–8760 (2017).
4. Williamson, C. J. et al. A large source of cloud condensation nuclei from new particle formation in the tropics. *Nature* **574**, 399–403 (2019).
5. Höpfner, M. et al. First detection of ammonia (NH_3) in the Asian summer monsoon upper troposphere. *Atmos. Chem. Phys.* **16**, 14357–14369 (2016).
6. Höpfner, M. et al. Ammonium nitrate particles formed in upper troposphere from ground ammonia sources during Asian monsoons. *Nat. Geosci.* **12**, 608–612 (2019).
7. Intergovernmental Panel on Climate Change. *Climate Change 2013: The Physical Science Basis* (Cambridge Univ. Press, 2013).
8. Dunne, E. M. et al. Global atmospheric particle formation from CERN CLOUD measurements. *Science* **354**, 1119–1124 (2016).
9. Kirkby, J. et al. Role of sulphuric acid, ammonia and galactic cosmic rays in atmospheric aerosol nucleation. *Nature* **476**, 429–433 (2011).
10. Andreae, M. O. et al. Aerosol characteristics and particle production in the upper troposphere over the Amazon Basin. *Atmos. Chem. Phys.* **18**, 921–961 (2018).
11. Lehtipalo, K. et al. Multicomponent new particle formation from sulfuric acid, ammonia, and biogenic vapors. *Sci. Adv.* **4**, eaau5363 (2018).
12. Zhao, B. et al. High concentration of ultrafine particles in the Amazon free troposphere produced by organic new particle formation. *Proc. Natl Acad. Sci.* **117**, 25344–25351 (2020).
13. Ge, C., Zhu, C., Francisco, J. S., Zeng, X. C. & Wang, J. A molecular perspective for global modeling of upper atmospheric NH_3 from freezing clouds. *Proc. Natl Acad. Sci.* **115**, 6147–6152 (2018).
14. Martin, R. V. et al. Space-based constraints on the production of nitric oxide by lightning. *J. Geophys. Res. Atmos.* **112**, D09309 (2007).
15. Lelieveld, J. et al. The South Asian monsoon—pollution pump and purifier. *Science* **361**, 270–273 (2018).
16. Wang, M. et al. Rapid growth of atmospheric nanoparticles by nitric acid and ammonia condensation. *Nature* **580**, 184–189 (2020).
17. Stolzenburg, D. et al. Enhanced growth rate of atmospheric particles from sulfuric acid. *Atmos. Chem. Phys.* **20**, 7359–7372 (2020).
18. Kürten, A. New particle formation from sulfuric acid and ammonia: nucleation and growth model based on thermodynamics derived from CLOUD measurements for a wide range of conditions. *Atmos. Chem. Phys.* **19**, 5033–5050 (2019).
19. Xiao, M. et al. The driving factors of new particle formation and growth in the polluted boundary layer. *Atmos. Chem. Phys.* **21**, 14275–14291 (2021).
20. Ehrhart, S. & Curtius, J. Influence of aerosol lifetime on the interpretation of nucleation experiments with respect to the first nucleation theorem. *Atmos. Chem. Phys.* **13**, 11465–11471 (2013).
21. Schobesberger, S. et al. Molecular understanding of atmospheric particle formation from sulfuric acid and large oxidized organic molecules. *Proc. Natl Acad. Sci.* **110**, 17223–17228 (2013).
22. Martin, S. T. Phase transitions of aqueous atmospheric particles. *Chem. Rev.* **100**, 3403–3454 (2000).
23. Wagner, R. et al. Solid ammonium nitrate aerosols as efficient ice nucleating particles at cirrus temperatures. *J. Geophys. Res. Atmos.* **125**, e2019JD032248 (2020).
24. Ullrich, R. et al. A new ice nucleation active site parameterization for desert dust and soot. *J. Atmos. Sci.* **74**, 699–717 (2017).
25. Oxtoby, D. W. & Kashchiev, D. A general relation between the nucleation work and the size of the nucleus in multicomponent nucleation. *J. Chem. Phys.* **100**, 7665–7671 (1994).
26. Kille, N. et al. The CU mobile solar occultation flux instrument: structure functions and emission rates of NH_3, NO_2 and C_2H_6. *Atmos. Meas. Tech.* **10**, 373–392 (2017).
27. Nault, B. A. et al. Chemical transport models often underestimate inorganic aerosol acidity in remote regions of the atmosphere. *Commun. Earth Environ.* **2**, 93 (2021).
28. Warner, J. X., Wei, Z., Strow, L. L., Dickerson, R. R. & Nowak, J. B. The global tropospheric ammonia distribution as seen in the 13-year AIRS measurement record. *Atmos. Chem. Phys.* **16**, 5467–5479 (2016).
29. Williams, J., Reus, M. D., Krejci, R., Fischer, H. & Ström, J. Application of the variability-size relationship to atmospheric aerosol studies: estimating aerosol lifetimes and ages. *Atmos. Chem. Phys.* **2**, 133–145 (2002).

[1]Center for Atmospheric Particle Studies, Carnegie Mellon University, Pittsburgh, PA, USA. [2]Department of Chemistry, Carnegie Mellon University, Pittsburgh, PA, USA. [3]Laboratory of Atmospheric Chemistry, Paul Scherrer Institute, Villigen, Switzerland. [4]Institute of Meteorology and Climate Research, Karlsruhe Institute of Technology, Karlsruhe, Germany. [5]Institute for Atmospheric and Environmental Sciences, Goethe University Frankfurt, Frankfurt am Main, Germany. [6]Institute for Atmospheric and Earth System Research (INAR), University of Helsinki, Helsinki, Finland. [7]Present address: Division of Chemistry and Chemical Engineering, California Institute of Technology, Pasadena, CA, USA. [8]Department of Meteorology, Stockholm University, Stockholm, Sweden. [9]Bolin Centre for Climate Research, Stockholm University, Stockholm, Sweden. [10]Institute for Ion Physics and Applied Physics, University of Innsbruck, Innsbruck, Austria. [11]Department of Chemical Engineering, Carnegie Mellon University, Pittsburgh, PA, USA. [12]CERN, the European Organization for Nuclear Research, Geneva, Switzerland. [13]CENTRA and Faculdade de Ciências da Universidade de Lisboa, Campo Grande, Lisbon, Portugal. [14]Leibniz Institute for Tropospheric Research, Leipzig, Germany. [15]Helsinki Institute of Physics, University of Helsinki, Helsinki, Finland. [16]Department of Chemistry & CIRES, University of Colorado Boulder, Boulder, CO, USA. [17]Faculty of Physics, University of Vienna, Vienna, Austria. [18]Department of Applied Physics, University of Eastern Finland, Kuopio, Finland. [19]Aerodyne Research, Inc., Billerica, MA, USA. [20]Finnish Meteorological Institute, Helsinki, Finland. [21]Atmospheric and Oceanic Sciences, Princeton University, Princeton, NJ, USA. [22]P. N. Lebedev Physical Institute of the Russian Academy of Sciences, Moscow, Russia. [23]Moscow Institute of Physics and Technology (National Research University), Moscow, Russia. [24]Department of Physics, University of Genoa & INFN, Genoa, Italy. [25]Department of Atmospheric and Oceanic Sciences, University of Colorado Boulder, Boulder, CO, USA. [26]Atmospheric Chemistry Department, Max Planck Institute for Chemistry, Mainz, Germany. [27]School of Earth and Environment, University of Leeds, Leeds, UK. [28]Institute Infante Dom Luíz, University of Beira Interior, Covilhã, Portugal. [29]Ionicon Analytik Ges.m.b.H., Innsbruck, Austria. [30]Joint International Research Laboratory of Atmospheric and Earth System Sciences, Nanjing University, Nanjing, China. [31]Aerosol and Haze Laboratory, Beijing Advanced Innovation Center for Soft Matter Science and Engineering, Beijing University of Chemical Technology, Beijing, China. [32]Department of Environmental Science (ACES), Stockholm University, Stockholm, Sweden. [33]Climate and Atmosphere Research Center, The Cyprus Institute, Nicosia, Cyprus. [34]Department of Engineering and Public Policy, Carnegie Mellon University, Pittsburgh, PA, USA. ✉e-mail: nmd@andrew.cmu.edu

Methods

The CLOUD facility

We conducted our measurements at the CERN CLOUD facility, a 26.1-m^3, electropolished, stainless-steel CLOUD chamber that allows new-particle-formation experiments under the full range of tropospheric conditions with scrupulous cleanliness and minimal contamination[9,30]. The CLOUD chamber is mounted in a thermal housing, capable of keeping the temperature constant in the range 208 K and 373 K with a precision of ±0.1 K (ref. [31]). Photochemical processes are initiated by homogeneous illumination with a built-in UV fibre-optic system, including four 200-W Hamamatsu Hg-Xe lamps at wavelengths between 250 and 450 nm and a 4-W KrF excimer UV laser at 248 nm with adjustable power. New particle formation under different ionization levels is simulated with and without the electric fields (±30 kV), which can artificially scavenge or preserve small ions produced from ground-level GCR. Uniform spatial mixing is achieved with magnetically coupled stainless-steel fans mounted at the top and bottom of the chamber. The characteristic gas mixing time in the chamber during experiments is a few minutes. The loss rate of condensable vapours and particles onto the chamber walls is comparable with the ambient condensation sink. To avoid contamination, the chamber is periodically cleaned by rinsing the walls with ultra-pure water and heating to 373 K for at least 24 h, ensuring extremely low contaminant levels of sulfuric acid $<5 \times 10^4$ cm^{-3} and total organics <50 pptv (refs. [32,33]). The CLOUD gas system is also built to the highest technical standards of cleanliness and performance. The dry air supply for the chamber is provided by boil-off oxygen (Messer, 99.999%) and boil-off nitrogen (Messer, 99.999%) mixed at the atmospheric ratio of 79:21. Highly pure water vapour, ozone and other trace gases such as nitric acid and ammonia can be precisely added at the pptv level from ultra-pure sources.

Instrumentation

Gas-phase sulfuric acid was measured using a nitrate chemical ionization APi-TOF (nitrate-CI-APi-TOF) mass spectrometer[34,35] and an iodide chemical ionization time-of-flight mass spectrometer equipped with a Filter Inlet for Gases and Aerosols (I-FIGAERO-CIMS)[36,37]. The nitrate-CI-APi-TOF mass spectrometer is equipped with an electrostatic filter in front of the inlet to remove ions and charged clusters formed in the chamber. A corona charger is used to ionize the reagent nitric acid vapour in a nitrogen flow[38]. Nitrate ions are then guided in an atmospheric pressure drift tube by an electric field to react with the analyte molecules in the sample flow. Sulfuric acid is quantified for the nitrate-CI-APi-TOF with a detection limit of about 5×10^4 cm^{-3}, following the same calibration and loss correction procedures described previously[9,32,39]. FIGAERO is a manifold inlet for a CIMS with two operating modes. In the sampling mode, a coaxial core sampling is used to minimize the vapour wall loss in the sampling line. The total flow is maintained at 18.0 slpm and the core flow at 4.5 slpm; the CIMS samples at the centre of the core flow with a flow rate of 1.6 slpm. Analyte molecules are introduced into a 150-mbar ion-molecule reactor, chemically ionized by iodide ions that are formed in a Po-210 radioactive source and extracted into the mass spectrometer. The sulfuric acid calibration coefficient for the I-FIGAERO-CIMS is derived using the absolute sulfuric acid concentrations measured with the pre-calibrated nitrate-CI-APi-TOF.

Gas-phase nitric acid was also measured using the I-FIGAERO-CIMS. Nitric acid concentration was quantified by measuring HNO_3/N_2 mixtures with known nitric acid concentrations, following similar procedures described previously[16]. The HNO_3/N_2 mixture was sourced from flowing 2 slpm ultra-pure nitrogen through a portable nitric acid permeation tube, at constant 40 °C. The permeation rate of nitric acid was determined by passing the outflow of the permeation tube through an impinger containing deionized water and analysing the resulting nitric acid solution through spectrophotometry.

Gas-phase ammonia was either measured or calculated. We measured ammonia using a proton transfer reaction time-of-flight mass spectrometer (PTR3-TOF-MS, or PTR3 for short)[40]. As a carrier gas for the primary ions, we used argon (ultra-high purity 5.0) to ensure that ammonium ions could not be artificially formed in the region of the corona discharge. Although the theoretical detection limit from peak height and width would be even smaller, the lowest concentration we were able to measure during the first fully ammonia-free runs of the beginning of the campaign was 10^9 cm^{-3}. An explanation for this is that, when concentrations of ammonia are low, effects of wall interaction of the highly soluble ammonia become important and the decay of ammonia in the inlet line becomes very slow. To reduce inlet wall contacts, we used a core-sampling technique directly in front of the instrument to sample only the centre 2 slpm of the 10 slpm inlet flow, but owing to frequent necessary on-site calibrations of volatile organic compounds, a Teflon ball valve was placed within the sample line that probably influenced measurements during times of low ammonia concentrations. At concentrations above about 2×10^9 cm^{-3} ammonia, however, the response of the instrument was very fast, so that, for example, changes in the chamber ammonia flow rate were easily detectable. Off-site calibrations showed a humidity-independent calibration factor of 0.0017 ncps/ppb. Calibrated data from the PTR3 agree very well with the Picarro above 10^{10} cm^{-3} (detection limit of the Picarro). The PTR3 also provides information about the overall cleanliness of the volatile organic compounds in the chamber. The technique was extensively described previously[40].

For ammonia concentrations below 10^9 cm^{-3}, we calculated concentration using the calibrated ammonia injection flow and an estimated first-order wall-loss rate. The wall-loss rate (k_{wall}) for ammonia inside the CLOUD chamber is confirmed to be faster than for sulfuric acid[41], and can be determined from the following expression[42]:

$$k_{wall} = \frac{A}{V}\frac{2}{\pi}\sqrt{k_e D_i} = C_{wall}\sqrt{D_i} \quad (1)$$

in which A/V is the surface-to-volume ratio of the chamber, k_e is the eddy diffusion constant (determined by the turbulent mixing intensity, not the transport properties of the gases) and D_i is the diffusion coefficient for each gas. C_{wall} is thus referred to as an empirical parameter of experiment conditions in the chamber. Here we first determine the k_{wall} for sulfuric acid and nitric acid to be 1.7×10^{-3} and 1.9×10^{-3} s^{-3}, respectively, by measuring their passive decay rates and subtracting the loss rate of chamber dilution for both (1.2×10^{-3} s^{-1}), as well as the loss rate of dimer formation for sulfuric acid (around 1.6×10^{-3} s^{-1} for 5×10^6 cm^{-3} H_2SO_4). The k_{wall} for sulfuric acid agrees with our measurements from previous campaigns[43]. We then derive the C_{wall} for sulfuric acid and nitric acid both to be 2.0×10^{-4} $torr^{-0.5}$ cm^{-1} $s^{-0.5}$, with $D_{H_2SO_4}$ of 74 torr cm^2 s^{-1} and D_{HNO_3} of 87 torr cm^2 s^{-1} (ref. [44]). Finally, we calculate the k_{wall} for ammonia to be 2.7×10^{-3} s^{-1}, with D_{NH_3} of 176 torr cm^2 s^{-1} (ref. [44]). Ammonia desorption from the chamber surface is a strong function of the temperature and is believed to be negligible at low temperatures[30]. Even after a long time exposure, ammonia desorption should be less than 1.6×10^6 cm^{-3}, according to previous parameterization of ammonia background contamination in the CLOUD chamber[41].

The composition of negatively charged ions and clusters were determined using an APi-TOF mass spectrometer[45]. The APi-TOF mass spectrometer is connected to the CLOUD chamber by means of a 1-inch (21.7-mm inner diameter) sampling probe, with coaxial core sampling to minimize the wall losses in the sampling line. The total sample flow is maintained at 20 slpm and the core sample flow for the APi-TOF mass spectrometer at 0.8 slpm. Because this instrument only measures charged clusters, the measurements were made during GCR conditions. Owing to a large temperature difference between the cold chamber (223 K) and the warm APi-TOF mass spectrometer (around 293 K), HNO_3–H_2SO_4–NH_3 clusters probably lose relatively

weakly bonded HNO_3 and NH_3 molecules. This resembles the chemical ionization process of detecting ammonia with the nitrate-CI-APi-TOF, in which HNO_3 and NH_3 molecules rapidly evaporate from the resulting ammonia nitrate cluster in the CI-APi-TOF vacuum regions[46].

Gas monitors were used to measure ozone (O_3, Thermo Environmental Instruments TEI 49C), sulfur dioxide (SO_2, Thermo Fisher Scientific Inc. 42i-TLE) and nitric oxide (NO, ECO Physics, CLD 780TR). Nitrogen dioxide (NO_2) was measured by a cavity attenuated phase shift nitrogen dioxide monitor (CAPS NO_2, Aerodyne Research Inc.) and a home-made cavity enhanced differential optical absorption spectroscopy (CE-DOAS) instrument. The relative humidity of the chamber was determined by dew point mirrors (EdgeTech).

Particle number concentrations were monitored by condensation particle counters (CPCs), including an Airmodus A11 nano Condensation Nucleus Counter (nCNC), consisting of a particle size magnifier (PSM) and a laminar-flow butanol-based CPC[47], as well as a butanol TSI 3776 CPC. Particle size distributions between 1.8 nm and 500 nm were measured by a nano-scanning electrical mobility spectrometer (nSEMS), a nano-scanning mobility particle sizer (nano-SMPS) and a long-SMPS. The nSEMS used a new, radial opposed migration ion and aerosol classifier (ROMIAC), which is less sensitive to diffusional resolution degradation than the DMAs[48], and a soft X-ray charge conditioner. After leaving the classifier, particles were first activated in a fast-mixing diethylene glycol stage[49] and then counted with a butanol-based CPC. The nSEMS transfer function that was used to invert the data to obtain the particle size distribution was derived using 3D finite element modelling of the flows, electric field and particle trajectories[50,51]. The two commercial mobility particle size spectrometers, nano-SMPS and long-SMPS, have been fully characterized, calibrated and validated in several previous studies[52–54].

Particle-phase chemical composition was quantified using a high-resolution time-of-flight aerosol mass spectrometer (HR-ToF-AMS, Aerodyne Research). The working principles of the HR-ToF-AMS have been explained in detail previously[55,56]. In brief, particles are focused by an aerodynamic lens and flash-vaporized by impact onto a hot surface at 600 °C under a high vacuum. The vapours are then ionized by 70-eV electrons and the ions are detected with a ToF mass spectrometer. Ionization efficiency calibrations were conducted before and after the campaign and the variation is within 30%. The particle collection efficiency was considered constant during the experiments because temperature and relative humidity in the chamber were fixed and the particle composition was dominated by ammonium nitrate.

INP were measured in real time at 215 K, as a function of ice saturation ratio (S_{ice}), by the mobile ice nucleation instrument of the Karlsruhe Institute of Technology (mINKA). mINKA is a continuous flow diffusion chamber with vertical cylindrical geometry[57], on the basis of the design of INKA[58,59]. A detailed description of the continuous flow diffusion chamber working principle is presented elsewhere[57]. Here, predefined scans of the water vapour saturation ratios were performed in the diffusion chamber every 30 min. For each scan, S_{ice} steadily increased from 1.2 to 1.8 while the temperature was kept constant. The errors associated to temperature and S_{ice} inside the diffusion chamber were derived from the uncertainty of the thermocouples attached to the instrument walls (±0.5 K)[59].

Determination of particle formation rate

The particle formation rate, $J_{1.7}$, is determined at 1.7-nm mobility diameter (1.4-nm physical diameter), here using a PSM. At 1.7 nm, a particle is normally considered to be above its critical size and, therefore, thermodynamically stable. $J_{1.7}$ is calculated using the flux of the total concentration of particles growing past a specific diameter (here at 1.7 nm), as well as correction terms accounting for aerosol losses owing to dilution in the chamber, wall losses and coagulation. Details were described previously[47].

Nucleation model

The nucleation model is on the basis of the thermodynamic model for H_2SO_4–NH_3 nucleation described in detail previously[18,19]. It is developed from the general dynamic equations[60], to calculate the production and losses for each cluster/particle size to determine the formation rates of the acid–base clusters. For HNO_3–H_2SO_4–NH_3 nucleation, we simplify the model simulations by extrapolating nano-Köhler-type activation by nitric acid and ammonia to clusters down to sulfuric acid trimers. Eighty size bins, ranging from one ammonium sulfate cluster to 300 nm, are used to capture the evolution of the size and composition of polydisperse particles.

In brief, we calculate the equimolar condensation flux of nitric acid and ammonia on the basis of the supersaturation of gas-phase nitric acid and ammonia over particle-phase ammonium nitrate[39,60]:

$$\Phi_i^v = k_c\,[C_i^v - a_i\,C_i^0] \tag{2}$$

in which Φ_i^v is the net condensation flux of nitric acid or ammonia, with vapour concentration C_i^v and saturation concentration C_i^0. The term a_i is the activity of species i at the condensed-phase surface of the particle and k_c is the condensation sink for vapours resulting from interaction with particles. The saturation concentrations of nitric acid and ammonia are estimated on the basis of the dissociation constant K_p (ref. [60]). When the vapours are unsaturated, particle-phase ammonium nitrate will evaporate to nitric acid and ammonia to reach the equilibrium.

We also include the Kelvin term ($K_{i,p}$) in the simulation to account for the increased activity ($a_i = a'_i\,K_{i,p}$) of a small curved cluster/particle:

$$K_{i,p} = 10^{(d_{K10}/d_p)} \tag{3}$$

in which $K_{i,p}$ scales with a 'Kelvin diameter' (d_{K10}) for decadal change and d_p is the diameter of the small cluster/particle. The Kelvin diameter for ammonium nitrate is estimated to be 5.3 nm by fitting the data from previous CLOUD experiments according to:

$$S = 10^{(d_{K10}/d_{act})} \tag{4}$$

in which S is the saturation ratio, calculated by means of dividing the product of measured concentrations of nitric acid and ammonia by the dissociation constant K_p and d_{act} is the activation diameter, at which the thermodynamic energy barrier for condensation is overcome and particles start to grow rapidly.

Determination of ice nucleation ability

During the experiments, aerosol particles were continuously sampled from the CLOUD chamber into the mINKA ice nucleation instrument, using an actively cooled sampling line for a consistent temperature profile. Particles were then subject to well-controlled ice supersaturated conditions; the ones that nucleated ice were selectively detected and counted by an optical particle counter (custom-modified Climet CI-3100, lower detection limit of about 1 µm) located at the outlet of the instrument. Background ice crystals were quantified before each saturation scan (for 2 min) and subtracted from the total ice number concentration of the corresponding measurement. The fraction of INP (f_{ice}) was calculated as the ratio of ice crystals number concentration to the total number of particles larger than 10 nm in diameter. The ice nucleation active surface site density (n_s)[61] was calculated as the ratio of ice number concentration to the total surface area of particles larger than 10 nm in diameter. The overall uncertainty of n_s is estimated to be ±40% (ref. [24]). Particle number and surface area concentrations were measured by the SMPS described in the 'Instrumentation' section.

In Extended Data Fig. 4, we provide a detailed summary of the measurement data recorded during the 'hotspot condition' experiment shown in Fig. 4a, in which we investigated the heterogeneous crystallization and ice nucleation ability of ammonium nitrate/sulfate particles produced directly from new particle formation. We first formed pure ammonium nitrate particles through nucleation of nitric acid and

ammonia vapours at 223 K and 15–30% relative humidity (over liquid water). When the evolution of the particle size distribution (Extended Data Fig. 4a) levelled off at a median diameter of around 100 nm, we turned on the UV lights and progressively injected SO_2 at 03:33 to gradually increase sulfuric acid concentration (Extended Data Fig. 4b). Consequently, in Extended Data Fig. 4c, aerosol mass spectrometer measurements show that particle composition was dominated by ammonium nitrate over the course of the experiment, whereas sulfate appeared approximately 1 h after the injection of SO_2. Finally, we show ice nucleation measurements in Extended Data Fig. 4d. Each vertical trajectory represents a saturation ratio scan in mINKA, colour-coded by the measured ice active fraction (f_{ice}). In each scan, we use a horizontal black dash to indicate an ice onset threshold corresponding to f_{ice} of 10^{-3}. Circles indicate the corresponding scans shown in Fig. 4a.

When the particulate sulfate-to-nitrate molar ratio is smaller than 0.0001, the ice nucleation threshold is detected at an ice saturation ratio (S_{ice}) of about 1.6, consistent with the homogeneous freezing threshold of aqueous solution droplets[62]. This finding shows that, if particles presented as absolutely pure ammonium nitrate (NH_4NO_3), they would exist as supercooled liquid droplets even at very low relative humidity, consistent with previous studies[22,63]. As the particulate sulfate-to-nitrate molar ratio gradually increases to about 0.017, the ice nucleation onset shifts to a lower S_{ice} of 1.2, caused by heterogeneous ice nucleation on crystalline ammonium nitrate particles[23]. Crystalline salts are known to be efficient INP at low temperatures when their deliquescence occurs at higher relative humidity compared with the humidity range of their heterogeneous ice nucleation activity[64]. The fact that the addition of sulfate can promote the crystallization of ammonium nitrate has already been observed in previous studies with particles nebulized in large sizes (around 1 μm) from bulk solutions of ammonium nitrate/sulfate[6,23,65]. But it is evidenced here for the first time in an in situ particle nucleation and crystallization experiment representative of upper tropospheric conditions.

Particle formation rate parameterization

According to the first nucleation theorem for multicomponent systems[25], we parameterize the particle formation rates ($J_{1.7}$) for the HNO_3–H_2SO_4–NH_3 nucleation scheme with the empirical formula:

$$J_{1.7} = k\,[H_2SO_4]^a\,[HNO_3]^b[NH_3]^c \quad (5)$$

in which vapour concentrations are in units of cm^{-3} and k, a, b and c are free parameters. This method has been validated by previous observations that the particle formation rates ($J_{1.7}$) vary as a product of power-law functions of nucleating vapours. For example, $J_{1.7}$ for ternary sulfuric acid, ammonia (and water) nucleation follows a cubic dependency on sulfuric acid[8] and a linear[8] or quadratic[19] dependency on ammonia; $J_{1.7}$ for multicomponent nucleation of sulfuric acid, biogenic oxidized organics and ammonia follows a quadratic dependency on sulfuric acid, a linear dependency on both organics[66] and ammonia[11]. The prefactor k accounts for effects of external conditions, such as temperature and relative humidity, thus differs in different environments.

To isolate variables, here we fit the power-law exponents for sulfuric acid, nitric acid and ammonia, respectively, to the dataset of experiments in which only the corresponding vapour concentration was varied. The red triangles, blue circles and yellow squares in Extended Data Fig. 5a–c (same experiments in Extended Data Fig. 1, Fig. 1 and Extended Data Fig. 2), respectively, show that $J_{1.7}$ depends on $[H_2SO_4]^3$ for sulfuric acid between 2.6×10^5 and 2.9×10^6 cm^{-3} (or 0.008 and 0.09 pptv), on $[HNO_3]^2$ for nitric acid between 2.3×10^8 and 1.7×10^9 cm^{-3} (or 7 and 52 pptv) and on $[NH_3]^4$ for ammonia between 1.7×10^8 and 4.9×10^8 cm^{-3} (or 5 and 15 pptv). The third power exponent for sulfuric acid is consistent with previously reported parameterizations for ternary H_2SO_4–NH_3 nucleation[8,19]. The fourth power exponent for ammonia, however, is larger than those in ternary[8,19] or multicomponent systems[11], which emphasizes the critical role of ammonia and suggests further bonding between ammonia and nitric acid molecules in the nucleating clusters. Next, we verify the exponents by refitting the product of $[H_2SO_4]^3$, $[HNO_3]^2$ and $[NH_3]^4$ to the full dataset. Extended Data Fig. 5d shows good consistency ($R^2 = 0.9$) of the parameterization among the three experiments, with a slope of 3.4×10^{-71} s^{-1} cm^{24} being the prefactor k:

$$J_{1.7} = 3.4 \times 10^{-71}[H_2SO_4]^3[HNO_3]^2[NH_3]^4 \quad (6)$$

This parameterization is representative of new particle formation in the Asian monsoon upper troposphere because our experimental conditions of 223 K and 25% relative humidity, as well as concentrations of sulfuric acid[67,68] and nitric acid[69,70], are within the upper tropospheric range, with ammonia[5,6] typical of Asian monsoon regions. One caveat, however, is that the cosmic radiation was at the ground level in our chamber, as shown with grey dot-dashed horizontal line in Extended Data Fig. 5d. The ion-pair production rate can be up to ten times higher in the ambient upper troposphere[71], potentially leading to further enhancement of $J_{1.7}$ by ion-induced nucleation, although the neutral channel dominates in our experiments.

Estimated temperature dependence of the particle formation rate

We did not cover the full temperature range in the upper troposphere, instead focusing on 223 K. However, to make the parameterization in the previous section more applicable for model simulations while not overstating the role of this mechanism, we provide some constraints on the temperature dependence of $J_{1.7}$ for HNO_3–H_2SO_4–NH_3 nucleation. Broadly, it is certain that particle formation involving HNO_3 will have a strong temperature dependence, becoming much slower as T increases.

We first present the temperature dependence of $J_{1.7}$ for pure HNO_3–NH_3 nucleation with the expression:

$$J_{1.7} = k(T)f([HNO_3], [NH_3]) \quad (7)$$

in which $k(T)$ is an empirical temperature-dependent rate constant and has the Arrhenius form

$$k(T) = e^{\left(-\frac{1}{T}\frac{E}{R}\right)}, \quad (8)$$

in which T is the absolute temperature (in Kelvin), E is the activation energy and R is the universal gas constant. $f([HNO_3],[NH_3])$ is a function of the ammonia and nitric acid concentrations (including the pre-exponential factor and free-fitting parameters). This expression is then fitted to the dataset in Fig. 3c in our previous study[16], in which $J_{1.7}$ were measured with only nitric acid, ammonia and water vapours added to the chamber, and the temperature was progressively decreased from 258 K to 249 K. Because the ammonia and nitric acid concentrations were kept almost constant during the temperature transition, we treat the $f([HNO_3],[NH_3])$ term as a constant to reduce the degrees of freedom. This expression with its two free parameters leads to a good agreement with the data, $R_2 = 0.96$. And the fitted $-E/R$ and $f([HNO_3],[NH_3])$ are 14,000 K and 3.2×10^{-26}, respectively.

Next, we apply the same $k(T)$ term to the HNO_3–H_2SO_4–NH_3 parameterization (equation (9)), assuming that the multicomponent nucleation follows a similar temperature dependence:

$$J_{1.7} = 2.9 \times 10^{-98} e^{\left(\frac{14{,}000}{T}\right)}[H_2SO_4]^3[HNO_3]^2[NH_3]^4 \quad (9)$$

Although this temperature-dependent parameterization may not be the final description of this process, it tracks the trend of $J_{1.7}$ well. In the event of 4×10^6 cm^{-3} H_2SO_4, 1.5×10^9 cm^{-3} HNO_3 and 5×10^8 cm^{-3} NH_3, the multicomponent nucleation is quenched ($J_{1.7} < 0.01$ cm^{-3} s^{-1}) above 268 K. This is consistent with the observations that nitric acid

and ammonia only contribute to the growth of ammonium sulfate particles at 278 K (ref. [16]). At 223 K, the parameterized $J_{1.7}$ is 306 cm^{-3} s^{-1}, matching our measurement in Fig. 2. And for the temperature in the upper troposphere and lower stratosphere (198 K), the parameterized $J_{1.7}$ is 8×10^5 cm^{-3} s^{-1}, which is still much slower than its kinetic limit of about 10^9–10^{10} cm^{-3} s^{-1}.

The EMAC global model

The ECHAM/MESSy Atmospheric Chemistry (EMAC) model is a numerical chemistry and climate simulation system that includes sub-models describing tropospheric and middle atmosphere processes and their interaction with oceans, land and human influences[72]. It uses the second version of the Modular Earth Submodel System (MESSy2) to link multi-institutional computer codes. Atmospheric circulation is calculated by the 5th generation of the European Centre Hamburg general circulation model (ECHAM5 (ref. [73])) and atmospheric chemical kinetics are solved for every model time step. For the present study, we applied EMAC (ECHAM5 version 5.3.02, MESSy version 2.54.0) in the T42L31ECMWF-resolution, for example, with a spherical truncation of T42 (corresponding to a quadratic Gaussian grid of approximately 2.8° by 2.8° in latitude and longitude) with 31 vertical hybrid pressure levels up to 10 hPa. EMAC uses a modal representation of aerosols dynamics (GMXe) that describes the aerosol size distribution as seven interacting log-normal distributions, of which four modes are soluble and three modes are insoluble. New particles are added directly to the nucleation mode. The applied model setup comprises the sub-model New Aerosol Nucleation (NAN) that includes new parameterizations of aerosol particle formation rates published in recent years[74]. These parameterizations include ion-induced nucleation. The ion-pair production rate, needed to calculate the ion-induced or ion-mediated nucleation, is described using the sub-model IONS, which provides ion-pair production rates[74].

The TOMCAT global model

The TOMCAT model is a global 3D offline chemical transport model[75,76]. It is run at approximately 2.8° spatial resolution, such as EMAC on a T42 grid, driven by ECMWF ERA-Interim reanalysis meteorological fields for the year 2008. We also used 31 hybrid sigma-pressure levels from the surface to 10 hPa. The dissolved fraction of gases in cloud water is calculated by means of an equilibrium Henry's law approach and set to zero for temperatures below −20 °C. The model includes GLOMAP aerosol microphysics[77] with nitrate and ammonium from the HyDIS solver[78] and the representation of new particle formation used by Gordon et al.[3]. The HyDIS solver adopts a sophisticated approach to the dissolution of nitric acid and ammonia into the aerosol phase that is a hybrid between a dynamic representation of the process, which accounts for the time needed for mass transport, and an equilibrium representation, which does not[78]. The main limitation of the solver is that it assumes all aerosol particles are liquid, which is probably a poor approximation in cold, dry conditions frequently found in the upper troposphere.

The cloud trajectories framework

We conducted a sensitivity study on ammonia transport processes and estimated the fraction remaining of ammonia vapour after convection from the boundary layer to the upper troposphere, using a cloud trajectories framework described in detail in Bardakov et al.[79,80]. In brief, trajectories from a convective system simulated with the large-eddy simulation (LES) model MIMICA[81] were extracted and a parcel representing the cloud outflow was selected for further analysis (Extended Data Fig. 8a). The meteorological profiles and clouds microphysics scheme used here were the same as in Bardakov et al.[80], producing altitude-dependent distributions of water and ice hydrometeors depicted in Extended Data Fig. 8. Partitioning of gas between vapour and aqueous phase along the trajectory was calculated on the basis of Henry's law constant adjusted to a cloud pH, $H^* = H \times 1.7 \times 10^{(9-pH)}$ following the expression for ammonia from Seinfeld and Pandis[60].

We then investigated the factors governing ammonia transport through the simulated convective system by varying: (1) the pH for the liquid water hydrometeors (Extended Data Fig. 8c); (2) the total amount of water in the system (Extended Data Fig. 8d); (3) the retention of ammonia molecules by the ice hydrometeors (Extended Data Fig. 8e). In our base-case simulation, the pH was assumed to have an altitude-dependent profile, reflecting the higher abundance of acids close to the surface and ranging from 4.5 to 5, in accordance with the representative pH values in the EMAC simulation. The base-case water content was as in Bardakov et al.[80] and the ice retention coefficient 0.05 in accordance with Ge et al.[13], with no further uptake on ice.

Atmospheric interpretation

This work focuses on the Asian monsoon region in part because this region is fairly extensive, but also because ammonia concentrations measured in this region are by far the highest in the upper troposphere. Although we frame this synergistic HNO_3–H_2SO_4–NH_3 nucleation in a scenario that suits the Asian monsoon upper troposphere, the physics applies more broadly — the colder the conditions are, the more important this mechanism is likely to be. To explore the importance of this synergistic nucleation to the atmosphere, we combine our experimental results, cloud resolving modelling and global-scale chemical transport modelling. On the basis of these constraints, the rate-limiting elements of new particle formation seem to be convective transport of ammonia and the production rate of particles in the mixing zone between convective outflow and the background upper free troposphere; however, confirmation of this will require extensive field and modelling studies.

Generally, nitric acid ranges between about 10^8 and 10^9 cm^{-3} (refs. [14,15]) and sulfuric acid between about 10^5 and 10^6 cm^{-3} (refs. [82,83]) in the tropical upper troposphere. The typical acid-excess conditions leave the principal uncertainty being ammonia levels, which are not yet well constrained. Although satellite-based ammonia measurements have provided a spatial distribution on a global scale, they are limited to cloud-free areas owing to blockage of the ammonia signal by optically thick clouds. However, deep convection followed by cloud glaciation may be a major source of upper tropospheric ammonia. This process may then not be captured by satellites as it occurs near clouds, with short time duration and high spatial heterogeneity. This may also explain why the in situ-measured ammonia concentrations are up to 40 times higher than those from satellite measurements[6].

Ammonia has no known chemical source in the atmosphere but is instead transported by cloud processes from the surface, whereas nitric acid and sulfuric acid vapours are formed primarily by out-of-cloud oxidation. Consequently, it is probable that this synergistic nucleation occurs initially in the outflow of convective clouds, in which the released ammonia mixes with pre-existing (background) nitric acid and sulfuric acid. Subsequently, as ammonia is titrated over several *e*-folding times (governed by the condensation sink in this mixing zone) and the outflow air fully mixes with the background air, nucleation conditions will shift from the ammonia-rich regime to the ammonia-limited regime. These highly dynamic processes are thus the key to constraining the climatic effects of this synergistic nucleation in Asian monsoon and potentially other convective regions. Nevertheless, current ambient measurements confirm the presence of ample ammonia, as well as particles comprised largely of ammonium nitrate[4], and our experiments show that synergistic HNO_3–H_2SO_4–NH_3 nucleation is a viable mechanism for new particle formation in the Asian monsoon upper troposphere. As global ammonia emissions continue to increase owing to agricultural growth and the warmer climate[84,85], the importance of this particle formation mechanism will increase.

Further, as there is almost no in situ composition measurement of clusters or newly formed particles in the upper troposphere, we can

only infer the major particle formation pathway from indirect evidence such as composition of precursor vapours or larger particles. Previously established mechanisms include binary and ternary sulfuric acid nucleation, which drive new particle formation over marine or anthropogenically influenced regions[1,4,86,87], nucleation by oxygenated organics, which dominates over pristine vegetated areas such as the Amazon basin[2,10,88], and nucleation by iodine oxidation products, which may be especially important in marine convection[89,90]. Over the Asian monsoon regions, however, mixed emissions of both inorganic and organic vapours may well complicate the particle formation mechanism. However, it has been demonstrated that ammonium nitrate can often explain more than half of the particulate volume in the upper troposphere[6]. This means that the HNO_3–NH_3 concentration is probably higher than the sum of all other condensable vapours (that is, sulfuric acid and oxygenated organics). And given that HNO_3–H_2SO_4–NH_3 nucleation is orders of magnitude faster than binary and ternary sulfuric acid nucleation at observed ammonia levels, we therefore infer that synergistic HNO_3–H_2SO_4–NH_3 nucleation is a major particle formation pathway in the Asian monsoon upper troposphere. It seems unlikely that this inorganic pathway and the organic pathways are antagonistic in growth, and without strong indications otherwise, it seems probable that they are more or less additive for nucleation itself. However, to further investigate interactions between different nucleation schemes, we would rely on further information on the source and identity of organic vapours that are present in the Asian monsoon upper troposphere.

Data availability

The full dataset shown in the figures is publicly available at https://doi.org/10.5281/zenodo.5949440. Source data are provided with this paper.

Code availability

The EMAC (ECHAM/MESSy) model is continuously further developed and applied by a consortium of institutions. The use of MESSy and access to the source code is licensed to all affiliates of institutions that are members of the MESSy Consortium. Institutions can become a member of the MESSy Consortium by signing the MESSy Memorandum of Understanding. More information can be found on the MESSy Consortium website (https://www.messy-interface.org). All code modifications presented in this paper will be included in the next version of MESSy. The TOMCAT model (http://homepages.see.leeds.ac.uk/~lecmc/tomcat.html) is a UK community model. It is available to UK (or NERC-funded) researchers who normally access the model on common facilities or who are helped to install it on their local machines. As it is a complex research tool, new users will need help to use the model optimally. We do not have the resources to release and support the model in an open way. Any potential user interested in the model should contact Martyn Chipperfield. The model updates described in this paper are included in the standard model library. The cloud trajectories model is publicly available at https://doi.org/10.5281/zenodo.5949440. Codes for conducting the analysis presented in this paper can be obtained by contacting the corresponding author, Neil M. Donahue (nmd@andrew.cmu.edu).

30. Duplissy, J. et al. Effect of ions on sulfuric acid-water binary particle formation: 2. Experimental data and comparison with QC-normalized classical nucleation theory. *J. Geophys. Res. Atmos.* **212**, 1752–1775 (2016).
31. Dias, A. et al. Temperature uniformity in the CERN CLOUD chamber. *Atmos. Meas. Tech.* **10**, 5075–5088 (2017).
32. Kirkby, J. et al. Ion-induced nucleation of pure biogenic particles. *Nature* **530**, 521–526 (2016).
33. Schnitzhofer, R. et al. Characterisation of organic contaminants in the CLOUD chamber at CERN. *Atmos. Meas. Tech.* **7**, 2159–2168 (2014).
34. Jokinen, T. et al. Atmospheric sulphuric acid and neutral cluster measurements using CI-APi-TOF. *Atmos. Chem. Phys.* **12**, 4117–4125 (2012).
35. Kürten, A. et al. Neutral molecular cluster formation of sulfuric acid–dimethylamine observed in real time under atmospheric conditions. *Proc. Natl Acad. Sci.* **111**, 15019–15024 (2014).
36. Lopez-Hilfiker, F. D. et al. A novel method for online analysis of gas and particle composition: description and evaluation of a Filter Inlet for Gases and AEROsols (FIGAERO). *Atmos. Meas. Tech.* **7**, 983–1001 (2014).
37. Wang, M. et al. Reactions of atmospheric particulate stabilized Criegee intermediates lead to high-molecular-weight aerosol components. *Environ. Sci. Technol.* **50**, 5702–5710 (2016).
38. Kürten, A., Rondo, L., Ehrhart, S. & Curtius, J. Performance of a corona ion source for measurement of sulfuric acid by chemical ionization mass spectrometry. *Atmos. Meas. Tech.* **4**, 437–443 (2011).
39. Tröstl, J. et al. The role of low-volatility organic compounds in initial particle growth in the atmosphere. *Nature* **530**, 527–531 (2016).
40. Breitenlechner, M. et al. PTR3: an instrument for studying the lifecycle of reactive organic carbon in the atmosphere. *Anal. Chem.* **89**, 5824–5831 (2017).
41. Kürten, A. et al. Experimental particle formation rates spanning tropospheric sulfuric acid and ammonia abundances, ion production rates, and temperatures. *J. Geophys. Res. Atmos.* **121**, 12–377 (2016).
42. McMurry, P. H. & Grosjean, D. Gas and aerosol wall losses in Teflon film smog chambers. *Environ. Sci. Technol.* **19**, 1176–1181 (1985).
43. Simon, M. et al. Molecular insight into HOM formation and biogenic new-particle formation over a wide range of tropospheric temperatures. *Atmos. Chem. Phys.* **20**, 9183–9207 (2020).
44. Tang, M., Cox, R. & Kalberer, M. Compilation and evaluation of gas phase diffusion coefficients of reactive trace gases in the atmosphere: volume 1. inorganic compounds. *Atmos. Chem. Phys.* **14**, 9233–9247 (2014).
45. Junninen, H. et al. A high-resolution mass spectrometer to measure atmospheric ion composition. *Atmos. Meas. Tech.* **3**, 1039–1053 (2010).
46. Kürten, A. et al. Observation of new particle formation and measurement of sulfuric acid, ammonia, amines and highly oxidized organic molecules at a rural site in central Germany. *Atmos. Chem. Phys.* **16**, 12793–12813 (2016).
47. Dada, L. et al. Formation and growth of sub-3-nm aerosol particles in experimental chambers. *Nat. Protoc.* **15**, 1013–1040 (2020).
48. Mui, W., Mai, H., Downard, A. J., Seinfeld, J. H. & Flagan, R. C. Design, simulation, and characterization of a radial opposed migration ion and aerosol classifier (ROMIAC). *Aerosol Sci. Technol.* **51**, 801–823 (2017).
49. Wimmer, D. et al. Performance of diethylene glycol-based particle counters in the sub-3 nm size range. *Atmos. Meas. Tech.* **6**, 1793–1804 (2013).
50. Mai, H. & Flagan, R. C. Scanning DMA data analysis I. Classification transfer function. *Aerosol Sci. Technol.* **52**, 1382–1399 (2018).
51. Mai, H., Kong, W., Seinfeld, J. H. & Flagan, R. C. Scanning DMA data analysis II. Integrated DMA-CPC instrument response and data inversion. *Aerosol Sci. Technol.* **52**, 1400–1414 (2018).
52. Jurányi, Z. et al. A 17 month climatology of the cloud condensation nuclei number concentration at the high alpine site Jungfraujoch. *J. Geophys. Res. Atmos.* **116**, D10204 (2011).
53. Tröstl, J. et al. Fast and precise measurement in the sub-20 nm size range using a Scanning Mobility Particle Sizer. *J. Aerosol Sci.* **87**, 75–87 (2015).
54. Wiedensohler, A. et al. Mobility particle size spectrometers: harmonization of technical standards and data structure to facilitate high quality long-term observations of atmospheric particle number size distributions. *Atmos. Meas. Tech.* **5**, 657–685 (2012).
55. Jayne, J. T. et al. Development of an aerosol mass spectrometer for size and composition analysis of submicron particles. *Aerosol Sci. Technol.* **33**, 49–70 (2000).
56. DeCarlo, P. F. et al. Field-deployable, high-resolution, time-of-flight aerosol mass spectrometer. *Anal. Chem.* **78**, 8281–8289 (2006).
57. Rogers, D. C. Development of a continuous flow thermal gradient diffusion chamber for ice nucleation studies. *Atmos. Res.* **22**, 149–181 (1988).
58. DeMott, P. J. et al. The Fifth International Workshop on Ice Nucleation phase 2 (FIN-02): laboratory intercomparison of ice nucleation measurements. *Atmos. Meas. Tech.* **11**, 6231–6257 (2018).
59. Schiebel, T. *Ice Nucleation Activity of Soil Dust Aerosols*. PhD thesis, KIT-Bibliothek (2017).
60. Seinfeld, J. H. & Pandis, S. N. *Atmospheric Chemistry and Physics* 2nd edn (Wiley, 2006).
61. Connolly, P. J. et al. Studies of heterogeneous freezing by three different desert dust samples. *Atmos. Chem. Phys.* **9**, 2805–2824 (2009).
62. Koop, T., Luo, B., Tsias, A. & Peter, T. Water activity as the determinant for homogeneous ice nucleation in aqueous solutions. *Nature* **406**, 611–614 (2000).
63. Cziczo, D. J. & Abbatt, J. P. D. Infrared observations of the response of NaCl, $MgCl_2$, NH_4HSO_4, and NH_4NO_3 aerosols to changes in relative humidity from 298 to 238 K. *J. Phys. Chem. A* **104**, 2038–2047 (2000).
64. Zuberi, B., Bertram, A. K., Koop, T., Molina, L. T. & Molina, M. J. Heterogeneous freezing of aqueous particles induced by crystallized $(NH_4)_2SO_4$, ice, and letovicite. *J. Phys. Chem. A* **105**, 6458–6464 (2001).
65. Schlenker, J. C. & Martin, S. T. Crystallization pathways of sulfate–nitrate–ammonium aerosol particles. *J. Phys. Chem. A* **109**, 9980–9985 (2005).
66. Riccobono, F. et al. Oxidation products of biogenic emissions contribute to nucleation of atmospheric particles. *Science* **344**, 717–721 (2014).
67. Möhler, O. & Arnold, F. Gaseous sulfuric acid and sulfur dioxide measurements in the Arctic troposphere and lower stratosphere: implications for hydroxyl radical abundances. *Geophys. Res. Lett.* **19**, 1763–1766 (1992).
68. Williamson, C. J. et al. Large hemispheric difference in ultrafine aerosol concentrations in the lowermost stratosphere at mid and high latitudes. Atmos. Chem. Phys. Discuss. 1–44 (2021).
69. Wespes, C. et al. First global distributions of nitric acid in the troposphere and the stratosphere derived from infrared satellite measurements. *J. Geophys. Res. Atmos.* **112**, D13311 (2007).

70. Popp, P. et al. Stratospheric correlation between nitric acid and ozone. *J. Geophys. Res. Atmos.* **114**, D03305 (2009).
71. Hirsikko, A. et al. Atmospheric ions and nucleation: a review of observations. *Atmos. Chem. Phys.* **11**, 767–798 (2011).
72. Jöckel, P. et al. Development cycle 2 of the modular earth submodel system (MESSy2). *Geosci. Model Dev.* **3**, 717–752 (2010).
73. Roeckner, E. et al. Sensitivity of simulated climate to horizontal and vertical resolution in the ECHAM5 atmosphere model. *J. Clim.* **19**, 3771–3791 (2006).
74. Ehrhart, S. et al. Two new submodels for the Modular Earth Submodel System (MESSy): New Aerosol Nucleation (NAN) and small ions (IONS) version 1.0. *Geosci. Model Dev.* **11**, 4987–5001 (2018).
75. Chipperfield, M. New version of the TOMCAT/SLIMCAT off-line chemical transport model: Intercomparison of stratospheric tracer experiments. *Q. J. R. Meteorol. Soc.* **132**, 1179–1203 (2006).
76. Monks, S. A. et al. The TOMCAT global chemical transport model v1.6: description of chemical mechanism and model evaluation. *Geosci. Model Dev.* **10**, 3025–3057 (2017).
77. Mann, G. et al. Description and evaluation of GLOMAP-mode: a modal global aerosol microphysics model for the UKCA composition-climate model. *Geosci. Model Dev.* **3**, 519–551 (2010).
78. Benduhn, F. et al. Size-resolved simulations of the aerosol inorganic composition with the new hybrid dissolution solver HyDiS-1.0: description, evaluation and first global modelling results. *Geosci. Model Dev.* **9**, 3875–3906 (2016).
79. Bardakov, R. et al. A novel framework to study trace gas transport in deep convective clouds. *J. Adv. Model. Earth Syst.* **12**, e2019MS001931 (2020).
80. Bardakov, R., Thornton, J. A., Riipinen, I., Krejci, R. & Ekman, A. M. L. Transport and chemistry of isoprene and its oxidation products in deep convective clouds. *Tellus B Chem. Phys. Meteorol.* **73**, 1–21 (2021).
81. Savre, J., Ekman, A. M. L. & Svensson, G. Technical note: Introduction to MIMICA, a large-eddy simulation solver for cloudy planetary boundary layers. *J. Adv. Model. Earth Syst.* **6**, 630–649 (2014).
82. Bates, T. S., Huebert, B. J., Gras, J. L., Griffiths, F. B. & Durkee, P. A. International Global Atmospheric Chemistry (IGAC) project's first aerosol characterization experiment (ACE 1): overview. *J. Geophys. Res. Atmos.* **103**, 16297–16318 (1998).
83. Hoell, J. M. et al. Pacific Exploratory Mission in the tropical Pacific: PEM-Tropics A, August-September 1996. *J. Geophys. Res. Atmos.* **104**, 5567–5583 (1999).
84. Erisman, J. W., Sutton, M. A., Galloway, J., Klimont, Z. & Winiwarter, W. How a century of ammonia synthesis changed the world. *Nat. Geosci.* **1**, 636–639 (2008).
85. Warner, J. X. et al. Increased atmospheric ammonia over the world's major agricultural areas detected from space. *Geophys. Res. Lett.* **44**, 2875–2884 (2017).
86. Twohy, C. H. et al. Deep convection as a source of new particles in the midlatitude upper troposphere. *J. Geophys. Res. Atmos.* **107**, AAC 6-1–AAC 6-10 (2002).
87. Lee, S.-H. et al. Particle formation by ion nucleation in the upper troposphere and lower stratosphere. *Science* **301**, 1886–1889 (2003).
88. Waddicor, D. A. et al. Aerosol observations and growth rates downwind of the anvil of a deep tropical thunderstorm. *Atmos. Chem. Phys.* **12**, 6157–6172 (2012).
89. Wang, S. et al. Active and widespread halogen chemistry in the tropical and subtropical free troposphere. *Proc. Natl Acad. Sci.* **112**, 9281–9286 (2015).
90. He, X.-C. et al. Role of iodine oxoacids in atmospheric aerosol nucleation. *Science* **371**, 589–595 (2021).

Acknowledgements We thank the European Organization for Nuclear Research (CERN) for supporting CLOUD with important technical and financial resources. This research has received funding from the US National Science Foundation (nos. AGS-1801574, AGS-1801897, AGS-1602086, AGS-1801329, AGS-2132089 and AGS-1801280), the European Union's Horizon 2020 programme (Marie Skłodowska-Curie ITN no. 764991 'CLOUD-MOTION'), the European Commission, H2020 Research Infrastructures (FORCeS, no. 821205), the European Union's Horizon 2020 research and innovation programme (Marie Skłodowska-Curie no. 895875 'NPF-PANDA'), a European Research Council (ERC) project ATM-GTP contract (no. 742206), an ERC-CoG grant INTEGRATE (no. 867599), the Swiss National Science Foundation (nos. 200021_169090, 200020_172602 and 20FI20_172622), the Academy of Finland ACCC Flagship (no. 337549), the Academy of Finland Academy professorship (no. 302958), the Academy of Finland (nos. 1325656, 316114 and 325647), Russian MegaGrant project 'Megapolis – heat and pollution island: interdisciplinary hydroclimatic, geochemical and ecological analysis' (application reference 2020-220-08-5835), Jane and Aatos Erkko Foundation 'Quantifying carbon sink, CarbonSink+ and their interaction with air quality' INAR project, Samsung PM2.5 SRP, Prince Albert Foundation 'the Arena for the gap analysis of the existing Arctic Science Co-Operations (AASCO)' (no. 2859), the German Federal Ministry of Education and Research (CLOUD-16 project nos. 01LK1601A and 01LK1601C), the Knut and Alice Wallenberg Foundation Wallenberg Academy Fellows project AtmoRemove (no. 2015.0162), the Portuguese Foundation for Science and Technology (no. CERN/FIS-COM/0014/2017) and the Technology Transfer Project N059 of the Karlsruhe Institute of Technology (KIT). The FIGAERO-CIMS was supported by a Major Research Instrumentation (MRI) grant for the US NSF AGS-1531284, as well as the Wallace Research Foundation. The computations by R.Bardakov were performed on resources provided by the Swedish National Infrastructure for Computing (SNIC) at the National Supercomputer Center (NSC). I.R. thanks the Max Planck Society for a sabbatical award. M.W. thanks Siebel Scholars Foundation for financial support.

Author contributions M.W., B.B., J.K. and N.M.D. planned the experiments. M.W., B.B., G.M., B.R., B.S., X.-C.H., J.S., W.S., R.M., B.L., H.L., H.E.M., F.A., P.B., Z.B., L.C., L.-P.D.M., J.D., H.F., L.G.C., M.G., R.G., V.H., A.K., K.L., V.M., D.M., S.M., R.L.M., B.M., T.M., A.O., T.P., M.P., A.A.P., A.P., M.Simon, Y.S., A.T., N.S.U., F.V., R.W., D.S.W., S.K.W., A.W., Y.W., M.Z.-W., M.Sipilä, P.M.W., A.H., U.B., M.K., R.C.F., J.C., R.V., I.E.-H., J.K., K.K. O.M., S.S. and N.M.D. prepared the CLOUD facility or measuring instruments. M.W., B.B., G.M., B.R., B.S., X.-C.H., J.S., W.S., R.M., B.L., H.E.M., A.A., L.C., L.G.C., M.G., M.H., V.H., J.E.K., N.G.A.M., D.M., R.L.M., B.M., A.R., M.Schervish, M.Simon, A.T., N.S.U., F.V., D.S.W., S.K.W., A.W., M.Z.-W., P.M.W., J.K. and K.K. collected the data. M.W., M.X., B.B., G.M., B.R., B.S., R.Bardakov, J.S., W.S., L.D., R.Baalbaki, B.L., D.S.W., S.K.W., A.W., I.R., T.C. and N.M.D. analysed the data. M.W., M.X., B.B., R.Bardakov, X.-C.H., J.S., W.S., R.M., L.D., R. Baalbaki., B.L., H.L., H.E.M., A.M.L.E., H.F., M.H., K.H., A.K., N.S.U., R.W., A.W., A.H., U.B., M.K., R.C.F., J.C., R.V., I.R., H.G., J.L., I.E.-H., D.R.W., T.C., J.K., O.M., S.S. and N.M.D. contributed to the scientific discussion. M.W., B.B., R.Bardakov, W.S., R.M., B.L., H.L., K.H., A.K., U.B., R.C.F., J.C., R.V., I.R., H.G., J.L., I.E.-H., T.C., J.K., O.M. and N.M.D. wrote the manuscript.

Competing interests The authors declare no competing interests.

Additional information

Supplementary information The online version contains supplementary material available at https://doi.org/10.1038/s41586-022-04605-4.

Correspondence and requests for materials should be addressed to Neil M. Donahue.

Peer review information *Nature* thanks Bernd Kärcher and the other, anonymous, reviewers for their contribution to the peer review of this work. Peer reviewer reports are available.

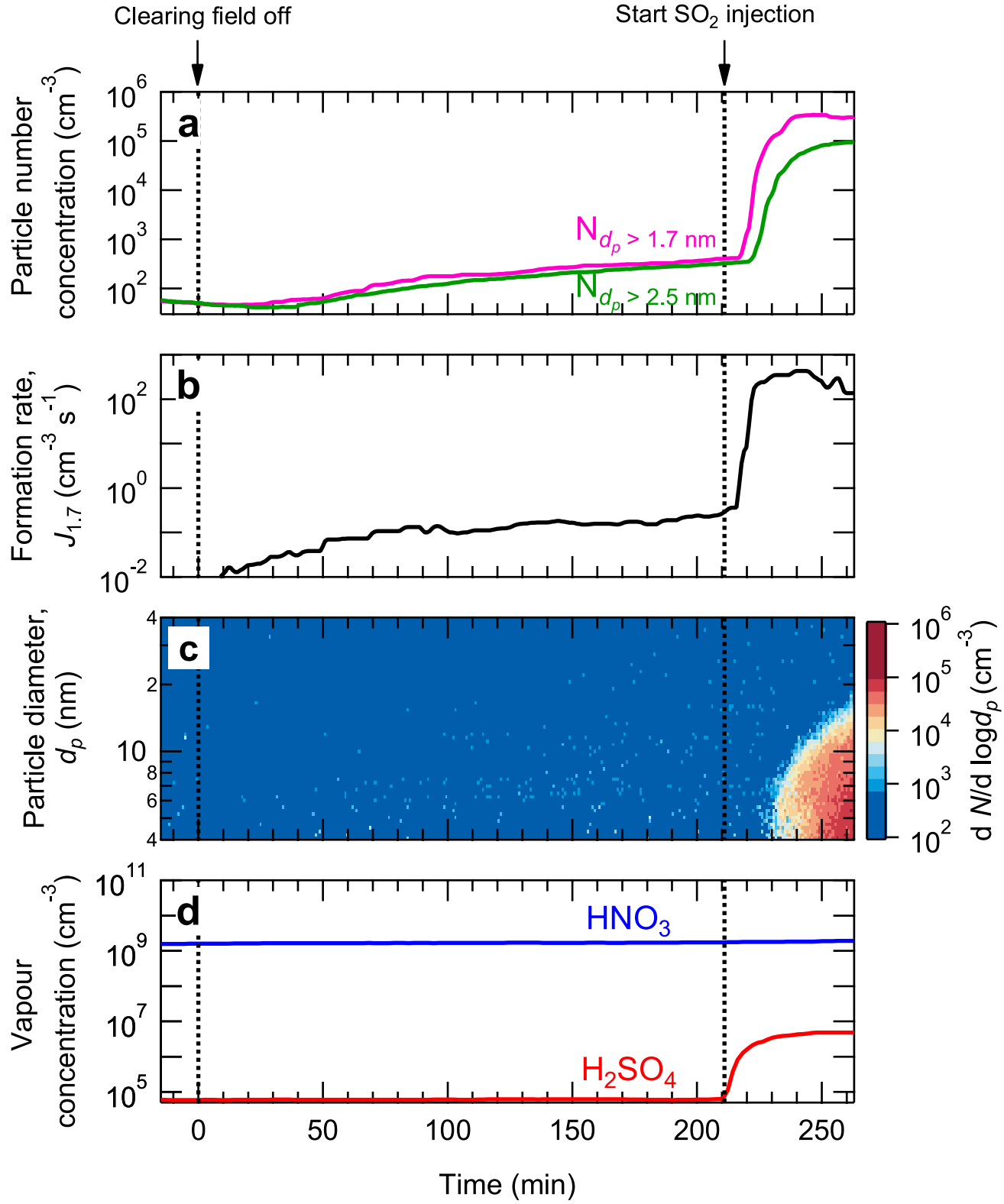

Extended Data Fig. 1 | See next page for caption.

Extended Data Fig. 1 | Enhancement of HNO_3–NH_3 particle formation by sulfuric acid. a, Particle number concentrations versus time at mobility diameters >1.7 nm (magenta) and >2.5 nm (green). The solid magenta trace is measured by a $PSM_{1.7}$ and the solid green trace is measured by a $CPC_{2.5}$. The fixed experimental conditions are about 6.5×10^8 cm^{-3} NH_3, 223 K and 25% relative humidity. **b**, Particle formation rate versus time at 1.7 nm ($J_{1.7}$), measured by a PSM. **c**, Particle size distribution versus time, measured by an SMPS. **d**, Gas-phase nitric acid and sulfuric acid versus time, measured by an I^- CIMS and a NO_3^- CIMS, respectively. We started the experiment by oxidizing NO_2 to produce 1.6×10^9 cm^{-3} HNO_3 in the presence of about 6.5×10^8 cm^{-3} ammonia. At time = 0 min, we turned off the high-voltage clearing field to allow the ion concentration to build up to a steady state between GCR production and wall deposition. The presence of ions (GCR condition) induces slow HNO_3–NH_3 nucleation, followed by relatively fast particle growth by nitric acid and ammonia condensation. We thus observe formation of both 1.7-nm and 2.5-nm particles by about one order of magnitude in about 3.5 h, with a slower approach to steady state because of the longer wall deposition time constant for the larger particles. Then, we increased H_2SO_4 in the chamber from 0 to 4.9×10^6 cm^{-3} by oxidizing progressively more injected SO_2 after 211 min, with a fixed production rate of nitric acid and injection rate of ammonia. Subsequently, particle concentrations increase by three orders of magnitude within 30 min. The overall systematic scale uncertainties of ±30% on particle formation rate, −33%/+50% on sulfuric acid concentration and ±25% on nitric acid concentration are not shown.

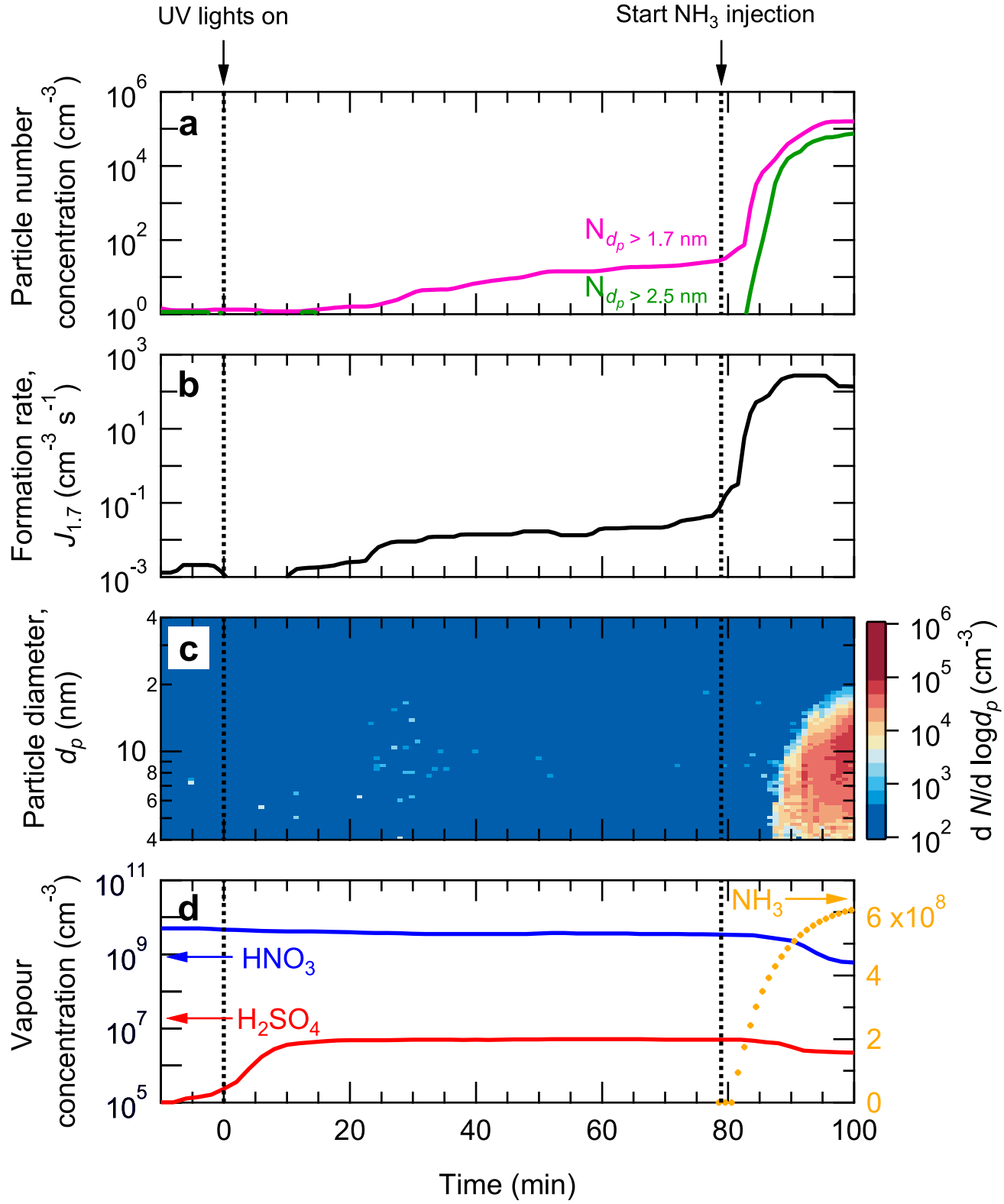

Extended Data Fig. 2 | See next page for caption.

Extended Data Fig. 2 | Enhancement of H_2SO_4–HNO_3 nucleation by ammonia. a, Particle number concentrations versus time at mobility diameters >1.7 nm (magenta) and >2.5 nm (green). The solid magenta trace is measured by a $PSM_{1.7}$ and the solid green trace is measured by a $CPC_{2.5}$. The fixed experimental conditions are 223 K and 25% relative humidity. **b**, Particle formation rate versus time at 1.7 nm ($J_{1.7}$), measured by a PSM. **c**, Particle size distribution versus time, measured by an SMPS. **d**, Gas-phase nitric acid and sulfuric acid versus time, measured by an I^- CIMS and a NO_3^- CIMS, respectively; gas-phase ammonia versus time, calculated with a first-order wall-loss rate. Before the experiment, we cleaned the chamber by rinsing the walls with ultra-pure water, followed by heating to 373 K and flushing at a high rate with humidified synthetic air for 48 h. We started with an almost perfectly clean chamber and only HNO_3, SO_2 and O_3 vapours present at constant levels. Sulfuric acid starts to appear by means of SO_2 oxidation soon after switching on the UV lights at time = 0 min, building up to a steady state of 5.0×10^6 cm^{-3} with the wall-loss timescale of about 10 min. Subsequently, we observe slow formation of 1.7-nm particles, yet they do not reach 2.5 nm during the course of a 2-h period with small growth rates and low survival probability. Then, owing to the injection of ammonia from 0 to around 6.5×10^8 cm^{-3} into the chamber after 80 min, a sharp increase in the rate of particle formation is observed with a fixed production rate of sulfuric acid and injection rate of nitric acid. The sulfuric acid concentration decreases slightly afterwards, owing to accumulated condensation sink from fast particle growth. The overall systematic scale uncertainties of ±30% on particle formation rate, −33%/50% on sulfuric acid concentration and ±25% on nitric acid concentration are not shown.

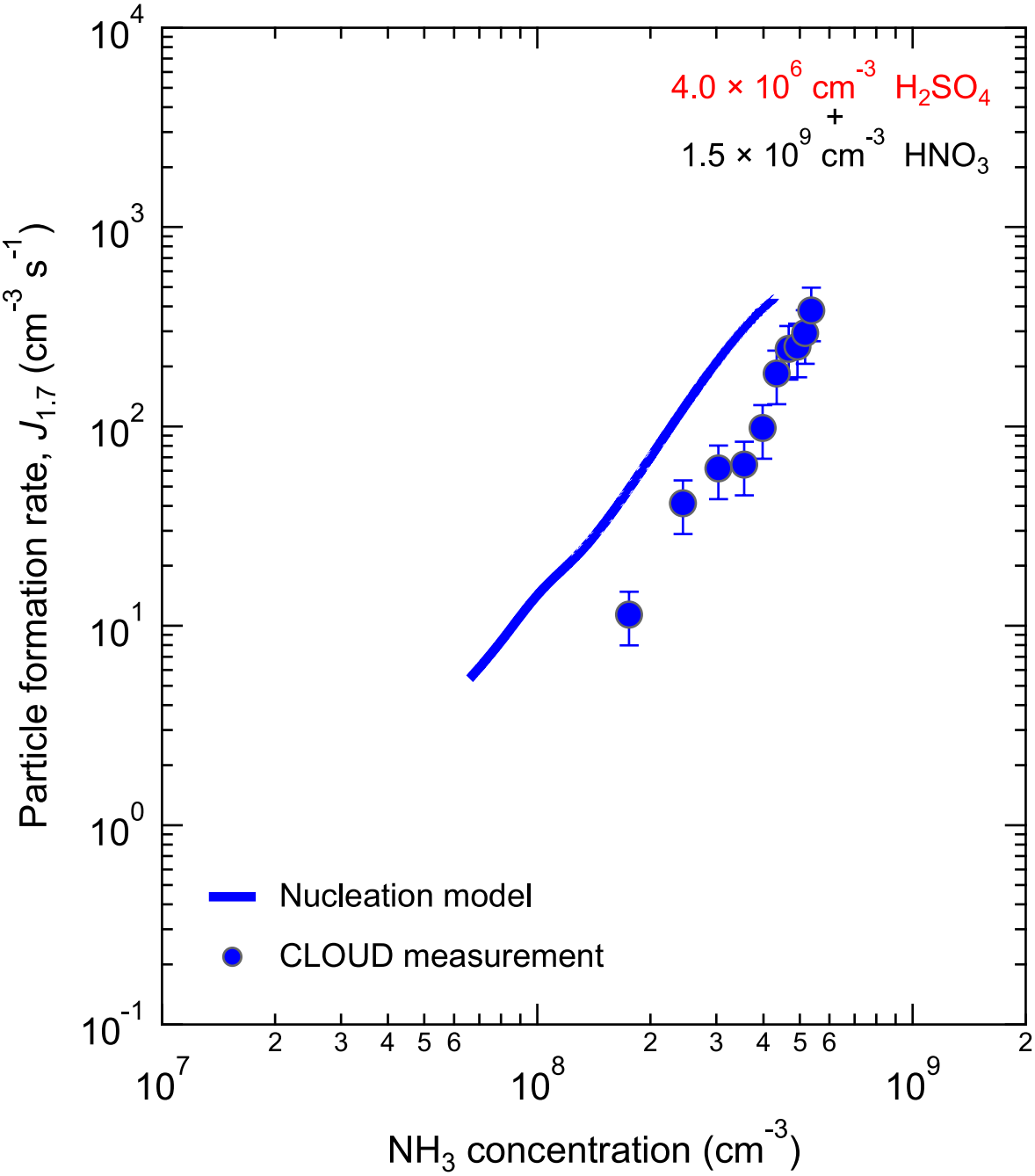

Extended Data Fig. 3 | Particle formation rates at 1.7 nm ($J_{1.7}$) versus ammonia concentration at 223 K and 25% relative humidity. Circles are the CLOUD measurements (the same as those in Fig. 2). The curve represents the model simulations on the basis of known thermodynamics and microphysics, including Kelvin effects, for nucleating clusters.

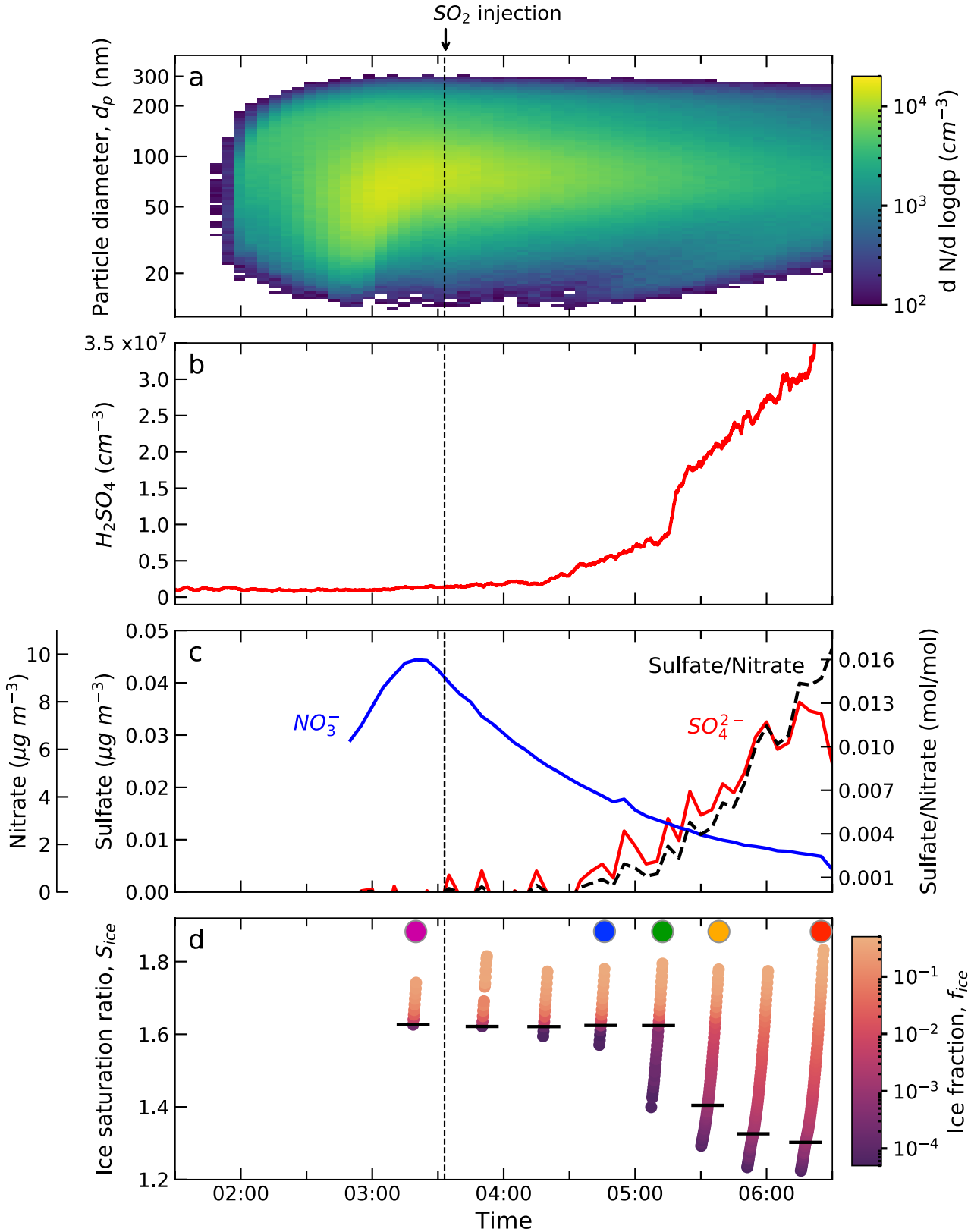

Extended Data Fig. 4 | Measurement of the ice nucleation ability of HNO_3–H_2SO_4–NH_3 particles versus sulfate-to-nitrate ratio. a, Particle size distribution versus time during the experiment, measured by an SMPS. **b**, Gas-phase sulfuric acid versus time, measured by a nitrate CIMS. **c**, Particle-phase chemical composition versus time, measured by an AMS. **d**, Fraction of INP at the nominal temperature of 215 K. The horizontal black dashes indicate the ice fraction threshold, $f_{ice} = 10^{-3}$. The coloured circles correspond to the sulfate-to-nitrate ratios shown in Fig. 4a.

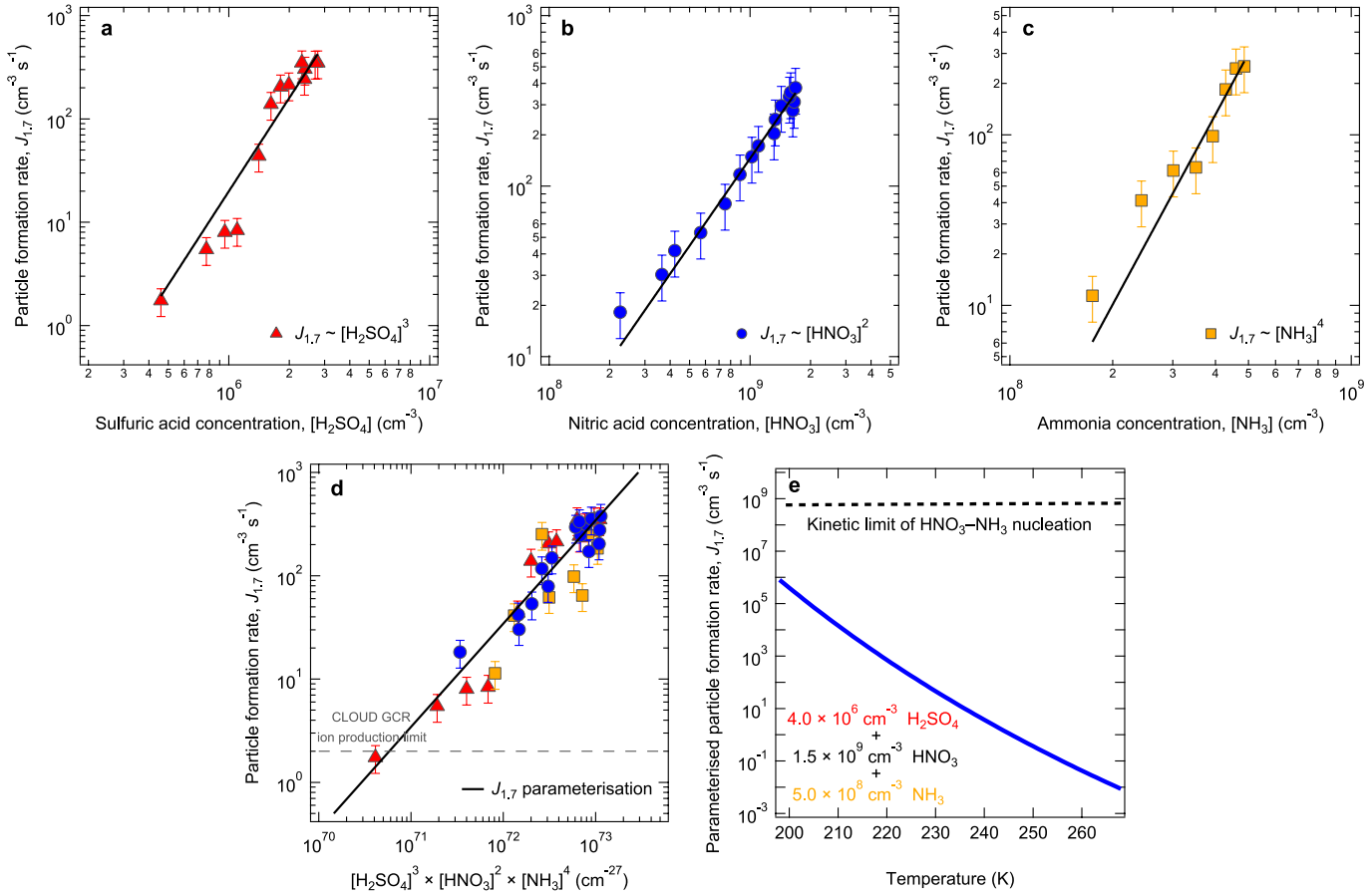

Extended Data Fig. 5 | Parameterization of the HNO_3–H_2SO_4–NH_3 particle formation rate. a–c Particle formation rate ($J_{1.7}$) as a function of H_2SO_4, HNO_3 and NH_3 vapour concentrations, respectively, at 223 K and 25% relative humidity. The red triangles, blue circles and yellow squares represent experiments while varying only the concentration of H_2SO_4 (Extended Data Fig. 1), HNO_3 (Fig. 1) and NH_3 (Extended Data Fig. 2), respectively. The H_2SO_4 concentration was varied between 4.6×10^5 and 2.9×10^6 cm^{-3}, HNO_3 between 2.3×10^8 and 1.7×10^9 cm^{-3} and NH_3 between 1.8×10^8 and 5.1×10^8 cm^{-3}. **d**, The multi-acid–ammonia parameterization (black line) on the basis of equation (6) with $k = 3.4 \times 10^{-71}$ s^{-1} cm^{24}. The grey dashed horizontal line shows a maximum of about 2 cm^{-3} s^{-1} ion-induced nucleation in the CLOUD chamber under GCR conditions, limited by the ion-pair production rate from GCR plus beam-background muons. The bars indicate 30% estimated total error on the particle formation rates, although the overall systematic scale uncertainties of −33%/+50% on sulfuric acid concentration and ±25% on nitric acid concentration are not shown. **e**, Temperature dependence of $J_{1.7}$ for HNO_3–H_2SO_4–NH_3 nucleation (blue curve) on the basis of equation (9) with $k = 2.9 \times 10^{-98}$ e$^{14{,}000/T}$ s^{-1} cm^{24}.

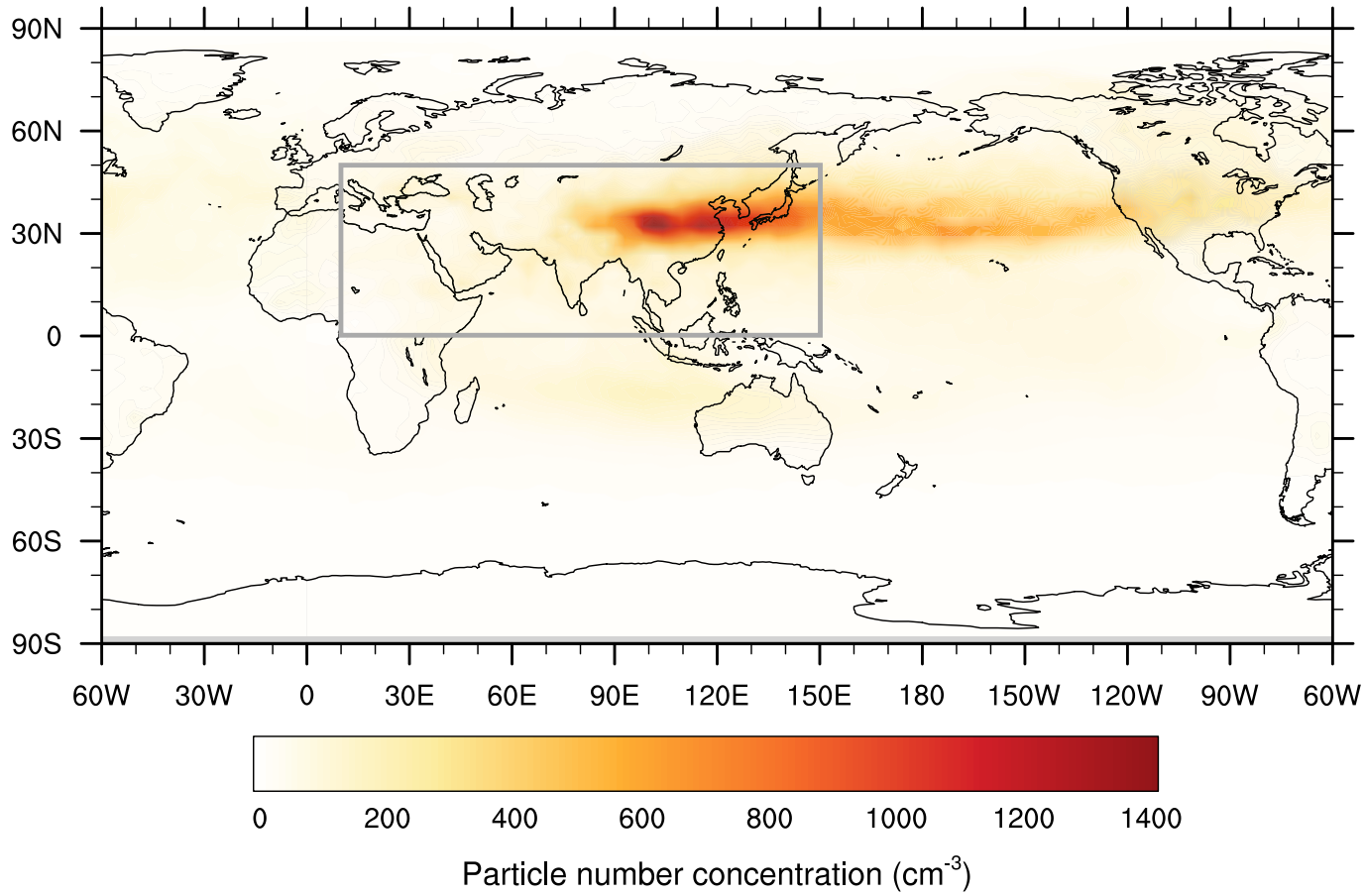

Extended Data Fig. 6 | Modelled contribution of HNO_3–H_2SO_4–NH_3 nucleation to upper tropospheric particles. Number concentrations of multi-acid new particles (nucleation mode) at 250-hPa altitude simulated in a global model (EMAC) with efficient vertical transport of ammonia. The particle formation rate is on the basis of the blue dashed curve in Fig. 2 and parameterization shown in Extended Data Fig. 5. The extra particle number concentrations are shown, that is, relative to the same model without multi-acid nucleation. High annually averaged particle numbers are expected in the monsoon region (grey rectangle) and adjacent regions.

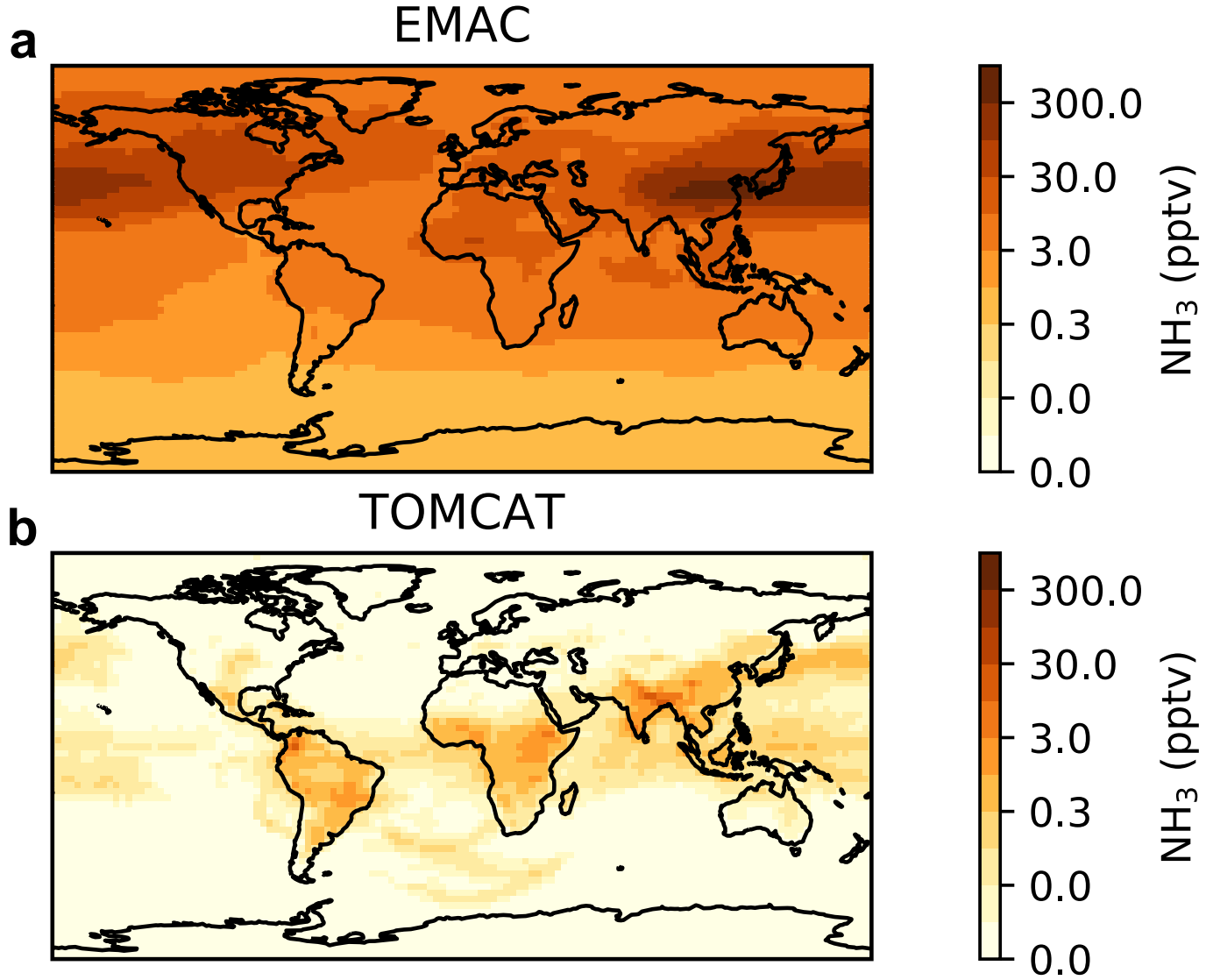

Extended Data Fig. 7 | Modelled annual mean ammonia mixing ratios at 250 hPa (11 km, about 223 K). a, The EMAC global model simulations are higher than the MIPAS satellite observations, although consistent with aircraft measurements[5,6]. **b**, The TOMCAT global model predicts much less ammonia (<1 pptv) in the upper troposphere.

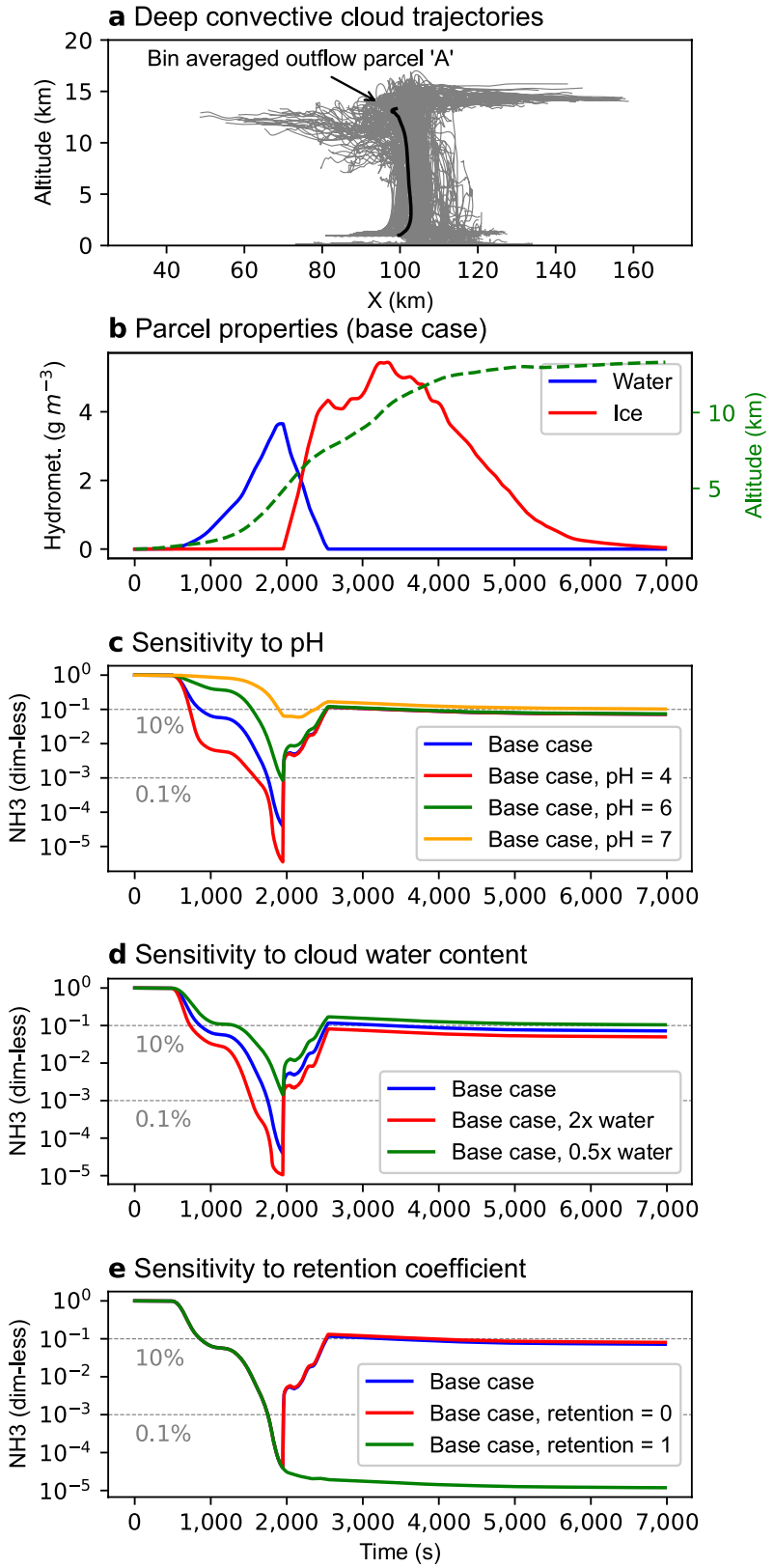

Extended Data Fig. 8 | Modelled transport of ammonia to the upper troposphere in deep convective clouds. a, Trajectories of the simulated convective cloud event (grey) and a selected parcel representing a buoyant parcel reaching the upper troposphere (black). **b**, The simulated evolution of parcel A altitude (green dashed trace) and the total mass concentration and phase of the cloud hydrometeors (red and blue curves). **c**–**e** Sensitivity of the predicted ammonia concentrations within parcel A to cloud water pH, total water amount and retention coefficient (by ice particles) as compared with the base-case simulation (blue trace in all figures).

Appendix C

Observations of Volatile Organic Compounds in the Los Angeles Basin during COVID-19

Van Rooy, P.; Tasnia, A.; Barletta, B.; Buenconsejo, R.; Crounse, J. D.; Kenseth, C. M.; Meinardi, S.; Murphy, S.; Parker, H.; Schulze, B.; Seinfeld, J. H.; Wennberg, P. O.; Blake, D. R.; Barsanti, K. C. Observations of Volatile Organic Compounds in the Los Angeles Basin during COVID-19. *ACS Earth Space Chem.* **2021**, *5* (11), 3045–3055. https://doi.org/10.1021/acsearthspacechem.1c00248.

ACS EARTH AND SPACE CHEMISTRY

http://pubs.acs.org/journal/aesccq

Article

Observations of Volatile Organic Compounds in the Los Angeles Basin during COVID-19

Paul Van Rooy, Afsara Tasnia, Barbara Barletta, Reina Buenconsejo, John D. Crounse, Christopher M. Kenseth, Simone Meinardi, Sara Murphy, Harrison Parker, Benjamin Schulze, John H. Seinfeld, Paul O. Wennberg, Donald R. Blake, and Kelley C. Barsanti*

Cite This: *ACS Earth Space Chem.* 2021, 5, 3045−3055

Read Online

ACCESS | Metrics & More | Article Recommendations | Supporting Information

ABSTRACT: Volatile organic compounds (VOCs) were measured in the Los Angeles (LA) Basin from mid-April to mid-July 2020 during the COVID-19 pandemic, as a part of the Los Angeles Air Quality Campaign (LAAQC). VOCs were quantified in over 450 samples using one- and two-dimensional gas chromatography with different detectors; mixing ratios were determined for 150 compounds associated with on- and off-road mobile, volatile chemical product, and biogenic sources. During the sampling period, traffic counts increased from ∼55% to ∼80% of pre-COVID levels. While the average afternoon combustion-derived VOCs and carbon monoxide (CO) mixing ratios did not change significantly between April−May and June−July, there was a shift in the distribution to higher mixing ratios in June−July, particularly for VOCs associated with gasoline evaporation. Compared to observations made in the last major air quality campaign in the LA Basin (CalNex-2010), emission ratios for 40 compounds relative to acetylene (VOC/acetylene) have remained similar, while emission ratios relative to CO (VOC/CO) have dropped to ∼60% of their 2010 values. This divergence in trends suggests that whereas mobile sources are still the dominant source of the combustion-derived VOCs measured in the LA Basin, there has been a shift in the mobile source sectors, with a growing contribution from sources that have lower CO/acetylene emission ratios, including off-road equipment and vehicles. In addition to the observed shift in source sector contributions, estimated OH exposure was 70−120% higher than in 2010.

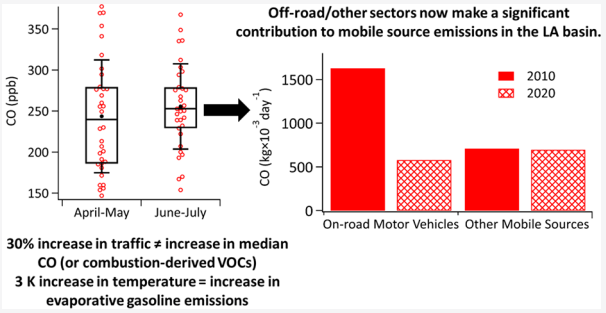

KEYWORDS: *VOCs, urban air quality, COVID-19, mobile source emissions, off-road emissions, VCPs*

1. HISTORICAL CONTEXT FOR THE 2020 OBSERVATIONS

During the 1950s, the Los Angeles (LA) Basin became infamous for its severely poor air quality. Since then, bans on open burning, regulation of emissions from electric power generation, and most notably, regulation of vehicle emissions and fuels have led to dramatic improvements in air quality.[1] Warneke et al.[2] showed that between 1960 and 2010, carbon monoxide (CO) and volatile organic compounds (VOCs) decreased substantially: a factor of ∼100 between 1960 and 2010, at a rate of ∼7.5% per year.[2] An exception to this decrease was short-chain alkanes (ethane and propane) associated with loss of processed natural gas and emissions from oil and gas production. In separate analyses of VOCs measured in the LA Basin during the 2010 California Research at the Nexus of Air Quality and Climate Change (CalNex-2010) campaign, Parrish et al.[1] and Warneke et al.[2] concluded that even though significant reductions in on-road vehicle emissions had been achieved, emissions from gasoline vehicles remained the dominant source of VOCs.

Early modeling studies of secondary organic aerosol (SOA) formation during CalNex-2010 demonstrated that oxidation of VOCs alone was insufficient (15−53%) to explain the observed SOA mass.[3] Various parametrizations were tested to consider the contribution of lower volatility emissions, including intermediate VOCs (IVOCs). Depending on the model variant, biogenic sources were predicted to account for 3−7% of observed SOA, diesel 16−27%, nonfossil (likely cooking) 19−35%, and gasoline 36−81%. More recent modeling studies of SOA formation during CalNex-2010 focused on the overall contribution of mobile source IVOCs and VOCs using updated emissions profiles for those sources, and the potential contribution of IVOCs from other sources.[4]

Special Issue: Mario Molina Memorial

Received: July 9, 2021
Revised: September 27, 2021
Accepted: October 9, 2021
Published: October 28, 2021

Lu et al.[4] reported that IVOCs from mobile sources increased the predicted peak SOA mass by 70%, but the increase did not represent observed ambient IVOCs or SOA mass, suggesting IVOCs are an important, but inadequately represented, source of SOA. An additional 12% of nonmobile gaseous organic emissions was required to match observed IVOCs (mobile IVOCs = 2.76×10^4 kg day^{-1}, nonmobile IVOCs = 3.07×10^4 kg day^{-1}), while an additional 14.8% of nonmobile gaseous organic emissions (nonmobile IVOCs = 6.85×10^4 kg day^{-1}) was required to match observed SOA. Lu et al.[4] noted that the additional amounts were likely unrealistic, and thus better constraints on sources and processes were still needed.

McDonald et al.[5] highlighted the importance of non-combustion source emissions in the LA Basin for atmospheric composition and chemistry more broadly. The addition of volatile chemical product (VCP) emissions was found to improve agreement between measured and predicted VOCs during CalNex-2010; particularly acetone, ethanol, and 1-propanol. Using chemical production statistics and indoor and outdoor measurements, they estimated that VCPs could contribute ~53% of VOC emissions, ~55% of VOC reactivity, and ~61% of SOA formation in the LA Basin in 2010. They also estimated that combustion source emissions contributed ~32% of the VOC emissions, ~37% of the VOC reactivity, and ~37% of the SOA formation.

Historical trends suggest that atmospheric composition and chemistry have changed since 2010. In the context of trace and greenhouse gas emissions, between 2010 and 2020 new vehicle emissions regulations have been implemented in California,[6] fuel economy standards have been updated,[6] and the on-road vehicle fleet has shifted toward hybrid and electric vehicles.[7] The influence of these changes on VOC and CO levels has not been quantified. Further, levels of nitrogen oxides (NO_x) have dropped within the LA Basin by an average of 49% (Figure S1), including in Pasadena, CA;[8] the effects of the last ten years of NO_x emissions reductions and changing OH levels on the VOC chemistry in the LA Basin are also poorly quantified.

2. THE LOS ANGELES AIR QUALITY CAMPAIGN (LAAQC)

LAAQC was organized to document atmospheric composition and diagnose the underlying emissions and photochemistry during the unprecedented shift in human activity associated with the COVID-19 pandemic and shelter-in-place restrictions. Over 450 samples were collected from April to July 2020 at a ground site in Pasadena, CA. The samples were analyzed for VOCs using one-dimensional gas chromatography (GC) with multiple detectors (including flame ionization (FID), electron capture (ECD), and mass spectrometry (MSD)) and two-dimensional gas chromatography with time-of-flight mass spectrometry (GC/GC-TOF-MS). Changes in mobile source patterns were well documented during LAAQC.[9−12] Using traffic counts obtained from Caltrans as one metric, travel across the LA Basin during LAAQC began at only ~55% of pre-COVID levels and increased approximately linearly to ~80% by the end of the campaign.[13] Other changes in human activity associated with urban emissions (e.g., ordering takeout, using personal care and cleaning products, using motorized landscaping equipment, etc.) are still being quantified.[14−18] The data collected during LAAQC were analyzed to (1) identify changes in VOC concentration and composition in the LA Basin during the COVID-19 pandemic associated with changes in human activity; and (2) quantify changes in VOC concentration and composition in the LA Basin since 2010 to better understand current composition and chemistry in this urban atmosphere. Changes in VOC sources during LAAQC, as well as changes in VOC sources and OH levels since 2010, are discussed.

3. EXPERIMENTAL METHODS

3.1. LAAQC Sampling. LAAQC was conducted from April 17 to July 19, 2020 in the midst of the COVID-19 pandemic; a state of emergency was issued on March 4, 2020 and shelter-in-place restrictions were issued on March 19, 2020. Air samples were collected from atop the Ronald and Maxine Linde Laboratory for Global Environmental Science on the Caltech campus in Pasadena, CA using canisters and adsorbent cartridges and analyzed for VOCs using GC with FID, ECD, and MSD (canisters) and GC/GC-TOF-MS (cartridges). Continuous measurements of trace gases, including CO, were collected using the Caltech air quality system (CITAQS).[13] Meteorological data, including temperature, wind speed, and wind direction, were collected at the Caltech Total Carbon Column Observing Network (TCCON) weather station.[19] Wind data were also obtained from the NOAA integrated surface database (ISD) accessed through Visual Crossing[20] to facilitate comparison with 2010. Afternoon wind speed was, on average, 3 m/s and wind direction was primarily from the west and southwest; nighttime wind speed was typically below the detection limit (<1.5 m/s) and wind direction was primarily from the east and northeast. Wind speeds and directions were relatively consistent throughout the measurement campaign (Figures S2−S3). Comparisons between 2020 and 2010 wind speeds and directions are shown in Figure S4 and calculated weekly back trajectories for LAAQC are shown in Figure S5.

3.2. UCI Canisters. A total of 314 whole air samples (WAS) were collected into evacuated 2-L electropolished stainless steel canisters using an automated 32-canister sampler (Atmospheric Technology Model 8001) capable of pressurizing the individual canisters to 20 psi. WAS canisters were collected three times per day between April 17 and July 19, 2020 at 05:30−06:30 PDT (hereafter referred to as "nighttime samples"), 09:00−10:00 PDT (hereafter referred to as "morning samples"), and 14:00−15:00 PDT (hereafter referred to as "afternoon samples").

Samples were analyzed at the University of California, Irvine (UCI) using a multi-column, multi-detector (FID, ECD, and MSD) GC system. A detailed description of the analytical techniques, including the use of standards and detection limits, precision, and accuracy for each reported compound can be found in Simpson et al.[21] Briefly, samples were cryogenically preconcentrated, vaporized, and split into five streams directed to a multi-column, multi-detector (FID, ECD, and MSD) GC system (Hewlett-Packard 6890 GC units). The various column and detector combinations allowed the identification and quantification of 92 VOCs across different classes of compounds, including hydrocarbons (C_2−C_{10}), alkyl nitrates (C_2−C_5), halogenated compounds, and sulfur compounds. The hydrocarbons and alkyl nitrates were analyzed using GC-FID, halogenated compounds using GC-ECD, and sulfur and all other compounds using GC-MSD.[21]

3.3. UCR Cartridges. A total of 154 dual sorbent bed (100 mg Tenax TA 35/60 and 200 mg Carbograph 1 TD 60/80 in series) cartridge samples were collected at a flow rate of ~250 ccm, at the same location as the canister samples. Cartridges were collected twice daily, 7 days per week, between April 17

https://doi.org/10.1021/acsearthspacechem.1c00248
ACS Earth Space Chem. 2021, 5, 3045−3055

and June 21, 2020; between June 24 and July 19, 2020 samples were collected twice daily on Wednesdays, Thursdays, Saturdays, and Sundays. The first sample was collected from 05:30−06:30 PDT (nighttime samples) and the second was collected from 14:00−15:00 PDT (afternoon samples). A glass fiber filter coated in sodium thiosulfate was mounted directly upstream of the cartridge to capture particles, and remove ozone (O_3) to prevent oxidation of compounds captured on the cartridge.[22,23] Samples were stored in a freezer on the Caltech campus before being transported to the University of California, Riverside (UCR) for analysis. Loading and travel blanks were also collected to correct for background contamination. Cartridges were analyzed at UCR using a Turbomatrix 650 automated thermal desorption (ATD) system (PerkinElmer, Waltham, MA) coupled to a Pegasus 4D GC/GC-TOF-MS (LECO Corp., St. Joseph MI). Details of the VOC analysis can be found in Hatch et al.,[24] in which the same approach was applied to speciation of VOCs emitted from biomass burning; errors in VOC mixing ratios were estimated to be ±30%. Data were analyzed using proprietary software from LECO (ChromaTOF) as well as in-house algorithms. A total of 58 compounds were identified and quantified across different compound classes including alkenes, higher alkanes (C_9−C_{14}), aromatics, aldehydes, ketones, terpenes, and halogenated compounds.

Nine compounds (octane, nonane, decane, 2-methylpentane, 2,3-dimethylpentane, *o*-xylene, *m*+*p*-xylene, toluene, and ethylbenzene) were quantified by both UCR and UCI in 130 paired samples, for a total of 1170 paired VOC measurements. The agreement was within ±50% for 84% of the paired VOC measurements and within ±25% for 58% of the paired measurements (Figure S6). Figure 1 shows the overall

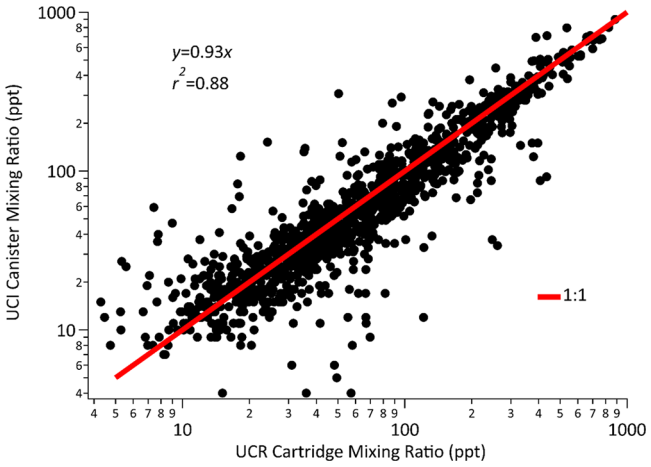

Figure 1. Mixing ratios of compounds (decane, octane, nonane, 2-methylpentane, 2,3-dimethylpentane, ethylbenzene, *o*-xylene, *m*+*p*-xylene, and toluene) quantified by both UCR and UCI.

correlation between the two data sets; the slope was 0.93 with an r^2-value of 0.88. This agreement is within the uncertainty of the UCR GC/GC-TOF-MS data, and is in the range reported by Hatch et al.[23] for biomass burning emissions (UCI vs UCR slope = 0.76 and r^2 = 0.82 across all samples, slope = 0.90 and r^2 = 0.95 when peat data were removed). Comparisons of individual compounds are shown in Figures S7−S15. For all overlapping compounds, the UCI WAS data were used in subsequent analysis due to the greater number of samples and higher precision and accuracy of the analytical methods.

3.4. Emission Ratio Calculations. Emission ratios (ERs), as defined by Warneke et al.,[25] were calculated for measured VOCs relative to CO and relative to acetylene (ethyne). ERs were calculated using the approach of de Gouw et al.[26] to account for reactive losses of VOCs with OH (OH-corrected ERs), the details of which are presented in Sections S3 and S4. First, the background CO level was calculated based on the average CO intercept of linear fits with *m*+*p*-xylene, 1,3,5-trimethylbenzene, and 1,2,4-trimethylbenzene (Figure S24). A value of 90 ± 15 ppb was calculated using the LAAQC-2020 data, which represents an ∼14−22% decrease from background CO levels of ∼105 ppb[3] and ∼115 ppb[26] reported for CalNex-2010. Next, the ratio of VOC to excess CO above background (VOC/ΔCO) was calculated for each VOC and plotted against the corresponding OH exposure (Figure S18). The OH-corrected ER to ΔCO, when OH exposure is zero, was then defined as the *y*-intercept. The error associated with OH-corrected ERs was calculated using the high and low values for background CO (105 and 75 ppb).

For OH-corrected ER to Δacetylene, the background acetylene was calculated as described in Section S4; the OH-corrected ER to Δacetylene was then defined as the *y*-intercept of the ratio of VOC to excess acetylene above background (VOC/Δacetylene) plotted against the corresponding OH exposure. ERs were also calculated using linear regression (see Section S4) from the nighttime data only (ER_{night}) for comparison with Borbon et al.[27] To account for reactive losses of VOCs with O_3 in the nighttime samples, O_3-corrected ERs_{night} were calculated analogously to OH-corrected ERs (see Section S4) based on de Gouw et al.[26] The OH-corrected ERs to ΔCO and ERs_{night} to CO and acetylene are summarized in Table 1, along with the ERs reported by Borbon et al.[27] and de Gouw et al.[26] OH-corrected ERs to acetylene and O_3-corrected ERs_{night} to ΔCO and Δacetylene are reported in Table S1. Following de Gouw et al.,[26] OH-corrected ERs and O_3-corrected ERs_{night} are relative to background-corrected CO (ΔCO) and to background-corrected acetylene (Δacetylene). Following Borbon et al.,[27] ERs_{night} are relative to total CO and to acetylene (not background corrected). Since constant values for background CO and acetylene were used in the ER calculations (see Section S3), ERs_{night} would not change if background corrections were applied.

3.5. OH Exposure Calculations. OH exposure ($[OH]\Delta t$) is a measure of atmospheric aging and represents the photochemical loss of reactive VOCs. In the derivation of OH-corrected ERs, OH exposure was estimated based on de Gouw et al.[26] using the ratio of benzene/1,2,4-trimethylbenzene (Figure S19) as an indicator of photochemical aging. The change in OH exposure relative to the past decade was also estimated based on Warneke et al.[29] Warneke et al.[29] used the ratio of weekday to weekend ERs to quantify the increase in OH exposure on weekends due to decreased NO_x. Here, the ratio of 2010 ER to 2020 ER was used to quantify the change in OH exposure between 2010 and 2020.

With daytime winds predominantly from the southwest, back trajectory analysis during CalNex-2010 showed air masses being transported from LA to Pasadena with approximate photochemical ages of up to 0.5 days.[3] Similar daytime wind direction and speeds were observed in 2020 (Figure S5). To account for photochemical loses, the relationship between

https://doi.org/10.1021/acsearthspacechem.1c00248
ACS Earth Space Chem. 2021, 5, 3045−3055

Table 1. 2020 and 2010 Emission Ratios (ERs) to CO and Acetylene

	OH-corrected ER (ppt [ppb ΔCO]$^{-1}$)		ER_{night} (ppt [ppb CO]$^{-1}$)		ER_{night} (ppt [ppt acetylene]$^{-1}$)		r^2 w/ CO	r^2 w/ acetylene
compound	2020	2010[a]	2020	2010[b]	2020	2010[c]	2020	2020
ethane	60.09 ± 8.02	16.5	58.34	18.4	18.22	4.16	0.76	0.72
ethene	6.80 ± 0.90	11.2	4.99	10.35	1.61	1.80	0.79	0.81
acetylene[d]	2.91 ± 0.44	6.4	2.96	5.87	–	–	0.90	–
1,2-propadiene	0.09 ± 0.01	–	0.07	–	0.02	–	0.79	0.73
propyne	0.10 ± 0.01	–	0.10	–	0.03	–	0.70	0.66
propane[d]	14.5 ± 3.33	–	14.45	11.2	4.71	2.05	0.74	0.80
propene	1.57 ± 0.22	4.1	1.07	3.74	0.34	–	0.77	0.76
i-butane[d]	2.67 ± 0.61	3.18	2.80	3.08	0.92	0.55	0.70	0.77
n-butane[d]	4.17 ± 0.96	4.94	4.44	4.42	1.47	0.78	0.70	0.75
1-butene	0.32 ± 0.04	0.39	0.17	0.34	0.06	0.05	0.67	0.67
i-butene	0.58 ± 0.08	0.9	0.27	–	0.08	–	0.35	0.33
trans-2-butene	0.06 ± 0.01	0.32	0.05	0.1	0.02	0.02	0.40	0.36
cis-2-butene	0.06 ± 0.01	0.28	0.04	0.09	0.01	0.02	0.42	0.37
i-pentane	4.62 ± 0.66	8.7	5.03	8.69	1.58	1.81	0.86	0.83
n-pentane	2.29 ± 0.31	3.4	2.42	3.26	0.76	0.65	0.83	0.81
1,3-butadiene	0.18 ± 0.02	0.4	0.10	0.35	0.03	0.06	0.55	0.56
1-pentene	0.14 ± 0.02	–	0.10	–	0.03	–	0.74	0.72
trans-2-pentene	0.06 ± 0.01	–	0.07	–	0.02	0.09	0.39	0.33
cis-2-pentene	0.03 ± 0.00	–	0.04	–	0.01	–	0.35	0.36
3-methyl-1-butene	0.05 ± 0.01	0.068	0.04	–	0.01	–	0.64	0.63
2-methyl-1-butene	0.12 ± 0.02	–	0.10	–	0.03	–	0.44	0.48
2-methyl-2-butene	0.07 ± 0.01	–	0.07	–	0.02	–	0.36	0.33
n-hexane	0.96 ± 0.12	1.39	1.10	1.13	0.34	0.21	0.48	0.44
n-heptane	0.45 ± 0.06	0.83	0.39	–	0.13	–	0.76	0.78
n-octane	0.22 ± 0.03	0.355	0.16	–	0.05	–	0.81	0.83
n-nonane	0.22 ± 0.03	0.326	0.16	0.22	0.05	0.04	0.73	0.74
n-decane	0.19 ± 0.03	0.3	0.10	0.18	0.03	0.04	0.56	0.64
2,2-dimethylbutane	0.14 ± 0.02	–	0.15	–	0.05	–	0.73	0.67
2,3-dimethylbutane	0.46 ± 0.06	–	0.45	–	0.14	–	0.88	0.83
2-methylpentane	1.17 ± 0.12	1.43	1.18	–	0.37	–	0.87	0.83
3-methylpentane	0.74 ± 0.02	1.39	0.78	–	0.24	–	0.78	0.74
2-methylhexane	0.45 ± 0.06	0.58	0.44	–	0.14	–	0.87	0.83
3-methylhexane	0.48 ± 0.07	0.58	0.47	–	0.15	–	0.87	0.84
2-methylheptane	0.17 ± 0.03	–	0.14	–	0.05	–	0.86	0.85
3-methylheptane	0.14 ± 0.02	–	0.12	–	0.04	–	0.89	0.87
2,4-dimethylpentane	0.37 ± 0.05	–	0.38	–	0.12	–	0.90	0.86
2,3-dimethylpentane	0.65 ± 0.09	–	0.64	–	0.20	–	0.89	0.85
2,2,4-trimethylpentane	1.01 ± 0.14	–	1.05	–	0.33	–	0.93	0.87
2,3,4-trimethylpentane	0.32 ± 0.04	–	0.33	–	0.10	–	0.94	0.89
cyclopentane	0.27 ± 0.04	–	0.24	–	0.08	–	0.77	0.75
methylcyclopentane	0.84 ± 0.04	1.34	0.81	–	0.25	–	0.76	0.72
cyclohexane	0.43 ± 0.06	0.53	0.35	–	0.11	–	0.79	0.81
methylcyclohexane	0.34 ± 0.05	0.43	0.29	–	0.09	–	0.79	0.83
benzene[d]	0.64 ± 0.17	1.26	0.76	1.3	0.24	0.23	0.82	0.83
toluene	2.84 ± 0.38	3.4	2.56	3.18	0.83	0.61	0.82	0.84
ethylbenzene	0.35 ± 0.05	0.61	0.33	0.57	0.10	0.10	0.91	0.89
m- and *p*-xylene	1.37 ± 0.18	2.07	1.29	1.79	0.41	0.34	0.90	0.89
o-xylene	0.50 ± 0.07	0.77	0.44	0.67	0.14	0.12	0.91	0.89
styrene	0.15 ± 0.02	0.36	0.07	0.22	0.03	0.04	0.32	0.38
i-propylbenzene	0.03 ± 0.00	0.0305	0.02	0.03	0.01	0.01	0.56	0.52
n-propylbenzene	0.08 ± 0.01	0.103	0.06	0.11	0.02	0.02	0.79	0.78
3-ethyltoluene	0.33 ± 0.05	0.44	0.25	–	0.08	–	0.88	0.88
4-ethyltoluene	0.15 ± 0.02	0.44	0.11	–	0.04	–	0.79	0.77
2-ethyltoluene	0.11 ± 0.02	0.123	0.07	0.12	0.02	0.02	0.74	0.76
1,3,5-trimethylbenzene	0.14 ± 0.02	0.39	0.10	0.31	0.03	0.06	0.77	0.80
1,2,4-trimethylbenzene	0.45 ± 0.06	0.79	0.31	0.62	0.10	0.12	0.79	0.80

[a]de Gouw et al.[26] [b]Borbon et al.[27] [c]Calculated using CalNex ground site data.[28] [d]Relatively unreactive compounds (k_{OH} < 5 × 10^{-12} cm^3 molecule^{-1} s^{-1}) were background corrected (see Section S3); correction values were 110, 294, 49, 79, and 60 ppt for acetylene, propane, *i*-butane, *n*-butane, and benzene, respectively.

https://doi.org/10.1021/acsearthspacechem.1c00248
ACS Earth Space Chem. 2021, 5, 3045−3055

ER_{day} and ER_{night} was approximated by a first-order loss equation (eq 1):

$$ER_{day} \cong ER_{night} \times e^{k_{OH}[OH]\Delta t} \quad (1)$$

where ER_{day} was calculated using linear regression from the daytime data only and $k_{OH} = -k_{VOC} + k_{CO}$. Then, to estimate the change in weekday OH exposure relative to 2010, the ratio of 2010 weekday ERs to 2020 weekday ERs was calculated (eq 2):

$$\frac{ER_{day(2010)} \times ER_{night(2020)}}{ER_{day(2020)} \times ER_{night(2010)}} \cong \frac{e^{k_{OH}([OH]t)_{2010}}}{e^{k_{OH}([OH]t)_{2020}}} = e^{-k_{OH}(([OH]\Delta t)_{2020} - ([OH]\Delta t)_{2010})} \quad (2)$$

This ratio was plotted against the rate constant (k) with OH for a subset of compounds; a fit was applied to the data, giving the change in weekday OH exposure between 2010 and 2020. The same method was applied to calculate the change in weekend OH exposure.

4. RESULTS AND DISCUSSION

4.1. Compounds, Sources, and Trends during LAAQC.

In Table S2, the average nighttime, morning, and afternoon mixing ratios are summarized for the 92 compounds identified and quantified using multi-column and multi-detector GC and 58 compounds using GC/GC-TOF-MS. Common sources for each compound are summarized in Table S3. Combustion source emissions include on- and off-road gasoline and diesel exhaust. In addition, there are evaporative fuel emissions from these sources which include contributions from light-duty cars and trucks ("passenger" vehicles), heavy-duty trucks, ocean-going vessels, recreational boats, construction equipment, farm equipment, and landscaping equipment. Nonmobile source emissions include VCPs and industrial cooking, with specific contributions from pesticides, coatings, inks, adhesives, cleaning agents and solvents, and personal care products.

While the broad changes in human activity during COVID-19 are still being examined, the change in travel demand in the LA Basin was striking. Between the beginning and end of the campaign, traffic counts increased by approximately 30%; the increase in average April−May traffic to average June−July traffic was approximately 10%.[13] Despite the increase in traffic, the average afternoon concentrations of CO and VOCs did not significantly increase; June−July mixing ratios were within one standard deviation of the April−May values (Figure 2). However, Figure 3 illustrates that the afternoon 25th percentile (Q1) mixing ratio, calculated for 54 compounds, increased substantially for some compounds. The Q1 mixing ratio of CO increased 23%, and acetylene increased 47%. CO, long-lived in the atmosphere, is a tracer of combustion sources; acetylene, also long-lived in the atmosphere, is emitted from gasoline exhaust and used to separate distinct sources of CO such as traffic and biomass burning.[30] Both CO and acetylene are useful tracers for on- and off-road mobile sources.

For the combined data set, April−July, acetylene was found to have the highest afternoon correlation with CO ($r^2 = 0.91$); the strength of relationship, defined by the r^2-value, indicates they were both primarily emitted from gasoline exhaust. Figure 3 illustrates that compounds with the greatest increase in

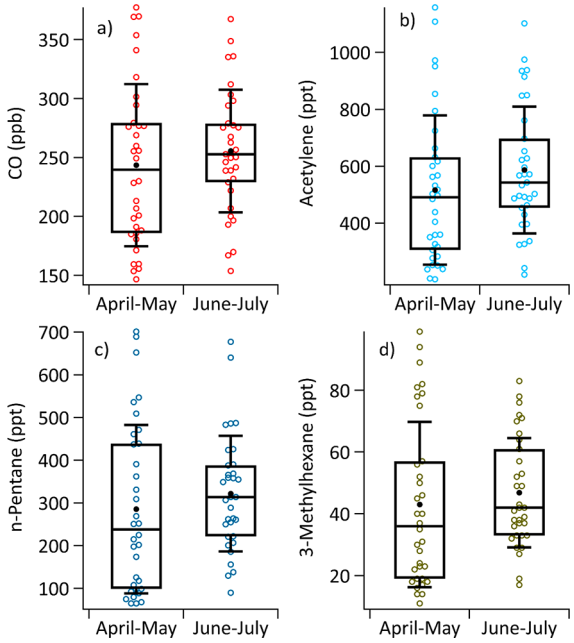

Figure 2. Box and whisker plots of (a) CO, (b) acetylene, (c) *n*-pentane, and (d) 3-methylhexane measured in April−May and June−July. The shaded circles indicate the afternoon mixing ratios of individual samples. The black dot indicates the mean mixing ratio. The whiskers represent one standard deviation from the mean. The black line represents the median, and the 25th and 75th percentiles are represented by the edges of the black box.

afternoon Q1 mixing ratios also have the strongest correlation with CO. VOCs with Q1 mixing ratios that increased >60% between April−May and June−July had an average r^2 with CO of 0.72, while VOCs with Q1 mixing ratios that increased or decreased <40% had an average r^2 with CO of only 0.35. This is consistent with combustion source emissions increasing between April−May and June−July while source emissions of the other measured VOCs were not increasing.

A majority of the VOCs with Q1 mixing ratios that increased >60% are emitted from both gasoline exhaust and gasoline evaporation.[5] The afternoon Q1 mixing ratio of *n*-pentane, a major component of gasoline vapor, increased by 119%, and 3-methylhexane, a component of both gasoline exhaust and vapor,[5] increased by 86%. While many of the compounds overlap between the two sources, the relative contributions of VOCs vary between gasoline exhaust and gasoline vapor emissions. For example, *n*-pentane makes up 8.7% of gasoline vapor and only 1.9% of gasoline exhaust.[5] VOC speciation profiles for gasoline exhaust and vapor were reported in McDonald et al.[5] To determine the extent to which the increase in Q1 mixing ratios for compounds emitted from mobile sources could be attributed to an increase in exhaust or evaporation, the percent increase in Q1 VOC mixing ratio was plotted against the corresponding ratio of gasoline vapor weight % to gasoline exhaust weight % in Figure 4 (e.g., for *n*-pentane, the vapor to exhaust ratio would be 8.7:1.9). Figure 4 illustrates that compounds with higher vapor to exhaust ratios had greater increases in afternoon Q1 mixing ratios, suggesting that evaporative emissions increased more than exhaust emissions between April−May and June−July. VOCs with a vapor to exhaust ratio of >1 increased, on average, 83%. The Q1 mixing ratio of isoprene, a biogenic VOC that exhibited strong positive correlation with temperature (r^2 = 0.89),

https://doi.org/10.1021/acsearthspacechem.1c00248
ACS Earth Space Chem. 2021, 5, 3045−3055

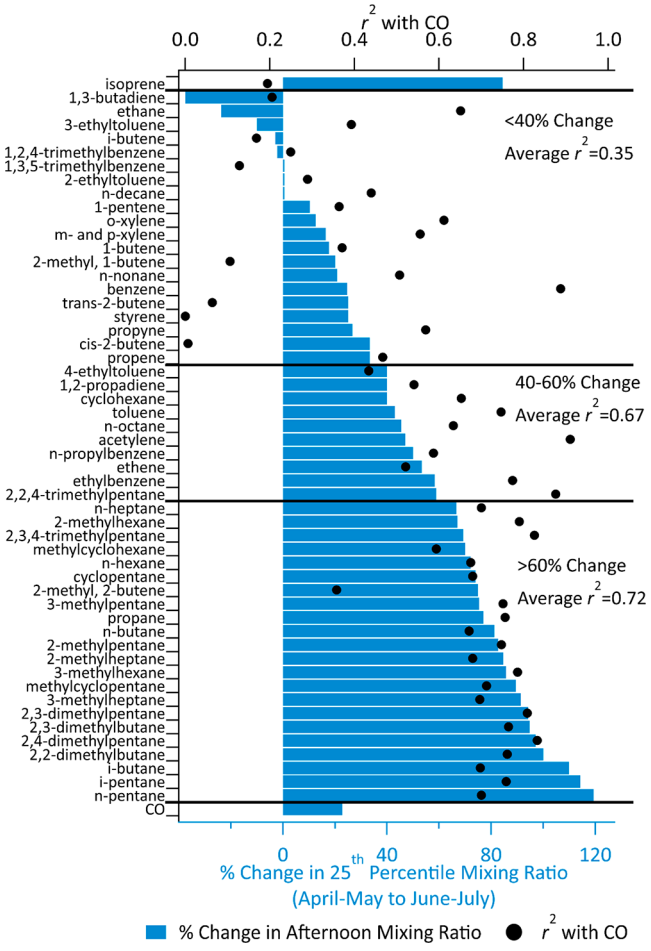

Figure 3. Percent change in the afternoon 25th percentile mixing ratio (Q1) from April−May to June−July for CO and a subset of VOCs (blue bars, bottom axis), plotted with the campaign r^2-value between the VOC and CO (black dots, top axis).

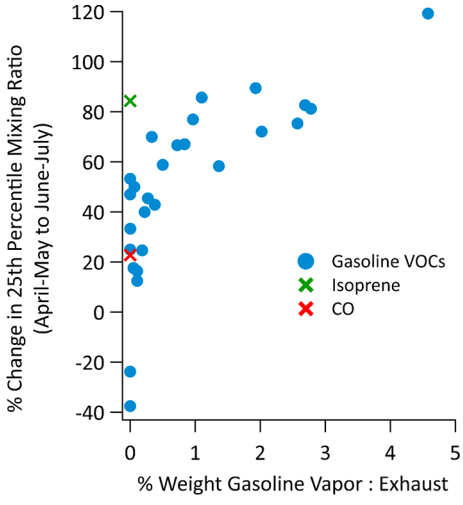

Figure 4. Percent change in the 25th percentile (Q1) mixing ratio from April−May to June−July plotted against the ratio of VOC weight (%) in gasoline vapor to VOC weight (%) in gasoline exhaust. VOCs are represented by blue dots, isoprene is represented by the green ×, and CO is represented by the red ×.

increased 84%. The Q1 temperature increased from 295.7 K in April−May to 298.6 K in June−July. These observations suggest that the increase in afternoon Q1 mixing ratios between April−May and June−July was largely due to an increase in temperature, and thus an increased contribution of measured VOCs from evaporative emissions.

In addition to VOCs associated with anthropogenic sources, a number of VOCs associated with biogenic sources were quantified during LAAQC, particularly terpenes. Terpenes are also emitted from anthropogenic sources; for example, fragrances have been reported to contribute significantly to terpene levels, especially limonene, in urban areas.[31] However, there was no clear evidence of a distinct contribution of anthropogenic sources to the terpenes quantified during LAAQC. Biogenic terpene emissions exhibit a light and temperature response and thus trend strongly with temperature.[32] During LAAQC, afternoon mixing ratios of α-pinene, camphene, and eucalyptol increased with temperature (Figure S23). However, β-pinene, β-myrcene, and limonene exhibited weaker temperature dependence, suggesting the primary driver of these terpenes changed during the campaign. In Figure 5 it

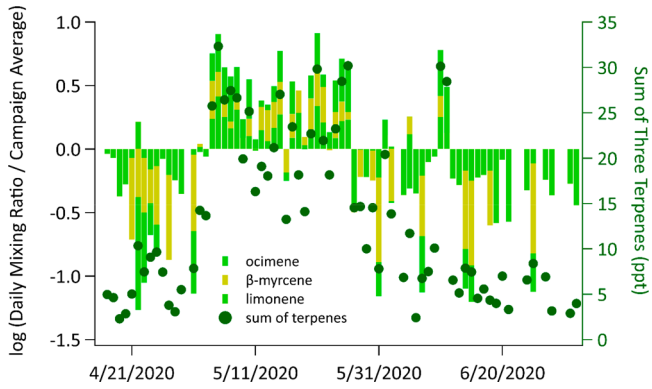

Figure 5. Log of daily afternoon mixing ratio normalized to campaign average afternoon mixing ratio for three terpenes (ocimene, β-myrcene, and limonene). Bars for the three compounds correspond to the left axis; values above zero indicate the daily summed concentration for the three compounds is greater than the campaign average summed concentration. The right axis corresponds to the total concentration for the three terpenes (green dots).

can be seen that the ocimene, β-myrcene, and limonene mixing ratios were elevated during the month of May. This trend is likely a result of higher emission rates from citrus trees during flowering.[33]

4.2. Changes in OH Exposure Since 2010. In 2010, Warneke et al.[29] reported that OH exposure ($[OH]\Delta t$) was 65−75% higher on weekends than on weekdays in Southern California due to a 35−50% decrease in NO_x levels on weekends. The lower NO_x levels on weekends have been attributed to reduced truck traffic.[34−37] Nussbaumer and Cohen[38] reported that NO_x levels in the LA Basin decreased up to ∼80% between 1994 and 2019, and remained lower on weekends compared to weekdays. On the basis of data obtained from a California Air Resources Board monitoring site located in Pasadena,[8] NO_x levels averaged over the April−July sampling period were an average of 50% lower than in 2020 than 2010; NO_x levels in 2020 were an average of 45% higher on weekdays compared to weekends (Table S4). The calculated OH exposures were used to probe the effect of changes in atmospheric composition, particularly NO_x levels, on OH exposure between 2010 and 2020.

https://doi.org/10.1021/acsearthspacechem.1c00248
ACS Earth Space Chem. 2021, 5, 3045−3055

Figure 6 illustrates the ratio of the 2010 ER to the 2020 ER for a subset of VOCs, plotted against their k_{OH}, measured on

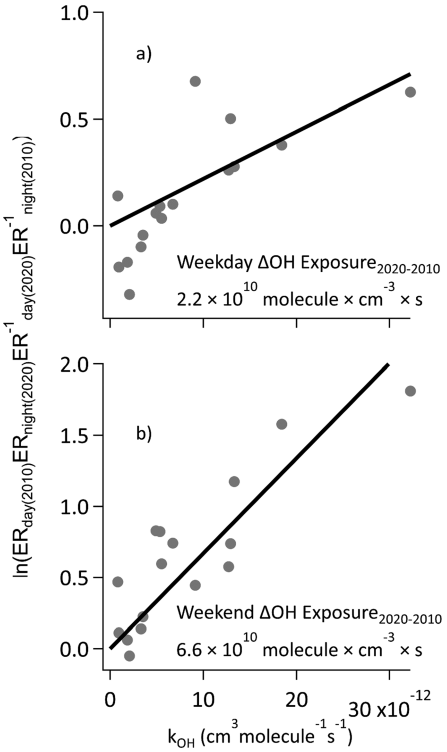

Figure 6. Increase in OH exposure between 2010 and 2020: (a) weekdays and (b) weekends. Each point represents a single VOC that was measured in both years; 2010 ER values were reported by Warneke et al.[29]

weekdays and weekends. Applying a linear fit to the data yielded an increase in weekday and weekend peak (afternoon) OH exposure by ~2.2 × 10^{10} molecules cm^{-3} s and ~6.6 × 10^{10} molecules cm^{-3} s, respectively, since 2010. The average peak OH exposure in 2010 was reported to be ~3 × 10^{10} molecules cm^{-3} s;[29] the weekly average change in OH exposure between 2010 and 2020 was calculated to be ~3.5 × 10^{10} molecules cm^{-3} s. Using the 2010 average peak OH exposure and calculated increase in weekly average change in peak exposure, the average peak OH exposure in 2020 was calculated to be ~6.5 × 10^{10} molecules cm^{-3} s. In comparison, using the ratio of benzene to 1,2,4-trimethylbenzene to estimate OH exposure (Section S4) resulted in an average peak OH exposure of 5.2 × 10^{10} molecules cm^{-3} s. Based on the similar wind speeds and directions (Figure S4), it can be assumed that transport time has remained relatively constant between 2010 and 2020, and thus the average peak OH concentration can be estimated using the ratio of average peak OH exposure in 2020 to 2010; by that approach, OH concentration has increased by a factor of 2, from ~4 × 10^6 molecules cm^{-3} in 2010 to ~8 × 10^6 molecules cm^{-3} in 2020.

The extent to which the OH concentrations are wholly representative of recent non-COVID periods, depends in part on whether the yet unknown trends in human activities and emissions significantly affected OH reactivity during the LAAQC sampling period. To evaluate whether the 2020 VOC mixing ratios were anomalously low during the sampling period, the average mixing ratios of three combustion-derived compounds (CO, acetylene, and *i*-pentane) and total non-methane hydrocarbons (NMHCs) measured during LAAQC-2020 were compared with average mixing ratios measured over the LA Basin during the NASA Student Airborne Research Program (SARP) between 2015 and 2019. It is expected that the mixing ratios of the shorter-lived compounds would be lower in the samples collected aloft than those collected at the Pasadena ground site. For all three individual compounds (Figures S25−S27) and total NMHCs (Figure S28), the median LAAQC values fall within the upper quartile of the SARP values. This suggests that the decreasing trends in OH are not an anomaly and more generally are expected based on trends in NO_x, and supports the use of the LAAQC-2020 data for comparisons with CalNex-2010.

4.3. Changes in VOCs, Sources, and Emission Ratios Since 2010. Coincident reductions in CO and VOCs over the decades prior to 2010 resulted in roughly constant ERs relative to CO and to acetylene.[2] The reductions resulted from improved vehicle emission control technologies and more stringent emissions standards. Anomalies from the observed trends, however, suggest the impact of other emissions sources. For example, several smaller alkanes (C2−C5), abundant in both processed and raw natural gas and associated gas (natural gas that was produced by oil wells),[39,40] did not follow the ~7.5% decrease per year over that time period. Peischl et al.[39] reported that nearly all ethane emissions measured in the LA Basin in 2010 could be attributed to such sources, as well as significant fractions of propane (~90%) and *n*-butane (~75%). Evaporated gasoline was identified as the primary source of *n*-pentane (~33%) and *i*-pentane (~50%) emissions; the remainder of *n*- and *i*-pentane was attributed to other mobile sources and natural gas.[39] As the on-road mobile source emissions of small alkanes decreased, other sources became more important and their ERs relative to CO increased.

Using the California Emissions Projection Analysis Model (CEPAM),[41] the California Air Resources Board (CARB) projected a reduction in emissions from on-road sources between 2010 and 2020, due to retirement of old vehicles and updates in regulations to on-road motor vehicles. Those regulations were assumed to result in negligible changes in the VOC composition of emissions, as supported by speciation profiles and associated documentation.[42,43] Figure 7 illustrates the estimated change in VOC and CO emissions from on-road motor vehicles, dominated by light-duty passenger vehicles and light-duty trucks, as reported in the CEPAM, and other mobile sources, dominated by off-road equipment. In 2010, on-road motor vehicles were projected to be the dominant contributor to mobile source CO (70%) and VOCs (65%) in the South Coast Air Basin. In 2020, other/off-road combustion and evaporative sources were projected to be the dominant contributor to mobile source CO (55%), and an equal contributor to VOC (50%) emissions. Thus, total VOCs from off-road sources were projected to drop 30% between 2010 and 2020, while total CO was projected to drop only 2%. In 2010, the most abundant off-road source of CO was riding mowers, which was projected to increase from 4.6 × 10^4 kg day^{-1} to 5.3 × 10^4 kg day^{-1} between 2010 and 2020. The most abundant off-road source of VOCs was gasoline evaporation from lawn mowers, which was projected to decrease from 7.8 × 10^3 kg day^{-1} to 4.3 × 10^3 kg day^{-1} between 2010 and 2020. The projected shift from on-road to other/off-road sectors as the dominant emitters of mobile source VOCs and CO likely changed measured VOCs levels and calculated ERs for

https://doi.org/10.1021/acsearthspacechem.1c00248
ACS Earth Space Chem. 2021, 5, 3045−3055

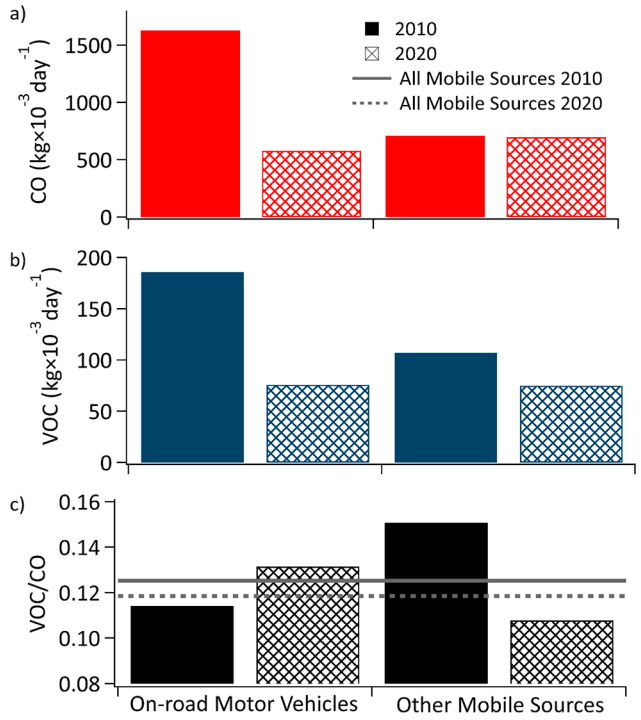

Figure 7. Projected emissions of (a) CO, (b) VOCs, and (c) the ratio of VOCs to CO from on-road motor vehicles and other/off-road mobile sources in the LA Basin. The solid line in (c) represents the 2010 VOC to CO ratio for all mobile sources (on-road motor vehicles + other mobile sources); the dotted line represents the 2020 VOC to CO ratio for all mobile sources. Projected emission values were obtained using the California Emissions Projection Analysis Model.[41]

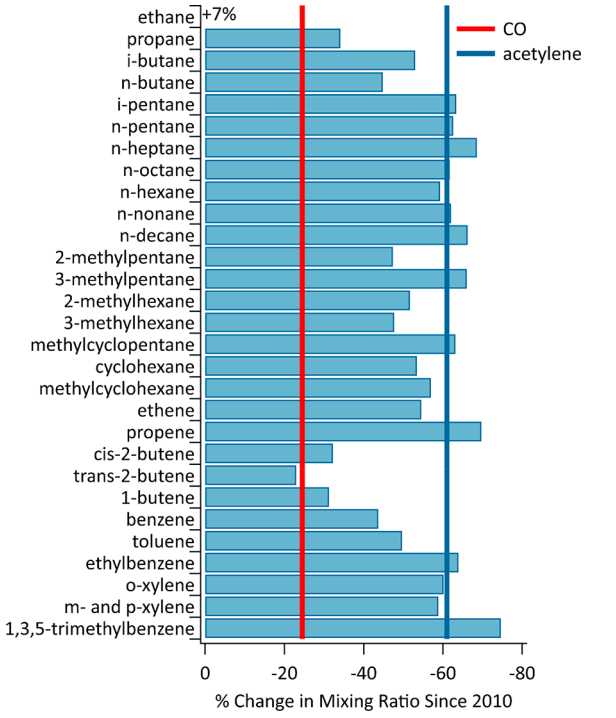

Figure 8. Percent change in VOC mixing ratios from 2010 to 2020 for CO (red line) and 30 VOCs, including acetylene (blue line). Average 2010 mixing ratios were calculated during the same times of day as samples collected during LAAQC using data in the CalNex-2010 database.[28]

compounds that have been historically emitted primarily by on-road mobile sources.

As illustrated in Figure 8, CO has dropped approximately 25% since 2010 while acetylene has dropped approximately 60%. Most VOCs followed acetylene, dropping ~60% since 2010. As noted previously, the correlation between CO and acetylene was strong in 2020, suggesting the dominant source of CO remains gasoline exhaust. ERs_{night} relative to acetylene remained constant between 2010 and 2020 (Figure 9, top), while ERs_{night} relative to CO and OH-corrected ERs to ΔCO dropped to ~60% of the 2010 values reported by Borbon et al.[27] and de Gouw et al.[26] (Figure 9, bottom). The divergence of CO and VOCs indicates a change in combustion source sectors, and is supported by the projected shift from on-road motor vehicles to other mobile/off-road sectors as equal or dominant contributors to mobile source CO and VOCs.

In Table S5, VOCs are classified as combustion, unknown, and noncombustion based on the 2010 vs 2020 ERs plotted in Figure 9. VOCs with ERs_{night} to acetylene within 25% of the 1:1 line and with ERs_{night} to CO and OH-corrected ERs to ΔCO within 25% of the 0.6:1 line were classified as combustion dominant (18 of 40 compounds). The majority of VOCs with ERs_{night} to acetylene that fell within 25% of the 1:1 line, also had ERs_{night} and OH-corrected ERs that fell within 25% of the 0.6:1 line; these VOCs likely were primarily from gasoline combustion. VOCs with ERs outside the 25% threshold were classified as noncombustion (15 of 40), and include small alkanes, butenes, and toluene. Small alkanes like ethane, propane, and butane are known to be emitted from natural gas and petroleum extraction.[39,40] The smaller change

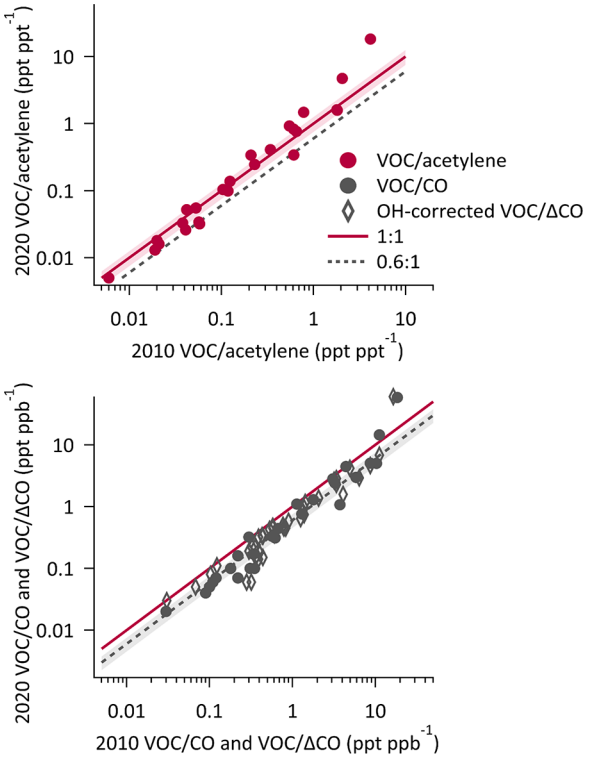

Figure 9. Relationship between 2010 and 2020 VOC ERs relative to acetylene (top) and CO (bottom). The solid burgundy line represents a slope of 1; the dashed gray line represents a slope of 0.6. Shading indicates ±25% from the line. 2010 VOC/CO emission ratios values were reported in Borbon et al.[27] 2010 VOC/acetylene emission ratios were calculated using CalNex-2010 VOC data.[28]

https://doi.org/10.1021/acsearthspacechem.1c00248
ACS Earth Space Chem. 2021, 5, 3045−3055

in butenes (average ~30%), may be due to the growing relative importance of biogenic butene sources.[44,45] Toluene was identified in Seltzer et al.[46] to be the fourth most abundant VOC emitted by VCPs, with a predicted emission rate of 0.37 kg person^{-1} year^{-1}. VOCs were classified as unknown (7 of 40) if only one or two of the three ERs (with acetylene, CO, or ΔCO) fell within the 25% threshold. The calculated OH-reactivity for VOCs classified as unknown was 0.06 s^{-1}; the calculated OH-reactivity for combustion and noncombustion VOCs was roughly equal, 0.37 s^{-1} and 0.36 s^{-1}, respectively.

5. CONCLUSIONS

As a part of the LAAQC, 150 VOCs were measured in the LA Basin during shelter-in-place restrictions associated with the COVID-19 pandemic (April 2020 to July 2020). Compounds that were identified (alkanes, alkenes, aldehydes, ketones, aromatics, etc.) are emitted from a variety of mobile, nonmobile, and biogenic sources. While traffic counts increased markedly during the measurement period, no significant change was observed in the mean VOC concentrations of combustion source emissions. Evaluation of the increases from April−May to June−July in Q1 mixing ratios of CO and acetylene (23% and 47%), as well as VOCs present in gasoline exhaust and evaporative emissions, suggest that the increase in traffic resulted in a relatively minor impact on gasoline exhaust emissions compared to gasoline vapor emissions.

A comparison of CO and VOC levels and ERs calculated from data collected during the CalNex-2010 campaign provided insight into the changing source contributions in the LA Basin, as well as changes in chemical composition and atmospheric reactivity. ERs relative to CO and ΔCO dropped to approximately 60% of their 2010 values, while ERs relative to acetylene remained constant. This suggests that sources with higher CO to acetylene ratios are becoming more important. Relative to 2010, the OH concentration increased 2-fold to approximately ~8 × 10^6 molecules cm^{-3}. OH reactivity was calculated for VOCs with ERs relative to acetylene that remained constant since 2010 (combustion VOCs) and for VOCs with ERs that did not remain constant (noncombustion VOCs); VOCs attributed to combustion vs noncombustion had roughly equal OH reactivity.

■ ASSOCIATED CONTENT

Supporting Information

The Supporting Information is available free of charge at https://pubs.acs.org/doi/10.1021/acsearthspacechem.1c00248.

Tables S1−S5: Emission ratios, average VOC mixing ratios, possible VOC sources, 2010 and 2020 NO_x data, and a list VOCs sorted by combustion vs noncombustion sources (XLSX)

Chemical and meteorological data, UCI vs UCR VOC mixing ratio comparisons, background CO and VOC calculations, emission ratio calculations, temperature dependence of terpene emissions, and trends in VOC mixing ratios (PDF)

■ AUTHOR INFORMATION

Corresponding Author

Kelley C. Barsanti − *Bourns College of Engineering, Center for Environmental Research and Technology, Riverside, California 92507, United States; Department of Chemical and Environmental Engineering, University of California, Riverside, California 92507, United States;* orcid.org/0000-0002-6065-8643; Email: kbarsanti@engr.ucr.edu

Authors

Paul Van Rooy − *Bourns College of Engineering, Center for Environmental Research and Technology, Riverside, California 92507, United States;* orcid.org/0000-0003-1193-0994

Afsara Tasnia − *Bourns College of Engineering, Center for Environmental Research and Technology, Riverside, California 92507, United States; Department of Chemical and Environmental Engineering, University of California, Riverside, California 92507, United States*

Barbara Barletta − *Department of Chemistry, University of California, Irvine, California 92697, United States*

Reina Buenconsejo − *Division of Chemistry and Chemical Engineering, California Institute of Technology, Pasadena, California 91125, United States*

John D. Crounse − *Division of Chemistry and Chemical Engineering and Division of Engineering and Applied Science, California Institute of Technology, Pasadena, California 91125, United States;* orcid.org/0000-0001-5443-729X

Christopher M. Kenseth − *Division of Chemistry and Chemical Engineering, California Institute of Technology, Pasadena, California 91125, United States;* orcid.org/0000-0003-3188-2336

Simone Meinardi − *Department of Chemistry, University of California, Irvine, California 92697, United States*

Sara Murphy − *Division of Geological and Planetary Sciences, California Institute of Technology, Pasadena, California 91125, United States*

Harrison Parker − *Division of Geological and Planetary Sciences, California Institute of Technology, Pasadena, California 91125, United States*

Benjamin Schulze − *Division of Geological and Planetary Sciences, California Institute of Technology, Pasadena, California 91125, United States*

John H. Seinfeld − *Division of Geological and Planetary Sciences and Division of Engineering and Applied Science, California Institute of Technology, Pasadena, California 91125, United States;* orcid.org/0000-0003-1344-4068

Paul O. Wennberg − *Division of Geological and Planetary Sciences and Division of Engineering and Applied Science, California Institute of Technology, Pasadena, California 91125, United States;* orcid.org/0000-0002-6126-3854

Donald R. Blake − *Department of Chemistry, University of California, Irvine, California 92697, United States*

Complete contact information is available at: https://pubs.acs.org/10.1021/acsearthspacechem.1c00248

Author Contributions

The study was conceived by KCB, JHS, DRB, and POW. All authors contributed to data collection, analysis, and/or interpretation. The manuscript was written largely by PVR and KCB, with contributions from AT, BB, JDC, HP, PS, and POW. The manuscript was edited through contributions of all authors. All authors have given approval to the final version of the manuscript.

Funding

PVR, AT, KCB acknowledge funding support from NSF RAPID award #2030049. BB, SM, and DRB acknowledge funding support from NSF RAPID award #2030112.

Notes

The authors declare no competing financial interest.

■ ACKNOWLEDGMENTS

The authors would like to sincerely thank Joost de Gouw for conversations during the campaign period in which he shared his knowledge of the composition and chemistry in the LA Basin. The authors would also like to thank Joost de Gouw and Carsten Warneke for the quality data collected during the CalNex-2010 campaign and subsequent analysis of that data, which were foundational to this study.

■ REFERENCES

(1) Parrish, D. D.; Xu, J.; Croes, B.; Shao, M. Air Quality Improvement in Los Angeles—Perspectives for Developing Cities. *Front. Environ. Sci. Eng.* **2016**, *10* (5), 11.

(2) Warneke, C.; de Gouw, J. A.; Holloway, J. S.; Peischl, J.; Ryerson, T. B.; Atlas, E.; Blake, D.; Trainer, M.; Parrish, D. D. Multiyear Trends in Volatile Organic Compounds in Los Angeles, California: Five Decades of Decreasing Emissions. *J. Geophys. Res. Atmospheres* **2012**, DOI: 10.1029/2012JD017899.

(3) Hayes, P. L.; Ortega, A. M.; Cubison, M. J.; Froyd, K. D.; Zhao, Y.; Cliff, S. S.; Hu, W. W.; Toohey, D. W.; Flynn, J. H.; Lefer, B. L.; Grossberg, N.; Alvarez, S.; Rappenglück, B.; Taylor, J. W.; Allan, J. D.; Holloway, J. S.; Gilman, J. B.; Kuster, W. C.; de Gouw, J. A.; Massoli, P.; Zhang, X.; Liu, J.; Weber, R. J.; Corrigan, A. L.; Russell, L. M.; Isaacman, G.; Worton, D. R.; Kreisberg, N. M.; Goldstein, A. H.; Thalman, R.; Waxman, E. M.; Volkamer, R.; Lin, Y. H.; Surratt, J. D.; Kleindienst, T. E.; Offenberg, J. H.; Dusanter, S.; Griffith, S.; Stevens, P. S.; Brioude, J.; Angevine, W. M.; Jimenez, J. L. Organic Aerosol Composition and Sources in Pasadena, California, during the 2010 CalNex Campaign. *J. Geophys. Res. Atmospheres* **2013**, *118* (16), 9233−9257.

(4) Lu, Q.; Murphy, B. N.; Qin, M.; Adams, P. J.; Zhao, Y.; Pye, H. O. T.; Efstathiou, C.; Allen, C.; Robinson, A. L. Simulation of Organic Aerosol Formation during the CalNex Study: Updated Mobile Emissions and Secondary Organic Aerosol Parameterization for Intermediate-Volatility Organic Compounds. *Atmos. Chem. Phys.* **2020**, *20* (7), 4313−4332.

(5) McDonald, B. C.; de Gouw, J. A.; Gilman, J. B.; Jathar, S. H.; Akherati, A.; Cappa, C. D.; Jimenez, J. L.; Lee-Taylor, J.; Hayes, P. L.; McKeen, S. A.; Cui, Y. Y.; Kim, S.-W.; Gentner, D. R.; Isaacman-VanWertz, G.; Goldstein, A. H.; Harley, R. A.; Frost, G. J.; Roberts, J. M.; Ryerson, T. B.; Trainer, M. Volatile Chemical Products Emerging as Largest Petrochemical Source of Urban Organic Emissions. *Science* **2018**, *359* (6377), 760−764.

(6) CFR. CFR. 49 CFR § 531.5 Fuel economy standards. https://ecfr.io/Title-49/Section-531.5 (accessed June 15, 2021).

(7) Alternative Fuels Data Center: Maps and Data. https://afdc.energy.gov/data/ (accessed June 15, 2021).

(8) Air Quality Data (PST) Query Tool. https://www.arb.ca.gov/aqmis2/aqdselect.php (accessed July 9, 2021).

(9) Gensheimer, J.; Turner, A. J.; Shekhar, A.; Wenzel, A.; Keutsch, F. N.; Chen, J. What Are the Different Measures of Mobility Telling Us About Surface Transportation CO2 Emissions During the COVID-19 Pandemic? *J. Geophys. Res.: Atmos.* **2021**, *126* (11), No. e2021JD034664.

(10) Turner, A. J.; Kim, J.; Fitzmaurice, H.; Newman, C.; Worthington, K.; Chan, K.; Wooldridge, P. J.; Köehler, P.; Frankenberg, C.; Cohen, R. C. Observed Impacts of COVID-19 on Urban CO2 Emissions. *Geophys. Res. Lett.* **2020**, *47* (22), No. e2020GL090037.

(11) Yang, J.; Wen, Y.; Wang, Y.; Zhang, S.; Pinto, J. P.; Pennington, E. A.; Wang, Z.; Wu, Y.; Sander, S. P.; Jiang, J. H.; Hao, J.; Yung, Y. L.; Seinfeld, J. H. From COVID-19 to Future Electrification: Assessing Traffic Impacts on Air Quality by a Machine-Learning Model. *Proc. Natl. Acad. Sci. U. S. A.* **2021**, *118* (26), e2102705118.

(12) Liu, J.; Lipsitt, J.; Jerrett, M.; Zhu, Y. Decreases in Near-Road NO and NO2 Concentrations during the COVID-19 Pandemic in California. *Environ. Sci. Technol. Lett.* **2021**, *8* (2), 161−167.

(13) Parker, H. A.; Hasheminassab, S.; Crounse, J. D.; Roehl, C. M.; Wennberg, P. O. Impacts of Traffic Reductions Associated With COVID-19 on Southern California Air Quality. *Geophys. Res. Lett.* **2020**, *47* (23), No. e2020GL090164.

(14) Eldeirawi, K.; Huntington-Moskos, L.; Nyenhuis, S. M.; Polivka, B. Increased Disinfectant Use among Adults with Asthma in the Era of COVID-19. *J. Allergy Clin. Immunol. Pract.* **2021**, *9* (3), 1378−1380.

(15) Koksoy Vayisoglu, S.; Oncu, E. The Use of Cleaning Products and Its Relationship with the Increasing Health Risks during the Covid-19 Pandemic. *Int. J. Clin. Pract.* **2021**, *75*, No. e14534.

(16) Antonioni, M. The Impact of COVID-19 on the Cosmetic and Personal Care Sectors: Trade Data & Analysis. https://blog.marketresearch.com/the-impact-of-covid-19-on-the-cosmetic-and-personal-care-sectors-trade-data-and-analysis (accessed June 16, 2021).

(17) Corley, J.; Okely, J. A.; Taylor, A. M.; Page, D.; Welstead, M.; Skarabela, B.; Redmond, P.; Cox, S. R.; Russ, T. C. Home Garden Use during COVID-19: Associations with Physical and Mental Wellbeing in Older Adults. *J. Environ. Psychol.* **2021**, *73*, 101545.

(18) Unnikrishnan, A.; Figliozzi, M. A. A Study of the Impact of COVID-19 on Home Delivery Purchases and Expenditures, 2020. https://archives.pdx.edu/ds/psu/33410.

(19) TCCON Weather. http://tccon-weather.caltech.edu/ (accessed June 16, 2021).

(20) Weather Data & Weather API. Visual Crossing. https://www.visualcrossing.com/ (accessed September 19, 2021).

(21) Simpson, I. J.; Blake, N. J.; Barletta, B.; Diskin, G. S.; Fuelberg, H. E.; Gorham, K.; Huey, L. G.; Meinardi, S.; Rowland, F. S.; Vay, S. A.; Weinheimer, A. J.; Yang, M.; Blake, D. R. Characterization of Trace Gases Measured over Alberta Oil Sands Mining Operations: 76 Speciated C_2−C_{10} Volatile Organic Compounds (VOCs), CO_2, CH_4, CO, NO, NO_2, NO_y, O_3 and SO_2. *Atmos. Chem. Phys.* **2010**, *10* (23), 11931−11954.

(22) Helmig, D. Ozone Removal Techniques in the Sampling of Atmospheric Volatile Organic Trace Gases. *Atmos. Environ.* **1997**, *31* (21), 3635−3651.

(23) Hatch, L. E.; Yokelson, R. J.; Stockwell, C. E.; Veres, P. R.; Simpson, I. J.; Blake, D. R.; Orlando, J. J.; Barsanti, K. C. Multi-Instrument Comparison and Compilation of Non-Methane Organic Gas Emissions from Biomass Burning and Implications for Smoke-Derived Secondary Organic Aerosol Precursors. *Atmos. Chem. Phys.* **2017**, *17* (2), 1471−1489.

(24) Hatch, L. E.; Jen, C. N.; Kreisberg, N. M.; Selimovic, V.; Yokelson, R. J.; Stamatis, C.; York, R. A.; Foster, D.; Stephens, S. L.; Goldstein, A. H.; Barsanti, K. C. Highly Speciated Measurements of Terpenoids Emitted from Laboratory and Mixed-Conifer Forest Prescribed Fires. *Environ. Sci. Technol.* **2019**, *53* (16), 9418−9428.

(25) Warneke, C.; McKeen, S. A.; de Gouw, J. A.; Goldan, P. D.; Kuster, W. C.; Holloway, J. S.; Williams, E. J.; Lerner, B. M.; Parrish, D. D.; Trainer, M.; Fehsenfeld, F. C.; Kato, S.; Atlas, E. L.; Baker, A.; Blake, D. R. Determination of Urban Volatile Organic Compound Emission Ratios and Comparison with an Emissions Database. *J. Geophys. Res. Atmospheres* **2007**, DOI: 10.1029/2006JD007930.

(26) de Gouw, J. A.; Gilman, J. B.; Kim, S.-W.; Lerner, B. M.; Isaacman-VanWertz, G.; McDonald, B. C.; Warneke, C.; Kuster, W. C.; Lefer, B. L.; Griffith, S. M.; Dusanter, S.; Stevens, P. S.; Stutz, J. Chemistry of Volatile Organic Compounds in the Los Angeles Basin: Nighttime Removal of Alkenes and Determination of Emission Ratios. *J. Geophys. Res. Atmospheres* **2017**, *122* (21), 11843−11861.

(27) Borbon, A.; Gilman, J. B.; Kuster, W. C.; Grand, N.; Chevaillier, S.; Colomb, A.; Dolgorouky, C.; Gros, V.; Lopez, M.; Sarda-Esteve, R.; Holloway, J.; Stutz, J.; Petetin, H.; McKeen, S.; Beekmann, M.; Warneke, C.; Parrish, D. D.; de Gouw, J. A. Emission Ratios of Anthropogenic Volatile Organic Compounds in Northern Mid-Latitude Megacities: Observations versus Emission Inventories in Los Angeles and Paris. *J. Geophys. Res. Atmospheres* **2013**, *118* (4), 2041−2057.
(28) US Department of Commerce. N. CalNex 2010 LA Ground Site Data Download. https://csl.noaa.gov/groups/csl7/measurements/2010calnex/Ground/DataDownload/index.php?page=/groups/csl7/measurements/2010calnex/Ground/DataDownload/ (accessed June 15, 2021).
(29) Warneke, C.; de Gouw, J. A.; Edwards, P. M.; Holloway, J. S.; Gilman, J. B.; Kuster, W. C.; Graus, M.; Atlas, E.; Blake, D.; Gentner, D. R.; Goldstein, A. H.; Harley, R. A.; Alvarez, S.; Rappenglueck, B.; Trainer, M.; Parrish, D. D. Photochemical Aging of Volatile Organic Compounds in the Los Angeles Basin: Weekday-Weekend Effect. *J. Geophys. Res. Atmospheres* **2013**, *118* (10), 5018−5028.
(30) Crounse, J. D.; DeCarlo, P. F.; Blake, D. R.; Emmons, L. K.; Campos, T. L.; Apel, E. C.; Clarke, A. D.; Weinheimer, A. J.; McCabe, D. C.; Yokelson, R. J.; Jimenez, J. L.; Wennberg, P. O. Biomass Burning and Urban Air Pollution over the Central Mexican Plateau. *Atmos. Chem. Phys.* **2009**, *9* (14), 4929−4944.
(31) Gkatzelis, G. I.; Coggon, M. M.; McDonald, B. C.; Peischl, J.; Aikin, K. C.; Gilman, J. B.; Trainer, M.; Warneke, C. Identifying Volatile Chemical Product Tracer Compounds in U.S. Cities. *Environ. Sci. Technol.* **2021**, *55* (1), 188−199.
(32) Guenther, A. B.; Jiang, X.; Heald, C. L.; Sakulyanontvittaya, T.; Duhl, T.; Emmons, L. K.; Wang, X. The Model of Emissions of Gases and Aerosols from Nature Version 2.1 (MEGAN2.1): An Extended and Updated Framework for Modeling Biogenic Emissions. *Geosci. Model Dev.* **2012**, *5* (6), 1471−1492.
(33) Baghi, R.; Helmig, D.; Guenther, A.; Duhl, T.; Daly, R. Contribution of Flowering Trees to Urban Atmospheric Biogenic Volatile Organic Compound Emissions. *Biogeosciences* **2012**, *9* (10), 3777−3785.
(34) Kim, S.-W.; McDonald, B. C.; Baidar, S.; Brown, S. S.; Dube, B.; Ferrare, R. A.; Frost, G. J.; Harley, R. A.; Holloway, J. S.; Lee, H.-J.; McKeen, S. A.; Neuman, J. A.; Nowak, J. B.; Oetjen, H.; Ortega, I.; Pollack, I. B.; Roberts, J. M.; Ryerson, T. B.; Scarino, A. J.; Senff, C. J.; Thalman, R.; Trainer, M.; Volkamer, R.; Wagner, N.; Washenfelder, R. A.; Waxman, E.; Young, C. J. Modeling the Weekly Cycle of NOx and CO Emissions and Their Impacts on O3 in the Los Angeles-South Coast Air Basin during the CalNex 2010 Field Campaign. *J. Geophys. Res. Atmospheres* **2016**, *121* (3), 1340−1360.
(35) Qin, Y.; Tonnesen, G. S.; Wang, Z. Weekend/Weekday Differences of Ozone, NOx, Co, VOCs, PM10 and the Light Scatter during Ozone Season in Southern California. *Atmos. Environ.* **2004**, *38* (19), 3069−3087.
(36) Pollack, I. B.; Ryerson, T. B.; Trainer, M.; Parrish, D. D.; Andrews, A. E.; Atlas, E. L.; Blake, D. R.; Brown, S. S.; Commane, R.; Daube, B. C.; de Gouw, J. A.; Dube, W. P.; Flynn, J.; Frost, G. J.; Gilman, J. B.; Grossberg, N.; Holloway, J. S.; Kofler, J.; Kort, E. A.; Kuster, W. C.; Lang, P. M.; Lefer, B.; Lueb, R. A.; Neuman, J. A.; Nowak, J. B.; Novelli, P. C.; Peischl, J.; Perring, A. E.; Roberts, J. M.; Santoni, G.; Schwarz, J. P.; Spackman, J. R.; Wagner, N. L.; Warneke, C.; Washenfelder, R. A.; Wofsy, S. C.; Xiang, B. Airborne and Ground-Based Observations of a Weekend Effect in Ozone, Precursors, and Oxidation Products in the California South Coast Air Basin. *J. Geophys. Res. Atmospheres* **2012**, DOI: 10.1029/2011JD016772.
(37) Yarwood, G.; Stoeckenius, T. E.; Heiken, J. G.; Dunker, A. M. Modeling Weekday/Weekend Ozone Differences in the Los Angeles Region for 1997. *J. Air Waste Manage. Assoc.* **2003**, *53* (7), 864−875.
(38) Nussbaumer, C. M.; Cohen, R. C. The Role of Temperature and NOx in Ozone Trends in the Los Angeles Basin. *Environ. Sci. Technol.* **2020**, *54* (24), 15652−15659.
(39) Peischl, J.; Ryerson, T. B.; Brioude, J.; Aikin, K. C.; Andrews, A. E.; Atlas, E.; Blake, D.; Daube, B. C.; de Gouw, J. A.; Dlugokencky, E.; Frost, G. J.; Gentner, D. R.; Gilman, J. B.; Goldstein, A. H.; Harley, R. A.; Holloway, J. S.; Kofler, J.; Kuster, W. C.; Lang, P. M.; Novelli, P. C.; Santoni, G. W.; Trainer, M.; Wofsy, S. C.; Parrish, D. D. Quantifying Sources of Methane Using Light Alkanes in the Los Angeles Basin, California. *J. Geophys. Res. Atmospheres* **2013**, *118* (10), 4974−4990.
(40) Rossabi, S.; Helmig, D. Changes in Atmospheric Butanes and Pentanes and Their Isomeric Ratios in the Continental United States. *J. Geophys. Res.: Atmos.* **2018**, *123* (7), 3772−3790.
(41) CEPAM: 2016 SIP − Standard Emission Tool. https://www.arb.ca.gov/app/emsinv/fcemssumcat2016.php (accessed June 22, 2021).
(42) Speciation Profiles Used in CARB Modeling. California Air Resources Board. https://ww2.arb.ca.gov/speciation-profiles-used-carb-modeling (accessed September 19, 2021).
(43) MSEI - Modeling Tools − EMFAC Software and Technical Support Documentation. California Air Resources Board. https://ww2.arb.ca.gov/our-work/programs/mobile-source-emissions-inventory/msei-modeling-tools-emfac-software-and (accessed September 19, 2021).
(44) Rhew, R. C.; Deventer, M. J.; Turnipseed, A. A.; Warneke, C.; Ortega, J.; Shen, S.; Martinez, L.; Koss, A.; Lerner, B. M.; Gilman, J. B.; Smith, J. N.; Guenther, A. B.; de Gouw, J. A. Ethene, Propene, Butene and Isoprene Emissions from a Ponderosa Pine Forest Measured by Relaxed Eddy Accumulation. *Atmos. Chem. Phys.* **2017**, *17* (21), 13417−13438.
(45) Tripathi, N.; Sahu, L. K.; Singh, A.; Yadav, R.; Patel, A.; Patel, K.; Meenu, P. Elevated Levels of Biogenic Nonmethane Hydrocarbons in the Marine Boundary Layer of the Arabian Sea During the Intermonsoon. *J. Geophys. Res.: Atmos.* **2020**, *125* (22), No. e2020JD032869.
(46) Seltzer, K. M.; Pennington, E.; Rao, V.; Murphy, B. N.; Strum, M.; Isaacs, K. K.; Pye, H. O. T. Reactive Organic Carbon Emissions from Volatile Chemical Products. *Atmos. Chem. Phys.* **2021**, *21* (6), 5079−5100.

A p p e n d i x D

The nano-scanning electrical mobility spectrometer (nSEMS) and its application to size distribution measurements of 1.5-25 nm particles

Kong, W.; Amanatidis, S.; Mai, H.; Kim, C.; Schulze, B. C.; Huang, Y.; Lewis, G. S.; Hering, S. V.; Seinfeld, J. H.; Flagan, R. C. The Nano-Scanning Electrical Mobility Spectrometer (NSEMS) and Its Application to Size Distribution Measurements of 1.5–25Nm Particles. *Atmospheric Measurement Techniques* **2021**, *14* (8), 5429–5445. https://doi.org/10.5194/amt-14-5429-2021.

Atmos. Meas. Tech., 14, 5429–5445, 2021
https://doi.org/10.5194/amt-14-5429-2021

Atmospheric Measurement Techniques
Open Access
EGU

The nano-scanning electrical mobility spectrometer (nSEMS) and its application to size distribution measurements of 1.5–25 nm particles

Weimeng Kong[1,a], Stavros Amanatidis[1], Huajun Mai[2], Changhyuk Kim[1,b], Benjamin C. Schulze[2], Yuanlong Huang[2], Gregory S. Lewis[3], Susanne V. Hering[3], John H. Seinfeld[1,2], and Richard C. Flagan[1,2]

[1]Division of Chemistry and Chemical Engineering, California Institute of Technology, Pasadena, CA 91125, USA
[2]Department of Environmental Science and Engineering, California Institute of Technology, Pasadena, CA 91125, USA
[3]Aerosol Dynamics Inc., Berkeley, CA, USA
[a]now at: California Air Resources Board, Sacramento, CA 95814, USA
[b]now at: Department of Environmental Engineering, Pusan National University, Busan, Republic of Korea

Correspondence: Richard C. Flagan (flagan@caltech.edu)

Received: 4 March 2021 – Discussion started: 11 March 2021
Revised: 1 July 2021 – Accepted: 1 July 2021 – Published: 9 August 2021

Abstract. Particle size measurement in the low nanometer regime is of great importance to the study of cloud condensation nuclei formation and to better understand aerosol–cloud interactions. Here we present the design, modeling, and experimental characterization of the nano-scanning electrical mobility spectrometer (nSEMS), a recently developed instrument that probes particle physical properties in the 1.5–25 nm range. The nSEMS consists of a novel differential mobility analyzer and a two-stage condensation particle counter (CPC). The mobility analyzer, a radial opposed-migration ion and aerosol classifier (ROMIAC), can classify nanometer-sized particles with minimal degradation of its resolution and diffusional losses. The ROMIAC operates on a dual high-voltage supply with fast polarity-switching capability to minimize sensitivity to variations in the chemical nature of the ions used to charge the aerosol. Particles transmitted through the mobility analyzer are measured using a two-stage CPC. They are first activated in a fast-mixing diethylene glycol (DEG) stage before being counted by a second detection stage, an ADI MAGIC™ water-based CPC. The transfer function of the integrated instrument is derived from both finite-element modeling and experimental characterization. The nSEMS performance has been evaluated during measurement of transient nucleation and growth events in the CLOUD atmospheric chamber at CERN. We show that the nSEMS can provide high-time- and size-resolution measurement of nanoparticles and can capture the critical aerosol dynamics of newly formed atmospheric particles. Using a soft x-ray bipolar ion source in a compact housing designed to optimize both nanoparticle charging and transmission efficiency as a charge conditioner, the nSEMS has enabled measurement of the contributions of both neutral and ion-mediated nucleation to new particle formation.

1 Introduction

Aerosol particles can either be emitted into the atmosphere directly from primary sources or generated through the nucleation of atmospheric condensable precursor vapors. Atmospheric nucleation, or new particle formation (NPF), is frequently observed across the globe under diverse environmental conditions, ranging from populated urban centers (Dunn et al., 2004; Wang et al., 2017; Yao et al., 2018; Wang et al., 2020) to remote areas such as forests or oceans (O'Dowd et al., 2002; Bonn and Moortgat, 2003; Paasonen et al., 2010; Dall'Osto et al., 2017), as well as in the free troposphere (Kulmala et al., 2004; Kerminen et al., 2018; Lee et al., 2019). Large-scale simulations and parameterizations suggest that NPF may generate half of the global cloud condensation nuclei (CCN; Merikanto et al., 2009; Gordon et al., 2017). In addition to their climate impact, ultrafine particles formed by nucleation can also have disproportionate adverse effects on human health (Brown et al., 2000).

To understand the formation and subsequent growth of freshly nucleated particles in the atmosphere and to evalu-

ate their impact on climate and human health requires measurement techniques that can enable particle size distribution measurements in the low nanometer regime. Nanoparticle sizing is often achieved using electrical mobility to separate charged particles according to the velocities with which they migrate in an electric field. The differential mobility analyzer (DMA) has long been the most widely used instrument to measure the size distribution of submicrometer ($< 1\,\mu m$) aerosol particles (Knutson and Whitby, 1975; Flagan, 1998). Most DMAs separate charged aerosol particles of different electrical mobilities by applying an electric field between two coaxial cylindrical electrodes that are parallel to a particle-free sheath flow. Classified particles from the DMAs are typically counted by a condensation particle counter (CPC) that uses supersaturated vapors to grow particle seeds before detection (Quant et al., 1992). This integrated instrument initially used stepwise variation in the voltage. By keeping the voltage applied between the electrodes constant at each step, particles are transmitted throughout the entire system under a steady field profile before they are counted by the CPC. This static-mode measurement system is referred to as the differential mobility particle sizer (DMPS) (Fissan et al., 1983). However, since the DMPS requires the system to reach a steady state before a reliable measurement can be made, the relatively long residence time of the particles in the DMA makes it less ideal in capturing transient aerosol activities. By continuously changing the voltage through an exponential ramp, the scanning electrical mobility spectrometer (SEMS; also known as the scanning mobility particle sizer, SMPS) considerably accelerates the particle classification using electrical mobility (Wang and Flagan, 1990).

While the traditional DMPS, SMPS, and SEMS systems can only detect particles with mobility-equivalent diameters above 10 nm, many efforts have focused on extending the classification range to smaller aerosol particles. The first major step in this direction was the Vienna short-column DMA that measured nanoparticles down to 3.5 nm (Winklmayr et al., 1991); the "nano-DMA", modified from the traditional long-column DMA design, can measure particle size distribution in the range of 3–50 nm (Chen et al., 1998). A radial DMA (RDMA) that classifies particles in a radial flow toward the center of parallel disk electrodes also demonstrated a high detection efficiency for particles between 3 and 10 nm (Zhang et al., 1995). Both designs have been extended to smaller sizes. Through meticulous aerodynamic design and very large sheath flow rates of up to $1000\,L\,min^{-1}$, Rosell-Llompart et al. (1996) refined the Vienna DMA into one instrument suitable for particle classification down to as small as 1 nm. Brunelli et al. (2009) developed an RDMA that could also classify 1 nm particles at much more modest flow rates, albeit at lower resolution. An alternate mobility analyzer design, the opposed-migration aerosol classifier (OMAC), uses a particle-free cross-flow instead of the parallel sheath flow in the DMAs to balance particle electrical migration. Since the aerosol being classified fills the space between the electrodes rather than occupying only a narrow slice of that space as in a DMA, this changes the scaling for where diffusion begins to degrade the resolution of the classifier, thereby enabling classification at lower voltages or operation at higher resolution than is possible with conventional DMAs (Flagan, 2004; Downard et al., 2011). A radial-flow form of this instrument, the radial opposed-migration ion and aerosol classifier (ROMIAC), has proven capable of measuring particles or ions approaching 1 nm in size and even separating peptide stereoisomers owing to its high resolving power when operated in voltage-stepping mode like a DMPS (Mui et al., 2013, 2017). The challenges with measuring particles in the low nanometer regime lie not only in classification, but also in particle detection. Some single-stage CPCs have been operated at sufficiently high supersaturation to activate particles as small as 1 nm in diameter, but in the experiment for which this instrument has been developed, wherein measurements must be made in a high-radiation environment, this can lead to ion-induced nucleation within the CPC. Therefore, we took a more conservative approach that has proven robust and effective for sub-10 nm particle detection, namely a two-stage CPC, in which the first stage employs a high-surface-tension, relatively low-vapor-pressure working fluid, typically diethylene glycol (DEG) in order to activate small particles with minimal risk of homogeneous nucleation (Iida et al., 2009; Jiang et al., 2011a), which was integrated with a DMA to produce the first SMPS system to measure size distributions approaching 1 nm (Jiang et al., 2011a) that agree closely with mass spectrometric data in the overlap region between the two methods (Jiang et al., 2011b). Owing to the low vapor pressure, the first stage does not grow particles to optically detectable size, so a second "booster" stage is used to grow the activated clusters and optically detect them. The second stage is typically a conventional CPC. The operation of two activation and growth systems in series compounds another challenge to SEMS and SMPS measurements; the residence time within the CPC can distribute counts of particles that exit the DMA over many time bins (Russell et al., 1995; Collins et al., 2002), thereby degrading the resolution of the instrument. This effect becomes increasingly important at scan rates that are fast relative to the response time of the CPC. Therefore, CPCs with a narrow distribution of residence times are preferred, particularly for one SEMS that targets the low nanometer range, in which the resolution is also compromised by Brownian diffusion.

In this work we show the development of a nano-scanning electrical mobility spectrometer (nSEMS) that features a fast-scanning OMAC and a two-stage CPC to acquire fast and accurate particle size distributions in the range of 1.5–25 nm. Here we describe the design and characterization of the scanning OMAC in detail as that is the unique component of the instrument which enables a sizing range that is not possible with a constant-flow DMA. A radial-flow version of the OMAC that is capable of classifying charged particles or ions as small as 1 nm in diameter (Mui et al., 2013, 2017)

is used in this instrument. The two-stage CPC includes a fast-mixing activation stage using DEG as a working fluid, followed by an eco-friendly, fast-response, water-based CPC (Hering et al., 2019). Other CPCs, either two-stage ones like the one we have employed or single-stage CPCs that are capable of counting particles as small as 1 nm, could be integrated into the nSEMS, so we limit our discussion of the two-stage CPC to its essential features, its integration into the nSEMS, and the resulting performance. The nSEMS analyzes a charged aerosol, which can be naturally charged or one that is processed through a charge conditioner (CC). The present paper focuses on nanoparticle sizing and detection downstream of the CC.

The integrated transfer function of the nSEMS system was derived based on both experimental results and finite-element modeling using COMSOL Multiphysics™. The nSEMS has been intensively used in the Cosmics Leaving OUtdoor Droplets (CLOUD) experiments at CERN, in which its size resolution and fast response have made it possible to follow very rapid growth of freshly nucleated nanoparticles and to identify a new mechanism for new particle formation in a highly polluted atmosphere (Wang et al., 2020). A comparison of nSEMS data with measurements from other well-calibrated particle sizing instruments at CLOUD confirms its capacity to provide reliable size distribution in the low nanometer size regime.

2 The nSEMS design and system features

The nSEMS was designed to capture critical aerosol dynamics during atmospheric nucleation and subsequent nanoparticle growth in both environmental chamber experiments and in ambient measurements. To this end, its design and operating parameters have been optimized to provide size distribution measurements with relatively high size resolution in the sub-25 nm range and with a fairly short duty cycle. The nSEMS classifies particles of different sizes according to their electrical mobilities, Z_p, which is defined as the ratio of particle migration velocity, v_m, to the electric field strength within the classifier, E:

$$Z_p = \frac{v_m}{E} = \frac{\phi e C_c}{3\pi\mu d_p}, \quad (1)$$

where ϕ is the net number of elementary charges, e, on the particle, C_c is the Cunningham slip correction factor that accounts for the noncontinuum effects, μ is the dynamic viscosity of air, and d_p is the particle diameter. Figure 1 shows a schematic of nSEMS main components. The aerosol enters the nSEMS after passing through a soft x-ray CC at a relatively high flow rate of 4.6 L min^{-1}. A smaller, 1.2 L min^{-1} polydisperse aerosol sample flow from the core of the larger flow is introduced into a ROMIAC, while the remainder is exhausted. The high flow rate through the CC and the core sampling flow spitter are designed to minimize losses of the highly diffusive nanoparticles. While the ROMIAC was originally designed to operate at constant voltage, the voltage is continuously varied in an exponential ramp in the nSEMS. Particles transmitted through the ROMIAC are counted using a two-stage CPC to capture the particle size distribution. Detailed operating parameters and default settings are summarized in Table 1.

Table 1. Default nSEMS operating parameters optimized for measurements of NPF events and nanoparticle growth. These settings enable particle size distribution measurements in the range of 1.5–25 nm, with a duty cycle of 1 min and a size classification resolution of $\mathcal{R}_{nom,nd} = 10$.

Parameter	Notation	Value
Instrument total sampling rate (L min^{-1})	Q_s	4.60[a]
ROMIAC polydisperse flow rate (L min^{-1})	Q_a	1.20
ROMIAC monodisperse flow rate (L min^{-1})	Q_c	1.20
ROMIAC incoming cross-flow flow rate (L min^{-1})	$Q_{x,in}$	12.0
ROMIAC outgoing cross-flow flow rate (L min^{-1})	$Q_{x,out}$	12.0
DEG feeding rate (L min^{-1})	Q_{DEG}	0.30
CPC sampling rate (L min^{-1})	Q_{CPC}	1.00[b]
Low electrode voltage (V)	V_{low}	20.0
High electrode voltage (V)	V_{high}	10 000
CPC sample conditioner temperature (°C)	T_{co}	20[c]
CPC DEG saturator temperature (°C)	T_{sat}	70
CPC sample condenser temperature (°C)	T_{cond}	10
Voltage ramp time (s)	t_{ramp}	50
Holding time at V_{low} (s)	t_{low}	4
Holding time at V_{high} (s)	t_{high}	2
Scan duty cycle (s)	t_{total}	60
CPC data recording interval (s)	t_c	0.20

[a] All flow-rate measurements have an uncertainty of ±2 %.
[b] The MAGIC™ water-based CPC is a special, high-flow-rate, concise CPC.
[c] All temperature measurements have an uncertainty of ±0.1 °C.

The CC used in this study employs a soft x-ray source to produce ion pairs from the gas molecules in order to bring the aerosol to a steady-state Fuchs charge distribution that enables estimation of the size distribution whose initial charge state is uncertain. The soft x-ray source has two advantages: (i) fewer regulatory hurdles than radio-isotope sources used for the same purpose and (ii) the ability to turn off the ion source in order to measure those particles in the sample that carry charge due to gas ionization by galactic or simulated cosmic rays. It was designed to minimize losses of the smallest particles. Preliminary characterization of the CC and data from numerous experiments, in which it has been applied to conventional DMAs in parallel with other DMAs using conventional CCs and to the nano-radial differential mobility analyzer (Brunelli et al., 2009), yield results consistent with the Wiedensohler (1988) approximation of the Fuchs charge distribution, with no apparent biases. Since mobility classified and therefore charged particles are used to determine the integrated instrument transfer function that is reported here, the key results from this paper are not affected by any minor deviations from the Fuchs charge distribution that is assumed in inverting data from the nSEMS. Details of the design and

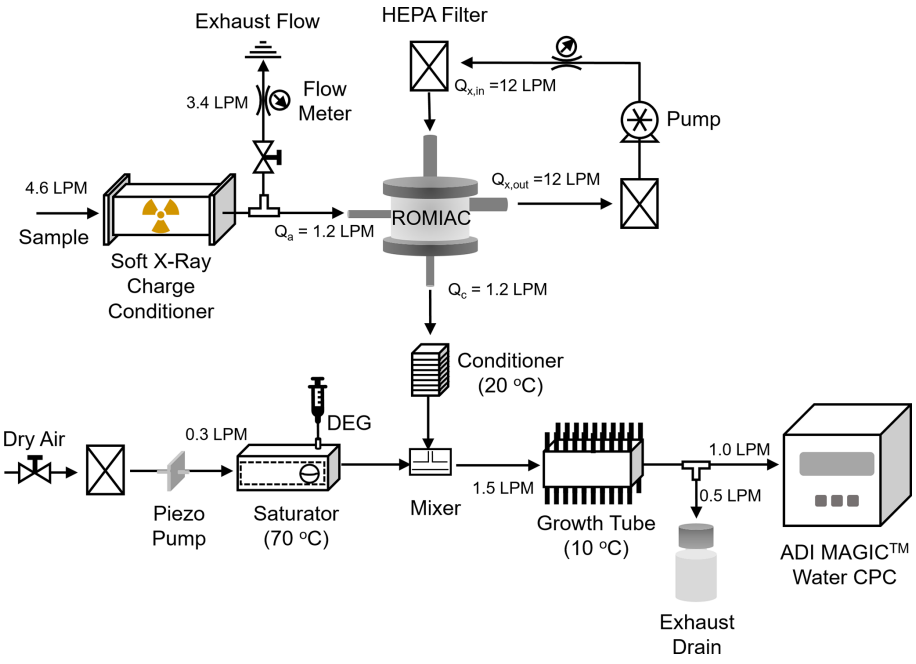

Figure 1. Schematic of the nSEMS main components: a radial opposed-migration ion and aerosol classifier (ROMIAC) and a two-stage condensation particle counter (CPC). The aerosol enters the nSEMS after passing through a soft x-ray CC at a high flow rate (4.6 L min^{-1}). Core sampling of that input sample flow is employed to minimize particle diffusional losses in the transport tubing and the CC. The ROMIAC is operated on exponentially increasing voltage ramps between 20 and 10 000 V of both positive and negative polarity at 1.2 and 12 L min^{-1} aerosol and cross-flows (Table 1). After exiting the classifier, monodisperse aerosol particles are mixed with 0.3 L min^{-1} diethylene glycol (DEG) vapor in the first stage of the CPC. This fast-mixing stage allows nanoparticles to grow through rapid vapor condensation before they enter the second "booster" CPC stage, a modified Aerosol Dynamics Inc. (ADI) MAGIC™ water CPC operated at a flow rate of 1.0 L min^{-1}, in which particles grow further and are optically detected.

quantitative calibration of the soft x-ray CC will be presented in a separate paper.

The charged nanoparticles transmitted through the aforementioned core sampling flow splitter enter the ROMIAC at a flow rate of 1.2 L min^{-1}, tangentially into a flow distribution channel, and then enter the classification region through a narrow slit. Unlike traditional DMAs, in which the particle-free sheath flow is parallel to the electrodes, the ROMIAC uses a 12 L min^{-1} recirculated, filtered cross-flow that enters and exits the classification region through screen electrodes (Flagan, 2004; Mui et al., 2013, 2017). For nondiffusive particles, the ideal resolving power of the classifier, $\mathcal{R}_{\mathrm{nom,nd}}$, is the same as that of a traditional DMA operating at the same flow-rate ratios, i.e.,

$$\mathcal{R}_{\mathrm{nom,nd}} = \frac{1}{\beta\,(1+|\delta|)}, \tag{2}$$

for all of the designs, configurations, or flow-rate ratios (Flagan, 1999, 2004). The two flow factors, the imbalance factor, δ, and the aerosol-to-cross-flow ratio, β, are defined as

$$\delta = \frac{Q_\mathrm{c} - Q_\mathrm{a}}{Q_\mathrm{a} + Q_\mathrm{c}}, \quad \beta = \frac{Q_\mathrm{a} + Q_\mathrm{c}}{Q_{x,\mathrm{in}} + Q_{x,\mathrm{out}}}, \tag{3}$$

where Q_a is the incoming polydisperse aerosol flow rate, Q_c is that of the outgoing classified sample flow, and $Q_{x,\mathrm{in}}$ and $Q_{x,\mathrm{out}}$ are the entering and exiting cross-flow rates. If the incoming flows are balanced with the outgoing flows ($Q_\mathrm{a} = Q_\mathrm{c}$; $Q_{x,\mathrm{in}} = Q_{x,\mathrm{out}}$), then the two factors can be simplified to $\delta = 0$ and $\beta = \mathcal{R}^{-1}_{\mathrm{nom,nd}}$. A resolution of $\mathcal{R}_{\mathrm{nom,nd}} = 10$ is generally sufficient to capture the critical cluster-to-ion formation process under ambient conditions. In order to get a reasonable size coverage to study the subsequent condensational or coagulational growth of newly formed nanoparticles, voltage is exponentially ramped between 20 and 10 000 V with a characteristic time,

$$\tau_\mathrm{s} = \frac{t_\mathrm{ramp}}{\ln\left(V_\mathrm{high}/V_\mathrm{low}\right)}, \tag{4}$$

of approximately 8 s. The mean residence time of the sample flow in the classifier, τ_f, is

$$\tau_\mathrm{f} = \frac{\mathcal{V}_\mathrm{class}}{Q_\mathrm{class}}, \tag{5}$$

with $\mathcal{V}_\mathrm{class}$ and $Q_\mathrm{class} = (Q_\mathrm{a} + Q_\mathrm{c})/2$ corresponding to the volume and aerosol flow rates in the classification region. For the ROMIAC, $\mathcal{V}_\mathrm{class} = \pi(R_2^2 - R_1^2)b$, where $R_1 = 0.24$ cm and $R_2 = 1.61$ cm are the inner and outer electrode radii, and $b = 1$ cm is the gap between the high-voltage and ground electrodes, resulting in a classification volume

$\mathcal{V}_{\text{class}} \simeq 8.0\,\text{cm}^3$. The resulting mean gas residence time at the nominal aerosol flow rate is $\tau_f \simeq 0.4\,\text{s}$. The mobility of the particles that are transmitted through an ideal, constant-voltage ROMIAC is

$$Z^*_{\text{p,ideal}} = \frac{\left(Q_{x,\text{in}} + Q_{x,\text{out}}\right) b}{2\pi \left(R_2^2 - R_1^2\right) V^*}, \tag{6}$$

where $Z^*_{\text{p,ideal}}$ can be treated as the centroid particle electrical mobility in scanning mode, assuming highly idealized flow and electric fields, and corresponds to the peak of the transfer functions (Zhang et al., 1995; Mui et al., 2017). V^* is the corresponding voltage applied to the central electrode when particles are detected by the CPC.

Most mobility-based particle sizing systems measure only one polarity of charged particles (usually positive) by employing a single-polarity high-voltage supply, but bipolar CCs such as the soft x-ray source used in this study produce ion pairs to bring the aerosol to a steady-state, "neutralized" state that contains both negatively and positively charged particles as they collide with ions of both polarities. Because ion properties, such as mass, mobility, and concentration, as well as experimental conditions, can all affect particle charging efficiency, and the ions produced by the soft x-rays can vary due to trace species in the gas, measuring only particles with single polarity may lead to uncertainties and variabilities in computing particle concentrations (Steiner et al., 2014; Chen et al., 2018; Kangasluoma et al., 2013). To optimize instrument performance and avoid potential variability in particle charging, the ROMIAC operates on a custom-built dual high-voltage supply with fast polarity-switching capability. In the default operating mode of the nSEMS, the polarity of the scanning voltage is switched at the start of every scan, but the polarity can also be fixed as either positive or negative, or it can be turned off to meet different scientific needs, i.e., to sample particles formed by ion-mediated nucleation. This feature not only helps to better understand the performance of bipolar diffusion charging, but it also enables measurement of the charge state of the sampled aerosol particles by deactivating the CC for some or all scans. This becomes an important feature when studying atmospheric nucleation as it enables discrimination between neutral and ion-mediated nucleation (Kirkby et al., 2016; Wagner et al., 2017).

Classified particles transmitted through the ROMIAC are subsequently detected by a two-stage CPC that enables particle counting approaching 1 nm in size (Iida et al., 2009; Jiang et al., 2011a). The first stage employs a fast-mixing condensational activation and growth reactor (Wang et al., 2002) that uses DEG as the working fluid to activate the nanoparticles. This activation stage is based upon the particle size magnifier (PSM) (Kousaka et al., 1982; Okuyama et al., 1984; Gamero-Castano and de la Mora, 2000; Sgro and de la Mora, 2004) in which a cool aerosol sample flow undergoes rapid turbulent mixing with a warm flow that is saturated with vapor to produce the supersaturated state that will activate and grow particles larger than a critical size. The detailed design incorporates modifications reported by Shah and Cocker (2005) that reduce the size of the mixing volume while maintaining the small growth tube, with a residence time of $\sim 10\,\text{ms}$. In the first stage used in this study, supersaturation is produced by turbulent mixing of a $0.3\,\text{L}\,\text{min}^{-1}$ flow of hot (e.g., 70 °C) DEG vapor with a $1.2\,\text{L}\,\text{min}^{-1}$ cold (20 °C) particle-laden flow. The downstream growth tube is cooled to 10 °C to accelerate particle growth and remove excess vapor. In contrast to the Airmodus particle size magnifier (PSM) and the CPC of Sgro and de la Mora (2004), on which the PSM is based, the mixing time in the activation stage of the present CPC has been minimized ($\sim 0.12\,\text{s}$) to speed up instrument response compared with $\sim 0.7\,\text{s}$. The design and initial experiments were performed with a TSI model 8210 CPC operating at a flow rate of $1.5\,\text{L}\,\text{min}^{-1}$ as the second detection stage. Owing to the slow response of that CPC, it was replaced with a modified, water-based ADI MAGIC™ CPC that serves as the second stage to grow particles sufficiently large for optical detection (Hering et al., 2019). Particle counts are recorded over the nSEMS size distribution scan at 5 Hz. The sample flow rate of the CPC is $1.00\,\text{L}\,\text{min}^{-1}$. Between the activation and booster stages, the flow is split between the water CPC and a smaller ($0.5\,\text{L}\,\text{min}^{-1}$) excess flow to minimize deposition of excessive DEG vapor in the intervening plumbing and to match the flow to the water CPC.

While this CPC can detect particles as small as 1 nm in diameter and the ROMIAC can classify particles of that small size (Mui et al., 2013, 2017), Kangasluoma et al. (2013) observed larger numbers of apparent particles smaller than 1.5 nm in diameter than were present in the calibration aerosol that they generated and attributed the excess particle counts to the activation of gas ions within the CPC. Lacking a definitive method for discriminating between gas ions and particles in the sub-1.5 nm size range, we do not report size distributions below 1.5 nm.

Data acquisition and instrument control for the nSEMS are accomplished with a National Instruments™ sbRIO-9637 CompactRIO single-board controller coupled with a field-programmable gate array (FPGA) module. The FPGA module, which is programmable using LabVIEW 2018, is capable of operating at clock speeds up to 40 MHz with optimized hardware and memory settings. The FPGA is controlled by a microprocessor that runs on a real-time Linux operating system (OS), greatly reducing the overhead and response lag associated with typical LabVIEW applications running on other platforms. The real-time OS and FPGA enable independent time loops for precise control of the voltage exponential ramp and recording of CPC concentrations. The board controller is connected to a Windows PC via Ethernet, enabling communication among different programs, visualization of real-time data, and online monitoring of critical parameters without compromising instrument timing.

3 Characterization of the nSEMS

Compared to the DMPS, the SEMS accelerates mobility-based size distribution measurements by classifying particles in a time-varying electric field and eliminating the transition time between measurement channels. Although the exponential voltage ramping allows investigation of rapidly evolving aerosol particles, it alters the particle trajectories in the classifier such that the transfer function may differ significantly from that expected for a DMPS. Numerical simulations of particle trajectories in a scanning cylindrical DMA have shown that the width of instrument transfer function for fast scans can be significantly greater than that for a static (constant-voltage) DMA (Collins et al., 2004; Mai and Flagan, 2018; Mai et al., 2018). Similarly, voltage scanning of the ROMIAC may distort the transfer functions from those seen in static-mode operation.

3.1 Finite-element modeling of particle transmission

Both numerical simulations and derivations of analytical solutions for idealized instruments have proven to be powerful tools in the study of the transfer functions of DMAs operating in scanning mode (Collins et al., 2004; Dubey and Dhaniyala, 2011). However, the ROMIAC geometry and particle trajectories are more complicated than those in long-column cylindrical DMAs. In order to fully understand the flows, electric field, and particle trajectories inside a scanning ROMIAC, particle transmission has been examined with finite-element simulations using COMSOL Multiphysics® (version 5.3).

We have solved Navier–Stokes and Maxwell equations for the flow and electric fields, respectively, using the "Laminar" and "Electrostatic" modules in COMSOL Multiphysics®. The time-varying electric field, $E(x, y, z, t)$, can be treated as quasi-steady-state:

$$E(x, y, z, t) = E_0(x, y, z) f(t), \tag{7}$$

where $E_0(x, y, z)$ is the electric field in the beginning of the voltage ramp at $V(t = 0) = V_{\text{low}}$, and $f(t)$ is the time variation factor depending on the characteristic ramping time τ_s defined in Eq. (4).

$$f(t) = \begin{cases} 1, & 0 \le t < t_{\text{low}} \\ e^{\frac{t - t_{\text{low}}}{\tau_s}}, & t_{\text{low}} \le t < t_{\text{low}} + t_{\text{ramp}} \\ \frac{V_{\text{high}}}{V_{\text{low}}}, & t_{\text{low}} + t_{\text{ramp}} \le t < t_{\text{low}} + t_{\text{ramp}} + t_{\text{high}} \end{cases} \tag{8}$$

Because the particles classified in the ROMIAC are sufficiently small that inertial effects can be neglected, particle motion is numerically simulated using the "Particle trajectories" module in COMSOL, with only the drag, electrostatic forces, and Brownian motion being considered, as the particles are assumed to be massless. The scanning ROMIAC transfer function for monodisperse particles can be written as

$$\Omega_{\text{ROMIAC}}\left(Z_p, \beta, \delta, t\right) = \frac{N_c(t)}{N_a}, \tag{9}$$

where N_a and N_c are the number of particles going in and coming out of the ROMIAC during the simulation. In order to determine the scanning ROMIAC transfer function with adequate time resolution, 200 particles are injected into the ROMIAC every 2.5 ms; simulations were performed for the default flows and voltage ramp settings listed in Table 1. The times at which particles enter and exit the scanning ROMIAC were recorded. Figure 2 shows an example of the finite-element solutions of the flow and electric fields for $d_p = 4$ nm particles. The modeled instrument response for particles with 13 different mobility diameters across the sizing range of the instrument is shown with solid lines in Fig. 3. The peak transmission ratio for particles larger than about 5 nm remains flat at approximately 60 % and progressively drops at smaller sizes. Simulation was also performed for different ramp times in order to compare the transfer function distortions that may result from fast voltage scanning (Fig. S1 in the Supplement).

3.2 Laboratory characterization of the ROMIAC

Although particle trajectory simulations using COMSOL Multiphysics® have proven very effective at retrieving particle transfer functions, they cannot fully capture the nonideal, three-dimensional behavior of particles inside the classifier due to the high computation cost (Mai and Flagan, 2018; Amanatidis et al., 2020). As a result, experimental calibrations are needed to closely examine the scanning ROMIAC performance. Figure 4 shows the tandem differential mobility analyzer (TDMA; Rader and McMurry, 1986) calibration setup used; aerosols of a known size are selected with a classifier (a constant-voltage ROMIAC or DMA for small, 1–20 nm, or large, 12–26.5 nm, respectively) before entering the nSEMS. Depending on the target size range, source particles were generated from electrosprayed tetra-alkyl ammonium solutions (Ude and de la Mora, 2005), a heated Nichrome hot-wire source (Peineke et al., 2006), or atomized sodium chloride solution. The polydisperse aerosols generated from the hot wire or the atomizer were size-selected by a ROMIAC or a cylindrical DMA operating at constant voltage to provide a narrow-mobility-distribution sample for nSEMS calibration. In order for the size-selected source particles to approximate a monodisperse aerosol, both the cylindrical DMA and the classifying ROMIAC were run at higher resolution than the nSEMS standard operating condition ($\mathcal{R}_{\text{nd}} \ge 10$ for both the classifying DMA and ROMIAC) using open-loop controlled sheath flow or cross-flow, respectively.

Due to perturbations of the electric field and imperfections in the instrument fabrication, particle transmission in any mobility analyzer can deviate from the designed performance. When the ROMIAC of the nSEMS is operated in static mode, correction factors can be determined empirically to account for any deviations from theoretical or numerical performance. In terms of particle sizing, an empirical mo-

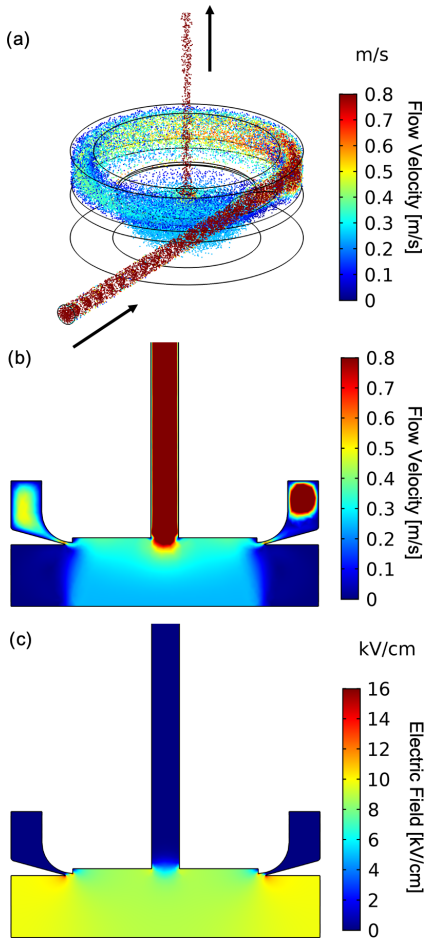

Figure 2. Example of finite-element simulations of the scanning ROMIAC at an aerosol flow rate of $Q_a = 1.2\,\mathrm{L\,min^{-1}}$ and a cross-flow rate of $Q_c = 12\,\mathrm{L\,min^{-1}}$, with particle diameter of $d_p = 4.0\,\mathrm{nm}$. **(a)** Particle trajectories over a 50 s upscan at $t \approx 25\,\mathrm{s}$. Cross-sectional view of **(b)** the flow velocity and **(c)** electric field distribution. The magnitude of the electric field corresponds to the maximum, 10 kV, electric potential. Particles enter the ROMIAC from the entrance slit that is tangential to the classification region and leave the ROMIAC from the slit perpendicular to the classification region.

bility correction factor, f_z, is calculated by comparing the experimental transfer function with the expected $Z^*_{p,ideal}$, as defined in Eq. (6), using the TDMA calibration setup (Mui et al., 2017). This correction factor, $f_z = Z^*_p/Z^*_{p,ideal}$, is estimated to be 1.03 for the ROMIAC classifier used in the nSEMS system.

3.3 Characterization of the two-stage CPC

In addition to the ROMIAC, nonideal performance of the two-stage CPC may also affect the nSEMS data acquisition and interpretation. Figure 5 shows the experimental setup that was used to measure the size-dependent detection efficiency of the two-stage CPC. The classifying ROMIAC was operated in static mode with a resolving power of $\mathcal{R}_{nd} = 14$. The hot-wire particle generator was set at similar conditions as shown in Fig. 4. Given that the hot-wire generator produces singly charged particles (Peineke et al., 2006), an aerosol electrometer was placed between the ROMIAC and the two-stage CPC to measure the total particle number concentrations coming out of the classifier. The plumbing upstream of the CPC was kept the same as on the integrated nSEMS system so that the resulting plumbing delays would be taken into account in this calibration. The CPC counting efficiency relative to that of the aerosol electrometer is shown in Fig. 6. The 50 % cutoff size is about 1.6 nm, and the counting efficiency reaches a plateau when particle-mobility-equivalent diameter is larger than about 2.1 nm ($d_p \geq 2.1\,\mathrm{nm}$). The empirically determined two-stage CPC counting efficiency was fitted with a logistic function:

$$\eta_{cpc} = \frac{\eta_{max}}{1 + e^{-k(d_p - d_{p,0})}}, \tag{10}$$

where $\eta_{max} = 1.01$, $k = 6.30\,\mathrm{nm^{-1}}$, and $d_{p,0} = 1.54\,\mathrm{nm}$ based on the calibration results.

In addition to detection efficiency, the delay in CPC response also complicates the transfer function of the system. When the classifier is operated at scanning mode, the slow response of the CPC may introduce a smearing effect and broaden the particle transfer functions. To account for this effect, the response of the two-stage CPC can be modeled as a plug flow reactor (PFR) in series with a continuous stirred-tank reactor (CSTR) to estimate its particle residence time distribution, $E_{cp}(t)$ (Russell et al., 1995; Collins et al., 2002; Mai et al., 2018):

$$\begin{aligned} E_{cp}(t) &= E_p(t) \star E_c(t) \\ &= \int_{-\infty}^{\infty} E_c(t') E_p(t - t') \mathrm{d}t' \\ &= \begin{cases} 0, & t < \tau_p \\ \frac{1}{\tau_c} e^{-\frac{t-\tau_p}{\tau_c}}, & t \geq \tau_p, \end{cases} \end{aligned} \tag{11}$$

where τ_p and τ_c are the mean residence time of the PFR and the CSTR, respectively, and $\star$ is the symbol for the convolution of two functions (Bracewell and Bracewell, 1986). The transfer function of the integrated nSEMS system, $\Omega_{nSEMS}(Z_p, \beta, \delta, t)$, can be written as

$$\Omega_{nSEMS}\left(Z_p, \beta, \delta, t\right) = \Omega_{ROMIAC}\left(Z_p, \beta, \delta, t\right) \star E_{cp}(t). \tag{12}$$

To explore the extent of this effect, the nSEMS was run with different voltage ramp times (10–1400 s, corresponding to a τ_s/τ_f value of 4–5600). At long voltage ramp times, e.g., at 1400 s, the nSEMS can be treated as operating in a quasi-static mode, wherein the CPC response time has no impact on the transfer functions. Figure 7 shows the experimentally determined particle transfer functions of the nSEMS

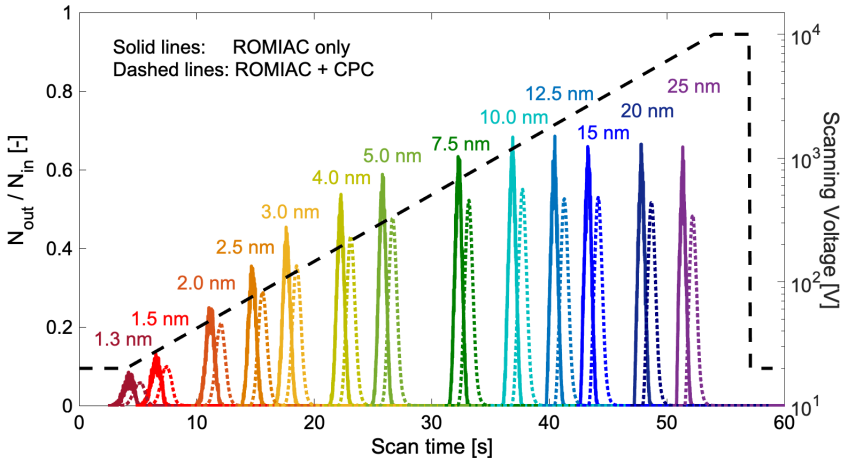

Figure 3. Simulated transfer function of the scanning ROMIAC with monodisperse input particles in the 1.3–25 nm size range. The transfer function is calculated as the ratio of the particle number at the exit and the entrance of ROMIAC over a voltage scan (dashed black line) with $t_{\mathrm{ramp}} = 50$ s. Solid lines show the transfer function of the classifier (scanning ROMIAC) only; dashed lines show the simulated ROMIAC transfer function coupled with the CPC residence time distribution (see Eq. 12). The integrated transfer function peaks (dashed lines) are used to compute the inversion kernel for nSEMS data inversion.

at different t_{ramp} for $d_{\mathrm{p}} = 18$ nm particles. The results indicate that the smearing effect is small when t_{ramp} is longer than 30 s ($\tau_{\mathrm{s}} \geq 4.83$ s). The residence time distribution is computed by deconvoluting the quasi-static nSEMS transfer function measured with $t_{\mathrm{ramp}} = 1400$ s from that measured with $t_{\mathrm{ramp}} = 50$ s. The resulting characteristic times for the CPC residence time distribution were $\tau_{\mathrm{c}} = 0.20$ s and $\tau_{\mathrm{p}} = 0.70$ s (Fig. S2). The dashed lines in Fig. 3 show the convoluted nSEMS transfer function, $\Omega_{\mathrm{nSEMS}}(Z_{\mathrm{p}}, \beta, \delta, t)$, combining the CPC residence time distribution in addition to the scanning ROMIAC simulation.

3.4 Derivation of the integrated instrument transfer function and data inversion

Data inversion is required to retrieve the particle size distribution of the source particles, $n(\log d_{\mathrm{p}})$, from the particle counts measured by the CPC, $\mathbf{R}_{\mathrm{nSEMS}}$, which can be represented in matrix form as

$$\mathbf{R}_{\mathrm{nSEMS}} = \mathbf{A}_{\mathrm{nSEMS}} \boldsymbol{N}, \tag{13}$$

where $\mathbf{A}_{\mathrm{nSEMS}}$ is often referred to as the inversion kernel for the instrument, and $\boldsymbol{N}$ is the vector of weights for the discretized representation of the particle size distribution, for which we use linear splines on $x = \log(d_{\mathrm{p}})$ (Mai et al., 2018). The time series instrument response can be written as $\mathbf{R}_{\mathrm{nSEMS}} = [R_{\mathrm{nSEMS},1}, R_{\mathrm{nSEMS},2}, \cdots, R_{\mathrm{nSEMS},I}]^{\mathrm{T}}$. With the default nSEMS voltage ramp time, $t_{\mathrm{ramp}} = 50$ s, and the CPC data recording frequency, $t_{\mathrm{c}} = 0.2$ s, the vector length for one complete scan is $I = 250$. The particle number counts recorded by the CPC in the ith time bin, $R_{\mathrm{nSEMS},i}$, can be represented as the integral of the total number of particles transmitted over the time interval $(i-1)t_{\mathrm{c}} \leq t < it_{\mathrm{c}}$.

$$\begin{aligned} R_{\mathrm{nSEMS},i} &= Q_{\mathrm{a}} \int_{(i-1)t_{\mathrm{c}}}^{it_{\mathrm{c}}} \int_{-\infty}^{\infty} n(x) \sum_{\phi} p_{\mathrm{charge}}(x,\phi) \\ &\quad \times \eta_{\mathrm{CPC}}(x,\phi) \Omega_{\mathrm{nSEMS}}(Z_{\mathrm{p}}(x,\phi), \beta, \delta, t)\, \mathrm{d}x\, \mathrm{d}t \\ &= Q_{\mathrm{a}} \int_{(i-1)t_{\mathrm{c}}}^{it_{\mathrm{c}}} \sum_{j} \int_{x_{j-1}}^{x_j} n(x) \sum_{\phi} p_{\mathrm{charge}}(x,\phi) \\ &\quad \times \eta_{\mathrm{CPC}}(x,\phi) \Omega_{\mathrm{nSEMS}}(Z_{\mathrm{p}}(x,\phi), \beta, \delta, t)\, \mathrm{d}x\, \mathrm{d}t \end{aligned} \tag{14}$$

The particle charging probability from the soft x-ray CC, $p_{\mathrm{charge}}(x,\phi)$, was assumed to be that of the Wiedensohler (1988) approximation and is computed separately for scans of negative and positive polarity. In order to obtain the instrument transfer function, $\Omega_{\mathrm{nSEMS}}(Z_{\mathrm{p}}(x,\phi), \beta, \delta, t)$, for each time bin, the simulated ROMIAC transfer functions were first fitted as a Gaussian function.

$$\Omega_{\mathrm{ROMIAC}}\left(Z_{\mathrm{p}}(x,\phi), \beta, \delta, t\right) = a \exp\left(-\frac{(t-b)^2}{2c^2}\right) \tag{15}$$

The three fitting parameters, a, b, and c, were then interpolated over the entire time vector with 250 bins. By substituting the interpolated parameters back into Eq. (15), a ROMIAC transfer function, $\Omega_{\mathrm{ROMIAC}}(Z_{\mathrm{p}}(x,\phi), \beta, \delta, t)$, was generated for each time bin. The fitted transfer functions were adjusted by the empirically determined mobility correction factor, f_z. The nSEMS transfer function for each time bin, $\Omega_{\mathrm{nSEMS}}(Z_{\mathrm{p}}(x,\phi), \beta, \delta, t)$, was then computed by the convolution of the ROMIAC transfer function and the CPC residence time distribution of Eq. (12). The inversion

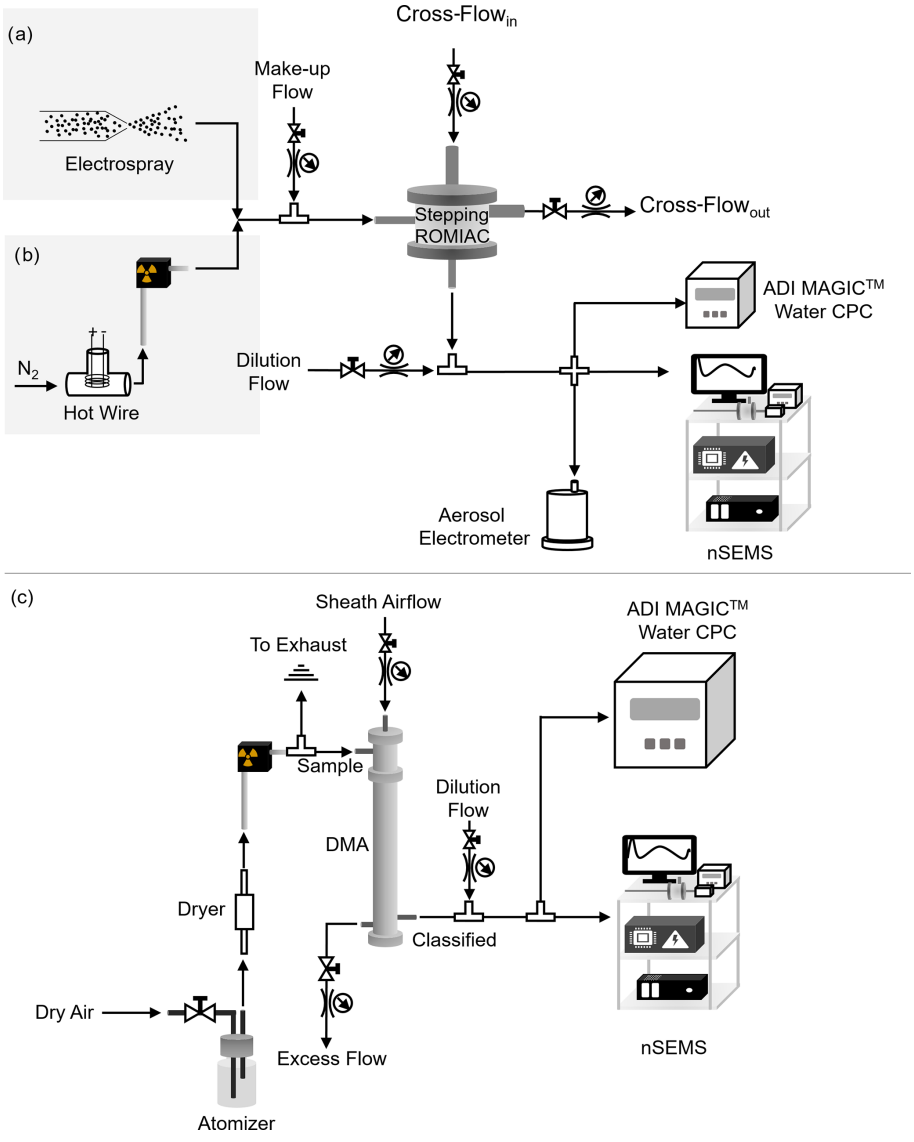

Figure 4. The experimental setup used for the nSEMS calibration and characterization in different particle size ranges. **(a)** < 3 nm size range: tetra-alkyl ammonium ions produced by an electrospray were classified using static ROMIAC as a classifier ($\mathcal{R}_{\mathrm{nom,nd}} \approx 10$) and an aerosol electrometer as a reference for the upstream particle number. The electrospray was operated at 3000 V and 25 cm H_2O pressure. The tetra-alkyl ammonium solutions were prepared with 10–20 mg salt in 1.5 mL methanol. **(b)** 1.5–20 nm size range: a heated Nichrome wire was employed as a hot-wire aerosol source, with a static ROMIAC as a classifier ($\mathcal{R}_{\mathrm{nom,nd}} \approx 10$) and both an aerosol electrometer and ADI MAGIC™ water CPC as upstream particle counters. The hot wire was operated in the range of 5.0–7.0 V and 4.5–6.5 A. **(c)** 12.0–26.5 nm size range: atomized sodium chloride was employed as an aerosol source, with a cylindrical differential mobility analyzer (DMA) as a classifier ($Q_{\mathrm{a}} = 0.5\,\mathrm{L\,min^{-1}}$, $Q_{\mathrm{sh}} = 5.8\,\mathrm{L\,min^{-1}}$, $\mathcal{R}_{\mathrm{nom,nd}} \approx 12$) and an ADI MAGIC™ water CPC as an upstream particle counter. Both **(b)** and **(c)** follow a TDMA calibration setup (Rader and McMurry, 1986), which uses a classifier at a constant voltage to select particles within a narrow range of sizes.

kernel matrix for the ith time bin and jth particle size bin thus becomes

$$A_{\mathrm{nSEMS},i,j} = Q_{\mathrm{a}} t_{\mathrm{c}} \int_{\log d_{p,j-1}}^{\log d_{p,j}} n(x) \sum_{\phi} p_{\mathrm{charge}}(x,\phi) \times \eta_{\mathrm{CPC}}(x,\phi)\Omega_{\mathrm{nSEMS}}(Z_{\mathrm{p}}(x,\phi),\beta,\delta,t)\,\mathrm{d}x. \quad (16)$$

We then applied a totally nonnegative least squares (TNNLS) algorithm to retrieve the sample particle size distribution from the inversion kernel and the particle number concentrations detected by the CPC, i.e., solving for $N = \mathbf{A}_{\mathrm{nSEMS}}^{-1}\mathbf{R}_{\mathrm{nSEMS}}$ (Merritt and Zhang, 2005; Mai et al., 2018).

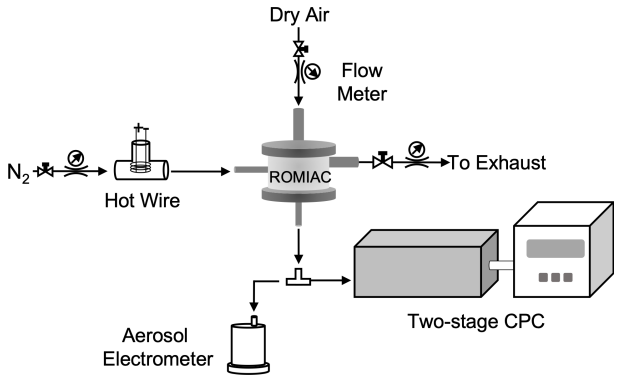

Figure 5. Experimental setup used to characterize the two-stage CPC detection efficiency. A hot-wire aerosol generator was used to provide aerosol samples. The ROMIAC was operated at static mode to provide stable, monodisperse aerosol particles for both the two-stage CPC and the aerosol electrometer. The ROMIAC aerosol and cross-flow rates were $Q_a = 2.5\,\mathrm{L\,min^{-1}}$ and $Q_x = 35.5\,\mathrm{L\,min^{-1}}$. The electrometer was pre-calibrated against a TSI 3760A butanol-based CPC and an ADI MAGIC™ water-based CPC.

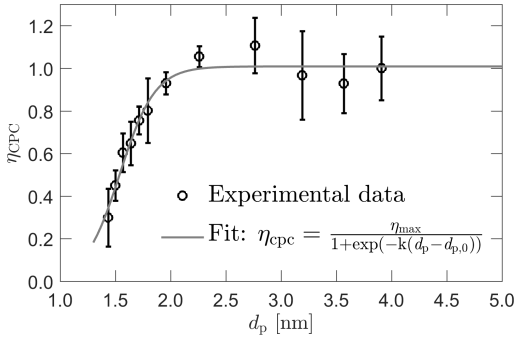

Figure 6. Detection efficiency of the two-stage CPC as a function of d_p, the mobility-equivalent particle diameter. The efficiency is corrected for the dilution due to the vapor flow. The size-dependent detection efficiency is fitted to a logistic function with fitting parameters $\eta_{max} = 1.01$, $k = 6.30\,\mathrm{nm^{-1}}$, and $d_{p,0} = 1.54\,\mathrm{nm}$. The fit is used to approximate the CPC detection efficiency, η_{cpc}, in the data inversion.

3.5 Calibration results

Figure 8 shows the nSEMS scanning response with size-selected particles of different mobility-equivalent diameters using the TDMA setup shown in Fig. 4b ($d_p \le 10.70\,\mathrm{nm}$) and Fig. 4c ($d_p \ge 12.00\,\mathrm{nm}$) with the default operating parameters listed in Table 1. The particles fed into the nSEMS using the TDMA setup were not monodisperse, which may have led to peak broadening and particle losses. In order to compare the experimental result with the simulation, we deconvoluted the CPC residence time distribution and the static classifier transfer function from the instrument response as

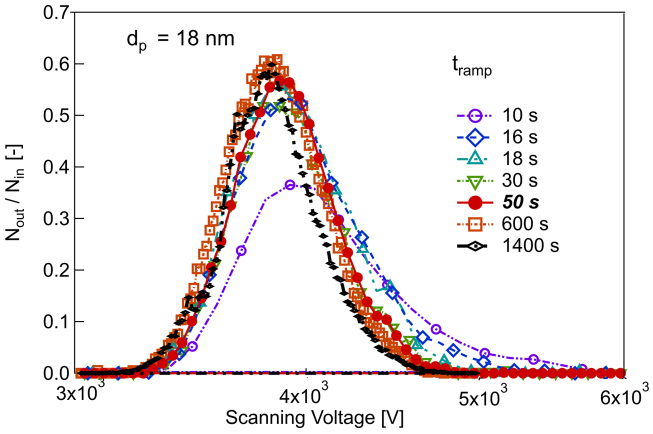

Figure 7. Effect of voltage ramp time, t_{ramp}, on the nSEMS scanning transfer function with $d_p = 18\,\mathrm{nm}$ input particles. The nSEMS voltage is increased exponentially from 20 V to 10 kV over ramp times within 10–1400 s, including the default $t_{ramp} = 50\,\mathrm{s}$. CPC smearing of the transfer function increases with decreasing t_{ramp} and becomes very pronounced at $t_{ramp} < 20\,\mathrm{s}$.

shown in Fig. 8 (Stolzenburg and McMurry, 2008):

$$\Omega_{\mathrm{ROMIAC}}\left(\tilde{Z}_p, \beta, \delta, t\right) = \begin{cases} \frac{R_{\mathrm{nSEMS},i}}{E_{cp}\Omega_{\mathrm{ROMIAC}}\left(\tilde{Z}_p,\beta,\delta,\sigma\right)}, & d_p < 12\,\mathrm{nm} \\ \frac{R_{\mathrm{nSEMS},i}}{E_{cp}\Omega_{\mathrm{DMA}}\left(\tilde{Z}_p,\beta,\delta,\sigma\right)}, & d_p \ge 12\,\mathrm{nm}, \end{cases} \quad (17)$$

where the dimensionless mobility, $\tilde{Z}_p$, is defined as the ratio of input particle electrical mobility and the ideal mobility, $Z^*_{p,ideal}$, as defined in Eq. (6),

$$\tilde{Z}_p = \frac{Z_p}{Z^*_{p,ideal}}, \quad (18)$$

and $\Omega_{\mathrm{ROMIAC}}(\tilde{Z}_p, \beta, \delta, \tilde{\sigma})$ and $\Omega_{\mathrm{DMA}}(\tilde{Z}_p, \beta, \delta, \tilde{\sigma})$ are the diffusing Stolzenburg transfer functions for the ROMIAC and long-column DMA operated at static mode, respectively:

$$\begin{aligned} &\Omega_{\mathrm{ROMIAC,DMA}}(\tilde{Z}_p, \beta, \delta, \tilde{\sigma}) \\ &= \frac{\tilde{\sigma}}{\sqrt{2}\beta(1-\delta)}\left[\epsilon\left(\frac{\tilde{Z}_p-(1+\beta)}{\sqrt{2}\tilde{\sigma}}\right)\right. \\ &+\epsilon\left(\frac{\tilde{Z}_p-(1-\beta)}{\sqrt{2}\tilde{\sigma}}\right)-\epsilon\left(\frac{\tilde{Z}_p-(1+\beta\delta)}{\sqrt{2}\tilde{\sigma}}\right) \\ &\left.-\epsilon\left(\frac{\tilde{Z}_p-(1-\beta\delta)}{\sqrt{2}\tilde{\sigma}}\right)\right], \end{aligned} \quad (19)$$

where ϵ is

$$\epsilon(x) = x\,\mathrm{erf}(x) + \frac{\exp\left(-x^2\right)}{\sqrt{\pi}}, \quad (20)$$

and erf(x) is the error function. The dimensionless diffusion factor, $\tilde{\sigma}$, is defined as

$$\tilde{\sigma}^2 = \frac{G_{\text{class}}}{Pe_{\text{mig}}} \tilde{Z}_{\text{p}}. \tag{21}$$

At ambient temperature, the migration Péclet number for singly charged particles can be approximated as a function of the static voltage:

$$Pe_{\text{mig}} = \frac{\phi e V}{kT} \approx \frac{V}{0.0255[V]}. \tag{22}$$

The dimensionless geometry factor for classifiers, G_{class}, which is estimated to be $G_{\text{LDMA}} = 2.55$ for the TSI 3081 LDMA at $\mathcal{R}_{\text{nd, DMA}} \approx 12$ and for the ROMIAC at $\mathcal{R}_{\text{nd, ROMIAC}} \approx 10$, can be computed as

$$G = \begin{cases} \frac{8}{3}, & \xi = 0 \\ \dfrac{4\left\{\begin{array}{l} \frac{4}{15}\left[\left(1-|\xi|^{5/2}\right)-(1-|\xi|)^{5/2}\right] \\ +\frac{1}{3}\left(\frac{\xi}{\alpha}\right)^2\left[\left(1-|\xi|^{3/2}\right)-(1-|\xi|)^{3/2}\right] \end{array}\right\}}{|\xi|(1-|\xi|)}, & 0<|\xi|<1 \\ 2\left[\frac{4}{3}+\left(\frac{1}{\alpha}\right)^2\right], & |\xi|=1, \end{cases} \tag{23}$$

where $\xi = \beta^{-1}(\tilde{Z}_{\text{p}} - 1)$ and $\alpha = L/b = 0.015\,\text{m}/0.01\,\text{m} = 1.5$ for the ROMIAC. The real resolution of the scanning ROMIAC can then be computed using the full width at half-maximum of the transfer function, $\Omega_{\text{ROMIAC}}(\tilde{Z}_{\text{p}}, \beta, \delta, t)$, (Flagan, 1999, 2004):

$$\mathcal{R} = \frac{Z_{\text{p}}^*}{\Delta Z_{\text{p,FWHM}}}. \tag{24}$$

The transmission efficiency can be calculated as the area under the transfer function normalized by the area of an ideal transfer function, which in non-dimensionless form is equivalent to the flow factor, β:

$$\eta = \frac{1}{\beta}\int \Omega_{\text{ROMIAC}}\left(\tilde{Z}_{\text{p}}, \beta, \delta, t\right) \mathrm{d}\tilde{Z}_{\text{p}} = \frac{1}{\beta}\int \frac{N_{\text{out}}(t)}{N_{\text{in}}} \mathrm{d}t. \tag{25}$$

Figure 9 shows the comparison of ROMIAC resolution and efficiency between the experiment, COMSOL simulation, and the theoretical limit calculated for the DMA and the OMAC operated in static mode (Flagan, 2004). The overall performance of the nSEMS shows convincing agreement with the finite-element simulation results in Fig. 3, which proves the feasibility of coupling laboratory calibrations with numerical simulation to predict the instrument response of a SEMS system. Compared to the simulation and theoretical calculation, the effect of diffusional degradation at low voltages remains minimal for the scanning ROMIAC system compared to other conventional nano-SMPS systems, as previously predicted for the static OMAC (Flagan, 2004; Downard et al., 2011). Figure 10 shows the nSEMS peak voltage (V^*) as a function of particle mobility when operated at a cross-flow rate of $Q_{\text{c}} = 12\,\text{L}\,\text{min}^{-1}$. The relatively high classification voltage ($\sim 35\,\text{V}$ at 1.47 nm) compared to DMAs further reduces diffusional degradation of the resolution (Flagan, 1999). In addition to the calibration results using the hot-wire or atomized particle sources, it also includes the signature peak of tetra-heptyl ammonium bromide (THAB) ions (see Fig. 4a for setup). Particle mobilities are calculated using Eq. (1) at given diameters, assuming that the particles are singly charged. The experimentally determined voltages at the transfer function peaks are in close agreement with those predicted by the COMSOL simulation in Fig. 3. From the laboratory characterization results, the method of using empirical data to adjust the simulated particle transmission has proven to be an efficient and effective way to derive SEMS or SMPS system transfer function. In addition, the nSEMS, as the first system that employs an opposed-migration classifier with continuously varying voltage, has also demonstrated the great potential of scanning OMAC systems for providing fast and accurate particle size information in the low nanometer regime without significant diffusional degradation.

4 Application to particle size distribution measurement

Atmospheric new particle formation and its subsequent growth have a great impact on aerosol number concentrations and the Earth's total energy budget. In order to better understand the climate significance of NPF, much research has attempted to study the mechanisms of nucleation and the growth rates of nanoparticles. For example, the CLOUD experiments at CERN have extensively probed the roles of sulfuric acid, ammonia, cosmic rays, and other atmospheric components in nucleation (Kirkby et al., 2011, 2016). To determine the particle formation and growth rates from atmospheric chamber experiments, the particle size distribution needs to be measured at high resolving power and with a short duty cycle. In addition to being able to capture the transient aerosol dynamics during NPF events, since most of the nucleation occurs in clean atmospheric conditions, the instrument must be capable of taking measurements at relatively low particle concentrations. The scan rate selected for this initial implementation was therefore a compromise between fast response and counting statistics.

The nSEMS was used with a 60 s scan for particle sizing in both the CLOUD 13 and the CLOUD 14 campaigns. Figure 11 shows a particle size distribution measured with nSEMS during an ion-induced nucleation event that simulated atmospheric nucleation and nanoparticle growth in an urban environment in CLOUD 13. The experiment was conducted in the presence of sulfuric acid, nitric acid, and ammonia at $-10\,^{\circ}\text{C}$ and 60 % RH. When particles reached $d_{\text{p}} \approx 4.6$ nm, nitric acid and ammonia started condensing rapidly onto the particles, resulting in a growth rate of $40\,\text{nm}\,\text{h}^{-1}$. This extremely fast growth from nitric acid and ammonia co-

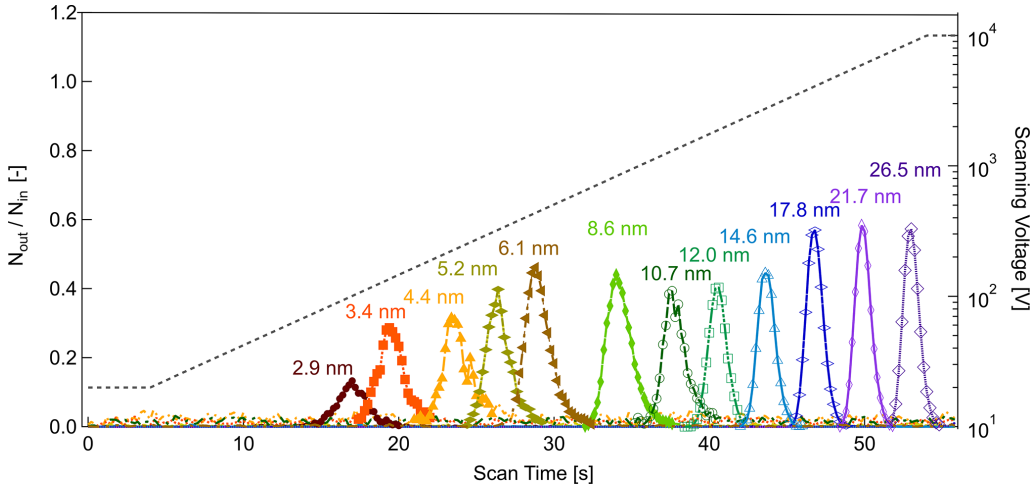

Figure 8. Experimental calibration of the nSEMS using the TDMA setup shown in Fig. 4. Particles entering the nSEMS were classified as described; the reported mobility-equivalent diameters were calculated based on the upstream classifier operating parameters. The nSEMS was operated at the default parameters listed in Table 1, with $t_{ramp} = 50$ s. The ratio of downstream to upstream particle counts of the nSEMS is shown as a function of time over the voltage scan, with input particles in the 2.9–26.5 nm range. The applied voltage is indicated by the dashed gray line. Only a fraction of the sizes used in the calibration are shown here for clarity; results from the complete size calibration summary are presented in Fig. 10.

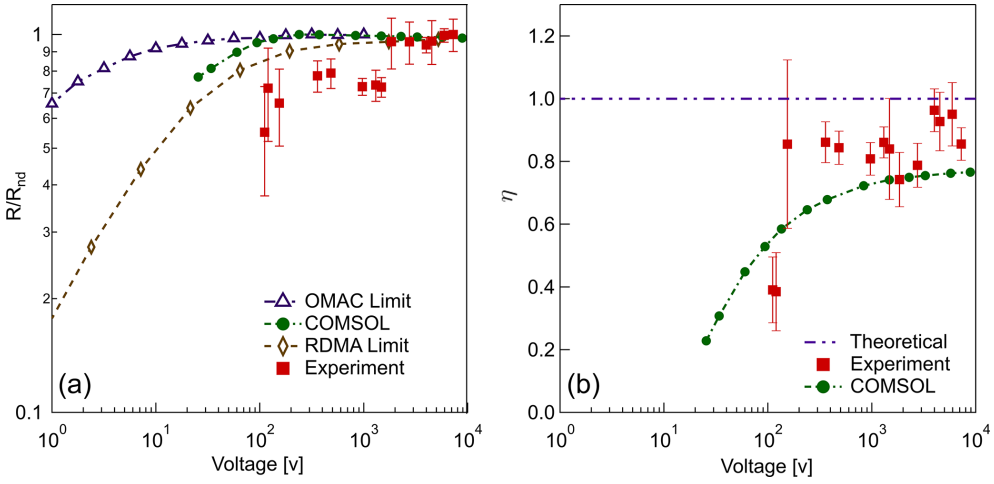

Figure 9. Comparison between experimental, simulated, and theoretical transfer functions. **(a)** The effect of operating voltage on classifier resolution calculated as the actual resolution based on the full width at half-maximum (FWHM) (Eq. 24) over $\mathcal{R}_{nd}$, the resolution at the non-diffusive regime (> 5000 V). **(b)** Particle transmission efficiency as a function of operating voltage. Transmission efficiency, η, is calculated as the ratio of the actual over the ideal area below the transfer function peak. The error bars represent 1 standard deviation of uncertainty from multiple experiments at one size.

condensation can generally persist for only a few minutes and activate only the largest of the initial small nuclei, before depleting the nitric acid supersaturation and turning off additional nucleation. Those few nuclei that activate are often present only in low concentrations (Wang et al., 2020). Consequently, the other conventional particle sizing instruments that are connected to the CLOUD chamber were not able to fully capture this rapid growth event; the concentrations were too low to be detected by the nano-SMPS (Tröstl et al., 2015). Moreover, the size of the particles evolved so fast that a higher size resolution was required than could be attained by the DMA train that measures six sizes in parallel with separate static DMAs (Stolzenburg et al., 2017). In the region where multiple instruments can capture the aerosol dynamics, the intercomparison between the results of different instruments showed reasonably good agreement. Combining these measurements also provided detailed particle growth information in rapidly evolving new particle formation events that the other instruments could follow (Wang et al., 2020). In addition to enabling high-resolving-

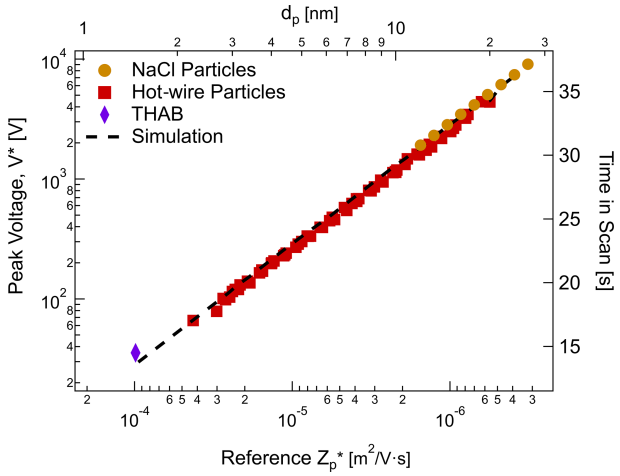

Figure 10. The nSEMS voltage at the peak transmission (V^*) as a function of the input reference particle mobility, Z_p^*. Symbols represent experimental results with tetra-heptyl ammonium bromide (THAB), hot-wire, and atomized NaCl particles produced using the setups shown in Fig. 4. The black dotted line demonstrates the voltage at peak transmission predicted by the finite-element simulations. The top axis shows the corresponding particle diameter, d_p, at a given mobility, Z_p^*, as defined in Eq. (1); the right axis shows the corresponding time in the scan.

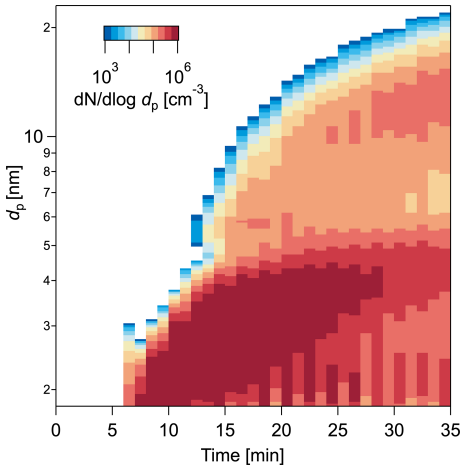

Figure 11. Particle size distribution measured by the nSEMS during a nucleation and growth event in the CLOUD 13 campaign with anthropogenic trace gases. The experiment was conducted at −10 °C and 60 % RH, with 24 pptv HNO_3, 2131 pptv NH_3, 0.46 pptv H_2SO_4, and 0.28 pptv highly oxygenated organic molecules (HOMs). The nSEMS high-voltage polarity was switched between scans to probe both positively and negatively charged particles from the soft x-ray CC. A clear bimodal size distribution was observed by the nSEMS due to the rapid co-condensation of nitric acid and ammonia (Wang et al., 2020). The activation diameter, d_{act}, for nitric acid condensation is around 4.6 nm.

power measurements of size distributions during rapid particle growth events, the nSEMS also provides valuable information on natural ion and charged particle concentrations in the chamber when operated with the CC switched off. The ability to measure the concentrations of positive and negative nanoparticles separately facilitates study of the role of ions in atmospheric nucleation and growth.

5 Conclusions

The design and performance of a novel nanoparticle size-classifying instrument, the nSEMS, have been evaluated. The concept of OMAC was first proposed in order to overcome the diffusional degradation at lower voltages of the DMA (Flagan, 2004). The radial form of the OMAC, the ROMIAC, was then designed to classify nanoparticles in the low nanometer regime with high resolving power in static mode (Mui et al., 2013, 2017). According to the ideal model of OMAC, particles are transmitted through the classification region parallel to the porous electrodes, and voltage variations would lead to excessive particle losses. A key feature of the ROMIAC design was to both introduce the sample and extract the classified ions or particles on the ground-electrode side of the classifier. The resulting trajectories, which can be seen in COMSOL Multiphysics™ simulations shown in Fig. S1, reduce losses associated with voltage scanning to acceptable levels, thereby enabling measurement acceleration by voltage scanning and operating as a SEMS. The ability to classify particles at low voltage with minimal diffusional degradation of the transfer function, combined with a fast-response CPC that minimizes residence time distribution related to the smearing effect, made it possible for the ROMIAC to be operated with fast exponential voltage ramping, greatly accelerating the measurement over that of static-mode operation. The nSEMS system, which was used with a soft x-ray CC in this study, combines a scanning ROMIAC as a classifier and a two-stage CPC as a particle detector, and it can provide highly resolved particle size distribution measurements in the 1.5–25 nm size range in 1 min or less (we did not push the bound on the scan rate in the initial application of the nSEMS at CLOUD). The integrated instrument transfer function, which can reproduce how particles are transmitted inside the nSEMS within 10 % uncertainty, has been derived by combining COMSOL finite-element analysis with empirical adjustments. The particle size distributions measured by the nSEMS employing the described data inversion method agree reasonably well with other instruments (Tröstl et al., 2015; Stolzenburg et al., 2017) used in the CLOUD experiment (Wang et al., 2020). However, uncertainties remain that are associated with particle charge distribution. When combined with a soft x-ray CC that can be switched off, the dual-polarity scanning feature of the nSEMS makes it possible to observe the effects of charges on the evolution of the size distribution as particles nucle-

ate and grow. Its dual-polarity capability will also facilitate characterization of the particle charge distribution in the low nanometer regime, thereby improving the instrumental transfer function and data inversion. Overall, this instrument is able to provide robust particle sizing information in the sub-25 nm region and is extremely powerful in examining atmospheric nucleation and the subsequent growth of nanoparticles.

Code and data availability. Data and code related to this article are available upon request to the corresponding author.

Supplement. The supplement related to this article is available online at: https://doi.org/10.5194/amt-14-5429-2021-supplement.

Author contributions. WK wrote the paper, analyzed the data, led the calibration of the instrument, and operated the instrument at CLOUD. SA led the construction the instrument as deployed to CLOUD, developed the data acquisition and control software, contributed to the calibration of the instrument, and contributed to the writing of the paper. HM built and conducted proof-of-concept experiments with the first prototype of the instrument and developed the finite-element simulation in developing the instrument response function. CK developed the soft x-ray charger used in the apparatus and did the initial construction of the two-stage condensation particle counter detector. BCS contributed to the construction and calibration of the instrument and operated it in CLOUD experiments. YH contributed to the development of the data analysis software and contributed to the writing of the paper. GSL developed the modified MAGIC CPC used as the second stage of the detector. SVH led the modifications of the MAGIC CPC for use in this instrument. JHS contributed to the analysis of the data and the writing of the paper. RCF led the project, development of the instrument, design of the experiments, and data analysis, along with contributing to the writing and editing of the paper.

Competing interests. The California Institute of Technology has a patent pending for the nSEMS. Aerosol Dynamics Inc. has a patent on the MAGIC CPC. No other conflicts of interest were identified.

Disclaimer. Publisher's note: Copernicus Publications remains neutral with regard to jurisdictional claims in published maps and institutional affiliations.

Special issue statement. This article is part of the special issue "The CERN CLOUD experiment (ACP/AMT inter-journal SI)". It is not associated with a conference.

Acknowledgements. The authors would like to thank the CLOUD experiment for providing the facility for instrument testing and operation. We gratefully acknowledge a generous gift from Christine and Dwight Landis to improve the data acquisition system of the instrument.

Financial support. This research has been supported by the National Science Foundation (grant nos. 1602086 and 1801329).

Review statement. This paper was edited by Charles Brock and reviewed by Juan Fernandez de la Mora and one anonymous referee.

References

Amanatidis, S., Kim, C., Spielman, S. R., Lewis, G. S., Hering, S. V., and Flagan, R. C.: The Spider DMA: A miniature radial differential mobility analyzer, Aerosol Sci. Technol., 54, 175–189, https://doi.org/10.1080/02786826.2019.1626974, 2020.

Bonn, B. and Moortgat, G. K.: Sesquiterpene ozonolysis: Origin of atmospheric new particle formation from biogenic hydrocarbons, Geophys. Res. Lett., 30, 1585, https://doi.org/10.1029/2003GL017000, 2003.

Bracewell, R. N. and Bracewell, R. N.: The Fourier transform and its applications, 2nd edn., vol. 31999, McGraw-Hill, New York, USA, 1986.

Brown, L. M., Collings, N., Harrison, R. M., Maynard, A. D., Maynard, R. L., Kim, C. S., and Jaques, P. A.: Respiratory dose of inhaled ultrafine particles in healthy adults, Philos. Trans. R. Soc. A, 358, 2693–2705, https://doi.org/10.1098/rsta.2000.0678, 2000.

Brunelli, N. A., Flagan, R. C., and Giapis, K. P.: Radial differential mobility analyzer for one nanometer particle classification, Aerosol Sci. Technol., 43, 53–59, https://doi.org/10.1080/02786820802464302, 2009.

Chen, D. R., Pui, D. Y. H., Hummes, D., Fissan, H., Quant, F. R., and Sem, G. J.: Design and evaluation of a nanometer aerosol differential mobility analyzer (Nano-DMA), J. Aerosol Sci., 29, 497–509, https://doi.org/10.1016/S0021-8502(97)10018-0, 1998.

Chen, X., McMurry, P. H., and Jiang, J.: Stationary characteristics in bipolar diffusion charging of aerosols: Improving the performance of electrical mobility size spectrometers, Aerosol Sci. Technol., 52, 809–813, https://doi.org/10.1080/02786826.2018.1479058, 2018.

Collins, D. R., Flagan, R. C., and Seinfeld, J. H.: Improved inversion of scanning DMA data, Aerosol Sci. Technol., 36, 1–9, https://doi.org/10.1080/027868202753339032, 2002.

Collins, D. R., Cocker, D. R., Flagan, R. C., and Seinfeld, J. H.: The scanning DMA transfer function, Aerosol Sci. Technol., 38, 833–850, https://doi.org/10.1080/027868290503082, 2004.

Dall'Osto, M., Beddows, D. C. S., Tunved, P., Krejci, R., Ström, J., Hansson, H.-C., Yoon, Y. J., Park, K.-T., Becagli, S., Udisti, R., Onasch, T., O´Dowd, C. D., Simó, R., and Harrison, R. M.: Arctic sea ice melt leads to atmospheric new particle formation, Sci. Rep., 7, 1–10, https://doi.org/10.1038/s41598-017-03328-1, 2017.

Downard, A. J., Dama, J. F., and Flagan, R. C.: An asymptotic analysis of differential electrical mobil-

ity classifiers, Aerosol Sci. Technol., 45, 727–739, https://doi.org/10.1080/02786826.2011.558136, 2011.

Dubey, P. and Dhaniyala, S.: A new approach to calculate diffusional transfer functions of scanning DMAs, Aerosol Sci. Technol., 45, 1031–1040, https://doi.org/10.1080/02786826.2011.579644, 2011.

Dunn, M. J., Jiménez, J.-L., Baumgardner, D., Castro, T., McMurry, P. H., and Smith, J. N.: Measurements of Mexico City nanoparticle size distributions: Observations of new particle formation and growth, Geophys. Res. Lett., 31, L10102, https://doi.org/10.1029/2004GL019483, 2004.

Fissan, H. J., Helsper, C., and Thielen, H. J.: Determination of particle size distributions by means of an electrostatic classifier, J. Aerosol Sci., 14, 354–357, https://doi.org/10.1016/0021-8502(83)90133-7, 1983.

Flagan, R. C.: History of electrical aerosol measurements, Aerosol Sci. Technol., 28, 301–380, https://doi.org/10.1080/02786829808965530, 1998.

Flagan, R. C.: On differential mobility analyzer resolution, Aerosol Sci. Technol., 30, 556–570, https://doi.org/10.1080/027868299304417, 1999.

Flagan, R. C.: Opposed Migration Aerosol Classifier (OMAC), Aerosol Sci. Technol., 38, 890–899, https://doi.org/10.1080/027868290505242, 2004.

Gamero-Castano, M. and de la Mora, J.: A condensation nucleus counter (CNC) sensitive to singly charged sub-nanometer particles, J. Aerosol Sci., 31, 757–772, https://doi.org/10.1016/S0021-8502(99)00555-8, 2000.

Gordon, H., Kirkby, J., Baltensperger, U., Bianchi, F., Breitenlechner, M., Curtius, J., Dias, A., Dommen, J., Donahue, N. M., Dunne, E. M., Duplissy, J., Ehrhart, S., Flagan, R. C., Frege, C., Fuchs, C., Hansel, A., Hoyle, C. R., Kulmala, M., Kürten, A., Lehtipalo, K., Makhmutov, V., Molteni, U., Rissanen, M. P., Stozkhov, Y., Tröstl, J., Tsagkogeorgas, G., Wagner, R., Williamson, C., Wimmer, D., Winkler, P. M., Yan, C., and Carslaw, K. S.: Causes and importance of new particle formation in the present-day and preindustrial atmospheres, J. Geophys. Res.-Atmos., 122, 8739–8760, https://doi.org/10.1002/2017JD026844, 2017.

Hering, S. V., Lewis, G. S., Spielman, S. R., and Eiguren-Fernandez, A.: A MAGIC concept for self-sustained, water-based, ultrafine particle counting, Aerosol Sci. Technol., 53, 63–72, https://doi.org/10.1080/02786826.2018.1538549, 2019.

Iida, K., Stolzenburg, M. R., and McMurry, P. H.: Effect of working fluid on sub-2 nm particle detection with a laminar flow ultrafine condensation particle counter, Aerosol Sci. Technol., 43, 81–96, https://doi.org/10.1080/02786820802488194, 2009.

Jiang, J., Chen, M., Kuang, C., and Attoui, M.: Electrical mobility spectrometer using diethylene glycol condensation particle counter for measuring aeerosol size distributions down to 1 nm, Aerosol Sci. Technol., 45, 510–521, https://doi.org/10.1080/02786826.2010.546817, 2011a.

Jiang, J., Chen, M., Eisele, F. L., Scheckman, J., Williams, B. J., Kuang, C., and McMurry, P. H.: First measurements of neutral atmospheric cluster and 1–2 nm particle number size distributions during nucleation events, Aerosol Sci. Technol., 45, 2–5, https://doi.org/10.1080/02786826.2010.546817, 2011b.

Kangasluoma, J., Junninen, H., Lehtipalo, K., Mikkilä, J., Vanhanen, J., Attoui, M., Sipilä, M., Worsnop, D., Kulmala, M., and Petäjä, T.: Remarks on Ion Generation for CPC Detection Efficiency Studies in the Sub-1-nm Size Range, Aerosol Sci. Technol., 47, 556–563, https://doi.org/10.1080/02786826.2013.773393, 2013.

Kerminen, V.-M., Chen, X., Vakkari, V., Petäjä, T., Kulmala, M., and Bianchi, F.: Atmospheric new particle formation and growth: review of field observations, Environ. Res. Lett., 13, 103003, https://doi.org/10.1088/1748-9326/aadf3c, 2018.

Kirkby, J., Curtius, J., Almeida, J., Dunne, E., Duplissy, J., Ehrhart, S., Franchin, A., Gagné, S., Ickes, L., Kürten, A., Kupc, A., Metzger, A., Riccobono, F., Rondo, L., Schobesberger, S., Tsagkogeorgas, G., Wimmer, D., Amorim, A., Bianchi, F., Breitenlechner, M., David, A., Dommen, J., Downard, A., Ehn, M., Flagan, R. C., Haider, S., Hansel, A., Hauser, D., Jud, W., Junninen, H., Kreissl, F., Kvashin, A., Laaksonen, A., Lehtipalo, K., Lima, J., Lovejoy, E. R., Makhmutov, V., Mathot, S., Mikkilä, J., Minginette, P., Mogo, S., Nieminen, T., Onnela, A., Pereira, P., Petäjä, T., Schnitzhofer, R., Seinfeld, J. H., Sipilä, M., Stozhkov, Y., Stratmann, F., Tomé, A., Vanhanen, J., Viisanen, Y., Vrtala, A., Wagner, P. E., Walther, H., Weingartner, E., Wex, H., Winkler, P. M., Carslaw, K. S., Worsnop, D. R., Baltensperger, U., and Kulmala, M.: Role of sulphuric acid, ammonia and galactic cosmic rays in atmospheric aerosol nucleation, Nature, 476, 429–433, https://doi.org/10.1038/nature10343, 2011.

Kirkby, J., Duplissy, J., Sengupta, K., Frege, C., Gordon, H., Williamson, C., Heinritzi, M., Simon, M., Yan, C., Almeida, J., Tröstl, J., Nieminen, T., Ortega, I. K., Wagner, R., Adamov, A., Amorim, A., Bernhammer, A.-K., Bianchi, F., Breitenlechner, M., Brilke, S., Chen, X., Craven, J., Dias, A., Ehrhart, S., Flagan, R. C., Franchin, A., Fuchs, C., Guida, R., Hakala, J., Hoyle, C. R., Jokinen, T., Junninen, H., Kangasluoma, J., Kim, J., Krapf, M., Kürten, A., Laaksonen, A., Lehtipalo, K., Makhmutov, V., Mathot, S., Molteni, U., Onnela, A., Peräkylä, O., Piel, F., Petäjä, T., Praplan, A. P., Pringle, K., Rap, A., Richards, N. A. D., Riipinen, I., Rissanen, M. P., Rondo, L., Sarnela, N., Schobesberger, S., Scott, C. E., Seinfeld, J. H., Sipilä, M., Steiner, G., Stozhkov, Y., Stratmann, F., Tomé, A., Virtanen, A., Vogel, A. L., Wagner, A. C., Wagner, P. E., Weingartner, E., Wimmer, D., Winkler, P. M., Ye, P., Zhang, X., Hansel, A., Dommen, J., Donahue, N. M., Worsnop, D. R., Baltensperger, U., Kulmala, M., Carslaw, K. S., and Curtius, J.: Ion-induced nucleation of pure biogenic particles, Nature, 533, 521–526, https://doi.org/10.1038/nature17953, 2016.

Knutson, E. O. and Whitby, K. T.: Aerosol classification by electric mobility: apparatus, theory, and applications, J. Aerosol Sci., 6, 443–451, https://doi.org/10.1016/0021-8502(75)90060-9, 1975.

Kousaka, Y., Niida, T., Okuyama, K., and Tanaka, H.: Development of a mixing type condensation nucleus counter, J. Aerosol Sci., 13, 231–240, https://doi.org/10.1016/0021-8502(82)90064-7, 1982.

Kulmala, M., Vehkamaki, H., Petaja, T., Dal Maso, M., Lauri, A., Kerminen, V.-M., Birmili, W., and McMurry, P.: Formation and growth rates of ultrafine atmospheric particles: A review of observations, J. Aerosol Sci., 35, 143–176, https://doi.org/10.1016/j.jaerosci.2003.10.003, 2004.

Lee, S.-H., Gordon, H., Yu, H., Lehtipalo, K., Haley, R., Li, Y., and Zhang, R.: New particle formation in the atmosphere: From molecular clusters to global climate, J. Geophys. Res.-Atmos., 124, 7098–7146, https://doi.org/10.1029/2018JD029356, 2019.

Mai, H. and Flagan, R. C.: Scanning DMA data analysis I. Classification transfer function, Aerosol Sci. Technol., 52, 1382–1399, https://doi.org/10.1080/02786826.2018.1528005, 2018.

Mai, H., Kong, W., Seinfeld, J. H., and Flagan, R. C.: Scanning DMA data analysis II. Integrated DMA-CPC instrument response and data inversion, Aerosol Sci. Technol., 52, 1400–1414, https://doi.org/10.1080/02786826.2018.1528006, 2018.

Merikanto, J., Spracklen, D. V., Mann, G. W., Pickering, S. J., and Carslaw, K. S.: Impact of nucleation on global CCN, Atmos. Chem. Phys., 9, 8601–8616, https://doi.org/10.5194/acp-9-8601-2009, 2009.

Merritt, M. and Zhang, Y.: Interior-point gradient method for large-scale totally nonnegative least squares problems, J. Optim. Theory Appl., 126, 191–202, https://doi.org/10.1007/s10957-005-2668-z, 2005.

Mui, W., Thomas, D. A., Downard, A. J., Beauchamp, J. L., Seinfeld, J. H., and Flagan, R. C.: Ion mobility-mass spectrometry with a radial opposed migration ion and aerosol classifier (ROMIAC), Anal. Chem., 85, 6319–6326, https://doi.org/10.1021/ac400580u, 2013.

Mui, W., Mai, H., Downard, A. J., Seinfeld, J. H., and Flagan, R. C.: Design, simulation, and characterization of a radial opposed migration ion and aerosol classifier (ROMIAC), Aerosol Sci. Technol., 51, 801–823, https://doi.org/10.1080/02786826.2017.1315046, 2017.

O'Dowd, C. D., Jimenez, J. L., Bahreini, R., Flagan, R. C., Seinfeld, J. H., Hämeri, K., Pirjola, L., Kulmala, M., Jennings, S. G., and Hoffmann, T.: Marine aerosol formation from biogenic iodine emissions, Nature, 417, 632–636, https://doi.org/10.1038/nature00775, 2002.

Okuyama, K., Kousaka, Y., and Motouchi, T.: Condensational growth of ultrafine aerosol particles in a new particle size magnifier, Aerosol Sci. Technol., 3, 353–366, https://doi.org/10.1080/02786828408959024, 1984.

Paasonen, P., Nieminen, T., Asmi, E., Manninen, H. E., Petäjä, T., Plass-Dülmer, C., Flentje, H., Birmili, W., Wiedensohler, A., Hõrrak, U., Metzger, A., Hamed, A., Laaksonen, A., Facchini, M. C., Kerminen, V.-M., and Kulmala, M.: On the roles of sulphuric acid and low-volatility organic vapours in the initial steps of atmospheric new particle formation, Atmos. Chem. Phys., 10, 11223–11242, https://doi.org/10.5194/acp-10-11223-2010, 2010.

Peineke, C., Attoui, M., and Schmidt-Ott, A.: Using a glowing wire generator for production of charged, uniformly-sized nanoparticles at high concentrations, J. Aerosol Sci., 37, 1651–1661, https://doi.org/10.1016/j.jaerosci.2006.06.006, 2006.

Quant, F. R., Caldow, R., Sem, G. J., and Addison, T. J.: Performance of condensation particle counters with three continuous-flow designs, J. Aerosol Sci., 23, 405–408, https://doi.org/10.1016/0021-8502(92)90435-X, 1992.

Rader, D. J. and McMurry, P. H.: Application of the tandem differential mobility analyzer to studies of droplet growth or evaporation, J. Aerosol Sci., 17, 771–787, https://doi.org/10.1016/0021-8502(86)90031-5, 1986.

Rosell-Llompart, J., Loscertales, I. G., Bingham, D., and de la Mora, J. F.: Sizing nanoparticles and ions with a short differential mobility analyzer, J. Aerosol Sci., 27, 695–719, https://doi.org/10.1016/0021-8502(96)00016-X, 1996.

Russell, L. M., Flagan, R. C., and Seinfeld, J. H.: Asymmetric instrument response resulting from mixing effects in accelerated DMA-CPC measurements, Aerosol Sci. Technol., 23, 491–509, https://doi.org/10.1080/02786829508965332, 1995.

Sgro, L. A. and de la Mora, J. F.: A simple turbulent mixing CNC for charged particle detection down to 1.2 nm, Aerosol Sci. Technol., 38, 1–11, https://doi.org/10.1080/02786820490247560, 2004.

Shah, S. D. and Cocker, D. R.: A fast scanning mobility particle spectrometer for monitoring transient particle size distributions, Aerosol Sci. Technol., 39, 519–526, https://doi.org/10.1080/027868291004652, 2005.

Steiner, G., Jokinen, T., Junninen, H., Sipilä, M., Petäjä, T., Worsnop, D., Reischl, G. P., and Kulmala, M.: High-resolution mobility and mass spectrometry of negative ions produced in a ^{241}Am aerosol charger, Aerosol Sci. Technol., 48, 261–270, https://doi.org/10.1080/02786826.2013.870327, 2014.

Stolzenburg, D., Steiner, G., and Winkler, P. M.: A DMA-train for precision measurement of sub-10 nm aerosol dynamics, Atmos. Meas. Tech., 10, 1639–1651, https://doi.org/10.5194/amt-10-1639-2017, 2017.

Stolzenburg, M. R. and McMurry, P. H.: Equations governing single and tandem DMA configurations and a new lognormal approximation to the transfer function, Aerosol Sci. Technol., 42, 421–432, https://doi.org/10.1080/02786820802157823, 2008.

Tröstl, J., Tritscher, T., Bischof, O. F., Horn, H.-G., Krinke, T., Baltensperger, U., and Gysel, M.: Fast and precise measurement in the sub-20 nm size range using a Scanning Mobility Particle Sizer, J. Aerosol Sci., 87, 75–87, https://doi.org/10.1016/j.jaerosci.2015.04.001, 2015.

Ude, S. and de la Mora, J. F.: Molecular monodisperse mobility and mass standards from electrosprays of tetraalkyl ammonium halides, J. Aerosol Sci., 36, 1224–1237, https://doi.org/10.1016/j.jaerosci.2005.02.009, 2005.

Wagner, R., Yan, C., Lehtipalo, K., Duplissy, J., Nieminen, T., Kangasluoma, J., Ahonen, L. R., Dada, L., Kontkanen, J., Manninen, H. E., Dias, A., Amorim, A., Bauer, P. S., Bergen, A., Bernhammer, A.-K., Bianchi, F., Brilke, S., Mazon, S. B., Chen, X., Draper, D. C., Fischer, L., Frege, C., Fuchs, C., Garmash, O., Gordon, H., Hakala, J., Heikkinen, L., Heinritzi, M., Hofbauer, V., Hoyle, C. R., Kirkby, J., Kürten, A., Kvashnin, A. N., Laurila, T., Lawler, M. J., Mai, H., Makhmutov, V., Mauldin III, R. L., Molteni, U., Nichman, L., Nie, W., Ojdanic, A., Onnela, A., Piel, F., Quéléver, L. L. J., Rissanen, M. P., Sarnela, N., Schallhart, S., Sengupta, K., Simon, M., Stolzenburg, D., Stozhkov, Y., Tröstl, J., Viisanen, Y., Vogel, A. L., Wagner, A. C., Xiao, M., Ye, P., Baltensperger, U., Curtius, J., Donahue, N. M., Flagan, R. C., Gallagher, M., Hansel, A., Smith, J. N., Tomé, A., Winkler, P. M., Worsnop, D., Ehn, M., Sipilä, M., Kerminen, V.-M., Petäjä, T., and Kulmala, M.: The role of ions in new particle formation in the CLOUD chamber, Atmos. Chem. Phys., 17, 15181–15197, https://doi.org/10.5194/acp-17-15181-2017, 2017.

Wang, J., McNeill, V. F., Collins, D. R., and Flagan, R. C.: Fast mixing condensation nucleus counter: Application to rapid scanning differential mobility analyzer measurements, Aerosol Sci. Technol., 36, 678–689, https://doi.org/10.1080/02786820290038366, 2002.

Wang, M., Kong, W., Marten, R., He, X.-C., Chen, D., Pfeifer, J., Heitto, A., Kontkanen, J., Dada, L., Kürten, A., Yli-Juuti, T., Manninen, H. E., Amanatidis, S., Amorim, A., Baalbaki, R.,

Baccarini, A., Bell, D. M., Bertozzi, B., Bräkling, S., Brilke, S., Murillo, L. C., Chiu, R., Chu, B., De Menezes, L.-P., Duplissy, J., Finkenzeller, H., Carracedo, L. G., Granzin, M., Guida, R., Hansel, A., Hofbauer, V., Krechmer, J., Lehtipalo, K., Lamkaddam, H., Lampimäki, M., Lee, C. P., Makhmutov, V., Marie, G., Mathot, S., Mauldin, R. L., Mentler, B., Müller, T., Onnela, A., Partoll, E., Petäjä, T., Philippov, M., Pospisilova, V., Ranjithkumar, A., Rissanen, M., Rörup, B., Scholz, W., Shen, J., Simon, M., Sipilä, M., Steiner, G., Stolzenburg, D., Tham, Y. J., Tomé, A., Wagner, A. C., Wang, D. S., Wang, Y., Weber, S. K., Winkler, P. M., Wlasits, P. J., Wu, Y., Xiao, M., Ye, Q., Zauner-Wieczorek, M., Zhou, X., Volkamer, R., Riipinen, I., Dommen, J., Curtius, J., Baltensperger, U., Kulmala, M., Worsnop, D. R., Kirkby, J., Seinfeld, J. H., El-Haddad, I., Flagan, R. C., and Donahue, N. M.: Rapid growth of new atmospheric particles by nitric acid and ammonia condensation, Nature, 581, 184–189, https://doi.org/10.1038/s41586-020-2270-4, 2020.

Wang, S. C. and Flagan, R. C.: Scanning electrical mobility spectrometer, Aerosol Sci. Technol., 13, 230–240, https://doi.org/10.1080/02786829008959441, 1990.

Wang, Z., Wu, Z., Yue, D., Shang, D., Guo, S., Sun, J., Ding, A., Wang, L., Jiang, J., Guo, H., Gao, J., Cheung, H. C., Morawska, L., Keywood, M., and Hu, M.: New particle formation in China: Current knowledge and further directions, Sci. Total Environ., 577, 258–266, https://doi.org/10.1016/j.scitotenv.2016.10.177, 2017.

Wiedensohler, A.: An approximation of the bipolar charge distribution for particles in the submicron size range, J. Aerosol Sci., 19, 387–389, https://doi.org/10.1016/0021-8502(88)90278-9, 1988.

Winklmayr, W., Reischl, G. P., Lindner, A. O., and Berner, A.: A new electromobility spectrometer for the measurement of aerosol size distributions in the size range from 1 to 1000 nm, J. Aerosol Sci., 22, 289–296, https://doi.org/10.1016/S0021-8502(05)80007-2, 1991.

Yao, L., Garmash, O., Bianchi, F., Zheng, J., Yan, C., Kontkanen, J., Junninen, H., Mazon, S. B., Ehn, M., Paasonen, P., Sipilä, M., Wang, M., Wang, X., Xiao, S., Chen, H., Lu, Y., Zhang, B., Wang, D., Fu, Q., Geng, F., Li, L., Wang, H., Qiao, L., Yang, X., Chen, J., Kerminen, V.-M., Petäjä, T., Worsnop, D. R., Kulmala, M., and Wang, L.: Atmospheric new particle formation from sulfuric acid and amines in a Chinese megacity, Science, 361, 278–281, https://doi.org/10.1126/science.aao4839, 2018.

Zhang, S.-H., Akutsu, Y., Russell, L. M., Flagan, R. C., and Seinfeld, J. H.: Radial differential mobility analyzer, Aerosol Sci. Technol., 23, 357–372, https://doi.org/10.1080/02786829508965320, 1995.

Appendix E

Efficacy of a portable, moderate-resolution, fast-scanning differential mobility analyzer for ambient aerosol size distribution measurements

Amanatidis, S.; Huang, Y.; Pushpawela, B.; Schulze, B. C.; Kenseth, C. M.; Ward, R. X.; Seinfeld, J. H.; Hering, S. V.; Flagan, R. C. Efficacy of a Portable, Moderate-Resolution, Fast-Scanning Differential Mobility Analyzer for Ambient Aerosol Size Distribution Measurements. *Atmospheric Measurement Techniques* **2021**, *14* (6), 4507–4516. https://doi.org/10.5194/amt-14-4507-2021.

Atmos. Meas. Tech., 14, 4507–4516, 2021
https://doi.org/10.5194/amt-14-4507-2021

Atmospheric Measurement Techniques
Open Access
EGU

Efficacy of a portable, moderate-resolution, fast-scanning differential mobility analyzer for ambient aerosol size distribution measurements

Stavros Amanatidis[1,2], Yuanlong Huang[3], Buddhi Pushpawela[1], Benjamin C. Schulze[3], Christopher M. Kenseth[1], Ryan X. Ward[3], John H. Seinfeld[1,3], Susanne V. Hering[2], and Richard C. Flagan[1,3]

[1]Division of Chemistry and Chemical Engineering, California Institute of Technology, Pasadena, CA 91125, USA
[2]Aerosol Dynamics Inc., Berkeley, CA 94710, USA
[3]Department of Environmental Science and Engineering, California Institute of Technology, Pasadena, CA 91125, USA

Correspondence: Richard C. Flagan (flagan@caltech.edu)

Received: 28 February 2021 – Discussion started: 8 March 2021
Revised: 20 May 2021 – Accepted: 24 May 2021 – Published: 18 June 2021

Abstract. Ambient aerosol size distributions obtained with a compact scanning mobility analyzer, the "Spider" differential mobility analyzer (DMA), are compared to those obtained with a conventional mobility analyzer, with specific attention to the effect of mobility resolution on the measured size distribution parameters. The Spider is a 12 cm diameter radial differential mobility analyzer that spans the 10–500 nm size range with 30 s mobility scans. It achieves its compact size by operating at a nominal mobility resolution $R = 3$ (sheath flow $= 0.9\,\mathrm{L\,min^{-1}}$; aerosol flow $= 0.3\,\mathrm{L\,min^{-1}}$) in place of the higher ratio of sheath flow to aerosol flow commonly used. The question addressed here is whether the lower resolution is sufficient to capture key characteristics of ambient aerosol size distributions. The Spider, operated at $R = 3$ with 30 s up- and downscans, was co-located with a TSI 3081 long-column mobility analyzer, operated at $R = 10$ with a 360 s sampling duty cycle. Ambient aerosol data were collected over 26 consecutive days of continuous operation, in Pasadena, CA. Over the 17–500 nm size range, the two instruments exhibit excellent correlation in the total particle number concentrations and geometric mean diameters, with regression slopes of 1.13 and 1.00, respectively. Our results suggest that particle sizing at a lower resolution than typically employed may be sufficient to obtain key properties of ambient size distributions, at least for these two moments of the size distribution. Moreover, it enables better counting statistics, as the wider transfer function for a given aerosol flow rate results in a higher counting rate.

1 Introduction

Mobility measurements of atmospheric aerosols in the 10–500 nm size range are important to atmospheric aerosol characterization (McMurry, 2000). Measurements aloft are especially important to understand aerosols in remote regions (Creamean et al., 2021; Herenz et al., 2018) and for mapping three-dimensional profiles (Mamali et al., 2018; Ortega et al., 2019; Zheng et al., 2021). Traditional mobility analyzers that span this size range are large and not suitable for most unmanned aerial vehicle (UAV) or tethered balloon payloads, which increasingly serve as platforms for aerosol characterization aloft. Moreover, aircraft measurements also require a fast scan time resolution to enable a good spatial resolution, as time is proportional to distance traveled in a moving platform.

To that end, Amanatidis et al. (2020) developed the "Spider DMA", a compact, lightweight, and fast differential mobility analyzer (DMA). The instrument was designed for 10–500 nm sizing, with an aerosol flow rate of $0.3\,\mathrm{L\,min^{-1}}$ to provide adequate counting statistics on ambient aerosol over the time window appropriate for moving platforms. Its compact size was achieved in part through reduction of mobility resolution. Instead of the typical ratio of sheath-to-aerosol flows of 10, the Spider DMA employs a flow ratio of 3. For given sample flow rate, the most commonly used flow rate ratio of 10 requires a larger sheath flow, which in turn requires a larger mobility analyzer to reach the same maximum particle size.

While high size resolution is important for specific applications, such as in laboratory calibrations that employ a DMA as a calibration aerosol source, it may not be critical for ambient size distribution measurements, wherein the particle distribution spans a much wider size range than the transfer function of the DMA. Lower DMA resolution has also been successfully employed for reconstructing aerosol dynamics process rates in chamber experiments (Ozon et al., 2021). In addition to the smaller physical size of the instrument, operating at lower resolution increases the particle count rate owing to the wider DMA mobility window, thereby reducing measurement uncertainty. This can be an important factor for low-concentration measurements. Moreover, the resulting lower sheath flow requirements enable the usage of more compact and less power-demanding pumps, which further facilitates the overall portability of the instrument.

The question explored in this paper is whether the moderate-resolution mobility sizing of the Spider DMA is sufficient to capture the important characteristics of atmospheric aerosol size distributions. We begin with the derivation of the Spider DMA transfer function through a combination of finite-element simulations and laboratory calibrations. We then present a field validation by comparison of ambient aerosol data from the new instrument with that obtained from a traditional long-column cylindrical DMA (LDMA) operated at a nominal resolution of $R = 10$ during nearly 1 month of continuous operation of the two co-located instruments.

2 Methods

2.1 Spider DMA

The prototype Spider DMA sizing system consists of the Spider DMA (Amanatidis et al., 2020) and the "MAGIC" (Moderated Aerosol Growth with Internal water Cycling) particle counter (Hering et al., 2014, 2019). The Spider is a compact mobility analyzer designed for applications requiring high portability and time resolution. It features a radial flow geometry and a sample inlet system that distributes the flow azimuthally through curved (spider-like) flow channels. The instrument was designed to operate at $0.3\,\mathrm{L\,min^{-1}}$ sample and $0.6–1.2\,\mathrm{L\,min^{-1}}$ sheath flow rates, offering size classification in the 10–500 nm size range. Owing to its small classification volume, the mean gas residence time in the classifier is on the order of ~ 1 s, making it possible to complete its voltage scan in times well below 60 s without significant smearing of its transfer function.

The MAGIC particle counter is a laminar-flow water-based condensation particle counter (CPC). It employs a particle growth tube chamber with three stages (cool, warm, and cool), in which ultrafine particles grow by heterogeneous water vapor condensation to $> 1\,\mu\mathrm{m}$ and are subsequently counted by an optical detector. The final stage of the MAGIC CPC growth tube (moderator) recovers excess water vapor, enabling long-term operation without the need of a reservoir or water refilling. The instrument operates at a sample flow rate of $0.3\,\mathrm{L\,min^{-1}}$ and has a 50 % detection cut point of ~ 6 nm.

2.2 Transfer function determination by finite-element modeling

Amanatidis et al. (2020) evaluated the Spider DMA transfer function in static mode based on the Stolzenburg (1988) transfer function model and its derivation for radial flow classifiers (Zhang et al., 1995; Zhang and Flagan, 1996). Here, we evaluate its transfer function in "scanning" mobility mode, wherein the electric field is varied continuously in an exponential voltage ramp (Wang and Flagan, 1990). The scanning transfer function was evaluated with 2D finite-element COMSOL Multiphysics simulations of flows, quasi-steady-state electric field, and particle trajectories. Simulations were performed for $0.9\,\mathrm{L\,min^{-1}}$ sheath and $0.3\,\mathrm{L\,min^{-1}}$ aerosol flow rates, scanning voltage in the range 5–5000 V, and 30 s exponential ramps for both up- and downscans. Particles were modeled with the "mathematical particle tracing" module, in which particle mass was assumed to be negligible since the electric field varies slowly, on a timescale that is long compared to the aerodynamic relaxation time of the particles being measured. Particle trajectories were calculated by assigning particle velocity vector components equal to the steady-state fluid field solution, combined with the axial velocity acquired from interaction with the time-varying electrostatic field. Moreover, a Gaussian random walk was employed in each time step of the solver to simulate particle Brownian motion, with a standard deviation proportional to particle diffusivity, i.e., $\mathrm{d}\sigma = \sqrt{2D\mathrm{d}t}$. Monodisperse particles were injected in regular intervals over the scan, varying from 0.025 s for large particles to 0.003 s for those in the diffusing size range to capture in sufficient detail the Brownian motion along the particle trajectories. Modeling was repeated for 10 discrete particle sizes, spanning the dynamic range of the classifier. Details on the Spider DMA geometry employed in the modeling, as well as an example with particle trajectories over the Spider voltage scan, are included in the Supplement (Figs. S1 and S2).

2.3 Experimental

The two sizing instruments, the Spider DMA and the LDMA system, were operated in parallel, sampling ambient air from a roof top at the Caltech campus in Pasadena, CA. Measurements were made between 16 May–11 June 2020 and were done as part of a study of the impacts of the COVID-19 pandemic shutdown on air quality. The experimental setup used is shown in Fig. 1. Ambient aerosol samples passed through a soft X-ray charge conditioner and were subsequently split between the two mobility sizing systems, thereby ensuring that the charge status of the aerosols seen by the two instru-

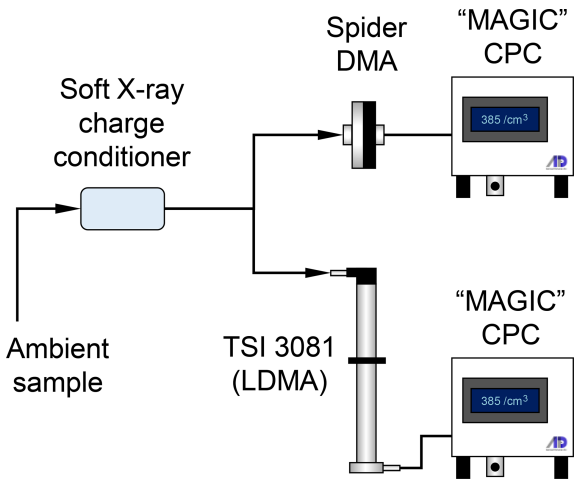

Figure 1. Schematic of the experimental setup used to evaluate the Spider DMA. The prototype instrument was operated at 0.9 L min^{-1} sheath and 0.3 L min^{-1} aerosol flow rates, with a scanning voltage program consisting of a 30 s upscan followed by a 30 s downscan. A TSI 3081 long-column DMA, operated at 3.0 L min^{-1} sheath and 0.3 L min^{-1} aerosol flows, with 240 s upscans, was used for comparison. Both sizing systems used an ADI "MAGIC" CPC as the particle detector.

ments was identical. The charge conditioner is a prototype device that was developed recently at Caltech. It is based upon a Hamamatsu soft X-ray source that directly ionizes the air around the incoming aerosol flow. Both DMA systems were operated in scanning mode. Both used a MAGIC water-based CPC as the detector. The size pre-cut stage in the inlet of both CPCs was removed to avoid additional smearing of the transfer functions.

The Spider DMA was operated at 0.9 L min^{-1} sheath and 0.3 L min^{-1} aerosol flow rates. A piezoelectric blower (Murata, MZB1001T02) was enclosed into a sealed housing to serve as a recirculating pump for the Spider sheath flow. The pump assembly weighs $\sim$ 60 g. Operating at a frequency of 24–27 kHz, this pump produces only very small pressure fluctuations that are effectively damped by the capacitance of the downstream filter. With feedback control, the pump attains a steady flow up to $\sim$ 1 L min^{-1} within about 1 s, making it well suited to operating in an environment in which the pressure varies slowly, as in UAV applications. The Spider DMA scanning program included a 30 s upscan followed by a 30 s downscan, during which the electrode voltage was exponentially varied between 5–5000 V. The voltage was held steady for an additional 2 s at each end of the voltage ramp to allow for incoming particles to transmit through the classifier. Particle counts over the scan were recorded with a 5 Hz rate.

The LDMA system was based on a TSI 3081 long-column DMA operated at 3.0 L min^{-1} sheath and 0.3 L min^{-1} aerosol flow rates, offering classification in the 17–989 nm size range. The scans consisted of an exponentially increasing (upscan) voltage ramp between 25–9875 V with a 240 s duration. As with the Spider DMA, the LDMA voltage was held constant at the beginning and end of the ramp. Owing to its longer mean flow residence time, the LDMA voltage hold periods were set at 40 s, bringing its overall duty cycle to 360 s. Particle counts for the LDMA system were recorded with a 2 Hz sampling rate. Data acquisition and instrument control (flows, high voltage) was performed with custom LabVIEW software for both systems.

2.4 DMA scanning conditions

Comparison of the scanning voltage conditions between the two DMAs requires accounting for differences in geometry, flow rates, and voltage scanning rates. The appropriate non-dimensional quantity that describes the DMA scanning rate is given by $\theta_s = \frac{\tau_{HV}}{t_g}$, the ratio of the exponential voltage ramp time constant, τ_{HV}, to the classifier mean gas residence time, t_g. At large θ_s values, typically $\theta_s > 10$, the rate at which the scanning voltage varies as particles transmit through the classifier is slow, and the transfer function approximates the "static" DMA transfer function. At small θ_s values, the scanning voltage changes quickly relative to the particle residence time, smearing the transfer function, which becomes pronounced as θ_s approaches unity (Russell et al., 1995; Collins et al., 2004). For the Spider DMA operating conditions, $\tau_{HV} = 4.34$ s and $t_g = 1.30$ s, resulting in $\theta_s = 3.35$. For the LDMA, $\tau_{HV} = 40.14$ s and $t_g = 7.52$ s, resulting in $\theta_s = 5.34$. Here, even though τ_{HV} of the LDMA is about 10 times larger (i.e., slower) than that of the Spider, its dimensionless scanning rate (θ_s) is only about 1.6 times smaller owing to its much longer flow residence time. In absolute terms, the scanning rate employed in both DMAs is moderate.

2.5 Data inversion and analysis

Particle size distributions were obtained by inverting the raw particle counts recorded over each voltage scan. Raw counts were smoothed prior to the inversion to minimize inversion artifacts. Locally weighted scatterplot smoothing (LOWESS) regression (Cleveland, 1979) was employed for the Spider DMA data with a 10 % smoothing window (i.e., 15 data points). The LDMA raw counts were smoothed by applying a moving average filter with a span of 5 data points. The smoothed data were then inverted by regularized non-negative least-squares minimization. Tikhonov regularization was used for both systems, with $\lambda = 0.140$ and $\lambda = 0.015$ regularization parameters for the Spider DMA and LDMA data, respectively. Those values were found to provide stable solutions without over-constraining the inversion results.

The inversion kernel for the Spider DMA system was based on the scanning transfer function of the Spider DMA obtained by finite-element modeling. In order to generate a

dense kernel required for the inversion, the modeled transfer function data were fitted to Gaussian distributions, whose parameters were subsequently fitted to analytical expressions that allowed generation of transfer functions at any instant (i.e., time bin) over the voltage scan. The Spider transfer functions were subsequently convoluted with a continuous stirred-tank reactor (CSTR) model (Russell et al., 1995; Collins et al., 2002; Mai et al., 2018) to take into account the time response of the MAGIC CPC. A 0.35 s time constant was used for the CSTR model in the Spider DMA system (Hering et al., 2017). The resulting transfer function was combined with a size-dependent transmission efficiency model described by Amanatidis et al. (2020) to take into account particle losses occurring at the Spider inlet, as those are not evaluated in the 2D finite-element modeling. Raw counts were shifted to earlier time bins to account for the 1.50 s plumbing time delay between the Spider outlet and the MAGIC CPC detector. Because the simulation enabled a strictly monodisperse "calibration" aerosol, the ratio of the number exiting the DMA during a particular counting time interval to the upstream particle number is the instrument transfer function. The kernel for the LDMA system was based on the scanning transfer function model derived recently by Huang et al. (2020). A CSTR model with a characteristic time of 0.35 s and a plumbing delay time of 0.95 s were used to incorporate the response of the MAGIC CPC used in the LDMA system.

The Wiedensohler (1988) fit to the Hoppel and Frick (1986) numerical evaluation of the Fuchs (1963) charge distribution has been used in the data inversion. Note that, since both instruments took samples from the same soft X-ray charge conditioner, any deviations from the assumed charge distribution will not affect the comparison between the two instruments.

3 Results

3.1 Spider scanning transfer function

Figure 2 shows the scanning transfer function of the Spider DMA evaluated by finite-element modeling. Results are plotted as a function of time in the scan for upscan and downscan voltage ramps. Each peak represents the ratio of particle number at the outlet to the inlet for a specific input particle size. Finite-element modeling data, shown with symbols, have been fitted to Gaussian distributions, shown with solid lines, which provide a close approximation to both upscan and downscan modeling data. As will be shown next, the Gaussian fits are subsequently employed to generate the transfer function at any time instance over the scan.

Comparison between upscan and downscan peaks reveals a distinct difference; downscan peaks have a higher maximum number ratio. Moreover, they are somewhat narrower than the upscan peaks. It should be noted that the transmission efficiency through the classification zone of a DMA is proportional to the area under the peak, rather than its maximum value. Hence, particle transmission over downscans is not necessarily higher than that over upscans. Here, the area of the Gaussian curves used to fit the transfer function modeling data was on average ∼3.5 % larger for downscans than upscans. This difference is likely due to the slightly asymmetrical shape of the downscan transfer function, which can be observed at the onset (i.e., lower left side) of each peak in Fig. 2b where the fitted curves are somewhat wider than the modeling data. A closer comparison between upscan and downscan fitting parameters is provided in the Supplement (Fig. S3). Diffusional broadening of the transfer function becomes important in the low-voltage region of each ramp, increasing the transfer function width as voltage decreases, though the broadening is less than would be seen with a higher-resolution DMA (Flagan, 1999).

The differences in the transfer function between upscans and downscans is the result of the scanning voltage operating mode and particle interaction with the boundary flow layers near the DMA electrode walls. Owing to the laminar flow profile, particles near the electrode walls acquire lower velocities than those in the middle of the electrode gap. Over downscans, a fraction of the incoming particles interacts with the boundary layer adjacent to the wall that houses the exit slit of the classifier. As voltage drops below a certain threshold, those particles reach the exit of the classifier, albeit with a time delay relative to particles of the same mobility whose trajectories did not interact with the boundary layer.

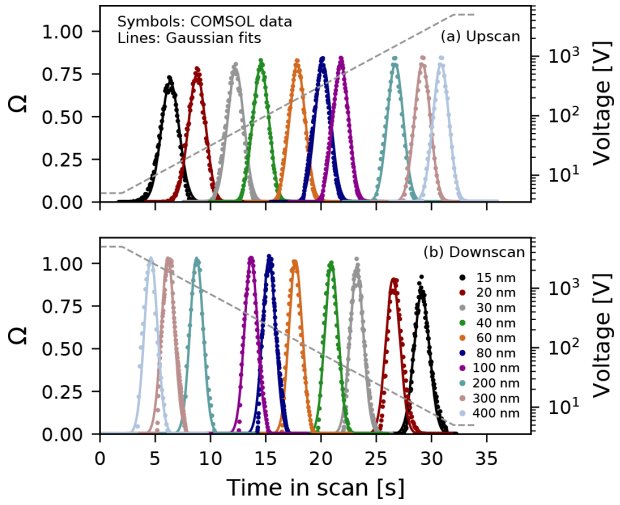

Figure 2. Finite-element modeling of the Spider DMA scanning transfer function for **(a)** upscan and **(b)** downscan exponential voltage ramps with 30 s duration and 0.9 L min^{-1} sheath and 0.3 L min^{-1} aerosol flow rates. Symbols correspond to finite-element modeling data (ratio of particle number at the outlet to the inlet), solid lines show Gaussian distributions fitted to the modeling data, and dashed lines indicate the scanning voltage program (values shown on right y axis).

This results in a particle exit time reallocation, which alters the shape of the downscan transfer function as the voltage drop becomes more rapid. This condition is inhibited over upscans, since the respective boundary layer is formed on the wall opposite to the exit flow and is exhausted through the excess flow.

Collins et al. (2004) and Mamakos et al. (2008) demonstrated the impact of scanning voltage on the transfer function of the cylindrical DMA. Over downscans, the transfer function deviates from the symmetric triangular or Gaussian shape and becomes skewed. The effect becomes larger for fast scans and is significant when the effective scan rate $\theta_s < 2$. This is also true for the Spider DMA, as shown in Fig. 2b; however the shape distortion is relatively small given the moderate Spider scan rate ($\theta_s = 3.4$). Moreover, in contrast to the cylindrical DMA, the boundary layers in the radial DMA are symmetric, which reduces the downscan distortion compared to its cylindrical counterpart. Over upscans, the width of the scanning transfer function broadens but retains its symmetric shape. For this reason, downscan data are often discarded in scanning DMA data analyses, as the more irregular shape of the transfer function is more difficult to parameterize. However, this strategy comes with a penalty in sampling time resolution, owing to the "dead" time associated with the discarded downscan that is required after each upscan. The dead time required depends on the classifier mean gas residence time (typically > 2–$3 \times t_g$) and the capacitance of the DMA high-voltage supply. As the Spider DMA scanning transfer function can be described with good fidelity for both upscans and downscans, both are included in the data analysis to maximize its time resolution.

Figure 3 shows the integrated transfer function of the Spider DMA system for the same operating conditions as those used in the experiments. The voltage program, shown in Fig. 3a, consists of a 2 s hold time at 5 V, followed by a 30 s upscan up to 5000 V, a 2 s hold time at 5000 V, and a 30 s downscan to 5 V. The classified particle size follows roughly the exponential increase and decrease of the voltage over the scan. The peaks shown in Fig. 3b consist of the Gaussian approximation of the Spider transfer function shown in Fig. 2, combined with the size and time response of the MAGIC CPC, and the size-dependent transmission efficiency in the Spider inlet (Amanatidis et al., 2020).

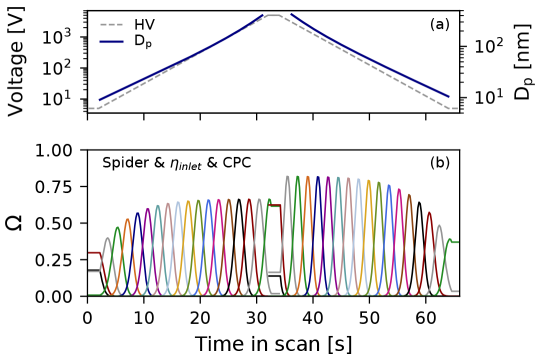

Figure 3. (a) Scanning voltage and classified particle size over the Spider DMA scan. **(b)** Transfer function of the integrated Spider DMA–MAGIC CPC system (ratio of particle number at the outlet to the inlet), consisting of the Spider DMA scanning transfer function combined with its inlet transmission efficiency and the MAGIC CPC response.

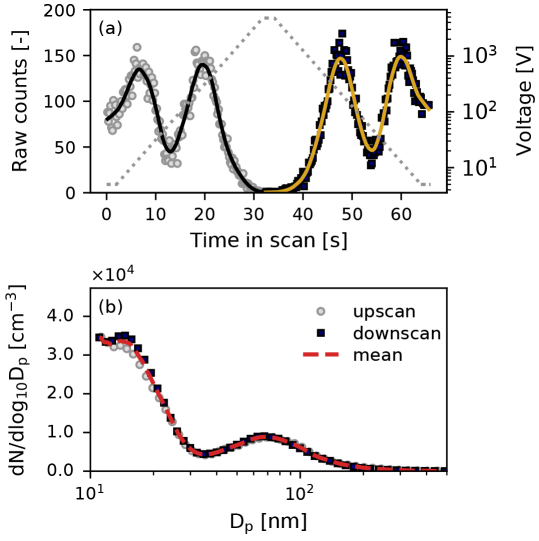

Figure 4. Example of Spider DMA data inversion. **(a)** Raw counts per time bin (symbols) recorded over the voltage ramp (up- and downscan). Solid lines indicate LOWESS smoothing to the raw counts. **(b)** Resulting size distributions after data inversion. The dashed line shows the mean of the up- and downscan distributions.

3.2 Data inversion example

Figure 4 demonstrates an inversion example for representative Spider DMA data. Particle raw counts recorded at each time bin over the upscan and downscan are shown in Fig. 4a. Smooth curves are fitted to the raw count data to minimize artifacts in the inversion process. The resulting size distributions, employing an inversion kernel based on the scanning transfer function in Fig. 3b, are shown in Fig. 4b. Up- and downscan distributions are almost identical in both shape and magnitude. The mean of the two distributions, as shown here, is used as the output of each scan. Overall, considering all measurement data collected in this work, upscan raw count data inversion yielded distributions with consistent but slightly higher (3.7 % ± 2.3 %) total particle number than downscans.

3.3 Instrument comparison

Figure 5 demonstrates the effect of sizing resolution on the counting rate of the downstream particle detector. As both the Spider DMA and the LDMA operated at the same aerosol flow rate, one would expect a higher counting rate for the

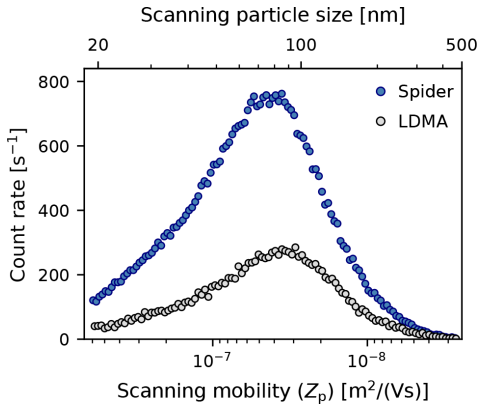

Figure 5. Sizing resolution effect on the particle count rate of the Spider DMA ($R = 3$) and LDMA ($R = 10$) systems. Data shown are the average of raw particle count rates during upscans over a period of 18 min (corresponding to 3 LDMA upscans and 17 Spider upscans) measured in the morning of 1 June 2020. Both systems operated at 0.3 L min^{-1} aerosol flow rate.

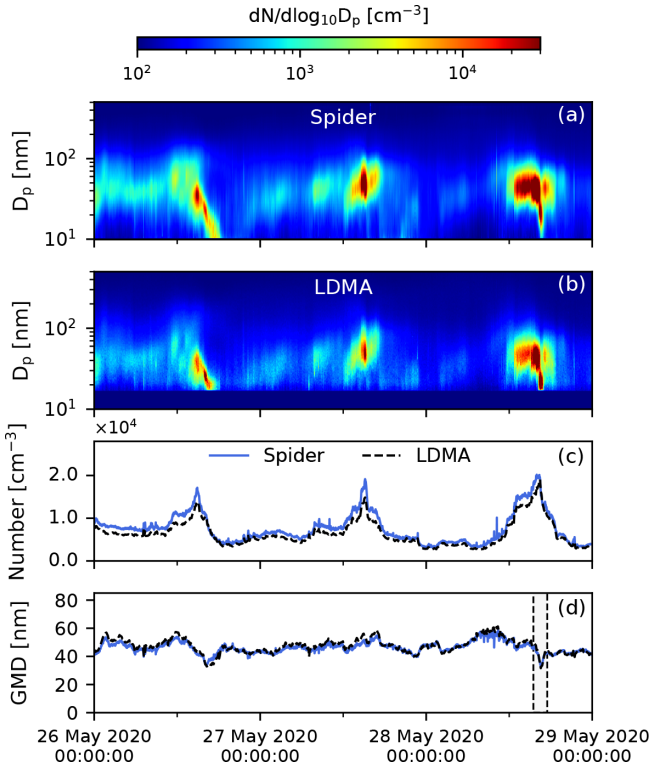

Figure 6. Evolution of the particle size distribution over a period of 3 d measured by **(a)** the Spider DMA and **(b)** the LDMA system. Corresponding total particle number and geometric mean diameter, calculated over the 17–500 nm size range, are shown in panels **(c)** and **(d)**, respectively. Solid blue color in panel **(b)** (size range < 17 nm) was used for no available data in the LDMA system. The dashed box in panel **(d)** indicates the time period shown in Fig. 7.

Spider DMA system owing to its wider transfer function. Indeed, as shown in Fig. 5, this was the case. The data presented here are the average of particle count rates during upscans over a period of 18 min (corresponding to 3 LDMA upscans and 17 Spider upscans). This example was selected as a representative comparison case since the resulting particle count distribution is centered near the middle of the overlapping mobility range. The integral of the counting rate with respect to scanning mobility for each instrument (i.e., area below the data points in Fig. 5) was larger by a factor of 3.325 in the Spider measurement than the LDMA; this is almost exactly the same as the inverse of the sizing resolution ratio (i.e., 10/3) of the two DMAs. In fact, this ratio was rather consistent (within $\pm 10\,\%$) despite the size distribution variation over the course of the day, corroborating that, for given aerosol flow rate, lower DMA resolution results in higher counting rates and thus enables better counting statistics.

Figure 6 illustrates an excerpt of the Spider and LDMA size distribution measurements over a time period of 3 d. The two instruments report similar diurnal variation in the particle size distribution, in both size and number concentration. Increased particle concentrations were recorded in the early afternoon of each day, a regular occurrence as particles from morning traffic are transported by the sea breeze from Los Angeles to Pasadena, where the measurements took place. Concentrations begin to drop later in the afternoon and through the evening, from about 15 000 cm^{-3} to below 5000 cm^{-3}. The geometric mean diameter (GMD) of the size distribution ranged between about 30–60 nm and was smaller over the high-number-concentration events recorded in the early afternoon.

Figure 7 shows the evolution of the size distribution over a period of 2 h in the afternoon of 28 May 2020 (indicated with a dashed box in Fig. 6d), measured with the Spider and the LDMA system. Since the measurement duty cycle of the two instruments was different (66 s for the Spider vs. 360 s for the LDMA), we employed 30 min averaging of the recorded size distributions. This corresponds to 5 scans for the LDMA and about 27 up- and downscans for the Spider. The shaded areas of the averaged distributions represent the variation over the averaging period. Starting from a mono-modal distribution with a peak at ~ 45 nm (panel a), the size distribution transitioned to a bi-modal one over a period of 60 min (panels b, c) before transitioning back to a mono-modal distribution (panel d). As indicated by the shaded areas, there was high variation in the aerosol concentration during this transition event. Overall, the measurement of the two instruments was in good agreement in terms of both sizing and concentration, suggesting that the lower sizing resolution in the Spider DMA was adequate in capturing the details of the size distribution. An animation video with side-by-side comparison of 30 min averaged distributions for the entire testing period is included in the video supplement (Amanatidis et al., 2021a).

Figure 8 compares the total number and geometric mean diameter measured by the two instruments over the entire

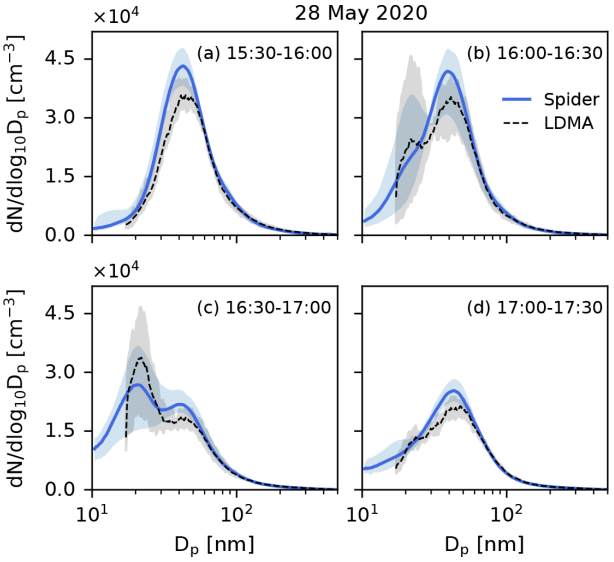

Figure 7. Evolution of the size distribution in the afternoon of 28 May 2020, as measured by the Spider and LDMA systems. Lines represent the mean of size distributions measured over a period of 30 min. Shaded areas demonstrate the variation of the size distribution over the averaging period, indicating maximum and minimum values.

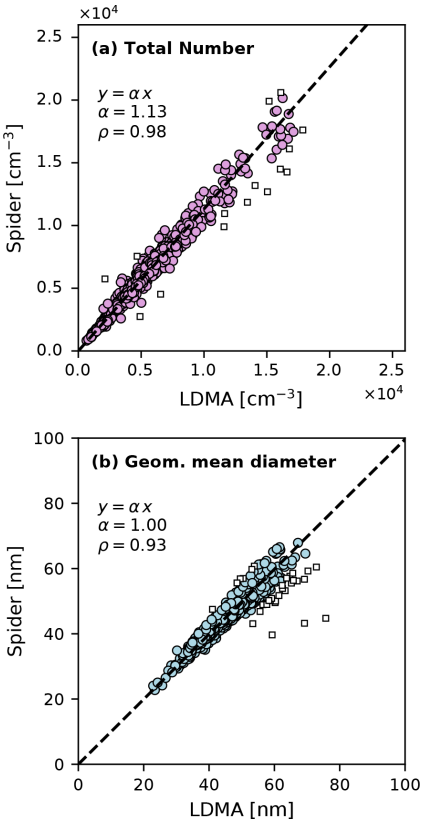

Figure 8. Comparison of **(a)** total particle number and **(b)** geometric mean diameter measured by the Spider and LDMA systems over a period of 26 d of continuous testing. Each point represents 1 h averaged data, calculated over the 17–500 nm size range where the two instruments overlap. Square symbols show outliers excluded from the regression analysis. Dashed lines represent a linear regression model (no intercept) fitted to the data. ρ values denote the Pearson correlation coefficient between the measurement data of the two instruments.

testing period. Each data point corresponds to a 1 h average of the size distribution measured by each instrument, calculated over the 17–500 nm size range where the two systems overlap. Overall, the comparison includes 550 h of measurement data. In order to identify outliers in the data, we employed the "RANSAC" (random sample consensus) algorithm (Fischler and Bolles, 1981). In this, random samples of the data are selected, analyzed, and classified as inliers and outliers through an iterative routine. The outliers identified are shown in Fig. 8 with open square symbols.

Next, a linear regression model (no intercept) was fitted to the data (excluding outliers) to evaluate the correlation between the two instruments. Since both instruments include measurement errors, we employed orthogonal distance regression (Boggs et al., 1987), where errors on both the dependent and independent variable are taken into account in the least-squares minimization. The resulting regression lines exhibit slopes of $\alpha = 1.13$ and $\alpha = 1.00$ for number concentration and GMD, respectively, suggesting an overall excellent agreement between the instruments. Moreover, Pearson correlation coefficients of $\rho = 0.98$ and $\rho = 0.93$ indicate a strong correlation for both metrics of the size distribution.

3.4 Operational observations

The prototype Spider DMA used in this study incorporated an electrostatic-dissipative plastic that failed after several months of continuous operation, causing arcing within the instrument at the highest voltages. The Spider DMA has been redesigned to eliminate this material and is currently being tested. This new Spider DMA has relatively minor changes to the classification region of the prototype presented here and employs the same moderate-resolution approach to maintain a compact size.

4 Summary and conclusions

We evaluated the performance of the Spider DMA, a highly portable particle sizer, in measuring ambient size distributions against a co-located particle sizer based on a TSI 3081 long-column differential mobility analyzer (LDMA). Comparison measurements were performed at the Caltech campus in Pasadena, CA, over a period of 26 d, between 16 May–11 June 2020, as part of a field campaign examining the effects of the COVID-19 shutdown on air quality. The Spider DMA system was operated at a lower nominal sizing resolution (0.9 L min^{-1} sheath and 0.3 L min^{-1} aerosol flow rates,

$R = 3$) than the LDMA ($3.0\,\mathrm{L\,min^{-1}}$ sheath and $0.3\,\mathrm{L\,min^{-1}}$ aerosol flow rates, $R = 10$) and at a higher time resolution (30 s vs. 240 s scans).

The transfer function of the Spider DMA was obtained by finite-element modeling at the conditions employed in the experiment, which included both up- and downscan exponential voltage ramps with 30 s duration. Owing to the Spider radial flow geometry and short gas flow residence time, distortion of the downscan transfer function shape is minimal at the scan rates employed, enabling usage of both upscan and downscan data, thereby increasing time resolution. Modeling data were fitted to Gaussian distributions and were combined with the experimentally determined transmission efficiency of the Spider DMA and the MAGIC particle counter response function to generate the inversion kernel of the combined system. Data inversion of the LDMA system was based on the semi-analytical model of the LDMA scanning transfer function derived by Huang et al. (2020).

Regression analysis of 550 h of measurement data showed an overall excellent correlation between the two instruments, with slopes of $\alpha = 1.13$ and $\alpha = 1.00$ and Pearson correlation coefficients of $\rho = 0.98$ and $\rho = 0.93$ in the reported particle number and geometric mean diameter, respectively. The present results suggest that two key characteristics of ambient size distributions, geometric mean diameter and number concentration, are sufficiently captured when operating the DMA at lower resolution than is typically employed. Moreover, use of lower resolution, where appropriate, has several distinct advantages. For the same aerosol flow rate and range in particle mobilities, reducing the nominal resolution reduces the required sheath flow and hence reduces the physical size of the DMA. In turn, this reduction in physical size at the same aerosol flow rate reduces the residence time within the classification region, enabling faster scans. Additionally, for the same aerosol flow, the wider mobility window increases the particle count rate, thereby improving measurement statistics. While some applications may require higher resolution, this study demonstrates the efficacy of lower-resolution measurements for ambient aerosol characterization and illustrates the commensurate advantages of faster measurements in a smaller package.

Code availability. The code used for data analysis in this work can be made available upon request from the authors.

Data availability. The Spider DMA and LDMA measurement data can be accessed from the Caltech data repository: https://doi.org/10.22002/D1.1998 (Amanatidis et al., 2021b)

Video supplement. This video supplement shows the evolution of the ambient aerosol size distribution in Pasadena, CA between 16 May–11 June 2020, as measured by the Spider DMA and LDMA systems (https://doi.org/10.22002/D1.1896, Amanatidis et al., 2021a).

Supplement. The supplement related to this article is available online at: https://doi.org/10.5194/amt-14-4507-2021-supplement.

Author contributions. SA performed the finite-element modeling for the Spider DMA instrument, analyzed its measurement data, generated the figures, and wrote the manuscript text. YH analyzed the LDMA instrument data and prepared the experimental setup. BP, BCS, CMK, and RXW collected the measurement data and provided technical maintenance to the instruments. JHS reviewed and provided editorial feedback on the manuscript. SVH and RCF planned the experiments and contributed to interpretation of the results and editing of the manuscript.

Competing interests. Richard C. Flagan and Stavros Amanatidis are inventors of the "Spider" DMA technology patent (US10775290B2), which is licensed to Susanne V. Hering's company. The rest of the authors declare that they have no conflict of interest.

Disclaimer. Neither the United States Government nor any agency thereof, nor any of their employees, makes any warranty, express or implied, or assumes any legal liability or responsibility for the accuracy, completeness, or usefulness of any information, apparatus, product, or process disclosed, or represents that its use would not infringe privately owned rights. Reference herein to any specific commercial product, process, or service by trade name, trademark, manufacturer, or otherwise does not necessarily constitute or imply its endorsement, recommendation, or favoring by the United States Government or any agency thereof. The views and opinions of authors expressed herein do not necessarily state or reflect those of the United States Government or any agency thereof.

Acknowledgements. The authors gratefully acknowledge support by the U.S. Department of Energy, Office of Science, and by the U.S. Department of Health and Human Services, Centers for Disease Control and Prevention.

Financial support. This research has been supported by the U.S. Department of Energy (grant no. DE-SC0013152) and the U.S. Department of Health and Human Services (grant no. OH010515).

Review statement. This paper was edited by Francis Pope and reviewed by three anonymous referees.

References

Amanatidis, S., Kim, C., Spielman, S. R., Lewis, G. S., Hering, S. V., and Flagan, R. C.: The Spider DMA: A miniature radial differential mobility analyzer, Aerosol Sci. Tech., 54, 75–189, https://doi.org/10.1080/02786826.2019.1626974, 2020.

Amanatidis, S., Huang, Y., Pushpawela, B., Schulze, B. C., Kenseth, C. M., Ward, R. X., Seinfeld, J. H., Hering, S. V., and Flagan, R. C.: Efficacy of a portable, moderate-resolution, fast-scanning DMA for ambient aerosol size distribution measurements (Version 1.0), CaltechDATA, https://doi.org/10.22002/D1.1896, 2021a.

Amanatidis, S., Huang, Y., Pushpawela, B., Schulze, B. C., Kenseth, C. M., Ward, R. X., Seinfeld, J. H., Hering, S. V., and Flagan, R. C.: Size distribution measurement datasets of the "Spider DMA" and "LDMA" particle sizers, collected in Pasadena, CA between 16 May–11 June 2020. (Version 1.0), CaltechDATA [data set], https://doi.org/10.22002/D1.1998, 2021b.

Boggs, P. T., Byrd, R. H., and Schnabel, R. B.: A Stable and Efficient Algorithm for Nonlinear Orthogonal Distance Regression, SIAM J. Sci. Stat. Comp., 8, 1052–1078, https://doi.org/10.1137/0908085, 1987.

Cleveland, W. S.: Robust Locally Weighted Regression and Smoothing Scatterplots, J. Am. Stat. Assoc., 74, 829–836, https://doi.org/10.1080/01621459.1979.10481038, 1979.

Collins, D. R., Flagan, R. C., and Seinfeld, J. H.: Improved inversion of scanning DMA data, Aerosol Sci. Tech., 36, 1–9, https://doi.org/10.1080/027868202753339032, 2002.

Collins, D. R., Cocker, D. R., Flagan, R. C., and Seinfeld, J. H.: The scanning DMA transfer function, Aerosol Sci. Tech., 38, 833–850, https://doi.org/10.1080/027868290503082, 2004.

Creamean, J. M., de Boer, G., Telg, H., Mei, F., Dexheimer, D., Shupe, M. D., Solomon, A., and McComiskey, A.: Assessing the vertical structure of Arctic aerosols using balloon-borne measurements, Atmos. Chem. Phys., 21, 1737–1757, https://doi.org/10.5194/acp-21-1737-2021, 2021.

Fischler, M. A. and Bolles, R. C.: Random sample consensus, Commun. ACM, 24, 381–395, https://doi.org/10.1145/358669.358692, 1981.

Flagan, R. C.: On Differential Mobility Analyzer Resolution, Aerosol Sci. Tech., 30, 556–570, https://doi.org/10.1080/027868299304417, 1999.

Fuchs, N. A.: On the stationary charge distribution on aerosol particles in a bipolar ionic atmosphere, Geofisica Pura e Applicata, 56, 185–193, https://doi.org/10.1007/BF01993343, 1963.

Herenz, P., Wex, H., Henning, S., Kristensen, T. B., Rubach, F., Roth, A., Borrmann, S., Bozem, H., Schulz, H., and Stratmann, F.: Measurements of aerosol and CCN properties in the Mackenzie River delta (Canadian Arctic) during spring–summer transition in May 2014, Atmos. Chem. Phys., 18, 4477–4496, https://doi.org/10.5194/acp-18-4477-2018, 2018.

Hering, S. V., Spielman, S. R., and Lewis, G. S.: Moderated, Water-Based, Condensational Particle Growth in a Laminar Flow, Aerosol Sci. Tech., 48, 401–408, https://doi.org/10.1080/02786826.2014.881460, 2014.

Hering, S. V., Lewis, G. S., Spielman, S. R., Eiguren-Fernandez, A., Kreisberg, N. M., Kuang, C., and Attoui, M.: Detection near 1-nm with a laminar-flow, water-based condensation particle counter, Aerosol Sci. Tech., 51, 354–362, https://doi.org/10.1080/02786826.2016.1262531, 2017.

Hering, S. V., Lewis, G. S., Spielman, S. R., and Eiguren-Fernandez, A.: A MAGIC concept for self-sustained, water-based, ultrafine particle counting, Aerosol Sci. Tech., 53, 63–72, https://doi.org/10.1080/02786826.2018.1538549, 2019.

Hoppel, W. A. and Frick, G. M.: Ion–aerosol attachment coefficients and the steady-state charge distribution on aerosols in a bipolar ion environment, Aerosol Sci. Tech., 5, 1–21, https://doi.org/10.1080/02786828608959073, 1986.

Huang, Y., Seinfeld, J. H., and Flagan, R. C.: Diffusional Transfer Function for the Scanning Electrical Mobility Spectrometer (SEMS), Aerosol Sci. Tech., 6826, 1–24, https://doi.org/10.1080/02786826.2020.1760199, 2020.

Mai, H., Kong, W., Seinfeld, J. H., and Flagan, R. C.: Scanning DMA Data Analysis II. Integrated DMA-CPC Instrument Response and Data Inversion, Aerosol Sci. Tech., 52, 1–35, https://doi.org/10.1080/02786826.2018.1528006, 2018.

Mamakos, A., Ntziachristos, L., and Samaras, Z.: Differential mobility analyser transfer functions in scanning mode, J. Aerosol Sci., 39, 227–243, https://doi.org/10.1016/j.jaerosci.2007.11.005, 2008.

Mamali, D., Marinou, E., Sciare, J., Pikridas, M., Kokkalis, P., Kottas, M., Binietoglou, I., Tsekeri, A., Keleshis, C., Engelmann, R., Baars, H., Ansmann, A., Amiridis, V., Russchenberg, H., and Biskos, G.: Vertical profiles of aerosol mass concentration derived by unmanned airborne in situ and remote sensing instruments during dust events, Atmos. Meas. Tech., 11, 2897–2910, https://doi.org/10.5194/amt-11-2897-2018, 2018.

McMurry, P. H.: A review of atmospheric aerosol measurements, Atmos. Environ., 34, 1959–1999, https://doi.org/10.1016/S1352-2310(99)00455-0, 2000.

Ortega, J., Snider, J. R., Smith, J. N., and Reeves, J. M.: Comparison of aerosol measurement systems during the 2016 airborne ARISTO campaign, Aerosol Sci. Tech., 53, 871–885, https://doi.org/10.1080/02786826.2019.1610554, 2019.

Ozon, M., Stolzenburg, D., Dada, L., Seppänen, A., and Lehtinen, K. E. J.: Aerosol formation and growth rates from chamber experiments using Kalman smoothing, Atmos. Chem. Phys. Discuss. [preprint], https://doi.org/10.5194/acp-2021-99, in review, 2021.

Russell, L. M., Flagan, R. C., and Seinfeld, J. H.: Asymmetric instrument response resulting from mixing effects in accelerated DMA-CPC measurements, Aerosol Sci. Tech., 23, 491–509, https://doi.org/10.1080/02786829508965332, 1995.

Stolzenburg, M. R.: An ultrafine aerosol size distribution measuring system, Doctoral dissertation, Department of Mechanical Engineering, University of Minnesota, Minneapolis, MN, USA, 1988.

Wang, S. C. and Flagan, R. C.: Scanning electrical mobility spectrometer, Aerosol Sci. Tech., 13, 230–240, https://doi.org/10.1080/02786829008959441, 1990.

Wiedensohler, A.: An approximation of the bipolar charge distribution for particles in the submicron size range, J. Aerosol Sci., 19, 387–389, https://doi.org/10.1016/0021-8502(88)90278-9, 1988.

Zhang, S.-H. and Flagan, R. C.: Resolution of the radial differential mobility analyzer for ultrafine particles, J. Aerosol Sci., 27, 1179–1200, https://doi.org/10.1016/0021-8502(96)00036-5, 1996.

Zhang, S.-H., Akutsu, Y., Russell, L. M., Flagan, R. C., and Seinfeld, J. H.: Radial Differential Mo-

bility Analyzer, Aerosol Sci. Tech., 23, 357–372, https://doi.org/10.1080/02786829508965320, 1995.

Zheng, G., Wang, Y., Wood, R., Jensen, M. P., Kuang, C., McCoy, I. L., Matthews, A., Mei, F., Tomlinson, J. M., Shilling, J. E., Zawadowicz, M. A., Crosbie, E., Moore, R., Ziemba, L., Andreae, M. O., and Wang, J.: New particle formation in the remote marine boundary layer, Nat. Commun., 12, 527, https://doi.org/10.1038/s41467-020-20773-1, 2021.